MULTINUCLEAR AND MULTIDIMENSIONAL NMR TOOLS FOR CHARACTERISATION OF PYROLYSIS BIO-OILS AND OTHER COMPLEX ORGANIC MIXTURES

Bridget Tang

Doctor of Philosophy

Aston University

May 2024

Aston University

MULTINUCLEAR AND MULTIDIMENSIONAL NMR TOOLS FOR CHARACTERISATION OF PYROLYSIS BIO-OILS AND OTHER COMPLEX ORGANIC MIXTURES

Bridget Tang

Doctor of Philosophy, 2024.

Abstract

Lignocellulosic biomass such as Brewers' Spent Grains (BSG) can be used to produce fuel. Unlike other biomass resources grown specifically to produce fuel, BSG is considered an agriculture waste, with low cost and high availability. Bio-oils or pyrolysis oils produced from lignocellulosic biomass, such as BSG, are a promising carbon-neutral energy source for replacing fossil fuels. Pyrolysis oils are made up of hundreds of small molecules, including many oxygen-containing compounds. The main disadvantage of pyrolysis oils, which renders them incompatible with current infrastructures, is their acidity.

Analyses of pyrolysis oils are required, particularly the identification and quantification of the acidic, oxygen-containing compounds. However, this is usually hindered due to the complex nature of the mixtures. Nuclear Magnetic Resonance (NMR) is a versatile tool widely used to analyse complex mixtures. However, ^{1}H NMR analysis of pyrolysis oils is limited due to the severe overlapping signals of the many species present. The main challenge is simplifying the spectra without compromising chemical information.

First, carbonyl-containing compounds are reacted with fluorine-containing reagents and the ^{19}F qNMR analysis was translated from high-field to low-field, benchtop NMR. Benchtop NMR offers a cheaper, simpler alternative to traditional NMR methods, making NMR techniques more accessible to a wide range of audience. Second, alcohol groups are reacted with phosphorus-containing reagents, followed by ^{31}P qNMR analysis. However, these spectra are still challenging due to the overlapping signals. Third, ^{31}P diffusion-ordered spectroscopy techniques reveal additional chemical information such as molecular weights, easing the identification of compounds present in a sample. Interpretation of diffusion coefficients using power law method is explored. An alternative method for interpreting diffusion coefficient is the using the Stokes-Einstein Gierer-Writz Estimation (SEGWE). The interpretation of protein diffusion coefficients and extending the SEGWE to mixed aqueous solvents was explored. Finally, both novel NMR and traditional techniques have been used in combination to characterise pyrolysis oils produced from BSG.

Keywords: brewers' spent grains, pyrolysis oil, lignin, nuclear magnetic resonance, low-field NMR, diffusion-ordered spectroscopy, protein diffusion-ordered spectroscopy

Publications

1. **Tang, B.**, Chong, K., Massefski, W. and Evans, R., 2022. Quantitative Interpretation of Protein Diffusion Coefficients in Mixed Protiated–Deuteriated Aqueous Solvents. *The Journal of Physical Chemistry B*, *126*(31), pp.5887-5895. DOI: https://doi.org/10.1021/acs.jpcb.2c03554

2. **Tang, B.**, Chong, K., Ragauskas, AJ. and Evans, R., 2023. Quantitative Low-field ^{19}F NMR Analysis of Carbonyl Groups in Pyrolysis Oils. *ChemSusChem,* p.e202300625. DOI: https://doi.org/10.1002/cssc.202300625

2a. **Tang, B.**, Chong, K., Ragauskas, AJ. and Evans, R., 2023. Front Cover: Quantitative Low-field ^{19}F NMR Analysis of Carbonyl Groups in Pyrolysis Oils (ChemSusChem 17/2023). *ChemSusChem,* p.e202301126 DOI: https://doi.org/10.1002/cssc.202301126

2b. **Tang, B.**, Chong, K., Ragauskas, AJ. and Evans, R., 2023. Cover Profile: Quantitative Low-field ^{19}F NMR Analysis of Carbonyl Groups in Pyrolysis Oils (ChemSusChem 17/2023). *ChemSusChem,* p.e202301127. DOI: https://doi.org/10.1002/cssc.202301127

Conferences & Seminars

2024   *Quantitative of Carbonyl Groups using Low-field ^{19}F NMR - Analysis of Bio-oils Produced from Brewers' Spent Grains*, Poster Presentation, 9th EUChemS Chemistry Congress, Dublin, Ireland

2024   Analysis of Bio-oils Produced from Brewers' Spent Grains – New Multinuclear and Multidimensional NMR Tools, Oral Presentation, RSC NMRDG Postgraduate Meeting, Brimingham, UK

2023   *Quantitative Low-field ^{19}F NMR Analysis of Carbonyl Groups in Pyrolysis Oils*, Oral Presentation, University of Tennessee, Knoxville, TN, USA

2023   *Quantitative Low-field ^{19}F NMR Analysis of Carbonyl Groups in Pyrolysis Oils*, Oral Presentation, Practical Application of NMR in Industry Conference (PANIC), Nashville, TN, USA

2022   *Quantitative interpretation of Diffusion Coefficients*, Oral Presentation, Chemistry Student Seminar Series, Massachusetts Institute of Technology, MA, USA

2022   *Quantitative Analysis of Carbonyl Compounds in Bio-oils using Low-field ^{19}F NMR, Poster Presentation*, SMASH NMR Conference, La Jolla, CA, USA

2022   *Quantitative Analysis of Carbonyl Compounds in Bio-oils using Low-field ^{19}F NMR* - **Awarded Runner Up Prize**, Poster Presentation, RSC NMRDG Postgraduate Meeting, Manchester, UK

2021   *Quantitative interpretation of Protein Diffusion Coefficients,* Poster Presentation, RSC NMRDG Postgraduate Meeting, Online

2021   Solid-state NMR Workshop, NMR Connect, Warwick University, UK

Awarded Grants

2024   NMR Discussion Group: Student Bursaries (£400.00)

2024   ABS Trusts: Travel Grant (£500.00)

2024   Early Career Researcher bursary: 9th EuChemS Chemistry Congress (£500.00)

2023   NMR Discussion Group: Student Bursaries (£400.00)

2023   ABS Trusts: Travel Grant (£1000.00)

2023   PANIC Student Travel Grant ($500.00)

2022   NMR Discussion Group: Student Bursaries (£400.00)

2022   Analytical Chemistry Trust Funds: Overseas Conference Travel Grant (£750.00)

2022   SMASH Student Scholarship ($1000.00)

Acknowledgements

Firstly, I would like to thank my main supervisor Dr. Robert Evans for all the invaluable guidance, support and opportunities throughout this project. This PhD wouldn't have been half as successful if it wasn't for you. You have been my biggest supporter since day one of my research career and the person I blame for getting me into NMR. You have been the best supervisor, mentor, and best friend I could've asked for. Team corgi!! I would also like to thank my associate supervisor Dr. Katie Chong, bio-oil queen, for all the guidance, support and always listening to my NMR talks during every quarterly. I'm extremely grateful to have both of you as my supervisors. I hope we can work together again in the near future!

A huge thank you is given to all my collaborators. This work would've not existed without you. Dr. Walter Massefski at Massachusetts Institute of Technology, thank you for introducing me to some protein NMR. Thank you for hosting us at MIT and giving me the opportunity to deliver my first seminar talk. Prof. Arthur Ragauskas at University of Tennessee, thank you for the invaluable contributions and hosting at UoT. Thank you to our local brewery Burning Soul Brewery, Birmingham, UK for providing feedstock for this research. Thank you to all staff in the Energy and Bioproduct Research Institute (EBRI), especially Dr. Sarah Asplin and Dr. Iram Razaq for your pyrolysis expertise. Thank you, James Hammerton (Jem), for keeping the NMR lab in check and running!

My PhD experience wouldn't have been so amazing without all of you, MB111 past and present! Thank you to those who have been here the last few months of my PhD, Alice, Nawal and Courtney, wish you guys the best of luck. Bawan and Hana, thank you for all those random hiking trips and standing with me in the post office for over an hour – I'm glad we didn't die from Bawan's driving. Lauren (La la), thank you for always making me laugh and I think we've actually lost the plot in design and build. Joe and Ben (my BRGRI buddies), thank you for all the crazy conversations and keeping me company when we worked late nights. Anisha, you are one of the most thoughtful, supportive, and kind friend I have ever met. Thank you for always being there for me when I needed it the most. Georgia, thank you for being there since the very start, I would not be able to do this journey without you, I owe you one! You have been there to celebrate every little milestone of this journey and one of the best friends I could ever ask for. I would also like to thank all the MEDIPOL exchange researchers, I have met some great friends from

5

across the world, thank you for all the various trips and memories that I will treasure forever.

To my family and my chosen family, I would like to thank some of my best friends, Bismah, Khadra, and Sean for the always checking up on me. Even though you still probably don't know what I'm doing (apart from Bismah), your unconditional love and support has made this journey easier. I would also like to thank my train buddy Emma Jordan you have been there every morning and evening to listen to my phosphorus NMR chats. I would like to thank my mum and my little sister Annie who have given me unlimited amounts of encouragement, love and support. Annie, I hope you have finally learnt what spin-spin coupling is. Last but very not least, this is for you, dad, thank you for your unconditional love and always pushing me to do the best! I wish you could see this, I miss you every day, but I hope you are resting well. I would not be here today without you all.

If I have missed anyone, sorry, I am deeply grateful to all those who have been part of this journey with me.

Contents

B.Tang, PhD Thesis, Aston University, 2024.

B.Tang, PhD Thesis, Aston University, 2024.

B.Tang, PhD Thesis, Aston University, 2024.

B.Tang, PhD Thesis, Aston University, 2024.

Abbreviations

^{13}C	carbon-13
^{19}F	fluorine-19
^{1}H	proton
^{31}P	phosphorus-31
$^{31}P\{^{1}H\}$	phosphorus decoupled proton
BSG	Brewers' Spent Grains
$CDCl_3$	deuteriated chloroform
CPD	composite pulse decoupling
D	diffusion coefficient
D_2O	deuterium oxide
DMF	dimethylformamide
DMSO	dimethyl sulfoxide
DOSY	Diffusion-ordered spectroscopy
EA	elemental analysis
FTIR	fourier transform infrared spectroscopy
GC/MS	gas chromatography mass spectrometry
H_2O	water
IDP	Intrinsically disordered protein
IS	Internal standard
MW	molecular weight
N_A	Avogadro's number
NHND	*endo*-*N*-hydroxy-5-norbornene-2,3-dicarboximide
NMR	nuclear magnetic resonance
NOE	nuclear Overhauser effect
rf	radiofrequency
PFG	pulsed field gradient
PFGSE	pulsed field gradient spin echo
PFGSTE	pulsed field gradient stimulated echo
Py-d_5	deuteriated pyridine
SEGWE	Stokes-Einstein-Gierer-Wirtz-Estimation
TMDP	2-chloro-4,4,5,5-tetramethyl-1,3,2-dioxaphospholane
TMP	trimethyl phosphate

List of Tables

B.Tang, PhD Thesis, Aston University, 2024.

List of Figures

B.Tang, PhD Thesis, Aston University, 2024.

16

B.Tang, PhD Thesis, Aston University, 2024.

19

B.Tang, PhD Thesis, Aston University, 2024.

B.Tang, PhD Thesis, Aston University, 2024.

B.Tang, PhD Thesis, Aston University, 2024.

CHAPTER 1 : INTRODUCTION TO BIOFUELS

1.1 Introduction to Biomass

Traditional fuels such as fossil fuels e.g coal, oil, and natural gas are limited.[1] Renewable energy is derived from natural processes that can be replenished constantly and replace traditional fuels.[2-4] Biomass is the term used to describe organic matter that comes from plants and animals.[5] Common biomass includes plant-based biomass from agriculture, animal residues, sewage sludge and forest residues. [6, 7] Plants grow by utilising sunlight, carbon dioxide and water to produce energy through a process known as photosynthesis[8], therefore, plant-based biomass can be considered a renewable resource for energy production.[9]
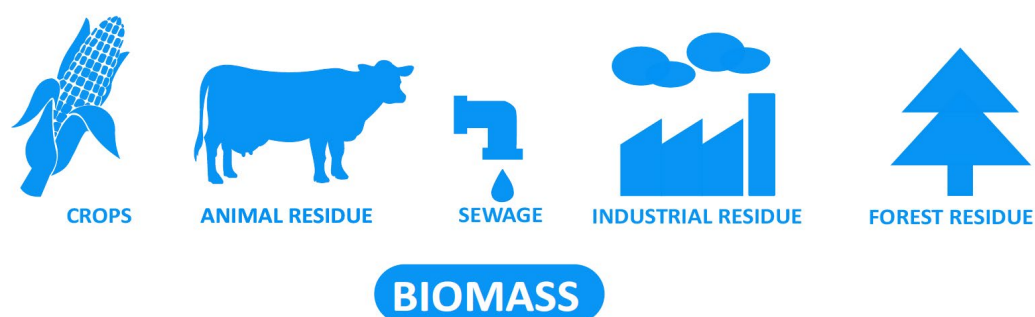
Figure 1.1.1 Schematic diagram of types of biomasses.

Plant-based biomass can act as a starting material for fuels.[10] There are two main paths to convert biomass into fuel: biological i.e bacterial decomposition and thermal i.e combustion, gasification and pyrolysis.[11-14] Biomass can be a substitute for coal in generating electricity via combustion.[15] Organic waste can be decomposed by bacteria to produce renewable fuel gases such as methane.[16] Biomass can also undergo gasification and pyrolysis processes producing gas and liquid fuels.[17, 18] In this body of work, there will be a focus on liquid fuels generated using pyrolysis processes.

1.2 Lignocellulose Biomass

Plant-based biomass is also known as lignocellulose biomass (Figure 1.2.1) as it mainly made up of biopolymers such as cellulose, hemicellulose, and lignin.[19, 20] These complex polymers help strengthen the plant cell walls.[21]
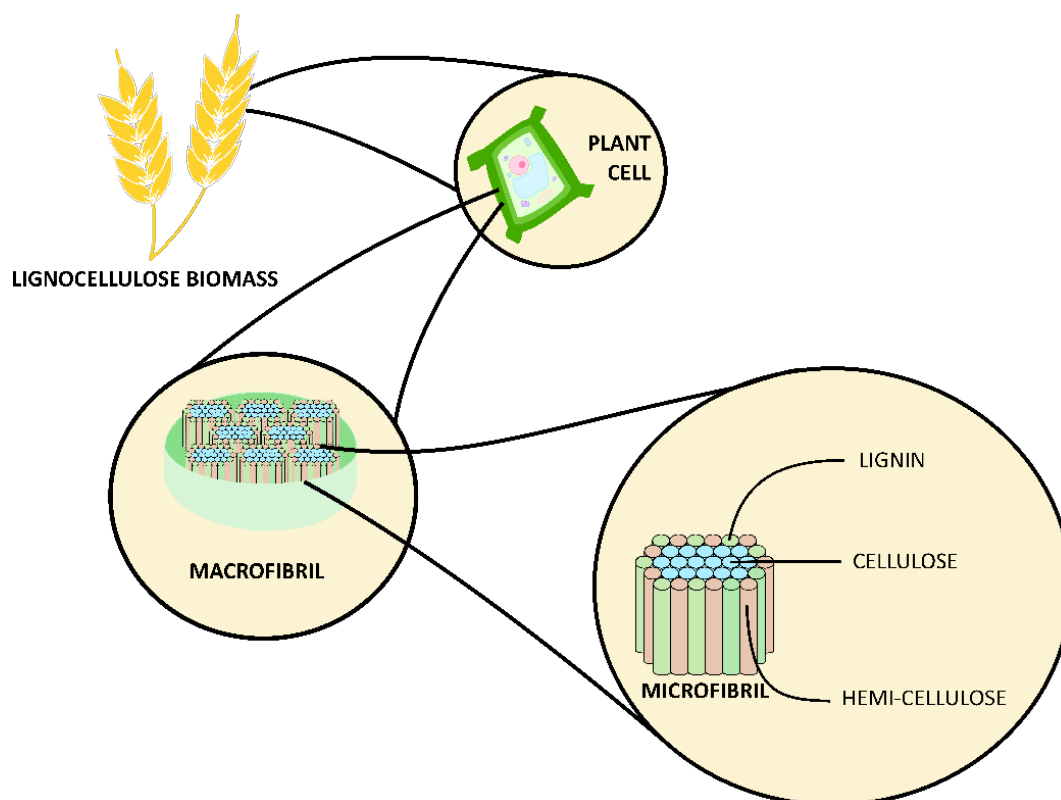
Figure 1.2.1 Schematic diagram of the components of lignocellulose plant cell walls.

Cellulose is a homogenous polysaccharide containing β-1,4-linked D-glucose units.[22] Hemicellulose, on the other hand, is a heterogeneous polysaccharide that contains several different sugar units including, both six-carbon sugars, such as mannose, galactose, glucose and 4-O-methyl-d-glucuronic acid, and five-carbon sugars, such as xylose and arabinose.[23] Moreover, hemicellulose itself can vary in terms of structure and physicochemical properties.[24] Lignin is made up of the monolignol units *p*-hydroxyphenyl (H), syringyl (S) and guaiacyl (G).[25, 26] Figure 1.2.2 shows the chemical structures of cellulose, hemicellulose and Figure 1.2.3 shows a typical hardwood lignin.
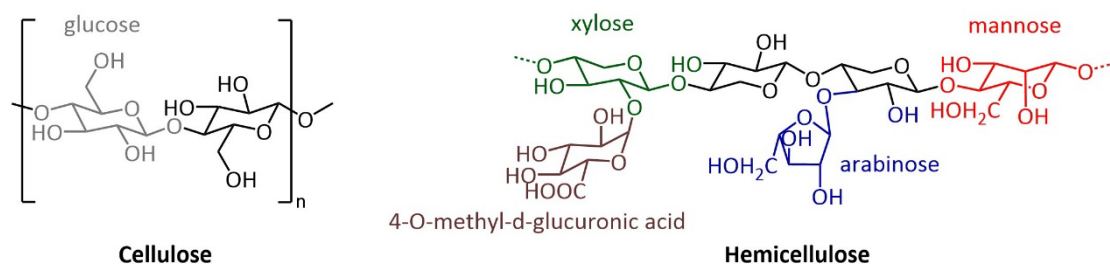
Figure 1.2.2 Chemical structure of a section of a cellulose and hemicellulose. The different sugar units, glucose - grey, xylose - green, mannose - red, 4-O-methyl-d-glucuronic acid -brown and arabinose - blue.
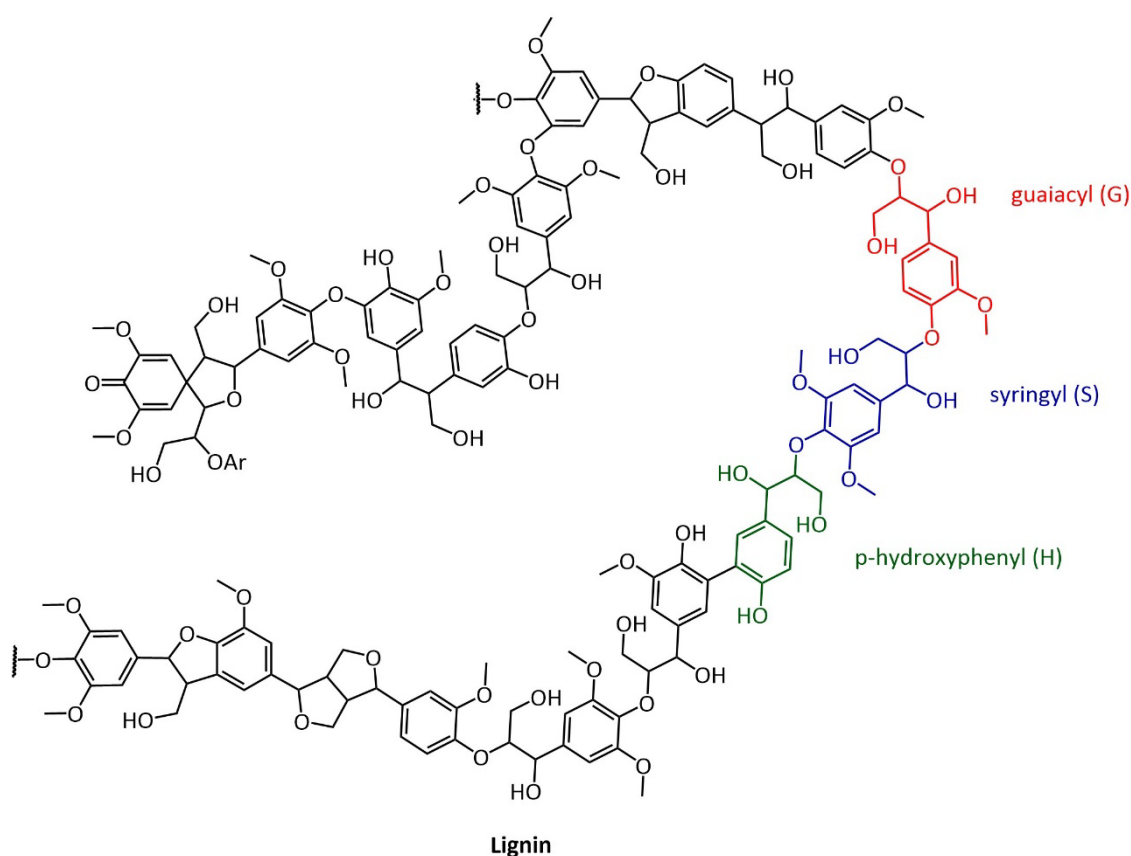
Figure 1.2.3 Chemical structure of a typical hardwood lignin, with monolignol units, p-hydroxyphenyl (H) - green, syringyl (S) - blue and guaiacyl (G) - red

Different types of biomass will have slightly different lignocellulose compositions. Table 1.2.1 shows the lignocellulosic composition of softwood, hardwood, and grasses. The type of biomass also plays a role in the monolignol distributions, where softwood is mostly guaiacyl units compared to hardwood and grasses. Grasses tend to have more syringyl units compared to wood-based biomass.

Table 1.2.1 Typical lignocellulose and monolignol compositions by weight for hardwood, softwood and grasses.[27-29]

	Lignocellulose composition (weight%)			Monolignol distribution (%)		
	Cellulose	Hemi-cellulose	Lignin	H	G	S
Softwood	46-50	19-22	21-29	<5	>95	0
Hardwood	40-46	17-23	18-25	0-8	25-50	45-75
Grasses	28-37	23-29	17-20	5-35	35-80	20-55

1.3 Brewers' Spent Grains

Beer is one of the most consumed beverages, with an annual production of around 1.9 billion hectolitres worldwide.[30] Beer is produced using four major ingredients: barley, hops, yeast and water.[31] The schematic diagram (Figure 1.2.1) shows a general process for beer production. The brewing process begins with the milling of malt grains creating a higher surface area.[32] The grains are then transferred to the mash tun, into which water is added and heated to make an "oatmeal". The oatmeal enters the lauter tun where the wort is separated and is transferred to the boil kettle. The Brewers' Spent Grains are removed from the laundering tun. Approximately 36.4 million tonnes of BSG of generated globally per annum.[33] As the wort is boiled, hops and other flavours are added.[34] Once the desired flavour is obtained, the mixture enters a whirlpool and heat exchanger. After cooling, yeast and oxygen are added to begin the fermentation process.[35] The beer passes a centrifuge and is transferred into a brite tank where it is carbonated. Finally, the final product is bottled or kegged.[36]
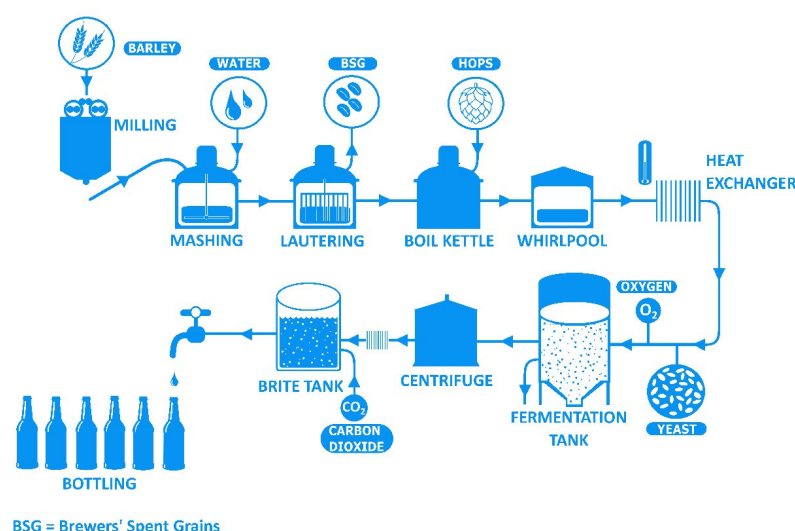
Figure 1.3.1 Schematic diagram of beer production process. Adapted from R. Willaert, The beer brewing process: Wort production and beer, Vrije Universiteit Brussel, 2007.[34]

The mashing process where water is added to the malted barley initiates the enzymatic hydrolysis of starch and proteins to produce a sugar-rich solution.[37] During the mashing process the waste produced is known as Brewers' Spent Grains (BSG).[38] This is one of the major by-products of the brewing process making up *ca.* 85% of the brewing waste.[39] The composition of BSG will also vary based on factors such as harvest time, malting and the process of mashing. BSG is made up of cellulose, hemicellulose, lignin and proteins, summarised in Table 1.3.1 .[40-43] Typically the monolignol distribution of H, G and S units are 24-31%, 56-57% and 18-20% respectively. The elemental analysis of BSG can also vary, some data is shown in Table 1.3.2. Unlike other biomass' resources, grown specifically to produce fuel, BSG is mainly considered as agricultural waste product which has a low cost and high availability.[44] BSG is rich in nutritive value and the majority of BSG is used either as a food additive or livestock feed.[45, 46] Other uses for BSG include paper manufacturing[47] and construction brick component.[48] BSG can also be used to produce added-value chemicals such as lactic acid[49], bioethanol[50] and xylitol.[51] Therefore, BSG is considered somewhat sustainable source of biomass without impacting on the land space and storage.[52]

Table 1.3.1 Summary of major chemical composition of Brewers' Spent Grains (BSG).

Composition (% dry weight)	Meneses *et al.* [40]	Xiros *et al.* [41]	Mussatto *et al.* [42]	Kanauchi *et al.* [43]
Cellulose	21.7	40.0	16.8	25.4
Hemicellulose	19.2	12.0	28.4	21.8
Lignin	19.4	11.5	27.8	11.9
Proteins	24.7	14.2	15.2	24.0
Ashes	4.2	3.3	4.6	2.4

Table 1.3.2 Elemental composition of Brewers' Spent Grains (BSG)

	C (%)	H (%)	N (%)	S (%)	O (%)
BSG [53]	46.6	6.85	3.54	0.74	42.26
BSG [54]	47.2	7.2	3.6	1.1	37.6

The major limitation hindering wider applications of BSG is storage. The rate of deterioration of BSG is rather fast[55] and it can spoil within a few days. This is due to the high water and a high sugar content making it optimal for microbial growth.[56] Several solutions to storage and prolonging the life of BSG have been proposed. The most effective method for preserving BSG has been factory drying.[57] This is where breweries

have a two-step processing plant where about 60% of the water content is reduced by pressing, followed by drying, thereby reducing the overall moisture content to below 10 %.[58] Drying the BSG has the additional advantage of reducing the volume, resulting in both a reduction in transport and storage cost.[30] The difficulty with drying BSG is the high energy cost associated with the process.[59]

1.4 Pyrolysis

Pyrolysis is the process of thermal degradation of material at a high temperature without the presence of oxygen.[60] Generally, pyrolysis of biomass produces three main products. [61-63] It produces char or biochar (solid), bio-oil or pyrolysis-oil (liquid) and syngas (gas). The distribution of the products depends on the biomass properties, but mainly the pyrolysis conditions.[64]

Cellulose, hemicellulose and lignin are each pyrolysed or degraded at different rates and by different mechanisms and pathways.[65] Cellulose has a relatively simple structure that depolymerises around 300 - 350 °C, producing cellulosic species.[66] Cracking and dehydration can also occur producing monosaccharides.[67] When dehydration has occurred, the cellulose is prone to crosslinking and ultimately forming char.[65] The primary products from depolymerisation are anhydrosugars such as levoglucosan.[68] Cracking of pyran rings convert the cellulose to light oxygenates such as furans, aldehydes, ketones and acids.[69] At temperatures above 300 °C the cellulose breaks down and produces liquid products, where the maximum yield of liquid product is produced at *ca*. 500 °C. Hemicellulose on the other hand is less thermally stable compared with cellulose and typically degrades at around 220 - 315 °C.[70] Xylose and pyranose can lead to biochar formation through multistep dehydration.[65] Lignin is much more thermally stable in comparison to both cellulose and hemicellulose.[71, 72] Lignin structures are connected through either ether i.e carbon-oxygen bonds or carbon-carbon bonds.[73, 74] These bonds are much harder to break than the glycosidic bonds in cellulose and hemicellulose.[75] Temperatures around 400 - 600 °C are required for the thermal degradation to occur.[76] Cracking lignin typically breaks down into aromatic rich liquid.[77, 78] The active aromatic species can also repolymerise and produce biochar.[79]

The different pyrolysis methods based on the products desired and reactor residence time. Slow pyrolysis, as the name suggests, is conducted on a relatively longer time

frame. It is usually carried out at lower temperatures, less than 500°C, with heating rates ranging from 0.1 to 2°C per second.[80] Slow pyrolysis is used to maximise the production of solid products.[81] On the other hand, fast pyrolysis, is typically carried out in a short resident time of less than 2 seconds at higher temperatures (500°C) with heating rates ranging from 10 to 200°C per second.[82] Fast pyrolysis is used to maximise the production of liquid products (75-80 wt%).[81, 83]

1.5 Brewers' Spent Grain Pyrolysis Oil

BSG is a lignocellulosic biomass, therefore, it can be processed into bio-oil via pyrolysis.[52, 84] Table 1.5.1 illustrates some of the resulting compounds identified from the fast pyrolysis of BSG at various temperatures using pyrolysis-gas chromatography/gas chromatography mass spectrometry or Py-GC/GCMS.

Table 1.5.1 Typical chemical compounds found in BSG pyrolysis oil produced at different temperatures.[85]

Chemical	Chemical formula	% Area of Peak			
		450°C	550°C	650°C	750°C
acetic anhydride	$C_4H_6O_3$	2.39	11.79	-	-
2-methyl-furan	C_5H_6O	2.18	-	4.44	4.93
2,3-butanedione	$C_4H_6O_2$	2.96	3.32	5.81	-
3-methyl-butanal	$C_5H_{10}O$	2.47	1.3	1.55	0.7
acetic acid	$C_2H_4O_2$	19.22	13.7	15.82	9.02
1-hydroxy-2-propanone	$C_3H_6O_2$	3.57	1.68	1.79	-
toluene	C_7H_8	0.71	1.15	5.31	11.02
pyrrole	C_4H_5N	2.31	2.32	2.06	3.34
3,3'-oxybis-propanenitrile	$C_6H_8N_2O$	2.11	1.36	1.66	-
1-methoxy-2-propyl acetate	$C_6H_{12}O_3$	10.01	31.16	12.09	4.86
furfural	$C_5H_4O_2$	9.85	7.15	8.79	5.41
1-decene	$C_{10}H_{20}$	-	-	0.83	1.95
2-furanmethanol	$C_5H_6O_2$	3.02	1.04	-	-
1-(acetyloxy)-2-propyl acetate	$C_5H_8O_3$	3.46	1.5	1.01	-
limonene	$C_{10}H_{16}$	-	1.57	0.97	-
2-cyclopentene-1,4-dione	$C_5H_6O_2$	1.33	1.12	-	-
6-oxa-bicyclo[3,1,0]hexan-3-one	$C_5H_6O_2$	1.8	0.57	-	-
5-methyl-2-furan carboxaldehyde	$C_6H_6O_2$	1.79	1.01	-	1.1
butyrolactone	$C_4H_6O_2$	0.54	0.49	-	-
2(5H)-furanone	C_4H_4O2	1.66	1.23	-	-
hexanoic acid	$C_6H_{12}O_2$	-	0.45	0.58	-
2-butoxiyethyl acetate	$C_8H_{16}O_3$	0.85	2.58	2.41	0.63
benzene acetaldehyde	$C_9H_{10}O$	0.8	0.36	0.67	-
1-dodecene	$C_{12}H_{24}$	-	-	0.67	1.3
phenol	C_6H_6O	-	-	0.88	2.06
dodecanal	$C_{12}H_{24}O$	0.5	1.18	-	--
2-methyloxy-4-vinylphenol	$C_9H_{10}O_2$	1.39	-	-	-

Borel *et al.*[85] show that the pyrolysis of BSG produces mixtures of compounds containing oxygen.Physicochemical properties such as the thermal degradation of products from pyrolysis of BSG have been studied. These showed that BSG had both high volatile matter content and high heating value, therefore, it has potential to produce pyrolysis oil.[86] The pyrolysis of BSG to produce fuel products still has many challenges to overcome to make the process cost-effective.[85, 87] Like pyrolysis oil produced from other biomass feedstock, BSG bio-oil poses similar issues with both a high content of oxygen-containing compounds [88] and a high-water content.[89] Pyrolysis oils typically have pH 2 to 3, which is very acidic when compared to bio-diesel (pH ~7).[53] Therefore, corrosion and related issues could still arise if used in current engines.[90]

1.6 Pyrolysis Oil and Upgrading Challenges

Whether the pyrolysis oil is produced via fast or slow pyrolysis processes, when lignocellulose biomass breaks down into smaller molecules, the product will mainly contain carbon, hydrogen and oxygen. Therefore, when using bio-oils as fuels, the major emissions are carbon dioxide (CO_2) and water (H_2O).[91] An advantage of the using of biomass-derived fuel is the ability to achieve a net zero emission of CO_2 gases, as the CO_2 released will be recycled via photosynthesis when the crops are replenished/replanted.[83, 92, 93] Biomass fuels also emit negligible amounts of sulfur oxide (SO_x) and nitrogen oxide (NO_x) compared to fossil fuels.[94]

Even though it may seem that pyrolysis oils are a good replacement for fossil fuels, there many challenges are still associated with the use of biofuels in current infrastructures. Bio-oils can be used directly in boilers.[95] Compared to petroleum fuel, bio-oils have some undesired properties therefore it cannot be used directly as transport fuel.[96] The main differences between traditional fuels and pyrolysis oil are low volatility, high water content, acidity, and high oxygen content.[54, 97, 98] Pyrolysis-oils typically contain a mixture of organic compounds such as alkanes, alkenes, aromatic hydrocarbons, alcohols, sugars, esters, ketones and aldehydes. The undesirable physiochemical properties include:

1. High water content - water content in bio-oil is around 15-30 wt% where the major contribution is the moisture present in the feedstock and the products of condensation during the pyrolysis reactions.[97] The main issue with high water content is that it decreases the heating value of the bio-oils. Therefore, the bio-oil is incompatible with current infrastructures due to the low heating values.[85, 98]

2. Corrosive - bio-oil produced from pyrolysis has a mixture of oxygen-containing compounds making up 35-40% of the composition.[99] Oxygen-containing compounds such as acetic acid, formic acid, syringic acid and phenol contribute to the acidity of the bio-oil, which makes the bio-oil corrosive especially at increasing temperatures.

3. Low heating value – the heating value of a fuel is the amount of heat is released during combustion. Compared to the conventional heating value for heavy petroleum (40 MJ/kg), pyrolysis oil has a heating value of 16-19 MJ/kg.[100, 101]

Upgrading bio-oil improves its properties to match existing fuel standards.[102, 103] Some of the common upgrading techniques used to produce higher-value products are summarised in Table 1.6.1.

B.Tang, PhD Thesis, Aston University, 2024.
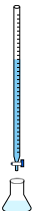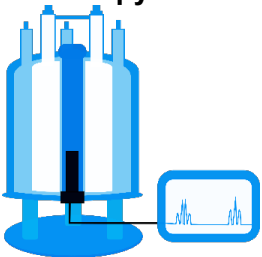
Table 1.6.1 Various upgrading method used to upgrade bio-oil, and their advantages and disadvantages.

Upgrading methods	Advantages	Disadvantages
Hydrotreating[104, 105] This is where hydrogenation takes place without simultaneous cracking. This process removes N, O, and S. Hydrogenation adds H_2	Hydrotreating process is cheaper and commercially available.	Poor quality of fuel is obtained due to high amounts of coke in product. The large amount of coke can result in deactivation of catalyst and block the reactor.
Cracking (hydro-cracking and catalytic cracking)[106, 107] This is where large hydrocarbons are broken down into smaller alkanes and alkenes. Hydrogenation with simultaneous cracking.	The production of large amounts of light products.	Specialist equipment is required that can withstand high temperature and pressures. Expensive catalysts are also needed for the catalytic cracking process.
Sub- or Super-critical fluid [108] Supercritical fluid is when the temperature and pressure of the sample exceed the fluids critical point. Such fluids can dissolve materials that are not normally soluble in the gas or liquid phase. This promotes gasification and liquefaction reactions.	It produces a higher oil yield, lowering the oxygen content and viscosity.	This can be achieved with a lower temperature however, the organic solvent required is not economically feasible.
Chemical Extraction[109, 110] This can be solvent extraction, distillation, or chemical modification	These techniques can produce high value chemicals such as phenols and volatile organic acids.	Other separation and refining methods may also be needed, thus adding to the cost.
Emulsification[111] This combines diesel and bio-oils with a surfactant.	Some improvements in stability and storage show promising ignition characteristics. It may also be a short-term solution for the use in diesel engines.	Even though the process is relatively simple and produces less corrosive fuels, the pH is still raised, and fuels can still be corrosive.
Esterification[112] This combines alcohols with carboxylic acids in the presence of a catalyst.	Reduces the number organic acids which improves the stability and long-term storage of the oil.	Reaction rates are slow therefore catalysts must be used. Esterification is a reversible process, therefore, esters can break down when exposed to water.

1.7 Pyrolysis Oil Characterisation

Current characterisation methods include oximation followed by titration, elemental analysis, Fourier-Transform Infrared spectroscopy, gas-chromatography/mass spectrometry and nuclear magnetic resonance spectroscopy. A brief summary of the advantages and disadvantage of each technique used to characterise pyrolysis-oils is summarised in the table below.

Table 1.7.1 Summary of characterisation techniques for bio-oil analysis, with their advantages and disadvantages.[113, 114]

Technique	Advantages	Disadvantages
Titrations[115-117]	Simple and reliable quantitative analysis.	Laborious and reactions >24 hours. No structural information.
Elemental Analysis[118-120]	Simple and reliable. Provides overall information on elemental components.	No information on structure or functional groups.
Fourier-Transform Infrared Spectroscopy (FTIR)[121, 122]	Identify functional groups.	It is mostly used for qualitative analysis.
Gas Chromatography Mass Spectrometry (GC/MS)[123-126]	Direct compound identification. Large MS database for ease of identification.	Not all compounds can be identified due to the volatility of the sample. Some bio-oil compounds are not in the library making them difficult to identify.
Nuclear Magnetic Resonance Spectroscopy[127-129]	Quantitative analysis is relatively quick compared to other methods. Functional groups can be derivatised with multinuclear containing reagents.	Overlap in spectrum makes it difficult to analyse. Reagents can be expensive.

1.8 Summary

Biomass could be one route to renewable fuel. However, with the increasing demand on land for food, there may be better option than growing crops for fuel. The brewing industry produces waste in the form of Brewer's Spent Grains (BSG) which is currently used mainly as feed for livestock. This offers an opportunity to have a low cost and readily available source of biomass. BSG can be thermally converted into bio-oil. However, there are still many issues that must be tackled before BSG can be used as commercial fuel. Major issues of pyrolysis oils include being too acidic as well as having high-water content. The acidity of pyrolysis oil is the main cause of corrosion in engines and storage. Typically, oxygen-containing functional group compounds (carbonyl, carboxyl, hydroxyl, phenolic) give bio-oil its acidic properties. Therefore, a better understanding of the chemical compositions of BSG pyrolysis oil is crucial for later storage, ageing and upgrading.

There are various techniques that can provide useful information about the chemical composition of pyrolysis oils. Oxygen/ oxygen-containing compounds in bio-oils can be quantified using oximation followed by titration, elemental analysis, gas chromatography and mass spectrometry. Chemical and structural information can be obtained using Fourier Transform Infrared Spectroscopy and Nuclear Magnetic Resonance. However, many of these techniques are laborious or multiple techniques are required to produce complementary data.

Nuclear Magnetic Resonance spectroscopy is a non-invasive and relatively quick approach to chemical characterisation. The ability to derivatise specifically oxygenated compounds and NMR can be used to study these chemicals alone. Developments in the field have enabled NMR to be applied to more complex systems, such as mixtures including bio-oils. Chapter 2 will explore:

- The theory of NMR techniques used throughout this work.
- Applications of multinuclear and multidimensional NMR techniques to characterise bio-oil.
- Followed by the research aims.

CHAPTER 2 : NUCLEAR MAGNETIC RESONANCE THEORY AND APPLICATIONS TO CHARACTERISE PYROLYSIS OIL

2.1 Introduction

Nuclear Magnetic Resonance (NMR) allows the analysis of molecular structures by observing and measuring the interaction of nuclear spins when placed into a magnetic field. Originally NMR techniques were confined to the physics community. The first NMR experiments in condensed matter were carried out by two groups of researchers Purcell (paraffin, 1945)[130] and Bloch (water, 1946)[131], for which they shared a Nobel Prize for physics in 1952. NMR came to the attention of chemists when the first ^{1}H NMR spectrum of ethanol was recorded, the three signals detected corresponding to the three proton environments in the molecule. This was the first demonstration of chemical shift.[132-134] Arnold et al. also observed that the intensities of the peaks were equal to the relative number of protons.[8] Chemical shift information combined with integral information can used to determine molecular structure.

2.2 Spin Physics

NMR is based on the fundamental idea that nuclei have intrinsic angular momentum, also known as 'spin'.[135, 136] For most chemical elements, at least one nuclide exhibits nuclear spin, also known as an 'NMR active' nuclei. The atoms nuclei have nuclear spin quantum number I with values:

$$I = 0,\ \frac{1}{2},\ 1,\ \frac{3}{2},\ 2,\ ....$$
Equation 2.2.1

Table 2.2.1 shows the natural abundances of common nuclei that are NMR active, their spin quantum number, magnetic moment, gyromagnetic ratio, and the typical chemical shift range they display. Chemical shift dispersion varies based on the electronic and chemical properties of the element, generally the heavier the nuclei, the larger the dispersion.

Table 2.2.1 Summary of important properties of common NMR nuclei that may be used in further chapters [137].

Isotope	Natural % Abundance	Spin (I)	Magnetic Moment (μ_N)	Gyromagnetic Ratio, γ (10^6 rad s^{-1} T^{-1})	Typical Chemical Shift Range (ppm)
[1]H	99.9	1/2	2.7927	267.52218744	0 - 15
[13]C	1.11	1/2	0.7022	67.2828	0 - 220
[17]O	0.04	5/2	−1.8930	−36.264	−100 - 1600
[19]F	100.00	1/2	2.6273	251.815	−500 - 500
[31]P	100.00	1/2	1.1305	108.291	−200 - 240

A nucleus with spin has a magnetic moment defined by:

$$\mu = \frac{h\gamma I}{2\pi}$$

Equation 2.2.2

where μ (JT^{-1}), the magnetic moment is proportional to γ, the gyromagnetic ratio of a given nuclei (rad s^{-1} T^{-1}), h, Planck's constant and I, the nuclear spin quantum number. When an external magnetic field B_0 is applied, the precession of the spin occurs at a rate dependent on the gyromagnetic ratio of the nuclei and the applied magnetic field strength. This is defined by the Larmor equation:

$$\omega_0 = \gamma B_0$$

Equation 2.2.3

where ω_0 is the intrinsic angular frequency (rad s^{-1}) and B_0 is the strength of the applied magnetic field (T). The frequency of precession in Hertz is given by the Larmor frequency:

$$\nu_0 = \frac{\gamma B_0}{2\pi}$$

Equation 2.2.4

Without a magnetic field applied, the energy level of spin-I has the same energy. When atoms are placed in an external magnetic field B_0 the energy levels become non-degenerate, with $2I + 1$ levels forming:

$$I_z = m_I \hbar$$

Equation 2.2.5

$$m_I = I, I-1, I-2, -1$$

Equation 2.2.6

Usually, the energy levels in a spin ½ nuclei are labelled as α (if it is parallel, meaning it is aligned with the applied field) or β (if it is antiparallel to the field). However, the assignment of alpha and beta state to parallel or antiparallel also depends on the sign of the gyromagnetic ratio. In the case for all the nuclei studied in this thesis their gyromagnetic ratio is positive. The energy of the transition is equal to the gap between the energy levels. For example, a nucleus such as a proton, with spin quantum number I = ½ will occupy one of two distinct energy levels as illustrated in the diagram Figure 2.2.1.
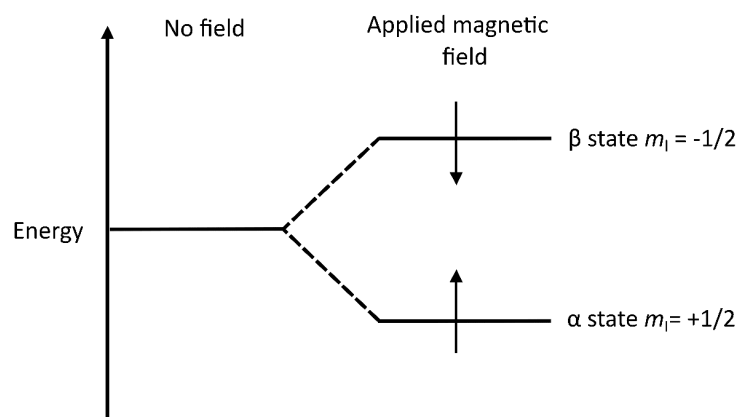
Figure 2.2.1 The energy gap splitting of spins when a magnetic field B_0 is applied.

The spins that are aligned with the applied magnetic field will have lower energy in comparison to those that are antiparallel to the field. The transition energy between the spin states is proportional to Planck's constant multiplied by the frequency of radiation associated with the transition. The difference between the two energy states, in J, is given by the equation:

$$\Delta E = h\nu = \frac{h\gamma B_0}{2\pi}$$

Equation 2.2.7

and therefore, the ratio of the two spin states is given by the Boltzmann distribution:

$$\frac{n_{\text{upper}}}{n_{\text{lower}}} = e^{-\frac{\Delta E}{k_B T}}$$

Equation 2.2.8

where n_{upper} and n_{lower} represents the number of nuclei in each spin state, k_B is the Boltzmann constant (1.38×10^{-23} J K^{-1}), and T is the temperature (K). As the difference between the energy levels are small, the population difference is also small. For a proton nucleus in a 9.4 T field, at 300 K, this energy gap is 2.64×10^{-25} J. The small excess of nuclear spins can be represented as a collective, the bulk magnetisation vector M_0. In a simple vector model, with a set of Cartesian coordinates, the static magnetic field is applied along the z-axis. At equilibrium the bulk magnetisation M_0 is the same as M_z. In the absence of a secondary field, i.e a radiofrequency pulse or rf pulse, the bulk magnetisation vector lies on the +z-axis as majority of the spins align with the magnetic field. Applying the vector model to a spin-echo experiment (Figure 2.2.2) where the chemical shift evolution is refocused and the signal detected is attenuated only by transverse relaxation. In this sequence a 90°_x rf pulse is applied, and the bulk magnetisation is transferred into the transverse plane for a delay time τ. A 180°_x pulse is then applied to refocus the chemical shift evolution. The net magnetisation will start to

precess around the z-axis at the Larmor frequency. The rotating magnetisation can be detected.
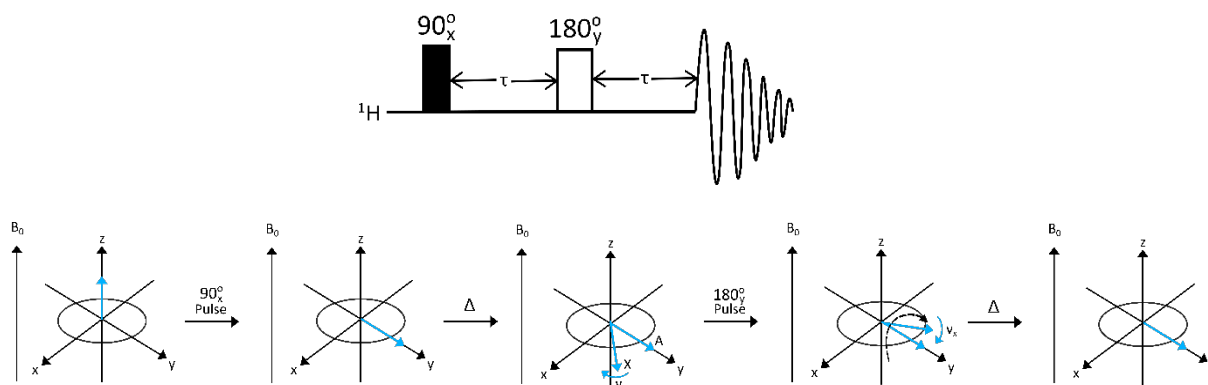
Figure 2.2.2 Spin-echo sequence and vector model representation. The bulk magnetisation vector (blue) aligns with the +z-axis in the direction of the magnetic field B₀. When a 90°ₓ radio frequency pulse is applied the bulk magnetisation is transferred to the transverse plane. A 180°ₓ pulse is then applied to invert and refocus the chemical shift evolution.

NMR spectrometry is a spectroscopic technique based on that nuclei have spin, when placed in a magnetic field the bulk magnetisation will align with the magnet. A small radio frequency pulse can be applied to disturb the equilibrium. The voltage induced in the coil by the precessing magnetisation is detected.

2.3 Instrument Design

In the modern-day, NMR has become a routine analytical technique used for structure elucidation and quantification. Original electromagnet spectrometers had a maximum field strength of 2.35 T, or equivalent to 100 MHz resonant frequency for protons, which is insufficient for the structural analysis of more complex molecules. NMR is an inherently insensitive technique due to the small energy gap, which results a small population difference. The development has largely been focused on improving the sensitivity of the NMR spectrometers.[138] One way to improve the sensitivity is to increase strength of the magnetic field, this increases the energy gap between the level and the population difference. The advancements in magnet technology and the ability to make super conducting electromagnets has enabled spectrometers to operate at high fields.[139, 140] Figure 2.3.1 is a schematic representation of a modern-day high-field NMR spectrometer. The superconducting materials are cooled using cryogens such as liquid helium. However, the use of cryogens is expensive and cryogenic cooling requires technical maintenance. Overall, NMR is not considered a low-cost analysis due to the high capital and maintenance cost. In particular, the cost of liquid helium has increased significantly

in the last decade due to a global helium shortage.[141, 142] High-field NMR spectrometers require a considerable investment and can cost over £10 million as a result, limiting the usage of NMR to larger and well-funded research facilities.
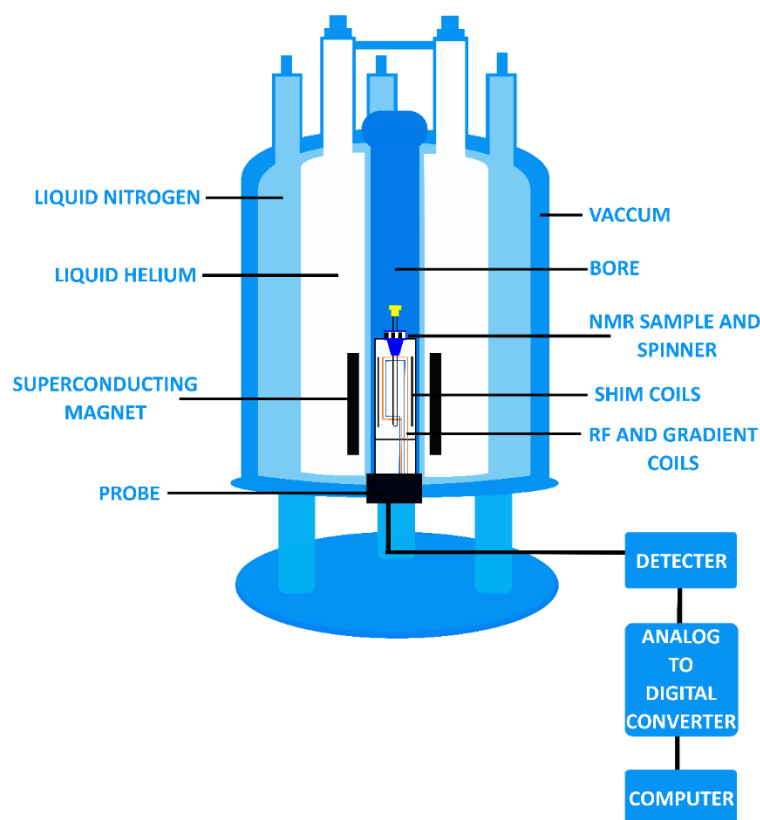
Figure 2.3.1 Schematic diagram of a modern-day spectrometer.

Moreover, a large amount of space is also required to house the spectrometer. This is especially true for material verification, such as quality control in an industrial setting or smaller academic institutes. In 2009, the first commercial benchtop NMR was launched. Benchtop NMR spectrometers typically utilise permanent magnets that generate a static magnetic field up to 2T or 80 MHz.[143] Permanent magnets do not require cryogenic cooling thus, reducing the technical maintenance and maintenance cost.[144] Using protiated solvents as the solvent system for analysis is made easier and possible as most benchtop spectrometers have an external locking system. The use of protiated solvents also reduces the cost of operations, for example DMSO costs ca. £35.70 (per 100 mL) and DMSO-d_6 costs ca. £307.00 (per 100 g). Typically, benchtop NMR spectrometer prices range from £30,000.00 to £150,000.00, providing a less expensive alternative to the high-field spectrometer which can cost up to £10 million.[140] Even though low-field NMR suffers from low sensitivity on account of the low field strengths

44

applied, it is not crucial to have the multiplicity resolution when analysing mixtures such as pyrolysis oils containing a vast number of compounds. Table 2.3.1 summaries the advantages and disadvantages of using high-field NMR and low-field NMR.

Table 2.3.1 Advantages and disadvantages of high-field NMR spectrometer and low-field NMR spectrometer.

High-Field NMR	Low-Field NMR
Higher Sensitivity ✓	✗ Lower Sensitivity
High Capital Cost ✗	✓ Low Capital Cost
Uses Cryogens ✗	✓ No Cryogens
Technical Maintenance ✗	✓ Less Maintenance
Deuteriated Solvents ✗	✓ Protiated Solvents
Central Facility ✗	✓ Benchtop Instrument

The following section gives an overview of how NMR techniques are currently applied to the analysis and characterisation of bio-oils.

2.4 Nuclear Magnetic Resonance Applications to Bio-oils

2.4.1 ^{1}H NMR Spectroscopy

Proton nuclei or ^{1}H have a ½ spin making it NMR active. The receptivity of a given nuclide depends on its natural abundance and gyromagnetic ratio. With a natural abundance of 99.9% and a large gyromagnetic ratio, protons are said to have a high receptivity. The chemical shift range is typically between 0 to 15 ppm. In principle, protons in different chemical environments produce a unique chemical shift. Protons exhibit *J*-coupling, also known as spin-spin or indirect dipole-dipole coupling. This arises from the indirect interaction of two nuclear spins, mediated through chemical bonds. ^{1}H-^{1}H coupling is responsible for the multiplicity or the complex splitting of resonance in NMR spectroscopy. Multiplicity patterns are useful for structure elucidation, based on n+1 rule, for example, a singlet peak has zero neighbouring protons, a doublet peak has one neighbouring proton, and a triplet peak has two neighbouring protons etc. However, this can lead to a highly crowded and complex spectra.

Pyrolysis oils are composed of hundreds of molecules, this results in a crowded spectrum making structural elucidation difficult. However, ^{1}H NMR can still provide

chemical information based on chemical shift values providing information on pyrolysis oil composition. Proton NMR has been one of the most versatile tools to characterise bio-refinery products. Figure 2.4.1 shows a stacked plot of ^{1}H NMR spectra of pyrolysis oils produced from six different feedstocks ((A) switch grass, (B) corn stover, (C) alfalfa stem, (D) guayule whole, (E) guayule bagasse, (F) chicken litter). Chemical shift values based on 400+ model compounds found in pyrolysis oils and plant-based natural products has been reported by various research groups producing a chemical shift library (Table 2.4.2).[145-147] ^{1}H NMR is commonly used as a complementary technique alongside FTIR for functional group analysis of pyrolysis oil products where results revealed by the ^{1}H NMR analysis were similar to the FTIR.[60, 148]
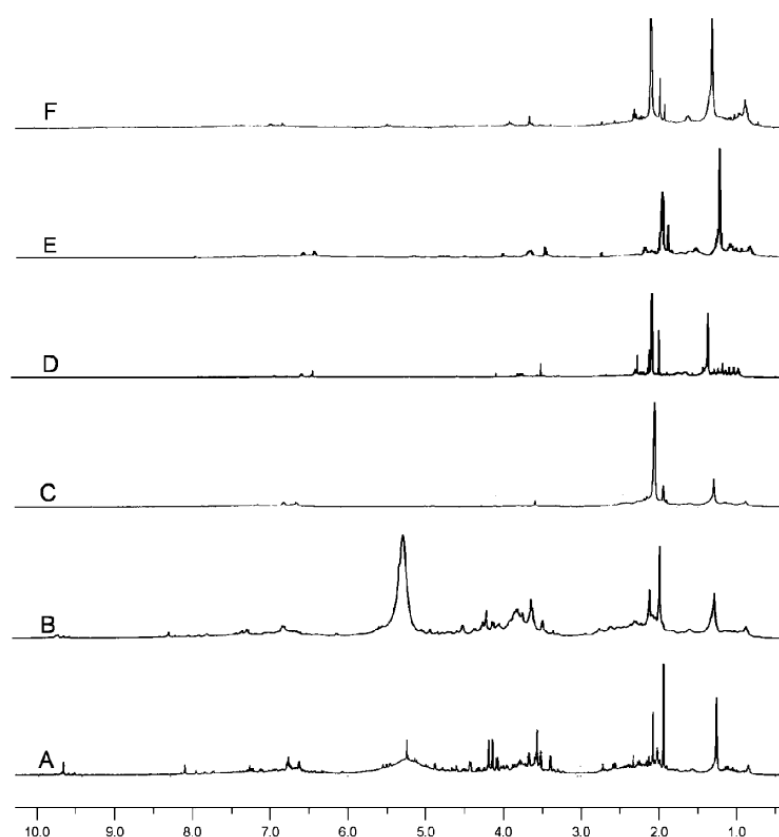
Figure 2.4.1 ^{1}H NMR spectra of bio-oil (A) switch grass, (B) corn stover, (C) alfalfa stem, (D) guayule whole, (E) guayule bagasse, (F) chicken litter. [147]

Table 2.4.1 Comparison of ^{1}H chemical shift integration regions of bio-oil samples in DMSO-d_6.

	Joseph et al. [146]	Ingram et al. [145]	Mullen et al. [147]
Functional Group	Chemical Shift (ppm)		
aliphatic	0 - 2	0.0 - 1.6	0.5 - 3.0
Aliphatic alcohol	2 - 3	1.6 - 2.2	-
ether, methoxy	3 - 4.2	2.2 - 3.0	3.0 - 6.0
Aliphatic OH, -C=C-, Ar-CH_2-O-	4.2 - 6	3.0 - 4.2	9.6 - 10.0
Aromatic, conjugated -C=C-	6 - 8.25	4.2 - 6.4	6.0 - 8.2
CHO, ArOH	8.25 - 11	6.4 – 8.0	-
carboxylic acids	11 - 12.5	8.0 - 10.0	9.6 - 10.0

Aside from identifying the types of compounds in pyrolysis oils it is also important to understand how much of a certain species is present. ^{1}H NMR techniques are inherently quantitative as the integrals equal the amount of protons in a sample. Mullen et al.[147] studied 6 bio-oil samples produced from wood-based, legume, and grass-based biomass. ^{1}H NMR was used to calculate the amount of compounds in the pyrolysis oils and upgraded pyrolysis oils based on the % of hydrogen.[149-151] Table 2.4.2 show how the % hydrogen content differs from different feedstock. However, the major overlapping region in the spectra makes it difficult to quantify specific compounds accurately. ^{1}H NMR has also been used alongside mass spectrometry techniques to show a decrease in oxygen-containing compounds and an increase of aromatic compounds when catalytic pyrolysis was used to produce pyrolysis oils.[152] Aside from the organic components of the pyrolysis oil, the water content of an oil is also important, as it affects the heating value of the pyrolysis oils. ^{1}H NMR has also been used to look at the water content of pyrolysis oils via the water addition method where results were compared with Karl Fischer techniques.[153, 154]

Table 2.4.2 Percentage of hydrogen based on the ^{1}H NMR analysis of Bio-oil produced from various feedstock.[147]

Functional group	Chemical Shift (ppm)	Percentage of Hydrogen (%)				
		switch grass	corn stover	alfalfa stem	guayule whole	guayule bagasse
alkanes	0.5 - 1.5	9.8	11.8	20.9	29.4	28.7
aliphatic	1.5 - 3.0	24.3	18.3	54.0	42.0	34.5
alcohol	3.0 - 4.4	21.3	20.5	7.2	10.4	12.5
methoxy/ carbohydrates	4.4 - 6.0	25.7	30.3	2.3	6.8	9.7
aromatics	6.0 - 8.5	17.5	15.1	15.1	11.2	15.6
aldehydes	9.5 - 10.1	1.3	1.7	-	0.2	0.5

The elucidation of pyrolysis-oil composition is essential for assigning the best application and upgrading process required. The major advantage of using NMR techniques is that bio-oils can be dissolved in various solvents dependent on solubility. ^{1}H NMR gives a good insight into both the chemical structures and functional groups present in bio-oil. It also allows some quantitative information such as hydrogen content, aromatic content, and water content. However, it does not yield chemical information, such as the types of hydroxyl groups within the sample, nor does it yield information on other functional groups that do not contain proton such as carbonyls. Overall, ^{1}H NMR has a narrow chemical shift range and bio-oils contain hundreds of hydrogen-containing compounds both of which result in a highly crowded spectrum. The overlap makes it very difficult to interpret and reduced the amount of information available. There are other NMR active nuclei such as ^{13}C which can be used to analyse pyrolysis oils.

2.4.2 ^{13}C NMR Spectroscopy

Carbon nuclei or ^{13}C, also have ½ spin making it NMR active. However, ^{13}C NMR has a lower receptivity compared to ^{1}H NMR. This is due to low natural abundance, ca. 1%, and a lower gyromagnetic ratio (Table 2.2.1). ^{13}C NMR has a larger chemical shift range, 0 to 200 ppm, this spreads the signals out making the spectrum less crowded. Carbons exhibit coupling with neighbouring protons making the spectrum more complex and difficult to interpret, as a result, ^{13}C NMR is often acquired with proton decoupling. The nomenclature of the decoupled spectrum is commonly shown as ^{13}C {^{1}H} for a proton decoupled carbon spectrum. Decoupling removes any unwanted J-coupling in the spectrum. As a result, multiplet structures are reduced to singlets. An additional advantage to decoupling is the increase in the signal-to-noise. The signal intensity present across a multiplet is now collected in a single, more intense, peak. Decoupling is typically classified as either homonuclear i.e where the decoupled and observed nuclides are the same, or heteronuclear i.e where the decoupled and observed nuclides are different. A simple way to describe spin decoupling is two spin- ½ nuclei, A and X share a mutual coupling of J Hz. A rf field is applied at the frequency of A spins. This induces a continuous and rapid transition between the α and β states. If the reorientation is really fast relative to the coupling constant, the X spin multiplet structure will collapse into a singlet as the lifetimes of the α and β states are no longer distinguishable. Therefore, if A spins are irradiated with a sufficiently strong pulse and the X spins display no coupling to A, it is said the spins are decoupled.

Scalar spin-spin decoupling is either used for a) selective decoupling of a single resonance to identify any coupling partners or b) non-selective decoupling, which is also known as broadband decoupling typically used to simplify the spectrum by decoupling one nuclide. Broadband heteronuclear decoupling has some practical issues such as decoupling species with larger coupling constants. To ensure decoupling is uniform across the spectrum a rf pulse that is effective over a larger frequency window is applied. A greater decoupling bandwidth can be achieved by increasing the decoupling power. However, increasing the power can ruin both the sample and probe due to increased temperature produced by the rf coil.

To achieve a larger bandwidth for decoupling composite pulse decoupling (CPD) have been introduced. The simplest CPD consists of a series of 90° or 180° pulses. Aside from reducing heating, CPD(s) have other practical uses such as it reduces imperfections in the original rf pulse. Table 2.4.3 shows common composite decoupling pulses. MLEV (Malcolm Levitt) utilises $(90_x°, 180°_y, 90°_x)_n$.[155] The WALTZ (wideband, alternating-phase, low-power for residual splitting) uses $(90_x°, 180°_x, 270°_{-x})_n$.[156] GARP (Globally Optimized Alternating Phase Rectangular Pulse) is a series of pulses that is computer-optimised.[157]

Table 2.4.3 Composite pulse sequences for broadband decoupling.[133]

Sequence	Bandwidth (γB_2) Hz
Continuous Wave	<0.1
MLEV-16	1.5
WALTZ-16	2.0
GARP	4.8

The simplest decoupling method (Figure 2.4.2 (a)) is where the decoupler is on throughout both the delay and acquisition. This method will allow decoupling of the one nuclide therefore, simplifying the spectrum and improving the signal-to-noise ratio. This method also produces a spectrum with some nuclear Overhauser effect (NOE) enhancement. NOE is the transfer of nuclear spin polarization from one population of spin active nuclei to another nuclei. This brings changes in resonance intensities resulting in a non-quantitative NMR spectrum.

The gated decoupling (Figure 2.4.2 (b)) experiment is when the decoupler is gated off before acquisition. Therefore, NOE developed during the delay will enhance the spectrum. The signal to noise enhancement will not be the same for all the nuclei, thus quantitative data will be lost. This results in a coupled spectrum as the decoupler is gated off, with NOE enhancement.

The inverse gated decoupling (Figure 2.4.2 (c)) experiment is designed for quantitative analysis.[158] It achieves this by minimising the signal-to-noise enhancement by NOE. The NOE develops and affects the longitudinal magnetisation, but it does not affect the transverse signals that are detected as the acquisition has already begun. This results in a decoupled spectrum without NOE. As the NOE enhancement is minimised, quantitative information can be yielded from integrating peaks.
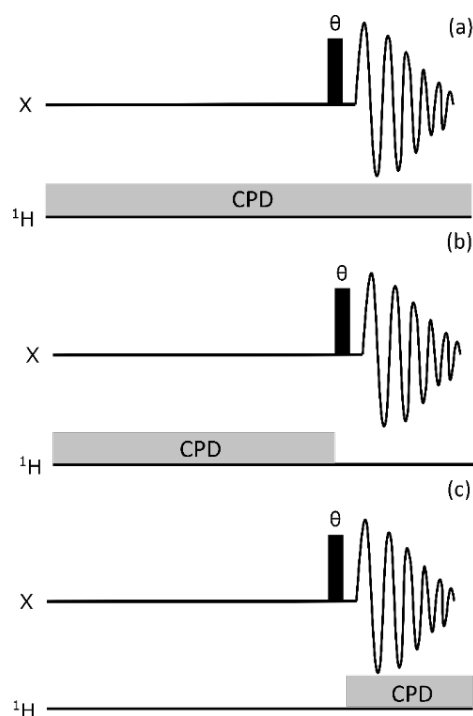
Figure 2.4.2 Heteronuclear decoupling pulse sequences that utilise composite pulse decoupling (a) 100% duty cycle (b) gated-decoupling sequence decoupling sequence (c) inverse-gated decoupling sequence.

Figure 2.4.3 shows the spectra of pyrolysis oil produced from different biomasses. Carbon NMR has a wider chemical shift range compared to ^{1}H NMR however, the ^{13}C NMR spectrum can still be quite crowded. Chemical shifts can provide information on the types of carbon containing compounds present. The chemical shifts for different carbon environments in bio-oils have been proposed by two main studies, these values

50

are summarised in the Table 2.4.4.[145, 146] However, the two studies reported slightly different chemical shifts for the methyoxy/hydroxyl groups and carbohydrates. Carbon NMR is useful when it comes to the analysis of functional groups that are not present in ^{1}H NMR, for example, carbonyl-containing compounds which play a major role in the acidity of pyrolysis oils. ^{13}C NMR has been used to identify carbonyl groups present in different fast pyrolysis products.[159-161] However, there is major overlaps in the carbonyl region of 163 to 215 ppm making it hard to distinguish between aldehydes, ketones, and carboxylic acids.
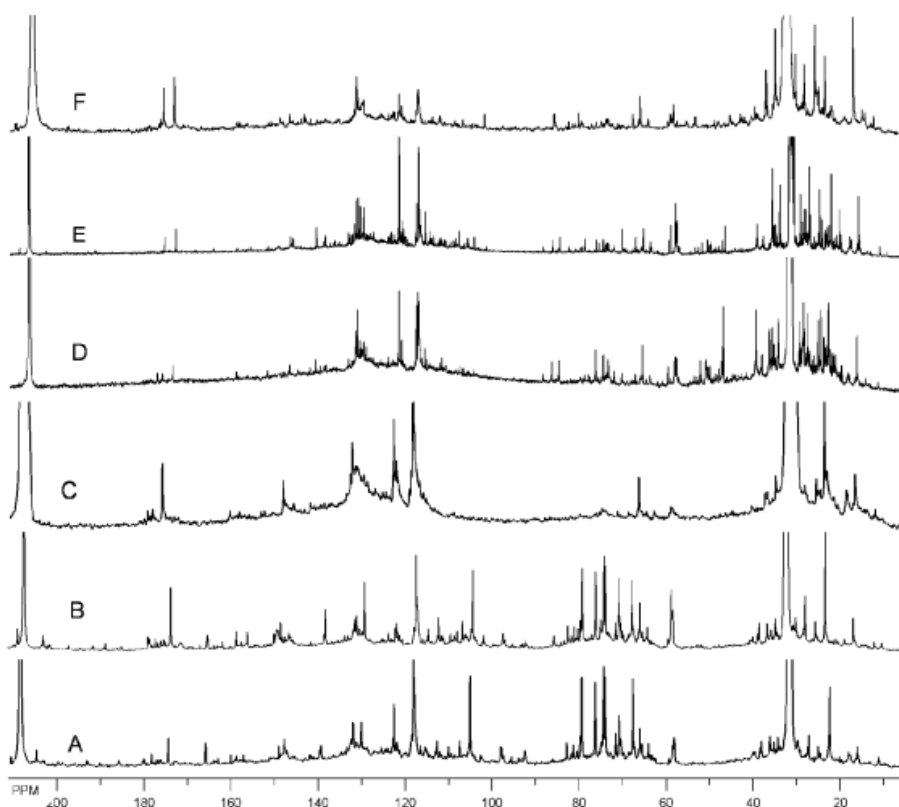
Figure 2.4.3 ^{13}C NMR spectra of bio-oil (A) switch grass, (B) corn stover, (C) alfalfa stem, (D) guayule whole, (E) guayule bagasse, (F) chicken litter [147].

Table 2.4.4 Summary of ^{13}C chemical shift integration regions of bio-oil samples

	Ingram *et al.* [145]	Joseph *et al.*[146]
Functional Group	Chemical Shift Range (ppm)	Chemical Shift Range (ppm)
Alkyl	0 - 54	0 - 54
Methoxy/ Hydroxyl	54 - 84	54 - 70
Carbohydrates	84 - 110	70 - 103
Aromatics/Alkenes	110 - 163	103 - 163
Carbonyls	163 - 215	163 - 215

Even though ^{13}C NMR spectra should be sparser due to the larger chemical shift range, bio-oil model compounds studied showed extensive overlap between the primary, secondary, and tertiary carbons in the region of 0 - 60 ppm making it difficult to distinguished between the different types of alkyl groups.[146] Distortionless Enhancement by Polarization Transfer (DEPT) are a library of experiments that can provide information of specific types of carbon atoms.[162, 163] In DEPT experiments, the proton pulse can be set at 45°, 90° or 135° resulting in experiments named DEPT-45, DEPT-90 and DEPT-135. DEPT-45 detects all protonated carbons, i.e. CH, CH_2 and CH_3, with the same phase. DEPT-90 gives only CH peaks. DEPT-135 detect all protonated carbons, but CH and CH_3 signals are positive while the CH_2 signals are negative. Figure 2.4.4 is a schematic representation of the DEPT experiments.
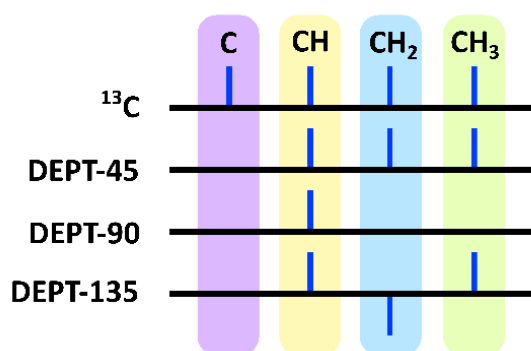
Figure 2.4.4 Schematic representation of ^{13}C NMR spectrum where all carbon peaks are present, DEPT-45 NMR spectrum all protonated carbons peaks are present, DEPT-90 NMR spectrum where only CH peaks, DEPT-135 NMR spectrum where CH and CH_3 signals are positive while the CH_2 signals are negative.

DEPT experiments have been used to investigate further the different types of carbon atoms in bio-oil. A combination of ^{13}C NMR, DEPT-45, DEPT-90 and DEPT-135 was used to analyse bio-oil produced from switchgrass, followed by mathematical manipulations to generate DEPT (Figure 2.4.5.) subspectra for CH, CH_2 and CH_3.[147, 164] The DEPT analysis more easily distinguishes between signals that are overlapped especially the ethers and methoxy groups.[147] A combination of DEPT-90 and DEPT-135 was proven able to identify methyl-aromatics and levoglucosan in bio-oil produced from oakwood and cottonwood.[165] DEPT has also been used in combination with standard ^{13}C NMR to estimate the ratio of non-oxygen-adjacent aliphatic carbons. It was found that the pyrolysis oils derivatised from rye grass had smaller protions of CH_1 compared to pyrolysis oils produced from oak, eel grass and barely straw.[166] Even though DEPT

can simplify the spectrum and reveal more structural information, the structural analysis of pyrolysis products remain highly challenging.
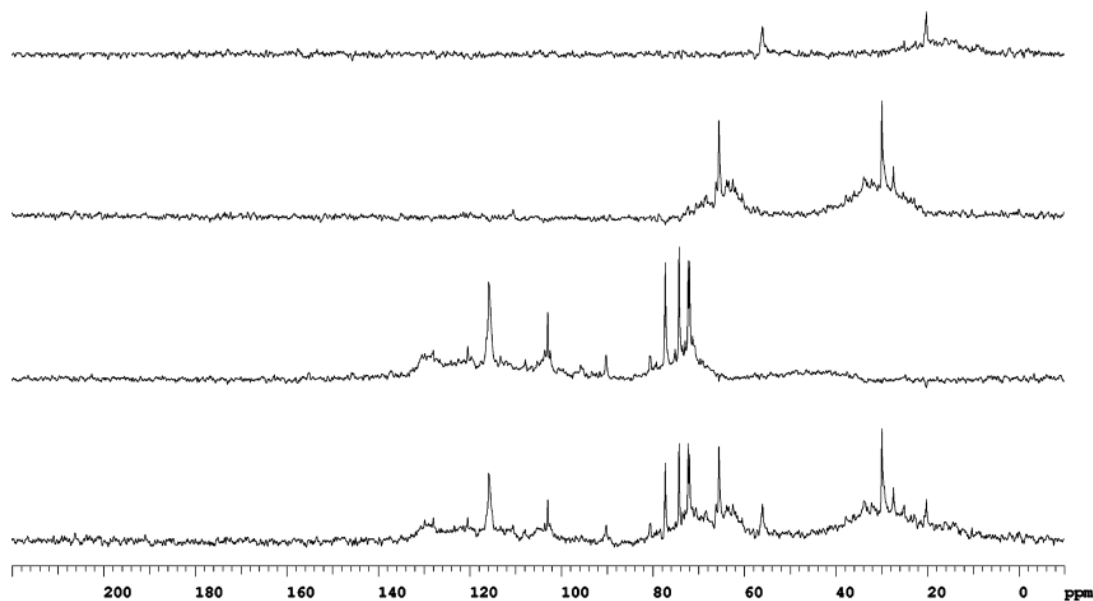
Figure 2.4.5 DEPT spectra of switchgrass bio-oil: (bottom) all protonated C, (second from bottom) CH, (third) CH2 and top (CH3).

Traditional one-dimensional NMR (1D NMR) techniques suffer from overlapping resonances making them difficult to interpret. NMR techniques are not limited to one-dimension, there are also two-dimensional NMR (2D NMR) experiments, and beyond which can provide more structural information. 2D NMR techniques have been used for the analysis of cellulose[167], lignin[167-169], and biomass[170]. An example of a 2D NMR experiment is the Heteronuclear Single Quantum Correlation (HSQC) spectroscopy. HSQC NMR is used to determine single bond correlations, often between proton and carbon, can be applied to other heteronuclei. HSQC has been used to characterise the pyrolytic sugars in three bio-oils.[171]

Figure 2.4.6 shows the 2D ^{1}H-^{13}C HSQC spectra of the fractions of bio-oil based on the different solubilities. The HSQC data provided chemical shift information of 27 different types of C-H bonds, more importantly it showed two different types of methoxyl groups present in the pyrolysis oils, which suggested rearrangements during the thermal treatment.[172, 173]
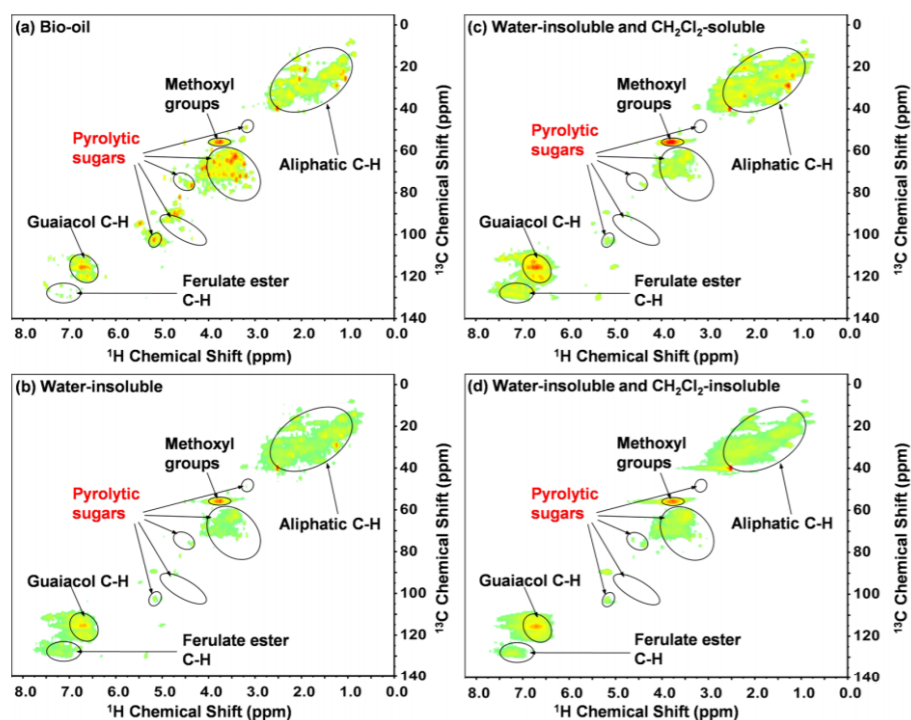
Figure 2.4.6 2D $^1H-^{13}C$ HSQC spectra of bio-oil B (produced from pine wood pyrolysis) and its fractions. (a) bio-oil B; (b) water-insoluble fraction of bio-oil B; (c) water-insoluble and CH_2Cl_2-soluble fraction of bio-oil B; and (d) water-insoluble and CH_2Cl_2-insoluble fraction of bio-oil B.[171]

^{13}C NMR techniques can reveal important structural information and quantification is also important, not all ^{13}C experiments are quantitative dependent on how the decoupling is achieved as described earlier. 1D ^{13}C NMR can be made more quantitative by using inverse gated decoupling experiment. Quantitative NMR experiments can also be denoted as qNMR. However, due to the inherently low signal-to-noise ratio of carbon-13 nuclei, to achieve a spectrum of good quality, usually a relatively long experimental time is required, for example for lignin sample *ca*. 72 hours is required.[174] The experimental time can be reduced by using relaxation agents such as chromium (III) acetylacetonate also known as Cr(acac)$_3$. Typically for absolute concentration determination, a known amount of standard compound is added to the sample, this is known as the internal standard or IS. The internal standard should contain the nucleus of interest and ideally the signal should not overlap with signals of interest. It is also beneficial for the IS to be chemically inert and produce a relatively simple spectrum for example a singlet peak. ^{13}C qNMR has been used to quantify different carbon containing compounds in both woody biomass pyrolysis oils and water-soluble fractions.[175] For carbonyl compounds it is relatively easy to quantify as there is little overlap in the ^{13}C spectrum.[166] However, Stankovikj *et al*. found that ^{13}C NMR techniques underestimated the number of carbonyl groups when compared to titration methods.[175, 176] Liu et al. used ^{13}C qNMR techniques

54

to compare the carbonyl content in raw and upgraded pyrolysis oils produced from rice husk. [177] It was found by NMR that the upgraded pyrolysis oil contained 68.4% less carbonyl compounds.[177] Alternatively, specific functional groups can be tagged by reacting it with a compound containing a different nucleus that is NMR active. For example, hydroxyl groups can undergo acetylation reaction with an alcohol and an acid catalyst followed by ^{13}C NMR analysis.[178-180] The carbon of the methyl and carboxyl groups after acetylation produce signal at 20.8 ppm and ~170 ppm respectively.[180] This region is integrated and compared to a known amount of internal standard (IS) such as trioxane.[180, 181]

Overall, the major advantages of ^{13}C NMR are the wider chemical shift range, resulting in a sparser spectrum and the ability to characterise functional groups, such as carbonyl groups that are not present in ^{1}H NMR. ^{13}C NMR is not limited to one dimension, and 2D techniques like ^{1}H-^{13}C HSQC offers more structural information such as the molecule connectivity compared to 1D ^{13}C NMR alone. It was able to resolve some overlapped peaks and thus confirming species present. However, 2D NMR techniques also suffer from overlapping, where the overlapping signals spread into two dimensions. In complex mixtures such as pyrolysis oils, the poor resolution due to overlapping can still make HSQC difficult to analyse. Quantification of compound is important, however, not all ^{13}C NMR experiments are suitable for quantification and thus, the choice of decoupling methods must be considered. For quantification, due to the low gyromagnetic ratio and natural abundance, toe achieve good signal-to-noise this typically experiments will take longer.

Pyrolysis oils are acidic due to the oxygen-containing compounds present, in an ideal world, the identification and quantification of these compounds by NMR could be detected using ^{17}O NMR. However, due to the low natural abundance of ^{17}O and negative gyromagnetic ratio, the receptivity would be too low. More importantly, ^{17}O nuclide has a spin quantum number I of 5/2 and is therefore quadrupolar, this results in broad signals. Any data collected would not be suitable for quantification. Alternatively, functional groups can be selectively reacted with reagents that contain NMR active nuclei such as ^{31}P and ^{19}F. Therefore, only specific functional groups of interest will be present in the NMR spectrum, this greatly reduces the number of signals and thus the complexity of the spectrum. The following section explores how derivatisation can be used to tag specific groups follow by NMR analysis.

2.4.3 ^{19}F NMR Spectroscopy

Like ^{1}H and ^{13}C nuclei, fluorine nuclei or ^{19}F, also has a nuclear spin of ½ making it NMR active. ^{19}F NMR has similar receptivity as ^{1}H NMR, this is due to the 100% natural abundance and high gyromagnetic ratio (Table 2.2.1). ^{19}F NMR also has a very large chemical shift range −500 to 500 ppm making the spectrum less crowded. One of the major limitations of ^{1}H NMR and ^{13}C NMR is the overlapping of signals resulting in a crowded spectrum. Spectra can also be simplified by looking at certain functional groups only, in this case the understanding the oxygen-containing compounds is crucial for ageing and upgrading of pyrolysis oils. Pyrolysis-oils naturally contain no fluorinated compounds; therefore, fluorine-containing agents can be used to derivatise compounds of interest, and the resulting ^{19}F NMR spectrum will directly correlate with the fluorine derivatives. Different derivatisation methods have been developed for the ease of identifying and quantifying of oxygen-containing compounds. This section will explore the different derivation methods as well as how ^{19}F NMR is applied to the characterisation of pyrolysis oils.

^{19}F NMR has been explored to analyse the types of hydroxyl groups in biomass, lignin and pyrolysis oils.[127, 182] The hydroxyl groups are reacted with a derivatisation agent followed by the ^{19}F qNMR analysis of the derived products. Barrelle *et al.* developed methods to quantity the phenolic and aliphatic hydroxyl groups. The hydroxyl groups would undergo fluorobenzylation producing fluorobenzyl ethers and fluorobenzoic acids respectively.[183] The internal standard 2-fluorobenzoic acid was used to quantify these products using ^{19}F qNMR. However, this method was rather cumbersome and significant overlap between the derivatisation agent and phenolic groups were observed.[184] Trifluoroacetic anhydride has been introduced as an alternative derivatisation reagent due the ease of use.[127, 182] The general reaction scheme is shown in Figure 2.4.7. 2-pentanol was used as the internal standard for ^{19}F qNMR analysis because it does not overlap any signals of interest.[127] One major advantage of this method is the trifluoroacetic anhydride has three equivalent fluorine nuclei in the compounds.[127, 185] This results in a higher sensitivity, and thus it can determine hydroxyl groups of minor species in a sample. However, the chemical shift range for the derivatised products spanned only *ca*. 2 ppm, making the spectrum highly crowded.[185] Kenny *et al*. proposes an alternative derivatisation agent, pentafluoropyridine can be used to tag hydroxyl groups in lignin.[186, 187] The internal standard 4,4-difluorobenzophenone was used for ^{19}F qNMR analysis. This derivatisation process was found to be safer due to low toxicity.[53]
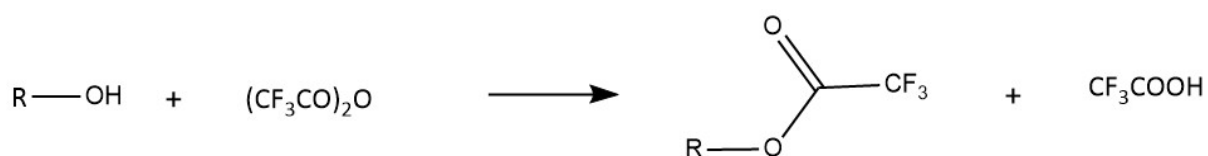
Figure 2.4.7 Reaction scheme of organic compound with -OH functional group reacting with trifluoroacetic anhydride to form the fluorine derivatised alcohol compound. The R group are residues of phenols, alcohols, aldehydes, sugars, or carboxylic acids.

Aside from ^{19}F derivatisation of hydroxyl groups in pyrolysis oils, fluorine-containing agents such as pentafluorophenyl hydrazine has been used to derivatise carbonyl groups in lignin.[188, 189] It was found that the derivatisation compound produced a rather complex spectrum.[55] This was because the phenyl ring contains non-equivalent fluorine atoms. Fluorophenyl hydrazine exhibits similar structural properties to pentafluorophenyl hydrazine but produces a simpler ^{19}F NMR spectrum.[190] The single peak produced by fluorophenyl hydrazine makes it simpler to quantify the carbonyl groups in the lignin by comparing the integrals to an internal standard.[191] Trifluoro compounds such as 4-(trifluoromethyl)phenyl hydrazine have a threefold increase NMR sensitivity without the loss of resolution compared to monofluoro compounds.[183]
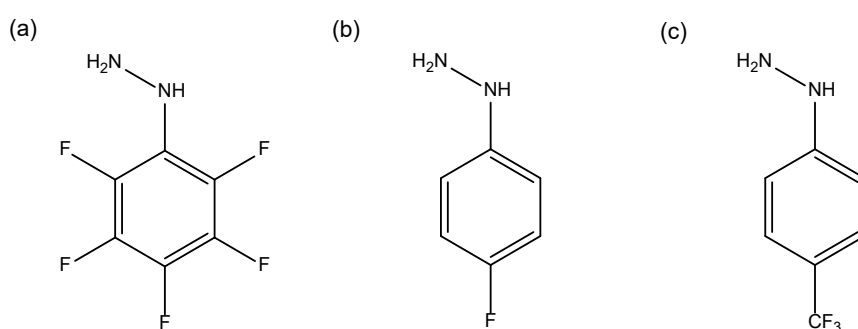
Figure 2.4.8 (a) pentafluorophenyl hydrazine (b) fluorophenyl hydrazine (c) 4-(trifluoromethyl)phenyl hydrazine

Huang *et al.*[192] used 4-trifluoromethylphenylhydrazine derivatisation methods (Figure 2.4.9) to characterise carbonyl groups pyrolysis oils followed by ^{19}F NMR spectroscopy. The derivatisation was conducted using 4-(trifluoromethyl)phenyl hydrazine over 24 hours in the dark. For the ^{19}F NMR method the bio-oil was dissolved in 500 µL of dimethylformamide (DMF), followed by 1 mL of a 50:50 (v/v) DMF-water. Constant *et al.* [193] optimised the method of the derivatisation of carbonyl groups using 4-(trifluoromethyl)phenyl hydrazine. In this study the derivatisation was conducted directly in the NMR tube, to avoid potential loss and other inaccuracies. Hydrazine reacts with

57

the carbonyl group to form a hydrazone with both E and Z isomer; the reaction scheme is shown Figure 2.4.9. The E isomer was usually found to be more stable hence being the major isomer present. Model compounds, industrial humin and kraft lignin samples were used in the study. Hexafluorobenzene was used as an external standard for chemical shift calibration. The chemical shifts (Figure 2.4.10) for non-conjugated carbonyls can be differentiated from the conjugated carbonyls. The conjugated carbonyls are found more downfield. Aliphatic carbonyls are observed between −59.3 and −59.5 ppm. The conjugated carbonyls are observed between −59.4 and −59.8 ppm. There are some overlap between the two regions, mainly the Z-hydrazone formation which can be seen in Figure 2.4.11(b).
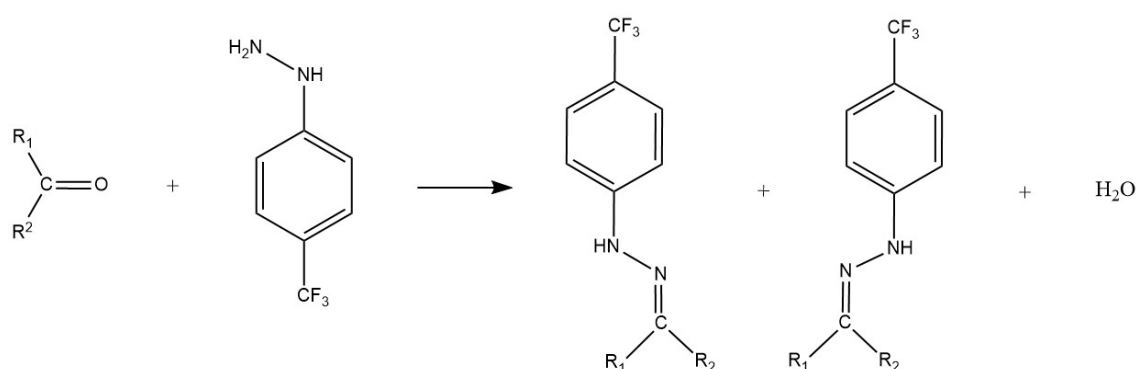
Figure 2.4.9 Reaction scheme of organic compound with carbonyl (C=O) functional group reacting with 4-(trifluoromethyl)phenylhydrazine to form the fluorine derivatised carbonyl compounds also known as hydrazone. Where the R group are residues of phenols, alcohols, aldehydes, sugars or carboxylic acids. For asymmetrical ketones, both E and Z isomers are typically observed. [193]
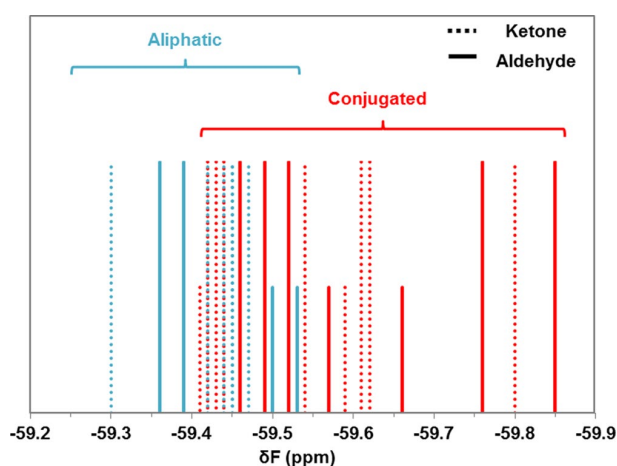
Figure 2.4.10 ^{19}F chemical shifts of the E,Z-hydrazones obtained after the reaction of a library of carbonyl-containing compounds with 4-(trifluoromethyl)phenyl hydrazine. The short lines represent the Z-hydrazones and the longer ones represent the E-hydrazones.
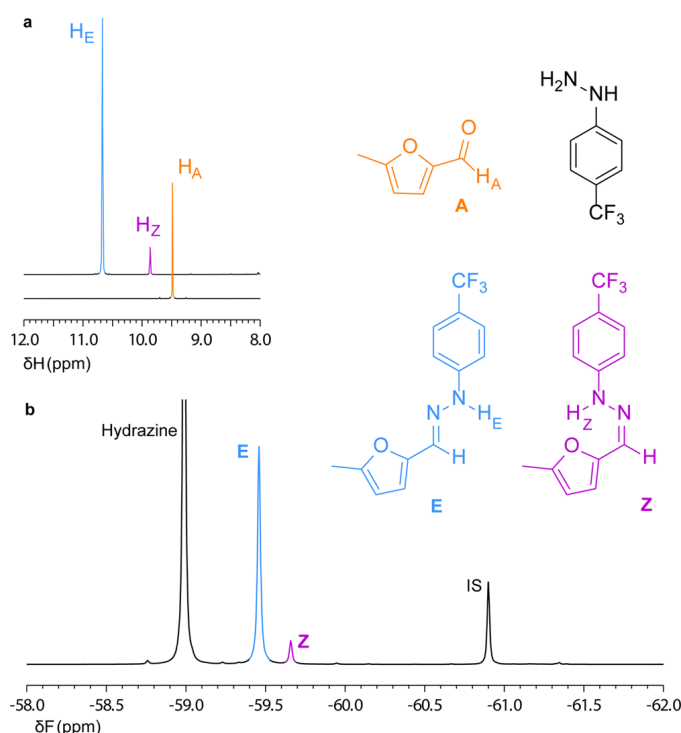
Figure 2.4.11 (a) ^{1}H NMR spectrum (8 to 12 ppm) of reaction mixture of 5-methylfuran-2-carbaldehyde and 4-(trifluoromethyl)phenyl hydrazine stacked on top of the spectrum of 5-methylfuran-2-carbaldehyde. (b) ^{19}F NMR spectrum of the reaction of 5-methylfuran-2-carbaldehyde and 4-(trifluoromethyl)phenyl hydrazine after derivatisation. [193]

Typically, the quantification of carbonyl groups in pyrolysis oils has been carried out using methods such as oximation followed by titration. The reaction is carried out for 48 hours, the hydroxylamine hydrochloride reacts with the carbonyl groups to form an oxime and HCl. Pyridine is added to mop up the HCL. The pyridine hydrochloride is titrated with NaOH, where the endpoint is around pH 4.7.[194] For the ^{19}F qNMR analysis of carbonyl groups, a ^{19}F NMR with a 90° pulse without proton decoupling is used. A large number of scans, typically >256 scans, and a long relaxation time *ca.* 25 s are typically required to achieve good signal-to-noise ratio and full relaxation of fluorine nuclei. To reduce the acquisition time, a relaxation agent such as chromium (III) acetylacetonate is added, this reduces the T_1 relaxation time of the fluorine nuclei about 10-fold. Different internal standards have been suggested, such as, 3-trifluoromethoxybenzioc acid and 1-methyl-4-(triflouromethyl)benzene. 1-methyl-4-(triflouromethyl)benzene was preferred as it was found to be more inert.[192] ^{19}F NMR methods have been compared with standard oximation followed by titrations. Results from both methods are summarised in the Table 2.4.5. The table shows that both methods produced comparable data for the total carbonyl content. But the advantage of using ^{19}F NMR methods compared to the traditional laborious method is the reduction of reaction time from 48 hours to 24 hours.

^{19}F NMR techniques can also distinguish between different types of carbonyl groups such as aldehydes, ketones and quinones.

Table 2.4.5 Summary of results from Huang et al. for the comparison of determination of carbonyl content using ^{19}F NMR and oximation methods.[192]

Sample	^{19}F NMR determination of carbonyl group content (mmol g^{-1})			Oximation determination of carbonyl group content (mmol g^{-1})
	Ketone/ Aldehyde	Quinone	Total	
Kraft lignin pyrolysis oil	1.04	0.34	1.38	1.32
Kraft lignin + ZSM-5 pyrolysis oil	0.90	0.37	1.27	1.20
Loblolly pine pyrolysis oil	4.21	0.53	4.74	4.68
Loblolly pine + ZSM-5 pyrolysis oil	3.29	0.88	4.17	4.05
Loblolly pine residue pyrolysis oil	3.27	0.53	3.80	3.71
Loblolly pine residue + ZSM-5 pyrolysis oil	3.31	0.58	3.89	3.77
P-1 (hardwood pilot-plant pyrolysis oil)	3.27	0.47	3.74	3.70
P-2 (hardwood pilot-plant pyrolysis oil)	3.53	0.62	4.15	3.99
P-3 (pine pilot-plant pyrolysis oil)	3.96	0.68	4.54	4.50

Overall, different ^{19}F-containing agents have been explored to derivatise hydroxyl groups and carbonyl groups. The major advantage of these methods is isolating specific functional groups which result in a sparser spectrum. The derivatisation methods have shorter experimental time compared to titration methods. ^{19}F NMR analysis also has its advantages of a large chemical shift range making it easier to analyse as well as the higher signal-to-noise ratio making it suitable for quantification.

Hydroxyl groups are oxygen-containing compounds that contribute to the acidity of bio-oils, therefore, understanding what type of hydroxyl groups are present and how much is in a sample is vital. However, hydroxyl groups are difficult to analyse using standard ^{1}H NMR. Hydroxyl protons are either labile protons, which exchange in aqueous solvents or otherwise highly overlapped with other signals. ^{19}F NMR methods have also been explored for the characterisation of hydroxyl groups. The process can be fairly long *ca.* 24 hours for the derivatisation alone, moreover, the overlap in the NMR spectrum makes

60

it difficult to analyse. In the next section the use of ^{31}P derivatisation agents and ^{31}P NMR is explored.

2.4.4 ^{31}P NMR Spectrocopy

Phosphorus nuclei or ^{31}P have a spin ½ making it NMR active. [31]P nuclei is 100 % naturally abundant, although the receptivity ratio is around 15% of the ^{1}H NMR due to its lower gyromagnetic ratio. ^{31}P NMR exhibits a large chemical shift range −200 to 240 ppm (Table 2.2.1). Phosphorus-containing compounds are not often found in bio-oils but can be added in a controlled manner. The relationships between the chemical shifts and structures, including the stereochemistry of organophosphorus compounds can be identified [195].In this section, the use of ^{31}P-containing compounds as tagging agents and thus the ^{31}P NMR analysis of hydroxyl groups will be explored.

The application of phosphorus-31 nuclear magnetic resonance (^{31}P NMR) has been used as a tool to quantify hydroxyl groups in coal[196], lignin and biodiesel[197], and more recently it has been applied to pyrolysis oil.[128] There are suitable ^{31}P-containing derivatising agent which can react with the hydroxyl group under mild conditions such as room temperature with an organic base. Model organic compounds, including aliphatic alcohols, aromatic acids, aliphatic acids, phenols, amines, and thiols have been derivatised by five different trivalent ^{31}P agents. All ^{31}P agents were synthesised from the reaction of diols and PCl_3[196, 198] with a general reaction scheme shown in Figure 2.4.12. The 5 chlorophospholanes synthesised for derivatisation applications shown in Figure 2.4.13 suitable derivatisation agents, and the derivatives were successfully characterised using ^{31}P NMR. However, the derivatised phenol and alcohol chemical shift overlapped, especially in the acid derivatives using the reagents Figure 2.4.13 structures (b) and (e).
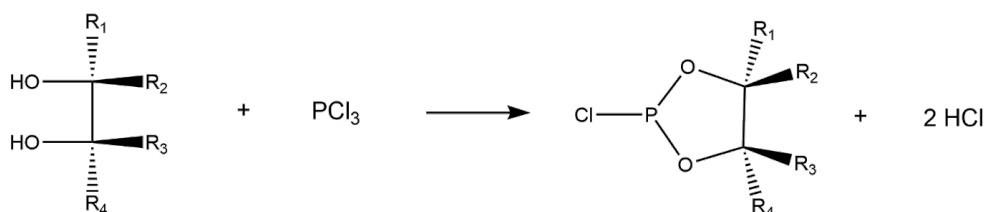
Figure 2.4.12 Reaction scheme of a generic diol reacting with phosphorus trichloride to produce possible phosphorus-containing derivatisation agents.
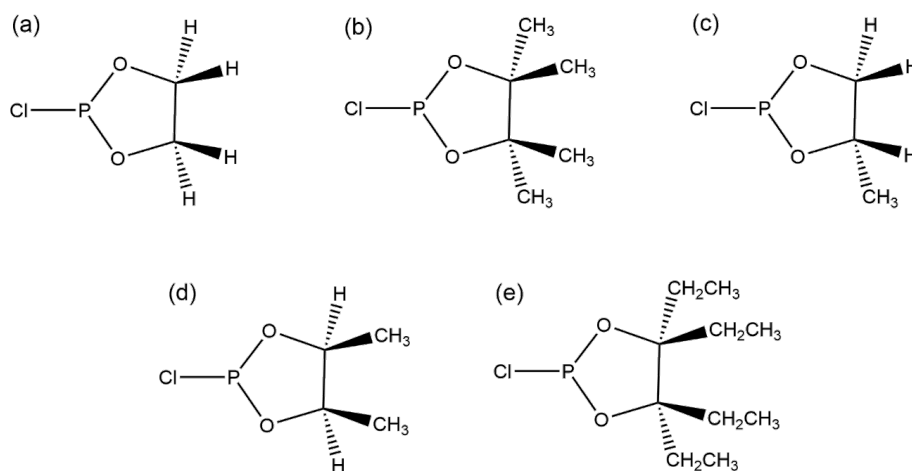
Figure 2.4.13 Five chlorophospholanes produced by reaction of diol and phosphorus trichloride as shown in reaction scheme (Figure 2.4.12) (a) 2-chloro-1,3,2-dioxaphospholane, (b) 2-chloro-4,4,5,5-tetramethyl-1,3,2-dioxaphospholane, (c) 2-chloro-4-methyl-1,3,2-dioxaphospholane, (d) 2-chloro-4,5-dimethyl-1,3,2-dioxaphospholane and (e)2-chloro-4,4,5,5-tetraethyl-1,3,2-dioxaphospholane.

Similar techniques were then applied in wood chemistry to characterise hydroxyl groups in lignin[199], where a collection of papers[200-205] utilised 2-chloro-1,3,2-dioxaphospholane (Figure 2.4.13 (a)) (CDP) as the phosphorus agent. This is shown in the reaction scheme Figure 2.4.14. This method aimed the characterise different hydroxyl groups using ^{31}P NMR of model compounds containing guaiacyl, syringyl, phenols, and carboxylic acids. The reaction was carried out in a pyridine and deuteriated chloroform solution. Pyridine is used as the organic base for the reaction. The role of the organic base is to mop-up the hydrogen chloride formed, driving the reaction to completion. The role of the deuteriated chloroform is to facilitate solubility, preventing the pyridine-HCl salt from precipitating[206] and acting as an NMR locking agent.[202] Various solvent systems can be chosen depending on the solubility of the substrate being analysed. Studies where lignins are less soluble in pyridine and chloroform mixtures utilise N,N-dimethylformamide (DMF) to facilitate solubility.[207] The main disadvantage of using CDP as the derivatisation agent was that the ^{31}P signal of e.g. derivatised phenolic, syringyl and primary hydroxyl would overlap.[208]
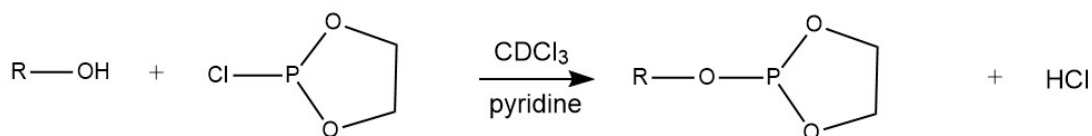
Figure 2.4.14 Reaction scheme of an organic compound with -OH functional group reacting with 2-chloro-1,3,2-dioxapholane (CDP) to form the phosphorus derivatised alcohol compound and hydrogen chloride. R group are residues of phenols, alcohols, aldehydes, sugars, or carboxylic acids.

A solution to the overlap in the ^{31}P NMR spectrum was replacing the CDP with a different phosphorus reagent 2-chloro-4,4,5,5-tetramethyl-1,3,2-dioxaphospholane (TMDP).[209] TMDP can react with various hydroxyl functional groups, and a generic reaction scheme is shown in Figure 2.4.15. Nowadays TMDP has been widely used in the biorefinery research to characterise and quantify the hydroxyl groups present.[128, 210] Protocols have been developed to analyse hydroxyl content of both lignin and tannin.[209] Lignin/tannin samples were prepared in a solvent mixture of deuteriated chloroform and pyridine with a volume ratio of 1.6:1. An excess of TMDP was added to ensure that all hydroxyl groups were completely phosphitylated. After a homogenous mixture has formed, it should be analysed straight away by ^{31}P NMR. TMDP has been used for other applications other than analysing lignin structure. More recently, it has been used to analyse biodiesel glycerol [197], biofuel precursors[206], and pyrolysis oil.[128]
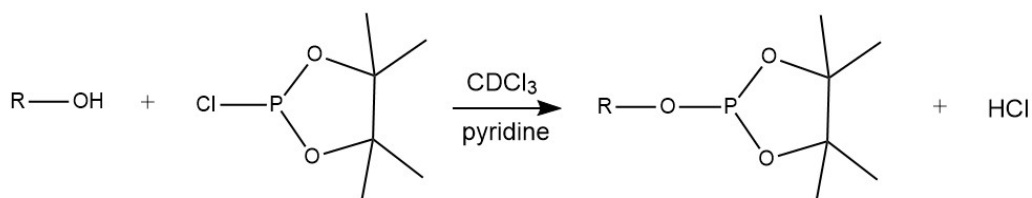
Figure 2.4.15 Reaction scheme of organic compound with -OH functional group reacting with 2-chloro-4,4,5,5-tetrmethyl-1,3,2-dioxapholane (TMDP) to form the phosphorus derivatised alcohol compound and hydrogen chloride. Where the R group consists of residues of phenols, alcohols, aldehydes, sugars, or carboxylic acids.

A known amount of internal standard can be added to the sample for absolute quantification. The internal standard must demonstrate stability and satisfactory resolution from the regions of interest in a ^{31}P NMR spectrum. Benzoic acid, cholesterol and cyclohexanol can all be derivatised. The derivatised products have all been previously used as an internal standards in ^{31}P NMR analysis of lignin. [207, 209] However, in some cases these internal standards overlapped with the peaks of interest. As a result, there is an underestimation of hydroxyl groups in samples. To address this issue,
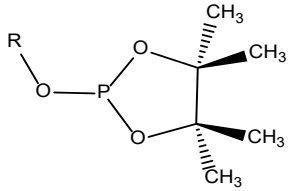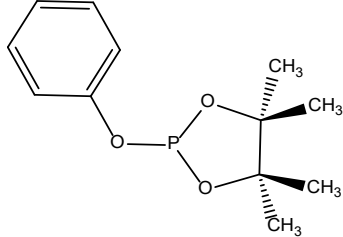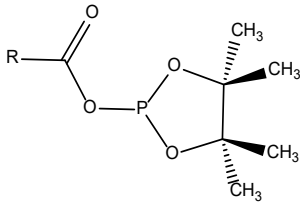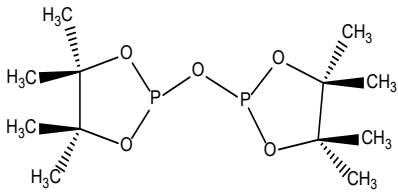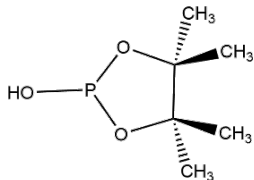
Ragauskas *et al.*[211] introduce *endo-N*-hydroxy-5-norbornene-2,3-dicarboximide (NHND) as an alternative internal standard. NHND was introduced so the baseline could be fully resolved from the lignin-derived resonances which allows for better quantitative analysis. Triphenylphosphine oxide (TPPO) has also been used as an internal standard for quantification in ^{31}P NMR.[212] Results also showed that the NHND was unstable after 12 hours of in-situ monitoring. Overall, studies found that the choice of phosphitylation agent and internal standard are key factors when looking at the qNMR of hydroxyl groups in bio-oil.

As mentioned in Section 2.4.2 not all pulse sequences are suitable for the acquisition of quantitative data. Typically, an inverse gated decoupling pulse sequence is used for qNMR. Firstly, decoupling allows multiplet structures to be simplified, improving the signal to noise ratio. Secondly, an inverse gated sequence is used to eliminate the nuclear Overhauser effects for quantitative purposes.[133] Extensive studies have been carried out to understand the spin-lattice relaxation times of ^{31}P.[213, 214] A commonly used relaxation agent in the study of lignin is chromium(III) acetylacetonate[213-215]. This typically reduces the relaxation delay from about 5 times 30 s to ≥10 s, which is required to ensure complete spin relaxation before applying other rf pulses. Some recommended parameters have been suggested in the ^{31}P protocol which are shown Table 2.4.6.[209] Typical chemical shift range of different -OH groups are shown in the Table 2.4.7. The derivatised product of TMDP reacted and water was shown to tautomerize. One of the products can be further reacted with TMDP resulting in a di-dervatised water as shown in Figure 2.4.16.

Table 2.4.6 Recommended ^{31}P NMR parameter conditions.[209]

Spectrometer Type	Bruker (this is noted as nomenclature below is manufacture specific)
Pulse program	Inverse gated decoupling pulse (zgig)
Nucleus	^{31}P
Spectral width (SW)	100 ppm
Relaxation delay (D1)	≥10 s
Number of scans (NS)	64 or more
Centre of the spectrum (O1P)	140 ppm

B.Tang, PhD Thesis, Aston University, 2024.

Table 2.4.7 Typical chemical shift range for different -OH functional groups, with examples structures derived with TMDP.

Hydroxyl Type	Chemical Shift Range (ppm)	Examples of derived structures with TMDP
Aliphatic	150.0 -145.5	
Phenolic	144.7 - 137.4	
Carboxylic acid	136.6 - 133.6	
TMDP	132.2	
Water	16.0	

B.Tang, PhD Thesis, Aston University, 2024.
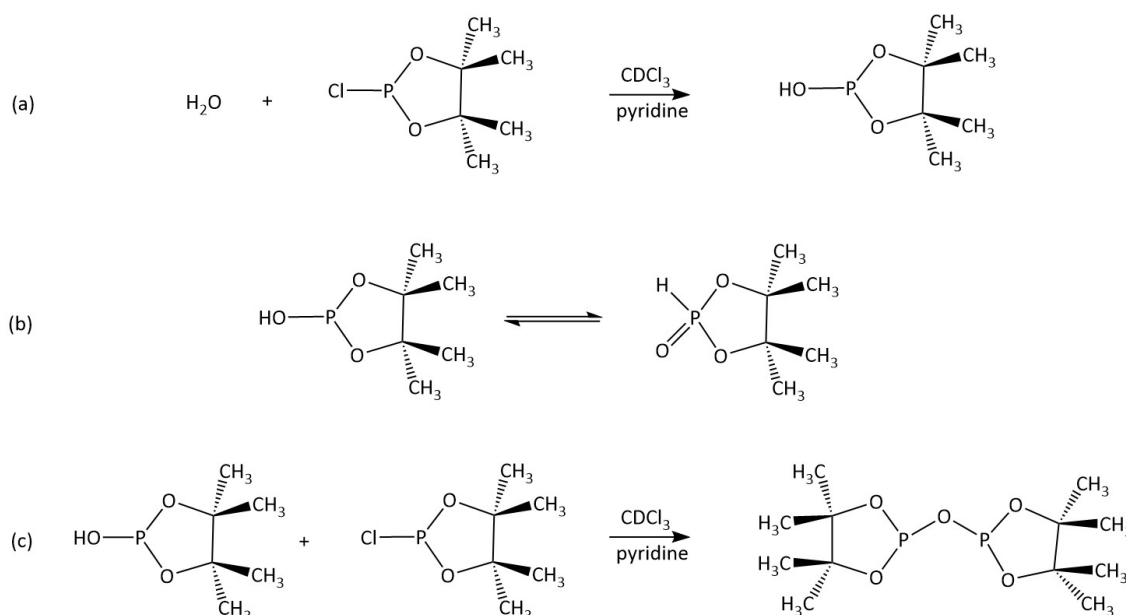
Figure 2.4.16 (a) Reaction of water with TMDP (b) tautomerization of the water derivatised TMDP and (c) the reaction of the water derived TMDP with TMDP.

TMDP derivatisation techniques have been successfully applied to bio-oils produced using loblolly pine as a feedstock.[128] Figure 2.4.17 shows the ^{31}P NMR spectrum of bio-oil produced from loblolly pine with cyclohexanol as an internal standard. This shows a larger chemical shift range compared to ^{19}F derivatised hydroxyl groups making it sparser and easier to analyse. More recently, this technique has been translated to low-field NMR for the quantitative analysis of alcohol groups in lignin.[216]
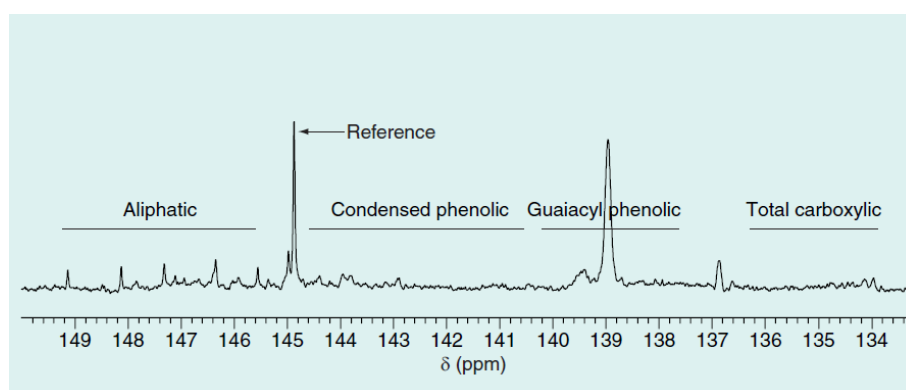
Figure 2.4.17 ^{31}P NMR spectrum of bio-oil from loblolly pine derivatised using TMDP. Cyclohexanol was used as the internal standard/ reference at 145 ppm[128] (blue background present in the original paper).

The major advantage of using ^{31}P NMR is the focus on types of hydroxyl groups present in pyrolysis oil samples. ^{31}P NMR has a larger chemical shift range reducing the

crowdedness of the spectrum and making it easier to analyse. It has a high signal-to-noise ratio which makes it suitable for quantification. The derivatisation of hydroxyl groups is quick (15 mins) compared to ^{19}F methods discussed in Section 2.4.3 (1 hour+). Nonetheless, every technique has its limitations. The major limitation is that the TMDP is not always commercially available, and the prohibitive cost is currently around £57.00/g or *ca.* £5.70 per sample in the United Kingdom. Therefore, this limits its uses in an industrial setting for 'screening' purposes. It is also very hydroscopic meaning that it is ideally handled in an inert environment. Another problem is that the derivatised samples are unstable after a long period (>12 hours), meaning that ^{31}P NMR analysis is required almost instantly after derivatization. Overall, the derivatisation of hydroxyl groups using phosphorus agents and using ^{31}P NMR as a technique to quantify various hydroxyl groups has been successful. However, spectral overlap can still be a problem when it comes to the analysis of pyrolysis oils. Aside from multinuclear NMR, there are also multidimensional NMR tools, in which Section 2.4.2 introduced a 2D technique known as HSQC. The following section explores multidimensional NMR tools and how they are used to characterise pyrolysis oils.

2.4.5 Diffusion-Ordered Spectroscopy

All molecules in liquid exhibit Brownian motion which is the random motion of particles suspended in a liquid. The random motion of particles is driven by the thermal energy of the system. This motion depends on physical parameters such as the size and shape of the molecule, such that larger the molecule the slower it moves, and small the molecule the quicker it moves. How far the molecules travel in the liquid in a given time will depend on its diffusion coefficient. The diffusion coefficient can be estimated by the Stokes-Einstein equation[217]:

$$D = \frac{k_b T}{6\pi\eta r_H} \qquad\qquad \text{Equation 2.4.1}$$

The equation predicts the diffusion coefficient, *D*, of a hard spherical particle with the radius, r_H, at infinite dilution in a continuum fluid with viscosity, η, at a given temperature. T. The thermal energy of the system, $k_b T$, this is balanced by the friction acting on the particle, $6\pi\eta r_H$. The original Stokes-Einstein equation are based on two assumptions: first, the solvent is a continuum, and second, that all solutes are spherical.

Pulsed-field gradient NMR (PFG-NMR) can be used to acquire self-diffusion data of different species. When magnetic field gradient, g_z, is applied along the z-axis, it adds a gradient term to the B in the Larmor Equation *2.2.3* to give the equation:

$$\omega = -\gamma(B + zg_z)$$
Equation 2.4.2

The gradient is applied for a duration, *δ*, this introduces an additional evolution of the phase of signals. The spins revert to the original precession frequency when the gradients are switched off. The positions of the spins are labelled based on the Larmor frequency and the phase angles that depend linearly on their height in the sample tube. The most basic pulse sequence used in diffusion NMR experiments is the pulse field gradient spin echo (PFGSE) shown in Figure 2.4.18. Without the gradients, the experiment is simply a spin-echo experiment where the chemical shift evolution is refocused and the signal detected is attenuated only by transverse relaxation. In this sequence, a 90° pulse is applied, followed by the first gradient that winds in a helix of phase into the sample. A 180° pulse is then applied to invert and refocus the chemical shift evolution. The second gradient pulse that has the same magnitude and duration as the first which unwinds the helix. If the spins remain in the same place as when the first gradient was applied, the signals completely refocus. The time between the two gradients is the diffusion delay period (*Δ*).
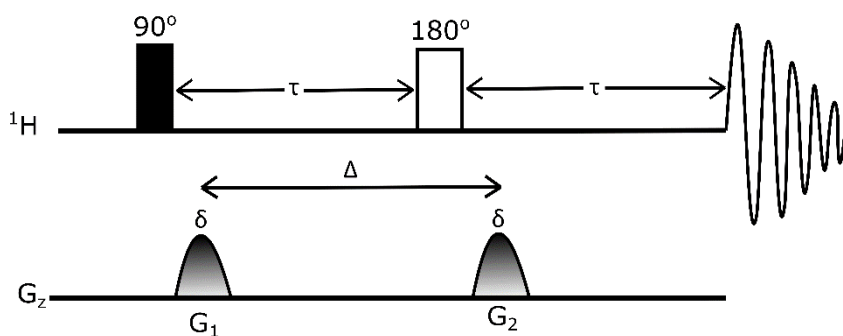
Figure 2.4.18 Pulse field gradient spin echo sequence.

Diffusion-ordered spectroscopy experiments are useful for the analysis of mixtures. There are some practical considerations. Diffusion is sensitive to both sample temperature and solvent viscosity; therefore, these must be kept constant during the experiment. The longer the diffusion delay period, the more time the molecule has, to travel through the NMR tube. As a result, long delays can lead to an increase in signal attenuation. However, increasing the diffusion delay, *Δ,* will induce attenuation from T_2

relaxation loss therefore, it is common to increase the diffusion gradient strengths while not altering the diffusion delay period. The signal attenuation (*S*) can be quantified using the Stejskal-Tanner equation[218]:

$$S = S_0 e^{-D\gamma^2 g^2 \delta^2 \Delta'}$$

Equation 2.4.3

The factors that control signal attenuation are the diffusion coefficient, *D,* the gyromagnetic ratio of the observed nuclide, *γ*, the strength of the applied gradient pulse, *g*, the length of the gradient pulse, *δ*, and the effective diffusion delay (*Δ'*) which allows for the effects of diffusion during the gradient pulse. The diffusion coefficient *D* can be calculated by linear plot of ln(*S/S₀*) vs gradient strength squared where the gradient of the straight line yields the diffusion data. In the spin-echo sequence, the key disadvantage is phase evolution during the diffusion delay period. When the 90° pulse is applied, the magnetisation is in the transverse plane which leads to the distortion of the signal. Therefore, the pulse field gradient stimulated spin echo sequence (PFGSTE) was introduced to overcome the issue. In this sequence (Figure 2.4.19) the 180° pulse is replaced by two 90° pulses. The magnetisation is only in the transverse plane for a duration of the first gradient pulse that is relatively short. It is flipped by the second 90° pulse, as a result, for the remainder of the diffusion period *Δ* the bulk magnetisation is in the longitudinal plane. The signal loss now depends on the T_1 relaxations and does not phase-evolve.
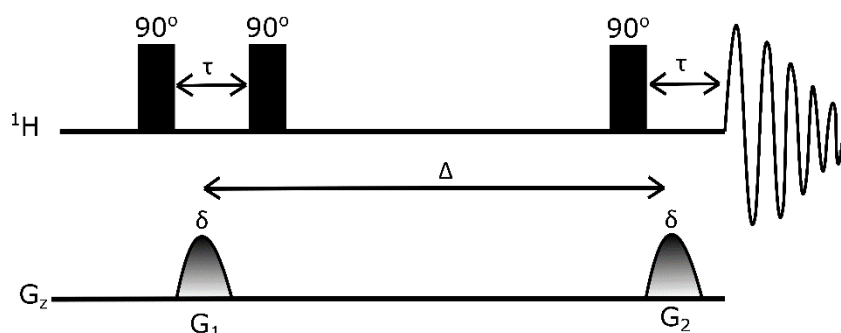
Figure 2.4.19 Pulse field gradient stimulated echo (PFGSTE) sequence. Each gradient pulse has the strength "g" and has a duration of δ. The diffusion delay time is Δ and τ is the variable diffusion delay parameter.

Diffusion NMR data are often presented in two-dimensional spectrum this is known as diffusion-ordered spectroscopy (DOSY).[219] One way to present the diffusion coefficient data is a pseudo-2D contour representation in which one axis presents the chemical shift and the other corresponds to the diffusion coefficients as shown in Figure 2.4.20. This

has been termed diffusion-ordered spectroscopy or DOSY. The data collected is a collection of 1D spectra recorded with increased gradient amplitudes. To extract the diffusion coefficient, the data-fitting process for individual peals involves the measure of decay of signal intensity as a function of applied gradient strength.
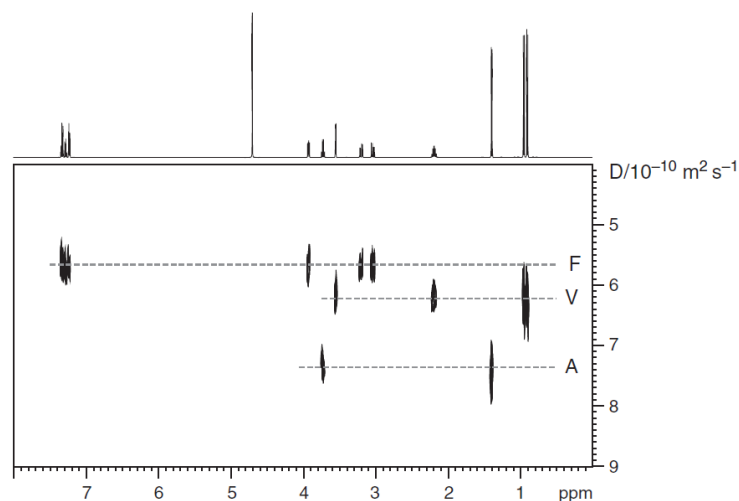
Figure 2.4.20 Example of 2D DOSY spetrum. The spectrum shows the separation of resonance from a mixture of L-amino acids, alanine (A) 7.73 × 10⁻¹⁰ m²s⁻¹, valine (V) 6.25 × 10⁻¹⁰ m²s⁻1 and phenylalanine (F) 5.67 × 10⁻¹⁰ m²s⁻¹ in aqueous solution at 298 K according to their diffusion coefficients[133].

Diffusion-ordered spectroscopy has been applied to the analysis of pyrolysis oils and extract additional information such as approximate molecular weights of species present. Mullen *et al.* [220] studied switchgrass pyrolysis oil produced at three temperatures (500°C, 600°C and 700°C). The diffusivity values were used to estimate the molecular weights of species using the Stokes-Einstein-Gierer-Wirtz-Estimation (SEGWE) approach.[221, 222] The study also showed that diffusion NMR techniques provide more information than typical pyrolysis oil characterisation protocols, including elemental analysis, GC/MS, GPC, and other standard NMR experiments (^{1}H and ^{13}C NMR). Figure 2.4.21 shows ^{1}H DOSY plot of the bio-oil produced at 500°C, 600°C and 700°C. However, due to the severely overlapping signal in the ^{1}H spectrum like shown in Figure 2.4.21, the diffusion coefficients could be misleading and should not be overinterpreted.

Figure 2.4.21 ^{1}H DOSY plot of the switchgrass bio-oil produced at 500°C (a), 600°C (b) and 700°C (c)

2.4.6 Coupled NMR Experiments

NMR experiments suffer from two general drawbacks. First, NMR spectroscopy is inherently insensitive, as discussed in Section 2.3. Second, spectra rapidly become crowded as peaks fill a limited chemical shift space and the fine structure introduced by couplings only further reduces resolution. There is a general solution. If different

71

functional groups can be selectively reacted, or derivatised, with reagents containing NMR-active nuclei other than ^{1}H, resolution can be greatly improved. First, ^{19}F and ^{31}P, for example, are more sensitive nuclei than ^{13}C. Second, only a sub-set of components of the mixture are represented in the final spectrum, with one peak per distinct species. In recent years, it has become of interest to couple various NMR experiments to solve overlapping peaks and improve the resolution of the NMR spectrum.

2-Dimensional Total Correlated Spectroscopy or TOCSY shows all coupling between nuclei connected in the spin system. 1D selective TOCSY means you can selectively choose the nuclei of interest and show which other protons it is connected to within the spin system. Lyu *et al.*[223] analysed model bio-oils representative of hydrogenation/hydrogenolysis reactions using DOSY plus 1D selective TOCSY. The four bio-oil models represented:

1. Products from 5-HMF hydrogenation/hydrogenolysis
2. Products from furfural hydrogenation/hydrogenolysis
3. Products from phenol hydrogenation
4. Products from ester groups hydrogenation

This review will use the results from the model oil produced by 5-HMF hydrogenation/hydrogenolysis (Figure 2.4.22) to demonstrate the advantages of coupling DOSY and 1D selective TOSCY together. Lyu *et al.* show that using ^{1}H DOSY (Figure 2.4.23) can help separate signals of model bio-oils based on their diffusion coefficient. However, the molecules (see scheme below) 2,5-dimethylfuran, DMF (D_{DMF} = 5.685×10^{-10} m^2 s^{-1}), and 2,5-bis-hydroxymethyl tetra-hydrofuran DMTHF (D_{DMTHF} 5.571×10^{-10} m^2 s^{-1}) have similar diffusion coefficients. In that case, signals in the DOSY spectrum (Figure 2.4.23) cannot be distinguished clearly, however the 1D selective TOCSY (Figure 2.4.24) of both DMTHF and DMF in the mixture were obtained where the peaks at 1.12 ppm and 2.20 ppm were selected respectively. The excited signals of both 1D selective TOCSY spectra was compared with ^{1}H NMR spectra (Figure 2.4.24) of both compounds, confirming the presence of DMTHF and DMF. This study suggests that DOSY is a suitable method for analysing mixtures without additional purification steps. However, when there is signal overlap in the diffusion dimension, the additional use of the 1D selective gradient TOCSY is beneficial for further identification of

compounds. [224] Limitations to this would be if the 1D spectrum were too crowded or not well resolved the selectivity of overlapping nuclei would be considerably harder.
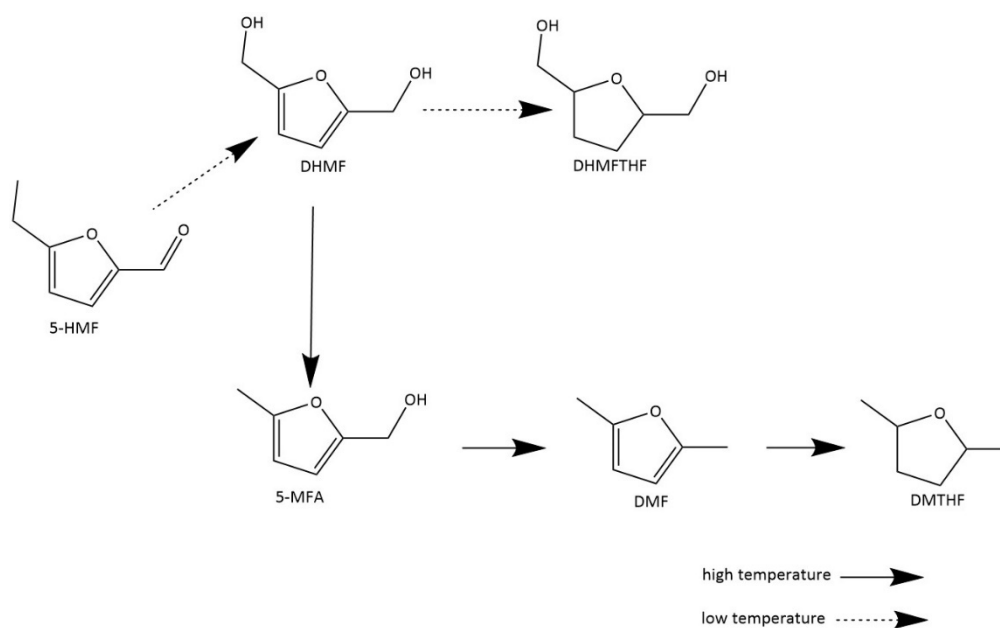
Figure 2.4.22 Products from 5HMF hydrogenation/hydrogenolysis reaction routes.
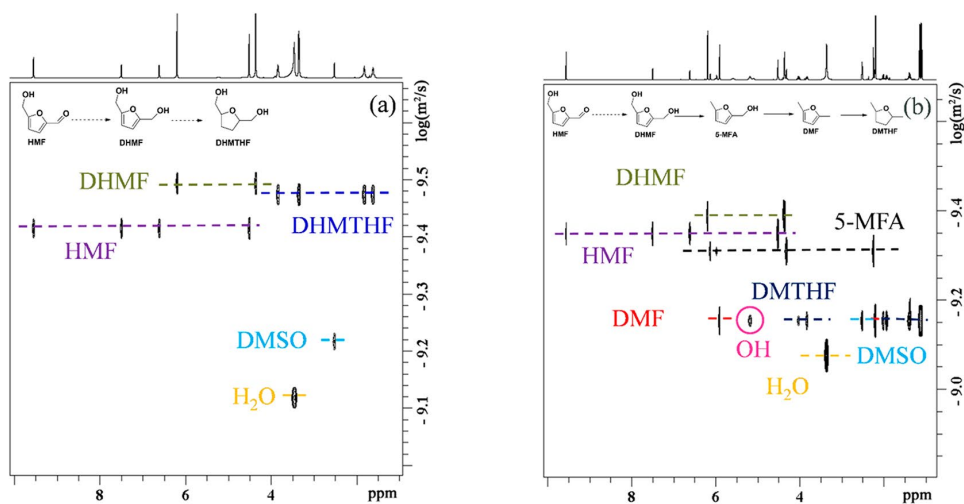
Figure 2.4.23 ^{1}H DOSY spectra of 5-HMF hydrogenation by two routes (Figure 2.6.15).

B.Tang, PhD Thesis, Aston University, 2024.
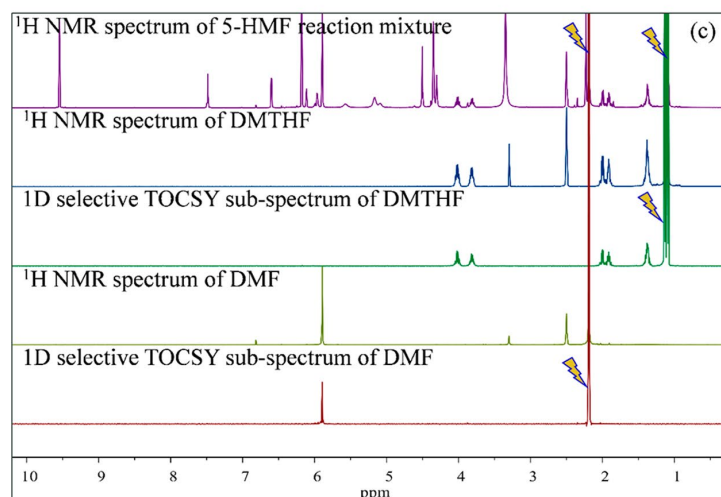
Figure 2.4.24 Stacked plot showing the 1D ^{1}H spectrum of the 5-HMF reaction (1-top), the 1D ^{1}H spectrum of DMTHF (2), 1D selective TOCSY of the sub-spectrum of the DMTHF which confirms the presence of DMTHF (3), the 1D ^{1}H spectrum of DMF (4), 1D selective TOCSY of the sub-spectrum of the DMF which confirms the presence of DMF (5-bottom).

Another major influence on resolution is the extensive multiplet structure that arises from scalar coupling which contributes to the overlap in spectra. Homonuclear and heteronuclear coupling can both produce multiplet structures. Earlier in the chapter, heteronuclear decoupling of the proton nuclei from the phosphorus nuclei was discussed. Pure shift methods (broadband homodecoupling) aims to improve spectral resolution by supressing the effects of homonuclear coupling interactions.[225] As a result of the broadband homodecoupling the multiplet signals are collapsed into singlets reducing the overlap.

Gresley *et al.*[226] reported the use of PSYCHE and PSYCHE-iDOSY experiments to verify signals for components in pyrolysis oil for the first time. The 1D ^{1}H NMR (Figure 2.4.25 (a)) of a crude bio-oil sample and four refined bio-oil samples were analysed, but the mixture's complexity made it difficult to quantify. Therefore, DOSY was used to help in the virtual separation of the overlapped peaks. Results suggested that DOSY is a good pseudo-separation technique for carboxylic acid and aldehyde proton signals in crude oil. However, some smaller peaks could not be seen due to the highly overlapped areas. PSYCHE-iDOSY reduced the chemical shift dimension error by reducing the multiplet structure to singlets however, this introduces large uncertainties in the diffusion domain due to the lower signal-to-noise ratio. Figure 2.4.26 shows a comparison of the DOSY plot and PSYCHE-iDOSY. The identification of five oxygen-containing compounds was assigned by Chenomx^{TM}. The identification of compounds was limited due to Chenomx^{TM}

being mainly a metabolite identifier. Even though, PSYCHE-iDOSY has potential to simplify and analyse complex mixtures, error in the diffusion domain compared to the DOSY spectra has increased and thus, reduced the resolution in the diffusion domain.
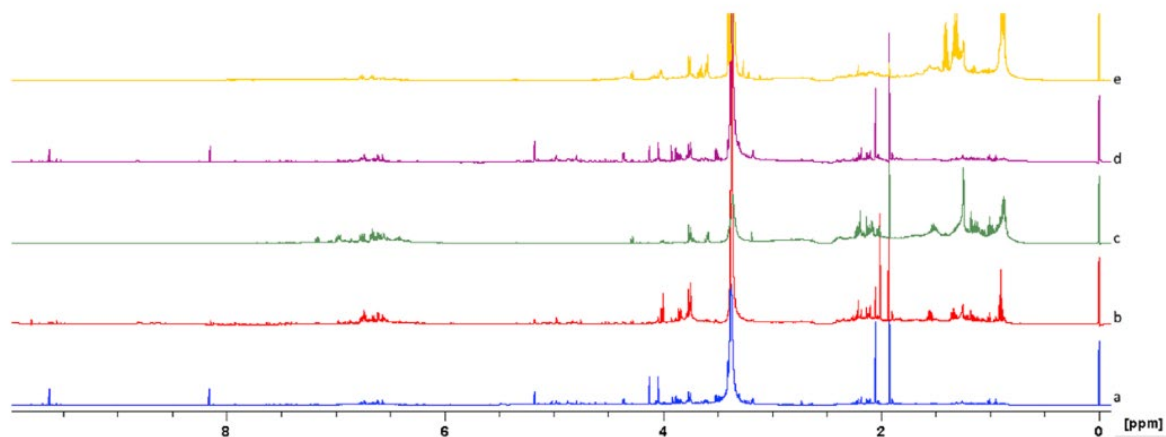
Figure 2.4.25 ^{1}H NMR spectra of (a) crude pyrolysis oil (b) upgrade 1: APO^{TM} (c) upgrade 2: APO^{TM} + hydrodeoxygenation (d) upgrade 3: volume reduction (e) upgrade 4: volume reduction + hydrodeoxygenation.[226]
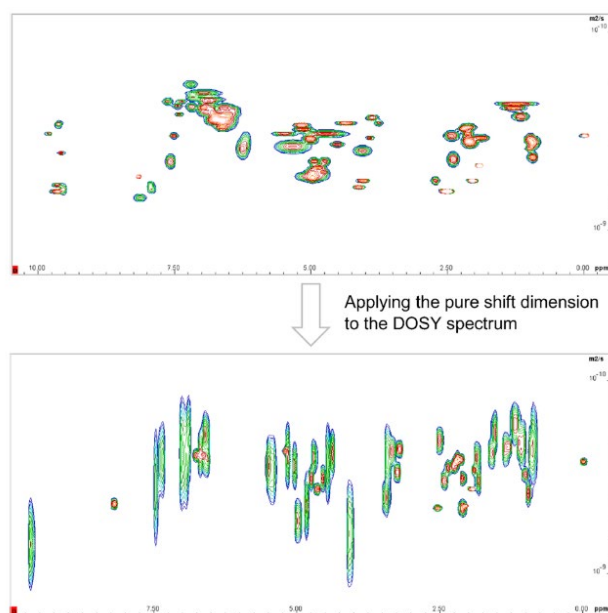
Figure 2.4.26 Comparison of the DOSY plot (top) and the PSYCHE-iDOSY plot (bottom) of the crude pyrolysis oil.[226]

More recently, PSYCHE and 1D-selective TOCSY-PSYCHE has also been used to analyse mixtures derived from hydrogenation and hydrogenolysis of biomass.[227] Four model mixtures and one real sample were analysed. The four model mixtures and the real sample contained different chemicals and represented different systems:

75

1. Sorbitol, ethylene glycol and 1,2 propylene glycol to represent the catalytic reaction system of sorbitol.
2. α-D-glycose, sorbitol and mannitol to represent the product mixture of glucose conversion.
3. Levulinic acid, γ-valerolactone, and 2-methyltetrahydrofuran to represent the hydrogenation of levulinic acid.
4. Tetrahydrofurfuryl alcohol, 1,2-pentanediol and 1,5-pentanediol to represent the most efficient catalytic hydrogenolysis of furfural derivative.
5. Real system reaction of levulinic acid hydrogenation conducted with Ru/TiO$_2$

All samples were dissolved in DMSO-d_6 and were analysed by standard ^{1}H NMR. For sample 2 the proton NMR spectrum was difficult to analyse due to the significant overlap in both the hydroxyl hydrogen region at 4.30 - 4.55 ppm and the alkyl region at 2.95 - 3.74 ppm. 1D PSYCHE was used to remove all homonuclear proton coupling simplifying the proton spectrum. This enabled analysis of nearly all of the hydroxyl protons. However, there were still some overlap of signals between 3.42 and 3.46 ppm. 1D selective TOCSY was then used to extract each component from the mixture, however could not resolve the overlapped signals. As a result of this, a combination of the two, TOCSY-PSYCHE technique was used. This led to a completely resolved spectrum, where the PSCHYE simplified the signals and using TOCSY separated the signals from individual spin systems. TOCSY-PSYCHE techniques were shown to be useful when combined in resolving overlapped signals. The technique was then employed to analyse real reaction system.

2.5 Summary

This chapter explores the theory, instrument design and applications of various nuclear magnetic resonance techniques. Each technique has many advantages and disadvantages and may be best to use as complementary techniques. The elucidation of pyrolysis-oil composition is essential for assigning the best application and upgrading process required. ^{1}H NMR offers a good insight into the chemical structure and some functional groups present in bio-oil. It also allows some quantitative information on the pyrolysis. However, it does not yield chemical information such as the types of hydroxyl groups within the sample. Nor does it yield information on other functional groups that do not contain proton such as carbonyls. ^{1}H NMR has a narrow chemical shift range and bio-oils contain hundreds of hydrogen-containing compounds both of which result in a

highly crowded spectrum. The overlap makes it very difficult to interpret and reduced the amount of information available.

^{13}C NMR produces a wider chemical shift range, resulting in a sparser spectrum and the ability to characterise functional groups such as carbonyl groups. ^{13}C NMR is not limited to one dimension, and 2D techniques like ^{1}H-^{13}C HSQC offers more structural information such as the molecule connectivity. It was able to resolve some overlapped peaks and thus confirming species present. In complex mixtures such as pyrolysis oils, the poor resolution due to overlapping can still make HSQC difficult to analyse. For quantification, due to the low gyromagnetic ratio and natural abundance, to achieve good signal-to-noise this typically experiments will take longer. Oxygen-containing compounds present in bio-oils are still challenging to analyse with ^{1}H and ^{13}C NMR alone.

The ability to tag specific functional groups with multinuclear-containing reagents followed by multinuclear NMR analysis was also explored. In particular the use of fluorine and phosphorus-containing compounds. Different ^{19}F-containing agents have been explored to derivatise hydroxyl groups and carbonyl groups. The major advantage of these methods is isolating specific functional groups which result in a sparser spectrum. The derivatisation methods have shorter experimental time compared to titration methods. ^{19}F NMR analysis also has its advantages of a large chemical shift range making it easier to analyse as well as the higher signal-to-noise ratio making it suitable for quantification. However, derivatisation methods can still take a long period of time.

Phosphitylation reactions were relatively quick in comparison to ^{19}F derivatisation methods. ^{31}P NMR offers an insight into the hydroxyl chemistry in bio-oil after derivatisation. It has a larger chemical range like makes the spectrum less crowded and easier to analyse. It has a high signal-to-noise ratio makes it suitable for quantification. Nowadays, it is the preferred method to analyse hydroxyl groups in bio-refinery products. The major limitation of this techniques is that the derivatisation agent can be expensive and not always available.

One-dimensional NMR technique explored in this section all share a limitation which is overlapping signals in the spectrum. More advanced NMR techniques such as DOSY, PSYCHE and TOCSY have also been useful in characterising structures in bio-oil.

2.6 Research Aims

Biomass could be a potential source of renewable energy. Brewers' Spent Grains are waste produced by the brewing industry. BSG can be turned into potential fuel replacements as fuels or added-value chemicals through process such as pyrolysis processes. Pyrolysis oils are often not suitable for direct use as fuel, mainly due to their acidic nature. The acidity of pyrolysis oils is mostly due to oxygen-containing compounds. An improved knowledge and understanding of the chemical compositions of BSG pyrolysis oil is critical for future storage, ageing and upgrading. However, pyrolysis oils are complex mixtures and difficult to analyse using current techniques. NMR spectroscopy offers an attractive method which can provide both structural analysis and quantitative analysis. Majority of analysis of pyrolysis oils in literature is either proton NMR or one-dimensional. However, more advanced NMR techniques are not widely used by the pyrolysis oil community.

The overall aim of this thesis is to develop multinuclear and multidimensional NMR tools to characterise pyrolysis oils produced from Brewers' Spent Grains. There is an opportunity for NMR tools to enable a better understanding of the chemical composition of pyrolysis oils. NMR methods are chemically specific and can be quantitative. However, there are still challenges in simplifying the spectra acquired and improving the spectral resolution. The rest of the thesis will explore and note that each chapter will be in paper format:

Chapter 3: Experimental Calibration

A new spectrometer was installed in the department and the performance of the spectrometer must be assessed prior to developing new NMR tools. The temperature stability and gradient strengths are very important for the acquisition of reliable and robust NMR data. This is especially true for diffusion coefficients measurements using pulsed field gradient NMR. Therefore, this chapter aims to evaluate and calibrate essential experimental parameters such as the temperature and gradient calibration constant.

Chapter 4: Quantitative Analysis of Carbonyl Groups in Fast Pyrolysis Oils Using Low-field ^{19}F NMR

Oxygen-containing compounds such as carbonyl groups contribute to the acidity of pyrolysis oils. It is vital to understand the types of carbonyl groups and quantify the amount of carbonyl groups in pyrolysis oils. Current methods of analysis have limitations as outlined in Chapter 1. Traditional titration methods are laborious and ^{19}F high-field NMR techniques can be costly. This limits techniques to larger institutions and research facilities. This chapter aims to improve current ^{19}F derivatisation methods and translate high-field NMR methods to cheaper benchtop NMR spectrometers.

Chapter 5: Quantitative Analysis of Hydroxyl Groups Using ^{31}P NMR

Oxygen-containing compounds such as hydroxyl groups are also a main contributor to pyrolysis oil acidity. Like all 1D NMR methods, the main limitation is in the available chemical shift range and highly crowded spectra. This chapter aims to improving current techniques and build the foundation for the developments of multinuclear and multidimensional techniques.

Chapter 6: Development of ^{31}P Diffusion-Ordered Spectroscopy

Diffusion NMR experiments separate signals in the diffusion domain improving spectral resolution. Diffusion coefficients provide information on the molecules' size, shape, and environment. There is a general correlation between molecular mass and the speed at which a molecule travels in solution, i.e the larger the molecule, the slower it moves through solution. This chapter aims to develop ^{31}P DOSY techniques. Combining the chemical shift information from 1D NMR spectrum and molecular weight information from DOSY could enable the easier identification of alcohols present in pyrolysis oils.

Chapter 7: Characterisation of Pyrolysis Oil Produced from Brewers' Spent Grains

Characterisation of pyrolysis oils have mostly been challenging due to the complexity of the samples. Due to limitations of current analytical techniques such as FTIR, EA, GCMS, and current NMR methodologies outlined in Chapter 1. Generally, the analysis

79

of the pyrolysis oils, especially the measurement, quantification and identification of oxygen-containing compounds, can still be very challenging. This chapter aims to brings together both current and newly-developed NMR? methodologies to better understand the composition of oxygen-containing species in both fast and slow BSG pyrolysis oils.

Chapter 8: Quantitative Interpretation of the protein Diffusion Coefficients in Mixed Protitated-Deuteriated Aqueous Solvent

The computational research was carried as part of a contingency plan due to COVID-19 lockdown. Diffusion coefficients of molecules can be interpreted quantitatively. Many chemical processes are carried out in mixed solvents. The diffusion of molecules in a mixed solution is still poorly understood. Current methods such as power laws or the Stokes-Einstein-Gierer-Wirtz-Estimation (SEGWE) equation have not been used to handle mixed solvent systems. The aims of this chapter are to extend current SEGWE methods to mixed solvents enabling the quantitative interpretation of protein diffusion coefficients.

CHAPTER 3 : EXPERIMENTAL CALIBRATION

3.1 Introduction

The NMR spectrometer used in the study was newly installed. The spectrometer can be equipped with different probes such as a Bruker iProbe or a Bruker diffusion probe (Figure 3.1.1). Before conducting this work, the spectrometer had not been used to conduct NMR experiments. Sample and instrument preparation are equally important to achieve accurate and precise NMR data. Therefore, preliminary studies on the performance of the spectrometer and subsequent calibration are needed to assure the users that subsequent measurements are suitably accurate. Many factors can affect the signal to noise or line shape and peak width of a sample, such as physical parameters (sample temperature, vibrations, NMR tube used) and experimental parameters.
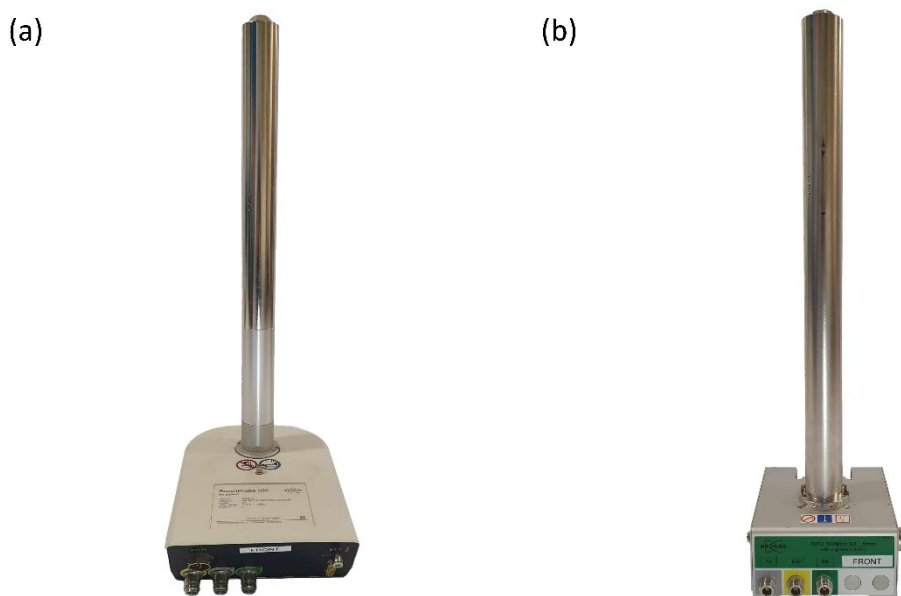
Figure 3.1.1 (a) Bruker iProbe SmartProbe^{TM} (b) Bruker Diffusion Probe (DiffBB probe).

Diffusion NMR experiments in particular, are susceptible to a range of experimental and instrumental parameters. For example, diffusion coefficients are highly dependent on the sample temperature. Sample temperature affects both the thermal energy of the system and the viscosity of the solvent. All modern spectrometers are equipped to monitor and regulate the temperature inside the probe. A schematic diagram of a probe with temperature regulation is shown in Figure 3.1.2. The temperature of the NMR probe is adjusted by passing heated or cooled compressed air across the sample. The variable temperature (VT) unit uses a thermocouple wire at the bottom of the probe to measure the temperature of the sample. The thermocouple is not in direct contact with the sample

but rather measures the temperature of the compressed air passing over it. Although the precision of the nominal temperature on the thermostat is typically ±0.1 K, the difference between the set temperature and the true sample temperature can be up to several Kelvin. To confirm the exact temperature of the sample, a chemically-inert liquid with a known temperature-dependent chemical shift can be used as an NMR thermometer. The method described in Findeisen *et al.* [228] was used, where deuteriated methanol was used to establish the relationship between the temperature stated by the spectrometer's VT unit and the actual temperature of the sample.
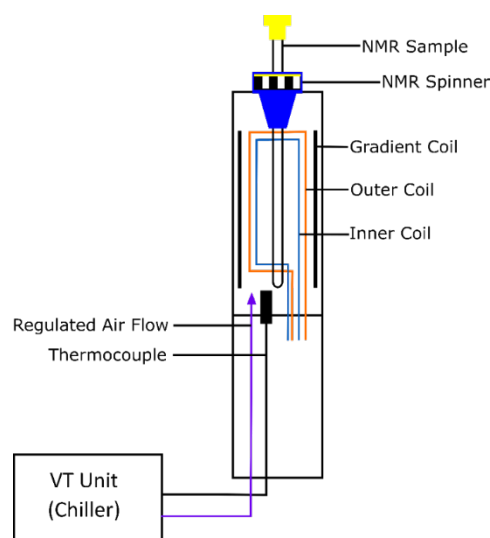
Figure 3.1.2 Schematic diagram of NMR probe with thermocouple.

The self-diffusion of molecules is measured using pulse-field gradient NMR or PFG-NMR. The gradient is produced by sending a current through the gradient coil in the probe. This generates a secondary magnetic field, which perturbs the main field. The resonance frequency of the protons will differ depending on position, encoding a spatial dependence in the signal. The size of the secondary field depends on the current passed through the coils. The percentage of current is converted to gradient strengths with the gradient calibration constant. The iProbe has a preset gradient calibration constant of 5.35 G mm^{-1}. The diffusion probe has a much larger gradient calibration constant of 170.1 G mm^{-1}. It is essential to evaluate the value of the gradient calibration constant using common solvents with well-known diffusion coefficients.

3.2 Experimental

3.2.1 Temperature Calibration

<u>Bruker iProbe SmartProbe^{TM} and Bruker Diffusion Probe (DiffBB probe)</u>

Deuteriated methanol (Sigma-Aldrich,99.9%) was used without further purification. The deuteriated methanol was sealed in a thick wall NMR tube under atmospheric pressure. Proton spectra consisting of 4 scans, with a total experimental duration of 7 seconds, were obtained at various temperatures (293 - 305 K).

3.2.2 Calibration Gradients

<u>Bruker iProbe SmartProbe^{TM}</u>

Three liquids with well-known diffusion coefficients were used for the gradient calibration. 1% H_2O in D_2O[229], DMSO[230] and cyclohexane[230] were all obtained from Sigma-Aldrich. All chemicals were used without further purification. Using the ^1H convection compensated sequence, the diffusion of each liquid was measured using the pre-set gradient calibration constant 5.35 G mm^{-1}.

<u>Bruker Diffusion Probe (DiffBB probe)</u>

Three liquids with well-known diffusion coefficients were used for the gradient calibration. DMSO[230], cyclohexane[230], 1-pentanol and squalane were all obtained from Sigma-Aldrich. All chemicals were used without further purification. All solvents were sealed under atmospheric pressure in a thick wall NMR tube. Using a ^{13}C DEPT45 SE sequence, the diffusion of each liquid was measured using the pre-set gradient calibration constant 170.1 G mm^{-1}.

3.3 Results and Discussion

3.3.1 Temperature Calibration

The 1D ^1H NMR spectrum of deuteriated methanol contains two peaks (Figure 3.3.1). The first peak is a pentet at 3.33 ppm corresponding to the proton present in the CHD_2OD, with a splitting pattern 1:2:3:2:1, this is due to the deuterium having a spin of 1 therefore following the 2*I*n+1rule. The second peak is a singlet further downfield, is the hydroxyl proton on the methanol. Because of hydrogen bonding in methanol, the chemical shift

84

of the singlet is temperature-dependent.[228] The relationship between the chemical shift and the temperature is given by the quadratic equation:

$$T = (-16.7467 \times (\Delta\delta)^2) - (52.5130 \times \Delta\delta) + 419.1381$$ *Equation 3.3.1*

Where $\Delta\delta$ is the difference in chemical shift of the two peaks.
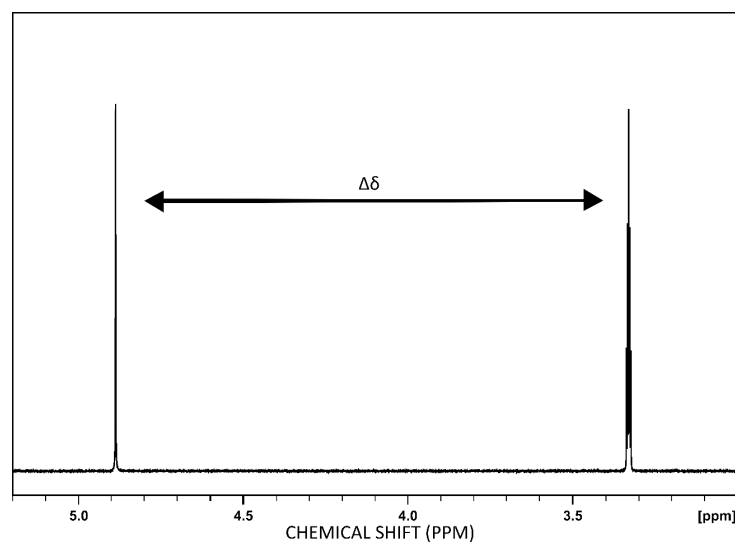
Figure 3.3.1 1D ^{1}H spectrum of deuteriated methanol, where Δδ is the difference between the chemical shifts of the singlet and the pentet peaks.

The temperature range measured was close to ambient temperature, reflecting the temperature range of expected future experiments. The chemical shift differences measured at each temperature were converted into sample temperature using Equation 3.3.1. The data is presented in Figure 3.3.2. The nominal temperature stated by the thermostat and the actual temperature differed by ~0.3 K. It is very important to know the actual sample temperature when conducting temperature sensitive experiments. This is especially true when conducting diffusion experiments, where the temperature will affect the thermal energy of the system and the solvent viscosity, and thus affecting the diffusion coefficient of the sample. An NMR thermometer should always be used to check the temperature, and the sample must be left to equilibrate to ensure it has reached the desired temperature.
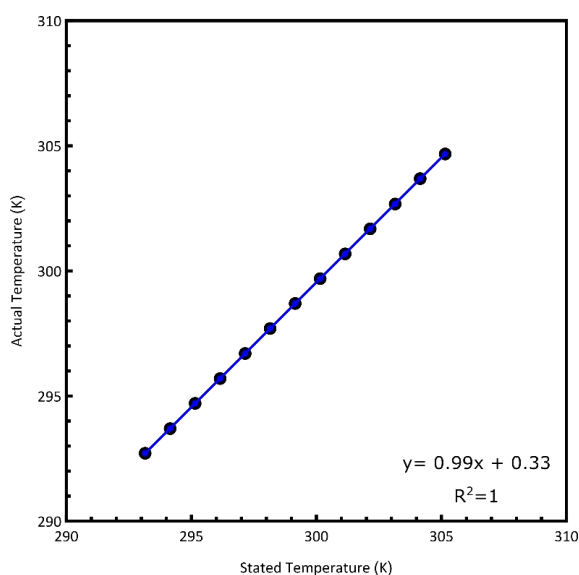
Figure 3.3.2 The relationship between the stated temperature of the spectrometer and the actual temperature of the NMR thermometer (methanol-d_4).

For the sample to reach the desired temperature after the temperature is changed, it may take longer to change than stated by the spectrometer. Therefore, the time required for the sample to reach thermal equilibrium must also be considered. The sample was left to equilibrate for 10 minutes throughout the temperature calibration before acquiring NMR data. If insufficient time is left before acquiring a spectrum, the sample temperature may be inhomogeneous or, worse, incorrect. This can be seen in, for example, the signal line shape or acquired diffusion coefficients. Figure 3.3.3 compares the nominal and actual temperature of the sample over 13 minutes. The temperature of the sample (methanol-d_4) was changed from 293 K to 304 K, and the time taken for this change was observed on the NMR thermostat. It clearly shows that the change in the temperature from the NMR thermostat reading quickly stabilised. The temperature change observed from the NMR thermometer was also relatively rapid (*ca.* 2 minutes). Note that the temperature was not fully stable, with minor fluctuations observed for *ca.* 3 minutes after the target temperature was reached; therefore, equilibration time must be considered when conducting any temperature measurements.

B.Tang, PhD Thesis, Aston University, 2024.
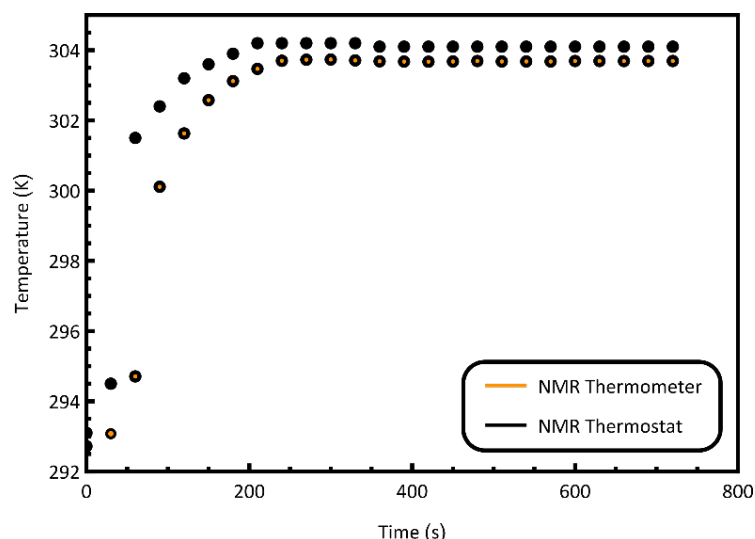
Figure 3.3.3 The nominal temperature was changed from 293 to 303 K. The time taken for stability of temperature after the initial change in nominal temperature of the NMR thermometer (methanol-d₄).

Same as the iProbe, the diffusion probe also requires a temperature calibration. A sample of methanol-d in a thick-walled tube was used to calibrate the temperature diffusion probe. The temperature range measured was close to ambient temperature, reflecting the temperature range intended for experiments. The chemical shift differences measured at each temperature were converted into sample temperature using Equation 3.3.1. and the data is presented in Figure 3.3.4. The nominal temperature stated by the thermostat and the actual temperature were different. Therefore, an NMR thermometer should always be used to check the temperature prior to any diffusion experiments, and the sample must be left to equilibrate to ensure it has reached the desired temperature.
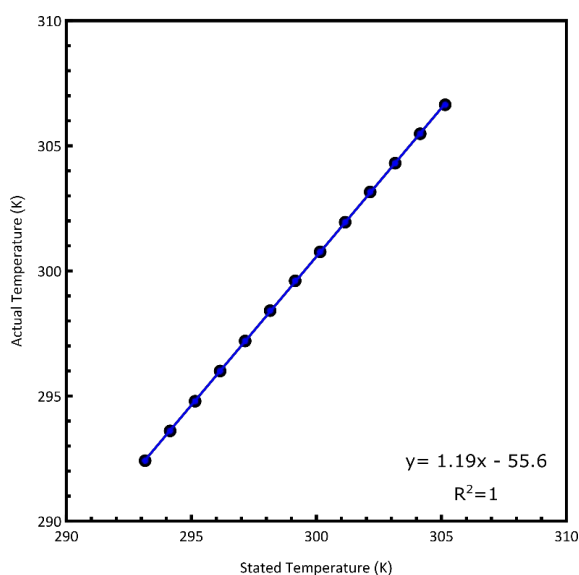
Figure 3.3.4 The relationship between the stated temperature of the spectrometer and the actual temperature of the NMR thermometer (methanol-d₄).

3.3.2 Attempted Gradient Calibration (teething problems)

The spectrometer had not been used for diffusion measurements since installation. Therefore, the diffusion coefficient of common solvents must be measured to correct the calibration constant as required. The initial 1D ^{1}H NMR spectrum of 1% H_2O in D_2O, which shows a sharp singlet at 4.70 ppm, is shown in Figure 3.3.5. The original peak width was 3.589 Hz prior to the diffusion experiment.
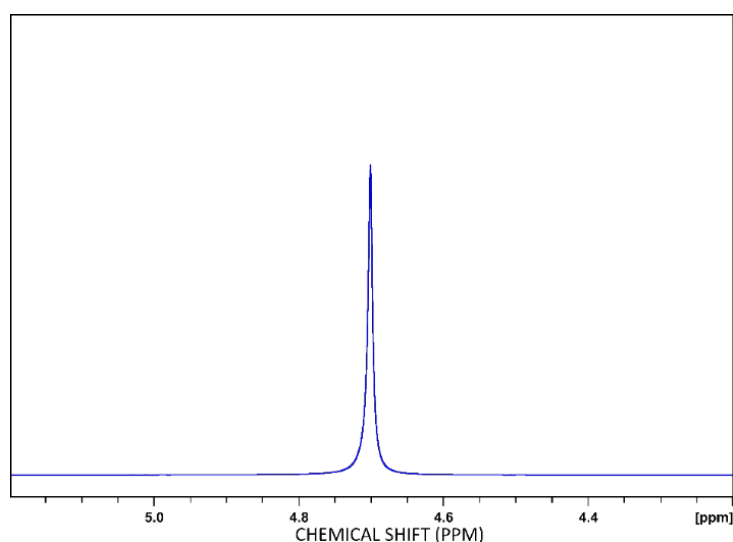
Figure 3.3.5 1D ^{1}H NMR spectrum of 1% H_2O in D_2O (peak at 4.70 ppm).

The double-stimulated echo bipolar pulse gradient pair (convection-compensated) pulse sequence (Figure 3.3.6 (a)) was used to measure the diffusion coefficient of 1% H_2O in D_2O. The sequence has 3 spoiler gradients to remove the unwanted coherences in the transverse plane. The diffusion of the 1% H_2O in D_2O was measured using the pre-set gradient calibration constant. However, when comparing the 1D spectrum from the first and last gradient, the peak at 4.70 ppm was no longer a sharp singlet, as shown in Figure 3.3.7. The peak width after the diffusion experiment had increased to 6.043 Hz.

(a)

(b)
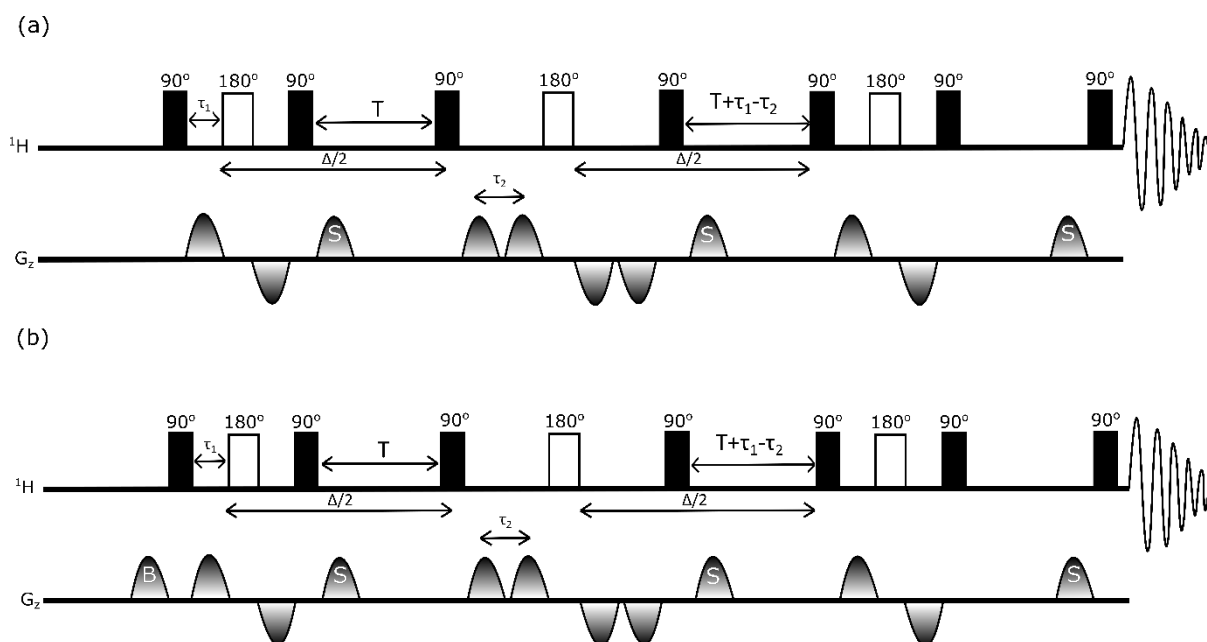
Figure 3.3.6 (a) Double stimulated echo bipolar pulse gradient pair pulse sequence (dstebpgp3s) (convection compensated sequence). The diffusion delay time (Δ) is split into two parts. The two adjacent sets of bipolar pulse pairs in the centre of the pulse sequence ensure that only the 180° pulse is required to refocus the signal. There are 3 spoiler gradients (gradients denoted with S) are used to remove any unwanted signals in the transverse plane. Each gradient pulse has the strength g and has a duration of δ. τ$_1$ and τ$_2$ are intergradient delays in the bipolar gradient pulse. T is the variable diffusion delay time parameter. (b) dstebpgp3s (same as Figure 3.3.2.2 (a)) with a balancing gradient denoted with B which balances out the three spoiler gradients.
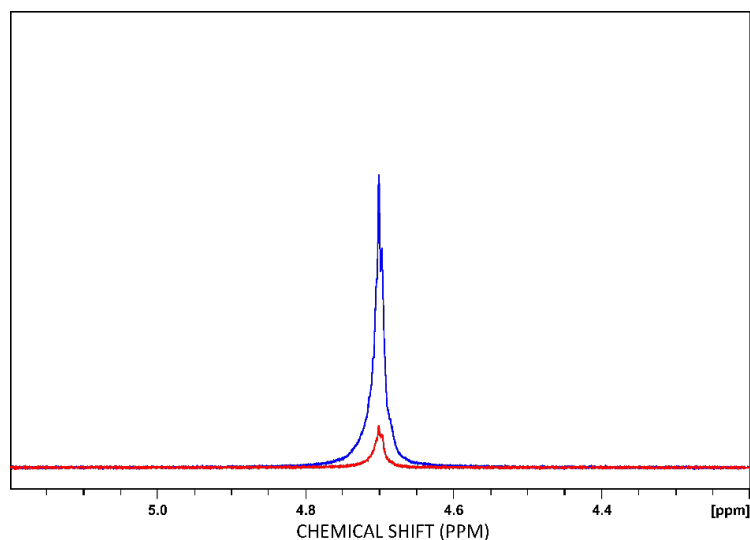
Figure 3.3.7 Stacked plot of the 1D spectrum of first (blue) and last (red) gradient using the double-stimulated-echo-bipolar-pulse-gradient-pair pulse sequence (peak 4.70 ppm, 1% H_2O in D_2O).

To ensure the changes in lineshape was not due to the choice of the pulse sequence, another convection compensated pulse sequence (Figure 3.3.6(b)) was used to measure the diffusion coefficient. The difference between this sequence and the last is that this sequence contains a balancing gradient to balance the spoiler gradients. However, similar results in the attenuation when looking at the stacked spectrum were obtained, with a slightly better line shape. However, the peak width (8.537 Hz) was broader than that of the initial proton, which had a peak width of 3.589 Hz (Figure 3.3.8).
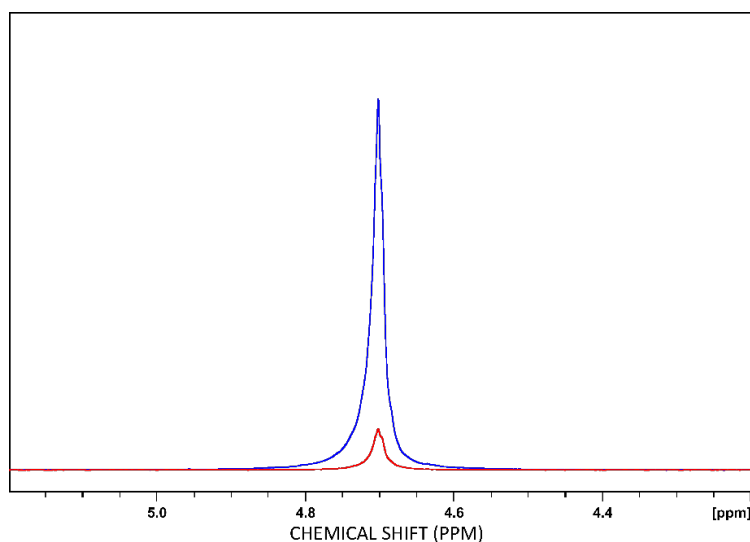
Figure 3.3.8 Stacked plot of the 1D spectrum of first (blue) and last (red) gradient using the double-stimulated-echo-bipolar-pulse-gradient-pair pulse sequence with the balancing gradient (peak 4.70 ppm, 1% H_2O in D_2O).

Another diffusion experiment was used to check if the pulse sequence choice affected the lineshape. A Oneshot diffusion experiment[231] (Figure 3.3.9) was carried out. Figure 3.3.10 illustrates the spectra acquired with the first, highest in blue and last, lowest in red gradients. Similar results were obtained where the line shape was not a sharp singlet.
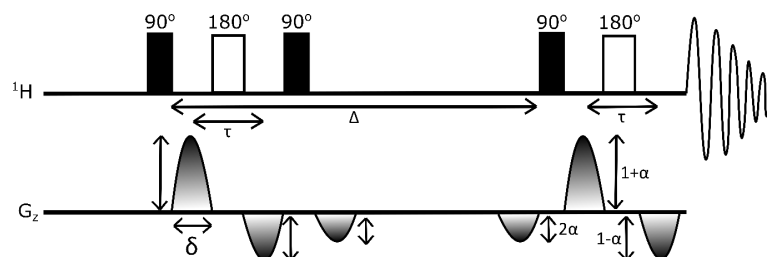
Figure 3.3.9 One-shot pulse sequence for measuring diffusion coefficient. The gradient pulse has a duration of δ. The gradient strength is changed by an imbalance factor (α). Any magnetisation not refocused by 180º pulse will be de-phased by the intensity factor 1+ α and 1- α and the two other gradients by the intensity 2α. The diffusion delay Δ and τ is an intergradient within the bipolar gradient pulse.
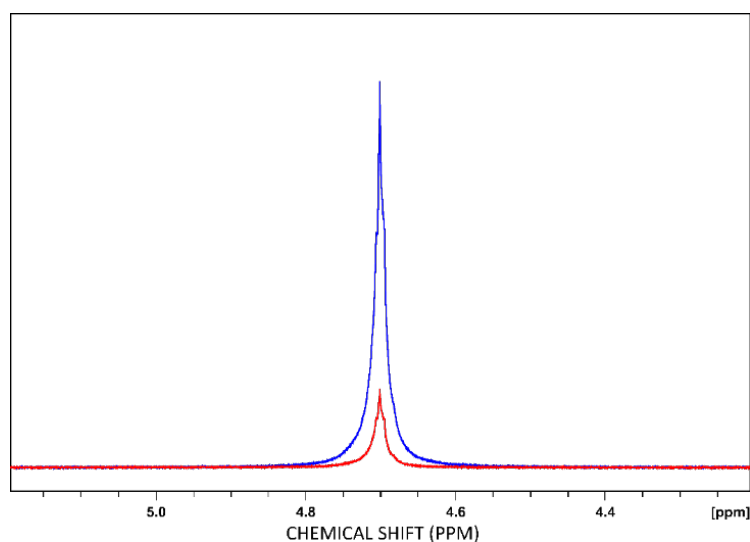
Figure 3.3.10 Stacked plot of the 1D spectrum of first (blue) and last (red) gradient using the One-shot pulse sequence (peak 4.70 ppm, 1% H_2O in D_2O).

After this, a standard 1D ^{1}H NMR spectrum was acquired to check the lineshape of the peak. Figure 3.3.11 illustrates a clear change in peak width from 3.589 Hz to 6.100 Hz; it is much broader than the peak at the start of the experiment. The sample was ejected from the spectrometer, and bubbles had formed in the sample. The formation of bubbles will have a major impact on how homogenous the sample is. The cause of the bubbles forming was unknown. However, there were possible proposals: the sample had been heated or rotated. Rotation of the sample is unlikely as the spectrum was acquired without rotation. The bubbles were removed, the sample was re-shimmed, and the same

one-shot diffusion experiment was acquired (Figure 3.3.12). There was an improvement in the peak width.
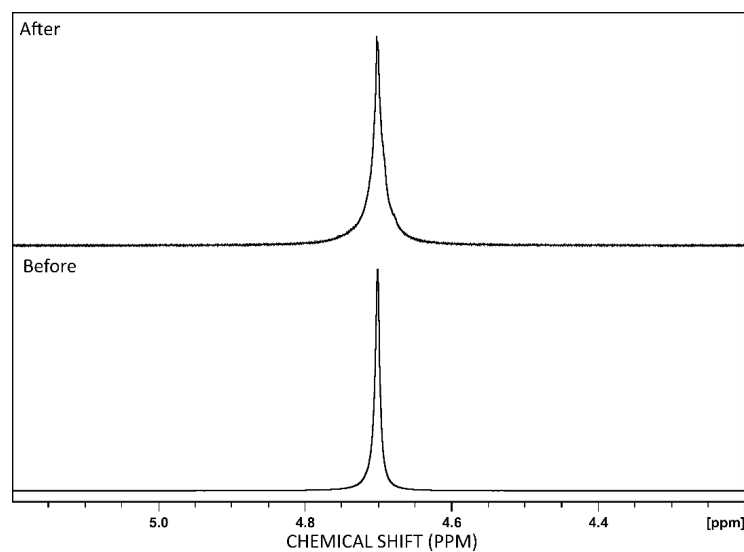
Figure 3.3.11 Plots of 1D ^1H NMR spectrum of 1% H_2O in D_2O (peak at 4.70 ppm) before (same spectrum as Figure 3.3.1) and after the series of diffusion experiments.
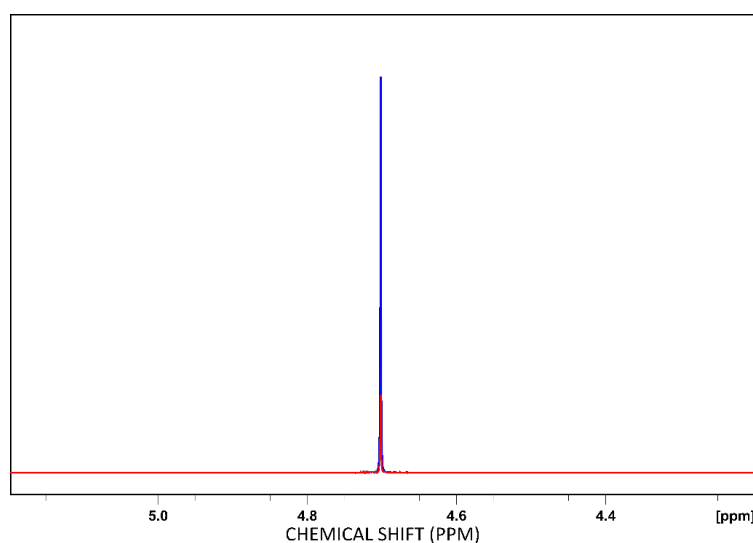
Figure 3.3.12 Stacked plot of the 1D spectrum of first (blue) and last (red) gradient using the One-shot pulse sequence (peak 4.70 ppm, 1% H_2O in D_2O), repeated experiment after the removal of bubbles and re-shimmed sample.

A series of proton experiments were acquired straight after to see if there were changes in the line shape over time. After each proton experiment, the sample was ejected to be examined for bubbles or other issues with the sample itself. No further bubbles were further observed. However, the line shape of the sample deteriorated with time, as shown in Figure 3.3.13.
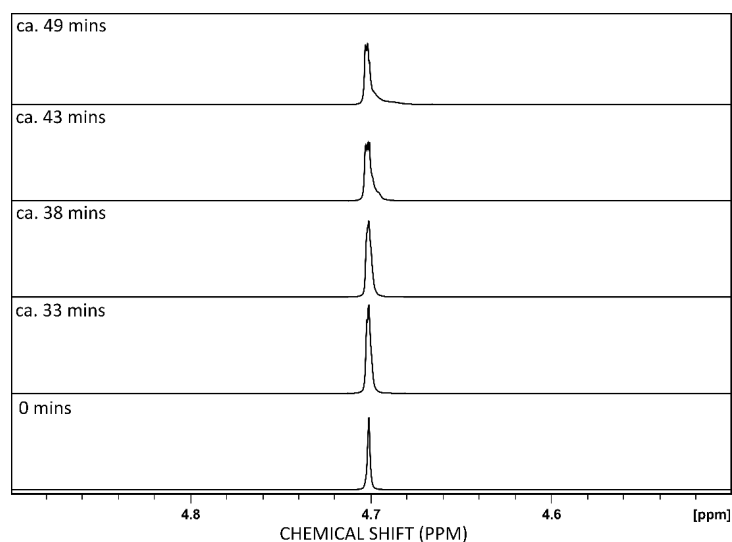
Figure 3.3.13 Stacked plot of 1D ^1H NMR spectrum of 1% H_2O in D_2O (peak at 4.70 ppm), showing the change in line shape over time.

To further investigate, experiments were carried out to eliminate possible causes of the change in line shape and peak width. Wear and tear from the usage of an NMR tube is common. Even small scratches in the tubes can cause sample inhomogeneity. Therefore, a series of 1D proton spectra of 1% H_2O in D_2O were measured in three thin-walled tubes. While 1D ^1H spectra of each sample were taken every minute, to simplify the results presented here, spectra from every 5 minutes for 15 minutes are shown in Figure 3.3.14. This figure compares the stacked plots of 1D ^1H spectra of 3 different samples of 1% H_2O in D_2O in thin-walled NMR tubes (where Figure 3.3.14 (a) is the same sample used to carry out previous experiments). The results from this set of experiments were conclusive with each other, and all samples were measured over 15 minutes. This was repeated with a thick-walled tube shown in Figure 3.3.14 (d). Overall, there is little to no line shape and peak width change. Therefore, this eliminated the possibility of the NMR tubes causing the inhomogeneity.
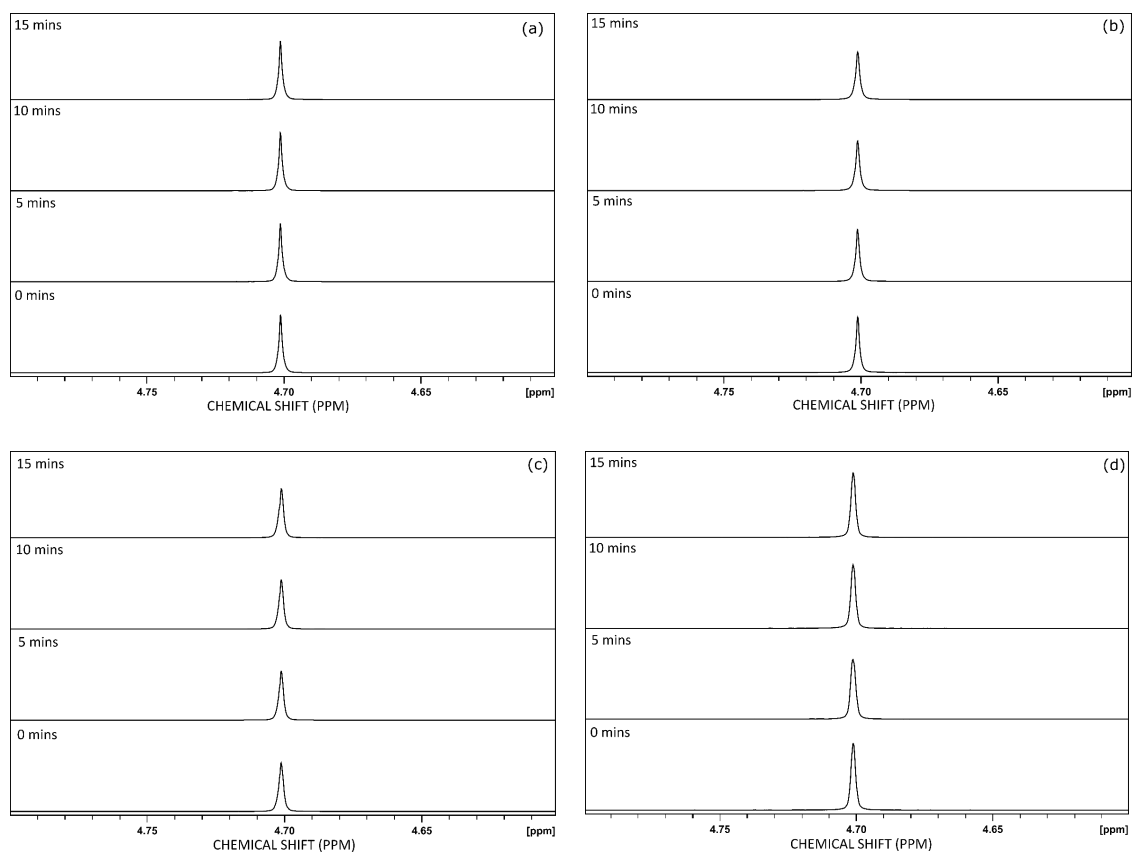
Figure 3.3.14 Stacked plot of 1D ^{1}H spectrum of 1% H_2O in D_2O (a) thin-wall tube sample 1 at 0 min peak width = 0.682 Hz and at 15 mins peak width = 0.658 Hz, (b) thin-wall tube sample 2 at 0 min peak width = 0.717 Hz and at 15 mins peak width = 0.848 Hz, (c) thin-wall tube sample 3 at 0 min peak width = 0.957 Hz and at 15 mins peak width = 0.957 Hz (d) thick-wall tube sample at 0 min peak width = 0.989 Hz and at 15 mins peak width = 0.982 Hz.

Changes in sample temperature may also change the line shape. The stability studies carried out previously were only for ~15 mins. Methanol-d_4 in a thick-walled NMR tube was chosen because it can act as both an NMR thermometer and an indicator of any instability of the shims. The temperature stability of the spectrometer was studied for 60 minutes to ensure the temperature was stable for longer experiments. 1D ^{1}H spectrum was measured every minute to monitor the temperature stability for 60 minutes. Figure 3.3.15 compares the 1D ^{1}H of methanol-d_4 spectra acquired immediately after the sample was inserted (0 minutes) and 60 minutes later. There were no changes in chemical shift, which indicates that there had been no changes in temperature. There were minor changes in line shape between 0 minutes and 60 minutes, which can be seen in Figure 3.3.16.

B.Tang, PhD Thesis, Aston University, 2024.
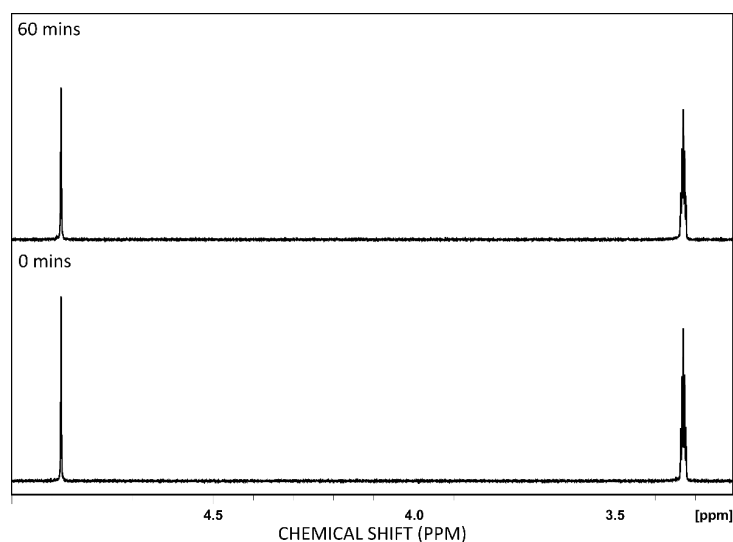
Figure 3.3.15 Stack plot of 1D ^{1}H NMR of methanol-d$_4$ at 0 minutes and at 60 minutes. After 60 minutes, there has been no change in chemical shift of the temperature-dependent singlet at ~4.9 ppm.
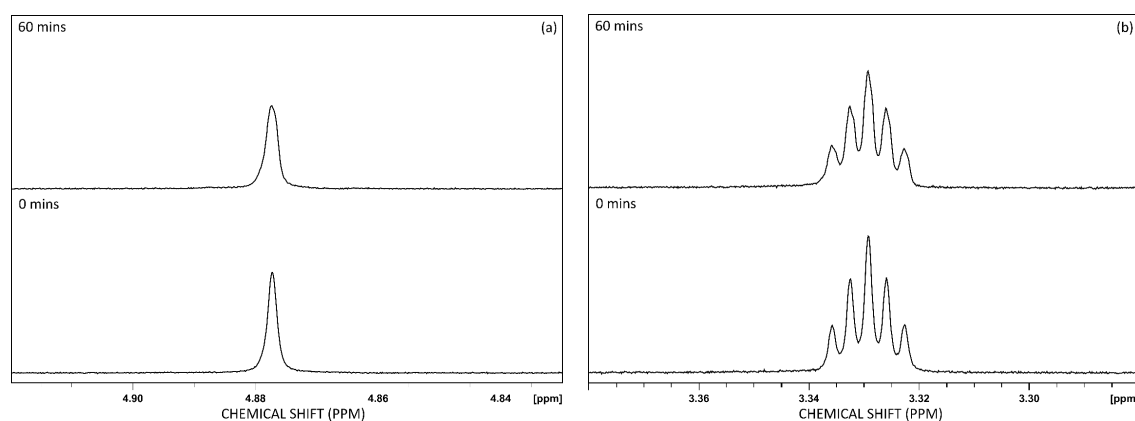
Figure 3.3.16 Stacked plot of 1D ^{1}H NMR of methanol-d$_4$ at 0 minutes and 60 minutes (a) singlet at 4.87 ppm at 0 mins peak width = 0.873 Hz and 60 mins peak width = 1.119 Hz (b) pentet at 3.33 ppm.

The cause of the change in line shape and width is unlikely due to the change in temperature or NMR tube used. It is unknown what caused bubble production in the very earliest experiments, as this was not reproduced in the other experiments at later dates. The change in line widths may have been caused by vibrations from road works outside the laboratory.

To understand the stability of the line width and line shape of the sample, further investigations were carried out where the sample containing deuteriated methanol in a

95

thick wall tube was monitored for 1 hour *in-situ* at a regulated temperature of 298 K with the airflow rate of 400 litres per hour (lph). The deuteriated methanol NMR spectrum contains a sharp singlet which can monitor changes in line shape. The 1D ^{1}H experiment was repeated 3 times on the same day with the same sample and conditions. Figure 3.3.17 shows the change in peak width compared with the original peak width. Repeat 1 (dark blue) showed an overall increase in peak width with cycles in the fluctuations of ~ 15 mins. However, this pattern was not reproducible in later experiments. In Repeat 2 (blue), the changes in peak width were more gradual, with none of the previous fluctuations observed. However, towards the end of the measurement, there was a steep increase in the peak width. This coincided with a large group of people entering the lab with clipboards. The overall change in peak width for repeats 1 and 2 was similar (change of 0.246 Hz and 0.228 Hz respectively). Repeat 3 (light blue) showed the least changes overall (0.06 Hz); there were still some fluctuations in peak width.
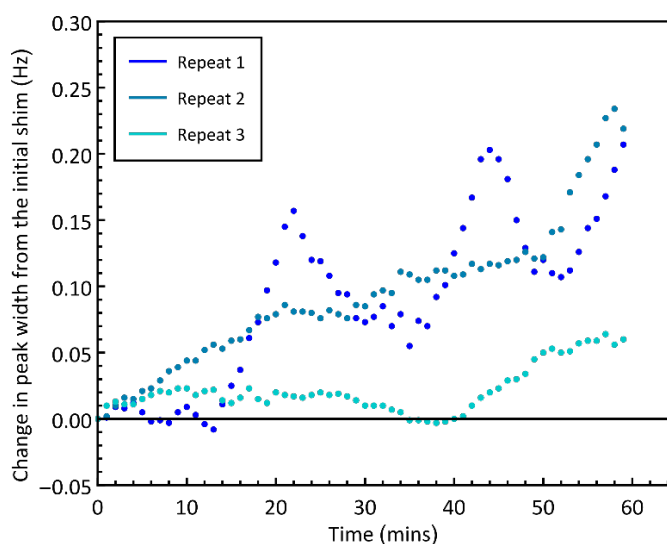
Figure 3.3.17 The change in peak width (Hz) from when the sample was first shimmed over time at 298 K at a constant air flow rate of 400 lph.

It was still not conclusive in what caused the fluctuation and changes in peak width. To ensure it was not any factors caused by the temperature regulation and to eliminate any other possibilities, this was repeated at two other air flow rates (350 lph and 450 lph). Figure 3.3.18 shows the results from the 3 different flow rates where the data set for 400 lph is repeated from earlier experiments in Figure 3.3.17. Results showed the most fluctuation at a higher flow rate (450 lph), whereas at lower flow rates (300 lph) there was a more gradual increase in peak width, which is expected as more air passes the

sample tube in the probe, the sample homogeneity can change. The overall change in peak width was similar across all three flow rates.
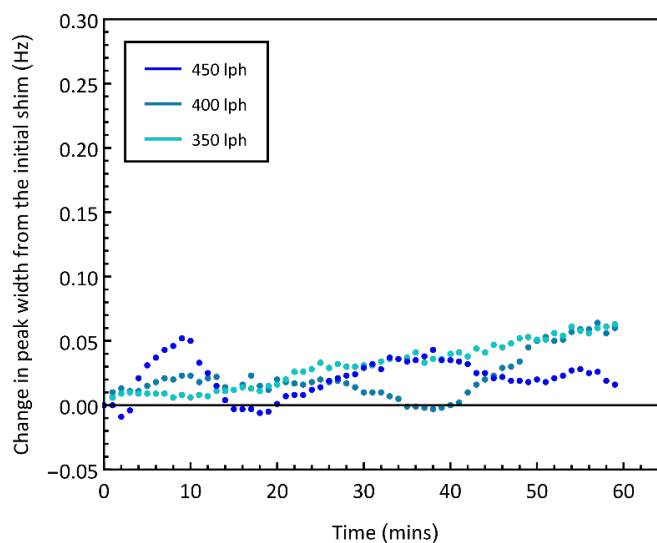
Figure 3.3.18 The change in peak width (Hz) from when the sample was first shimmed over time at 298 K at various air flow rates.

As the change in line shape was less than 0.10 Hz over the typical duration of a diffusion NMR experiment, the gradient calibration was repeated, where the double-stimulated-echo bipolar-pulse-gradient-pair pulse sequence with the balancing gradient was used to measure the diffusion coefficient of 1% H_2O in D_2O. Figure 3.3.19 shows the 1D ^1H NMR spectrum 1% H_2O in D_2O used to perform this gradient calibration. The peak at 4.70 ppm is a sharp singlet from the water. Figure 3.3.20 shows the initial diffusion experiment containing two gradients (where blue is the first, highest gradient and red is the last, lowest gradient) used to check parameters before a longer experiment was acquired. The peaks are sharp singlets, and the attenuation is around 90%.

B.Tang, PhD Thesis, Aston University, 2024.
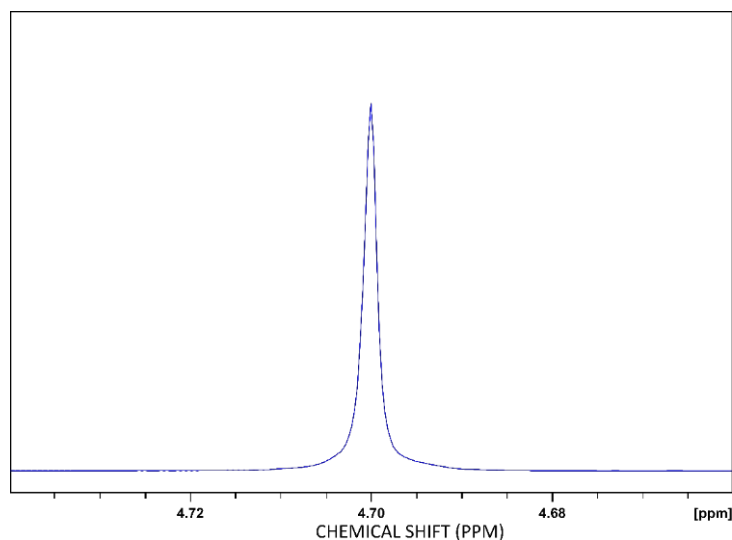
Figure 3.3.19 1D ^{1}H NMR spectrum of 1% H_2O in D_2O (peak at 4.70 ppm).
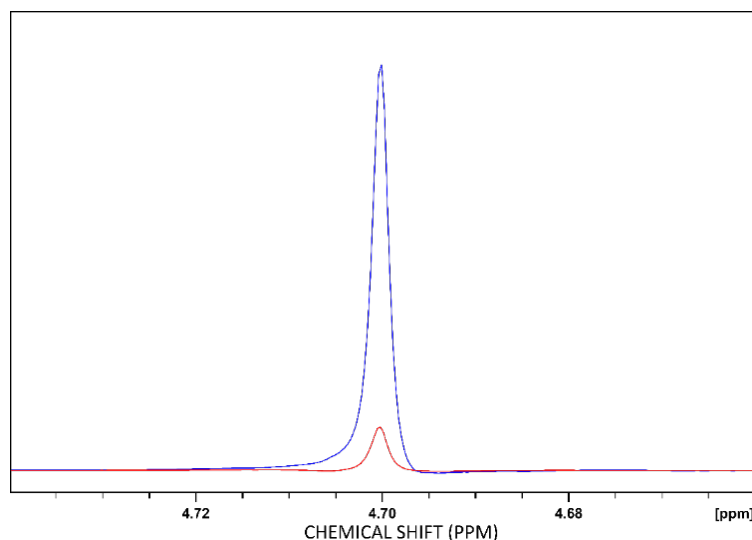
Figure 3.3.20 Stacked plot of the 1D spectrum of first (blue) and last (red) gradient using the double-stimulated-echo-bipolar-pulse-gradient-pair pulse sequence with the balancing gradient (peak 4.70 ppm, 1% H_2O in D_2O). Full diffusion experiment with 2 gradients.

Therefore, a full diffusion experiment with 16 gradient increments was acquired with the same timing parameter. Figure 3.3.21 shows the full diffusion experiment containing the first and highest gradient (blue) and the last and lowest gradient (red). While the peak width did not change over the duration of the experiment, there were distortions in the line shape observed. Figure 3.3.22 compares 1D ^{1}H spectrum before and after the diffusion experiment, where there is a clear change in lineshape.

98
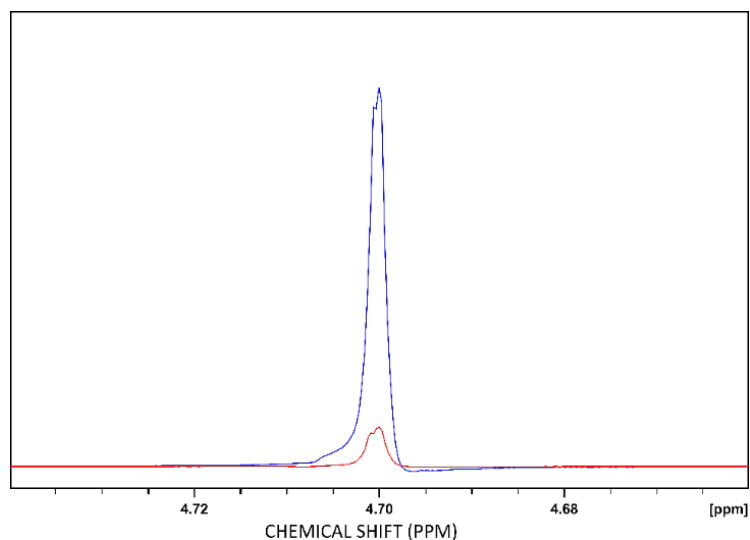
Figure 3.3.21 Stacked plot of the 1D spectrum of first (blue) and last (red) gradient using the double-stimulated-echo-bipolar-pulse-gradient-pair pulse sequence with the balancing gradient (peak 4.70 ppm, 1% H_2O in D_2O). Full diffusion experiment with 16 gradients.
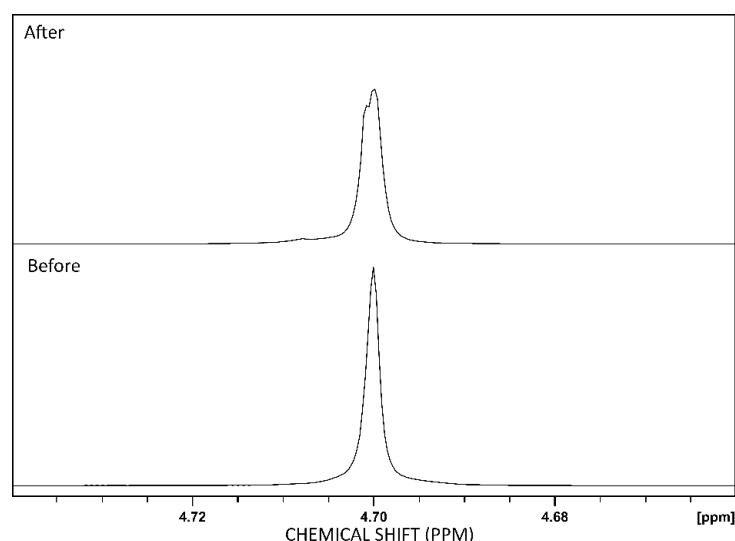
Figure 3.3.22 Plots of 1D ^1H NMR spectrum of 1% H_2O in D_2O (peak at 4.70 ppm) before (same spectrum as Figure 3.3.1) and after the diffusion experiments.

The change in line shape in the diffusion experiments could be because the spectrometer was new, and no diffusion experiments had yet been performed. As diffusion experiments require currents to be put through the gradient coils, on initial attempts at the gradient calibration, some heating may have been produced as currents were applied for the first time, resulting in distortions in the lineshape of the sample. It is common for the shims to drift in new magnets, and around 6 months of settle time is required. Stability tests were performed monthly after the magnet installation, where a

99

¹H NMR spectrum was acquired every minute for 60 minutes and only the first acquisition was shimmed. Figure 3.3.23 shows the changes of peak width over 60 minutes for each month from December 2020 to June 2021 and overall, after February the magnet stability improved and less fluctuations in peak width was observed. In December 2020, there were fluctuations up to *ca.* 0.2 Hz change in peak width compared to June 2021 with minor fluctuation where overall changes after one hour were less than 0.02 Hz. The chart (Figure 3.3.24) shows the change in linewidth at the end of each hour for each month this procedure was completed also indicating the shims became more stable. Once the magnet had stabilised, more advanced experiments could be run.
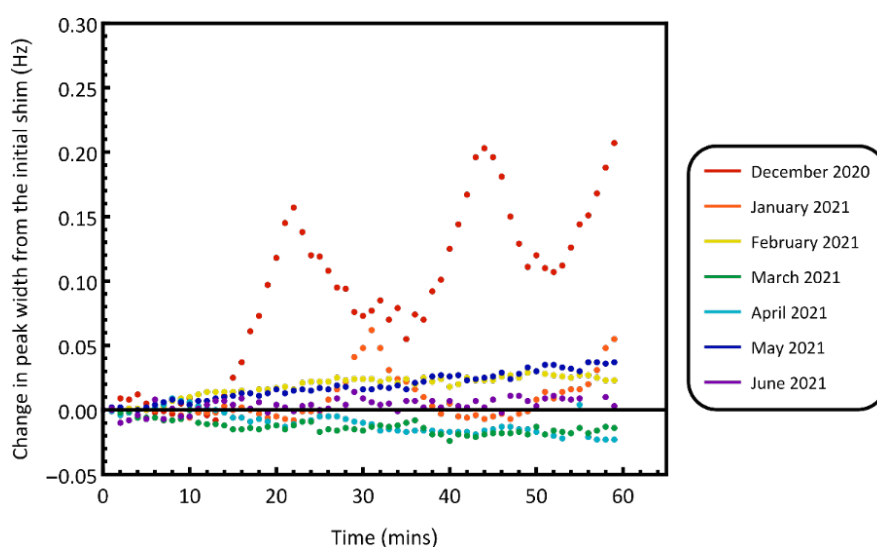
Figure 3.3.23 Changes in peak width (Hz) as a function of time at 298 K from December 2020 to June 2021.
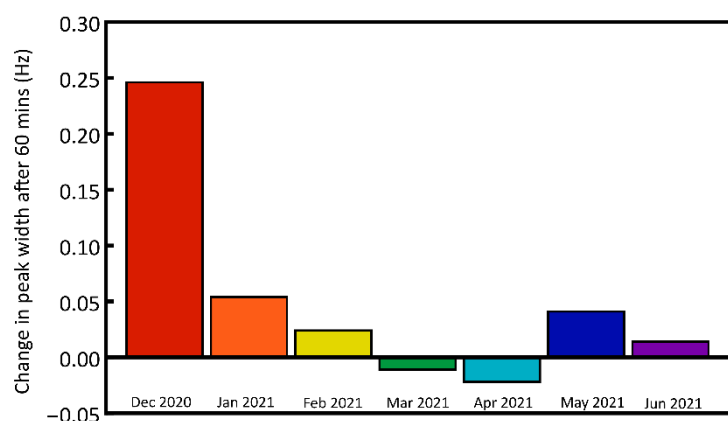
Figure 3.3.24 Bar chart of the change in peak width after 60 minutes from the initial acquisition from December 2020 to June 2021.

3.3.3 Gradient Calibration

The nominal gradient strength (SmartProbe iProbe) provided by the z-gradient probe installed on the spectrometer is 53.5 G cm^{-1}. The diffusion coefficients of three solvents, 1% H2O in D2O, DMSO, and cyclohexane, were acquired and compared with literature data at 298 K. The three solvents were chosen as they span a range of diffusion coefficients, and their diffusion coefficients have been widely reported. Figure 3.3.25 summarises the different gradient strengths required to achieve a 10% and 90% for a proton diffusion experiment where Δ = 0.2 s, δ = 0.001 s and γ = 267522187 rad s^{-1} T^{-1}. These values were calculated using the Stejskal-Tanner Equation. The initial diffusion coefficients and literature values are recorded in Table 3.3.1.
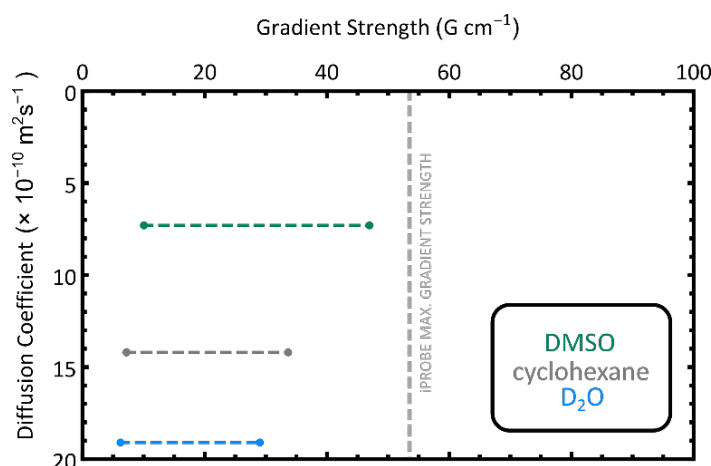
Figure 3.3.25 Estimated gradient strength required to achieve a 10% to 90% attenuation for a proton diffusion experiment using the Stesjkal-Tanner Equation where Δ = 0.2 s δ = 0.001 s and γ = 267522187 rad s^{-1} T^{-1}. DMSO (green), cyclohexane (grey) and D2O (blue), where the iProbe maximum gradient strength is ca. 53.5 G cm^{-1} shown by the dashed grey line.

Table 3.3.1 Comparison of literature and measured diffusion coefficients for DMSO, cyclohexane and 1% H2O in D2O with the original gradient calibration constant of 53.5 G cm^{-1}.

Solvent	D_{lit} × 10^{-10} m^{2}s^{-1}	D_{exp} × 10^{-10} m^{2}s^{-1}
DMSO	7.3 [230]	6.4 (± 0.1)
Cyclohexane	14.2 [230]	12.7 (± 0.1)
1% H$_2$O in D$_2$O	19.1 [229]	17.1 (± 0.1)

The difference in the experimental data and literature values shows a systematic error in the gradient calibration, larger than the experimental error due to the fitting of the Stejskal-Tanner Equation (Equation 2.4.3). The measured diffusion coefficients were all

smaller than expected. Figure 3.3.26 illustrates the relationship between the literature and measured values. The gradient contribution to signal attenuation is a squared term in the equation. To compensate for this error, a factor of $\sqrt{0.8922}$ was applied to the initial calibration, producing the new gradient calibration constant of 50.5 G cm^{-1}.
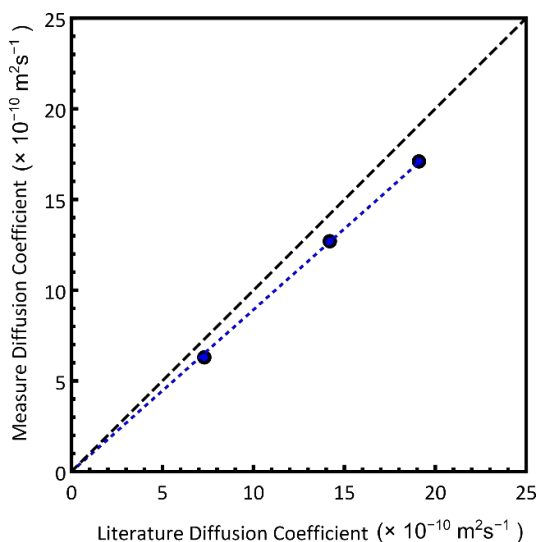
Figure 3.3.26 The relationship between the expected and measured diffusion coefficients for DMSO, cyclohexane, and 1% H$_2$O in D$_2$O pre gradient calibration.

The diffusion coefficients of the solvents were measured again using the new gradient calibration value. The results are shown in Table 3.3.2, and Figure 3.3.27 illustrates the corrected relationship between the experimental and literature diffusion coefficients. The DOSY plot of deuteriated water before and after the gradient correction is also shown in Figure 3.3.28.

Table 3.3.2 Comparison of literature and measured diffusion coefficients for DMSO, cyclohexane and 1% H$_2$O in D$_2$O with the new gradient calibration constant of 50.5 G cm^{-1}.

Solvent	D_{lit} × 10^{-10} m^{2}s^{-1}	D_{exp} × 10^{-10} m^{2}s^{-1}
DMSO	7.3 [230]	7.3 (± 0.1)
Cyclohexane	14.2 [230]	14.2 (± 0.1)
1% H$_2$O in D$_2$O	19.1 [229]	19.1 (± 0.1)
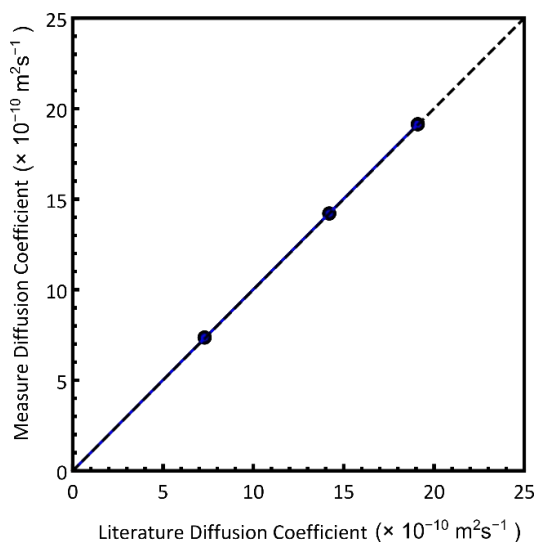
Figure 3.3.27 The relationship between the expected and measured diffusion coefficients for DMSO, cyclohexane, and 1% H_2O in D_2O after gradient calibration.
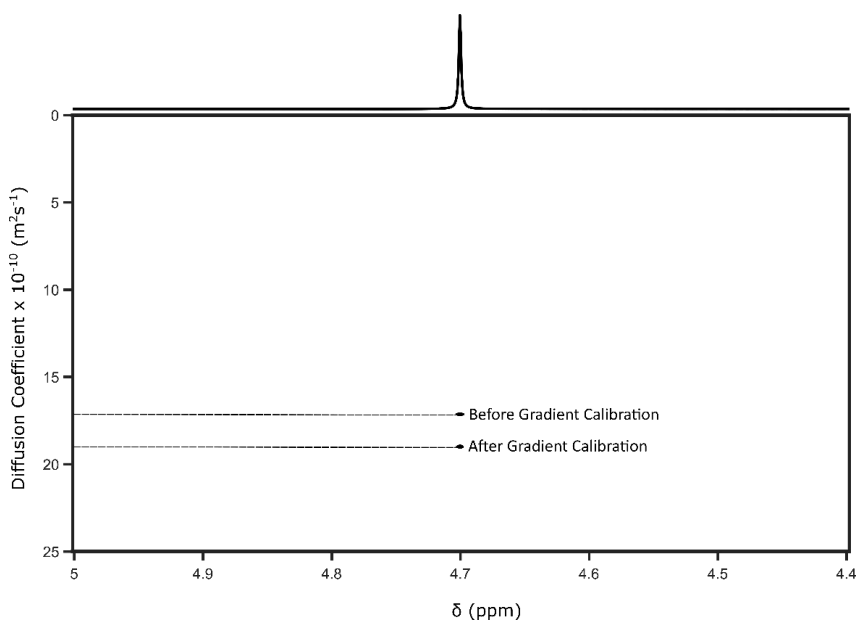
Figure 3.3.28 DOSY spectrum of 1% H_2O in D_2O before and after gradient calibration.

The diffusion probe has larger gradient coils that can produce a larger nominal gradient strength of 1700 G cm^{-1}. Figure 3.3.29 summarises different compounds with a range of diffusion coefficients with the estimated gradient strength required to achieve a 10% and 90% attenuation (for a proton diffusion experiment where Δ = 0.1 s, δ = 0.001 s and γ = 267522187 rad s^{-1} T^{-1}). The estimated gradients required for a 90% attenuation for the slowest moving species ($D_{squalane}$ = 0.290 × 10^{-10} m^2 s^{-1}) is 333.1 G cm^{-1}, only utilising about ~20% of the maximum gradient. Therefore, the choice of solvents and a proton diffusion experiment will not prove suitable for this probe.

B.Tang, PhD Thesis, Aston University, 2024.
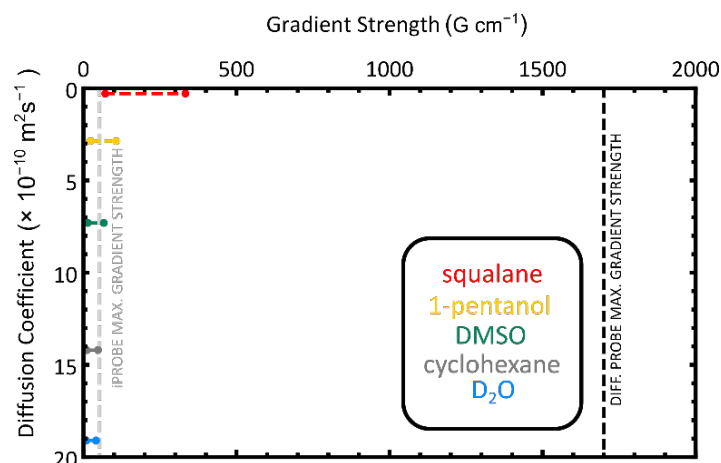
Figure 3.3.29 Estimated gradient strength required to achieve a 10% to 90% attenuation for a proton diffusion experiment using the Stejskal-Tanner Equation where Δ = 0.1 s δ = 0.001 s and γ = 267522187 rad s⁻¹ T⁻¹. Squalane (red), 1-pentanol (yellow), DMSO (green), cyclohexane (grey) and D₂O (blue) where the iProbe maximum gradient strength is ca. 53.5 G cm⁻¹ shown by the dashed grey line.

An alternative method must be chosen to utilise the full range of gradient strengths as the liquids in Figure 3.3.29 only use ~20% of the maximum gradient strength. There are two methods: finding an even more viscous and slow-moving liquid or choosing a diffusion experiment with different nuclei. Carbon-13 has a fourfold lower γ = 67282800 rad s⁻¹ T⁻¹, compared to the proton γ = 267522187 rad s⁻¹ T⁻¹; therefore, to achieve the same amount of attenuation, the gradient pulse area approximately 16 times larger is required. Calculated using the Stesjkal-Tanner equation, a summary of the gradient strengths required to achieve a 10% and 90% for a carbon diffusion experiment where Δ = 0.1 s δ = 0.001 s and γ = 67282800 rad s⁻¹ T⁻¹ is summarised in Figure 3.3.30. The estimated gradients required for a 90% attenuation of the slowest moving species ($D_{squalane}$ = 0.290 × 10⁻¹⁰ m² s⁻¹) is 1323.1 G cm⁻¹. Therefore, using a carbon experiment a larger range of gradients can be utilised.

Gradient Strength (G cm⁻¹)
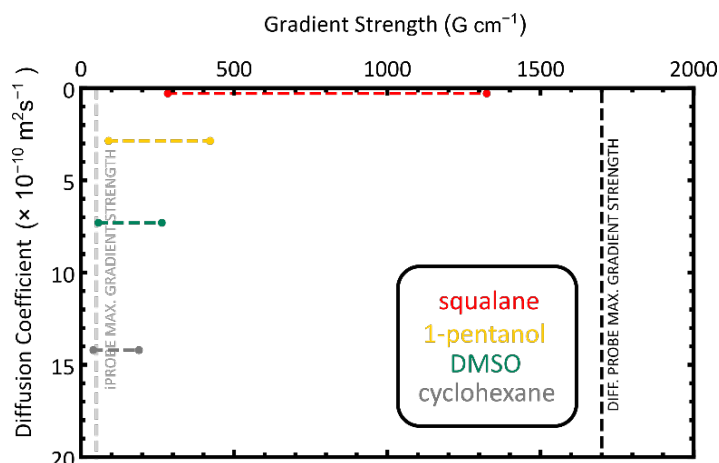
Figure 3.3.30 Estimated gradient strength required to achieve a 10% to 90% attenuation for a carbon diffusion experiment using the Stejskal-Tanner Equation where Δ = 0.1 s δ = 0.001 s and γ = 267522187 rad s⁻¹ T⁻¹. Squalane (red), 1-pentanol (yellow), DMSO (green) and cyclohexane (grey) where the iProbe maximum gradient strength is ca. 53.5 G cm⁻¹ shown by the dashed grey line and diffusion probe maximum gradient is 1700 G cm⁻¹ shown by the black dashed line.

Acquiring ^{13}C diffusion NMR data requires a different experimental NMR strategy. The combination of DEPT with spin echo to produce a DEPTSE pulse sequence is illustrated in Figure 3.3.31. A spin echo sequence was chosen over a stimulated echo as there is negligible problem with J modulation when diffusion encoding using ^{13}C and, this turn, this avoids throwing away 50% of the signal in a stimulated-echo (STE). However, as this pulse sequence is not convection compensated, thick-walled tubes were used to minimise effects due to convection.
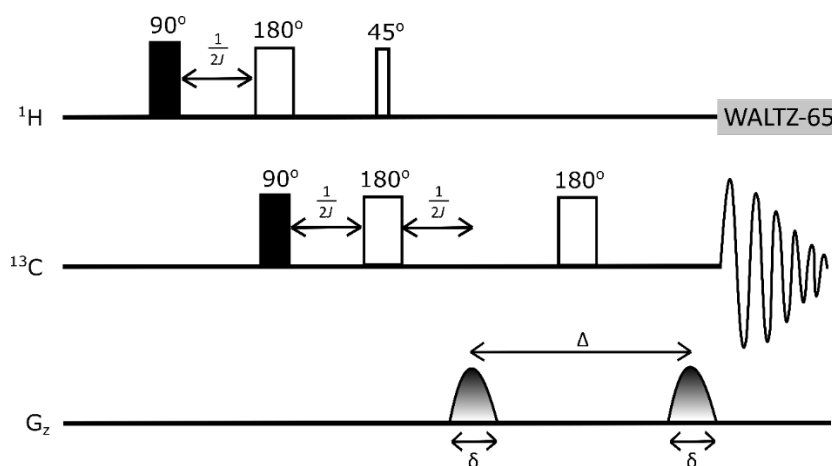
Figure 3.3.31 Distortionless Enhancement by Polarisation Transfer (DEPT) with a pulse field gradient spin echo sequence, diffusive delay time Δ, the gradient pulse has gradient strength g with a duration δ.

B.Tang, PhD Thesis, Aston University, 2024.

The diffusion coefficients of the solvents were measured with the original calibration constant for the diffusion probe. The diffusion coefficients and literature values are recorded in Table 3.3.3. The results are shown in Figure 3.3.32, which illustrates the linear relationship between the experimental and literature diffusion coefficients. This suggests that the original calibration constant was correct. Therefore, no further action was required to obtain accurate diffusion coefficient data using a diffusion probe.

Table 3.3.3 Comparison of literature and measured diffusion coefficients for squalane, 1-pentanol, DMSO and cyclohexane with the gradient calibration constant of 1701 G cm^{-1}.

Solvent	D_{lit} $\times 10^{-10}$ m^{2}s^{-1}	D_{exp} $\times 10^{-10}$ m^{2}s^{-1}
Squalane	0.29	0.29 (± 0.03)
1-Pentanol	2.9	2.97 (± 0.02)
DMSO	7.3 [230]	7.20 (± 0.02)
Cyclohexane	14.2 [230]	14.3 (± 0.10)
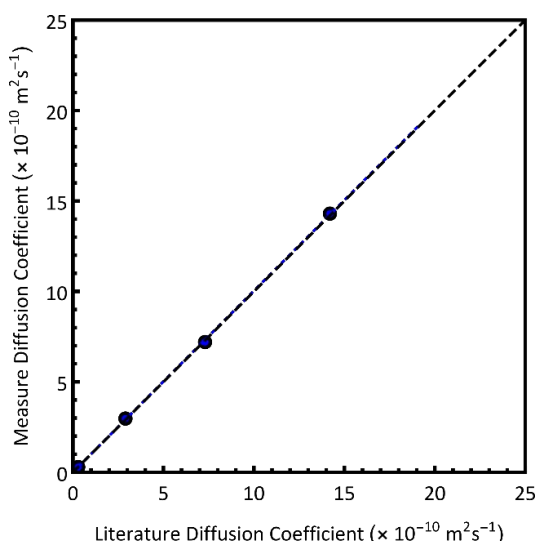
Figure 3.3.32 The relationship between the expected and measured diffusion coefficients for DMSO, cyclohexane, and 1% H$_2$O in D$_2$O after gradient calibration.

3.4 Conclusions

In this chapter, the essential experimental parameters, particularly the accuracy of the spectrometer temperature and the gradient calibration constant, have been evaluated for both regular probe (iProbe) and diffusion probe (DiffBB) on the 500 MHz magnet. Understanding and correcting these parameters ensures that all diffusion NMR data collected for further experiments are as precise and accurate as possible. From the study

of sample temperature, it was expected that the nominal temperature stated by the spectrometer was not the actual temperature within the sample tube. A linear conversion was obtained between the actual temperature (using the standard NMR thermometer) and the nominal temperature. The time taken for the temperature to change was also analysed, and in conclusion, the sample was stable after 6 minutes. However, 10 minutes of waiting time would be more suitable. It is very important to know the actual sample temperature, especially when conducting diffusion experiments, where the temperature will affect the thermal energy of the system and the solvent viscosity, and thus affecting the diffusion coefficient of the sample. An NMR thermometer should always be used to check the temperature, and the sample must be left to equilibrate to ensure it has reached the desired temperature.

In the course of this work, some worrying issues emerged particularly in the early stages of running the magnet. The stability of the shims was also evaluated, and the line shape of the samples and peak width improved over time. This is likely due to the newly installed magnet. It is common for the shims to drift in new magnets, and around 6 months of settle time is required. Stability tests were performed monthly after the magnet installation, over 7 months the magnet stability improved.

Once stabilised, gradient calibrations could be performed. The strength of the pulsed field gradient of the iProbe was also calibrated using three common solvents whose diffusion coefficients are well-known and described in the literature. The diffusion coefficients of DMSO, cyclohexane and 1% H_2O in D_2O were measured at 298 K and compared with literature data. It was found that there was a systematic error in the diffusion coefficient across all species. The gradient calibration constant was changed and repeats of the experiments were carried out. The diffusion coefficients within the expected values were obtained.

The 500 MHz magnet was supplied with a diffusion probe (DiffBB probe), containing much larger gradients powered by a larger amplifier. It was found that proton diffusion experiments were not suitable for calibrating diffusion probes, due to these much larger gradients. Alternatively, a carbon DOSY experiment was chosen. Due to the lower gyromagnetic ratio of carbon, larger gradients are required to achieve the same diffusion attenuation of signal. The diffusion coefficients of squalene, 1-pentanol, DMSO, and

cyclohexane were compared to literature data. It was found that the diffusion coefficients were in the expected range, and the diffusion probe did not need further correction of the calibration constant.

CHAPTER 4 : QUANTITATIVE ANALYSIS OF CARBONYL GROUPS IN FAST PYROLYSIS OIL USING ^{19}F LOW-FIELD NMR

4.1 Introduction

Oxygen-containing compounds are the main contributor to the acidity of the pyrolysis oils. These compounds typically being aldehydes, ketones, quinones, hydroxyl, carboxylic and phenolic groups. Such carbonyl-containing compounds have a negative effect on the stability of the pyrolysis oil. Acidity of the pyrolysis oil causes corrosion in storage and usage.[90, 100, 101] These oils can be enhanced either physically or chemically. The identification and quantification of the oxygen-containing compounds is crucial for characterisation and upgrading processes. However, the identification and quantification of carbonyl groups in pyrolysis oil is difficult. Current semi-quantitative/quantitative techniques including Fourier Transform Infrared Spectroscopy (FTIR), oximation by titration, and derivatisation using 4-(trifluoromethyl)phenyl hydrazine followed by ^{19}F NMR methods. FTIR is generally a semi-quantitative technique that primarily looks at functional groups where the spectra band ratios are compared.[176, 192] Oximation reactions tend to be laborious, the carbonyl groups are reacted with hydroxylamine hydrochloride for >30 hr, followed by a titration with hydrogen chloride.[192, 232] During the oximation reaction the hydroxylamine hydrogen chloride reacts with carbonyl containing compounds such as aldehydes and ketones present in the pyrolysis oil. The reaction yields an oxime and hydrochloric acid as shown in reaction Scheme 4.1. The reaction is an equilibrium where pyridine is added to 'mop-up' the excess HCl which drives the reaction to completion. The pyridine and HCl form pyridine hydrochloride salt. This is titrated against NaOH with an end-point around pH 4.7.
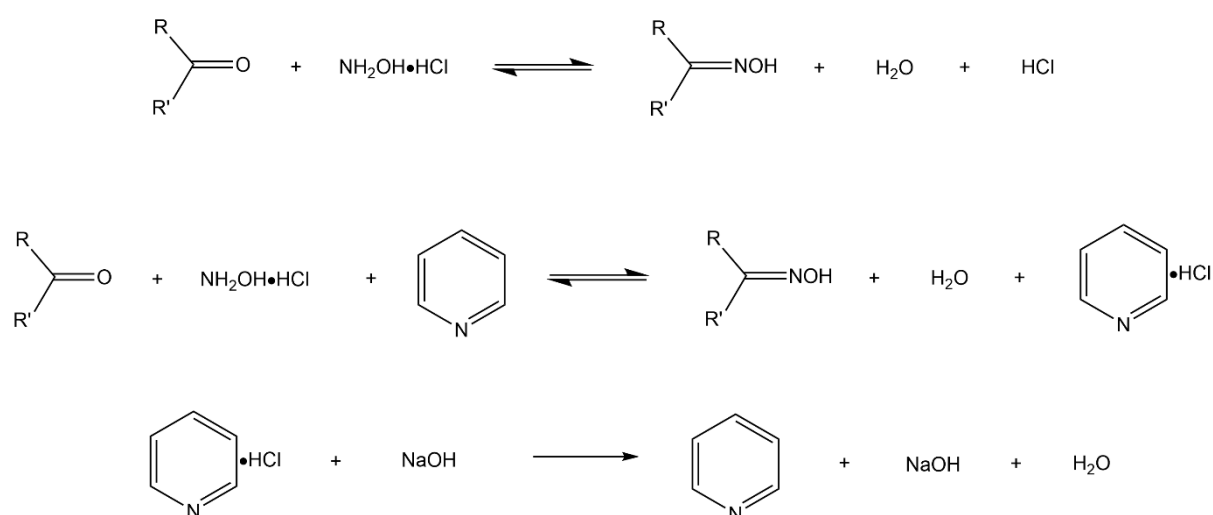
Scheme 4.1 Reaction scheme of carbonyl-containing compound with hydroxylamine hydrochloride producing oxime and HCl. The reaction is shifted towards the oxime in the presence of pyridine. Pyridine hydrochloride is titrated with sodium hydroxide.

110

B.Tang, PhD Thesis, Aston University, 2024.

Quantification of total carbonyl content is then calculated using the equation:

$$mol\ of_{C=O}\ per\ gram\ of\ oil = \frac{Volume_{NaOH} \times N_{NaOH}}{Dry\ Weight\ of\ the\ Oil\ (g)}$$

Equation 4.1.1

Derivatisation methods add a tagging agent to isolate molecules with certain functional groups of interest for analysis. The different methods of the derivatisation of carbonyl groups using 4-(trifluoromethyl)phenyl hydrazine followed by NMR analysis were explored in Chapter 2. The derivatisation method in this chapter will be based on general reaction scheme is shown in Figure 4.1.1(reproduced from Figure 2.4.9). A summary of the derivatisation methods are as follow, the Sevillano *et al*. method dissolves the lignin in DMF:H_2O solution followed by the 100 mg derivatisation agent. This solution was left to react for 1 day in the dark.[191] The derivatised mixture was precipitated using 100 mL of water with 3 drops of phosphoric acid. The sample was filtered using a sintered glass crucible and dried at 40°C. Huang *et al*. also follows a similar procedure, 60 mg bio-oil sample is dissolved in 500 μL of DMF.[192] 1 mL of the 50:50 DMF-water (v/v) mixture containing 110 mg of 4-(trifluoromethyl)phenyl hydrazine was added. The mixture was left in the dark to react at room temperature for 24 hours. The sample is then precipitated using pH HCl solution, followed by freezing, thawing and drying. Constant *et al*. dissolves *ca*. 150 mg of sample and 10 mg of 1-methyl-4-(trifluoromethyl)benzene the internal standard (IS) in DMSO-d_6.[193] 0.8 mmol of 4-(trifluoromethyl)phenyl hydrazine was dissolved in 300 mL DMSO-d_6. The derivatisation agent was added dropwise to the sample. The solution is transferred to a standard NMR tube and left to react in a pre-heated oven at 40°C for 16 hours. In all these cases, 4-(trifluoromethyl)phenyl hydrazine is reacted to form hydrazones. Following the derivatisation process ^{19}F NMR analysis has always been typically carried out using high-field NMR spectrometers.
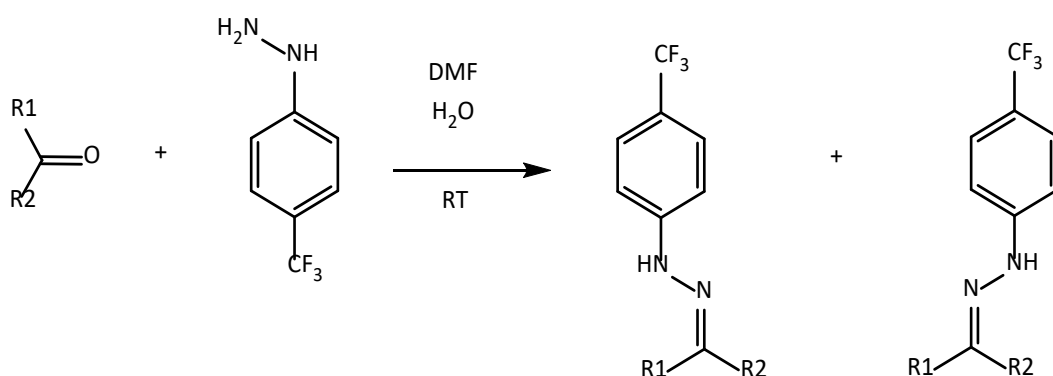
Figure 4.1.1 Reaction scheme of carbonyl-containing compound derivatised by 4-(trifluoro methyl)phenyl hydrazine.

Quantification of carbonyl content was calculated using the equation[192] where IR is the integration ratio:

$$mol\ of_{C=O}\ per\ gram\ of\ oil\ = \frac{IR\ \times n_{(IS\ in\ NMR\ sample)}\ (mol)}{Dry\ Weight\ of\ the\ Oil\ (g)}$$

Equation 4.1.2

In Chapter 2, Section 2.3 the advantages and disadvantages of high-field NMR spectrometers and low-field NMR spectrometers were compared. Overall, high-field NMR required a large capital cost and technical maintenance which limits the usage of NMR to larger research facilities. The cost and maintenance of NMR spectrometers is also limiting factor for material verification such as quality control in an industrial setting.[233] However, there has been an increased use for low-field NMR in the analysis of mixtures such as over-counter drugs[234], edible oils[235] and crude oil-water biphasic mixtures[236]. Even though low-field NMR suffers from sensitivity, it is not crucial to have the multiplicity resolution when analysing mixtures containing a vast number of compounds. Recently, low-field benchtop NMR has been used for quantitative ^{31}P NMR analysis of alcohol groups in lignin.[237] This chapter will focus on developing low-field ^{19}F NMR methods to identification and quantification of carbonyl containing species.

4.2 Experimental

4.2.1 Materials

All reagents used as model compounds were obtained commercially, the origin and purity of these compounds used in this study are reported in the Appendix 2 (Table A2.1). 4-(trifluoromethyl)phenyl hydrazine and dimethylformamide was purchased from Sigma-Aldrich and Fisher Scientific respectively. All chemicals were used without any further purification. All pyrolysis oil was provided by the Energy and Bioproducts Research Institute (EBRI). Pyrolysis oil produced from oak, willow, Virginia mallow and miscanthus was all produced from fast pyrolysis in a 300 g h^{-1} continuous bubbling fluidised bed reactor.

4.2.2 Elemental Analysis

Elemental Analysis of all oils was varied out on a Flash 2000 elemental analyser. Carbon, hydrogen, nitrogen and sulphur (CHNS) content were analysed in triplicate, and the average values were taken. The oxygen content of the oils was found by difference.

4.2.3 Oximation Followed by Titration

The oximation of pyrolysis oil was carried out using the following procedure: Hydroxylamine hydrochloride solution was prepared by dissolving 17.50 g of hydroxylamine hydrochloride in 80.00 g of deionised water, the solution was transferred to a 500 mL volumetric flask, the volumetric flask was filled to the mark with anhydrous ethanol. Pyridine solution was prepared by adding 10 mL of pyridine into a 500 mL volumetric flask, the volumetric flask was filled with anhydrous ethanol. For the oximation reaction *ca*. 0.40 g of pyrolysis oil reacted with 10.00 mL of hydroxylamine solution and 20 mL of pyridine solution were combined in a sealed flask. The reaction was left stirring for 48 hours at room temperature. The reaction mixture was transferred to a 100.00 mL volumetric flask and filled with anhydrous ethanol. Aliquots of 25.00 mL were taken and titrated with 0.5 M sodium hydroxide solution. The titration endpoint (pH = ~4.5) was measured using a micro pH electrode probe.

4.2.4 ^{19}F NMR Analysis

The derivatisation of pyrolysis oil was carried out using the following procedure: 110 mg of 4-(trifluoro methyl)phenyl hydrazine was dissolved in 1 mL of 50:50 DMF and water (v/v). This solution was added to a solution of pyrolysis oil (*ca*. 30 mg) dissolved in 500 μL dimethylformamide (DMF) in a 20 mL vial. The mixture was stirred in the dark for 24 hours at room temperature. The derivatised pyrolysis oil was purified by adding 20 mL of pH 2.0 water, where the pH 2.0 water was prepared by diluting 5N HCl with deionised water. The sample was placed in a freezer to allow precipitation to occur. The frozen sample was melted to room temperature. The aqueous layer was carefully discarded, and the product was washed multiple times with pH 2.0 water to remove excess 4-(trifluoromethyl)phenyl hydrazine. The precipitant was then air dried for 24 hours. The dried sample was then dissolved in protiated DMSO for NMR analysis, where 3-(trifluoromethoxy) benzoic acid was used as an internal standard (IS). Figure 4.2.1 shows hexafluorobenzene (C_6F_6) was used as an external standard (ES) for the chemical shift calibration at −164.9 ppm. All low-field NMR was carried out using a Magritek Spinsolve 43 MHz benchtop NMR. All high-field NMR was carried out using Bruker AVANCE NEO 500 MHz. All data was processed using MestReNova 10 software.
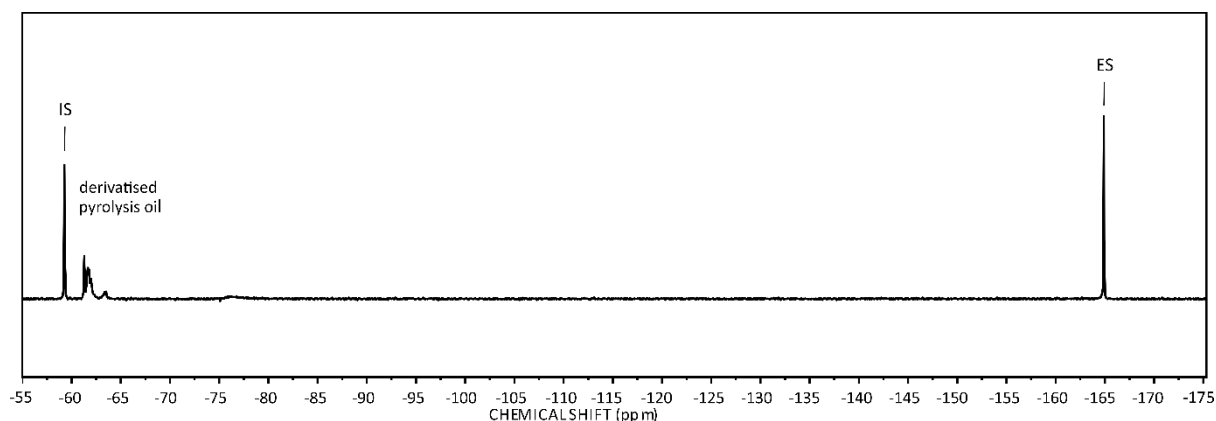
Figure 4.2.1 ^{19}F NMR spectrum of hexafluorobenzene used as the external standard (−164.9 ppm) at 43 MHz.

4.3 Results and Discussion

4.3.1 Method Development of ^{19}F Low-Field NMR Technique

4.3.1.1 Qualitative Analysis of Carbonyl Groups Using Low-field NMR

One of the advantages of using the benchtop NMR is that data can be acquired using protiated solvents which are cheaper than their deuteriated counterpart. As a proof of concept that low-field ^{19}F NMR can be used to distinguish between different fluorine environments in derivatised pyrolysis oil, simple mixtures model carbonyl-containing compounds were studied. Starting with the simplest ketone, acetone was derivatised using the procedure described in Section 4.2.4. The derivatised product was dissolved in protiated DMSO and analysed using low-field NMR. Model compound had the same chemical shift regardless of the choice of protiated solvent or deuteriated solvent. In the Appendix 2, Figure A2.1 shows stacked spectra of different fluorine-containing compounds in DMSO-d_6 and protiated DMSO. The chemical shifts are tabulated below:

Table 4.3.1 Summary of the chemical shift for standard fluorine-containing compounds in DMSO and DMSO-d6.The spectra can be found in Appendix 2, Figure A2.1.

Figure A2.1	Chemical and Solvent	Chemical Shift
(a)	3-(trifluoromethoxy) benzoic acid,	−59.3
	3-(trifluoromethyl) benzoic acid and	−63.8
	C_6F_6 in DMSO-d_6	−164.0
(b)	3-(trifluoromethoxy) benzoic acid in DMSO-d_6	−59.3
(c)	3-(trifluoromethoxy) benzoic acid in DMSO	−59.3
(d)	3-(trifluoromethyl) benzoic acid in DMSO-d_6	−63.8
(e)	3-(trifluoromethyl) benzoic acid in DMSO	−63.8
(f)	C_6F_6 DMSO-d_6	−164.9
(g)	C_6F_6 in DMSO	−164.9

The reaction was proven successful via ^{19}F NMR analysis using a low-field spectrometer shown in Figure 4.3.1. The product and the internal standard should show two species present in the spectrum this can be seen in Figure 4.3.1(a). However, to confirm the signal at −61.63 ppm belonged to the derivatised acetone and not unreacted derivatisation agent, the sample was spiked with a small amount of 4-(trifluoro)phenyl hydrazine this can be seen in Figure 4.3.1 (b), where three signals are present. As a final assessment, the ^{19}F spectrum of the internal standard and derivatisation agent was acquired Figure 4.3.1 (c) as well as the ^{19}F spectrum of the internal standard only was acquired Figure 4.3.1 (d) confirms the peak at −61.63 ppm belongs to the derivatised acetone. This also proves low-field NMR can provide chemical information of simple mixtures displaying singlet peaks produced by the different fluorine environments which are resolved enough to be assigned to different compounds.
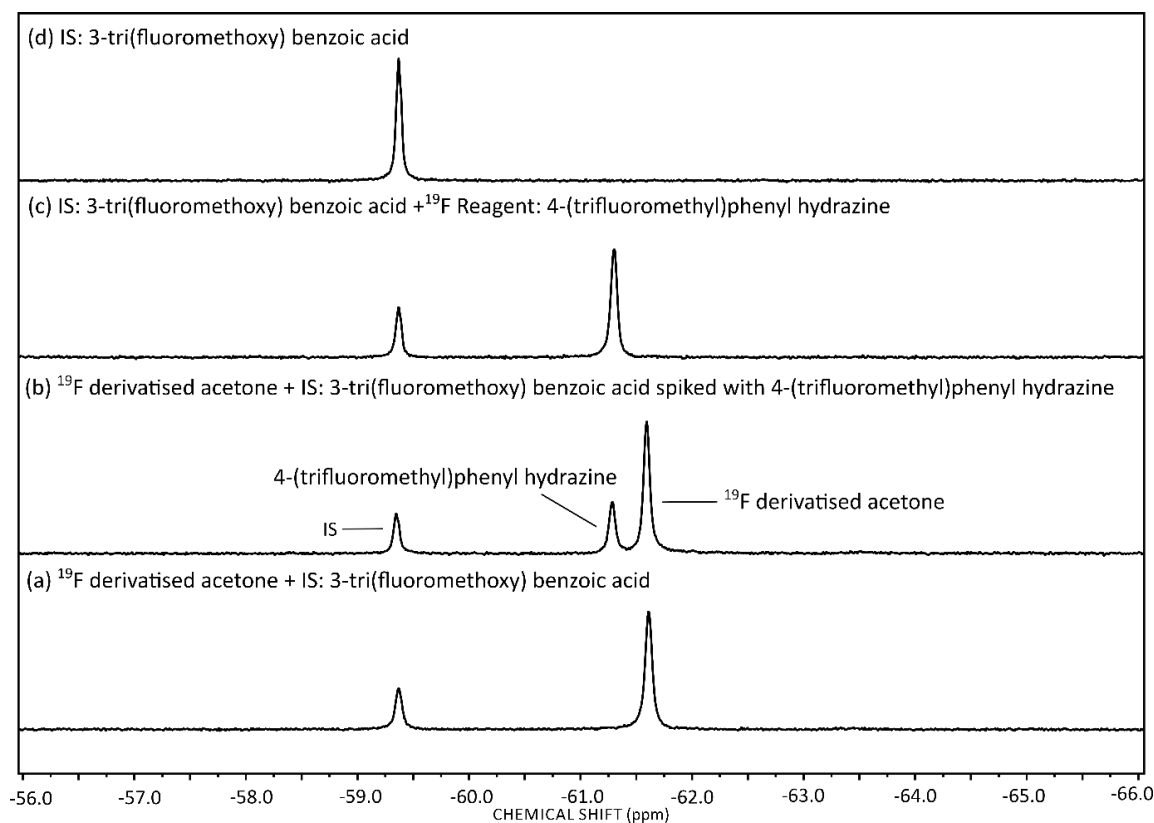
Figure 4.3.1 (a) ^{19}F NMR spectrum of derivatised acetone and internal standard (IS) 3-(trifluoromethoxy) benzoic acid (b) ^{19}F NMR spectrum of derivatised acetone, internal standard (IS) 3-(trifluoromethoxy) benzoic acid and 4-(trifluoromethyl)phenyl hydrazine. (c) ^{19}F NMR spectrum of derivatised acetone and 4-(trifluoromethyl)phenyl hydrazine (d) internal standard (IS) 3-(trifluoromethoxy) benzoic acid. All data acquired on the benchtop NMR spectrometer at 43 MHz.

4.3.1.2 Generation of ^{19}F Chemical Shift Map of Derivatisation Compounds

Having shown the reaction works, the next step is to develop a comprehensive chemical shift map. Derivatisation of model compounds followed by analysis using the low-field NMR spectrometer was used to produce a chemical shift map which will then be used for integration. Figure 4.3.2 shows the stacked plot of the derivatised model compounds. A summary of the chemical shift can be found in Appendix 2 (Table A2.2) where all chemical shifts were referenced using hexafluoro benzene (-164.9 ppm). The chemical shift for the 4-(trifluoromethyl)phenyl hydrazine derivatised ketone is *ca.* -61.0 to -61.7 (red), 4-(trifluoromethyl)phenyl hydrazine derivatised aldehyde is *ca.* -61.7 to -61.9 (blue) and 4-(trifluoromethyl)phenyl hydrazine derivatised quinone -61.9 to -64.0 (black). A summary of the chemical shift area for ketones, aldehyde and quinones is represented in a schematic diagram (Figure 4.3.3).
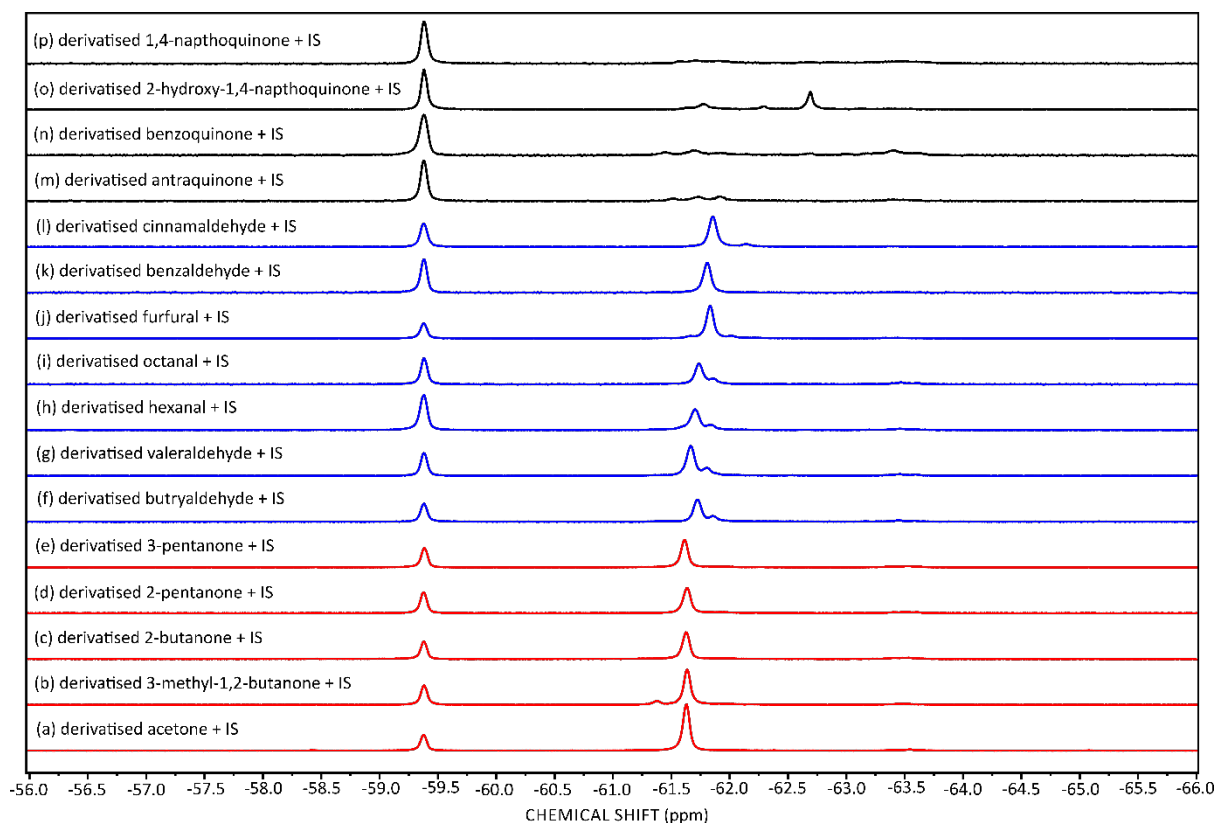
Figure 4.3.2 ^{19}F NMR stack plot of derivatised model compounds containing carbonyl groups at 43 MHz, where the aldehydes are shown in red, ketones are in blue and quinones are in black with the internal standard 3-(trifluoromethoxy) benzoic acid at −59.8 ppm.
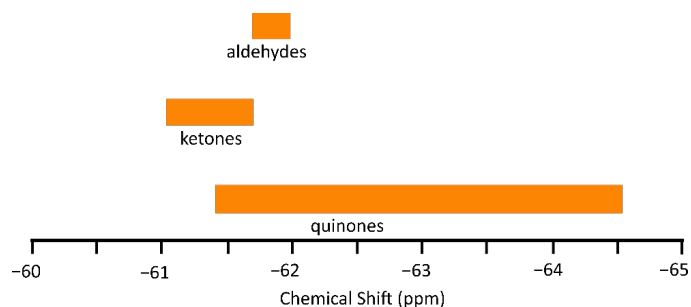
Figure 4.3.3 Schematic representation of ^{19}F NMR chemical shift regions for carbonyl compounds derivatised using 4-(trifluoro)phenyl hydrazine.

4.3.1.3 Selection of Internal Standard

Unlike other quantification techniques, NMR methods do not require a calibration curve. The key factor to quantification is successfully determining the peak integral in an NMR spectrum. This has been predominantly calculated using integration where the computer calculates the sum of the data points within the spectral region. The integrals of the peak of interests are compared to the integral of the internal standard. The selection of internal

standard is crucial for quantitative analysis. Avoiding overlap between the peaks of interest and the internal standard is vital to get accurate integrals. There are a number of internal standards that are mentioned fit for quantification purposes in literature such as 3-tri(fluoromethoxy)benzoic acid[192], 1-methyl-4-(trifluoromethyl)benzene[193] and 2-fluoroguaiacyl benzoate.[192] However, there was ambiguity in the primary literature as to which internal standards have actually been used. Theoretically any fluorine-containing compound that demonstrates stability and satisfactory resolution from the peaks of interest can be used as an internal standard. Two different fluorinated compounds (Figure 4.3.4) were originally chosen as potential candidates for quantification, these being 3-(trifluoromethoxy)benzoic acid and 3-(trifluoromethyl)benzoic acid. First, both compounds were mentioned in literature and second, trifluoromethyl groups increase the sensitivity by three-fold compared to monofluorinated agents.
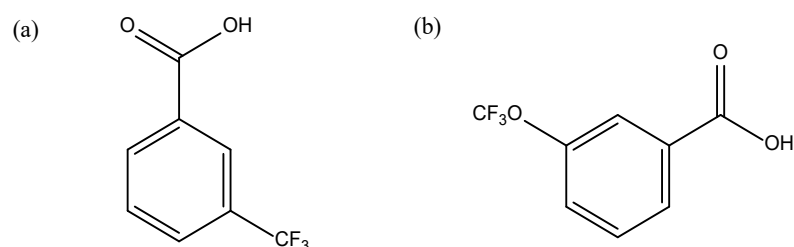
Figure 4.3.4 (a) 3-(trifluoromethyl)benzoic acid (b) 3-(trifluoromethoxy)benzoic acid.

Figure 4.3.5, and Figure A2.2 in the Appendix 2, show that the different internals standards, 3-(trifluoromethoxy)benzoic acid and 3-(trifluoromethyl)benzoic acid respectively, are located away from the derivatised acetone peak. However, as oils contain more than one carbonyl-containing compound it is important to test this with a real sample. In this study pyrolysis oil produced from spruce was used to determine a suitable internal standard for quantification. Figure 4.3.5 shows the two internal standards with the spruce pyrolysis oil (a) 3-(trifluoromethoxy)benzoic acid (*ca.* –59.3 ppm) and (b) 3-(trifluoromethyl)benzoic acid (*ca.* –63.8 ppm). It was found that 3-(trifluoromethyl)benzoic acid as the internal standard would overlap with the peaks of interest around –64 ppm, therefore for future studies the internal standard 3-tri(fluoromethoxy)benzoic acid was used.
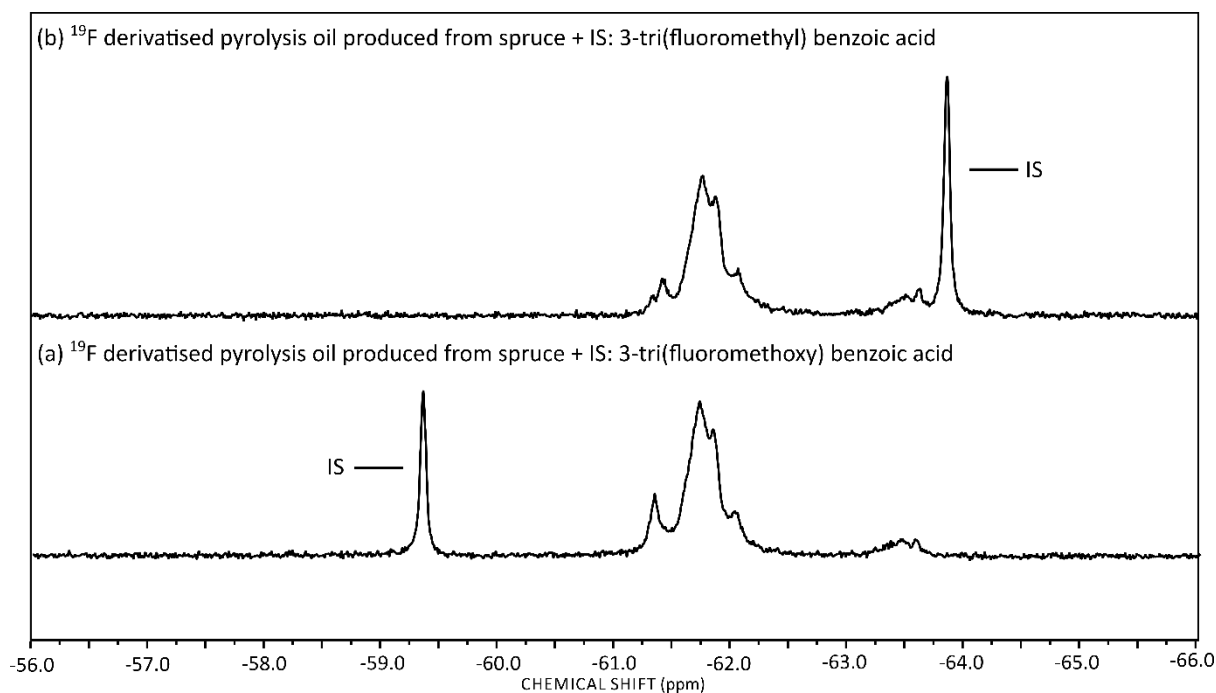
Figure 4.3.5 (a) ^{19}F NMR derivatised pyrolysis oil produced from spruce and internal standard 3-(trifluoromethoxy) benzoic acid at −59.8 ppm (b) ^{19}F NMR derivatised pyrolysis oil produced from spruce and internal standard 3-(trifluoromethyl) benzoic acid at −63.8 ppm.

4.3.1.4 Quantitative ^{19}F NMR Analysis

Model bio-oils were produced to show that low-field NMR can be used to get accurate integrals for quantification analysis. The model oils were generated by combining different amounts of aldehyde, ketone and quinone model compounds. Table 4.3.2 shows the mole composition of each model oil.

Table 4.3.2 Summary of the mole composition of the model carbonyl-containing compounds in each model oil.

Compound	Model Oil 1 ($\times 10^{-4}$ mol)	Model Oil 2 ($\times 10^{-4}$ mol)	Model Oil 3 ($\times 10^{-4}$ mol)	Model Oil 4 ($\times 10^{-4}$ mol)
acetone	2	4	2	2
octanal	1	1	2	1
furfural	1.8	1.8	1.8	3.6
1,4-benzoquinone	0.3	0.3	0.3	0.3

The model oils were derivatised using the procedure outlined in Section 4.2.4. 1D ^{19}F NMR data was acquired on the benchtop NMR. Figure A2.3 shows the integrated NMR spectrum, with all the data used to calculate the amount of carbonyl groups summaries in the Appendix 2, Tables A2.2(a) and (b). Figure 4.3.6 shows a graph summarising the

119

theoretical amount of ketones, aldehydes and quinones in the model oils compared with the quantification via NMR spectroscopy. There are some overlaps in the quinone regions with the ketones and aldehydes. This technique is limited due to the overlap and relatively small chemical shift range for the derivatised compound. NMR proves able to provide chemical information on the compounds compared to other traditional techniques where elemental analysis only give the percentage of oxygen and oximation followed by titration can only give a total amount of carbonyl groups.
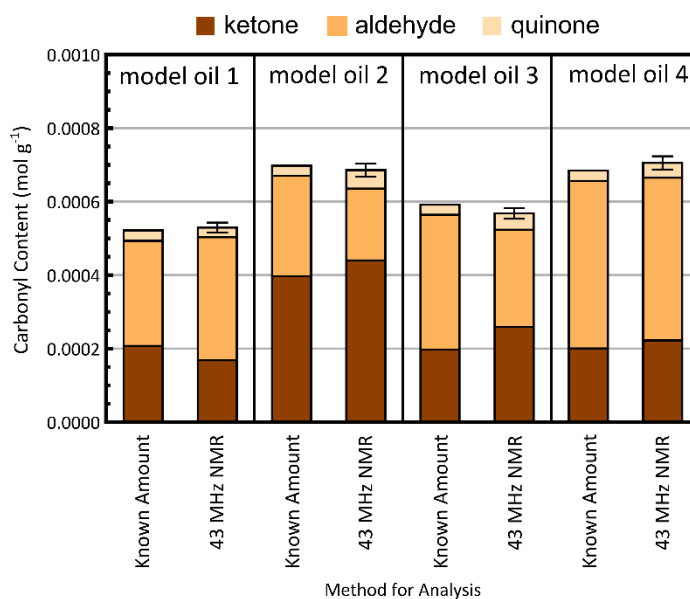
Figure 4.3.6 Graph comparing the theoretical amount of ketones, aldehydes and quinones with the quantification carried out using 19F NMR spectroscopy technique.

4.3.1.5 Optimisation of Derivatisation Process and ^{19}F NMR Analysis

The derivatisation methods described by Sevillano et al., Huang et al. and Constant *et al.* all use the derivatisation agent 4-(trifluoromethyl)phenyl hydrazine, as outlined in the introduction (Section 4.1).[191-193] The original method by Sevillano *et al.* was developed to analyse carbonyl content in lignin.[191] Huang et al. used a similar method, where the main difference was in the methods used for purification of the product.[192] The revised experimental methods by Constant *et al.* method results in a shorter experimental time 16 hours compared to 24 hours.[193] By carrying out the reaction in the NMR tube, there are no losses due to sample transfer. However, the lack of any purification step results in a significant peak at *ca.* −59 ppm in the final ^{19}F NMR spectrum in Reference 188 due to left-over derivatisation agent. The derivatisation agent peak could overlap with peaks of interest leading to an over estimation of carbonyl groups. Overall, Huang *et al.* method was more favoured for the study of pyrolysis oil, as the method was originally applied to

similar samples and the purification step is important to remove the excess derivatisation agent is important for accurate quantification of carbonyl groups.[192] Following Huang *et al*. method, it was found that 60 mg for bio-oils were found to be not reproducible for these specific types of bio-oils.[192] For example, the derivatisation of the bio-oil produced from willow was repeated in triplicate, however as shown in Figure 4.3.7 the expected peaks between −61 ppm and −61.7 ppm which belong to derivatised aldehydes were missing. This can also be visually seen in the derivation process, when the samples are precipitated with the pH2 water, the water would be colourless, suggesting that all the derivatisation agent was used. It is important to have an excess of the derivatisation agent for all carbonyl-containing compounds to be derivatised. The amount of bio-oil was reduced to 30 mg per reaction. This was found to be more reproduceable. Figure A2.4 shows the ^{19}F NMR spectrum of derivatised bio-oil in triplicate, where the NMR all look identical as well as the integrals being similar to each other.
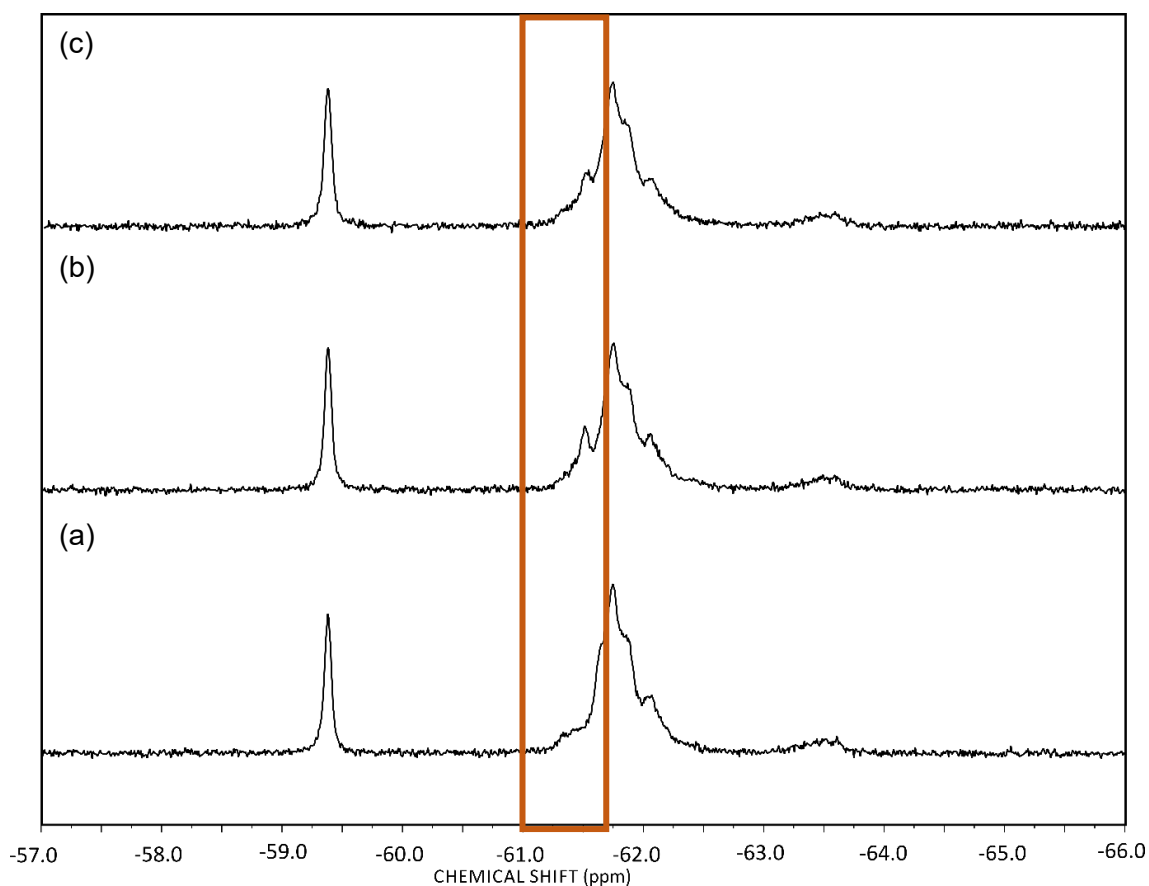
Figure 4.3.7 Stacked ^{19}F NMR of derivatised pyrolysis oil produced from willow in triplicate. The highlighted are between −61 and −61.7 ppm which belongs to the derivatised aldehydes were missing.

4.3.2 Analysis of Pyrolysis Oil

4.3.2.1 Elemental Analysis

All pyrolysis oil were provided by the Energy and Bioproducts Research Institute (EBRI). Pyrolysis oil produced from oak, willow, Virginia mallow and miscanthus were all produced from fast pyrolysis in a 300 g h^{-1} continuous bubbling fluidised bed reactor. The pyrolysis oils were characterised previously by Banks *et al*..[238] There was some time difference between the initial analysis and this study. The elemental analysis giving the CHNS composition of the oils were re-acquired, checking the oil composition. Table 4.3.3 shows a summary of the original data[238] and the re-acquired data for the elemental composition of the oils, where the oxygen content was calculated by a difference. All the data was within the instrument error of 5% and concordant to values reported in the original paper.[238] However, elemental analysis only provides the full oxygen content as a weight percentage but cannot give information such as structure or functional groups which are crucial to identify the oxygen-containing compounds pyrolysis oils for upgrading. Other analytical techniques are needed to identify and quantify the oxygen-containing compounds.

Table 4.3.3 Elemental analysis results for pyrolysis oil produced from various feedstocks (oak, willow, Virginia mallow and miscanthus).

Pyrolysis sample	Run	C (%)	H (%)	N (%)	S (%)	O (%)
Oak	Paper [238]	49.77	5.88	0.31	0.00	44.04
	Average	46.97	6.07	0.30	0.00	46.66
Willow	Paper[238]	48.63	5.78	0.77	0.00	44.82
	Average	45.01	6.83	0.85	0.00	47.31
Virginia Mallow	Paper[238]	48.40	5.91	0.42	0.00	45.27
	Average	47.17	6.73	0.42	0.00	45.68
Miscanthus	Paper[238]	47.02	5.54	0.47	0.00	46.97
	Average	49.00	7.04	0.28	0.00	43.68

4.3.2.2 Oximation Reaction Followed by Titration

As described in the introduction the carbonyl content can be determined using oximation reactions followed by titration. The reactions were carried out as described in Section 4.2.3. These reactions also as part of the quality control. Each reaction was done in

B.Tang, PhD Thesis, Aston University, 2024.

triplicate and an average was taken. The total carbonyl content was calculated using Equation 4.1.1. The results are summarised in Table 4.3.4.

Table 4.3.4 Summary of the total carbonyl groups of the different pyrolysis oils analysed using oximation reaction followed by titration.

Pyrolysis sample	Total Carbonyl Content (mol g⁻1)
Oak	0.00599
Willow	0.00461
Virginia Mallow	0.00558
Miscanthus	0.00492

4.3.2.3 Quantitative ^{19}F NMR Analysis

The carbonyl content of four fast-pyrolysis oils produced from different feedstocks (oak, willow, Virginia mallow and miscanthus) were derivatised and analysed using ^{19}F NMR methods outlined in Section 4.2.4. Figure 4.3.8 depicts spectra acquired on both high-field NMR and low-field NMR spectrum. All the data for the other pyrolysis oils are located in the Appendix 2, Figures A2.4-6.
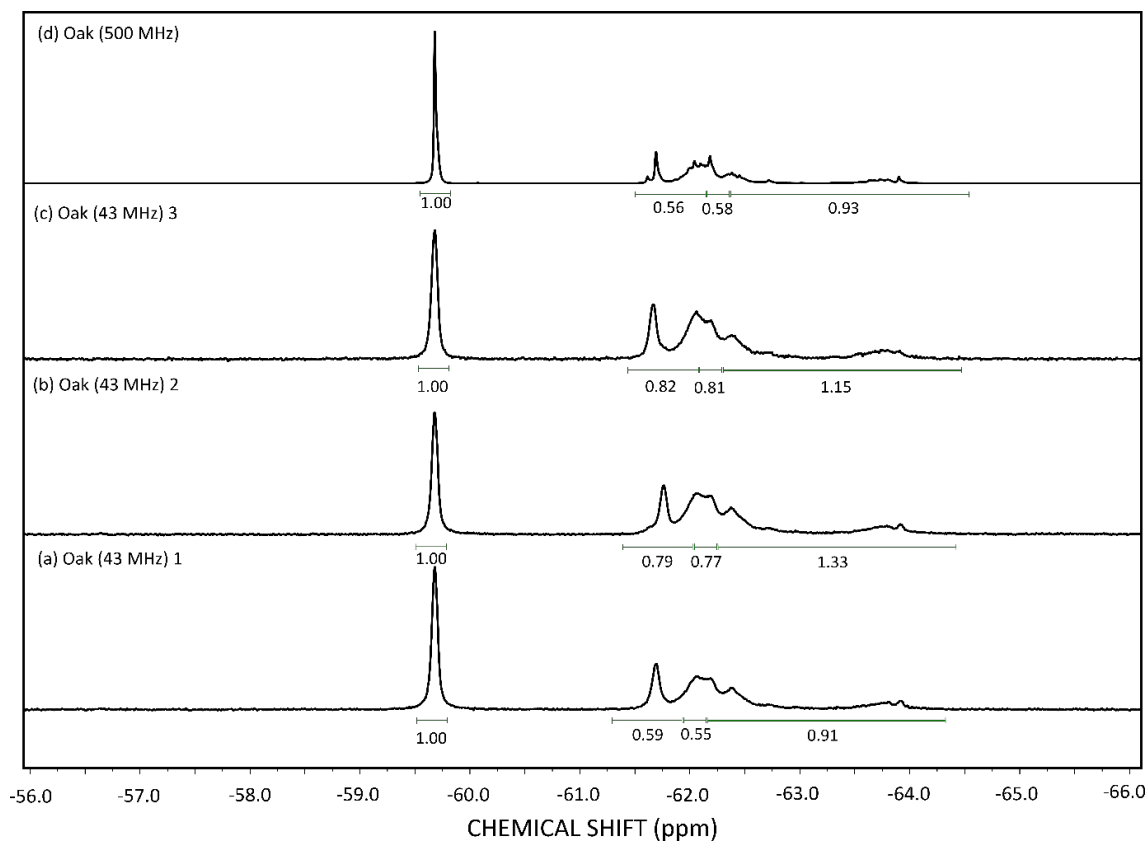
Figure 4.3.8 Stacked Plot of ^{19}F NMR spectra of derivatised pyrolysis oil produced from oak at 43 MHz in triplicate (a-c) and ^{19}F NMR spectrum of derivatised pyrolysis oil produced from oak at 500 MHz.

123

The estimate of the total carbonyl group content from both low-field (43 MHz) and high-field (500 MHz) ^{19}F NMR analysis (ketone, aldehydes and quinones) was comparable to the total carbonyl content values determined by the oximation method (OT), as shown in Figure 4.3.9. ^{19}F NMR methods are more efficient compared to traditional methods as they require less time, less sample and simpler procedures. Overall, it was found that wood-based biomass i.e. oak and willow tend to have more aldehyde and ketones whereas grass-based biomass i.e Virginia Mallow and miscanthus tended to produce more quinones. Quinones are known to form from the oxidation of phenolic compounds. For example 1,4-benzoquinone can be formed from the oxidation of *p*-hydroxyphenyl compounds.[239] Grass-based feedstocks typically contain between 5-35% *p*-hydroxyphenyl units compared to 0-8% in wood-based feedstocks. This suggests that grass-based feedstocks could produce pyrolysis oil that contains more quinones compared to hardwood feedstocks.
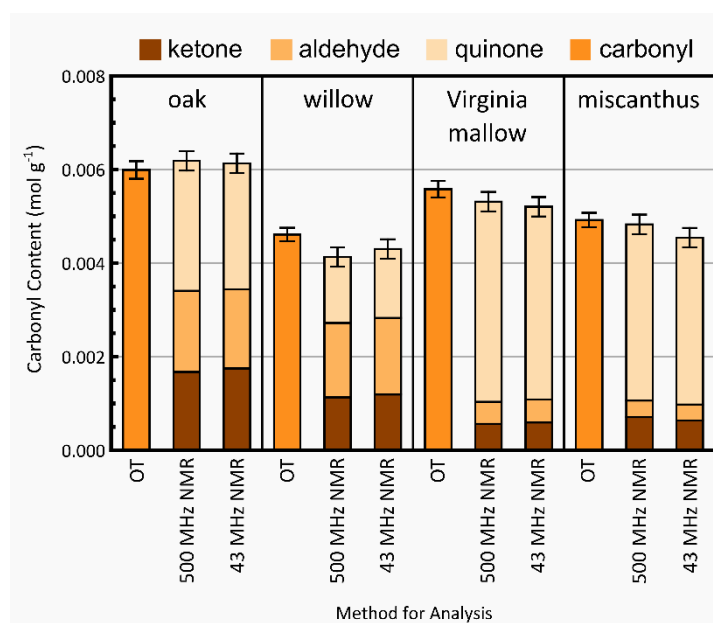
Figure 4.3.9 Graph comparing the quantification of ketones, aldehydes and quinones in pyrolysis produced from oak, willow, Virginia Mallow and Miscanthus using different methodologies, oximation followed by titration (OT), High-field NMR spectroscopy (500 MHz) and low-field NMR spectroscopy (43 MHz).

Elemental analysis gives a total percentage of oxygen present in the sample but cannot give any quantitative information about certain types of oxygen-containing compounds. Traditional methods such as oximation followed by a titration provide an estimate of total carbonyl content. However, titration methods do not provide information on the types of carbonyl groups present, which is an important factor when deciding on the route of upgrading. NMR also has an advantage over titration methods as it is able to provide

additional chemical information such as the type of carbonyl group. Even-though low-field NMR compared high-field NMR is less sensitive, the technique offers similar information to high-field NMR. Benchtop spectrometers are compact requiring minimal space, it does not require a large investment or technical maintenance making NMR techniques more accessible in places such as industry and smaller research institutions.

4.4 Conclusion

Low-field NMR proves able to distinguish between different fluorine environments. Derivatised model compounds containing carbonyl groups were used to build a chemical shift map. For the first time low-field NMR was used to quantify the amount of carbonyl groups in four pyrolysis oil produced from different feedstock. The results showed that the total carbonyl content provided by NMR spectroscopy was comparable to estimation provided by titrations methods. More importantly the results from the low-field NMR provide a detailed description of the different carbonyl environments comparable to quantification using high-field NMR analysis. Low-field benchtop NMR is an attractive option for routine quality control as the resolution and multiplicity of signals are not crucial for ^{19}F NMR analysis of pyrolysis oil.

4.5 Further Work

Current methods using sum integration is known to be sensitive to any phase or baseline distortions, but assuming these can be corrected using software. The main problem with this technique, it suffers from significant overlap of peaks. Especially in this case where the derivatisation produces compounds that lie in a tight range of chemical shifts. One way to overcome this issue is using other methods such as Global Spectral Deconvolution (GSD) for the estimation of integrals.[240] GSD provide advantages over sum integration even though it requires a spectrum to be correctly phased it is relatively insensitive to baseline distortions. More importantly it efficiently deals with overlapping peaks by modelling the experimental lineshape using a generalised Lorentzian function.[241] However, GSD was designed for automatic spectral analysis and can over interpret as it was not intended for accurate quantitative analysis.

^{19}F-containing derivatisation agents can be used to selectively isolate different functional groups for example pentafluoropyridine can be used to selectively isolate hydroxyl

groups. The analysis has only been carried out using high-field NMR. An alternative route could be exploring the chemistry of derivatisation agents not limited to fluorine nuclei further separate the signals in the chemical shift domain. Reducing the overlap of signals will improve the resolution of the spectrum, thus, easing the identification and quantification of carbonyl containing compounds.

CHAPTER 5 : QUANTITATIVE ANALYSIS OF HYDROXYL GROUPS USING ^{31}P NMR

5.1 Introduction

Pyrolysis oils are typically acidic resulting in both storage and commercial usage issues. Understanding the chemical composition of the oils and what contributes to the acidic nature of bio-oils is an important starting point. Typically, oxygen-containing compounds such as phenol and carboxylic acids contribute to the acidity of pyrolysis oils. There are various techniques that can be used to quantify hydroxyl content such as redox titration, FTIR and GC/MS. These techniques are useful, providing important information but have limitations. Redox titration is a laborious procedure that can only quantify hydroxyl content but cannot distinguish between different chemical species containing those functional groups. FTIR can be used to distinguish between different functional groups, however it is usually used purely qualitatively due to the broad peak in the -OH region. GC/MS can be used for quantification of various chemicals, however due to instrument limitations, not all components of bio-oil can be detected as outlined in Chapter 1.

NMR offers a non-invasive and non-destructive alternative approach to bio-oil characterisation. Proton NMR analysis can be carried out in various solvent systems. The functional groups of interest are hydroxyl groups which are labile protons and often absent from proton spectrum. Due to the complexity of bio-oil, coupled with the narrow chemical shift range of ^{1}H NMR, typical proton NMR spectra are highly crowded and may not yield information such as the identification of specific compounds. This is demonstrated in Figure 5.1.1, the 1D ^{1}H spectrum of a derivatised bio-oil in mixed pyridine/CDCl$_3$ solution.

B.Tang, PhD Thesis, Aston University, 2024.
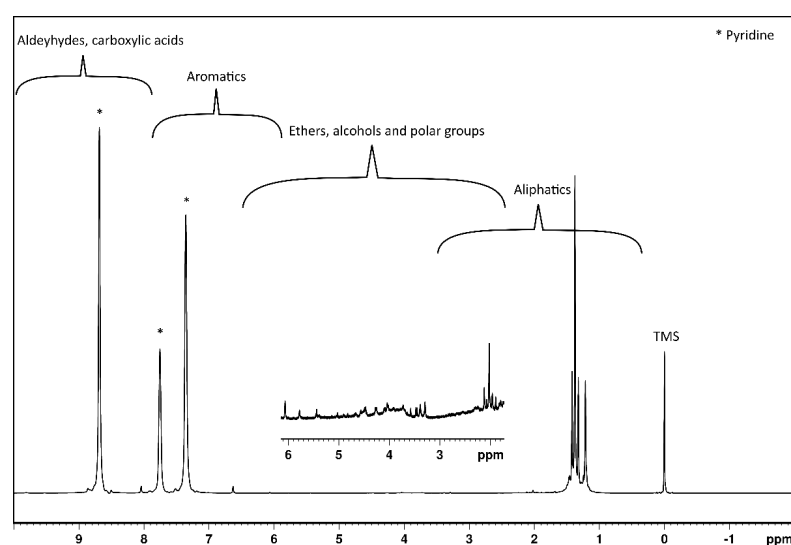
*Figure 5.1.1 ^{1}H NMR of bio-oil produced from spruce feedstock in a CDCl$_3$:pyridine solution where the * belong to pyridine peaks. The ether, alcohol and polar groups region was enlarged due to the low signal intensities.*

One way to simplify the spectrum and target specific functional groups is using derivatisation methods. Hydroxyl groups can be derivatised by phosphorus-containing compounds such as 2-chloro-4,4,5,5-tetramethyl-1,3,2-dioxaphospholane (TMDP). This effectively tags the hydroxyl group with a phosphorus containing compound which can then be analysed using ^{31}P NMR. NMR can also be used for quantitative analysis when an internal standard is used. A common internal standard that can be used for qNMR of bio-oils is *endo-N*-hydroxy-5-norbornene-2,3-dicarboximide (NHND). In this chapter, the refining of current methodologies will be explored. Pyrolysis oils contain hundreds of small alcohols and are very complicated samples. Therefore, hand sanitisers were used for this study as an intermediate complex sample. The active ingredients in hand sanitiser are ethanol, isopropyl alcohol, and n-propanol. Glycerol is a tri-alcohol, and this is added to hand sanitisers to prevent skin dryness. The effectiveness of the hand sanitisers is closely related to the amount of alcohol present. Typically, the higher the alcohol content, the more effective the hand sanitiser is. Alcohol content should range between 60-95% alcohol to be most effective. [242, 243] The refined methodology was also applied to a real pyrolysis oil produced from Spruce.

5.1.1 Materials

All reagents used as model compounds were obtained commercially, the origin and purity of these compounds used in this study are reported in Appendix 3 (Table A3.1). Tetramethyl silane, 99.9 %, chloroform-*d* (CDCl$_3$), 99.8% and pyridine, 99.5%, extra dry over molecular sieve was purchased from Acros organics. Chromium(III) 2,4-pentanedionate,97% was purchased from Fischer Scientific. Trimethylphosphate ≥99%, 2-chloro-4,4,5,5-tetramethyl-1,3,2-dioxaphospholane (TMDP), 95%, *endo-N*-hydroxy-5-norbornene-2,3-dicarboximide (NHND), 97%, guaiacol, ≥98%, phenol, 99%, and furfural, 99% was purchased from Sigma-Aldrich, UK.

The hand sanitisers used were off the shelf and were used without any further processing. The bio-oil used was produced at Aston University using a Norwegian Spruce feedstock in a 1 kg h^{-1} fast pyrolysis rig. All chemicals were used without any further purification.

B.Tang, PhD Thesis, Aston University, 2024.

Figure 5.1.2 shows the four different hand sanitisers that were used in this study with the respective ethanol content given in percentage by weight or % (w/w).
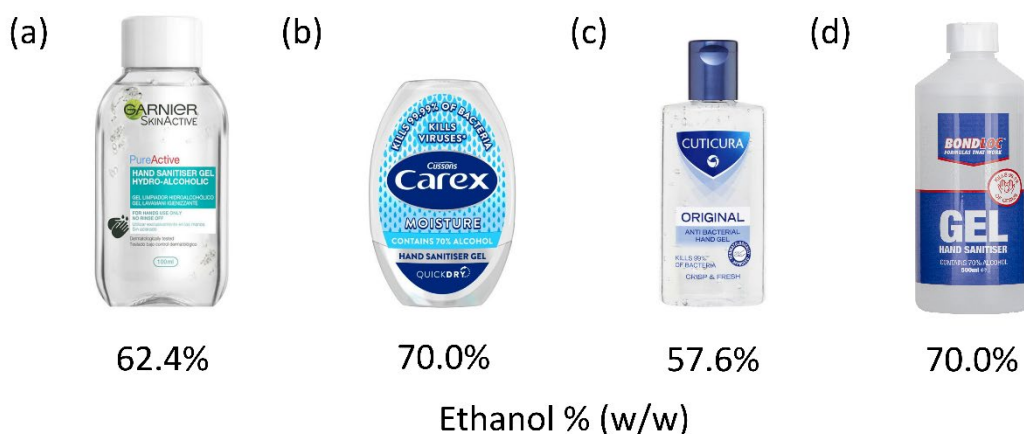
Figure 5.1.2 Hand sanitisers (a) Garnier PureActive hand sanitiser gel (b) Carex moisture hand sanitiser gel (c) Cuticura original hand sanitiser gel (d) Bondloc hand sanitiser gel

5.1.2 ^{31}P Derivatisation Reaction of Hydroxyl Groups

This section describes the preparation of solvents, internal standards required for the derivatisation reaction, and NMR analysis.

Solvent A

A stock solvent solution of 1:1.6 volume ratio of $CDCl_3$ and anhydrous pyridine was prepared and dried over molecular sieves.

Internal Standard:

0.1M internal standard was prepared by adding NHND (0.018 g) to solution A (1 mL). A relaxation agent, chromium (III) 2,4-pentadienoate (5 mg) was dissolved in the solution. The weight of the entire solution was recorded. The internal standard was stored over molecular sieves.

Derivatisation reaction:

IS solution (0.1 mL) was transferred into a glass vial equipped with a PTFE-lines silicone septum. The weight of the 0.1 mL IS solution was recorded. Bio-oil (30 mg) was weighed into the same vial. The actual weight of the sample was recorded. Solvent A (0.7 mL) was added using a gastight syringe into the same vial and was left stirring until mixture was homogenous. For the derivatisation reaction an excess of TMDP (*ca.* 0.2 mL) was added using a gastight syringe. The reaction was left for 10 minutes to stir. The solution was then transferred to a 5 mm NMR tube with a Pasteur pipette and analysed immediately. The reason being the phosphitylation derivative of NHND was not stable over a long period of time.

NMR Analysis:

NMR acquisitions were acquired using a Bruker NEO 500 MHz spectrometer equipped with a RT-DR-BF/^{1}H-5mm-Z SP iProbe unless specified. All hand sanitiser data was acquired using a Bruker AVANCE 300 MHz equipped with a 5mm PABBO BB-1H Z-GRD probe. All ^{31}P data was acquired with 10 seconds pulse delay and 64 scans at 298.15 K. All NMR data was processed using Topspin.

5.1.3 Alcohol Content by Dichromate Oxidation followed by Redox Titration

This section describes the preparation of solutions, reaction and titration method.

Acid dichromate solution:

125 mL of DI water was added to 70 mL of concentrated sulfuric acid in a 500 mL conical flask. The flask was swirled under cold tap water. 0.75 g of potassium dichromate was added to the solution. The solution was then made up to 250 mL in a volumetric flask with DI water.

Sodium thiosulfate solution:

A solution of 0.03 M of sodium thiosulfate was prepared by dissolving 3.72 g of sodium thiosulfate in 500 mL distilled water in a volumetric flask.

Potassium iodide solution:

A solution of 1.2 M of potassium iodide was prepared by dissolving 5 g of solid potassium iodide in 25 mL of distilled water in a volumetric flask.

Preparation of sample:

0.4 g of sample of interest was dissolved in 100 mL of distilled water.

Blank titration:

A blank titration was carried by pipetting 10 mL of the dichromate solution into a 250 mL conical flask. 100 mL of distilled water and 1 mL of iodine solution was added to the flask. The titration was carried out by titrating the blank with the sodium thiosulfate solution. When the colour changes from brown to yellow, a small quantity of starch was added to the conical flask resulting in the solution changing to a dark blue. Sodium thiosulfate was added until the solution was colourless. The volume was recorded and repeated for concordant results.

Oxidation reaction:

1 mL of sample and 10 mL of dichromate solution was pipetted into a 250 mL conical flask. The flask was sealed with a rubber bung and left to stir overnight. The titration procedure was the same as the titration procedure used for the blank titration. The titrations are governed by the following three reactions, with the end-point indicated by the change of colour from blue to colourless.

(a) Oxidation of ethanol to ethanoic acid.

$2Cr_2O_7^{2-} + 16H^+ + 3C_2H_5OH \rightarrow 4Cr^{3+} + 11H_2O + 3CH_3COOH$
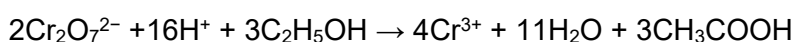
(b) Determination for unreacted dichromate by adding potassium iodide solution.

$Cr_2O_7^{2-} + 14H^+ + 6I^- \rightarrow 2Cr^{3+} + 3I_2 + 7H_2O$
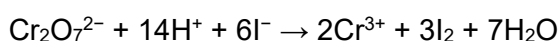
(c) Titration of iodine with sodium thiosulfate.

$2S_2O_3^{2-} + I_2 \rightarrow S_4O_6^{2-} + 2I^-$
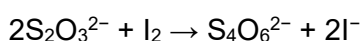
5.2 Results and Discussion

5.2.1 Initial Qualitative Analysis of Hydroxyl Group Using ^{31}P NMR

As a proof of concept that ^{31}P NMR can be used to distinguish between various hydroxyl groups simple mixtures containing hydroxyl groups and model oils were studied. Both ^{31}P and ^{31}P{^{1}H} have been chosen to characterise hydroxyl groups. While ^{31}P{^{1}H} simplifies the spectrum and with a suitable pulse sequence can be used for quantification purposes, ^{31}P also plays a role in the characterisation as it generates information such as connectivity, which helps with identification of compounds. The derivatisation of cyclohexanol with TMDP was carried out using the procedure described in Section 5.1.2 where 0.1mL of 0.1M trimethyl phosphate was added as a chemical shift standard. The 1D ^{31}P spectrum was used to confirm the derivatisation. The full analysis is shown in Table 5.2.1. Figure 5.2.1 shows the stacked plot of the full spectrum of ^{31}P NMR and the ^{31}P{^{1}H} NMR of derivatised cyclohexanol. The peak at 145.19 ppm is the derivatised cyclohexanol. Note that with ^{31}P NMR experiments the excitation bandwidth can cause artefacts in peaks far from the centre of the spectrum. This was not observed in these experiments. However, the presence of off resonance effects can be easily observed in a series of experiments with different transmitter centres.
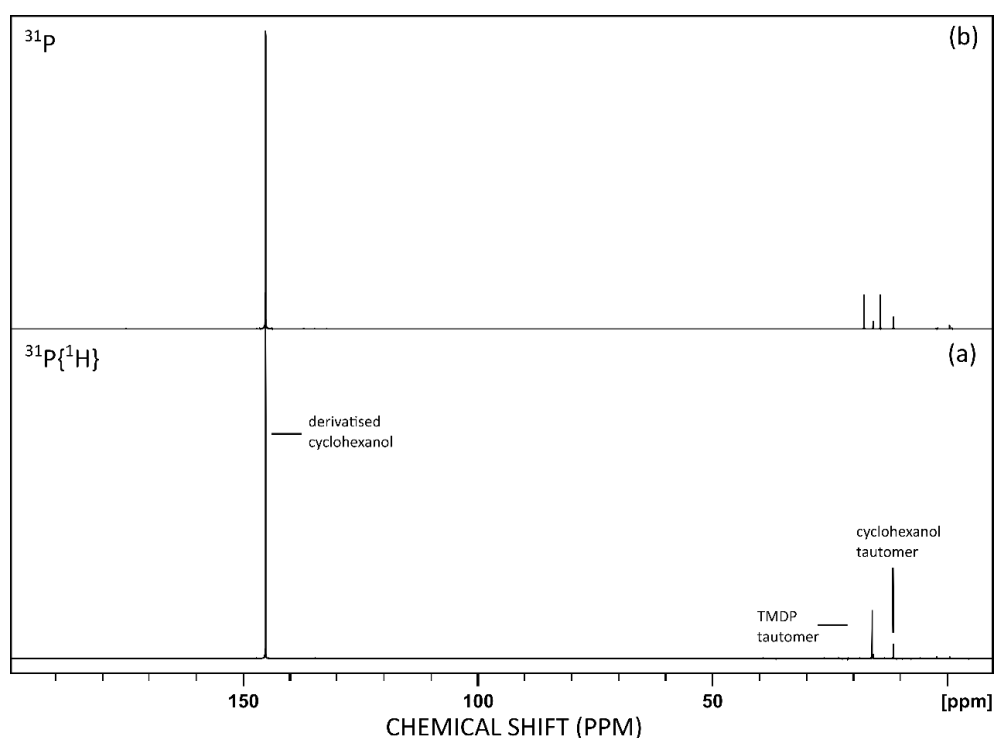
Figure 5.2.1 Stacked plot of the full spectrum 0-200 ppm of derivertised cyclohexanol (a) ^{31}P{^{1}H} NMR and (b) ^{31}P NMR. The enlarge spectrum between −5 and 30 ppm (Figure 5.2.2)

Enlarging the spectrum between −5 and 30 ppm (Figure 5.2.2) reveals additional peaks which could be due to the tautomerisation of TMDP (16.10 ppm) - the mechanism is shown in Figure 2.4.16, water (15.77 ppm) and cyclohexanol (11.44 ppm). Identification can be made based on the multiplicity pattern in the ^{31}P spectrum. There are also small peak motifs in the baseline that are present in the 1D ^{31}P{^{1}H} spectrum but not the 1D ^{31}P spectrum (Figure 5.2.2). These artefacts are known as cyclic sidebands, they are caused by peaks with larger coupling constants (*J* values) of the phosphorus and proton in the TMDP tautomer.
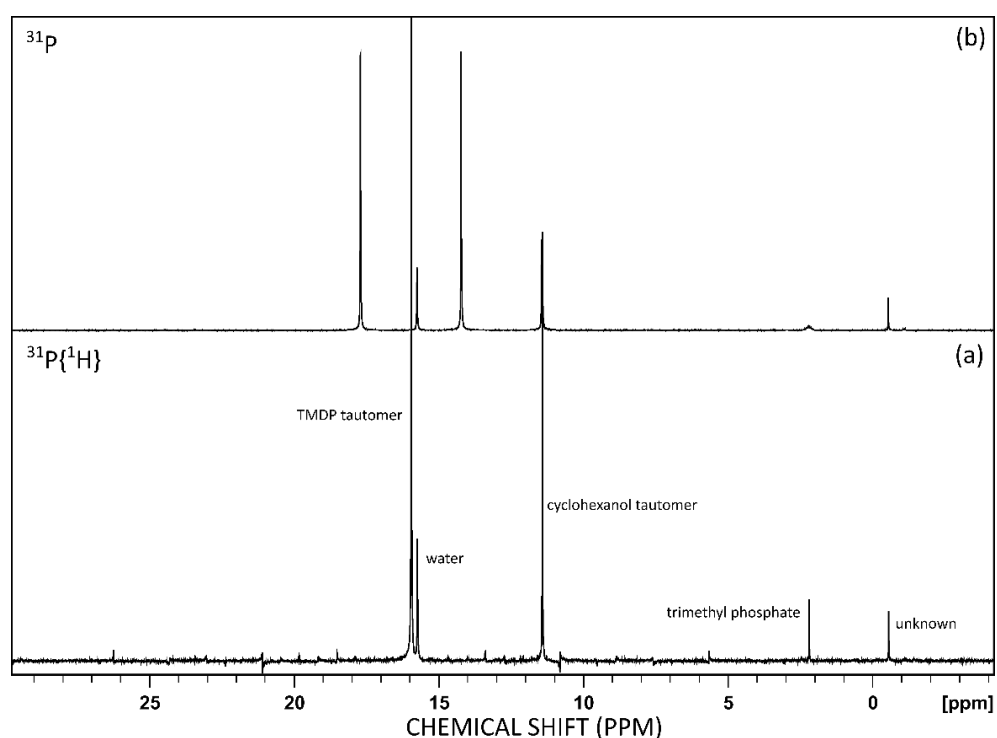
Figure 5.2.2 Stacked plot of derivertised cyclohexanol between −5-30 ppm (a) ^{31}P{^{1}H} NMR and (b) ^{31}P NMR.

Table 5.2.1 ^{31}P NMR peak assignments for derivatisation of cyclohexanol using TMDP (Figure 5.2.1 is the full spectrum).

Chemical Shift (ppm)	^{31}P/^{31}P Decoupled Multiplicity	Compound
-0.46	s/s	Unknown
2.20	oct/s	Trimethyl phosphate (reference)
11.44	d/s	Cyclohexanol/TMDP tautomer
15.77	s/s	Mono-derivatised water
16.10	d/s	TMDP tautomer
132.20	s/s	Di-derivatised water
145.19	d/s	Derivatised cyclohexanol
174.90	s/s	Unreacted TMDP

5.2.2 Optimisation of CPD decoupling sequence to Reduce Cyclic Sidebands

The cyclic sidebands of the TMDP tautomer can be reduced, a way to reduce these artefacts would be using a higher power decoupler. But using a higher power can cause both convection in the sample and damage to the probe. Other ways to improve the decoupling without using a large power output is by using different decoupling sequences. The role of the composite pulse decoupling (CPD) is to decouple the proton from the phosphorus. CPD typically require less power and sample heating can be kept to a minimum. Common CPDs were chosen and compared. The signal to noise ratio of the cyclic sideband was measured and summarised in Table 5.2.2. The typical CPD used for ^{31}P{^{1}H} spectrum was the WALTZ-16.[209] The signal-to-noise ratio of the cyclic sideband at *ca.* 18.45 ppm was found to be 6.19. The WALTZ-16 CPD was compared to the related sequences, GARP (10.6), WALTZ-64 (6.08) and BI-WALTZ-16 (1.98). The cyclic side bands in the GARP spectrum are visible even without any enlargements, whereas they are not viable in the BI-WALTZ spectrum. Overall, it was found that the bi-level WALTZ-16 composite decoupling pulse most effectively reduced artefacts (Figure 5.2.3).
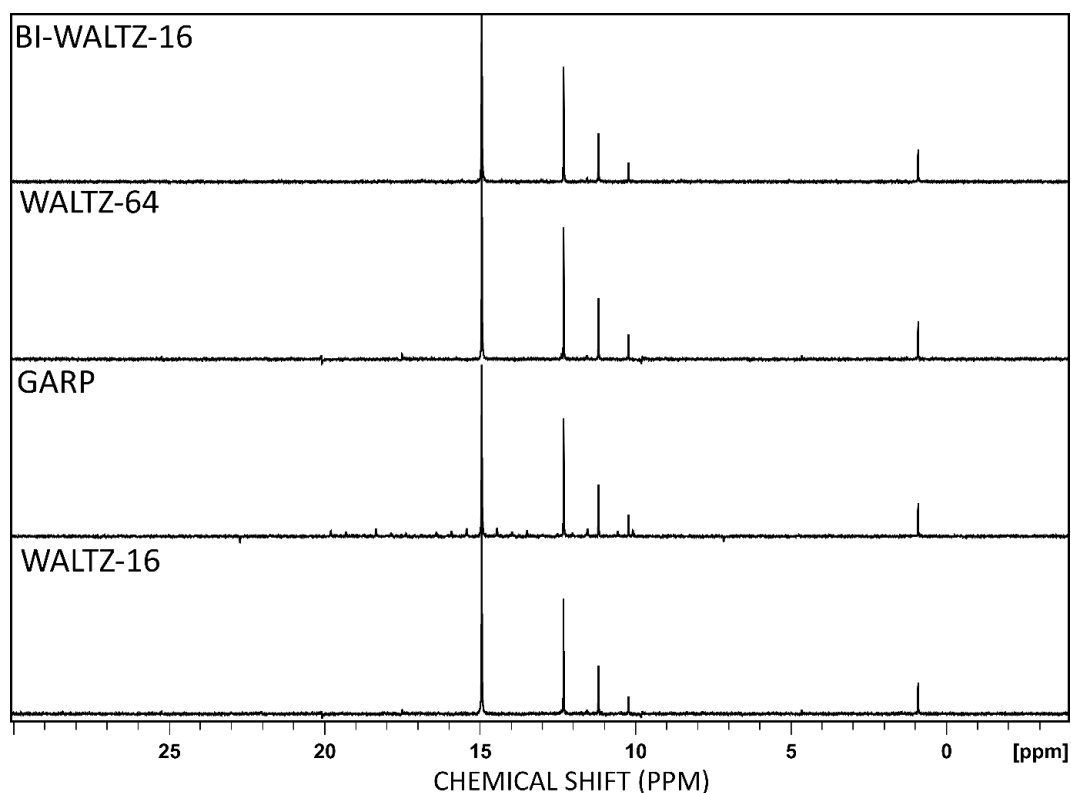
Figure 5.2.3 Stacked plot of $^{31}P\{^1H\}$ spectrum from −5-30 ppm aquired using different CPD(s).

Table 5.2.2 Summary of the different CPD used and the signal to noise ratio of the cyclic sideband at ca. 18.45 ppm.

CPD	SIGNAL TO NOISE RATIO (18.45ppm)
BI-WALTZ-16	1.98
WALTZ-64	6.08
GARP	10.6
WALTZ-16	6.19

5.2.3 Optimisation of Power Levels for Bi-level WALTZ-16 CPD

Bi-level decoupling utilises a low power radiofrequency irradiation during the relaxation delay, followed by a higher power during the acquisition in order to decouple over a wide bandwidth.[244] Many instrument manufacturers do not express the output power in Watts. For example, this work is carried out on Bruker instruments, where the output power, P, is typically express in decibels (dB). The unit is defined as

$$dB = −10 \times \log_{10}(P) \qquad \text{Equation 5.2.1}$$

therefore, the larger the number, the lower the power. For the probe being used for most of the work, the pre-set power levels were 5.69 dB and 8.67 dB. The first step for optimising the power level was to understand the power required to fully decouple the proton from the phosphorus. The aim was to decouple the peak 15.1 ppm. Figure 5.2.4 shows a stacked plot of each spectrum at the various power levels and Table 4.3.3 is a summary of power levels used as well as the signal to noise of the cyclic side bands. The two power levels were both set to the lowest power at 8.67 dB and incremented in steps. It was found that at least 7 dB was required to fully decouple the proton from the phosphorus. The second step for optimising the power level was to reduce the cyclic sidebands around the TMDP tautomer peak at 15.10 ppm. From 7 dB the power was incremented up to 5.69 dB which was the highest pre-set power level. The power level was not exceeded past the pre-sets for the probe as having high currents flowing through the coil can damage and break the probe. It was found that 5.69 dB was optimal. At 5.69 dB the cyclic sideband was the smallest with a signal to noise ratio of 2.01 compared with at 7 dB the signal to noise ratio was 6.71.

5.69 dB   SNR:2.01

6.00 dB   SNR:2.99

6.50 dB   SNR:6.07   Fully decoupled

7.00 dB   SNR:6.71

7.10 dB   SNR:7.09

7.20 dB   SNR:7.96

7.30 dB   SNR:8.28   Partially decoupled

7.40 dB   SNR:8.34

7.50 dB   SNR:8.46

8.00 dB   SNR:9.33

8.67 dB   SNR:10.76   Coupled

25   20   15   10
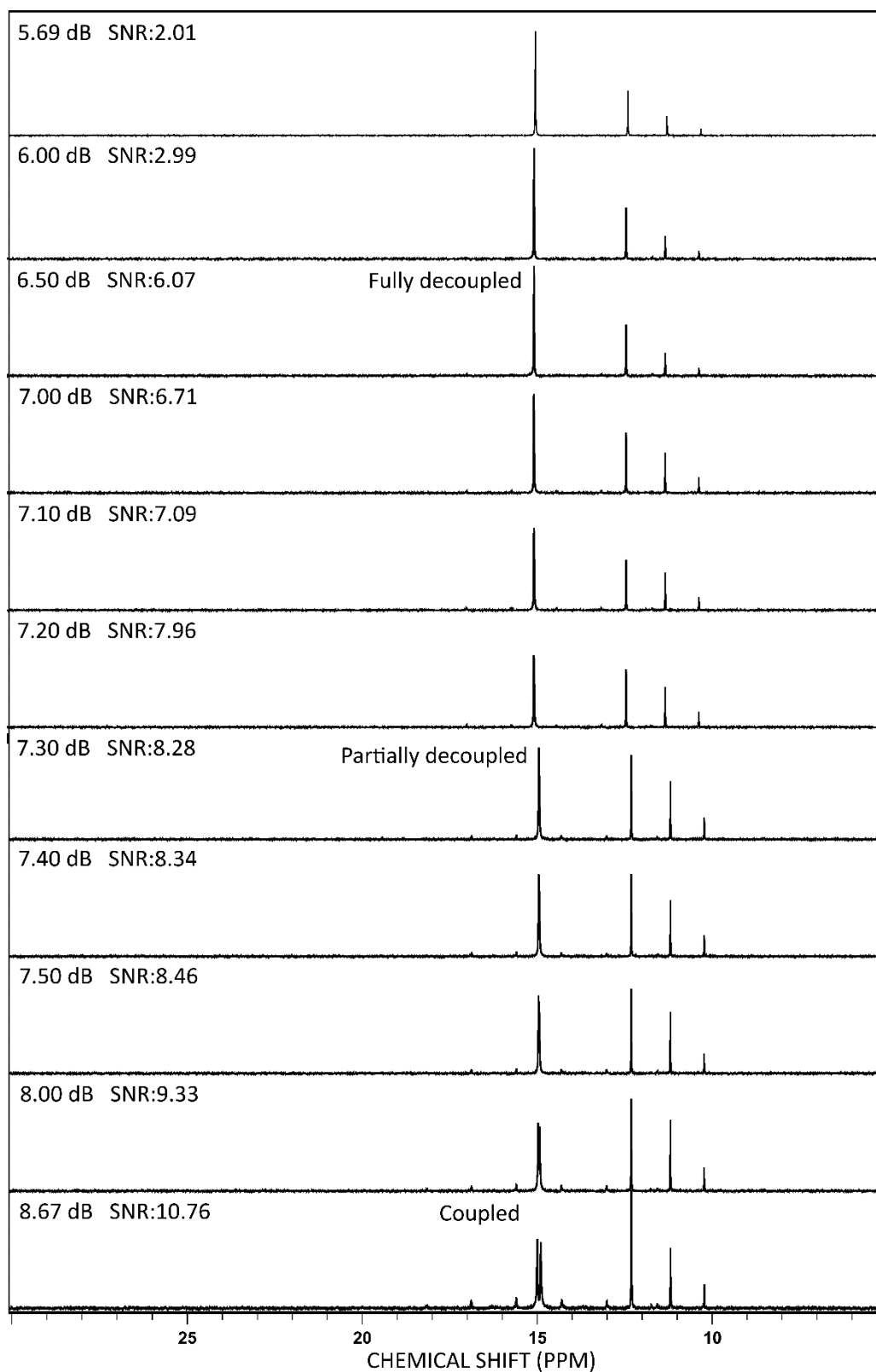
CHEMICAL SHIFT (PPM)

Figure 5.2.4 St Stacked plot of $^{31}P\{^{1}H\}$ spectrum from −5-30 ppm aquired with the bi-level WALTZ-16 CPD at power levels between 8.67 dB and 5.69 dB.

138

5.2.4 Qualitative Analysis of Different Hydroxyl Groups using ^{31}P NMR and Generation of Chemical Shift Map

The choice of a bi-level CPD and power levels are now optimised with a power level of 5.69 dB. ^{31}P {^{1}H} NMR can be used to identify and quantify hydroxyl groups that have been derivatised using TMDP. As a simple test, to understand how ^{31}P NMR can be used in a qualitative manner looking at different hydroxyl groups, three sample were prepared. First sample contained one alcohol, cyclohexanol. Second sample contained two alcohols, cyclohexanol and ethanol. Third sample contained three alcohols, cyclohexanol, ethanol and methanol. All samples were derivatised using the procedure in *Section 5.1.2*. Figure 5.2.5 shows a stacked plot of the ^{31}P and ^{31}P{^{1}H} NMR spectrum top and bottom respectively, where each sample is colour coded cyclohexanol (black), cyclohexanol and ethanol (blue), cyclohexanol, ethanol and methanol (red). In spectra (a) and (b) there is a peak at 174.90 ppm and 132.20 ppm that is not present in the other spectrum this is the unreacted TMDP and di-derivatised water respectively. Figure 5.2.6 shows the same stacked plot from 140-150 ppm. In all spectra at 145.19 ppm there is a singlet and doublet respectively. The doublet corresponds to the derivatised cyclohexanol following the n+1 rule, where the phosphorus is coupled to a proton. In spectrum (c) and (d) as well as (e) and (f) at 146.73 ppm there is a singlet and triplet respectively. The triplet corresponds to the derivatised ethanol where the phosphorus is coupled to two protons. In spectrum (e) and (f) at 148.03 ppm there is a singlet and quartet respectively. The triplet corresponds to the derivatised methanol where the phosphorus is coupled to three protons. These peak motifs are also repeated more shielded (see Figure 5.2.7), doublet (11.44 ppm), triplet (12.42 ppm), and quartet (13.35 ppm). These could be tautomers of the derivatised alcohols. There is also a singlet and singlet at 15.77 ppm in spectrum (a) and (b) as well as (c) and (d), this corresponds to the mono-derivatised water tautomer. At 16.10 ppm there is a doublet in the ^{31}P spectrum and a singlet in the ^{31}P{^{1}H} this corresponds to the TMDP tautomer. Overall using ^{31}P NMR can be used to distinguish between different hydroxyl groups.
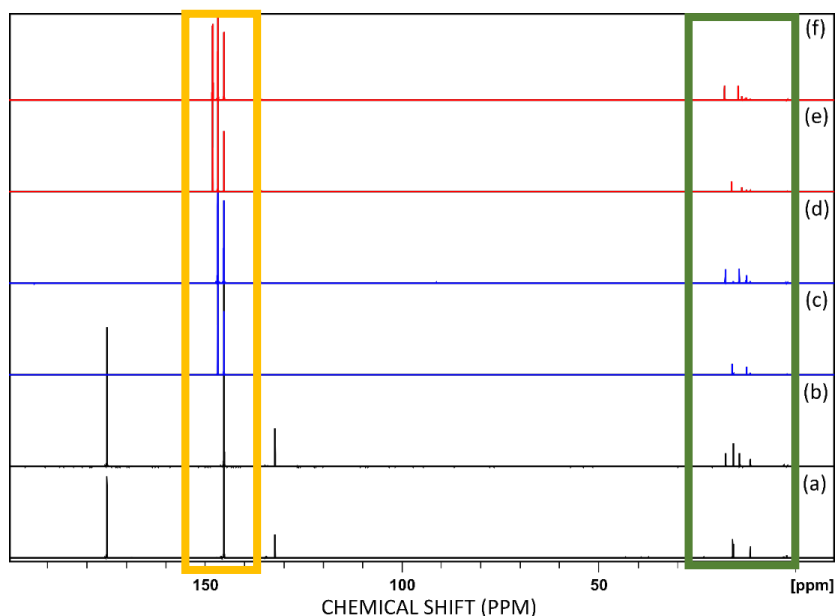
Figure 5.2.5 Stacked plot of full spectrum from 0-200 ppm (a) 1D $^{31}P\{^{1}H\}$ spectrum of derivatised cyclohexanol (b) 1D ^{31}P spectrum of derivatised cyclohexanol (c) 1D $^{31}P\{^{1}H\}$ spectrum of derivatised cyclohexanol and ethanol (d) ^{31}P spectrum of derivatised cyclohexanol and ethanol (e) 1D $^{31}P\{^{1}H\}$ spectrum of derivatised cyclohexanol, ethanol and methanol (f) 1D ^{31}P spectrum of derivatised cyclohexanol, ethanol and methanol. From 140-150 ppm in orange is expanded in Figure 4.3.6, and 10-20 ppm in green is expanded in Figure 4.3.7.
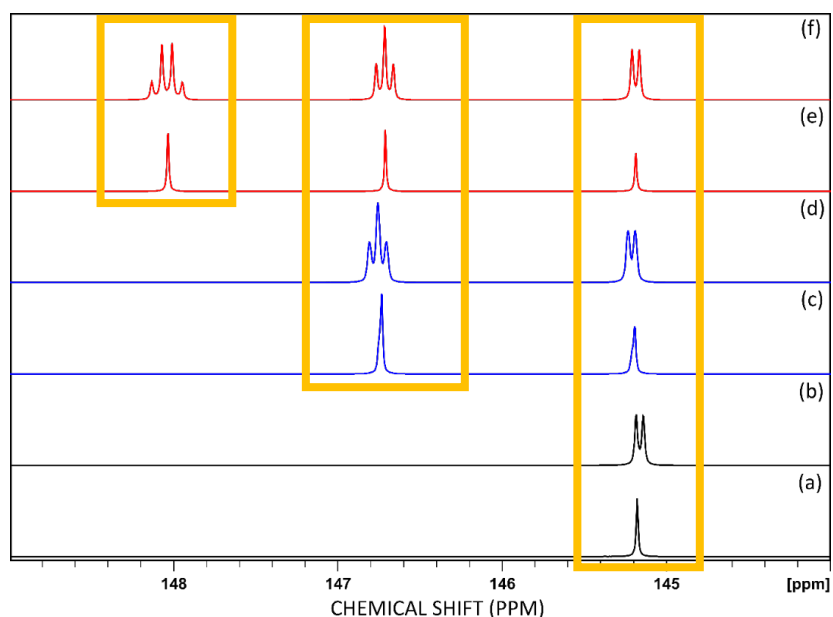
Figure 5.2.6 Stacked plot of spectrum from 140-150 ppm (a) 1D $^{31}P\{^{1}H\}$ spectrum of derivatised cyclohexanol (b) 1D ^{31}P spectrum of derivatised cyclohexanol (c) 1D $^{31}P\{^{1}H\}$ spectrum of derivatised cyclohexanol and ethanol (d) ^{31}P spectrum of derivatised cyclohexanol and ethanol (e) 1D $^{31}P\{^{1}H\}$ spectrum of derivatised cyclohexanol, ethanol and methanol (f) 1D ^{31}P spectrum of derivatised cyclohexanol, ethanol and methanol.
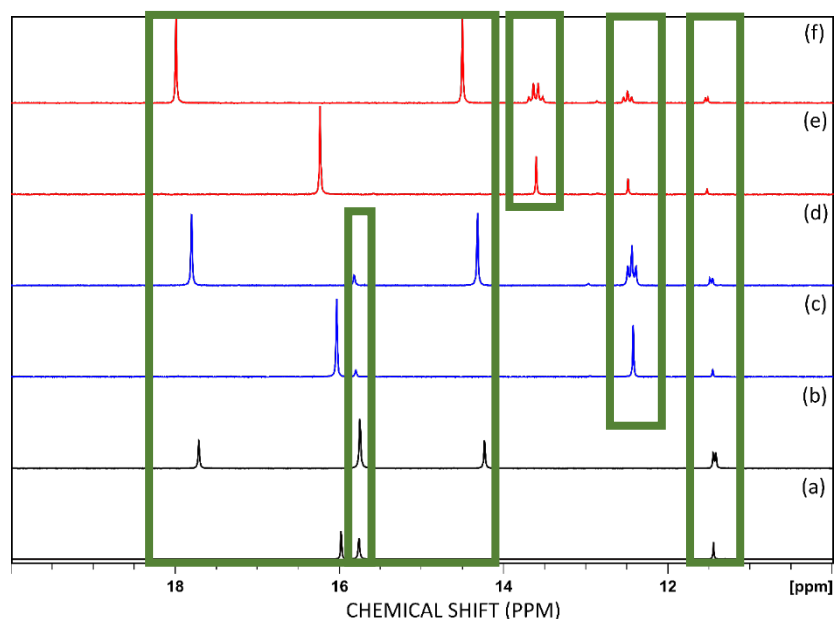
Figure 5.2.7 Stacked plot of spectrum from 10-20 ppm (a) 1D $^{31}P\{^1H\}$ spectrum of derivatised cyclohexanol (b) 1D ^{31}P spectrum of derivatised cyclohexanol (c) 1D $^{31}P\{^1H\}$ spectrum of derivatised cyclohexanol and ethanol (d) ^{31}P spectrum of derivatised cyclohexanol and ethanol (e) 1D $^{31}P\{^1H\}$ spectrum of derivatised cyclohexanol, ethanol and methanol (f) 1D ^{31}P spectrum of derivatised cyclohexanol, ethanol and methanol.

Having shown that ^{31}P NMR can be used to distinguish between different derivatised alcohols, the next step is to develop a comprehensive chemical shift map using known literature data and 10 other model compounds containing alcohol groups. The derivatisation of model compounds followed by ^{31}P NMR analysis was used to produce a chemical shift map which will later be used for identification and integration. Figure 5.2.8 shows the stacked plot of the derivatised model compounds. A summary of the chemical shifts can be found in Appendix 3 where all chemical shifts were referenced using the di-derivatised water signal (−132.2 ppm). The chemical shifts for the TMDP derivatised primary alcohol are *ca*. 146.1 to 148.0 ppm, TMDP derivatised secondary alcohol is *ca*.144 to 146.0 ppm, TMDP derivatised tertiary and aromatic alcohols (phenols) is *ca*. 137.7 to 142.2 ppm and TMDP derivatised carboxylic acids is *ca*. 134.3 to 136 ppm. A summary of the chemical shift from this study and chemical shifts reported in Li *et al* [245] (Appendix 3) are represented in a schematic diagram (Figure 5.2.9).
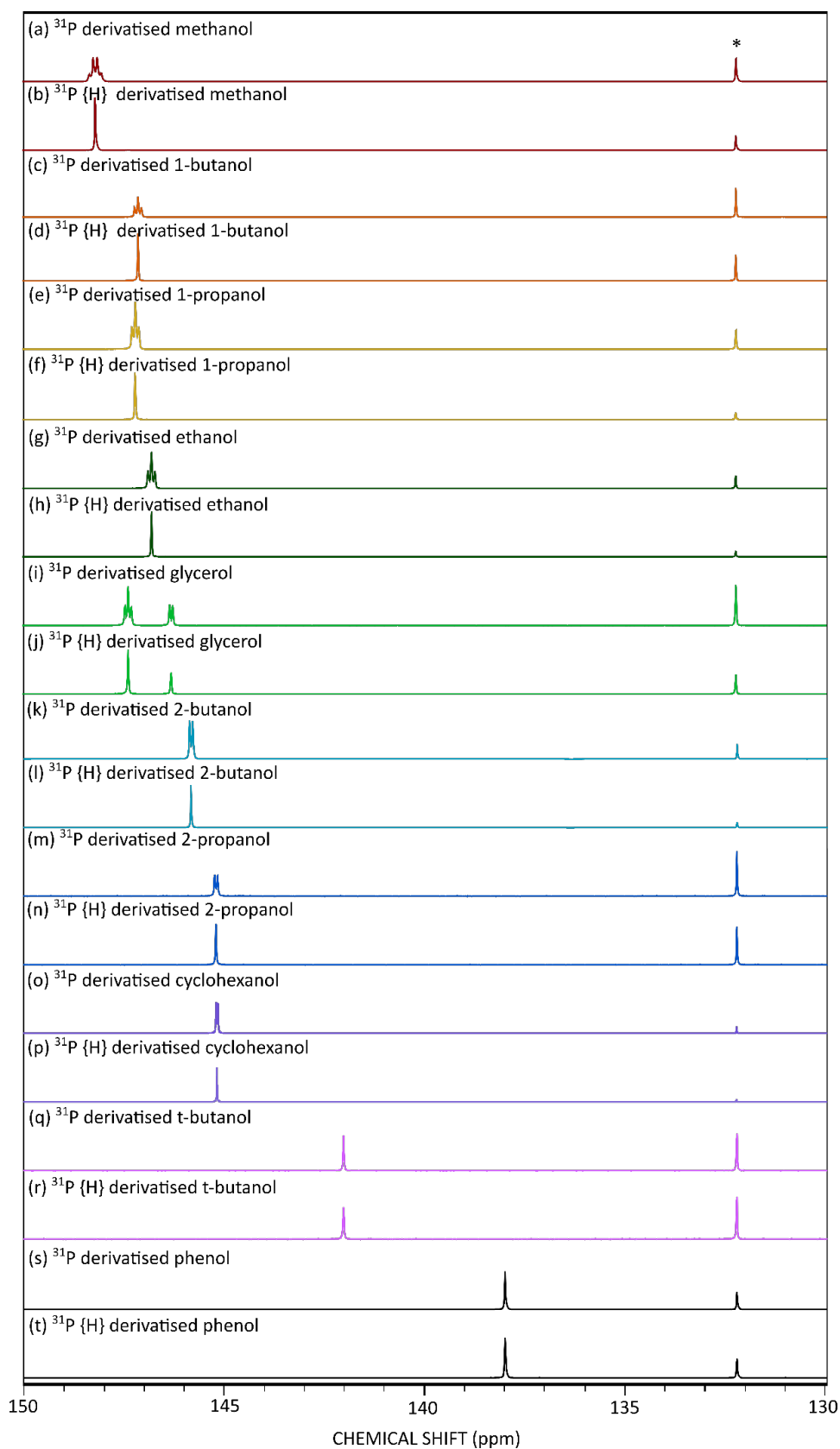
*Figure 5.2.8 Stacked plot of 1D ^{31}P NMR and ^{31}P {^1H} NMR spectra of derivatised ten model compounds containing alcohol groups with chemical shift reference di-derivatised water (−132.2 ppm). *The di-derivatised water used for chemical shift referencing.*
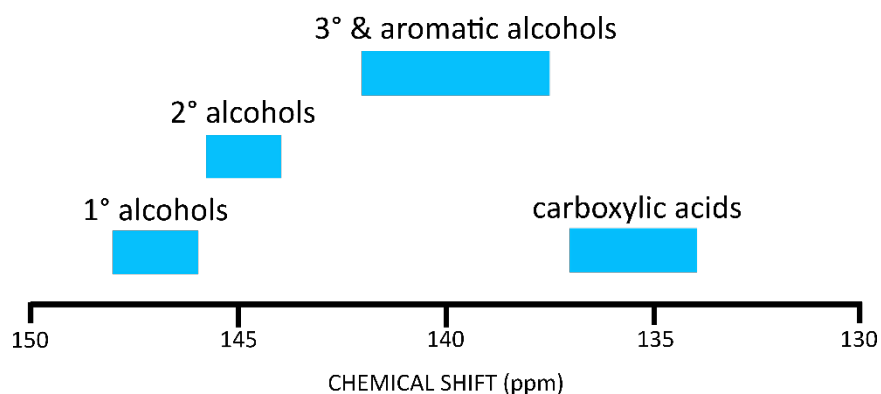
Figure 5.2.9 Schematic representation of ^{31}P NMR chemical shift regions for alcohol containing compounds derivatised using 2-chloro-4,4,5,5-tetramethyl-1,3,2-dioxaphospholane (TMDP)

5.2.5 ^{31}P Inverse Gated Decoupling for qNMR

^{31}P NMR can be used to distinguish various hydroxyl groups as shown in Section 5.2.4. More importantly quantifying these oxygen-containing compounds will help understand the acidity of the oils. Cyclohexanol was derivatised using the methods outlined in Section 5.1.2, with NHND as an internal standard for quantification. For quantification purposes ^{31}P inverse gated decoupling sequence was used to reduce any signal induced by NOE. Figure 5.2.10 (a) shows the derivatised cyclohexanol, however none of the other species present was derivatised. More TMDP was added and left to react for another 10 minutes. Figure 5.2.10 (b) shows the fully derivatised sample. For quantitative purposes it is important for the excess TMDP peak to be present at *ca*. 174.93 ppm to ensure that all species have been fully derivatised.
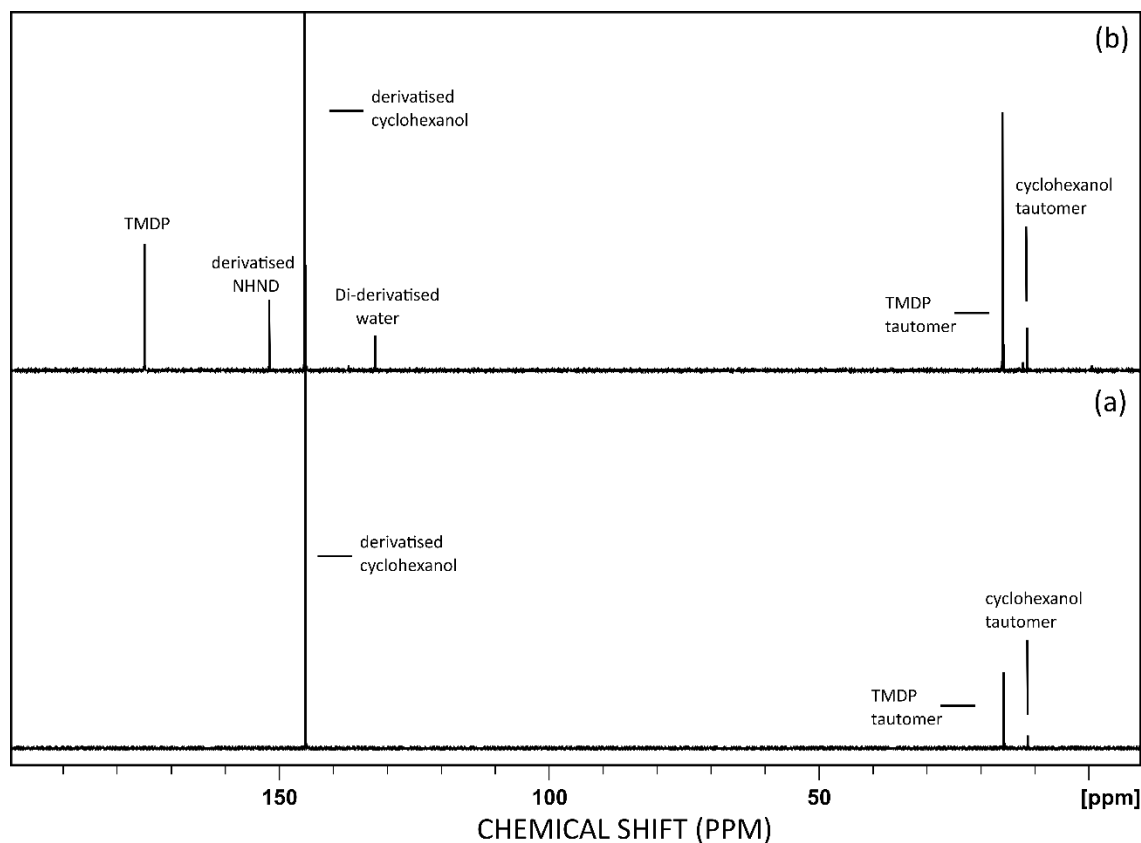
Figure 5.2.10 Stacked plot of the full $^{31}P\{^1H\}$ NMR spectrum 0-200 ppm of derivatised cyclohexanol (a) partial dervatisated (not enough TMDP was added) (b) fully derivatisated (excess TMDP was added)

Unlike other techniques such as gas chromatography where a calibration curve is required to enable quantification, NMR integrals in qNMR techniques are quantitative. To understand how accurate the quantification technique is, a calibration curve should be produced for a range of concentrations. Concentrations up to 1 M of cyclohexanol was prepared in a pyridine and CDCl$_3$ mixture. The samples were derivatised using the methods outlined in Section 5.1.2. The integrals of the peak of interest were compared with the integral of the internal standard. Different approaches have been discussed in literature used to determine the amount of internal standard that should be used but none have a definitive answer.[246] One way to determine the amount of internal standard is through an experimental design in order to determine the optimal concentration needed. [247, 248] Some studies suggests that to improve the accuracy a large amount of the internal standard should be added.[249] However, Haefelfinger *et al.* suggests that the internal standard peak height should be similar to that of the analyte of interest.[250] In this study, the internal standard signal should be similar to the peaks of interest because if a large amount of internal standard was used the signals of the analyte would be lower, resulting in inaccuracies.

144

The actual moles are calculated using the following equations:

$$n_{(NHND\ in\ solution)}\ (mmol) = \frac{M_{(NHND)}\ (g)}{179.17\ (g/mol)} \times 97\% \times 1000 \qquad \text{Equation 5.2.2}$$

$$n_{(NHND\ in\ NMR\ sample)}\ (\text{mmol}) = \qquad \text{Equation 5.2.3}$$
$$\frac{n_{(NHND\ in\ solution)}\ (\text{mmol})}{M_{(IS\ solution)}\ (\text{g})} \times M_{(0.1\ mL\ of\ IS\ solution)}(\text{g})$$

$$R = \frac{I_{OH}}{I_{NHND}} \qquad \text{Equation 5.2.4}$$

$$mmol\ of\ OH\ per\ gram\ of\ sample = \qquad \text{Equation 5.2.5}$$
$$\frac{R \times n_{(NHND\ in\ NMR\ sample)}\ (mmol)}{Dry\ weight\ of\ Sample\ (g)}$$

The calibration curve was created using a larger range of concentrations to gauge how accurate the technique can be, especially at lower concentrations. The lower concentrations are chosen to reflect typical ranges for bio-oils reported in literature[128]. Figure 5.2.11 shows the calibration curve between 0 moles and 9.84×10^{-4} moles. The calibration curve had a R^2=0.99 and all the points lay inside the orange shaded region which shows the 95% confidence. There are deviations in the calculated moles compared to the theoretical moles, which is summarised in Table 5.2.3. Overall, ^{31}P NMR can accurately predict the hydroxyl content in a sample however, limitations of the technique must be considerations when the hydroxyl content are at very low concentrations.

B.Tang, PhD Thesis, Aston University, 2024.

Table 5.2.3 Theoretical and calculated moles based on the intgral ratio of -OH and NHND for a range of concentration from 0.01 – 1 M.

Concentration (M)	Theoretical moles (mol)	Integration Ratio I_{OH}/I_{NHND}	Calculated moles (mol)	Percentage difference compared to theoretical (%)
1.00**	0.000984	248.9696	0.001020	3.66
0.75	0.000738	174.7620	0.000723	−2.04
0.50	0.000492	130.0000	0.000541	9.95
0.25	0.000246	62.2294	0.000261	5.88
0.10	0.000098	18.9771	0.000081	−18.05
0.075	0.000074	17.9000	0.000075	2.18
0.05	0.000049	10.5329	0.000044	−10.46
0.025	0.000025	6.2329	0.000026	6.43
0.00	0	0.0000	0	0
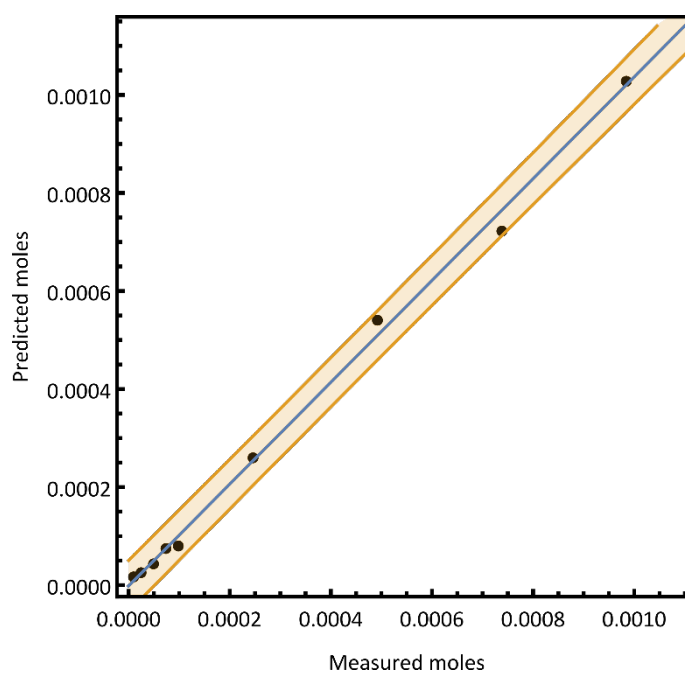
Figure 5.2.11 Calibration curve of ^{31}P qNMR. The predicted moles vs the measured moles calculated from the integral ratios between the derivatised cyclohexanol and NHND.

5.2.6 Qualitative ^{31}P NMR analysis of a model pyrolysis oil

Qualitative analysis of singular and simple alcohol mixtures using ^{31}P NMR techniques were proven successful in Section 5.2.4. Mixtures of model organic compounds were prepared to simulate dewatered bio-oil. Various oxygenated compounds were chosen based on bio-oil composition reported in the literature.[251] Two different model oils with different compositions were prepared. The components of the two model oils are

B.Tang, PhD Thesis, Aston University, 2024.

summarised in Table 5.2.4. Model bio-oil 1 was composed of furfural, acetic acid, phenol and ethanol. Model oil 2 was made up of acetic acid, guaiacol, methanol, cyclohexanol, and furfural. Heptane was added to represent the non-oxygenated compounds in bio-oil. Figure 5.2.12 shows the full ^{31}P spectrum for both oils, the area of interest from 130-160 ppm in orange is expanded in Figure 5.2.13, and from −5-30 ppm in green is expanded in Figure 5.2.14. The qualitative analysis is summarised in Table 5.2.5. Similar to Section 5.2.4 the compounds produced main peaks between 130 – 180 ppm where chemical shifts were compared to chemical shift map produced earlier.[245] Similar patterns were repeated in the more shielded region between 0 – 20 ppm. However, in this case it was harder to identify the individual peaks in the shielded region. Firstly, data was typically acquired between 120 ppm to 200 ppm in literature, therefore there are no chemical shift reports between 0 – 30 ppm. Secondly, as the phosphorus is not coupled to hydrogen, only singlet peaks were produced in both ^{31}P and the $^{31}P\{^{1}H\}$, this results in an increase in difficulty in peak assignments.

Table 5.2.4 Composition of Model Oil 1 and Model Oil 2.

Model Oil 1 Composition	Model Oil 2 Composition
Acetic acid	Acetic acid
Phenol	Guaiacol
Ethanol	Methanol
Furfural	Cyclohexanol
Heptane	Furfural
	Heptane
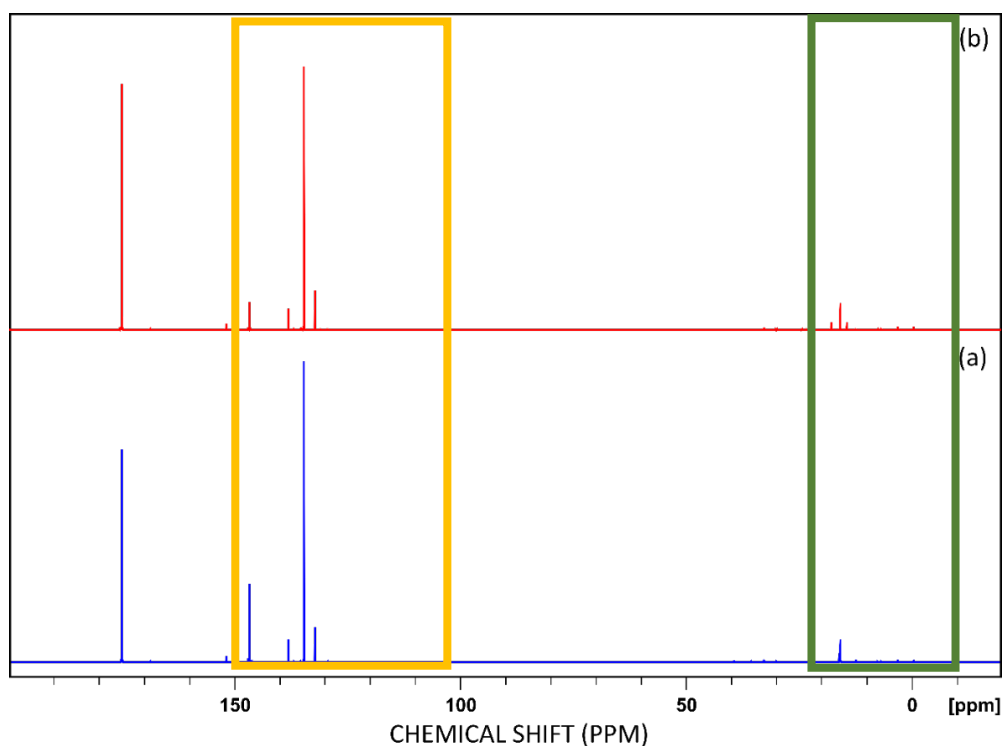
Figure 5.2.12 Stacked plot of full spectrum from −20-200 ppm (a) 1D $^{31}P\{^{1}H\}$ spectrum of derivatised model oil 1 (b) 1D ^{31}P spectrum of derivatised model oil 1. From 130-160 ppm in orange is expanded in Figure 4.3.11, and −5-30 ppm in green is expanded in Figure 4.3.12.
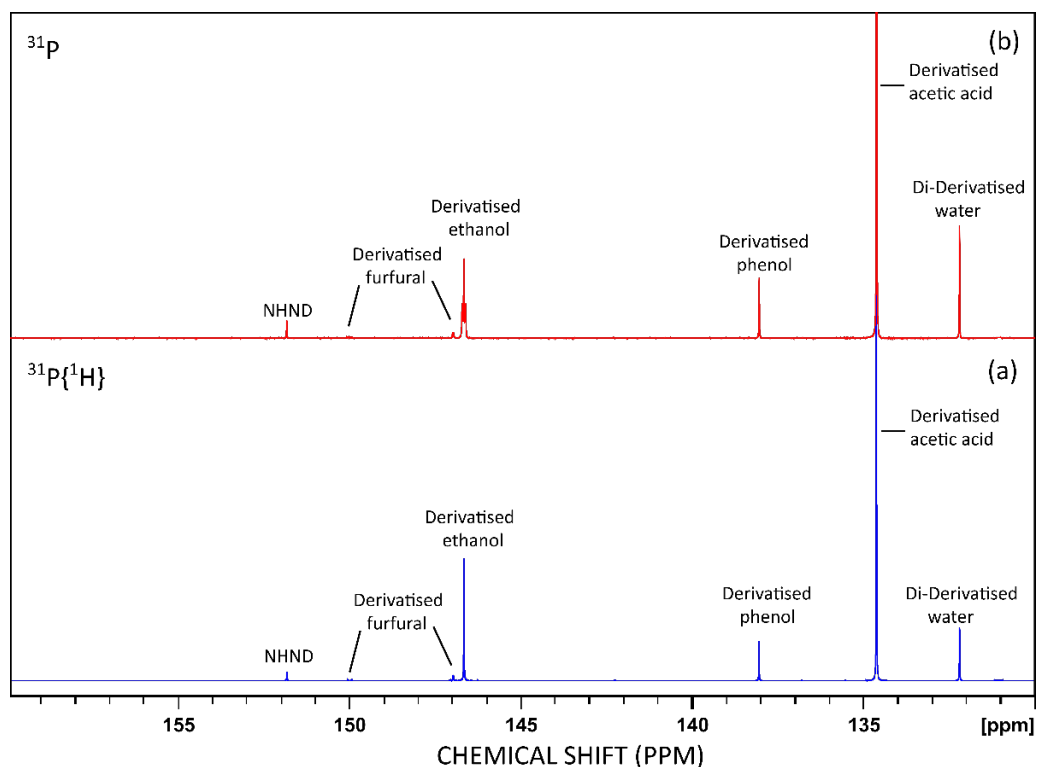
Figure 5.2.13 Stacked plot of spectrum from 130-160 ppm (a) 1D $^{31}P\{^{1}H\}$ spectrum of derivatised model oil 1 (b) 1D ^{31}P spectrum of derivatised model oil 1.

B.Tang, PhD Thesis, Aston University, 2024.
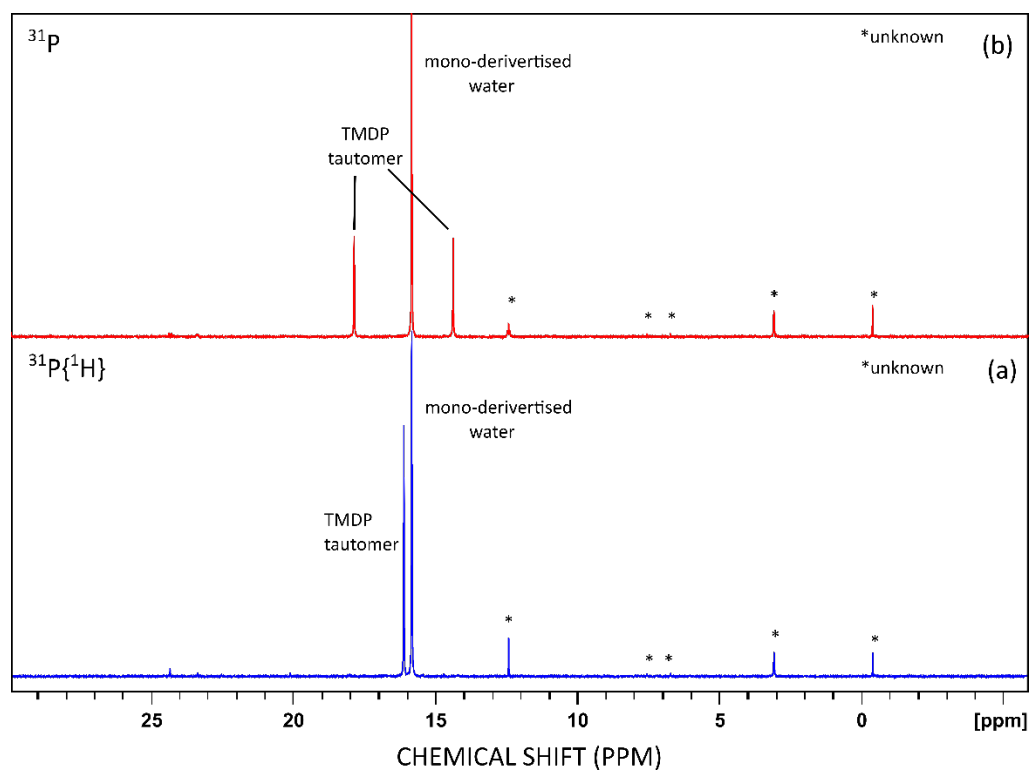
*Figure 5.2.14 Stacked plot of spectrum from −5-30 ppm (a) 1D $^{31}P\{^1H\}$ spectrum of derivatised model oil 1 (b) 1D ^{31}P spectrum of derivatised model oil 1. *unknown peaks*

Table 5.2.5 ^{31}P NMR assignment of model oil 1.

^{31}P/ ^{31}P Decoupled Chemical Shift (ppm)	^{31}P/ ^{31}P Decoupled Multiplicity	Compound
−0.39	singlet/singlet	Unknown
3.07	singlet/singlet	Unknown or acetic acid/TMDP tautomer
6.73	singlet/singlet	Unknown or phenol/TMDP tautomer
7.56	singlet/singlet	Unknown or furfural/TMDP tautomer
12.43	triplet/singlet	Ethanol/TMDP tautomer
15.82	singlet/singlet	Mono-derivatized water
16.12	doublet/ singlet	TMDP tautomer
132.20	singlet/singlet	Di-derivatised water
134.62	singlet/singlet	Derivatised acetic acid
138.05	singlet/singlet	Derivatised phenol
146.66	triplet/singlet	Derivatised ethanol
146.97	singlet/singlet	Derivatised furfural
150.00	doublet of doublet/doublet	Derivatised furfural
151.84	singlet/singlet	NHND internal standard
174.93	singlet/singlet	Unreacted TMDP

Model bio-oil 2 was composed of furfural, acetic acid, guaiacol, cyclohexanol and methanol. Figure 5.2.15 shows the full ^{31}P spectrum for both oils, the areas of interest from 130-160 ppm in orange are expanded in Figure 5.2.16, and those from −5-30 ppm in green are expanded in Figure 5.2.17. The qualitative analysis is summarised in Table 5.2.6. Similar to model bio-oil 1, the compounds in model bio-oil 2 produced significant peaks between 130 – 10 ppm where chemical shifts were compared to Li *et al.*[245] Similar patterns were repeated more shielded between −5 - 30 ppm. Again, it was hard to assign the singlets found at the low chemical shift. In order to assign them, each compound will need to be analysed separately to deduce accurate chemical shift values for compounds shielded.
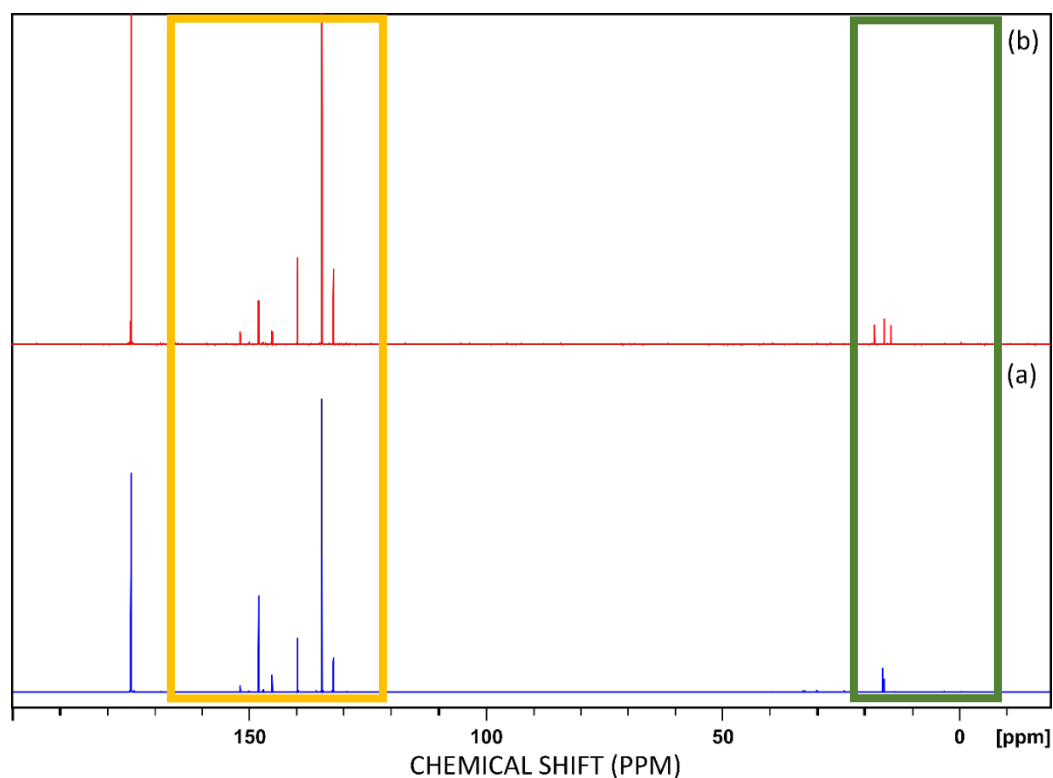
Figure 5.2.15 Stacked plot of full spectrum from −20-200 ppm (a) 1D $^{31}P\{^1H\}$ spectrum of derivatised model oil 2 (b) 1D ^{31}P spectrum of derivatised model oil 2. From 130-160 ppm in orange is expanded in Figure 4.3.15, and −5-30 ppm in green is expanded in Figure 4.3.15.
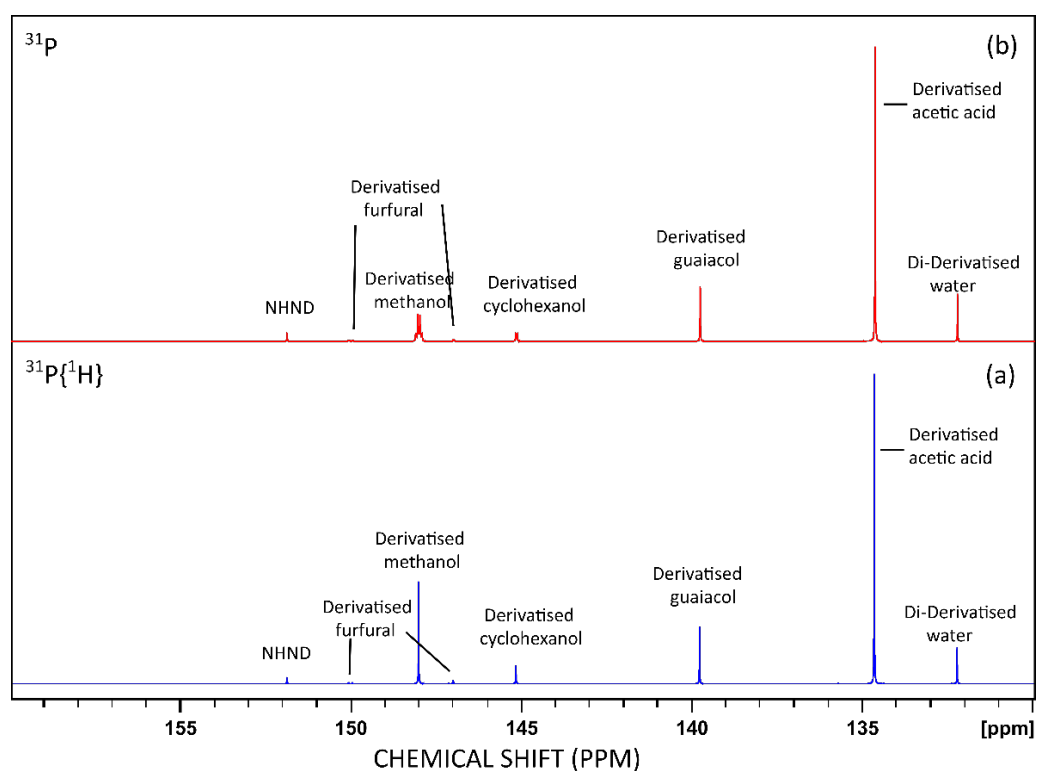
Figure 5.2.16 Stacked plot of spectrum from 130-160 ppm (a) 1D $^{31}P\{^1H\}$ spectrum of derivatised model oil 2 (b) 1D ^{31}P spectrum of derivatised model oil 2.
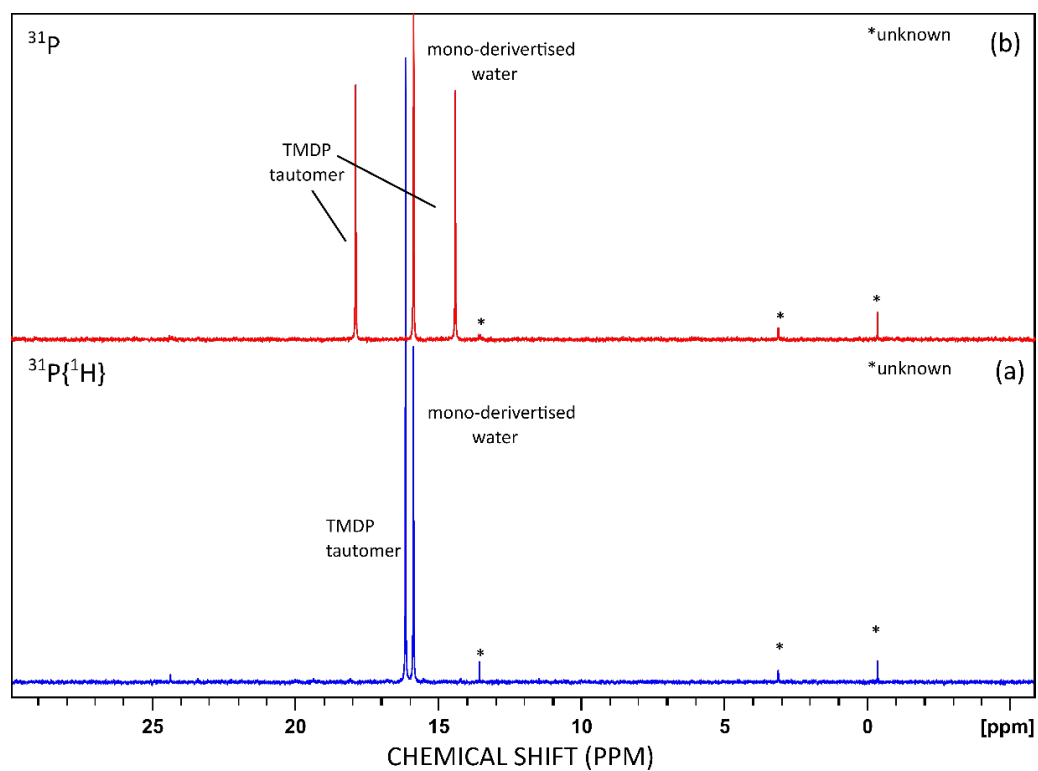
*Figure 5.2.17 Stacked plot of spectrum from −5-30 ppm (a) 1D $^{31}P\{^1H\}$ spectrum of derivatised model oil 2 (b) 1D ^{31}P spectrum of derivatised model oil 2. *unknown peaks.*

Table 5.2.6 ^{31}P NMR assignment of Model oil 2.

^{31}P/ ^{31}P Decoupled Chemical Shift (ppm)	^{31}P/ ^{31}P Decoupled Multiplicity	Compound
-0.39	singlet/singlet	Unknown
3.14	singlet/singlet	Unknown or acetic acid/TMDP tautomer
6.73	singlet/singlet	Unknown or guaiacol /TMDP tautomer
13.56	Quartet/singlet	Methanol/TMDP tautomer
15.82	singlet/singlet	Mono-derivatized water
16.12	doublet/ singlet	TMDP tautomer
132.20	singlet/singlet	Di-derivatized water
134.62	singlet/singlet	Derivatized acetic acid
139.75	singlet/singlet	Derivatized guaiacol
145.13	doublet/singlet	Derivatized cyclohexanol
146.97	singlet/singlet	Derivatized furfural
148.99	quartet/singlet	Derivatized methanol
150.00	doublet of doublet/doublet	Derivatized furfural
151.84	singlet/singlet	NHND internal standard
174.93	singlet/singlet	Unreacted TMDP

Overall, ^{31}P NMR techniques were able to distinguish between different derivatised alcohol containing compounds in simple mixtures, providing structural information about the alcohol themselves. ^{31}P qNMR was also able to provide accurate qualitative data on the amount of hydroxyl content, however, there is a limitation to detection, as a result, data should not be over interpreted especially at lower concentrations.

5.2.7 Analysis of Hand Sanitisers

Pyrolysis oils contain hundreds of small alcohols and are very complicated samples. Therefore, hand sanitisers were used for this study as an intermediate complex sample. The active ingredients in hand sanitiser are ethanol, isopropyl alcohol, and n-propanol. Glycerol is a tri-alcohol, and this is added to hand sanitisers to prevent skin dryness.

One analytical technique that could be used to analyse the alcohol content of the hand sanitisers is NMR. However, ^{1}H NMR alone can be difficult to interpret when it comes to mixtures. In addition, the ethanol peaks are so large, they can crowd out and overlap with peaks from less concentrated species present. Figure 5.2.9 shows a ^{1}H NMR of a hand sanitiser, where the peats at 1.19 ppm and 3.63 ppm belongs to the ethanol. There are some overlaps between the regions of 3.5 – 4 ppm, where the species are less concentrated making them difficult to identify and quantify. Quantitative analysis of alcohol content can also be determine using redox titration methods, however, these methods tend to be laborious. Therefore, ^{31}P derivatisation methods followed by NMR analysis could be a quicker alternative to identify and quantify alcohols present in hand sanitizers.
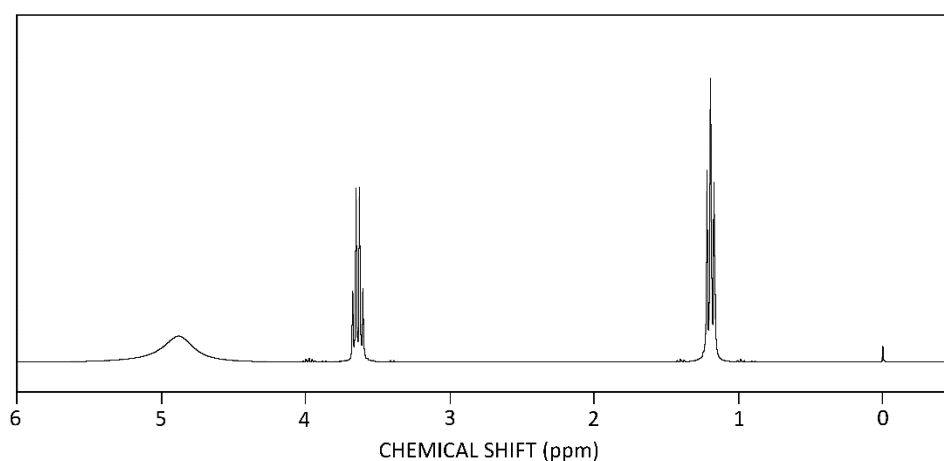
Figure 5.2.18 ^{1}H NMR spectrum of hand sanitiser (Garnier) with TMS as chemical shift reference (0 ppm).

5.2.7.1 Redox Titration

As described in the introduction, the alcohol content can be determined using redox titration methods. The reactions were carried out as described in Section 5.1.3. Each reaction was completed in triplicate and an average was taken. An example of how the % (w/w) of alcohol content was calculated is shown below and the results are summarised in Table 5.2.7. All data can be found in Appendix 3 (Section A3.4), where the error is the total apparatus error.

Sample (hand sanitiser) mass: 0.406g in 100 mL $\therefore$ 0.00406g in 1 mL

Initial amount of $Cr_2O_7^{2-}$:

$$n = CV = 0.01 \text{ M} \times \frac{10}{1000} = 1 \times 10^{-4} \text{ moles}$$

Equation 5.2.6

Titre: 12.4 cm^3 of 0.03 M thiosulfate need for titration for Garnier sample

Moles of thiosulfate:

$$n = CV = 0.03 \text{ M} \times \frac{12.4}{1000} = 3.72 \times 10^{-4} \text{ moles}$$

Equation 5.2.7

6 moles of $S_2O_3^{2-}$ reacts with 1 mole of $Cr_2O_7^{2-}$, $Cr_2O_7^{2-}$ remaining:

$$\therefore \frac{3.72 \times 10^{-4}}{6} = 6.2 \times 10^{-5} \text{ moles}$$

Equation 5.2.8

Moles of $Cr_2O_7^{2-}$ reacted with alcohol:

$$1 \times 10^{-4} - 6.2 \times 10^{-5} = 3.8 \times 10^{-5} \text{ moles}$$

Equation 5.2.9

Moles of ethanol in the hand sanitiser: 2:3 ratio

$$3.8 \times 10^{-5} \times 1.5 = 5.7 \times 10^{-5} \text{ moles}$$

Equation 5.2.10

Mass of ethanol in hand sanitiser: (MW_{Ethanol} = 46.07 gmol^{-1})

$$m = 5.7 \times 10^{-5} \times 46.07 = 2.626 \times 10^{-3} \text{g}$$

Equation 5.2.11

Ethanol (%w/w):

$$\frac{2.626 \times 10^{-3}}{4.06 \times 10^{-3}} \times 100 = 64.4$$

Equation 5.2.12

Table 5.2.7 Summary of the alcohol content of different hand sanitisers determined by redox titration.

Hand sanitiser	Average of the amount alcohol using titration
	%(w/w)
Garnier	64.4 ± 3.27
Carex	69.5 ± 3.52
Cuticura	56.3 ± 2.86
BondLoc	71.1 ± 3.61

5.2.7.2 Qualitative ^{31}P NMR Analysis

All four different hand sanitisers were derivatised and analysed using ^{31}P NMR methods outlined in Section 5.1.2. Figure 5.2.19 shows the ^{31}P {^{1}H} NMR spectra for each hand sanitiser, (a) Garnier, (b) Carex, (c) Cuticura and (d) Bondloc. Chemical shift for all

spectra were referenced using the di-derivatised water peak at 132.2 ppm. Each sample contains an internal standard derivatised NHND at 151.8 ppm, this is later used for quantification. The derivatised ethanol peak can be found at 146.6 ppm in all samples. The peaks at 147.4 ppm and 146.3 ppm belong to the derivatised glycerol. In the Cuticura sample, shown in Figure 5.2.19 (c), has an additional peak at 145.6 ppm. Both the chemical shift and ^{31}P NMR spectrum (Figure A3.7 (b)), where the singlet peak splits into a doublet, suggest it is a secondary alcohol. However, it is inconclusive whether this peak belongs to 2-propanol, typically at 145.2 ppm, or 2-butanol, typically found at 145.8 ppm. The Bondloc sample shown in Figure 5.2.19 (d) also contains an additional peak at 145.1 ppm where the singlet peak splits into a doublet in the ^{31}P NMR spectrum (Figure A3.7 (d)). Based on that information, it is likely that the peak at 145.1 ppm belongs to 2-propanol.
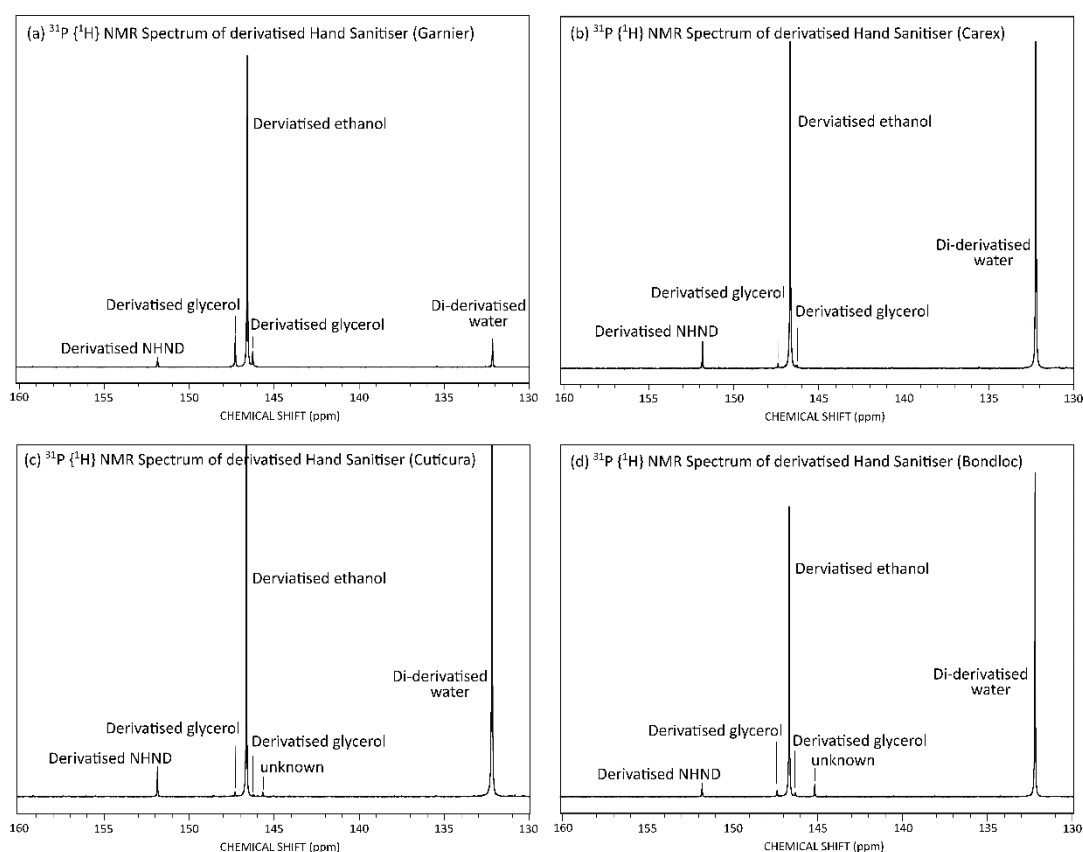
Figure 5.2.19 ^{31}P {1H} spectrum of hand sanitisers derivatised with TMDP (a) Garnier (b) Carex (c) Cuticura (d) Bondloc.

5.2.7.3 Quantitative ^{31}P NMR Analysis

The ethanol content of four hand sanitisers i.e Garnier, Carex, Cuticura and Bondloc can be found using ^{31}P qNMR methods. Figure 5.2.20 shows a ^{31}P {^{1}H} NMR spectrum of

derivatised Garnier hand sanitiser. The derivatised NHND peak and derivatised ethanol peak were integrated, where the integration ratio is 37.8. All data for the other hand sanitisers are located in Appendix 3. The estimation of ethanol is based on the integration ratio internal standard (*ca*. 151 ppm) used and ethanol peak.
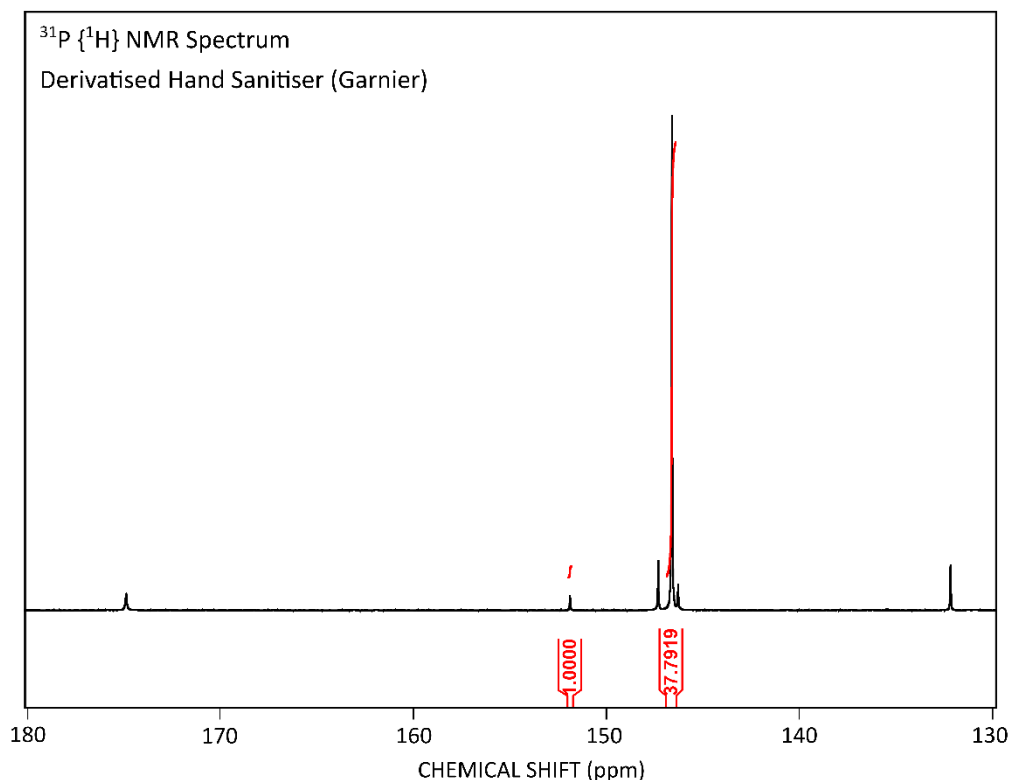
Figure 5.2.20 ^{31}P {^{1}H} NMR spectrum of hand sanitiser (Garnier) derivatised with TMDP, where the intergrated peak at 151.8 ppm is the derivatised NHND, the intergal set to 1.000 and the intgrated peak at 146.6 ppm, integral calculated as 37.79 is the derivatised ethanol.

An example of how the %(w/w) of ethanol was calculated using the integration is shown below.

Internal Standard:

$$n_{NHND} = \frac{m}{mr} \times purity \times 1000 =$$

$$\frac{0.0388}{179.17} \times 97\% \times 1000 = 0.21 \text{ mmol}$$

Equation 5.2.13

Quantity of IS in NMR tube:

$$n_{NHND \, in \, NMR \, tube} = \frac{n_{NHND} \times M_{(0.1 \, mL \, of \, IS \, solution)}}{M_{IS \, solution}} =$$

$$\frac{0.21 \times 0.1125}{2.513} = 0.00940 \text{ mmol}$$

Equation 5.2.14

Integration ratio:

$$R = 37.8 \text{ (integration from NMR)} \qquad \text{Equation 5.2.15}$$

Moles of ethanol (mmol):

$$n_{OH} = \frac{R \times n_{NHND \, in \, NMR \, tube}}{M_{handsanitser}} = \frac{37.8 \times 0.00940}{0.0263} \qquad \text{Equation 5.2.16}$$
$$= 13.5156 \text{ mmol g}^{-1}$$

Convert mmol/g to %(w/w) by multiplying by the molecular mass:

$$\frac{13.5156}{1000} = 0.0135156 \text{ mol g}^{-1} \qquad \text{Equation 5.2.17}$$

$$0.0135156 \text{ mol g}^{-1} \times 46.07 \text{ g mol}^{-1} \times 100 = 64.4 \text{ \%} \qquad \text{Equation 5.2.18}$$

Using redox titration method (Section 5.1.3), the Garnier branded hand sanitiser was determined to contain 64.4 ± 3.3 %(w/w) alcohol content. From ^{31}P {^{1}H} NMR spectrum it was found that the hand sanitiser contains ethanol and glycerol and the ethanol content determined from was found to be 63.3 ± 1.9 % (w/w). Both methods were comparable to the label stating that the hand sanitiser should contain 62.4 % (w/w) ethanol. Similarly, using titration methods, the Carex branded hand sanitiser was determined to contain 69.5 ± 3.5 % (w/w) alcohol content. From ^{31}P {^{1}H} NMR spectrum it was found that the hand sanitiser contains ethanol and glycerol and the ethanol content determined from was found to be 70.8 ± 2.2% (w/w). Both methods were comparable to the label stating that the hand sanitiser should contain 70 % (w/w) ethanol. Using titration methods, the Cuticura branded hand sanitiser was determined to contain 56.3 ± 2.9 % (w/w) alcohol content. From NMR methods it was found that the hand sanitiser contains derivatised ethanol, glycerol peak and additional alcohol peak. The ethanol content determined was found to be 55.9 ± 1.8 % (w/w) and additional alcohol was found to be 0.4 ± 1.8 % (w/w), therefore a total of 56.3 % (w/w). Both methods estimated the same amount of alcohol content in then hand sanitiser, it was also similar to the label stating that the hand sanitiser should contain 57.5% (w/w) ethanol. Using titration methods, the Bondloc branded hand sanitiser was determined to contain 71.1 ± 3.6 % (w/w) alcohol content. From NMR methods it was found that the hand sanitiser contains derivatised ethanol, glycerol peak and additional alcohol peak. The ethanol content determined was found to be 70.3 ± 2.1 % (w/w) and unknown alcohol was found to be 2.6± 2.1 % (w/w), therefore

a total of 72.9 % (w/w). Both methods estimated the same amount of alcohol content in then hand sanitiser, it was also similar to the label stating that the hand sanitiser should contain 70%(w/w) ethanol. ^{31}P derivatisation reactions typically take *ca*. 15 minutes compared to oxidation of alcohol followed by titration where the reaction typically takes over *ca*. 12 hours. Overall, the ethanol content determined using ^{31}P NMR techniques were comparable to the redox titration methods. These were also compared to the label on the hand sanitiser and both methods agree with the label. This is summarised in Figure 5.2.21, note that the bars representing the alcohol content obtained from ^{31}P NMR for the Cuticura and Bondloc are shown in turquoise and grey representing the two different alcohols present. The advantage of NMR techniques compared to titration methods is the ability to distinguish between different types of alcohol groups and thus quantifying them individually.
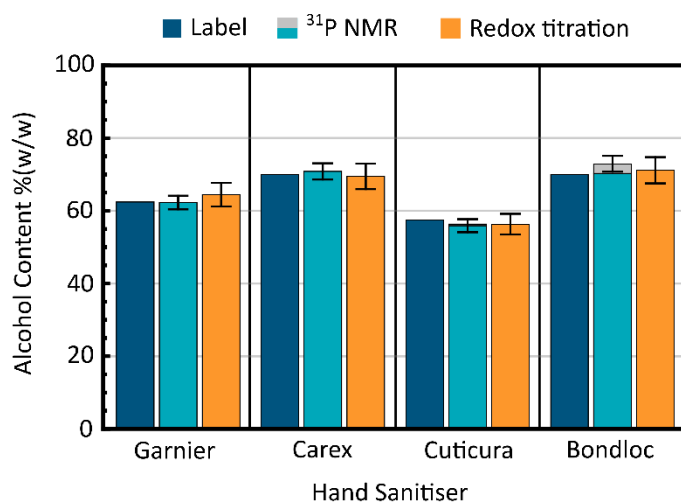
Figure 5.2.21 Graph comparing the quantification of ethanol in different brands of hand sanitisers using ^{31}P NMR methods and redox titration methods.

5.2.8 ^{31}P NMR Analysis of Pyrolysis Oil

^{31}P NMR techniques were applied to a bio-oil produced from a spruce feedstock. The samples were derivatised using the method in Section 5.1.2. Figure 5.2.22 shows the stacked plot of the ^{31}P NMR and ^{31}P {^{1}H} NMR spectrum of derivatised bio-oil produced from spruce. The decoupled spectrum shows a sparser, simplified, spectrum. The hydroxyl groups are assigned based on chemical shift values reported in literature and chemical shift map produced in Section 5.2.4[209]. It is difficult to identify and distinguish individual compounds when a spectrum is crowded. This is one of the main reasons ^{1}H

NMR struggles to identify compounds mixtures like bio-oil. For ^{31}P qNMR analysis, the spruce oil was found to contain 0.00315 mol g^{-1} of primary alcohol, 0.00038 mol g^{-1} secondary alcohol, 0.00126 mol g^{-1} of tertiary/aromatics alcohols and 0.00029 mol g^{-1} of carboxylic acids. These were calculated based on the integration regions shown in Figure A3.11.
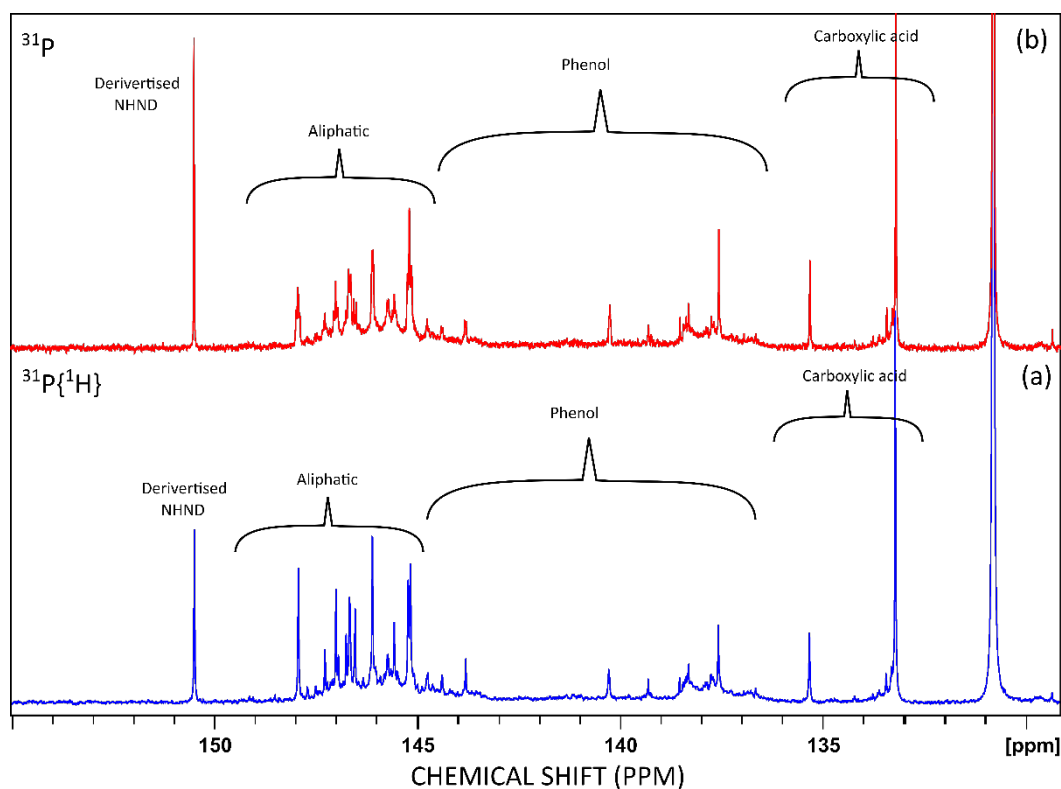
Figure 5.2.22 Stacked plot of spectrum from 130-160 ppm (a) 1D ^{31}P{^{1}H} spectrum of derivatised bio-oil produced from spruce feedstock (b) 1D ^{31}P spectrum of derivatised bio-oil produced from spruce feedstock.

5.3 Conclusion

This chapter introduces and improves current ^{31}P NMR methodologies for the characterisation of bio-oil. ^{1}H NMR struggles to distinguish between various hydroxyl groups in the sample. Derivatisation of only the hydroxyl groups using ^{31}P-contianing agents result in a single peak for each hydroxyl group in the sample. To further reduce the crowding of the spectrum, ^{31}P{^{1}H} NMR was employed. An inverse gated sequence can be used to acquire quantitative data. The ^{31}P and ^{31}P{^{1}H} experiments were optimised, and the bi-level WALTZ-16 composite decoupling pulse was used to minimise spectral artefacts that arise from compounds with larger coupling constants. When model oils were studied, additional peaks were observed at low chemical shifts, which could be due to either rearrangement or tautomerisation of the derivatised compound.

Overall, ^{31}P NMR enabled the qualitative analysis of alcohol containing samples in both hand sanitisers and pyrolysis oils. For real-world samples such as hand sanitiser, ^{31}P qNMR techniques were used to detect alcohol level accurately. These findings were also compared to label on the sample and more traditional methods such as oxidation followed by redox titration.

When it came to the identification of peaks in real hand sanitisers, the major limitation is that the chemical shift range of secondary alcohols are close together and all secondary alcohols would exhibit the same splitting pattern. For example, the Bondloc sample contains an extra peak at 145.1 ppm. Based on purely 1D ^{31}P NMR data, chemical shift, and splitting pattern, it is determined likely to belong to 2-propanol. However, other possibilities remain. This chapter introduces the foundations for further development of methodologies such as ^{31}P DOSY. By developing diffusion-based techniques, such as ^{31}P DOSY, it will enable the estimations of molecular weights of compounds, and thus, confirming species present in bio-oil. By coupling chemical shift values as well as molecular weight information, this should enable ease of identification of oxygenated species present. Development of these methods will be explored in the next chapter.

CHAPTER 6 : DEVELOPMENT OF ^{31}P DIFFUSION-ORDERED SPECTRSCOPY

6.1 Introduction

Chapter 5 explored the use of 2-chloro-4,4,5,5-tetramethyl-1,3,2-dioxaphospholane (TMDP) to selectively derivatise hydroxyl groups followed by ^{31}P {^{1}H} NMR. ^{31}P NMR has a larger chemical shift range than ^{1}H NMR, which increases the chemical shift dispersion. Using ^{31}P {^{1}H} NMR experiments, decoupling significantly simplifies the spectrum easing the analysis. The resulting spectrum with fewer peaks, decoupling to remove multiple signals and larger chemical shift ranges all combine to produce a sparser spectrum. The selection of only the hydroxyl groups also simplified the spectrum and allows the identification of different alcohols. However, as shown in previous chapter, based on chemical shift, and coupling information alone, there remains some ambiguity in identifying the all the alcohols present in the hand sanitisers samples.

Molecular self-diffusion in a liquid originates from the random movement of the molecules present. Encoding spatial information using gradients in diffusion-based experiments enable the separation of signals in a second, diffusion, dimension resulting in further simplification and improved resolution. Diffusion coefficients provide information on the molecules' size, shape, and environment. There is a general correlation between molecular mass and the speed at which a molecule travels in solution, i.e the larger the molecule, the slower it moves and the small the molecule, the fast it moves through solution. This, in turn, infers chemical information, such as the molecular weight. In this chapter, the developments of ^{31}P DOSY experiments and the use of internal calibration are explored to estimate molecular weights of unknown species.

6.2 Experimental

6.2.1 Materials

All reagents used as model compounds were obtained commercially, the origin and purity of these compounds used in this study are reported in the Appendix 3 (Table A3.1). Acros organics supplied Tetramethyl silane, 99.9 %, chloroform-*d* (CDCl$_3$), 99.8% and pyridine, 99.5%, extra dry over molecular sieve. Chromium(III) 2,4-pentanedionate,97% was purchased from Fischer Scientific. Trimethylphosphate ≥99%, 2-chloro-4,4,5,5-tetramethyl-1,3,2-dioxaphospholane (TMDP), 95%, *endo-N*-hydroxy-5-norbornene-2,3-dicarboximide (NHND) was purchased from Sigma-Aldrich.

6.2.2 Methods

The following procedure for derivatisation is the same as Section 5.2.2

Solvent A

A stock solvent solution of 1:1.6 volume ratio of $CDCl_3$ and anhydrous pyridine was prepared and dried over molecular sieves.

Internal Standard:

0.1M internal standard was prepared by adding NHND (0.018 g) to solution A (1 mL). A relaxation agent, chromium (III) 2,4-pentadienoate (5 mg) was dissolved in the solution. The weight of the entire solution was recorded. The internal standard was stored over molecular sieves.

Derivatisation reaction:

IS solution (0.1 mL) was transferred into a glass vial equipped with a PTFE-lined silicone septum. The weight of the 0.1 mL IS solution was recorded. Bio-oil (30 mg) was weighed into the same vial. The actual weight of the sample was recorded. Solvent A (0.7 mL) was added using a gastight syringe into the same vial and was left stirring until the mixture was homogenous. For the derivatisation reaction an excess of TMDP (*ca.* 0.2 mL) was added using a gastight syringe. The reaction was left for 10 minutes to stir. The solution was then transferred to a 5 mm NMR tube using a Pasteur pipette and analysed immediately because the phosphitylation derivative of NHND is not stable over a long period of time.

NMR Analysis:

All NMR acquisition were acquired using Bruker AVANCE 300 MHz equipped with a 5mm PABBO BB-1H Z-GRD probe. The z-gradient coil producing a calibrated maximum gradient of 55.7 G cm^{-1}.[252] Data was acquired using 10 increments, equally spaced in gradient squared. All data was measured at 298 K. For all data acquired using Oneshot sequences, gradient ranged from 20% to 80% of the maximum. For all data acquired

using convection compensated sequences, gradient ranged from 10% to 90%. The error in width of peak is calculated based on the fit of the data to the Stejskal-Tanner (Equation 2.4.3). All diffusion data was processed using DOSYToolBox [253], where 5 Hz of line broadening was used.

6.3 Results and Discussion

6.3.1 Development of ^{31}P DOSY pulse sequence

6.3.1.1 ^{31}P Oneshot Sequence

Trimethyl phosphate (TMP) was chosen as the test compound for the development of the ^{31}P DOSY sequence as it is an inert, simple molecule that contains both hydrogen and phosphorus atoms. As it is single compound, regardless of nuclei chosen, the measured diffusion coefficient of both nuclei should be the same. The ^{31}P Oneshot diffusion sequence is based on the ^{1}H Oneshot sequence.[231] The observed nuclei added, were changed from proton to phosphorus with the proton decoupled using an inverse gated decoupling pulse sequence. The decoupler was optimised in Chapter 5. The full pulse sequence for BRUKER instruments can be found in Appendix 4.
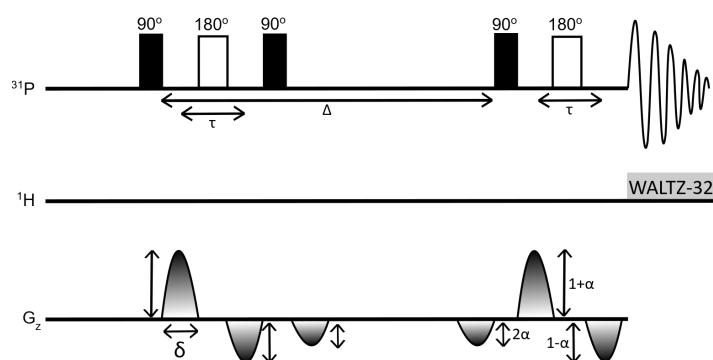
Figure 6.3.1 Oneshot pulse sequence for measuring diffusion coefficient with a WALTZ-32 decoupling sequence. The gradient pulse has a duration of δ. The gradient strength is changed by an imbalance factor (α). Any magnetisation not refocused by 180º pulse will be de-phased by the intensity factor 1+ α and 1- α and the two other gradients by the intensity 2α. The diffusion delay Δ and τ is an intergradient within the bipolar gradient pulse.

The diffusion coefficient of trimethyl phosphate in D_2O was measured at 298 K using the ^{1}H Oneshot diffusion sequence. The doublet peak at 3.7 ppm belongs to the trimethyl phosphate and the diffusion coefficient was found to be $7.70 \pm 0.01 \times 10^{-10}$ m^2 s^{-1}. The diffusion coefficient was then measured using the ^{31}P Oneshot sequence. The singlet peak at 2.23 ppm belongs to the trimethyl phosphate, where the diffusion coefficient was

165

found to be $7.62 \pm 0.02 \times 10^{-10}$ m^2 s^{-1}. Therefore, it was found that the diffusion coefficient of trimethyl phosphate in D$_2$O for both ^{1}H and ^{31}P diffusion experiments were concordant.
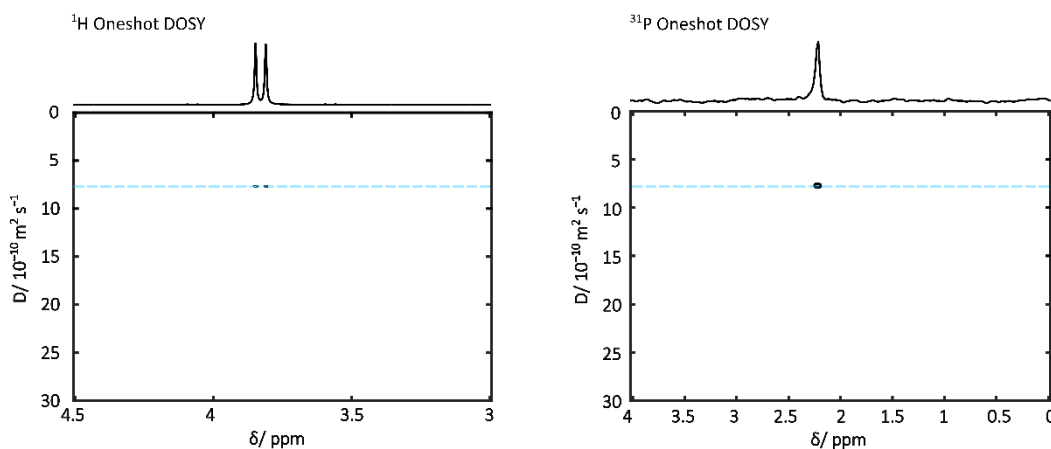
Figure 6.3.2 ^{1}H DOSY spectrum of trimethyl phosphate in D$_2$O acquired using Oneshot sequence (left hand side) and ^{31}P DOSY spectrum of trimethyl phosphate in D$_2$O acquired using Oneshot sequence (right hand side).

However, the derivatisation reaction in Chapter 5 is not carried out in D$_2$O, but a mixture of CDCl$_3$ and pyridine. Therefore, to test the robustness of the sequence, the diffusion coefficient of trimethyl phosphate dissolved in pyridine-d_5 and CDCl$_3$ was measured. It was found that the diffusion coefficients of trimethyl phosphate in pyridine-d_5 for ^{1}H and ^{31}P Oneshot diffusion experiments were $12.9 \pm 0.03 \times 10^{-10}$ m^2 s^{-1} and $24.9 \pm 0.22 \times 10^{-10}$ m^2 s^{-1}, respectively. The diffusion coefficient of trimethyl phosphate in CDCl$_3$ for ^{1}H and ^{31}P Oneshot diffusion experiments were $24.5 \pm 0.14 \times 10^{-10}$ m^2 s^{-1} and $28.3 \pm 0.48 \times 10^{-10}$ m^2 s^{-1}, respectively. For both solvents, diffusion coefficient increased in the ^{31}P Oneshot DOSY experiment compared to the ^{1}H Oneshot DOSY.
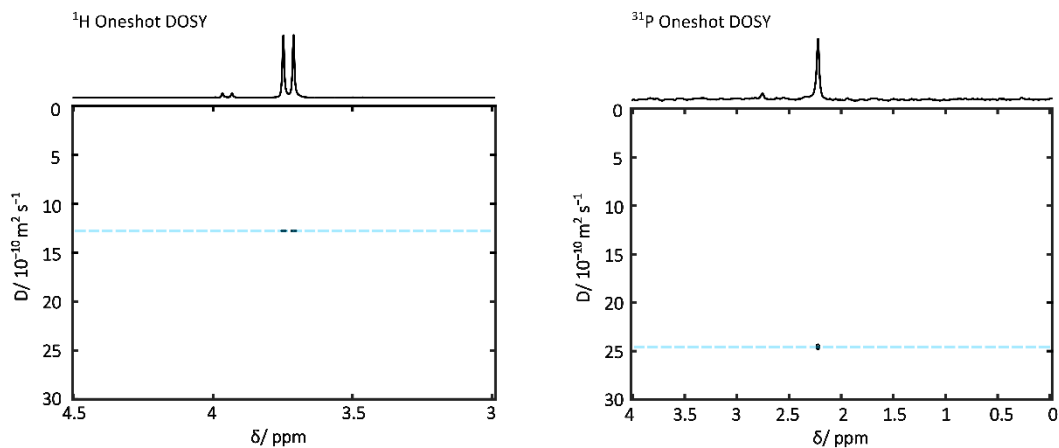
Figure 6.3.3 ^1H DOSY spectrum of trimethyl phosphate in pyridine-d_5 acquired using Oneshot sequence (left-hand side) and ^{31}P DOSY spectrum of trimethyl phosphate in pyridine-d_5 acquired using Oneshot sequence (right-hand side).
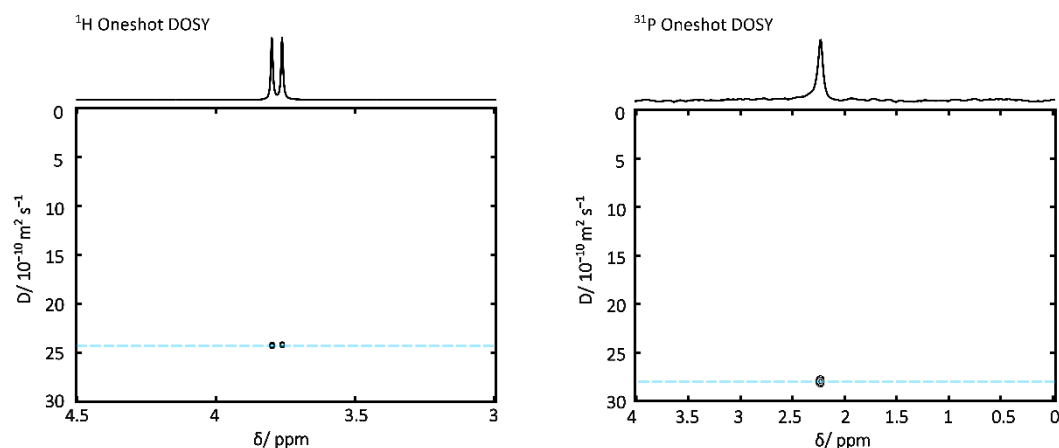
Figure 6.3.4 ^1H DOSY spectrum of trimethyl phosphate in CDCl$_3$ acquired using Oneshot sequence (left-hand side) and ^{31}P DOSY spectrum of trimethyl phosphate in CDCl$_3$ acquired using Oneshot sequence (right-hand side).

Usually, a larger diffusion coefficient suggests that the solute is moving quicker. This could be due to different reasons, such as the size of the solute, viscosity of the solvent or temperature of the sample. The size of the solute can be ruled out because the H and P nuclei are from the same species. A composite pulse decoupling (CPD) is used to decouple the proton from the phosphorus simplifying the spectrum. The decoupler requires a small amount of power, potentially heating the sample. As a result, there may be a greater chance of convection causing the molecules to diffuse faster than expected.[133]

6.3.1.2 Convection

Liquid state NMR experiments are susceptible to temperature variation in the sample. This is especially true for experiments that uses pulsed field gradients such as diffusion NMR experiments, even though the temperature of the NMR experiments can be controlled using the variable temperature unit, the flow of gas enters at the base of the probe which can result in the base of the sample being cooler than the top. Any temperature gradient in the sample will lead to a convective liquid. Resulting in problems such as signal loss and an overestimation of diffusion coefficients.

The most well-known form of convection is known as Rayleigh-Bénard convection, which arises when the sample at the bottom of the tube is warmer than the top. The warmer liquid then rises to the top and the cooler liquid sinks. The resulting temperature gradient $\frac{dT}{dz}$ will lead to convection when it reaches a critical value. The Rayleigh number, Ra, describes the relationship between the buoyancy and viscosity of a fluid.[254] This is described by the equation:

$$Ra = \frac{g\beta\rho^2 c_p R^4 \frac{dT}{dz}}{\eta\kappa} \qquad \text{Equation 6.3.1}$$

where g is the acceleration due to gravity (m s^{-2}), β (K^{-1}) is the volumetric thermal expansion coefficient, ρ (kg m^{-3}) is the density of a liquid at a given temperature, c_p (J kg^{-1} K^{-1}) the specific heat capacity, R is the cylinder internal radius, $\frac{dT}{dz}$ is the vertical temperature gradient (K m^{-1}), η (Pa s) is the viscosity of the liquid at a given temperature and κ is the thermal conductivity (W m^{-1} K^{-1}). As noted earlier, Rayleigh-Bernard convection only occurs when the temperature gradient exceeds a critical value. However, in literature in the case of chloroform in a thin-walled tube, a vertical gradient less than 0.3 K cm^{-1} was enough for sample to be convective. This demonstrates that in typical NMR experiments, there are also horizontal temperature gradient. Convection driven by horizontal temperature gradient does not exhibit critical behaviour. The maximum convection velocity depends on the solvent used. For a horizontal temperature gradient in a conducting tube, it can be estimated by:

$$v_{max} = \frac{R^3 g\beta\rho}{\sqrt{108}\eta}\frac{dT}{dx} = \chi\frac{R^3 g}{\sqrt{108}}\frac{dT}{dx} \qquad \text{Equation 6.3.2}$$

The quantity χ (K^{-1} m^{-2}) measures of the ease in which a given liquid convects under a horizontal temperature gradient. This can be calculated using the equation:

$$\chi = \frac{\beta\rho}{\eta} \qquad \text{Equation 6.3.3}$$

The thermal volumetric expansion, density and viscosity are temperature-dependant. Figure 6.3.5 shows a schematic diagram of how each parameter varies with temperature. The viscosity (Figure 6.3.5 (a)) of a liquid generally decreases as temperature increases, as molecules have more kinetic energy and move more quickly and interact for a shorter time. Density (Figure 6.3.5 (b)) decreases due to molecules having more kinetic energy, therefore the particles move quickly and spreading further apart, thus, occupying a larger volume and decreasing the density. The volumetric expansion coefficient, (Figure 6.3.5 (c)) increases with temperature. As a result, the ease of convection is also temperature dependant, where χ increases as the temperature increases.
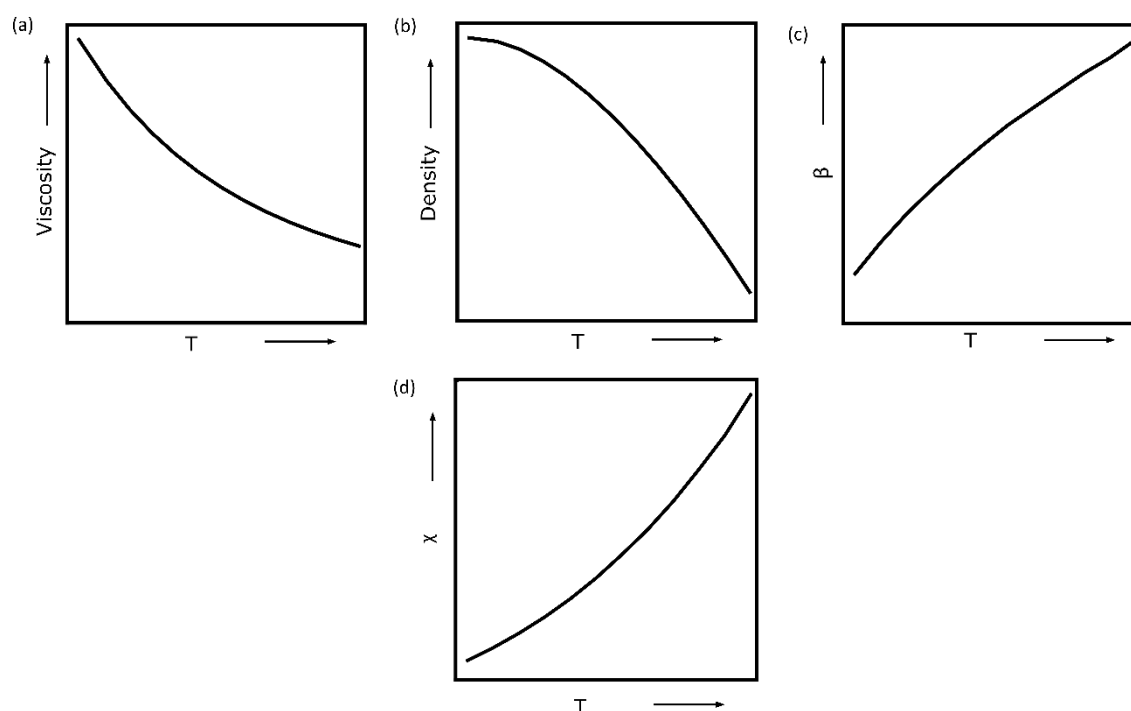
Figure 6.3.5 Schematic diagram of how temperature effects (a) viscosity, (b)density, (c) volumetric expansion coefficient and (d) ease of convection.

Section 6.2.2 described a reaction that uses a mixed solvent system of $CDCl_3$ and pyridine. To determine how convective a solvent is, values of χ must be evaluated. However, obtaining data for χ in literature can be difficult, particularly for deuteriated solvents. Values of β, ρ and η for chloroform, H_2O and D_2O can be found in Table 6.3.1, hence X can be calculated for these solvents.

Table 6.3.1 Physical parameters for determining the rate of convection driven by a horizontal temperature gradient for protiated and deuteriated forms of common solvents at 298 K.

Solvent	β $/10^{-3}$ K^{-1}	ρ $/10^3$ kg m^{-3}	η $/10^{-3}$ Pa s	X /K^{-1} m^{-2}
Chloroform	1.27	1.479	0.542	3.4655
H_2O	0.257	0.997	0.89	0.2876
D_2O	0.172	1.044	1.095	0.1639

The parameters above must be obtained from literature or calculated to estimate the likelihood of convection. The literature readily provides the densities of a solvent at different temperatures.[255-257] Equation 6.3.5 where m is the mass (kg) ρ is the density (kg m^{-3}), and V_m is the molar volume (m^3 mol^{-1}).

$$\rho = \frac{m}{V_m}$$

Equation 6.3.4

$$\therefore V_m = \frac{m}{\rho}$$

Equation 6.3.5

β can be found by:

$$\beta = \frac{1}{V_m}\left(\frac{\partial V_m}{\partial T}\right)$$

Equation 6.3.6

The volumetric thermal expansion can be obtained by plotting molar volume as a function of T. The volume data can be fitted to a quadratic equation:

$$V_m = a + bT + cT^2$$

Equation 6.3.7

$$\beta = \frac{(a + bT + cT^2)'}{a + bT + cT^2}$$

Equation 6.3.8

$$\therefore \beta = \frac{b + 2cT}{a + bT + cT^2}$$

Equation 6.3.9

Alternatively, the volume data can also be interpolated; however, this less effective with smaller data sets. For pyridine, a different macro was used, as small number of values for β could be found, while no consistent density data was identified. [258] This required a different approach, were β at 298 K was extrapolated. Table 6.3.2 shows the volumetric thermal expansion, density, viscosity, and ease of convection for solvents of interest. Where the macro in Appendix 4 was used to calculate β. For example, for H_2O, the density data at various temperature was found in literature.[255] The volume of water is found by multiplying the molecular mass of water (18.015 g mol^{-1}) by the density of water at a temperature. The volume is plotted against temperature this is shown by the blue

dots in Figure 6.3.6. The data is fitted to a quadratic equation which is shown by the red dashed line in Figure 6.3.6.
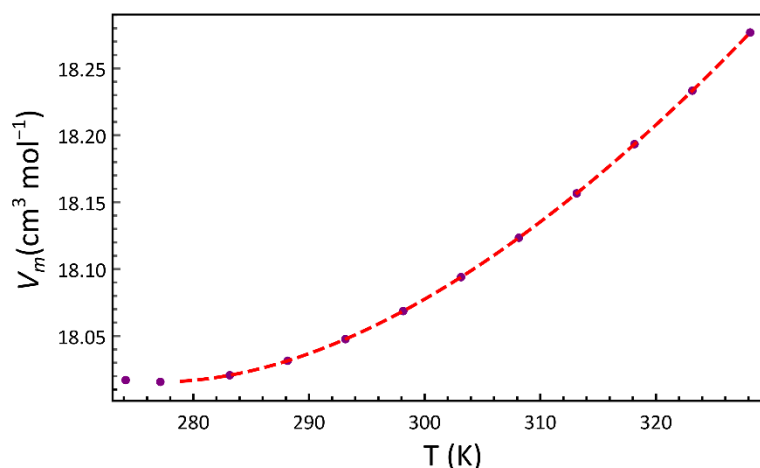
Figure 6.3.6 Plot of temperature vs volume calculated using Equation 6.3.5 (blue dot) and the fitting of the quadratic equation (red dashed line)

Where the quadratic equation was found to be:

$$V_m = 24.5311 - 0.047736\ T + 0.0000874\ T^2$$

Therefore, at 298.15 K:

$$\beta = \frac{-0.047736 + 0.000174817 \times 298.15}{24.5311 - 0.047736 \times 298.15 + 0.0000871 \times 298.15^2} = 0.000243\ \mathrm{K}^{-1}$$

Using this method, the thermal expansion coefficient at 298.15 K for H_2O was found to be 0.243 K^{-1} this is concordant to data found in literature β =0.25 K^{-1}.[259] Overall, it was found that from least convective to most convective solvents of interest are as follows D_2O (χ=0.164 $K^{-1}\ m^{-2}$), pyridine (χ=1.201 $K^{-1}\ m^{-2}$) and chloroform-*d* (χ=3.664 $K^{-1}\ m^{-2}$).

*Table 6.3.2 Physical parameter determining the rate of convection driven by a horizontal temperature gradient for protiated and deuteriated forms of common solvents at 298 K *estimated values using macros written in this thesis.*

Solvent	β /10^{-3} K^{-1}	ρ /10^3 kg m^{-3}	η /10^{-3} Pa s	X /K^{-1} m^{-2}
Chloroform	1.27	1.479	0.542	3.465
Chloroform-*d*	1.29*	1.500	0.528	3.664
H$_2$O	0.257	0.997	0.890	0.288
D$_2$O	0.172	1.044	1.095	0.164
Pyridine	1.08*	0.982	0.879	1.201
Pyridine-*d$_5$*	1.03*	1.050	0.945	1.144

There are two types of strategies commonly used to deal with convection, either adapt experimental conditions e.g sample geometry, to reduce the rate of convection or use pulse sequences that are designed to compensate for the effects of convection. Methods that reduce the rate of convection include using thinner diameter NMR tube for example thick-walled NMR tubes. Convection-compensated pulses are designed to refocus the effects of constant velocity flow along the field gradient direction. However, at extreme temperatures neither would be sufficient by itself. Thick-walled tubes are easily obtained, experiments using thick-walled NMR tube was the step taken to address convection.

The diffusion coefficient of TMP in D$_2$O in a thick-walled NMR tube was measured using the ^{1}H and ^{31}P Oneshot sequence. The diffusion coefficients were found to be 7.67 ± 0.01 × 10^{-10} m^2 s^{-1} and 7.86 ± 0.40 × 10^{-10} m^2 s^{-1} respectively, and these results were comparable to those in the thin-walled tube. Earlier calculations showed that pyridine-*d$_5$* and CDCl$_3$ are more susceptible to convective flow than D$_2$O. Therefore, the diffusion coefficient of TMP was also measured in pyridine-*d$_5$* and CDCl$_3$. The diffusion coefficient of TMP in pyridine-*d$_5$* was measured using the ^{1}H and ^{31}P Oneshot sequence where the diffusion coefficients were found to be 11.06 ± 0.02 × 10^{-10} m^2 s^{-1} and 11.96 ± 0.59 × 10^{-10} m^2 s^{-1} suggesting that the thick-walled tube was sufficient to suppress most of the effects of convection. However, when the diffusion coefficient of TMP in CDCl$_3$ in a thick-walled NMR tube was measured using the ^{1}H and ^{31}P Oneshot sequence, the diffusion coefficients were found to be 15.45 ± 0.04 × 10^{-10} m^2 s^{-1} and 18.95 ± 0.67 × 10^{-10} m^2 s^{-1} respectively. These results were less comparable, suggesting that for very convective solvents like CDCl$_3$, a think-walled tube is not enough to suppress the effects of convection.
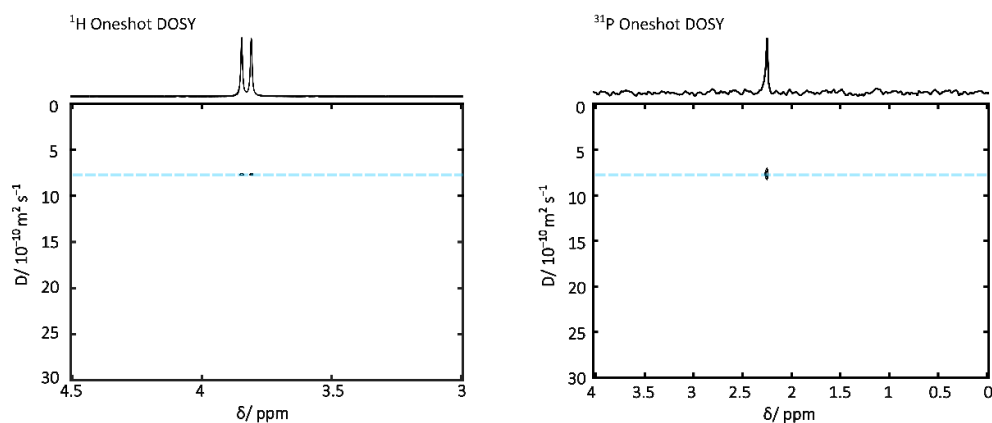
Figure 6.3.7 ^{1}H DOSY spectrum of trimethyl phosphate in D_2O acquired using Oneshot sequence in a thick-walled tube (left-hand side) and ^{31}P DOSY spectrum of trimethyl phosphate in D_2O acquired using Oneshot sequence in a thick-walled tube (right-hand side).
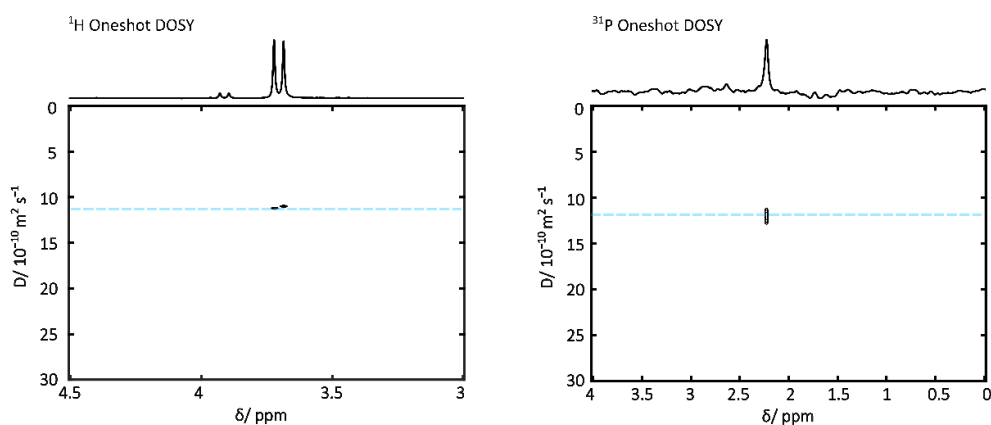
Figure 6.3.8 ^{1}H DOSY spectrum of trimethyl phosphate in pyridine-d_5 acquired using Oneshot sequence in a thick-walled tube (left-hand side) and ^{31}P DOSY spectrum of trimethyl phosphate in pyridine-d_5 acquired using Oneshot sequence in a thick-walled tube (right-hand side).
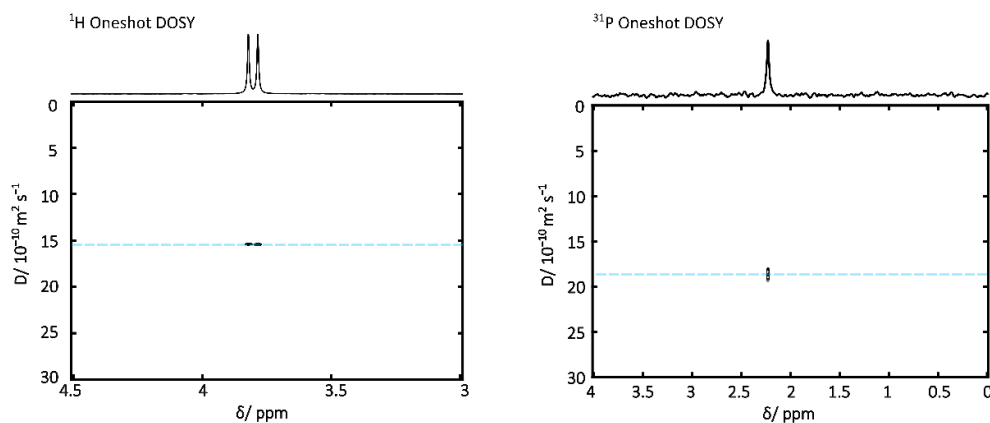
Figure 6.3.9 ^{1}H DOSY spectrum of trimethyl phosphate in $CDCl_3$ acquired using Oneshot sequence in a thick-walled tube (left-hand side) and ^{31}P DOSY spectrum of trimethyl phosphate in $CDCl_3$ acquired using Oneshot sequence in a thick-walled tube (right-hand side).

173

6.3.1.3 ^{31}P Convection Compensated Squenece

Similar to the ^{31}P Oneshot diffusion sequence, the convection compensated ^{31}P DOSY sequences were based on the double stimulated echo using bipolar gradient pulse, 3 spoiler pulsers and a balancing pulse at the start. The combined with an inverse gated proton decoupling sequence. The full pulse sequence for BRUKER instruments can be found in Appendix 4.
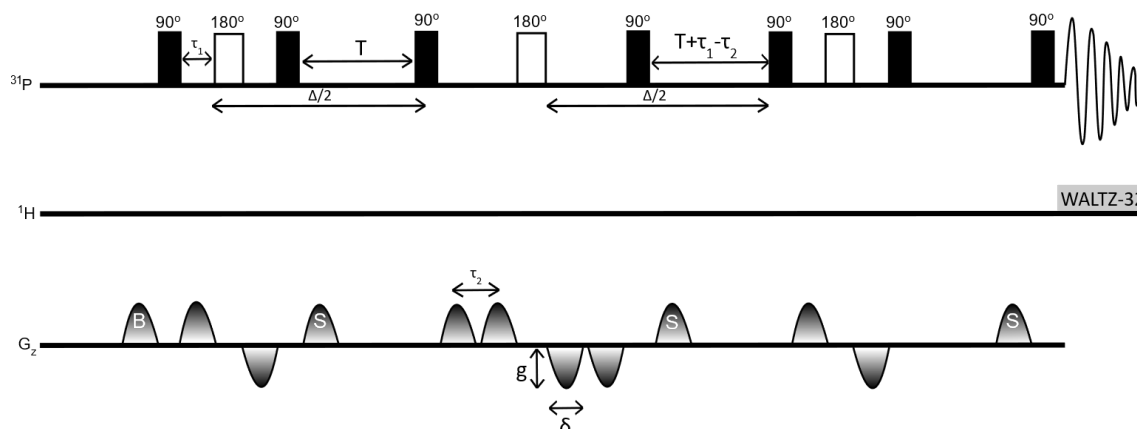
Figure 6.3.10 Double stimulated echo bipolar pulse gradient pair pulse sequence with a WALTZ-32 decoupling sequence (dstebpgp3s) (convection compensated sequence). The diffusion delay time (Δ) is split into two parts. The two adjacent sets of bipolar pulse pairs in the centre of the pulse sequence ensure that only the 180° pulse is required to refocus the signal. There are 3 spoiler gradients denoted with S are used to remove any unwanted signals in the transverse plane. Each gradient pulse has the strength, g and has a duration of δ. $τ_1$ and $τ_2$ are intergradient delays in the bipolar gradient pulse. T is the variable diffusion delay time parameter with a balancing gradient denoted with B which balances out the three spoiler gradients.

The ^{31}P convection compensated sequence was tested with the three different samples. To ensure the convection compensated sequence was adequate enough to compensate for the amount of convection, the diffusion coefficients of TMP in different solvents were measured in both thick-walled and standard NMR tubes.
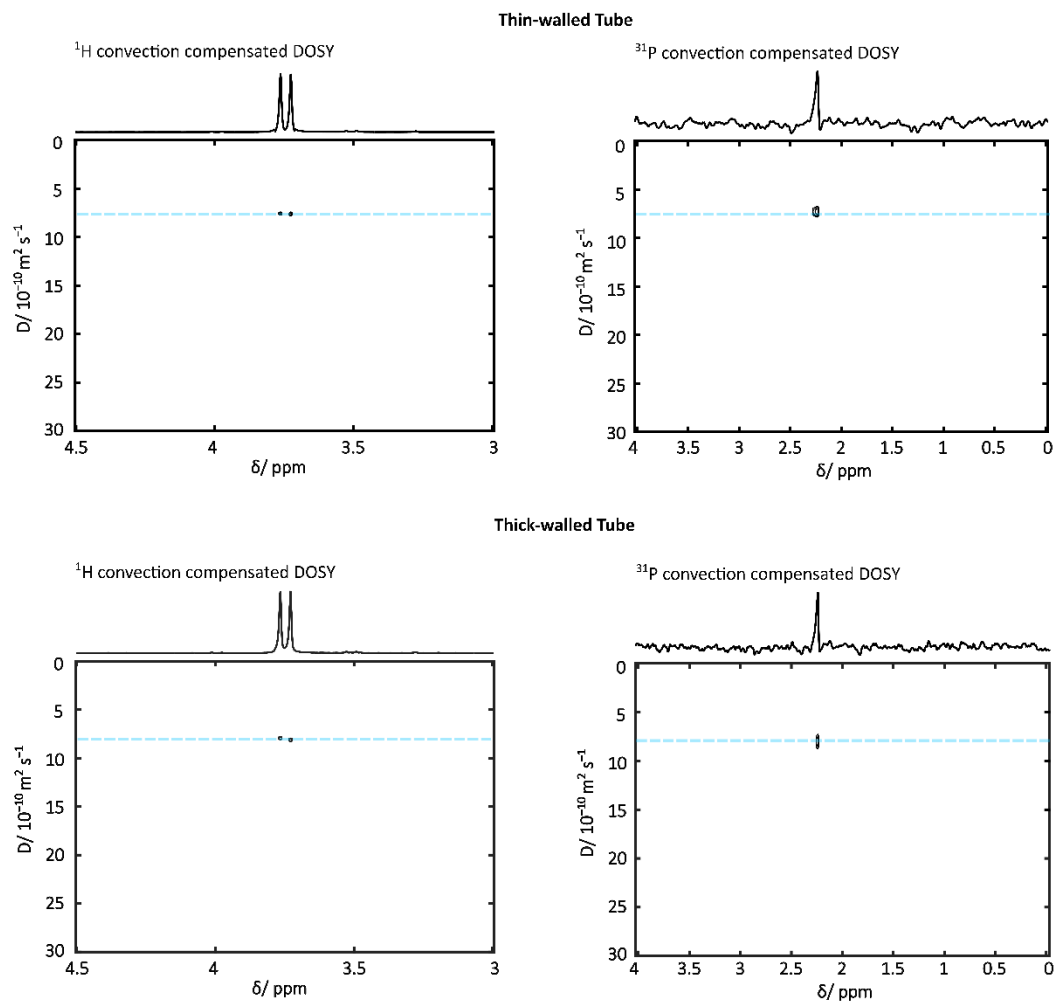
Figure 6.3.11 ^{1}H DOSY spectrum of trimethyl phosphate in D$_2$O acquired using convection compensated sequence in a thin-walled tube (top left-hand side), ^{31}P DOSY spectrum of trimethyl phosphate in D$_2$O acquired convection compensated sequence in a thin-walled tube (top right-hand side), ^{1}H DOSY spectrum of trimethyl phosphate in D$_2$O acquired using convection compensated sequence in a thick-walled tube (bottom left-hand side) and ^{31}P DOSY spectrum of trimethyl phosphate in D$_2$O acquired convection compensated sequence in a thick-walled tube (bottom right-hand side).
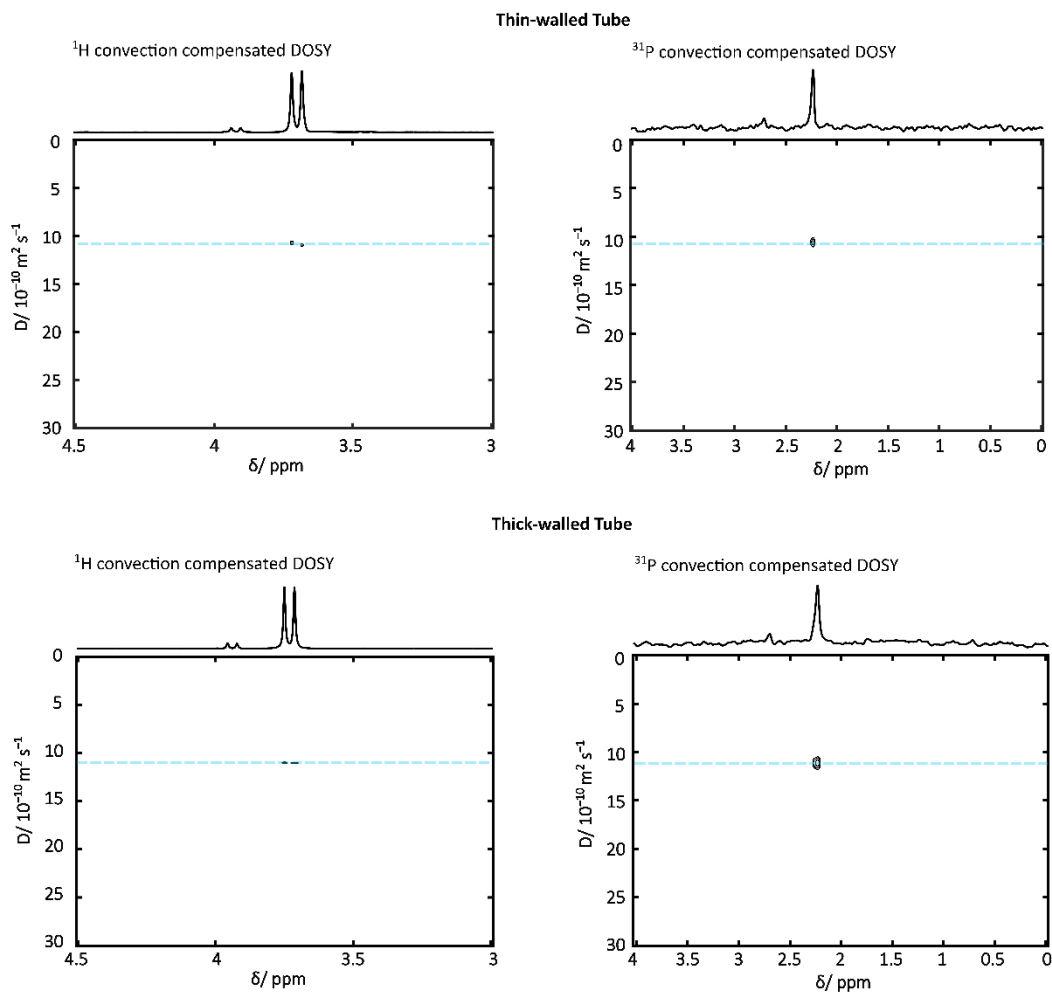
Figure 6.3.12 ¹H DOSY spectrum of trimethyl phosphate in pyridine-d₅ acquired using convection compensated sequence in a thin-walled tube (top left-hand side), ³¹P DOSY spectrum of trimethyl phosphate in pyridine-d₅ acquired convection compensated sequence in a thin-walled tube (top right-hand side), ¹H DOSY spectrum of trimethyl phosphate in pyridine-d₅ acquired using convection compensated sequence in a thick-walled tube (bottom left-hand side) and ³¹P DOSY spectrum of trimethyl phosphate in pyridine-d₅ acquired convection compensated sequence in a thick-walled tube (bottom right-hand side).
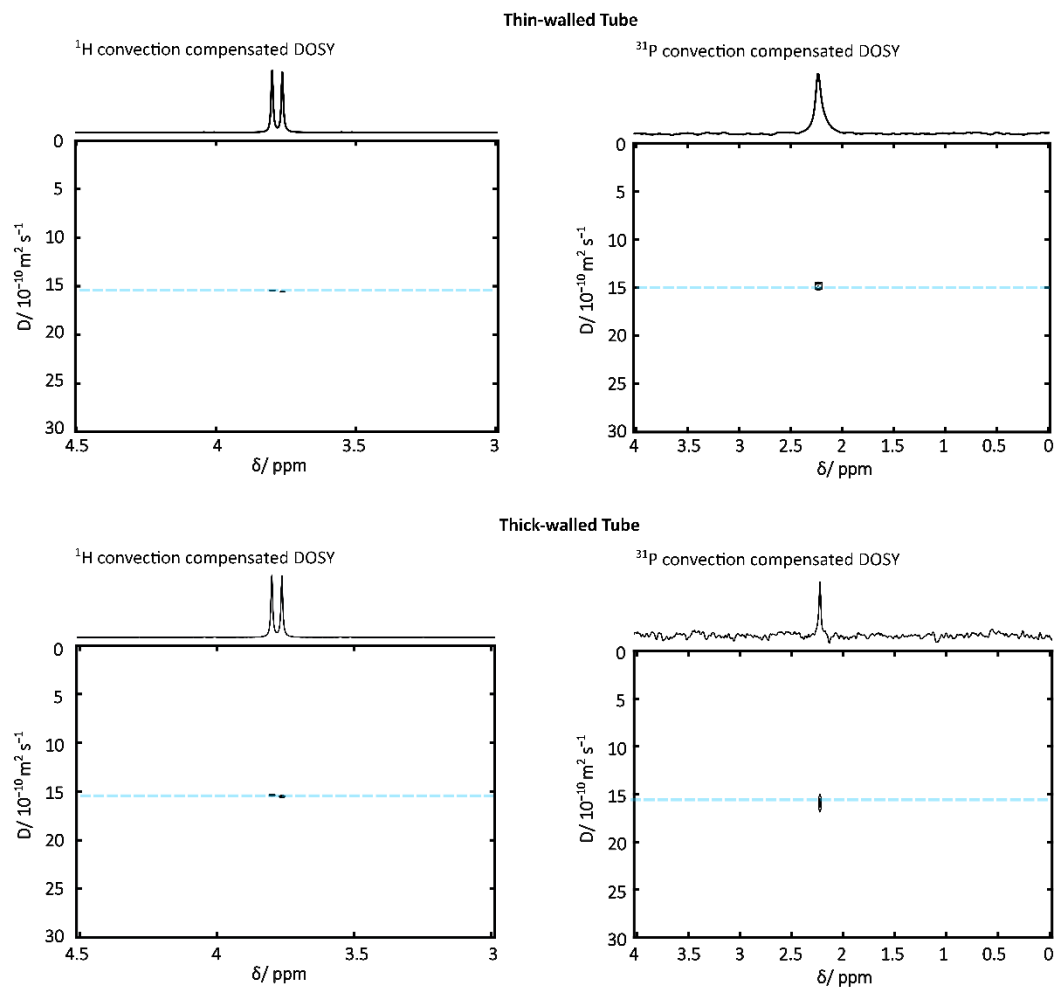
Figure 6.3.13 ^{1}H DOSY spectrum of trimethyl phosphate in CDCl$_3$ acquired using convection compensated sequence in a thin-walled tube (top left-hand side), ^{31}P DOSY spectrum of trimethyl phosphate in CDCl$_3$ acquired convection compensated sequence in a thin-walled tube (top right-hand side), ^{1}H DOSY spectrum of trimethyl phosphate in CDCl$_3$ acquired using convection compensated sequence in a thick-walled tube (bottom left-hand side) and ^{31}P DOSY spectrum of trimethyl phosphate in CDCl$_3$ acquired convection compensated sequence in a thick-walled tube (bottom right-hand side).

In Section 6.3.1.2 it was estimated that D$_2$O was the least susceptible to convective flow, and chloroform-*d* was the most susceptible to convective flow. This phenomenon can be seen in the experimental data collected so far, where the diffusion coefficients of TMP in the different solvents are summarised in Figure 6.3.14. In D$_2$O, where convection is unlikely to have an effect on the diffusion coefficients, the diffusion coefficients measured using both ^{1}H and ^{31}P and both Oneshot sequences and convection compensated sequences were comparable in both standard and thick-walled NMR tubes. With solvents that are more likely to convect such as pyridine-*d$_5$*, the effects of convection can be seen in the difference of diffusion coefficient of TMP measured using the ^{1}H Oneshot

sequence ($12.9 \pm 0.03 \times 10^{-10}$ m^2 s^{-1}) and ^{31}P Oneshot sequence ($24.7 \pm 0.22 \times 10^{-10}$ m^2 s^{-1}). Using a thick-walled NMR tube does reduce the ease of convection. However, the diffusion coefficient of TMP measured using the ^{31}P Oneshot sequence was still slightly higher than expected ($11.9 \pm 0.59 \times 10^{-10}$ m^2 s^{-1}). The diffusion coefficients measured using the convection compensated sequences were all concordant. With solvents that easily convects, such as chloroform-d, the thick-walled tube alone was not sufficient to reduce the rate of convection in the ^{31}P Oneshot experiment where the diffusion coefficient of TMP was found to be $18.9 \pm 0.67 \times 10^{-10}$ m^2 s^{-1} compared with ^{1}H Oneshot, where the diffusion coefficient was found to be $15.4 \pm 0.04 \times 10^{-10}$ m^2 s^{-1}. Overall, the diffusion coefficients measured for TMP in D2O, pyridine-d_5 and chloroform-d solvent using a convection compensated sequence were all in agreement. Therefore, all ^{31}P DOSY for the rest of this chapter will be acquired using the convection compensated sequence.
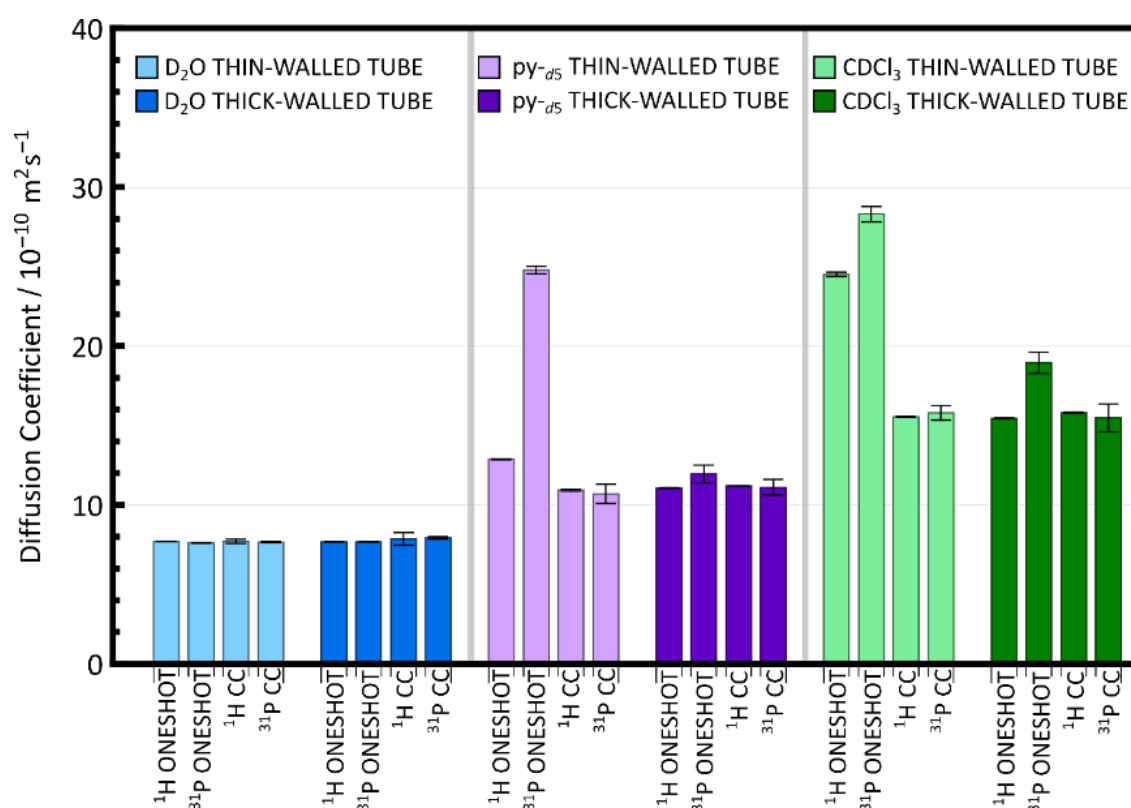
Figure 6.3.14 Summary of diffusion coefficients of TMP measured in D2O, pyridine-d5, CDCl3 using both ^{1}H and ^{31}P one shot and convection compensated pulse sequences in a thin-walled tube compared to those measured in the thick-walled tube.

The derivatisation reaction was carried out in a mixed solution, it was important to understand how mixed solvents could affect the diffusion of molecules. Therefore, as a

final test, trimethyl phosphate dissolved in $CDCl_3$:pyridine (1:1.6 v/v) mixture in a thin-walled tube was used to test the robustness of the ^{31}P convection compensated sequence. The diffusion coefficient of trimethyl phosphate dissolved in $CDCl_3$:pyridine was measured using the proton convection compensated sequence and phosphorus convection compensated sequence (Figure 6.3.15). The diffusion coefficient of trimethyl phosphate was found to be $12.1 \pm 0.1 \times 10^{-10}$ $m^2\,s^{-1}$ for the ^1H convection compensated sequence and $11.63 \pm 0.2 \times 10^{-10}$ $m^2\,s^{-1}$ for the ^{31}P convection compensated sequence.
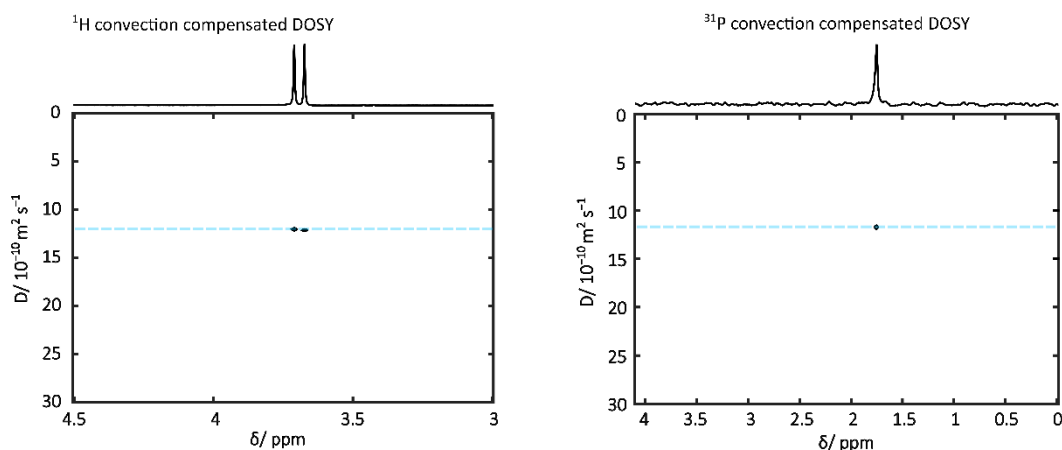
Figure 6.3.15 ^1H DOSY spectrum of trimethyl phosphate in $CDCl_3$:pyridine acquired using convection compensated sequence (left-hand side) and ^{31}P DOSY spectrum of trimethyl phosphate in $CDCl_3$:pyridine acquired using convection compensated sequence (right-hand side).

For real samples, in the derivation method (Section 6.2.2) a relaxation agent was added to the samples for qNMR. As a final test, the diffusion coefficient of trimethyl phosphate dissolved in $CDCl_3$:pyridine with the relaxation agent $Cr(acac)_3$ was measured using the proton convection compensated sequence and phosphorus convection compensated sequence. The diffusion coefficient was found to be $12.1 \pm 0.1 \times 10^{-10}$ m^2 s^{-1} (^1H convection compensated sequence) and $11.9 \pm 0.15 \times 10^{-10}$ m^2 s^{-1} (^{31}P convection compensated sequence). These were also comparable to the diffusion coefficients without the $Cr(acac)_3$, therefore, the relaxation agent used did not affect diffusion measurements.

B.Tang, PhD Thesis, Aston University, 2024.
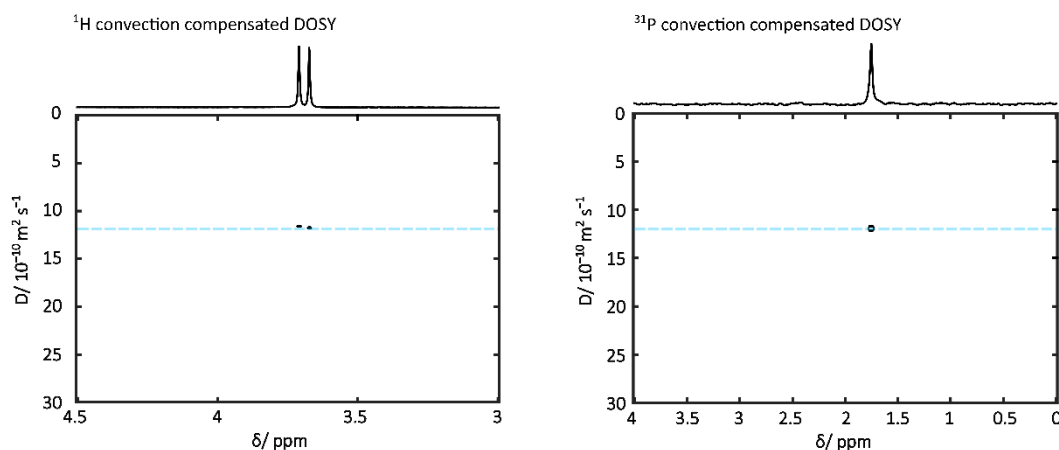
Figure 6.3.16 ^{1}H DOSY spectrum of trimethyl phosphate in CDCl$_3$:pyridine with Cr(acac)$_3$ acquired using convection compensated sequence (left-hand side) and ^{31}P DOSY spectrum of trimethyl phosphate in CDCl$_3$:pyridine with Cr(acac)$_3$ acquired using convection compensated sequence (right-hand side).

6.3.2 Internal Calibration with Model Compounds

Diffusion coefficients can be used to infer chemical information such as size of a molecule, smaller the molecule the quicker it diffuses through a liquid and larger the molecule the slower it diffuses. There are two different approaches to obtain quantitative measurements on the size or molecular weight of a species based on their diffusion coefficient. Power laws is one approach in deduce molecular weight information from diffusion coefficients. The diffusion coefficient can be expressed in terms of the molecular weight, MW, raised to an empirical negative power, $-\alpha$, as such, $D \propto MW^{-\alpha}$. Use of these methods requires calibration curves, a Log D vs Log MW, plot for a particular set of calibration compounds. All power-law based methods follow the same approach, where the diffusion coefficient of a series of reference compounds are measured, and a double logarithmic plot is used to generate the two parameters needed for the power law. The power law generated is then used to estimate the molecular weight of the unknown compounds based on the experimental diffusion coefficient or to predict the diffusion coefficient based on the molecular weight.

Internal calibration, as the name suggests, indicates that the species used to generate a calibration curve are all contained within the sample. The diffusion coefficients are measured synchronously with the unknown. Typically, a minimum of three co-solutes are added to the sample to provide parameters for the power law. This is more reliable than using only two co-solutes. Not all compounds are suitable as internal standards, as

they must be inert, soluble, non-aggregating and cover a suitable range of molecular weights for the analytes to be studied.

All NMR samples were prepared in thin-walled tubes. During the derivatisation process, TMDP derivatises any alcohol groups, the NHND and any water within the sample. Therefore, every sample will contain the derivatised NHND, di-derivatised water and unreacted TMDP. Therefore, an extra compound was added; in this case TMP has been chosen as its chemical shift is far away from the peaks of interest and it is inert. Table 6.3.3 contains the compounds used for an internal calibration and their ^{31}P NMR chemical shifts.

Table 6.3.3 Compounds used for the internal calibration with their chemical shift.

Compound	Chemical Shift (ppm)
TMP	3.3
Di-derivatised water	132.2
Derivatised NHND	151.8
Unreacted TMDP	174.9

To test this, a simple alcohol (ethanol) was derivatised using the methods in (Section 6.2.2). The ethanol was treated as an 'unknown' alcohol. The ^{31}P DOSY was carried out using the ^{31}P convection compensated sequence. Figure 6.3.17 shows the ^{31}P DOSY of the TMDP (174.9 ppm), derivatised NHND (151.8 ppm), derivatised ethanol (146.5 ppm) and di-derivatised water (132.2 ppm). The molecular weights of the internal standards and their measured diffusion coefficients are shown in Table 6.3.4
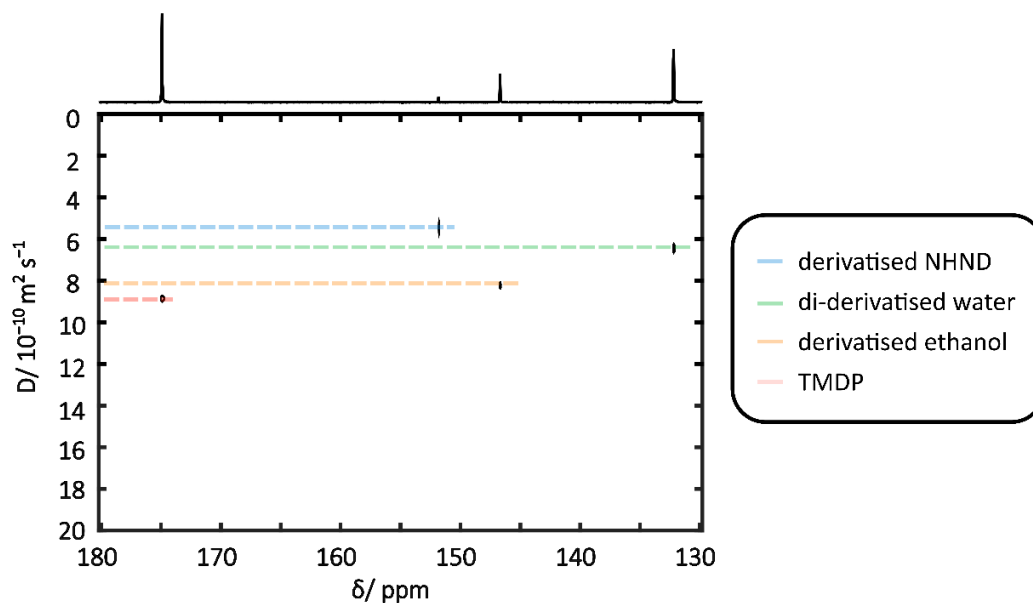
Figure 6.3.17 ^{31}P DOSY spectrum of TMDP, derivatised NHND, derivatised ethanol and diderivatised water.

Table 6.3.4 Molecular weight, log MW, measured diffusion coefficient and log D of internal calibrants.

Compound	MW	log MW	D	log D
	g mol^{-1}		/ 10^{-10} m^2 s^{-1}	
TMP	140.1	2.14	10.1 ± 0.38	−8.99
Di-derivatised water	310.2	2.49	6.65 ± 0.12	−9.18
Derivatised NHND	325.3	2.51	6.34 ± 0.30	−9.19
TMDP	182.6	2.26	8.93 ± 0.05	−9.04

By plotting log *MW* against log *D* of the internal calibrants, a power law is generated, where the molecular weight of the derivatised alcohol can be estimated from their diffusion coefficient. Using the equation generated:

$$\log D = -0.548 \log MW - 7.815$$

The molecular weight of the derivatised alcohol can be estimated from the diffusion coefficient. The estimated molecular weight will be the molecular weight of the derivatised alcohol. Therefore, for a mono-derivatised alcohol, the estimated derivatised molecular weight minus 146.1 g mol^{-1} will be the molecular weight of the alcohol. In this case, peak at 146.5 ppm had a diffusion coefficient of 8.57 × 10^{-10} m^2 s^{-1}, therefore from this, the estimated molecular weight of the derivatised alcohol is 192.2 g mol^{-1}. Therefore, the mono-derivatised alcohol has a molecular weight of 46.1 g mol^{-1}. Based on chemical

shift information and the estimated molecular weight, which is the same as that of ethanol, 46.1 g mol^{-1}. It can be confirmed that the derivatised alcohol was ethanol.

$$\log D = -0.548 \log MW - 7.815$$
$$R^2 = 0.99$$

Figure 6.3.18 log D vs log MW plot of internal calibrants, TMDP, derivatised NHND, di-derivatised water and TMP for the estimation of MW of derivatised ethanol.

Table 6.3.5 Measured diffusion coefficient, log D, log MW, estimated MW of derivatised compound, estimated MW of alcohol of interest.

D / 10^{-10} m^2 s^{-1}	log D	log MW	MW_{est} (derivatised compound) g mol^{-1}	MW_{est} g mol^{-1}	Compound	%Error Actual MW
8.57 ± 0.13	-9.07	2.28	192.2	46.1 ± 5.4	ethanol	0.02

Following that, a simple mixture of three different alcohols was derivatised. Figure 6.3.19 shows the ^{31}P DOSY of the derivatised alcohol mixture. The molecular weights of the internal standards and their measured diffusion coefficients are shown in Table 6.3.6.

B.Tang, PhD Thesis, Aston University, 2024.
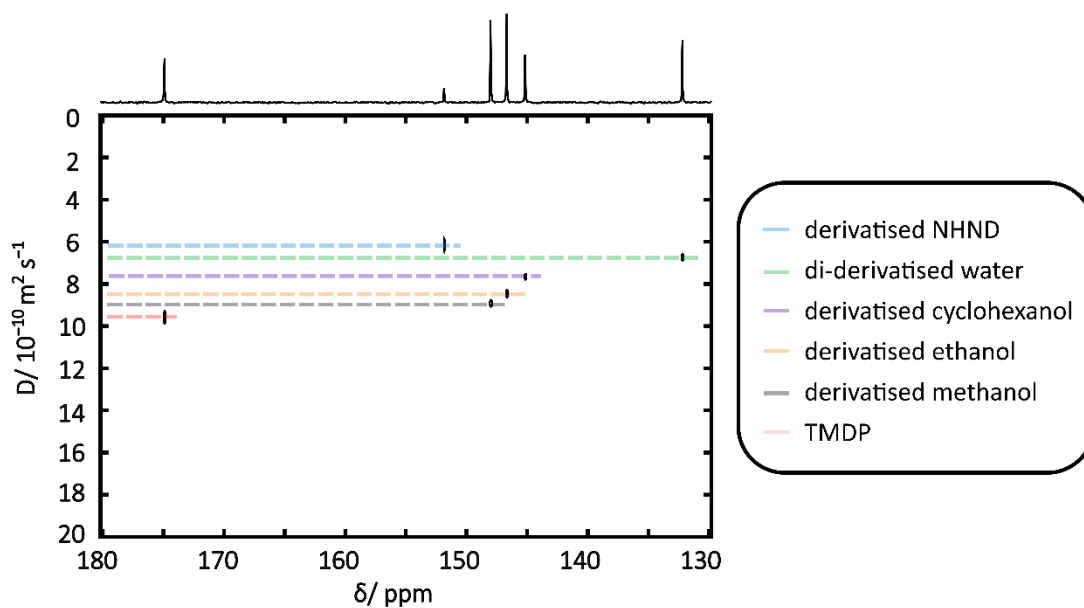
Figure 6.3.19 ^{31}P DOSY spectrum of TMDP, derivatised NHND, derivatised ethanol, derivatised methanol and derivatised cyclohexanol and di-derivatised water.

Table 6.3.6 Molecular weight, log MW, measured diffusion coefficient and log D of internal calibrants.

Compound	*MW*	log *MW*	*D*	log *D*
	g mol^{-1}		/ 10^{-10} m^2 s^{-1}	
TMP	140.1	2.14	9.64 ± 0.26	−9.01
Di-derivatised water	310.2	2.49	6.51 ± 0.08	−9.19
Derivatised NHND	325.3	2.51	5.87 ± 0.27	−9.23
TMDP	182.6	2.26	9.38 ± 0.18	−9.03

By plotting log *MW* against log *D* of the internal calibrants, a power law is generated, where the molecular weight of the derivatised alcohol can be estimated from their diffusion coefficient. The equation generated:

$$\log D = -0.595 \log MW - 7.716$$

was used to estimate the MW of the mixed alcohols. This can confirm that the alcohols are methanol, ethanol and cyclohexanol.

$$\log D = -0.595 \log MW - 7.716$$
$$R^2 = 0.94$$

Figure 6.3.20 log D vs log MW plot of internal calibrants, TMDP, derivatised NHND, di-derivatised water and TMP for the estimation of MW of derivatised compounds.

Table 6.3.7 Measured diffusion coefficient, log D, log MW, estimated MW of derivatised compound, estimated MW of alcohol of interest.

D / 10^{-10} m^2 s^{-1}	$\log D$	$\log MW$	MW_{est} (derivatised compound) g mol^{-1}	MW_{est} g mol^{-1}	Compound	%Error Actual MW
8.75 ± 0.09	−9.06	2.25	180.5	34.4 ± 3.2	methanol	7.2
8.52 ± 0.11	−9.07	2.27	188.7	42.6 ± 4.2	ethanol	7.4
7.35 ± 0.06	−9.13	2.38	241.9	95.9 ± 3.3	cyclohexanol	4.3

In order to test the robustness of the technique, an unknown alcohol-containing sample was supplied with the label Sample X. The identity of the alcohol was not revealed to eliminate any bias. Figure 6.3.19 shows the ^{31}P DOSY where the peak at 145.6 ppm belongs to the derivatised sample X. The molecular weights of the internal standards and their measured diffusion coefficients are shown in Table 6.3.8.
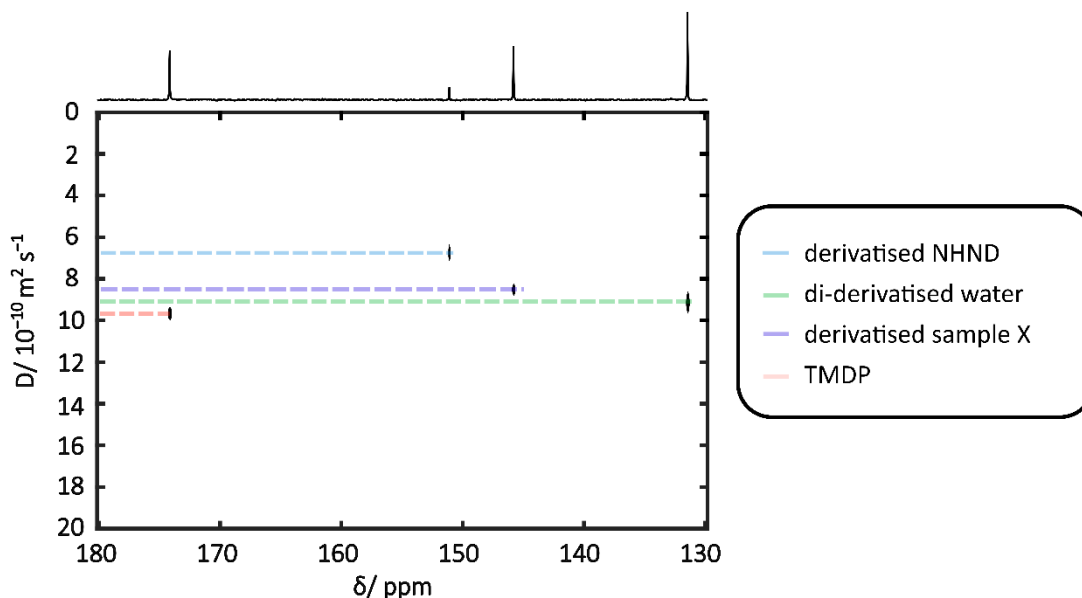
Figure 6.3.21 ^{31}P DOSY spectrum of derivatised sample X.

Table 6.3.8 Molecular weight, log MW, measured diffusion coefficient and log D of internal calibrants.

Compound	MW	log MW	D	log D
	g mol^{-1}		/ 10^{-10} m^2 s^{-1}	
TMP	140.1	2.14	9.48 ± 0.35	−9.02
Di-derivatised water	310.2	2.49	6.17 ± 0.05	−9.21
Derivatised NHND	325.3	2.51	5.08 ± 0.25	−9.29
TMDP	182.6	2.26	9.17 ± 0.11	−9.04

By plotting log *MW* against log *D* of the internal calibrants, a power law is generated, where the molecular weight of the derivatised alcohol can be estimated from their diffusion coefficient. The equation generated:

$$\log D = -0.707 \log MW - 7.475$$

was used to estimate the *MW* of the sample X from the acquired diffusion coefficient. Derivatised sample X had a diffusion coefficient of 6.33×10^{-10} m^2 s^{-1}, based on the power law above, the estimated molecular weight of sample X was found to be 127.9 g mol^{-1}. The ^{31}P multiplicity follows the n+1 rule. Therefore, based on the doublet peak at 146.5 ppm in the ^{31}P NMR spectrum and the estimated molecular weight, sample X was determined to be 1-phenylethanol (*MW* = 122.1 g mol^{-1}).

$$\log D = -0.707 \log MW - 7.475$$
$$R^2 = 0.90$$

Figure 6.3.22 log D vs log MW plot of internal calibrants, TMDP, derivatised NHND, di-derivatised water and TMP for the estimation of MW of derivatised sample X.

Table 6.3.9 Measured diffusion coefficient, log D, log MW, estimated MW of derivatised compound, estimated MW of alcohol of interest.

D / 10^{-10} m^2 s^{-1}	ln D	ln MW	MW_{est} (derivatised compound) g mol^{-1}	MW_{est} g mol^{-1}	Sample X	%Error Actual MW
6.33 ± 0.05	−9.19	2.43	271.7	127.9 ± 1.0	1-phenylethanol	4.8

6.3.3 Applications to hand sanitisers

Bio-fuels contain hundreds of compounds and are very complex. Simpler systems were first characterised to test the methodology developed here. In this section, ^{31}P DOSY convection compensated methods was tested on a model hand sanitiser made up of a mixture of ethanol and glycerol. The model hand sanitiser sample had roughly similar concentrations of ethanol and glycerol for easy analysis. Figure 6.3.23 shows the ^{31}P DOSY of the derivatised alcohol mixture. Based on the chemical shifts, the peaks at 147.4 ppm and 146.2 ppm belong to glycerol as expected, and the peak at 146.7 ppm belongs to ethanol. The molecular weights of the internal calibrants and their measured diffusion coefficients are shown in Table 6.3.10.

B.Tang, PhD Thesis, Aston University, 2024.
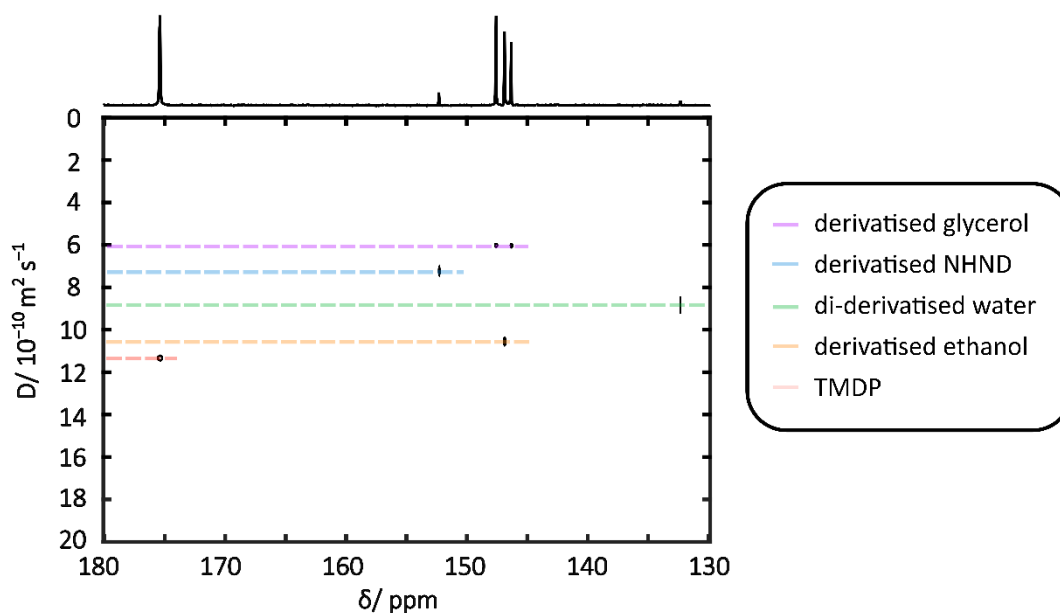
Figure 6.3.23 ^{31}P DOSY spectrum of derivatised model hand sanitiser.

Table 6.3.10 Molecular weight, log MW, measured diffusion coefficient and log D of internal calibrants.

Compound	*MW* g mol^{-1}	log *MW*	*D* / 10^{-10} m^2 s^{-1}	log *D*
TMP	140.1	2.14	11.9 ± 0.11	−8.92
Di-derivatised water	310.2	2.49	8.86 ± 0.03	−9.05
Derivatised NHND	325.3	2.51	7.22 ± 0.13	−9.14
TMDP	182.6	2.26	11.39 ± 0.04	−8.95

By plotting log *MW* against log *D* of the internal calibrants, a power law is generated, where the molecular weight of the derivatised alcohols can be estimated from their diffusion coefficient. The equation generated:

$$\log D = -0.533 \log MW - 7.760$$

was used to estimate the *MW* of the model hand sanitiser from the acquired diffusion coefficient. Glycerol contains three alcohols groups; therefore, it will be tri-derivatised. The estimated derivatised molecular weight minus 3 × 146.1 g mol^{-1} will be the molecular weight of the underivatised alcohol. In this case, peaks at 147.4 ppm and 146.2 ppm had a diffusion coefficient of 6.02 × 10^{-10} m^2 s^{-1}, indicating that the tri-derivatised alcohol had an estimated molecular weight of 546.0 g mol^{-1}. Therefore, the tri-derivatised alcohol has a molecular weight of 107.7 g mol^{-1}, which is similar to that of glycerol (92.1 g mol^{-1}). The estimated molecular weight of the peak at 146.7 ppm was found to be 44.3 g mol^{-1}, similar to that of ethanol (46.1 g mol^{-1}).
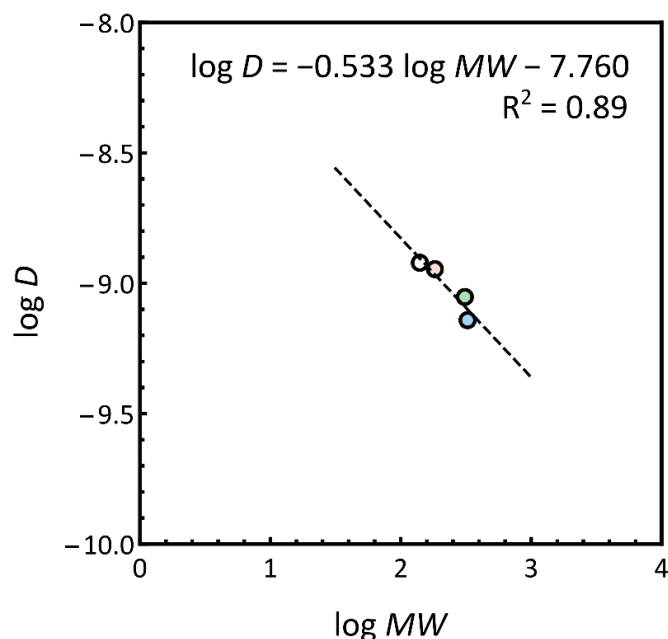
$$\log D = -0.533 \log MW - 7.760$$
$$R^2 = 0.89$$

Figure 6.3.24 log D vs log MW plot of internal calibrants, TMDP, derivatised NHND, di-derivatised water and TMP for the estimation of MW of derivatised compounds in model hand sanitiser.

Table 6.3.11 Measured diffusion coefficient, log D, log MW, estimated MW of derivatised compound, estimated MW of alcohol of interest.

D	$\ln D$	$\ln MW$	MW_{est} (derivatised compound)	MW_{est}	Compound	%Error Actual MW
/ 10^{-10} m^2 s^{-1}			g mol^{-1}	g mol^{-1}		
6.02 ± 0.03	-9.22	2.73	546.0	107.7 ± 5.1	glycerol	16.9
10.6 ± 0.08	-8.98	2.28	190.4	44.3 ± 2.7	ethanol	3.7

Real-life samples may not be as ideal as the model hand sanitiser. Therefore, this technique must be tested on real-life samples. For the four hand sanitisers studied in Chapter 5, two of the samples were found to contain an unknown peak at *ca*. 145.1 ppm. Based on the chemical shift and multiplicity pattern, whether the peak belonged to 2-propanol (isopropanol) or 2-butanol was inconclusive. Diffusion techniques can provide molecular weight information and thus, confirm which alcohol is present. The four hand sanitisers were derivatised, and the diffusion coefficients of the species were measured. The ^{31}P DOSY spectrum of the derivatised Garnier sample is shown in Figure 6.3.25 containing, TMDP (174.9 ppm), derivatised NHND (151.9 ppm), derivatised glycerol (147.4 ppm and 146.3 ppm), derivatised ethanol (146.6 ppm) and di-derivatised water

B.Tang, PhD Thesis, Aston University, 2024.

(132.2 ppm), where the measured diffusion coefficients for the internal calibrants are shown in Table 6.3.12.
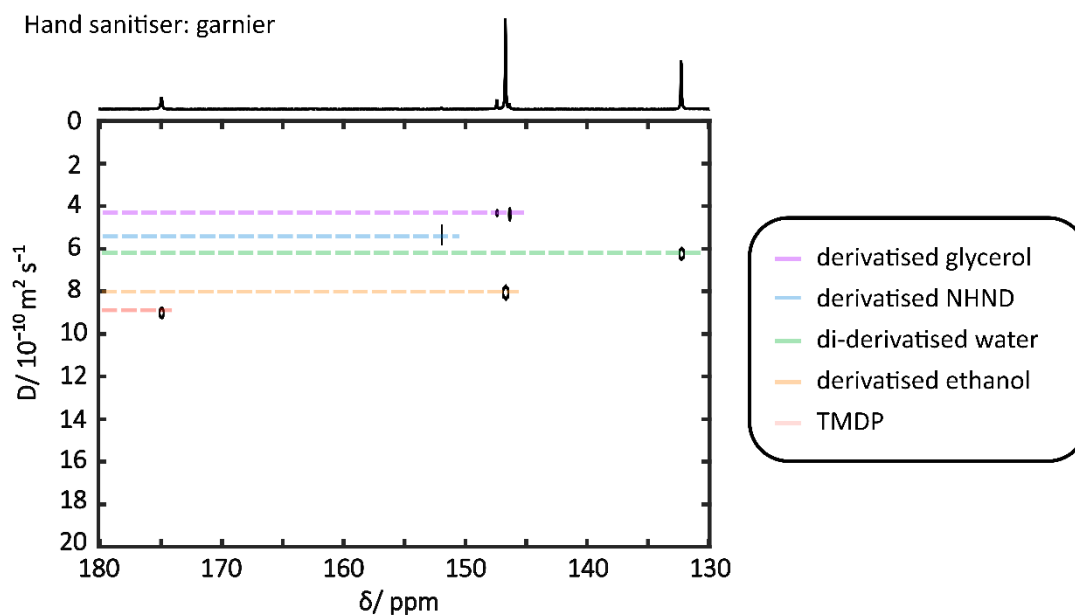
Figure 6.3.25 ^{31}P DOSY spectrum of derivatised Garnier hand sanitiser.

Table 6.3.12 Molecular weight, log MW, measured diffusion coefficient and log D of internal calibrants.

Compound	*MW* g mol^{-1}	log *MW*	*D* / 10^{-10} m^2 s^{-1}	log *D*
TMP	140.1	2.14	8.88 ± 0.22	−9.05
Di-derivatised water	310.2	2.49	6.24 ± 0.12	−9.20
Derivatised NHND	325.3	2.51	5.33 ± 0.53	−9.27
TMDP	182.6	2.26	9.02 ± 0.12	−9.04

By plotting log *MW* against log *D* of the internal calibrants, a power law is generated, where the molecular weight of the derivatised alcohols can be estimated from their diffusion coefficient. The equation generated:

$$\log D = -0.598 \log MW - 7.7736$$

was used to estimate the *MW* of the alcohols present in the hand from the acquired diffusion coefficient. The at 147.4 ppm and 146.3 ppm peak had a measured diffusion coefficient of 4.30×10^{-10} m^2 s^{-1}. The estimated molecular weight was found to be 93.2 g mol^{-1}, similar to that of glycerol (92.1 g mol^{-1}). The peak at 146.7 ppm had a measured diffusion coefficient of 7.99×10^{-10} m^2 s^{-1}. The estimated molecular weight was found to be 42.2 g mol^{-1}, similar to that of ethanol (46.1 g mol^{-1}). The hand sanitiser contained glycerol and ethanol as expected.

Figure 6.3.26 log D vs log MW plot of internal calibrants, TMDP, derivatised NHND, di-derivatised water and TMP for the estimation of MW of derivatised compounds in Garnier hand sanitiser.

Table 6.3.13 Measured diffusion coefficient, log D, log MW, estimated MW of derivatised compound, estimated MW of alcohol of interest.

D / 10^{-10} m^2 s^{-1}	ln D	ln MW	MW_{est} (derivatised compound) g mol^{-1}	MW_{est} g mol^{-1}	Compound	%Error Actual MW
4.30 ± 0.16	−9.37	2.72	531.5	93.2 ± 1.2	glycerol	1.2
7.99 ± 0.13	−9.10	2.27	188.2	42.2 ± 5.2	ethanol	8.4

The hand sanitiser (Carex) contained glycerol and ethanol however, due to low signal to noise ratio, only the ethanol peak was present in the DOSY spectrum. The ^{31}P DOSY spectrum of the derivatised Carex sample containing the derivatised ethanol (146.6 ppm) is shown in Figure 6.3.27. The measured diffusion coefficients for the internal calibrants are shown in Table 6.3.14.

Hand sanitiser: carex
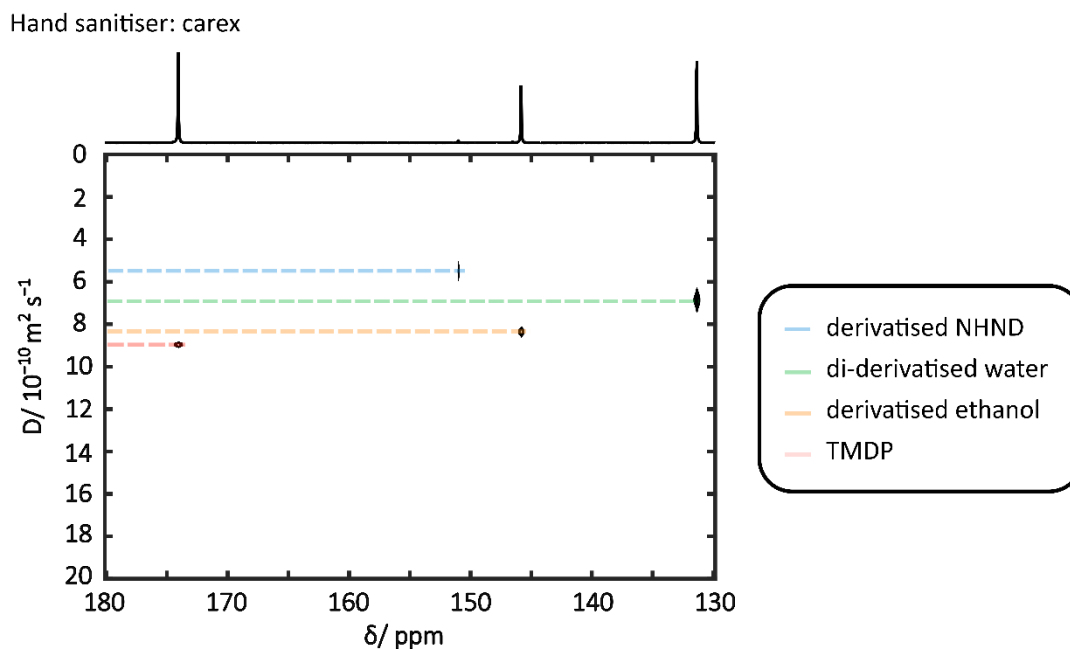
Figure 6.3.27 ^{31}P DOSY spectrum of derivatised Carex hand sanitiser.

Table 6.3.14 Molecular weight, log MW, measured diffusion coefficient and log D of internal calibrants.

Compound	*MW* g mol^{-1}	log *MW*	*D* / 10^{-10} m^2 s^{-1}	log *D*
TMP	140.1	2.14	9.27 ± 0.20	−9.03
Di-derivatised water	310.2	2.49	6.30 ± 0.21	−9.20
Derivatised NHND	325.3	2.51	5.57 ± 0.43	−9.25
TMDP	182.6	2.26	9.03 ± 0.04	−9.04

A power law is generated by plotting log *MW* against log *D* of the internal calibrants, where the molecular weight of the derivatised alcohols can be estimated from their diffusion coefficient. The equation generated:

$$\log D = -0.601 \log MW - 7.719$$

was used to estimate the *MW* of the alcohols present in the hand from the acquired diffusion coefficient. The peak at 146.7 ppm had a measured diffusion coefficient of 8.20 × 10^{-10} m^2 s^{-1}. The estimated molecular weight was estimated to be 42.3 g mol^{-1}, similar to that of ethanol (46.1 g mol^{-1}).

Figure 6.3.28 log D vs log MW plot of internal calibrants, TMDP, derivatised NHND, di-derivatised water and TMP for the estimation of MW of derivatised compounds in Carex hand sanitiser.

Table 6.3.15 Measured diffusion coefficient, log D, log MW, estimated MW of derivatised compound, estimated MW of alcohol of interest.

D / 10^{-10} m^2 s^{-1}	ln D	ln MW	MW_{est} (derivatised compound) g mol^{-1}	MW_{est} g mol^{-1}	Compound	%Error Actual MW
8.20 ± 0.09	−9.08	2.27	188.3	42.3 ± 3.5	ethanol	8.2

As detailed in the previous chapter, the ^{31}P NMR spectrum of the derivatised hand sanitiser Cuticura contains an extra peak at 145.1 ppm. Based on purely 1D ^{31}P NMR data, chemical shift and splitting pattern, it is determined likely to belong to 2-propanol. However, there was some ambiguity in its assignment, other secondary alcohols such as 2-butanol could be responsible. [31]P DOSY could be used to determine if that unknown peak belonged to 2-propanol. However, due to the low signal-to-noise ratio, the peak at 145.1 ppm was too small to select. The signal-to-noise ratio of the glycerol peak at 146.2 ppm was also low; therefore, it was unable to be picked during the peak picking. This resulted in only one of the glycerol peaks being present in the final DOSY spectrum.
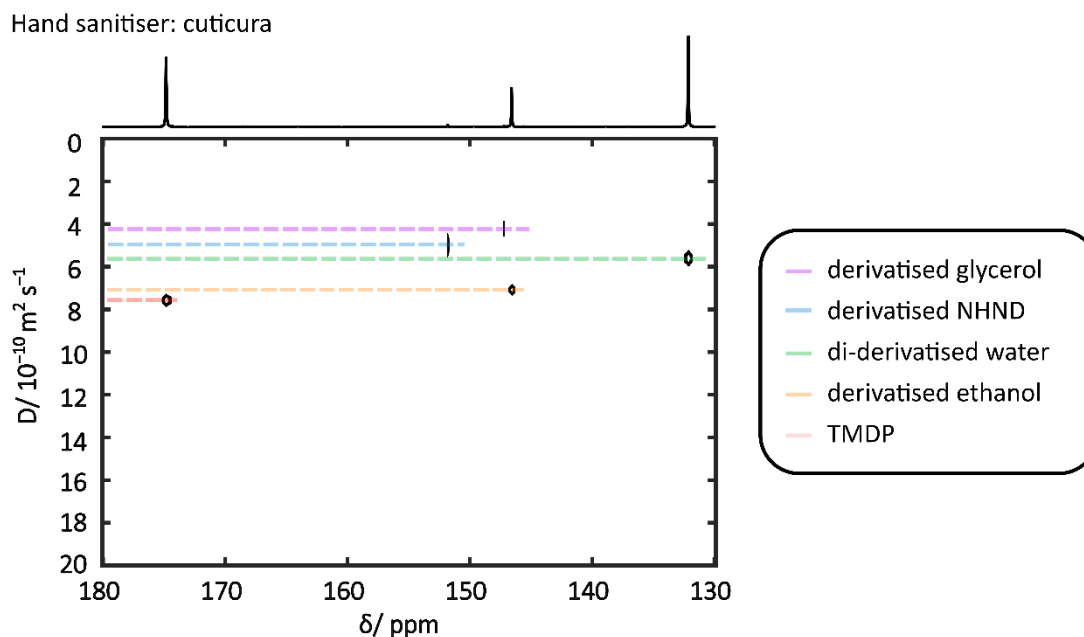
Figure 6.3.29 ^{31}P DOSY spectrum of derivatised Cuticura hand sanitiser.

Table 6.3.16 Molecular weight, log MW, measured diffusion coefficient and log D of internal calibrants.

Compound	*MW*	log *MW*	*D*	log *D*
	g mol^{-1}		/ 10^{-10} m^2 s^{-1}	
TMP	140.1	2.14	8.03 ± 0.80	−9.12
Di-derivatised water	310.2	2.49	5.64 ± 0.14	−9.30
Derivatised NHND	325.3	2.51	5.00 ± 0.34	−9.25
TMDP	182.6	2.26	7.57 ± 0.10	−9.10

By plotting the graph (Figure 6.3.30) of Log *D* against Log *MW* of the internal standard and a power law equation is generated. The equation generated:

$$\log D = -0.541 \log MW - 7.792$$

was used to estimate the *MW* of the alcohols present in the hand from the acquired diffusion coefficient. The 147.4 ppm and 146.3 ppm peak had a measured diffusion coefficient of 4.04 × 10^{-10} m^2 s^{-1}. The estimated molecular weight was found to be 95.3 g mol^{-1}, similar to that of glycerol (92.1 g mol^{-1}). The peak at 146.7 ppm had a measured diffusion coefficient of 7.11 × 10^{-10} m^2 s^{-1}. The estimated molecular weight was 41.4 g mol^{-1}, similar to that of ethanol (46.1 g mol^{-1}). The hand sanitiser contained glycerol and ethanol as expected. However, for this sample, it was still inconclusive whether if the unknown alcohol at 145.1 ppm was 2-propanol or 2-butanol on the basis of the 1D ^{31}P NMR alone.

194

$$\log D = -0.541 \log MW - 7.792$$
$$R^2 = 0.95$$

Figure 6.3.30 log D vs log MW plot of internal calibrants, TMDP, derivatised NHND, di-derivatised water and TMP for the estimation of MW of derivatised compounds in Cuticura hand sanitiser.

Table 6.3.17 Measured diffusion coefficient, log D, log MW, estimated MW of derivatised compound, estimated MW of alcohol of interest.

D / 10^{-10} m^2 s^{-1}	ln D	ln MW	MW_{est} (derivatised compound) g mol^{-1}	MW_{est} g mol^{-1}	Compound	%Error Actual MW
4.04 ± 0.30	−9.39	2.72	533.5	95.3 ± 66.2	glycerol	3.4
7.11 ± 0.09	−9.15	2.27	187.4	41.4 ± 4.5	ethanol	10.2

The hand sanitiser Bondloc also contained an extra peak at 145.1 ppm. Based on purely 1D ^{31}P NMR data, chemical shift, and splitting pattern alone, it is determined to likely belong to 2-propanol or 2-butanol. The additional peak at 145.1 ppm, had a diffusion coefficient of 7.15×10^{-10} m^2 s^{-1}.

Hand sanitiser: bondloc
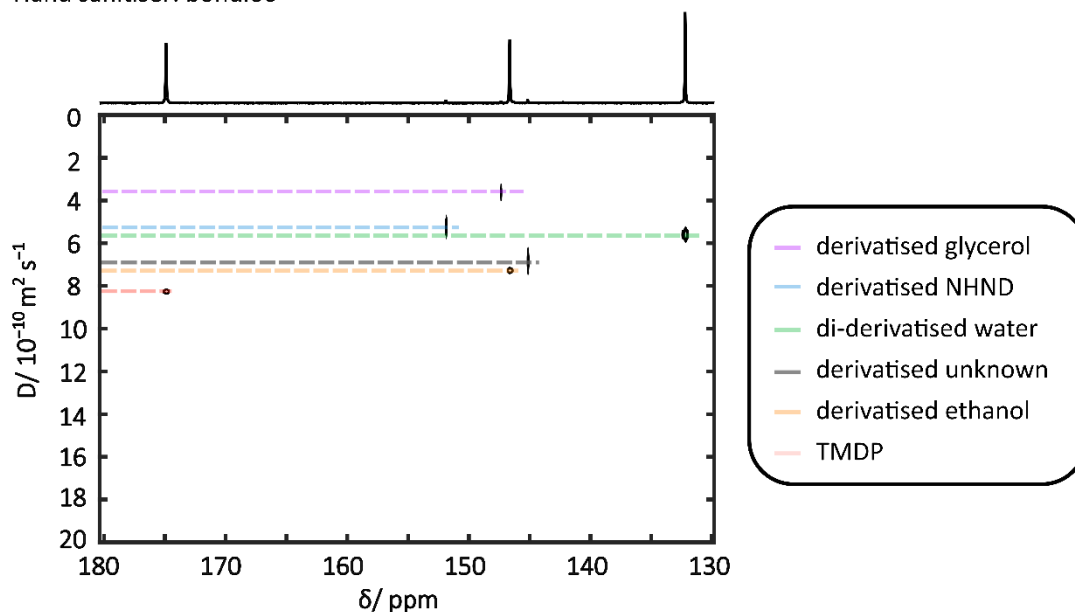
Figure 6.3.31 ^{31}P DOSY spectrum of derivatised Bondloc hand sanitiser.

Table 6.3.18 Molecular weight, log MW, measured diffusion coefficient and log D of internal calibrants.

Compound	*MW* g mol^{-1}	log *MW*	*D* / 10^{-10} m^2 s^{-1}	log *D*
TMP	140.1	2.14	8.39 ± 0.55	−9.08
Di-derivatised water	310.2	2.49	5.59 ± 0.20	−9.25
Derivatised NHND	325.3	2.51	5.48 ± 0.52	−9.26
TMDP	182.6	2.26	8.10 ± 0.24	−9.09

A power law equation is generating by plotting the graph (Figure 6.3.32) of ln D against ln MW of the internal standard. The equation generated:

$$\log D = -\,0.551 \log MW - 7.875$$

was used to estimate the *MW* of the alcohols present in the hand from the acquired diffusion coefficient. Based on the diffusion coefficients, the hand sanitiser contained glycerol and ethanol as expected. From the experimental diffusion coefficient of 7.15 × 10^{-10} m^2 s^{-1}, using the power law above, the unknown alcohol was estimated to have a molecular weight of 57.1 g mol^{-1} which is close to the molecular weight of 2-propanol (60.1 g mol^{-1}).

$$\log D = -0.551 \log MW - 7.875$$
$$R^2 = 0.95$$

Figure 6.3.32 log D vs log MW plot of internal calibrants, TMDP, derivatised NHND, di-derivatised water and TMP for the estimation of MW of derivatised compounds in Bondloc hand sanitiser.

Table 6.3.19 Measured diffusion coefficient, log D, log MW, estimated MW of derivatised compound, estimated MW of alcohol of interest.

D / 10^{-10} m^2 s^{-1}	ln D	ln MW	MW_{est} (derivatised compound) g mol^{-1}	MW_{est} g mol^{-1}	Compound	%Error Actual MW
4.19 ± 0.29	−9.38	2.73	537.6	99.3 ± 61.5	glycerol	7.8
7.32 ± 0.23	−9.14	2.30	194.9	46.8 ± 10.6	ethanol	5.9
7.15 ± 0.27	−9.15	2.31	203.2	57.1 ± 13.2	isopropanol	4.9

6.4 Conclusion

1D ^{31}P NMR analysis of hydroxyl groups can still be challenging when it comes to the identification of compounds. One way to improve the resolution of the spectra further is to extend it into a second dimension. Diffusion NMR techniques separate the signals based on the diffusion coefficient in the diffusion domain. Novel NMR pulse sequences can be produced by combining existing sequences. In this chapter, a novel ^{31}P Oneshot sequence was developed, and model compounds were tested using the sequence. However, for CDCl$_3$ the diffusion coefficient measured using ^{31}P DOSY sequence compared with the ^{1}H DOSY sequence was quite different. This is likely caused by convection. The effects on convection were also explored and should always be

considered when running diffusion-based experiments. The ease of convective flow experienced by solvents can be calculated by the volumetric thermal expansion coefficient multiplied by the density and divided by the viscosity of a solvent at a given temperature. The volumetric expansion for common solvents can be found in the literature. However, it can be difficult to find, particularly so for deuteriated solvents. Macros were written to calculate the volumetric expansion coefficient (β) based on quantities more readily available in the literature such as density.

To reduce the effects of convection, thick-walled NMR tubes were used. However, it was found that for solvents that easily convect such as $CDCl_3$, even thick-walled NMR tubes were not enough to compensate for the convection. Therefore, a novel ^{31}P convection-compensated DOSY sequence was written to remove for the effects of convection from the acquired diffusion data. The robustness of the sequence was tested using the same model compound trimethylphosphate. It was found that the diffusion coefficients measured using ^{31}P convection compensated sequence were comparable to those measured using ^1H DOSY sequences.

To test this methodology, simple systems containing one alcohol, three alcohols and unknown alcohol were derivatised using TMDP, and the diffusion coefficients of these compounds were measured using the ^{31}P convection compensated DOSY sequence. It was found that by using internal standards to create a calibration curve, and thus generating a power law, linking Log *MW* to Log *D*, the molecular weight of the derivatised alcohols could be accurately estimated using the experimental diffusion coefficient. This method was then applied to the four hand sanitisers studied in Chapter 5. Two hand sanitisers had an extra peak in the 1D ^{31}P NMR spectrum. It was found that for hand sanitiser Cuticura, due to low concentration of the species, the signal to noise ratio was low, therefore, the unknown peak was unsuccessfully identified. For the Bondloc sample, based on the chemical shift, multiplet pattern in the ^{31}P NMR, and the molecular weight estimated were from the diffusion coefficient using the power law method, it was successfully confirmed that the unknown peak at 145.1 ppm was isopropanol. However, to further confirm that unknown peak at 145.1 ppm is isopropanol, a DOSY of the derivatised isopropanol can be performed.

CHAPTER 7 : CHARACTERISATION OF PYROLYSIS OIL PRODUCED FROM BREWERS' SPENT GRAINS

7.1 Introduction

The characterisation of pyrolysis oils in general can be challenging due to the nature of the oils. Limitations of current analytical techniques were explored in Chapter 1. Pyrolysis oils are produced from Brewers' Spent Grains via both slow and fast pyrolysis techniques. In this chapter, both traditional techniques typically used to characterise bio-oils and the novel NMR techniques developed in previous sections of this thesis are brought together to characterise these pyrolysis oils.

Figure 7.1.1 From left to right, Brewers' Spent Grains, bio-char and bio-oil.

7.2 Experimental

7.2.1 Feedstock

The biomass feedstock Brewers' Spent Grains (BSG) were donated by Burning Soul Brewery, Birmingham, UK (logo below). The BSG feedstock was dried in the oven at 105 °C for 24 hours and was used without any further purification.

7.2.2 Slow Pyrolysis Processing

The slow pyrolysis experiments were carried out in a 100 g h^{-1} continuous bench-scale auger pyrolysis system shown in Figure 7.2.1. The system was designed and constructed at the Energy and Bioproduct Research Institute (EBRI), Aston University, UK.

B.Tang, PhD Thesis, Aston University, 2024.
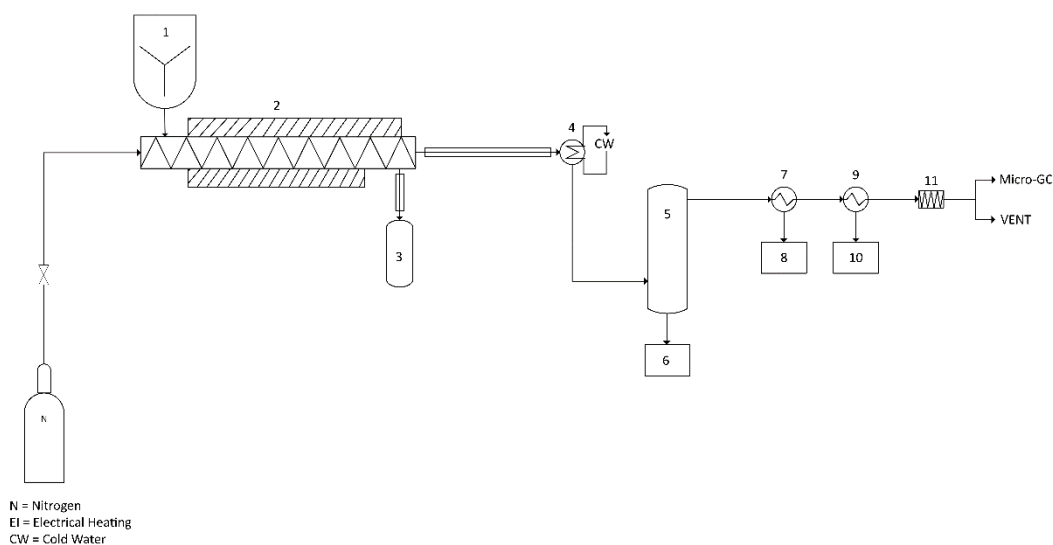
Figure 7.2.1 Slow pyrolysis rig setup: (1) feed hopper, (2) Auger reactor (3) char pot, (4) water-cooled condenser (5) electrostatic precipitator, (6) liquid bio-oil collector, (7) dry ice/acetone condenser, (8) liquid bio-oil collector, (9) dry ice/acetone condenser, (10) liquid bio-oil collector and (11) cotton wool filter.

Biomass was continuously fed by speed regulated volumetric screw (2) through the Auger reactor. Slow pyrolysis processing parameters are shown in Table 7.2.1.

Table 7.2.1 Slow pyrolysis processing parameters.

Parameter	Slow Pyrolysis
Pyrolysis temperature (°C)	550
Run time (mins)	120
Biomass moisture content (%)	1.5
Biomass used (g)	200

All experiments were carried out with the aim of achieving an average pyrolysis temperature of 550 °C. As the vapours leave the auger reactor (2), the char is collected in the char pot (3). The vapours then pass through a water-cooled condenser (4) at 12 °C. The aerosols were separated using an electrostatic precipitator (ESP, 5). The condensed bio-oil from the ESP was collected in a round bottom flask (6). Following the ESP, the gases passed through two dry ice/acetone condenser (7 & 9) in series, which is referred to as condenser 1 (8) and condenser 2 (10) respectively. Finally, remaining gases are passed through a cotton wool filter (11).

B.Tang, PhD Thesis, Aston University, 2024.

7.2.3 Fast Pyrolysis Processing

The fast pyrolysis experiments were carried out in a 100 g h^{-1} continuous bubbling fluidised-bed reactor at the Energy and Bioproduct Research Institute (EBRI), Aston University, UK. The reactor is shown in Figure 7.2.2.
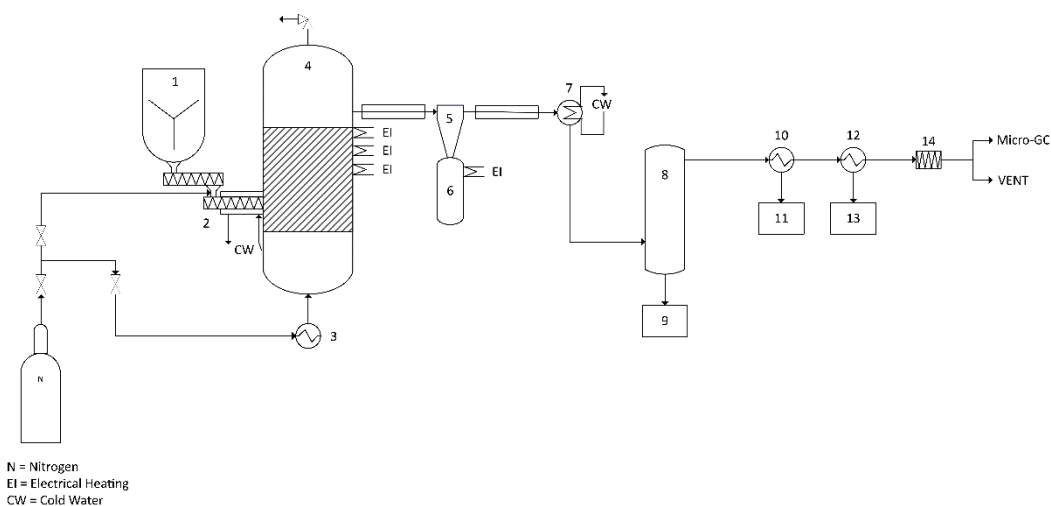
Figure 7.2.2 Fast pyrolysis rig setup: (1) feed hopper, (2) fast screw, (3) nitrogen preheater, (4) bubbling fluidised-bed reactor (5) cyclone (6) char pot, (7) water-cooled condenser, (8) electrostatic precipitator, (9) liquid bio-oil collector, (10) dry ice/acetone condenser, (11) liquid bio-oil collector, (12) dry ice/acetone condenser, (13) liquid bio-oil collector and (14) cotton wool filter.

Biomass was continuously fed by speed regulated twin metering screws (2) to a single fast screw into the bubbling fluidised-bed reactor. Fast pyrolysis processing parameters are shown in Table 7.2.2.

Table 7.2.2 Fast pyrolysis processing parameters.

Parameter	Fast Pyrolysis
Pyrolysis temperature (°C)	550
Run time (mins)	120
Biomass moisture content (%)	1.5
Biomass used (g)	200

All experiments were carried out with the aim of achieving an average pyrolysis bed temperature of 550 °C. As the vapours leave the reactor it passes through a cyclone (5) and char is collected in the char pot (6). The vapours then pass through a water-cooled condenser (7) at 12 °C. The aerosols were separated using an electrostatic precipitator

B.Tang, PhD Thesis, Aston University, 2024.

(ESP, 8). The condensed bio-oil from the ESP was collected in a round bottom flask. Following the ESP, the gases passed through two dry ice/acetone condenser (9 and 11) in series, which is referred to as condenser 1 (10) and condenser 2 (12) respectively. Finally, remaining gases are passed through a cotton wool filter.

7.2.4 Water Content Analysis

Volumetric Karl-Fischer (KF) titration was used to determine the water content of all the pyrolysis liquid products. A Mettler Toledo V20 KF titrator was used with Hydranal (R) K as a working medium and Hydranal (R) Composite 5 K as a titrant. All analyses were performed in triplicate with the water content being calculated automatically, based on the weight of the bio-oil sample injected. Prior to analysis, the KF instrument was calibrated with HPLC grade water.

Karl-Fischer titrations are based on the reaction:

$2H_2O + SO_2 + I_2 \rightarrow H_2SO_4 + 2HI$
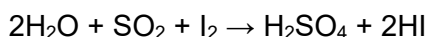
This is facilitated by the KF reagents as the reactions:

$ROH + SO_2 + R'N \rightarrow [R'NH]SO_3R + H_2O + I_2 + 2R'N \rightarrow 2[R'NH]I + [R'NH]SO_4R$
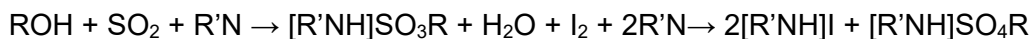
The amount of iodine that is used up is dependent on the amount of water present in the sample. The current change from the platinum electrodes, together with the mass of the sample and titration time to reach the end-point combined, allows the instrument to determine the sample's water content by mass.

7.2.5 pH Analysis

A Fisherbrand™ accumet™ FE150 Benchtop pH meter was used to measure the pH of the BSG pyrolysis oils. Prior to each measurement, the pH meter was calibrated using Mettler Toledo pH buffers with pH of 4, 7 and 10. Calibrations were repeated for each sample and the probe was cleaned with DI water between samples to ensure no cross-contamination occurred.

7.2.6 Elemental Analysis (CHNS/O)

Elemental analysis of all oils was carried out on a Flash 2000 elemental analyser. Carbon, hydrogen, nitrogen, and sulphur content were analysed in triplicate, and the average values were taken. The oxygen content of the oils was found by difference.

7.2.7 Fourier Transformation Infrared Spectroscopy (FTIR)

FTIR was used to analyse functional groups present in the oil. All FTIR data was collected on a Thermo Nicolet 380 spectrometer. A small amount of liquid sample was placed on the diamond plate. 16 scans were used for all experiments.

7.2.8 Gas-Chromatography Mass Spectrometry (GC/MS)

The chemical composition of the BSG fast pyrolysis oil and the organic layer of the BSG slow pyrolysis oil were analysed using a Shimadzu GCMS-QP2012 SE. The bio-oil samples were mixed with analytical grade acetone 1:4 (v:v) and was further diluted 1:1 (v:v) to create a GC sample. For each analysis, 1 μ of GC sample was injected into the GC column where helium was used as the carrier gas. To separate the pyrolysis oil components, a Rtx-5MS was used (30m,0.25mm id., 0.25 μm df). The injection port was kept at 280 °C, and a 1:75 split ratio was used. The GC oven was held at 50 °C for 2 minutes, then heated at 5 °Cmin^{-1} to 290 °C and held at this temperature for 8 mins. Proposed peak assignments (m/z=45 – 300) were made from mass spectra detection using the NIST17 MS library and from assignments in literature.

7.2.9 Nuclear Magnetic Resonance Spectroscopy: Low-field ^{19}F qNMR analysis of Carbonyl Groups

Procedure as described in Chapter 4 and reproduced here.

110 mg of 4-(trifluoro methyl)phenyl hydrazine was dissolved in 1 mL of 50:50 DMF and water (v/v). This solution was added to a solution of pyrolysis oil (*ca*. 30 mg) dissolved in 500 μL dimethylformamide (DMF) in a 20 mL vial. The mixture was stirred in the dark for 24 hours at room temperature. The derivatised pyrolysis oil was purified by the addition of 20 mL of pH 2.0 water, where the pH 2.0 water was prepared by the dilution of 5N HCl in deionised water. The sample was placed in a freezer to allow precipitation to occur. The frozen sample was melted to room temperature. The aqueous layer was carefully discarded, and the product was washed multiple times with pH 2.0 water to

remove excess 4-(trifluoromethyl)phenyl hydrazine. The precipitant was then air dried for 24 hours. The dried sample was then dissolved in protiated DMSO for NMR analysis, where 3-(trifluoromethoxy) benzoic acid was used as an internal standard (IS). Hexafluorobenzene (C_6F_6) was used as an external standard (ES) for the chemical shift calibration at −164.9 ppm. All low-field NMR was carried out using a Magritek Spinsolve 43 MHz benchtop NMR.

7.2.10 Estimation of Carbonyl Content using Oximation Followed by Titration

The oximation of pyrolysis oil was carried out using the following procedure: Hydroxylamine hydrochloride solution was prepared by dissolving 17.50 g of hydroxylamine hydrochloride in 80.00 g of deionised water. The solution was transferred to a 500 mL volumetric flask, the volumetric flask was filled to the mark with anhydrous ethanol. Pyridine solution was prepared by adding 10 mL of pyridine into a 500 mL volumetric flask, the volumetric flask was filled with anhydrous ethanol. For the oximation reaction *ca*. 0.40 g of pyrolysis oil reacted with 10.00 mL of hydroxylamine solution and 20 mL of pyridine solution were combined in a sealed flask. The reaction was left stirring for 48 hours at room temperature. The reaction mixture was transferred to a 100.00 mL volumetric flask and filled with anhydrous ethanol. Aliquots of 25.00 mL were taken and titrated with 0.5 M sodium hydroxide solution. The titration endpoint (pH = ~4.5) was measured using a micro pH electrode probe.

7.2.11 Nuclear Magnetic Resonance Spectroscopy: ^{31}P qNMR & ^{31}P DOSY analysis of Alcohol Groups

Procedure as described in Chapter 5 & 6 and reproduced here.

Solvent A

A stock solvent solution of 1:1.6 volume ratio of $CDCl_3$ and anhydrous pyridine was prepared and dried over molecular sieves.

Internal Standard:

0.1M internal standard was prepared by adding NHND (0.018 g) to solution A (1 mL). A relaxation agent, chromium (III) 2,4-pentadienoate (5 mg) was dissolved in the solution.

The weight of the entire solution was recorded. The internal standard was stored over molecular sieves.

Derivatisation reaction:

IS solution (0.1 mL) was transferred into a glass vial equipped with a PTFE-lines silicone septum. The weight of the 0.1 mL IS solution was recorded. Bio-oil (30 mg) was weighed into the same vial. The actual weight of the sample was recorded. Solvent A (0.7 mL) was added using a gastight syringe into the same vial and was left stirring until mixture was homogenous. For the derivatisation reaction an excess of TMDP (*ca.* 0.2 mL) was added using a gastight syringe. The reaction was left for 10 minutes to stir. The solution was then transferred to a 5 mm NMR tube with a Pasteur pipette and analysed immediately. The reason being the phosphitylation derivative of NHND was not stable over a long period of time.

NMR Analysis:

All NMR acquisition were acquired using Bruker AVANCE 300 MHz equipped with a 5mm PABBO BB-1H Z-GRD probe. The z-gradient coil producing a calibrated maximum gradient of 55.7 G cm^{-1}.[252] Data was acquired using 10 increments, equally spaced in gradient squared. All data was measured at 298 K. For all data acquired using Oneshot sequences, gradient ranged from 20% to 80% of the maximum. For all data acquired using convection compensated sequences, gradient ranged from 10% to 90%. The error in width of peak is calculated based on the fit of the data to the Stejskal-Tanner Equation (Equation 2.4.3). All diffusion data was processed using DOSYToolBox [253], where 5 Hz of line broadening was used.

7.3 Results and Discussion

The BSG feedstock was dried at 105 °C in the oven for 24 hours to removed most of the water as possible from the feedstock. This is important as the initial water content of the feedstock influences the amount of water in the final pyrolysis oil. After drying, the feedstock had a moisture content of *ca.* 1.5 wt. %. The slow pyrolysis process produced three main products: char, pyrolysis oil and gases. The char content made up 35.1 wt. %, 42.1 wt. % being organic liquid yield and gas yield, 22.8 wt. % was calculated by difference. The slow pyrolysis oil produced was a biphasic pyrolysis oil containing an

organic layer (upper layer) and an aqueous layer (lower layer). The organic layer was a thick brown tar-like substance, and the aqueous layer was a less viscous yellow liquid. For all the characterisation techniques the organic and aqueous layers were analysed separately and will be referred to as the BSG slow pyrolysis oil organic layer and BSG slow pyrolysis oil aqueous layer. The fast pyrolysis process also produced three main products, char, pyrolysis oil and gases. The char content made up 6.1 wt. %, 57.5 wt. % being organic liquid yield and gas yield, 36.4 wt. % was calculated by difference. The fast pyrolysis oil produced was a thick brown tar-like substance and two fractions of yellow liquid were collected in the two condensers. Throughout this chapter these will be referred to BSG fast pyrolysis oil, BSG fast pyrolysis oil condenser 1 and BSG fast pyrolysis oil condenser 2 respectively. The mass balance for both slow pyrolysis and fast pyrolysis processes are depicted in the Figure 7.3.1.
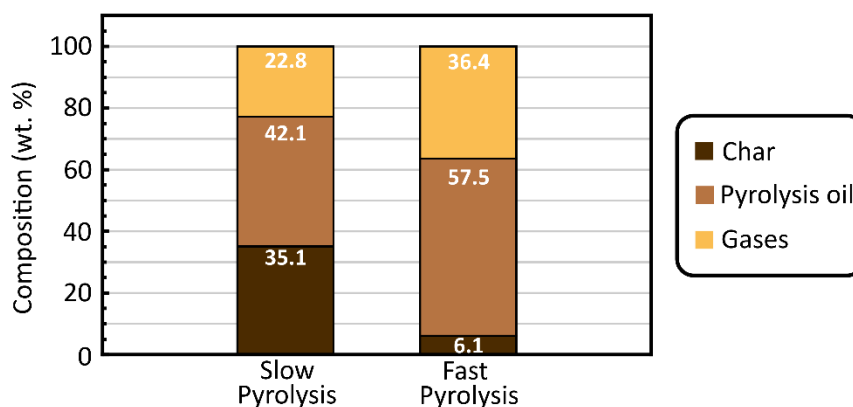
Figure 7.3.1 Mass balance, composition of products (char, pyrolysis oil and gases) produced from both slow pyrolysis and fast pyrolysis of Brewers' Spent Grains.

Different analytical techniques were used to characterise the pyrolysis oils produced from Brewers' Spent Gains. Water content of pyrolysis fuels are important as this directly influences the heating value of the pyrolysis oil. The water content in pyrolysis oils is mostly related to the initial feedstock moisture. The water content was determined using the automated Mettler Toledo V20 241 Karl-Fischer (KF). The average water content of the pyrolysis oils is presented in Table 7.3.1. The water content for the BSG slow pyrolysis oil organic layer was 2.43 wt. % and the aqueous layer contained 54.17 wt. %. The organic layer has less water compared to typical pyrolysis oils 15-30 wt. %, suggesting suitability as a potential fuel replacement. The BSG slow pyrolysis aqueous layer contained more water (54.17 wt. %) as expected. For fast pyrolysis-oils the water

B.Tang, PhD Thesis, Aston University, 2024.

content also relates to the dehydration reactions that occurs during the fast-pyrolysis process. The water content for BSG fast pyrolysis oil was found to be 27.08 wt. %. BSG fast pyrolysis oils from condenser 1 and condenser 2 both found to have a large content of water (49.13 wt.% and 61.10 wt. %). This suggests the fast pyrolysis oils found in the condensers were similar to the aqueous phase of slow pyrolysis oil.

Table 7.3.1 Water content (wt. %) of pyrolysis oils produced from Brewers' Spent Grains.

Sample	Water Content (wt. %)
BSG Slow Pyrolysis Oil Organic Layer	2.43
BSG Slow Pyrolysis Oil Aqueous Layer	54.17
BSG Fast Pyrolysis Oil	27.08
BSG Fast Pyrolysis Oil Condenser 1	49.13
BSG Fast Pyrolysis Oil Condenser 2	61.10

Table 7.3.2 shows the pH of different pyrolysis oils in literature. [238, 260-267] Due to oxygen-containing compounds, pyrolysis oils are relatively acidic (pH 2 to 4), compared to conventional fuels which may lead to corrosion. The pH of pyrolysis oils was analysed using a Fisherbrand™ accumet™ FE150 Benchtop pH meter, where the results of each pyrolysis oil is summarised in Table 7.3.3. [267] The pH of all the pyrolysis oils were found to be in the range of ca. pH 5.5 to 6.55. This suggests that the pyrolysis oils produced from BSG is more suitable as potential fuel replacements as they are less acidic compared with other pyrolysis oils from other biomass feedstocks.

Table 7.3.2 pH of pyrolysis oils produced from different feedstocks from literature.

Property	Pine [260]	Mallee [261]	Poplar[26] [2]	Acacia[2] [63]	Oak [238, 264]	Eucalyptus [265]	Beech wood[266]
pH	2.4	3	3.0 - 3.9	2.5	2.7	1.8-2.9	2.5 – 2.8

Table 7.3.3 pH of pyrolysis oils produced from Brewers' Spent Grains.

Sample	pH
BSG Slow Pyrolysis Oil Organic Layer	6.19
BSG Slow Pyrolysis Oil Aqueous Layer	6.51
BSG Fast Pyrolysis Oil	5.86
BSG Fast Pyrolysis Oil Condenser 1	6.00
BSG Fast Pyrolysis Oil Condenser 2	6.04

Oxygen content of pyrolysis oils from different feedstocks are presented in Table 7.3.5.[238, 260-267] The oxygen content varies between 22 % and 72%. Elemental analysis provides the different percentage composition of C, H, N, and S where the analysis was carried out in triplicate. Table 7.3.4 shows a summary of the elemental compositions of the pyrolysis oils, where the oxygen content was calculated by a difference. The BSG slow pyrolysis oil organic layer and BSG fast pyrolysis oil had the most carbon content 66.32 % and 53.82 % respectively. This suggests most of the organic species are in found in the organic layers. The large amounts of oxygen in BSG slow pyrolysis oil aqueous layer (75.48 %), BSG fast pyrolysis oils from condenser 1 (93.16 %) and condenser 2 (85.4 %) are likely due to the high-water content. More importantly, there was more oxygen in the BSG fast pyrolysis oil (31.71 %) in comparison to the BSG slow pyrolysis organic layer (19.20 %). Oxygen-containing compounds contribute to the acidity, therefore, these results are also in agreement with earlier pH results. The BSG pyrolysis oils was found to have a lower oxygen content compared to typical pyrolysis oils. This also suggests it can be a potential fuel replacement. The upgrading techniques discussed in Chapter 1 are used to remove the oxygen-containing compounds from pyrolysis oils. Most of the upgrading techniques require high energy cost or expensive catalysis. If the pyrolysis oils produced have less oxygen to begin with, less upgrading will be required. Reduction in upgrading processes will make producing pyrolysis oils more financially viable.

Table 7.3.4 CHNS/O analysis of pyrolysis oils produced from Brewers' Spent Grains.

Sample	C (%)	H (%)	N (%)	S (%)	O (%)
BSG Slow Pyrolysis Oil Organic Layer	66.32	8.14	6.33	0.00	19.20
BSG Slow Pyrolysis Oil Aqueous Layer	12.61	7.80	4.12	0.00	75.48
BSG Fast Pyrolysis Oil	53.82	7.61	6.87	0.00	31.71
BSG Fast Pyrolysis Oil Condenser 1	4.31	0.89	1.64	0.00	93.16
BSG Fast Pyrolysis Oil Condenser 2	6.73	5.79	2.07	0.00	85.40

Table 7.3.5 CHNO of pyrolysis oils produced from different feedstocks from literature.

Sample	C (%)	H (%)	N (%)	O (%)
Pine[260]	45.70	7.00	<0.1	47.0
Mallee[261]	52.00	8.00	0.0	40.0
Poplar[262]	28.52 – 29.59	6.87 – 8.72	0.67 – 0.92	62.1 – 72.56
Acacia[263]	57.17- 66.52	5.98 – 8.28	0.14 – 3.17	22.03 – 36.14
Oak[238, 264]	48.69	6.97	<0.5	43.80
Eucalyptus[265]	63.00	6.70	0.0	30.10
Beech wood[266]	58.10	11.37	0.37	30.08

To better understand the chemical composition of these pyrolysis oils, Fourier transform infrared spectroscopy can be used to identify the main functional groups present. Figure 7.3.2 shows the FTIR spectra of the BSG slow pyrolysis oil organic layer (dark blue) and aqueous layer (light blue), with the assignments of peaks summarised in Table 7.3.6. The O-H group, which is typically linked with water, is represented by a peak in both FTIR spectra at 3260 cm^{-1} and 3257 cm^{-1} respectively. This peak is significantly more prominent in the aqueous layer due to the increased water content. Both spectra also showed the pyrolysis oils contained carbonyl C=O (1708 cm^{-1} and 1716 cm^{-1} respectively), alkenes C=C (1646 cm^{-1} and 1630 cm^{-1} respectively), amines N-H / alcohols O-H (1460 cm^{-1} and 1412 cm^{-1} respectively) and ester C-O-C (1212 cm^{-1} and 1217 cm^{-1} respectively). However, the organic layer contained strong peaks at 2921 cm^{-1} and 2850 cm^{-1} corresponding to alkanes C-H compared to the aqueous layer. Interestingly the aqueous layer contained a peak at 1541 cm^{-1} which is not present in the organic layer Peaks in this region typically belong to nitro compounds. Since nitro compounds are typically yellow and slightly soluble in water, this may also explain the yellow colour of the aqueous layer.
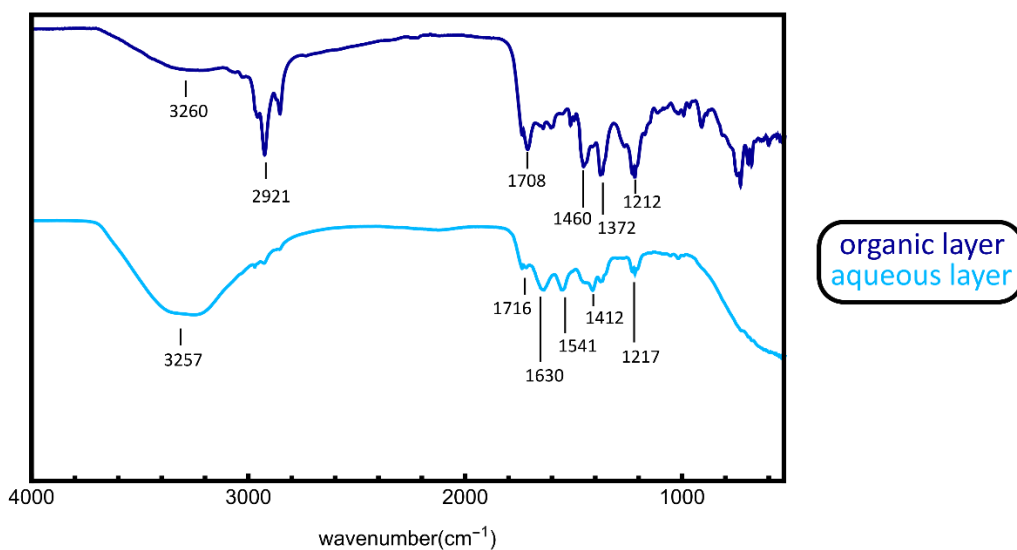
Figure 7.3.2 Stacked plot of FTIR spectra of derivatised BSG slow pyrolysis oil where the top spectra is the organic layer, and the bottom spectra is the aqueous layer.

Table 7.3.6 FTIR analysis of slow pyrolysis oils produced from Brewers' Spent Grains.

BSG Slow Pyrolysis Oil Organic Layer		
Wavenumber (cm^{-1})	**Functional Group**	**Class of Compound**
3260	O-H stretching	alcohol/water
2921, 2850	C-H stretching	alkanes
1646	C=C stretching	alkene
1708	C=O stretching	carboxylic acid/ aldehyde/ketone
1460	N-H or O-H	amine/ carboxylic acid
1372	O-H bending	alcohol
1212	C-O stretching	aromatic ester
BSG Slow Pyrolysis Oil Aqueous Layer		
Wavenumber (cm^{-1})	**Functional Group**	**Class of Compound**
3257	O-H stretching	alcohol/water
1716	C=O stretching	carboxylic acid/ aldehyde/ketone
1630	C=C stretching	alkene
1541	N-O stretching	nitro compound
1412	O-H bending	carboxylic acid
1217	C-O stretching	aromatic ester

Figure 7.3.3 shows the FTIR spectra of the BSG fast pyrolysis oil organic layer (top, dark blue), condenser 1 (middle, blue) and condenser 2 (bottom, light blue), with the assignments of peaks summarised in Table 7.3.7. Similar to the FTIR spectrum for the BSG slow pyrolysis oils, the peak at 3221 cm^{-1}, 3257 cm^{-1}, and 3275 cm^{-1} respectively belongs to water (O-H group). This peak is much stronger in the condenser 1 and condenser 2 which is comparable to the higher water content. All three spectra also showed the pyrolysis oils contained carbonyl C=O (1704 cm^{-1}, 1716 cm^{-1} and 1738 cm^{-1}

respectively) and alkenes C=C (1648 cm⁻¹, 1630 cm⁻¹ and 1633 cm⁻¹ respectively). Amines N-H/ alcohols O-H (1453 cm⁻¹, 1412 cm⁻¹ and respectively) and ester C-O-C (1240 cm⁻¹ and 1217 cm⁻¹ respectively) were found in the BSG fast pyrolysis oil, BSG fast pyrolysis oil condenser 1 and BSG fast pyrolysis oil condenser 2. BSG fast pyrolysis oil contained strong peaks at 2921 cm⁻¹ and 2850 cm⁻¹ corresponding to alkanes C-H compared to the condenser 2. Furthermore, it is important to note that, only the BSG fast pyrolysis oil condenser 1 contained a peak at 1541 cm⁻¹ which is normally associated with nitro compounds and is absent from the organic layer. FTIR is useful for the identification of functional groups present, however, no other chemical information could be determined from FTIR alone.
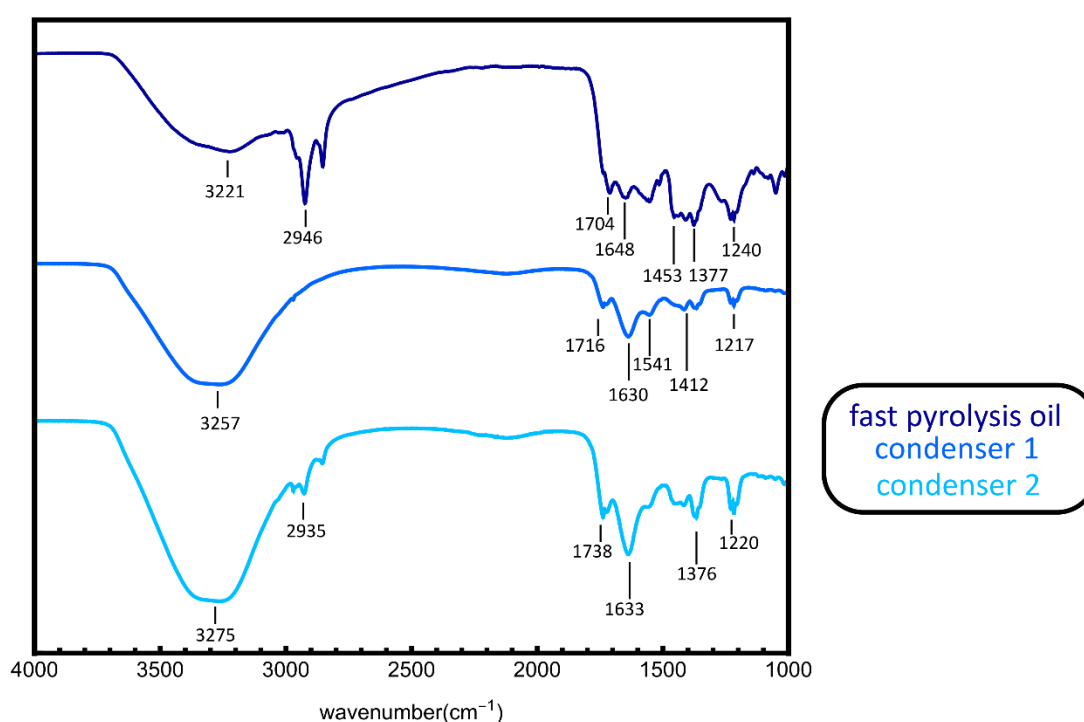
Figure 7.3.3 Stacked plot of FTIR spectra of derivatised BSG fast pyrolysis oil produced from Brewers' Spent Grains, where the top spectra is the pyrolysis oil, middle spectra is from condenser 1 and the bottom spectra is from condenser 2.

Table 7.3.7 FTIR analysis of fast pyrolysis oils produced from Brewers' Spent Grains.

BSG Fast Pyrolysis Oil		
Wavenumber (cm^{-1})	**Functional Group**	**Class of Compound**
3221	O-H stretching	alcohol/water
2946, 2922, 2853	C-H stretching	alkanes
1704	C=O stretching	carboxylic acid/ aldehyde/ketone
1648	C=C stretching	alkene
1453	N-H or O-H	amine/ carboxylic acid
1377	O-H bending	alcohol
1240	C-O stretching	aromatic ester
BSG Fast Pyrolysis Oil Condenser 1		
Wavenumber (cm^{-1})	**Functional Group**	**Class of Compound**
3257	O-H stretching	alcohol/water
1716	C=O stretching	carboxylic acid/ aldehyde/ketone
1630	C=C stretching	alkene
1541	N-O stretching	nitro compound
1412	O-H bending	carboxylic acid
1217	C-O stretching	aromatic ester
BSG Fast Pyrolysis Oil Condenser 2		
Wavenumber (cm^{-1})	**Functional Group**	**Class of Compound**
3275	O-H stretching	alcohol/water
2935, 2923, 2854	C-H stretching	alkanes
1738	C=O stretching	carboxylic acid/ aldehyde/ketone
1633	C=C stretching	alkene
1376	O-H bending	alcohol
1220	C-O stretching	aromatic ester

Gas-chromatography with mass spectroscopy (GC/MS) allows the identification of compounds where the separation of compounds is based on the affinity to the stationary phase (GC) and then the identification of compound according to *MW* (MS). GC/MS was only performed on the BSG slow pyrolysis organic layer and the BSG fast pyrolysis oil, because the gas chromatography column was not suitable for aqueous layer analysis. The resulting chromatogram for the BSG slow pyrolysis oil organic layer is shown in Figure 7.3.4 and that for the BSG fast pyrolysis oil is shown in Figure 7.3.5. Appendix 6 summarises the compounds identified in the pyrolysis oil using the NIST17 MS library.
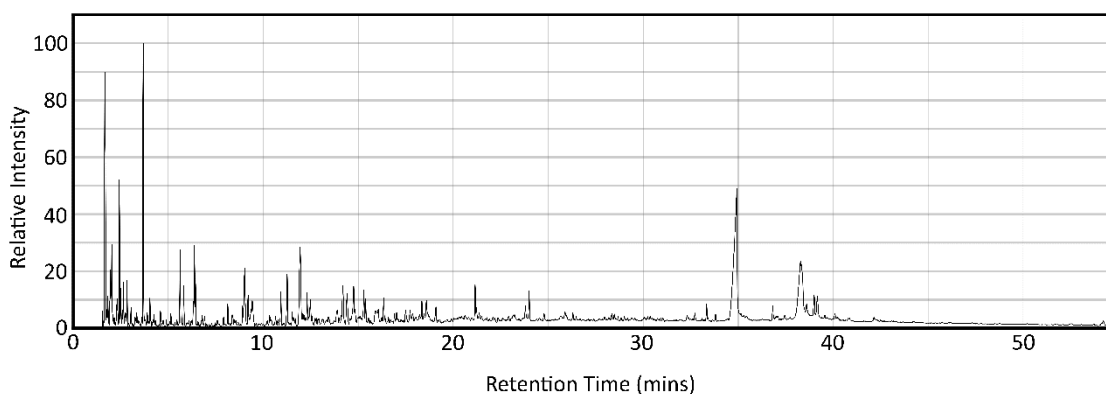
Figure 7.3.4 GC/MS chromatogram for BSG slow pyrolysis oil organic layer.
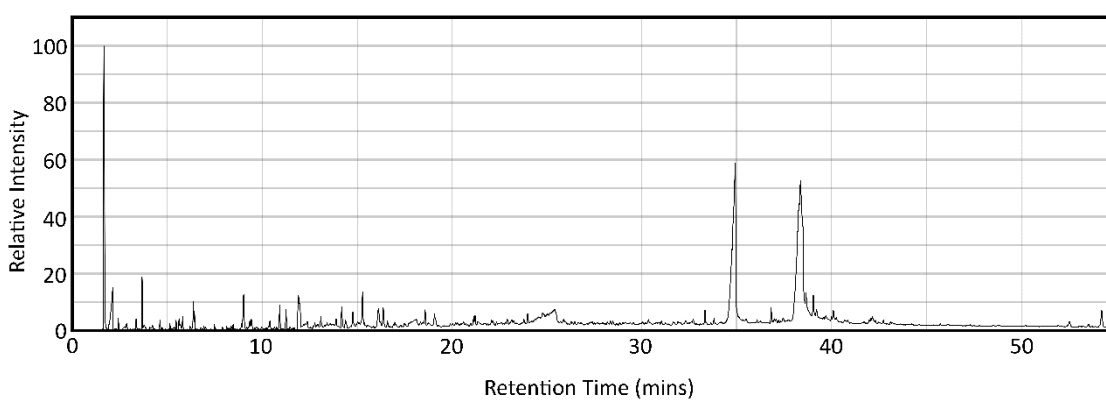
Figure 7.3.5 GC/MS chromatogram for BSG fast pyrolysis oil.

The area under the peak is often considered proportional to the amount of analyte injected, however, different compounds give different peak areas and intensities in GC/MS. However, for these studies GC/MS was used to estimate the amounts of oxygen containing species. An alternative method for fully quantitative data would be to produce calibration curves for each individual compound. The pyrolysis composition determined using GC/MS is summarised in Figure 7.3.6. Both BSG slow-pyrolysis oil organic layer and BSG fast pyrolysis oil contained a similar amount of amides 11.45 % and 12.32 % respectively. These results are also concordant with the elemental analysis results, where both contained similar amounts of nitrogen. The BSG fast pyrolysis oil also contained more aldehydes and ketones (total 33.9 %) than the slow pyrolysis organic layer (total 0.72%). The BSG fast pyrolysis oil had slightly more hydroxyl-containing compounds (total: 37.96 %) compared to BSG slow pyrolysis organic layer (total: 36.46 %). Overall, from the GC/MS data the BSG fast pyrolysis oil contained more oxygen-containing species than the BSG slow pyrolysis organic layer. These results are

also similar to elemental analysis where the BSG fast pyrolysis oil contained more oxygen compared to the BGS slow pyrolysis organic layer.
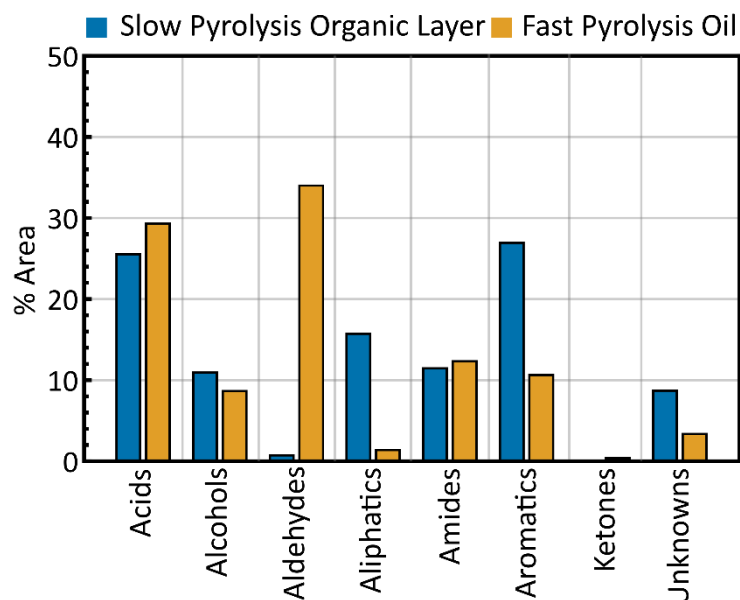
Figure 7.3.6 Composition of BSG pyrolysis oil produced from slow pyrolysis and fast pyrolysis.

GC/MS techniques typically can only analyse 30-40 % of compounds present due to solubility limitations and not all compounds can be identified. For absolute quantification, calibrations of that compound must be produced which can be difficult for mixtures such as bio-oils. In this case, GC/MS could not be performed on the aqueous layers of the pyrolysis oils, therefore, other techniques such as NMR were used to characterise these pyrolysis oils.

Derivatisation methods also enable the analysis of particular certain functional groups. Carbonyl and hydroxyl content is particularly important as they contribute to fuel acidity. The carbonyl content of the BSG pyrolysis oil was accessed by derivatisation followed by ^{19}F low-field NMR analysis, as outlined in Section 7.2.9. Figure 7.3.7 depicts spectra of ^{19}F derivatised BSG slow pyrolysis oil organic layer (dark blue) and aqueous layer (light blue). The internal standard 3-tri(fluoromethoxy) benzoic acid was used for quantification of ketones, aldehydes and quinones in the pyrolysis oils. The integration regions are those outlined in the chemical shift map in Section 4.3.1.2.

B.Tang, PhD Thesis, Aston University, 2024.
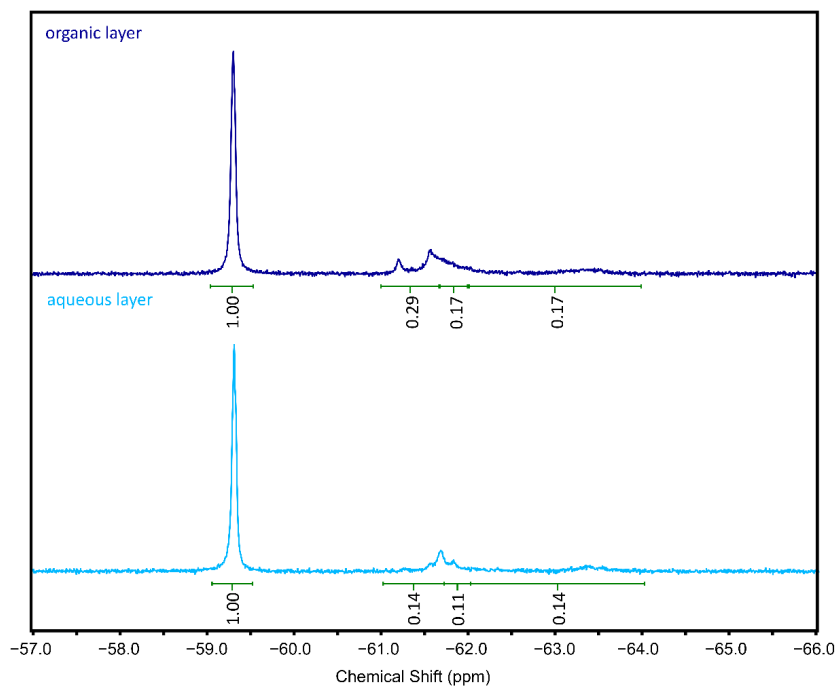
Figure 7.3.7 Stacked plot of ^{19}F NMR spectra of derivatised BSG slow pyrolysis oil at 43 MHz, where the top spectra is organic layer, and the bottom spectra is the aqueous layer.
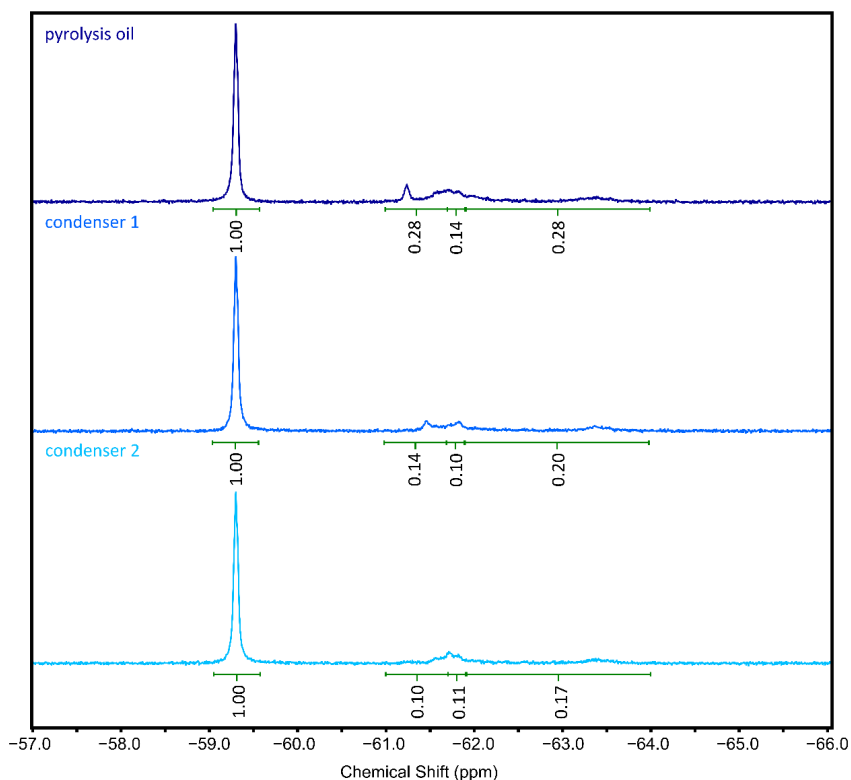
Figure 7.3.8 Stacked plot of ^{19}F NMR spectra of derivatised BSG fast pyrolysis oil produced from Brewers' Spent Grains at 43 MHz, where the top spectra is pyrolysis oil, middle spectra is from condenser 1 and the bottom spectra is from condenser 2.

216

The estimate of the total carbonyl group content from low-field (43 MHz) NMR analysis of ketone, aldehydes and quinones was comparable to the total carbonyl content values determined by the oximation method (OT) as shown in Figure 7.3.9. It was found that the slow pyrolysis organic layer contained more carbonyls than slow pyrolysis aqueous layer. Fast pyrolysis oil also had more carbonyl-containing species than the aqueous fractions from the BSG fast pyrolysis process condenser 1 and condenser 2. Overall, the BSG fast pyrolysis oil contained more carbonyl compounds *ca*. 0.00181 mol g^{-1} when compared to the BSG slow pyrolysis organic layer *ca*. 0.00137 mol g^{-1}. While there were similar amounts of aldehyde-containing compounds in both samples, there were more ketones and quinones present in the fast pyrolysis oil than the slow pyrolysis organic layer. These results are concordant with those found from GCMS, where there are more carbonyl-containing compounds in the BSG fast pyrolysis oil compared to the BSG slow pyrolysis organic layer.
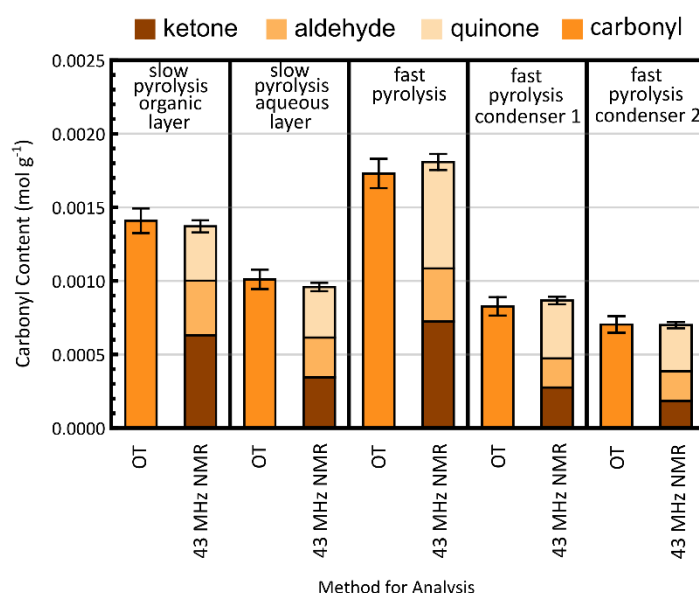
Figure 7.3.9 Bar chart comparing the quantification of ketones, aldehydes and quinones in BSG slow pyrolysis oil organic layer, BSG slow pyrolysis oil aqueous layer, BSG fast pyrolysis oil, BSG fast pyrolysis condenser 1 and BSG fast pyrolysis condenser 2 using both oximation followed by titration (OT) and low-field NMR spectroscopy (43 MHz).

The hydroxyl contents of the BGS pyrolysis oils were obtained by derivatisation using TMDP outlined in Section 7.2.11 followed by NMR analysis. Figure 7.3.10 depicts the spectrum of ^{31}P {^{1}H} NMR derivatised BSG slow pyrolysis oil organic layer. The internal standard derivatised NHND at *ca*. 151.8 ppm was used for quantification of different types of hydroxyl groups present in the pyrolysis oils. The integration regions are those outlined in the chemical shift map in Section 5.3.4. The chemical shifts for the TMDP

derivatised primary alcohol are *ca*. 146.1 to 148.0 ppm, TMDP derivatised secondary alcohol is *ca*.144 to 146.0 ppm, TMDP derivatised tertiary and aromatic alcohols is *ca*. 137.7 to 142.2 ppm and TMDP derivatised carboxylic acids is *ca*. 134.3 to 136 ppm.
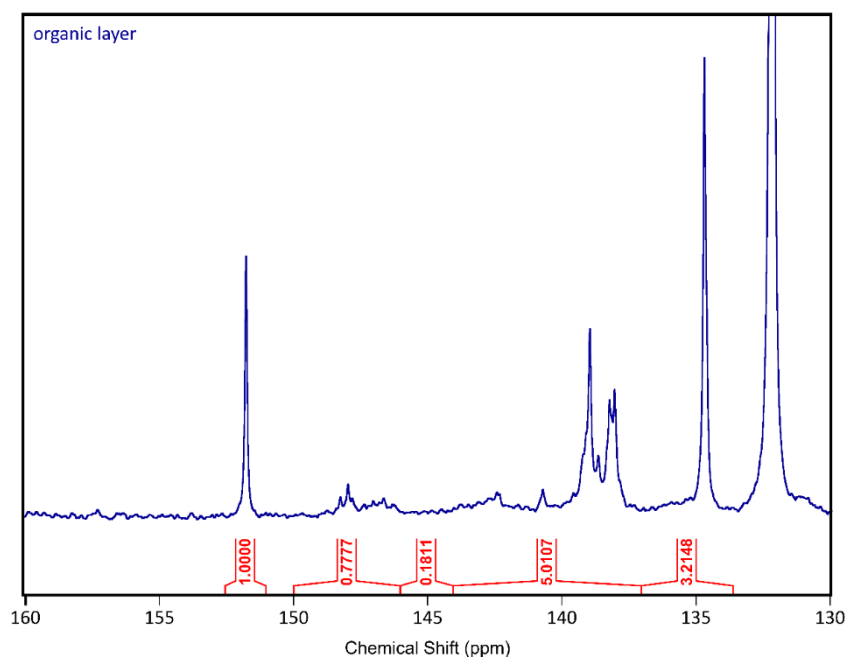
Figure 7.3.10 ^{31}P{^{1}H} NMR spectrum of derivatised BSG slow pyrolysis oil organic layer.

Figure 7.3.11 shows the spectrum of the ^{31}P {^{1}H} derivatised BSG pyrolysis oil aqueous layer. However, there are no peaks in the regions of interest (130 ppm to 160 ppm) due to there being a high-water content, all the derivatisation agent has reacted with the water. The only peak resulted from derivatisation was the mono-derivatised water peak at 15.7 ppm. The derivatisation agent is relatively expensive, and an unknown amount is required to fully derivatise the BSG slow pyrolysis oil aqueous layer. Previous analysis also suggests that the majority of product present is water; a ^{1}H NMR spectrum was acquired to confirm this. Figure 7.3.12 shows the ^{1}H NMR spectrum of the slow pyrolysis aqueous layer acquired without locking. The most dominant peak at *ca*. 4.7 ppm belongs to water. There are also several peaks at lower intensities at around 0-2 ppm which are most likely to be aliphatic compounds.
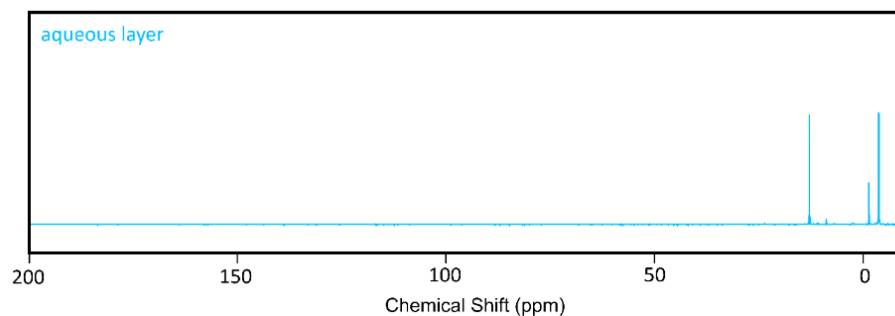
Figure 7.3.11 ^{31}P{^{1}H} NMR spectrum of derivatised BSG slow pyrolysis oil aqueous layer.
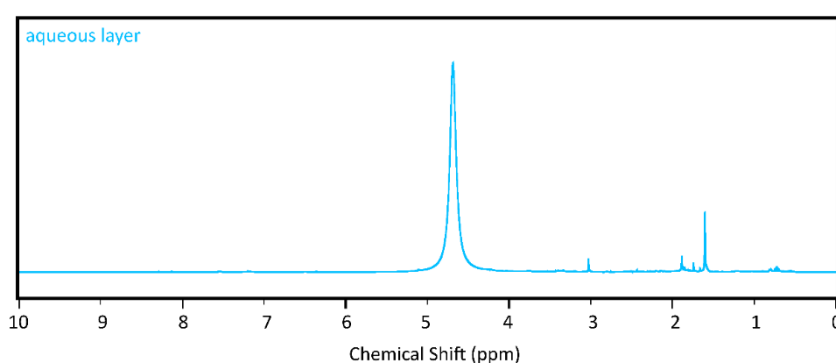
Figure 7.3.12 ^{1}H NMR spectrum of BSG slow pyrolysis oil aqueous layer.

Figure 7.3.13 depicts the spectrum of ^{31}P {^{1}H} derivatised BSG fast pyrolysis oil. The internal standard derivatised NHND at *ca*. 151.8 ppm was used for quantification of different types of hydroxyl groups present in the pyrolysis oils. The integration regions are those outlined in the chemical shift map in Section 5.3.4 and earlier in this section.
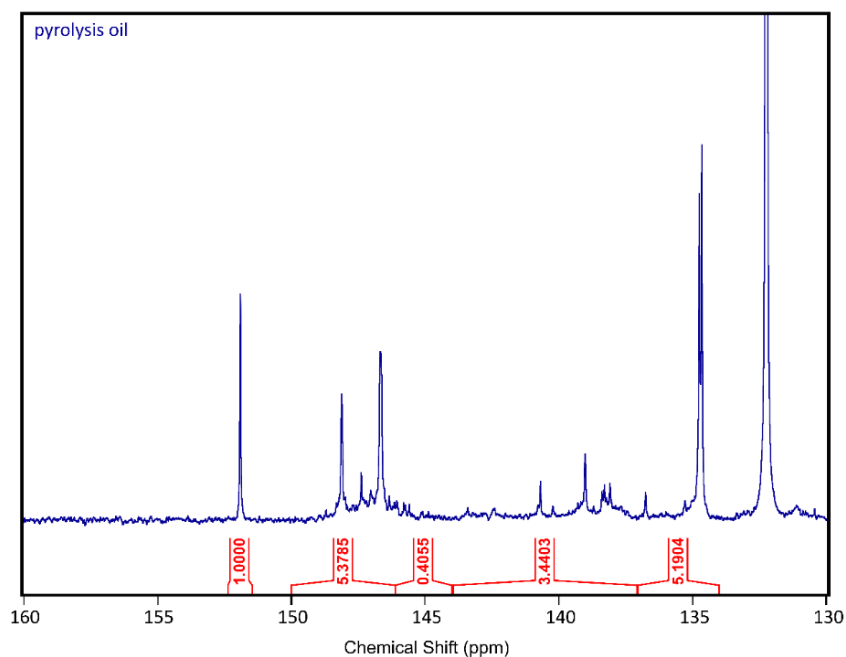
Figure 7.3.13 $^{31}P\{^1H\}$ NMR spectrum of derivatised BSG fast pyrolysis oil.

Based on previous results for the BSG slow pyrolysis oil aqueous layer where it was predominantly water, ^1H NMR spectrum was acquired for both BSG fast pyrolysis oil condenser 1 and condenser 2. Both spectra had a dominant peak at *ca.* 4.7 ppm which shows that water is major product in the samples. Both spectra also had peaks at lower intensities of around 0-2 ppm which are likely to be aliphatic compounds.
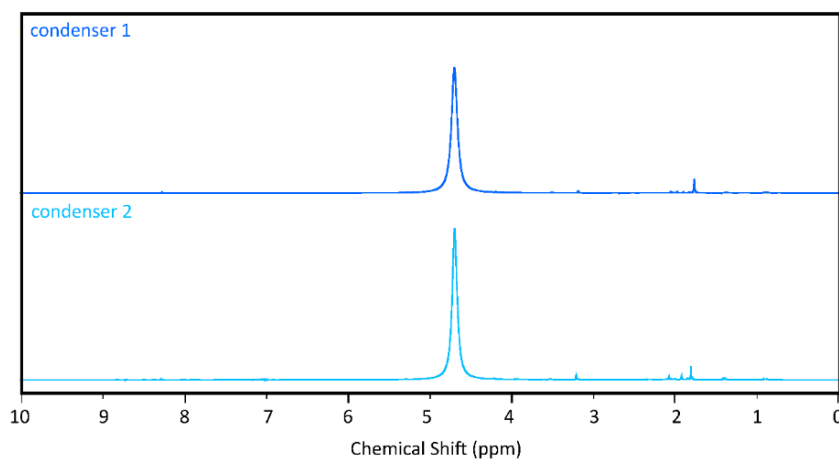
Figure 7.3.14 ^1H NMR spectrum of BSG slow pyrolysis oil aqueous layer, where the top spectra is from condenser 1 and the bottom spectra is from condenser 2.

Only the BSG organic layer of the slow pyrolysis and the BSG fast pyrolysis oils showed measurable concentration of alcohol using ^{31}P NMR methods. The estimate of the total hydroxyl group content from ^{31}P NMR methods is shown in Figure 7.3.15. Using ^{31}P NMR techniques it was found that slow pyrolysis oil contained ca. 0.00084 mol g^{-1} of carboxylic acids. The BSG fast pyrolysis oil contained more carboxylic acids ca. 0.00153 mol g^{-1}. Overall, the fast pyrolysis oil contained more hydroxyl compounds total: 0.00424 mol g^{-1} when compared to the BSG slow pyrolysis organic layer total: 0.00241 mol g^{-1}. These results correspond to previous GC/MS data, where the BSG fast pyrolysis oil contains more hydroxyl compounds (alcohols and acids) in comparison the BSG slow pyrolysis oil organic layer.
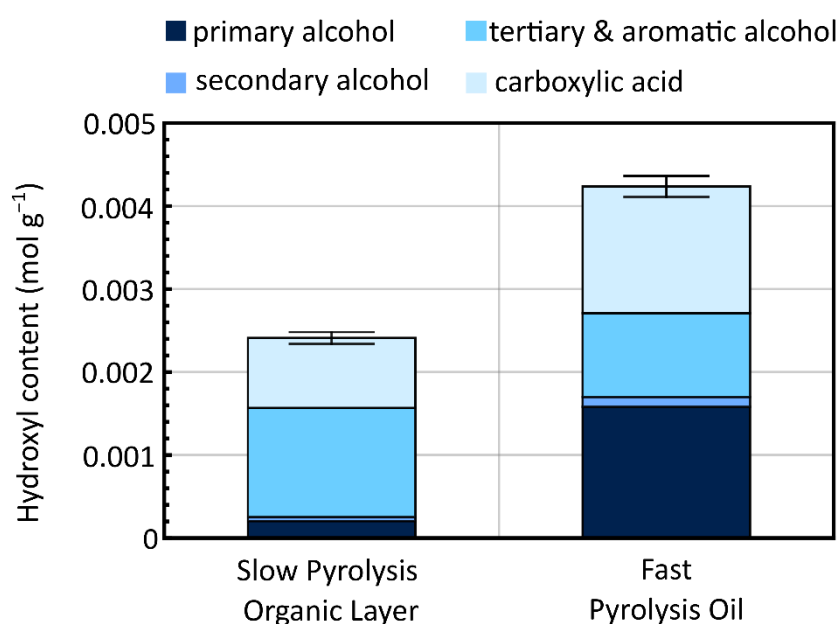
Figure 7.3.15 Graph comparing the quantification of different alcohol in BSG slow pyrolysis oil organic layer and BSG fast pyrolysis oil found using ^{31}P NMR spectroscopy.

It is still challenging to identify hydroxyl compounds present using 1D ^{31}P NMR techniques due to the overlapping peaks. ^{31}P DOSY techniques can be used to separate signals out in the diffusion domain. ^{31}P DOSY techniques were applied to the BSG slow pyrolysis organic layer and the BSG fast pyrolysis oil to further identify hydroxyl-containing compounds. The ^{31}P DOSY was carried out using the ^{31}P convection compensated sequence as described in Section 7.2.11. The DOSY spectrum of the derivatised slow pyrolysis oil is shown in Figure 7.3.16. Only the largest peaks in the spectrum were selected to ensure for the maximum signal-to-noise ratio. The molecular weights of the internal standards and their measured diffusion coefficients are shown in

B.Tang, PhD Thesis, Aston University, 2024.

Table 7.3.8. The peak at 151.8 ppm belongs to the derivatised NHND and the peak at 132.2 ppm belongs to the di-derivatised water. The unknown alcohol peaks were in the expected regions for tertiary and aromatic alcohols *ca.* 137.7 to 142.2 ppm, and also carboxylic acids *ca.* 134.3 to 136.0 ppm. Qualitatively analysis of the DOSY spectrum, the peaks in the carboxylic acid region suggests there is a smaller acid (134.6 ppm) with a diffusion coefficient of 6.06×10^{-10} m^2 s^{-1} and a bigger acid (135.0 ppm) with a diffusion coefficient of 3.92×10^{-10} m^2 s^{-1}.
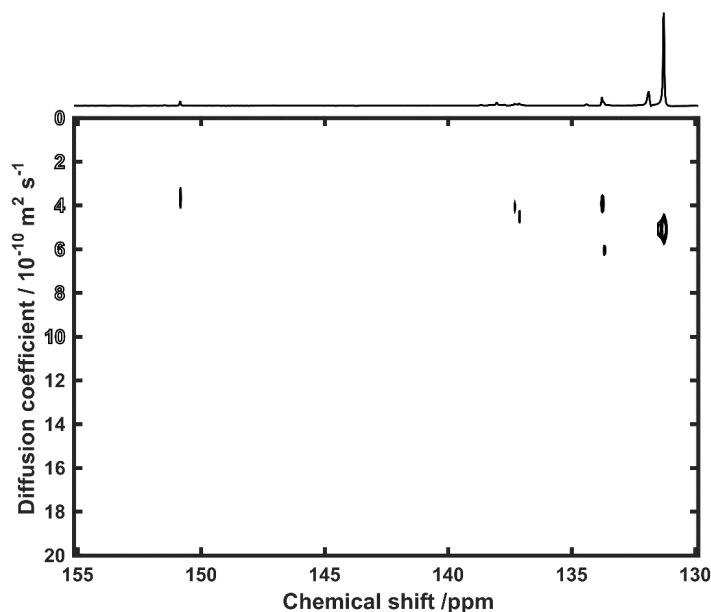
Figure 7.3.16 ^{31}P DOSY spectrum of derivatised slow pyrolysis oil.

Table 7.3.8 Molecular weights, log MW, measured diffusion coefficients and log D of internal calibrants.

Compound	*MW*	log *MW*	*D*	log *D*
	g mol^{-1}		/ 10^{-10} m^2 s^{-1}	
TMP	140.1	2.14	8.58	−9.06
Di-derivatised water	310.2	2.49	5.08	−9.29
Derivatised NHND	325.3	2.51	3.92	−9.41
TMDP	182.6	2.26	6.79	−9.16

A power law is generated by plotting the log *MW* against log *D* of the internal calibrants, where the molecular weight of the derivatised alcohol can be estimated from their diffusion coefficient. The equation generated:

$$\log D = -0.800 \log MW - 7.351$$

was used to estimate the *MW* of the unknown alcohols can be estimated. The measured diffusion coefficient of the unknown alcohols and estimated molecular weights of the derivatised alcohol is shown in Table 7.3.9.
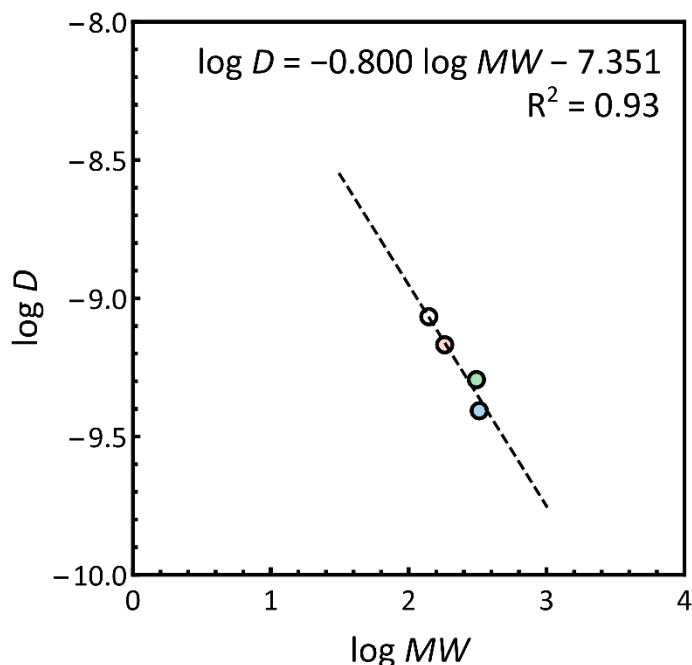
Figure 7.3.17 log D vs log MW plot of internal calibrants, TMDP, derivatised NHND, di-derivatised water and TMP for the estimation of MW of derivatised compounds in derivatised slow pyrolysis oil sample.

Table 7.3.9 Diffusion coefficient, log D, log MW, and estimated MW for derivatised compounds in derivatised slow pyrolysis oil sample.

ppm	*D*	log *D*	log *MW*	*MW*$_{est}$ (derivatised compound)
	/ 10^{-10} m^2 s^{-1}			g mol^{-1}
134.6	6.06	−9.21	2.46	290.4
135.0	3.92	−9.40	2.79	618.7
138.1	4.51	−9.34	2.69	485.1
138.4	4.06	−9.39	2.76	582.1

An additional complication for pyrolysis oil sample is that the unknown molecules could be mono-, di- or tri- etc. derivatised, corresponding to mono-, di-, and tri- alcohols respectively. This adds to the difficulty in interpretation. The estimated molecular weights for mono-, di- and tri- derivatised hydroxyl-containing compounds can be found in Table 7.3.10. The peak at 134.6 ppm (carboxylic acid region) was found to have an estimated

molecular weight of 144.30 g mol^{-1} this is similar to that of cinnamic acid (148.2 g mol^{-1}), the peak at 135.0 ppm (carboxylic acid region) has an estimated molecular weight for a tri-derivatised 180.5 g mol^{-1} which is similar to that of caffeic acid (180.2 g mol^{-1}), the peak at 138.1 ppm (tertiary/aromatic region) has an estimated molecular weight for a di-derivatised 192.9 g mol^{-1} which is similar to that of syringic acid (198.2 g mol^{-1}) and the peak at 138.4 ppm (tertiary/aromatic region) has an estimated molecular weight of 289 g mol^{-1} which is similar to 5,5'-methylenebis(2-methoxy-4-methylphenol) (288.3 g mol^{-1}). Cinnamic acid, caffeic acid, syringic acid and 5,5'-methylenebis(2-methoxy-4-methylphenol) are typical products found in pyrolysis oils of lignocellulose biomass. [268-270] The structures and their molecular weights are shown in Figure 7.3.18.

Table 7.3.10 Estimated MW of mono-, di- and tr-derivatised alcohol.

ppm	MW_{est} mono-derivatised	MW_{est} di-derivatised	MW_{est} tri-derivatised	Compound
	g mol^{-1}	g mol^{-1}	g mol^{-1}	
134.6	144.3	-	-	cinnamic acid (148.2 g mol^{-1})
135.0	472.7	326.5	180.5	caffeic acid (180.2 g mol^{-1})
138.1	339.0	192.9	-	syringic acid (198.2 g mol^{-1})
138.4	436.1	289.9	-	5,5'-methylenebis(2-methoxy-4-methylphenol) (288.3 g mol^{-1})

cinnamic acid
MW=148.2 g mol^{-1}

caffeic acid
MW=180.2 g mol^{-1}

syringic acid
MW=198.2 g mol^{-1}

5,5'-methlyenebis(2-methoxy-4-methylphenol)
MW=288.3 g mol^{-1}
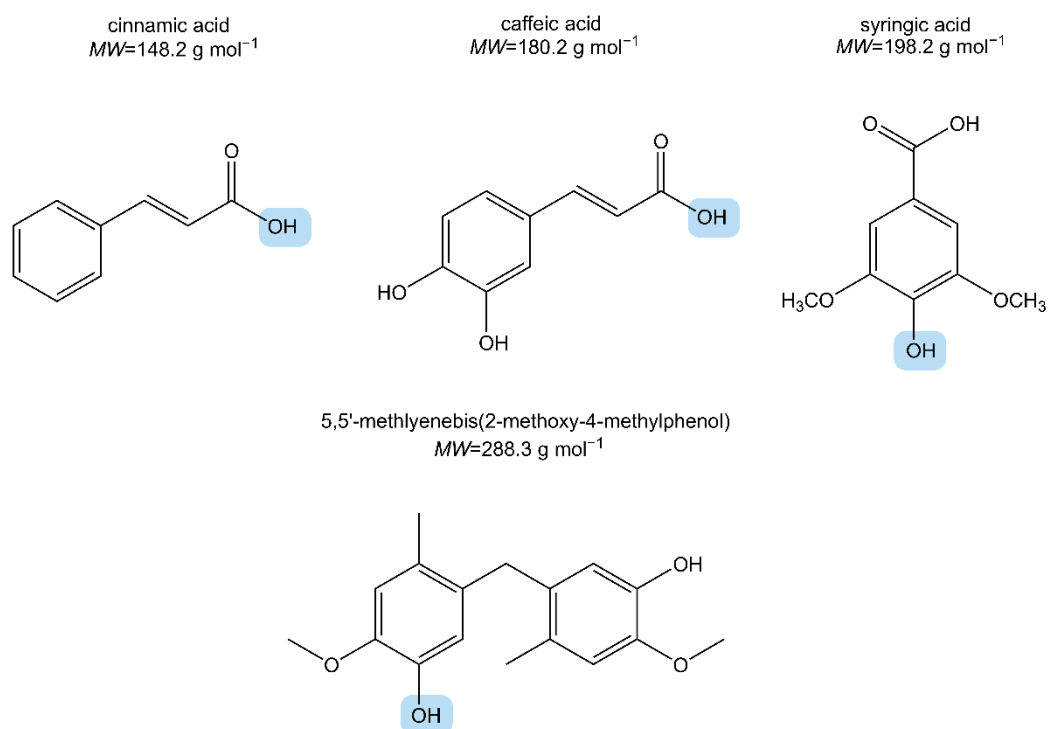
Figure 7.3.18 structure of potential compounds found in slow pyrolysis oil, cinnamic acid, caffeic acid, syringic acid and 5,5'-methylenebis(2-methoxy-4-methylphenol).

The [13]P DOSY spectrum of the derivatised fast pyrolysis oil is shown in Figure 7.3.19. Only the largest peaks in the spectrum were selected to ensure for the maximum signal-to-noise ratio. The molecular weights of the internal standards and their measured diffusion coefficients are shown in Table 7.3.11. The peak at 151.8 ppm belongs to the derivatised NHND and the peak at 132.2 ppm belongs to the di-derivatised water. As with the previous sample, all unknown alcohol peaks were in the expected regions for tertiary and aromatic alcohols, ca. 137.7 to 142.2 ppm, and also carboxylic acids, ca. 134.3 to 136.0 ppm.
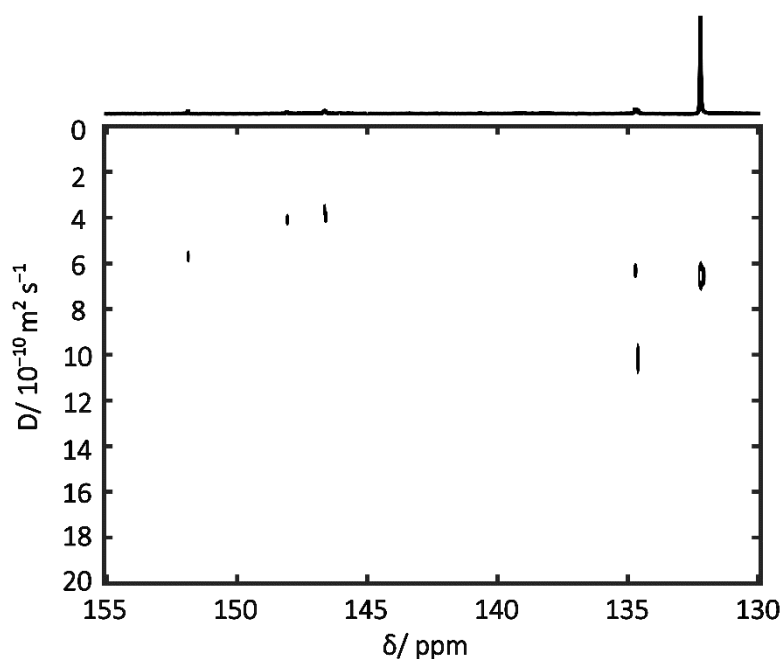
Figure 7.3.19 ^{1}P DOSY spectrum of derivatised fast pyrolysis oil.

Table 7.3.11 Molecular weights, log MW, measured diffusion coefficients and log D of internal calibrants.

Compound	MW	log MW	D	log D
	g mol^{-1}		/ 10^{-10} m^2 s^{-1}	
TMP	140.1	2.14	8.23	−9.08
Di-derivatised water	310.2	2.49	5.33	−9.27
Derivatised NHND	325.3	2.51	5.20	−9.28
TMDP	182.6	2.26	8.57	−9.07

A power law is generated by plotting the log *MW* against log *D* of the internal calibrants, where the molecular weight of the derivatised alcohol can be estimated from their diffusion coefficient. The equation generated:

$$\log D = -0.622 \log MW - 7.712$$

was used to estimate the MW of the unknown alcohols can be estimated. The measured diffusion coefficient of the unknown alcohols and estimated molecular weights of the derivatised alcohol is shown in Table 7.3.12.
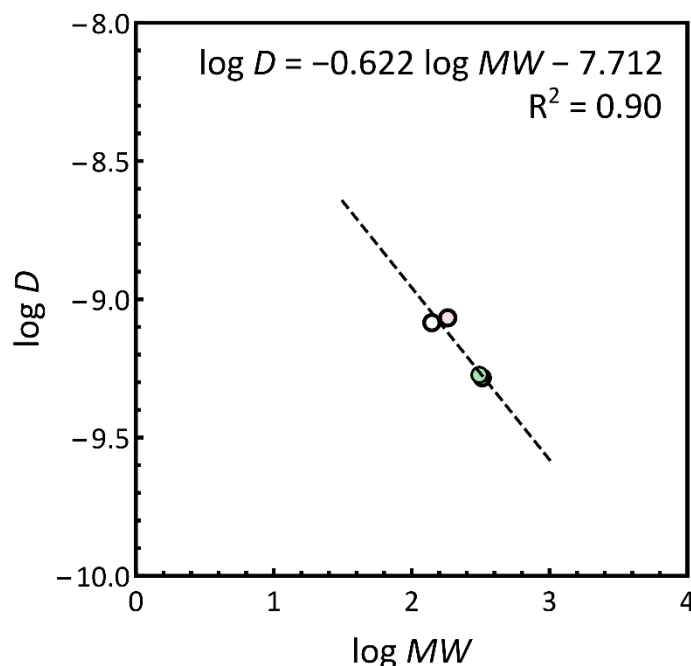
$$\log D = -0.622 \log MW - 7.712$$
$$R^2 = 0.90$$

Figure 7.3.20 log D vs log MW plot of internal calibrants, TMDP, derivatised NHND, di-derivatised water and TMP for the estimation of MW of derivatised compounds in derivatised fast pyrolysis oil sample.

Table 7.3.12 Diffusion coefficients, log D, log MW, and MW of estimated for derivatised compounds in derivatised slow pyrolysis oil sample.

ppm	D	log D	log MW	MW_{est} (derivatised compound)
	/ 10^{-10} m^2 s^{-1}			g mol^{-1}
134.7	9.99	−9.00	2.07	117.2
134.9	6.05	−9.21	2.42	262.1
146.6	3.89	−9.41	2.72	533.1
148.1	4.17	−9.38	2.68	477.1

The estimated molecular weights for mono- and di-derivatised hydroxyl-containing compounds can be found in Table 7.3.13. The assignment of chemical compound was based on the chemical shift values and estimated molecular weight compounds. The peak at 134.7 ppm belongs to carboxylic acid had a diffusion coefficient of 9.99 ± 0.38 × 10^{-10} m^{2}s^{-1} suggesting it could be a small molecule. However, the estimated molecular weight was found to be −28.9 g mol^{-1}, suggesting there are limitations to the technique. This could be due to the larger error in the diffusion coefficient estimated for that peak, however, even when that was taken into consideration, the estimated molecular weights

were still negative. The measured diffusion coefficient was also outside of the calibration curve produced, therefore, there may be some inaccuracies in the estimated molecular weight.

The peak at 134.9 ppm (carboxylic acid region) was found to have an estimated molecular weight of 116.0 g mol^{-1}, this is similar to that of benzoic acid (122.1 g mol^{-1}), the peak at 146.6 ppm (primary alcohol region) has an estimated molecular weight for a di-derivatised 240.9 g mol^{-1} similar to that of 1-(phenyl)-2-phenoxy-1,3-propanediol (244.3 g mol^{-1}), and the peak at 148.1 ppm (primary alcohol region) had an estimated molecular weight for a di-derivatised alcohol of 185.0 g mol^{-1} which is similar to that of coniferyl alcohol (180.2 g mol^{-1}). Benzoic acid, 1-(phenyl)-2-phenoxy-1,3-propanediol and coniferyl alcohol are typical products found in pyrolysis oils of lignocellulose biomass.[271-273]

Table 7.3.13 estimated MW of mono-, di- and tr-derivatised alcohol.
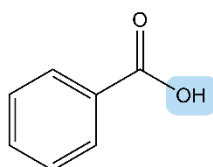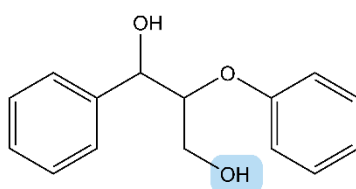
ppm	MW$_{est}$ mono-derivatised g mol^{-1}	MW$_{est}$ di-derivatised g mol^{-1}	Compound
134.7	−28.9	-	-
134.9	116.0	-	Benzoic acid (122.1 g mol^{-1})
146.6	387.0	240.9	1-(phenyl)-2-phenoxy-1,3-propanediol (244.3 g mol^{-1})
148.1	331.1	185.0	Coniferyl alcohol (180.2 g mol^{-1})
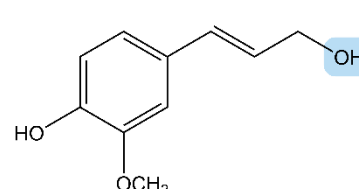
Figure 7.3.21 structure of potential compounds found in fast pyrolysis oil, benzoic acid, 1-(phenyl)-2-phenoxy-1,3-propanediol and coniferyl alcohol.

7.4 Summary

BSG was used to produce a slow pyrolysis oil and a fast pyrolysis oil. Figure 7.4.1 summarises the pH, water content and elemental composition of the two pyrolysis oils. Figure 7.4.2 summarises the amounts of different oxygen-containing species, including the overall concentrations of hydroxyl- and carbonyl- containing species, such as alcohols, acids, ketones, and aldehydes present in the pyrolysis oils.

BSG Slow Pyrolysis Oil   **BSG Fast Pyrolysis Oil**
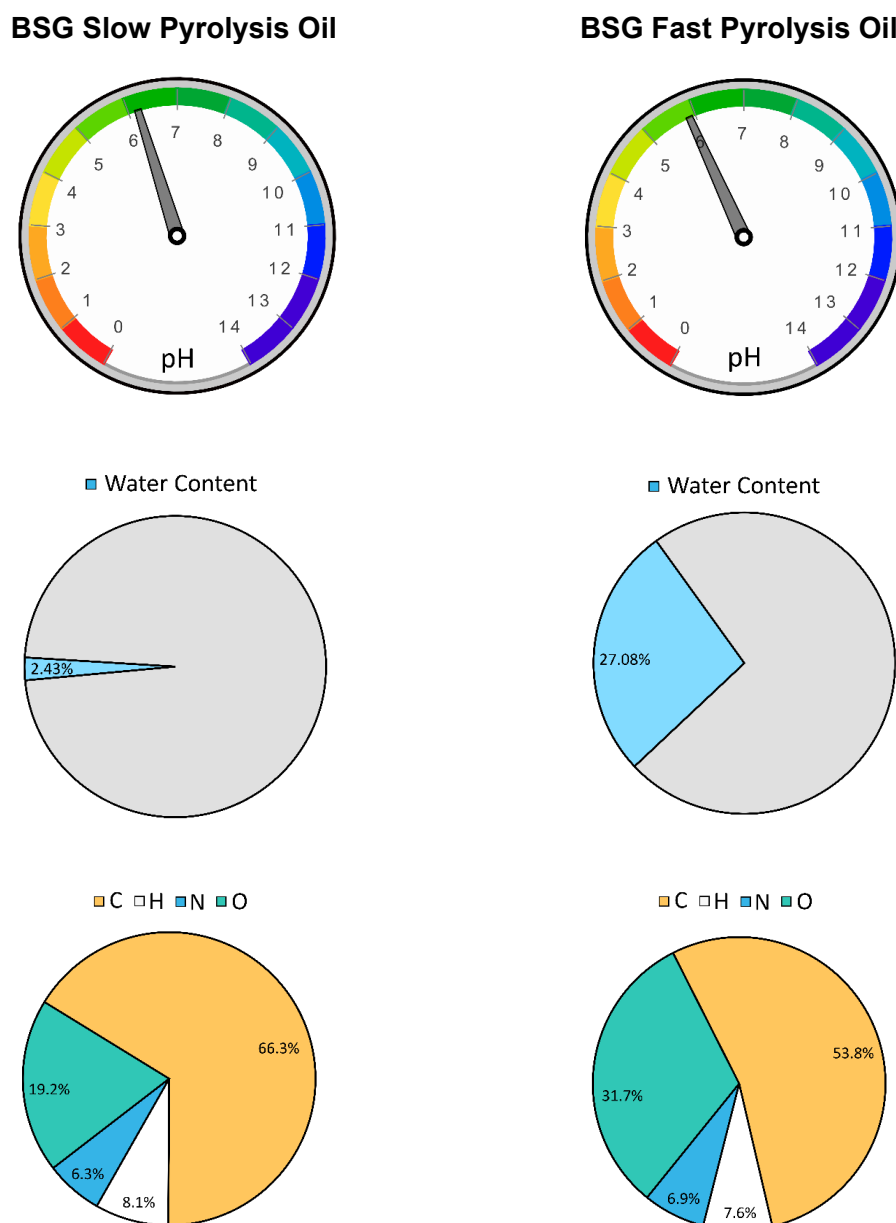
Figure 7.4.1 Infographic summarising the pH, water content and elemental composition of the BSG slow pyrolysis oil and BSG fast pyrolysis oil.

B.Tang, PhD Thesis, Aston University, 2024.

BSG Slow Pyrolysis Oil

BSG Fast Pyrolysis Oil
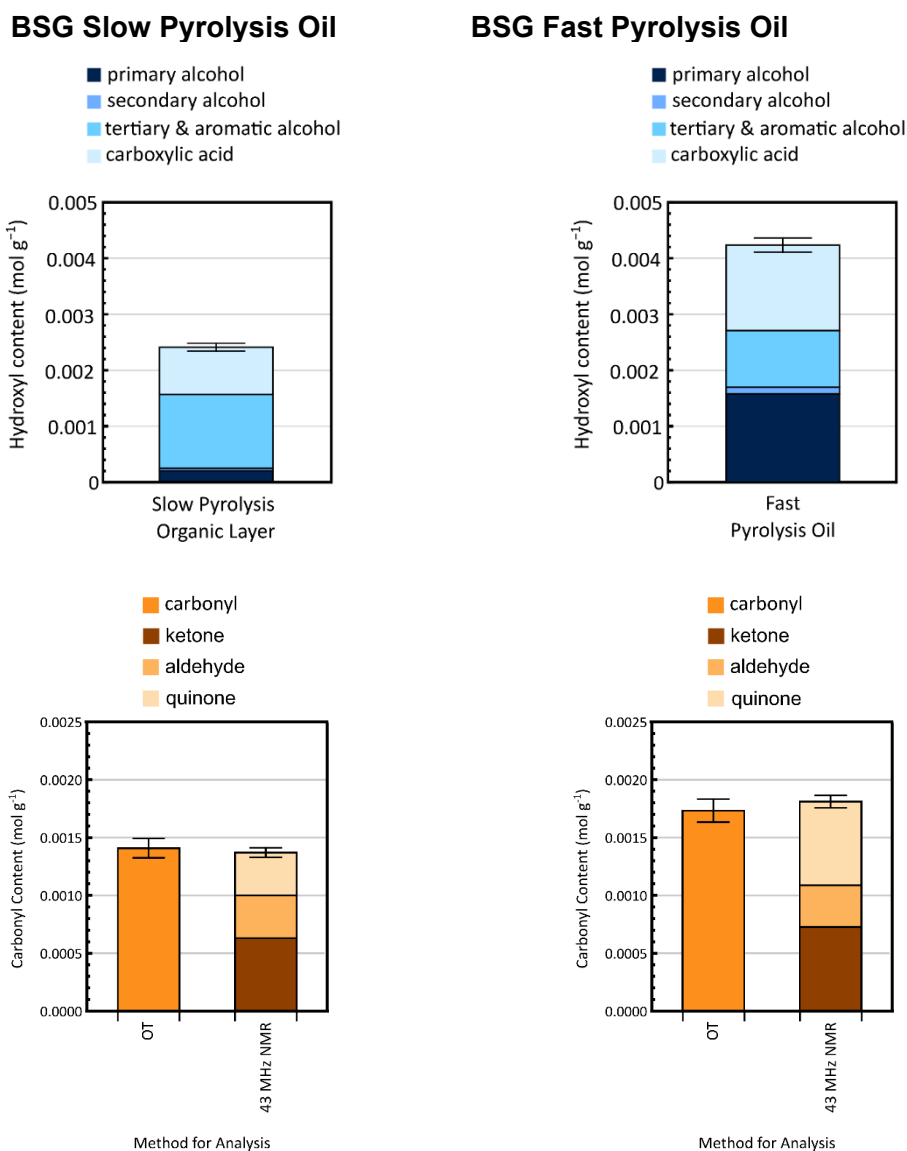
Figure 7.4.2 Infographic summarising the overall concentrations of hydroxyl and carbonyl containing species, such as alcohols, acids, ketones, and aldehydes present in the pyrolysis oils. This figure is reproduced from data present earlier in the chapter.

7.5 Conclusion

Brewers' Spent Grains was used as a feedstock to produce pyrolysis oils using two different method: slow pyrolysis and fast pyrolysis. Slow pyrolysis techniques produced a biphasic liquid product. Fast pyrolysis produced a singly phased oil, and two predominantly aqueous-phase liquid products. It was found that the organic phase of the pyrolysis oil produced using slow pyrolysis contained the least water *ca*. 2.43 %, and the fast pyrolysis oil contained *ca*. 27.08 %. The low water content suggests that these oils maybe a potential for producing fossil fuel replacements, fuel additives or upgrading to added-value chemicals.

Typical pyrolysis oils have a pH around 2 to 3 which makes them unsuitable for use in current infrastructures. As a result, for BSG pyrolysis oils to be considered as a fuel replacement other physical chemical property such as acidity must be considered. The pH of the slow pyrolysis oil organic layer *ca*. 6.19 compared to the slightly more acidic fast pyrolysis oil with a pH *ca*. 5.86. This shows that pyrolysis oils produced from Brewers' Spent Grains used as a biofuel, either as boiler fuel where no specialist burners are required or can be used as marine fuel directly.

Oxygen-containing compounds such as hydroxyl and carbonyl compounds contribute to the acidity of pyrolysis oils. Further analysis was conducted to better understand the chemical composition of these pyrolysis oils. Understanding what oxygen-containing molecules are present, as well as how much of them, is particularly important. The elemental composition of the pyrolysis oils was analysed using CHSN/O. BSG slow pyrolysis oil organic layer contained 19.2 % oxygen and BSG fast pyrolysis oil contained 31.71 % oxygen. FTIR confirmed that the pyrolysis oils contained a variety of functional group. GC/MS was used to identify some of the compounds present. However, this was only performed on the organic layers of the sample. Overall GC/MS data also indicates there were less oxygen-containing compounds (alcohol, acids, aldehydes and ketones) in the slow pyrolysis oil (37.18 % Area) in comparison to the fast pyrolysis oil organic layer (71.86 % Area).

However, because GC/MS techniques were semi quantitative, the oxygen-containing compounds were identified and quantified by derivatisation of specific functional groups and multinuclear qNMR techniques. ^{19}F low-field NMR techniques were used to quantify the carbonyl content, which was then compared to standard methods, oximation followed by titration It was found that the fast pyrolysis oil contained more carbonyl-containing compounds than the slow pyrolysis organic layer. The ^{31}P NMR techniques were used to quantify the alcohol groups, and the fast pyrolysis oil contained more hydroxyl-containing compounds than the slow pyrolysis oil organic layer.

Overall, for an extensive study of oxygen-containing species present in the pyrolysis oils, this chapter combined the use of current techniques and novel NMR techniques. Based on all the different types of analysis, pyrolysis oils produced from Brewers' Spent Grains via the fast pyrolysis process contained more oxygen-containing compounds than those

produced via the slow pyrolysis process. The upgrading techniques explored in Chapter 1, mostly focus on the removal of oxygen-containing compounds. However, these techniques generally require high energy consumption and high cost. The less oxygen-containing compounds, the less upgrading required. Overall, these BSG pyrolysis oils contained very small amounts of oxygen-containing compounds and thus, potentially a viable option for boiler fuels or marine fuel. However, some upgrading may still be required for BSG to be feasible as fuel alternatives.

7.6 Further works

A comprehensive study of these pyrolysis oils is needed to further evaluate the feasibility of these pyrolysis as renewable replacements of traditional fuels.

1. Heating Values – the amount of heat released during the combustion of pyrolysis oils.
2. TAN (Total acid number) – the quantity of KOH required to neutralise the acid component.
3. Flash Point – the minimum temperature at which a liquid gives off vapour at a sufficient concentration to for an ignitable mixture with air.

Even though the use of $^{31}P\{^1H\}$ NMR simplifies the spectrum, however there are still overlapping regions on the spectrum. As a result, the data interpretation was still challenging.

1. Identifying/ synthesising other derivatisation agents that could disperse the signals across the chemical shift domain.

The interpretation of the ^{31}P DOSY was more challenging than expected.

1. The crowdedness of the spectrum and low signal-to-noise meaning it was difficult to select all the peaks.
2. Better choice of internal calibrants i.e., a wider molecular weight range, as well as using extra internal standard as the TMDP concentration can vary from sample to sample depending on how much had been used up.
3. An extensive library/ machine learning of diffusion data for the compounds in bio-oil can be produced for a rapid and precise way to characterise bio-oil samples.

4. Once these protocols are developed, they can be implemented on NMR software or as standalone packages.

233

CHAPTER 8 : QUANTITATIVE INTERPRETATION OF PROTEIN DIFFUSION COEFFICIENTS IN MIXED PROTIATED-DEUTERIATED AQUEOUS SOLVENT

8.1 Introduction

Molecular self-diffusion in a liquid originates from the random movement of the molecules present. Diffusion-ordered nuclear magnetic resonance spectroscopy (DOSY) has become a routine technique for the measurement of self-diffusion coefficients of molecules[219]. Typically, the diffusion information in a DOSY spectrum is used for qualitative analysis, for example, to identify signals from the same species. Figure 8.1.1 is a DOSY spectrum of 0.4 mM lysozyme at 278.15 K in 0:100 $H_2O:D_2O$. It shows the signals belong to the same species with a diffusion coefficient of 0.528×10^{-10} m^2s^{-1}. Diffusion coefficients provide information on the molecules' size, shape, and environment. This, in turn, infers chemical information, such as the molecular weight of unknown species, its aggregation or association with other species and can reveal changes in structure, such as when protein denature. More recently, diffusion coefficients have been used for quantitative analysis. While there is a general correlation between molecular mass and the speed at which a molecule travels in solution, i.e the larger the molecule, the slower it moves, the wide range of possible molecular shapes, solute-solvent interactions and fundamental problems with diffusion theories make quantitative techniques difficult to interpret.
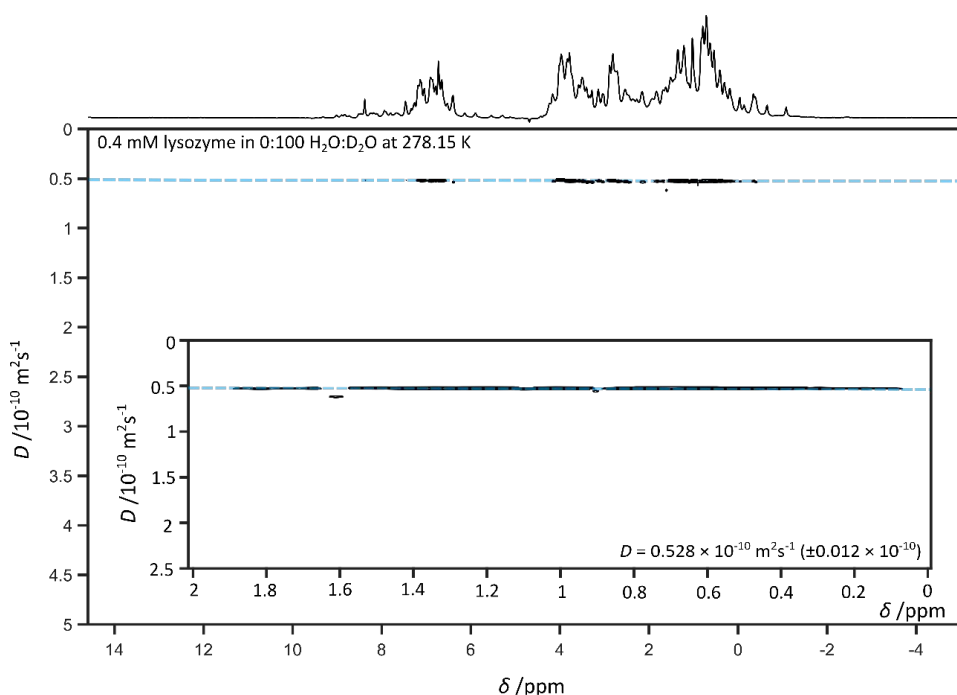
Figure 8.1.1 DOSY spectrum of 1 mM lysozyme at 5°C in 10:90 $H_2O:D_2O$ with solvent suppression.

B.Tang, PhD Thesis, Aston University, 2024.

Many chemical processes are studied in mixed solvent systems, however, the diffusion behaviour of molecules in mixed solutions, such as deuteriated and protiated solvents, are still poorly understood. In Chapter 5 & 6, derivatisation reactions are carried out in a mixed solvent system (pyridine and $CDCl_3$). In Chapter 6, the use of internal calibrations and the generation of a power law was explored to gain quantitative information based on the diffusion coefficients. In this chapter other methods that can be used to predict the diffusion coefficients based on their molecular weight, solvent composition and sample temperature will be explored.

Power laws, such as Equation 8.1.1, to correlate between diffusion coefficients, *D*, and molecular mass, *MW*, for a homologous series in a particular solvent at a given temperature. A plot of log *D* against log *MW*, as in Equation 8.1.2 for structurally similar compounds, can be used to infer unknown molecular weights from experimentally acquired diffusion coefficients. Globular proteins are an example of chemical species where the value of 1/δ tends towards 0.33. Some studies relate the protein gyration and hydrodynamic radii to the number of residues present.[274-276] Jones and Wilkins *et al*. and Whitehead *et al*. both also reported globular proteins tended towards 0.33 and measurements in strongly denaturing solutions increased values approaching 0.6. [275, 276]

$$D = K \cdot M^{-\left(\frac{1}{\delta}\right)}$$
Equation 8.1.1

$$\log D = -\left(\frac{1}{\delta}\right) \cdot \log MW + \log K$$
Equation 8.1.2

Alternative methods have been developed to accurately predict and correlate diffusion coefficient with molecular weight. Discussion of the diffusion of small molecules all starts with the Stokes-Einstein Equation (Equation 8.1.3)[217]. This equation predicts the diffusion coefficient of a species, *D*, by balancing the thermal energy of the system, defined as $k_b T$, where k_b is the Boltzmann constant and *T* is the given temperature, with the friction acting on the particle, assuming that the particle is a hard sphere with the hydrodynamic radius r_H, at an infinite dilution in a continuum fluid with the viscosity *η*.

$$D = \frac{k_b T}{6\pi \eta r_H}$$
Equation 8.1.3

The Stokes-Einstein equation works well for nanometre and larger sized species. However, the equation fails to accurately predict the diffusion coefficient for small molecules. The approximation fails for small molecules due to two well-established

reasons. First, small molecules are not hard spheres but can exhibit different molecular shapes, are flexible, interact with solvents to different degrees, and can have very different densities.

The friction caused by molecular shape can modify the friction factor, f_s. Small molecule shapes can be better approximated as ellipsoids. Ellipsoids can be described as either prolate or oblate, and this is defined by their aspect ratio (*b/a*), where b is the major axis and a is the minor axis. Perrin analysed the effect of shape factor on diffusion coefficients[277], showing molecular shape only becomes important when the aspect ratios are high, as depicted in Figure 8.1.2, i.e. where molecules are thin rods or wide disks. The Perrin shape friction factor f_s can be included in the denominator of the Stokes-Einstein equation. Equation 8.1.5 and Equation 8.1.6 for prolate and oblate ellipsoids respectively. Where aspect ratios are lower than 5, which is true for most small molecules, the effects on *D* are usually less than 10% and, therefore, can be safely ignored.

$$D = \frac{kT}{6\pi\eta f_s r_H}$$

Equation 8.1.4

$$\text{Prolate ellipsoid:} f_s = \frac{\sqrt[2]{1 - \left(\frac{b}{a}\right)^2}}{\left(\frac{b}{a}\right)^{\frac{3}{2}} ln\left(\frac{a}{b}\sqrt[2]{1 - \left(\frac{b}{a}\right)^2}\right)}$$

Equation 8.1.5

$$\text{Oblate ellipsoid:} f_s = \frac{\sqrt[2]{\left(\frac{b}{a}\right)^2 - 1}}{\left(\frac{b}{a}\right)^{\frac{3}{2}} arctan\left(\sqrt[2]{\left(\frac{b}{a}\right)^2 - 1}\right)}$$

Equation 8.1.6
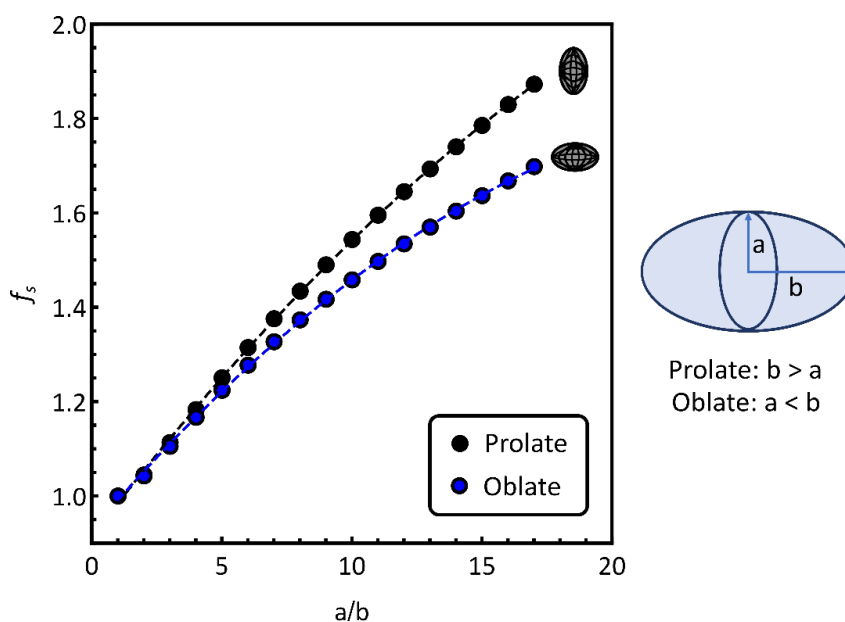
Figure 8.1.2 The dependence of f_s shape factor according to Perrin's equations for prolate and oblate molecules.

Second, solvent systems are neither infinitely dilute nor a continuum fluid. A continuum fluid is one where the discrete molecules of the fluid are neglected, and the solvent can be thought of as a uniform substance throughout. Real solvents, being small molecules themselves, have various geometries and are not infinitely small compared to the solute. Therefore, the interactions between the solvents and solutes also contribute to the friction. It was proposed that, for small molecules, the denominator of the Stokes-Einstein equation could be $6\pi\eta r_H$ for a stick boundary and $4\pi\eta r_H$ for a non-stick, or slip, boundary, as shown in Equation 8.1.7 and Equation 8.1.8.

$$Stick - boundary\ condition\ D = \frac{kT}{6\pi\eta r_H}$$

Equation 8.1.7

$$Slip - boundary\ condition\ D = \frac{kT}{4\pi\eta r_H}$$

Equation 8.1.8

Instead of using either 4 or 6, corresponding to the slip or stick boundaries, the equation proposed by Sutherland (Equation 8.1.9)[278] introduced a numerical factor that depends on the radius ratio of the solute and solvent, β. When β is zero, the denominator reduces to 4; when β approaches infinity, the denominator approaches 6, reproducing the Stoke-Einstein equation.

$$D = \frac{kT}{6\pi\eta r_H}\left(\frac{\beta r_H + 3\eta}{\beta r_H + 2\eta}\right)$$

Equation 8.1.9

An improved model for variable solvent friction factor was derived by Gierer and Wirtz (Equation 8.1.10), based on micro friction theory[279]. Here α is defined as the ratio of the radius of the solute to that of the solvent. When the solvent and solute are the same size, f_{GW} reduces from 6 to 3. This model was also empirically re-derived by Chen and Chen by fitting with experimental data, giving Equation 8.1.11[254].

$$f_{GW} = \left(\frac{3\alpha}{2} + \frac{1}{1+\alpha}\right)^{-1} where, \alpha = \frac{r_s}{r}$$

Equation 8.1.10

$$f_{Chen} = (1 + 0.695a^{2.234})^{-1}$$

Equation 8.1.11

As the shape factors are ignored and all molecules are also assumed to be spherical. The hydrodynamic radius of the solute can be re-written based on the assumption that all molecules are spherical and have the same effective density. The average effects of flexibility and solvation factors that are otherwise impossible to include can be approximated by an effective density of the solute molecules. A set of experimental diffusion coefficient measured at 25 °C, for 109 combinations of 44 solutes and 5 common solvents was used to calculate an effective density, ρ_{eff} = 627 kg m^{-3} [221, 222].

Combining these three simplifications results in the Stokes-Einstein-Gierer-Wirtz-Estimation (SEGWE) (Equation 8.1.12) which links the diffusion coefficient obtained at a given temperature to the solute and solvent molecular weights through a single parameter ρ_{eff}.[221, 222, 280] This approach simplifies α, the ratio of the solvent and solute radii, required in the Geier-Wirtz friction to the cube root of the ratio of the solvent and solute molecular weights.

$$D = \frac{k_B T\left(\frac{3\alpha}{2} + \frac{1}{1+\alpha}\right)}{6\pi\eta\sqrt[3]{\frac{3MW}{4\pi\rho_{eff}N_A}}} \quad where, \alpha = \frac{r_s}{r} = \sqrt[3]{\frac{MW_s}{MW}}$$

Equation 8.1.12

8.2 Development of SEGWE Model for Mixed Solvents

Diffusion coefficients strongly depend on the temperature of the system. Firstly, the temperature affects the thermal energy of the system. If the system has more energy, the faster the solute will diffuse through the solution. Secondly, the solvent viscosity also depends on the temperature. A fluid is a substance with no fixed shape and can be easily deformed. Viscosity refers to a fluid's resistance to flow. A fluid with low viscosity will have less resistance to flow, meaning it will flow easier and quicker, and vice versa. For example, water has a lower viscosity than honey; therefore, water flows easier and quicker than honey. The temperature dependence of viscosity can be described by an Arrhenius-like equation known as Andrade's Equation (Equation 8.2.1)[281, 282]. The parameters *a* and *b* can be found for a given solvent by plotting the logarithm of viscosity against the reciprocal of temperature. These Arrhenius parameters have been collated for common deuteriated and protiated solvents in Evans *et al*.[221]

$$\eta = ae^{\frac{b}{T}}$$

Equation 8.2.1

The SEGWE model is a good estimation of diffusion coefficients of small molecules in a solvent with viscosity at a given temperature. Neither general power law nor SEGWE methods are designed to handle samples containing mixed solvents. There are various prediction models for viscosity in literature. Most of these are useful descriptions for pure liquids. However, there is surprisingly little consensus on predicting the viscosity of mixed liquids. This is complicated due to non-ideal mixing and intermolecular forces such as hydrogen bonding. Mixing fluids with different viscosities changes the viscosity of the whole system; therefore, it would be useful to accurately predict the viscosities of a mixture, enabling the prediction of diffusion coefficients of solutes in mixed solvents.

Several equations for the calculation of viscosities of mixtures have been proposed. There are two main types: those containing interaction parameters and those without. The equations containing the interactive parameter tend to be more accurate; however, this parameter is usually determined using experimental results and is entirely empirical.

One of the most commonly used empirical equations without an interactive parameter is the Kendall-Monroe equation (Equation 8.2.2)[283, 284], where the equation describes the viscosity of the mixed solvent $\eta_{1,2}$ as the weighted average of the cube-root viscosities of the pure liquid. $\eta_{1,2}$ is the viscosity of the mixed system, x_1 is the molar fraction of

component 1, η_1 is the viscosity of component 1, x_2 is the molar fraction of component 2 and η_2 is the viscosity of component 2. The equation was developed to analyse binary liquid mixtures with zero adjustable parameters. However, this equation has little meaningful theoretical substantiation.

$$\eta_{1,2}^{1/3} = x_1\eta_1^{1/3} + x_2\eta_2^{1/3}$$

Equation 8.2.2

Other models used to calculate the viscosity of mixed solvents include physical properties such as densities of the pure component, as shown in Equation 8.2.3[285, 286]. Typically, this equation is used for salt solutions in water. x_1 and x_2 are the volume concentrations of the two pure substances in the mixture, ρ_1 and ρ_2 are their densities and η_1 and η_2 are their viscosities.

$$\eta_{1,2} = \frac{x_1\rho_1 + \rho_2 x_2}{x_1\dfrac{\rho_1}{\eta_1} + x_2\dfrac{\rho_2}{\eta_2}}$$

Equation 8.2.3

A mixing rule for viscosity was originally proposed by Eyring, subsequently updated by Nissan and Grunberg (Equation 8.2.4)[287, 288]. The Nissan-Grunberg model is functionally similar to the mixing rule derived by Arrhenius, where an additional interactive term can be added to the equation for a more accurate prediction[289]. The term is usually experimentally determined.

$$ln\,(\eta_{1,2}) = x_1 ln\,(\eta_1) + x_2 ln\,(\eta_2)$$

Equation 8.2.4

Many chemical processes are carried out in various solvent mixtures. The diffusion behaviour of molecules in mixed solutions is still poorly understood. The following section will explore how mixed solvents, thus mixed viscosities affect the diffusion coefficients of a solute. The simplest mixture is a mix of deuteriated and protiated solvents such as deuterium oxide and water. Mixed protiated-deuteriated solvents are commonly used in the NMR study of proteins. The viscosity-modified model will be tested with a number of proteins in various composition of water and deuterium oxide. However, proteins further complicate matters as they can exhibit a range of structures, from the highly structured to the intrinsically disordered.

8.3 Experimental

Unless otherwise specified, all data was collected at the Department of Chemistry Instrumentation Facility (DCIF) at Massachusetts Institute of Technology. All DOSY measurements were carried out on a 600 MHz Bruker AVANCE NEO spectrometer, using a 5mm helium-cooled QCI-F cryoprobe equipped with a *z*-gradient coil producing

241

a calibrated maximum gradient of 55.37 G cm^{-1}. The gradients were calibrated using the standards and method of Holz and Weingartner[230]. Temperature calibration was done with both methanol-d_4 and ethylene glycol[228, 290].

All DOSY data was acquired using a stimulated echo NMR pulse sequence with bipolar pulsed field echoes and longitudinal eddy current delay[291], with additional excitation sculpting used to suppress the solvent signals[292, 293]. In total, diffusion coefficients of five different globular, monomeric proteins with molecular weights ranging from 6500 to *ca.* 66500 g mol^{-1} were acquired.

Table 8.3.1 summarises all proteins studied in this work with their molecular weights.

Table 8.3.1 Summary of proteins studied and their molecular weights.

Protein	Molecular weight g mol^{-1}
aprotinin	6500
ubiquitin	8579
lysozyme	14307
myoglobin	16700
bovine serum albumin (BSA)	66463

Data were acquired using 16 gradients, incremented in equal steps of gradient squared. These arrays ranged from 5% to 95% of the maximum for aprotinin, ubiquitin, myoglobin and BSA at all temperatures, and lysozyme at both 298.15 K and 310.15 K. For lysozyme data sets at 278.15 K, 283.15 K and 288.15 K, the gradients ranged from 2 % to 98 % of the maximum. All diffusion-encoding gradients used smoothed square shaped pulses, with a gradient shape factor of 0.9. Experiment timing parameters, Δ and δ, are summarised in Table 8.3.2. Data was processed using GNAT[294], using a Lorentzian line broadening of 10 Hz. Peaks between 0.5-1.5 ppm (alkyl region) and 6.5-7.5 ppm (aromatic region) were used to obtain the diffusion coefficients, and the largest error from the region was reported. The error in width of peak is calculated based on the fit of the data to the Stejskal-Tanner Equation (Equation 2.4.3). The diffusion coefficients of the alkyl region and aromatic region do not differ significantly. This can be seen in the DOSY spectra. All DOSY spectra for all protein samples, at all sample temperatures and for all sample compositions can be found in Appendix 5.

B.Tang, PhD Thesis, Aston University, 2024.

Table 8.3.2 Summary of experimental parameters.

Sample(s)	Δ (s)	δ (s)
0.4 mM lysozyme at 273.15 K	0.1	0.0055
0.4 mM lysozyme at 293.15 K	0.1	0.0050
0.4 mM lysozyme at 288.15 K	0.1	0.0045
0.4 mM lysozyme at 298.15 K	0.1	0.0035
0.4 mM lysozyme at 310.15 K	0.1	0.0030
0.4 mM aprotinin at 298.15 K	0.1	0.0030
0.4 mM ubiquitin at 298.15 K	0.1	0.0030
0.4 mM myoglobin at 298.15 K	0.1	0.0035
0.4 mM BSA at 298.15 K	0.1	0.0045
0.2 mM lysozyme at 298.15 K	0.1	0.0035
0.4 mM lysozyme at 298.15 K	0.1	0.0035
0.8 mM lysozyme at 298.15 K	0.1	0.0035
1.6 mM lysozyme at 298.15 K	0.1	0.0035
3.2 mM lysozyme at 298.15 K	0.1	0.0035

8.4 Results and Discussion

The diffusion coefficients of lysozyme in different aqueous solvent compositions at temperatures ranging from 273.15 to 310.15 K were measured using diffusion-ordered spectroscopy. A summary of the diffusion coefficients of lysozyme in various solvent compositions and at different temperatures is shown in Figure 8.4.1. All DOSY spectra of lysozyme corresponding to the data in Figure 8.4.1 can be found in Appendix 5. As the temperature increases, there is an increase in the thermal energy of the system; molecules move quicker, the solvent becomes less viscous and the diffusion coefficient increases. In 0:100 $H_2O:D_2O$, the diffusion coefficient was 0.53×10^{-10} m^2s^{-1} at 273.15 K compared to 1.40×10^{-10} m^2s^{-1} at 310.15 K. The diffusion coefficient of lysozyme also increases with an increase in the percentage of water. In 0:100 $H_2O:D_2O$ the diffusion coefficient was found to be 0.53×10^{-10} m^2s^{-1} compared to 0.70×10^{-10} m^2s^{-1} in 90:10 $H_2O:D_2O$ at 273.15 K.
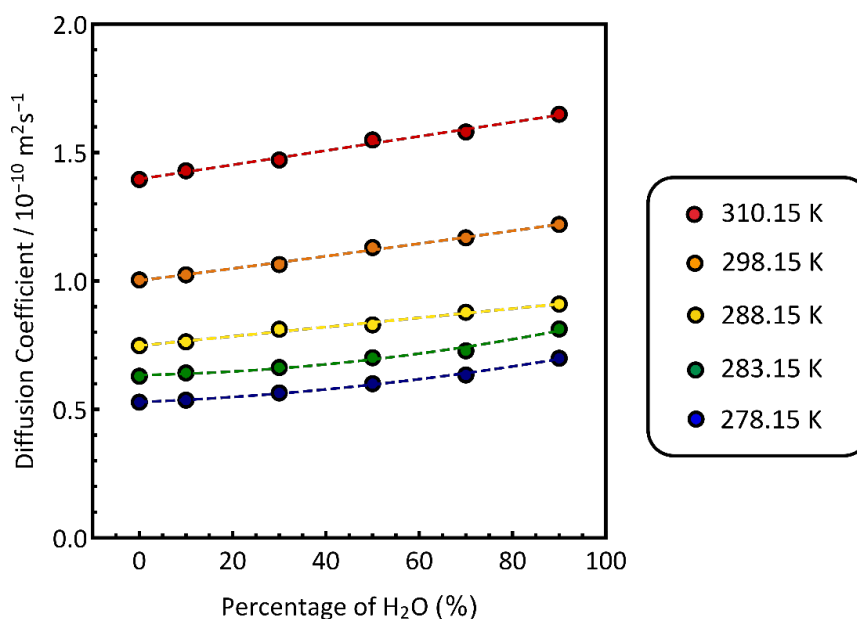
Figure 8.4.1 Measured diffusion coefficient of 1 mM lysozyme at temperatures ranging from 273.15 - 310.15 K, with a range of solvent compositions 90:10 $H_2O:D_2O$, 70:30 $H_2O:D_2O$, 50:50 $H_2O:D_2O$, 30:70 $H_2O:D_2O$, 10:90 $H_2O:D_2O$.

While the effect of deuteriation on solvents may sometimes be overlooked, it will affect the solvent viscosity. The effect of deuteriation on the solvent viscosity depends on two factors: the number of protons per molecule replaced by a heavier isotope and the role of hydrogen bonding in the liquid[295]. The viscosity of liquids at a given temperature can be calculated using Andrade's equation (Equation 8.2.1). Figure 8.4.2 shows that H_2O (protiated solvent) and D_2O (deuteriated solvent) not only have different viscosities, differing by ca. 25% at room temperature, but these viscosities also have different temperature dependencies. This is also true for other protiated solvents and their deuteriated counterparts (see Appendix 5.2). Figure 8.4.3 shows the ratio between the viscosity of the protiated solvents and their deuteriated counterpart at various temperatures. The viscosity ratios $\left(\frac{\eta_H}{\eta_D}\right)$ are not 1: there are differences between the protiated and deuteriated.
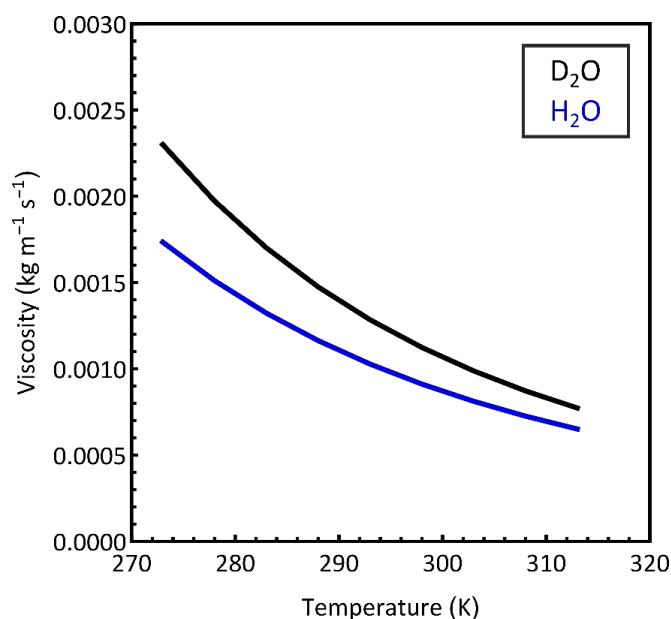
Figure 8.4.2 Viscosity of H_2O (blue) and D_2O (black) at temperatures from 275 to 315 K, calculated using Andrade's equation.
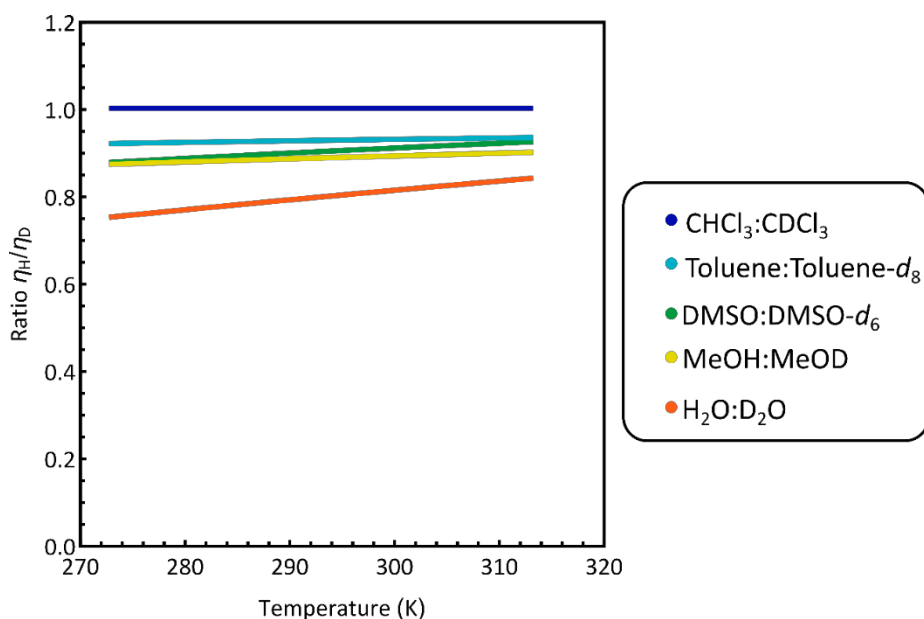
Figure 8.4.3 Ratio of viscosities of protiated solvents and their deuteriated counter parts.

All three models from Equation 8.4.1 to Equation 8.4.3 were combined with Andrade's equation (Equation 8.2.1) for predicting the viscosity of mixed solvents. This enables the prediction of viscosities of solvent mixtures using the Arrhenius-like parameters *a* and *b* of both pure components. All three models predicted similar viscosities for solvent mixtures of H_2O:D_2O; this is shown in Figure 8.4.4, the percentage difference between

245

the Kendall-Monroe (cubic) equation and the Nissan-Grunberg model, and Figure 8.4.5, the percentage difference between the density equation and the Nissan-Grunberg model. Both graphs show that the prediction of viscosities is very similar, with less than 0.3% difference. However, looking at the final forms of the combined equations is instructive. The Kendall-Monroe equation (Equation 8.4.1) requires cubing, which will introduce a number of additional terms. The rearrangement of Equation 8.4.2 also introduces additional terms based on the solvent density. The Nissan-Grunberg model (Equation 8.4.3) keeps the form of Andrade's equation. For the aqueous system studied here, it has been assumed that the liquids will mix ideally, and the interactive parameter can be ignored. The Nissan-Grunberg model was chosen for the present study as it is the simplest model and the final form is intuitive. However, when liquids do not mix ideally the interactive parameter can used. Note that adding a simple additive interaction parameter to Equation 8.2.4 results in a multiplication e^A where A is the interactive parameter, increasing or decreasing the viscosity compared to ideal mixing.

$$\eta_{1,2}^{1/3} = x_1 a_1^{1/3} e^{\frac{b_1}{3T}} + x_2 a_2^{1/3} e^{\frac{b_2}{3T}}$$

Equation 8.4.1

$$\eta_{1,2} = \frac{x_1 \rho_1 + \rho_2 x_2}{x_1 \frac{\rho_1}{(a_1 e^{\frac{b_1}{T}})} + x_2 \frac{\rho_2}{(a_2 e^{\frac{b_2}{T}})}}$$

Equation 8.4.2

$$\eta_{1,2} = a_1^{x_1} a_2^{x_2} e^{(\frac{x_1 b_1 + x_2 b_2}{T})}$$

Equation 8.4.3
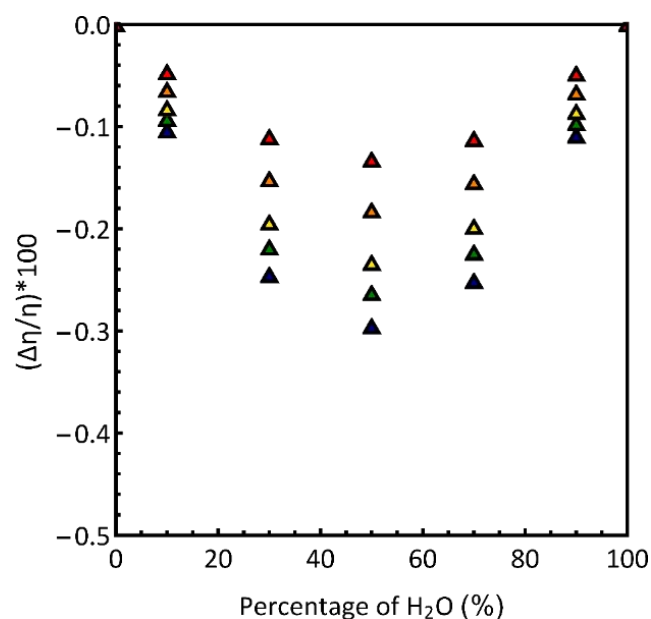
Figure 8.4.4 Percentage differences (($\eta_{GN} - \eta_{KM}/\eta_{GN}$)×100) in estimates of viscosity, calculated using the Kendall-Monroe (cubic) and the Grunberg-Nissan equations, for mixed $H_2O{:}D_2O$ solvents, at temperatures between 273 and 310 K.
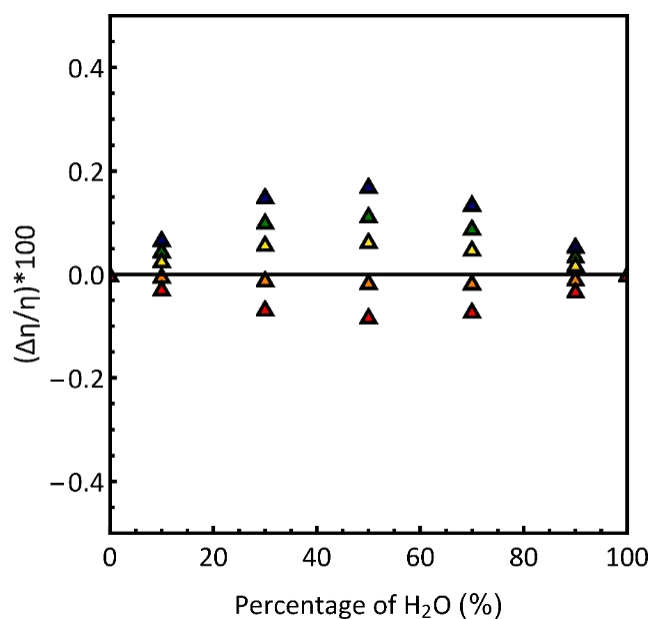
Figure 8.4.5 Percentage differences $\left(\left(\eta_{GN} - \eta_{density}/\eta_{GN}\right)×100\right)$ in estimates of viscosity, calculated using the density and the Grunberg-Nissan equations, for mixed $H_2O{:}D_2O$ solvents, at temperatures between 273 and 310 K.

Even though the radii of H_2O and D_2O can be reasonably assumed to be the same, they still influence the Gierer-Wirtz friction term. Without the Gierer-Wirtz friction term, simply combining the Stokes-Einstein equation with the mixed viscosity model, the diffusion

247

coefficients are underestimated. The estimated diffusion coefficients by the Stokes-Einstein equation and modified SEGWE for mixed solvents are shown in Figure 8.4.6. Overall, Figure 1.4.6 (b) shows fitting of experimental diffusion coefficients against estimated diffusion coefficients for 0.4 mM of lysozyme at various temperatures ranging from 273.15 to 310.15 K and a range of solvent compositions. Overall, the modified SEGWE equation for mixed solvents was able to accurately predict the diffusion coefficient of lysozyme, with an $R^2 = \sqrt{0.9996}$. We propose a model that can predict the diffusion coefficients of proteins based on their molecular weight, solvent composition, and sample temperature.

$$D = \frac{k_B T \left(\frac{3\alpha}{2} + \frac{1}{1+\alpha}\right)}{6\pi\eta \sqrt[3]{\frac{3MW}{4\pi\rho_{eff}N_A}}} \quad \text{where, } \alpha = \frac{r_s}{r} = \sqrt[3]{\frac{MW_s}{MW}} \text{ and}$$

Equation 8.4.4

$$\eta_{1,2} = a_1^{x_1} a_2^{x_2} e^{\left(\frac{x_1 b_1 + x_2 b_2}{T}\right)}$$

(a)   (b)
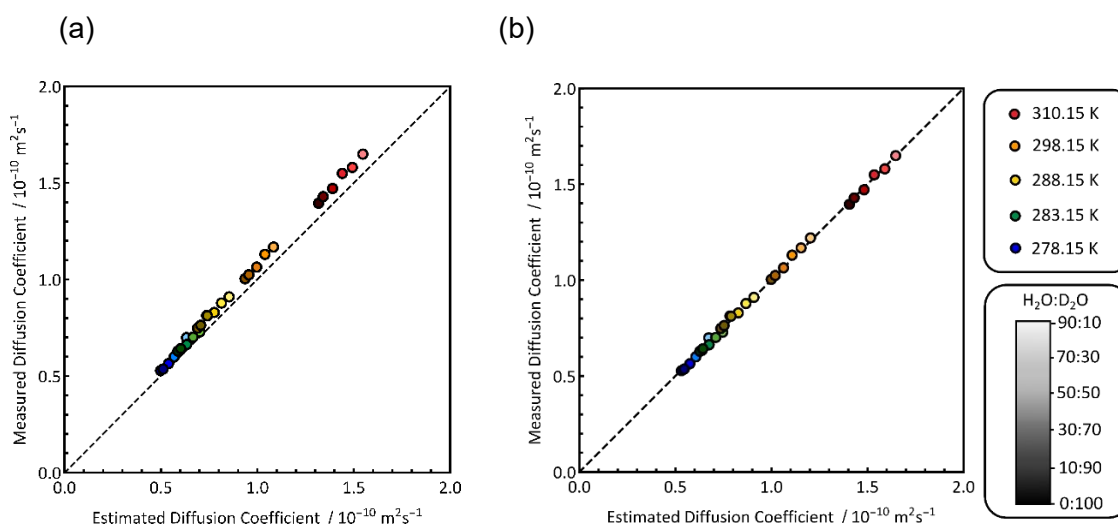
Figure 8.4.6 Measured diffusion coefficients plotted against estimated diffusion coefficient for 0.4 mM lysozyme at temperatures ranging from 273.15 - 310.15 K, with a range of solvent compositions 90:10 H_2O:D_2O, 70:30 H_2O:D_2O, 50:50 H_2O:D_2O, 30:70 H_2O:D_2O, 10:90 H_2O:D_2O, 0:100 H_2O:D_2O where 90:10 H_2O:D_2O is the lightest shade and 0:100 H_2O:D_2O is the darkest shade. (a) Stokes-Einstein equation with viscosity modifications for mixed solvent (b) SEGWE equation with viscosity modifications for mixed solvent.

To further test the extended SEGWE model, diffusion coefficients were acquired for 4 other proteins, aprotinin, ubiquitin, myoglobin and BSA, at the same temperature (298.15 K) in different aqueous compositions. These proteins were chosen as they exhibit a range of molecular weights. Figure 8.4.7 shows the plots of the experimental diffusion coefficients versus those predicted using the extended SEGWE method. The extended

B.Tang, PhD Thesis, Aston University, 2024.

SEGWE equation accurately predicted the diffusion coefficient of ubiquitin, lysozyme and myoglobin. The SEGWE method performs well with an RMS error 4.4%. While the proteins were chosen as a representative set of monomeric, globular proteins, both aprotinin and BSA diffusion coefficients were underestimated using the extended SEGWE model. This could result from the shapes the protein adopts in solution. Deviations from a spherical globular protein, result in greater friction and lower diffusion coefficients than expected.
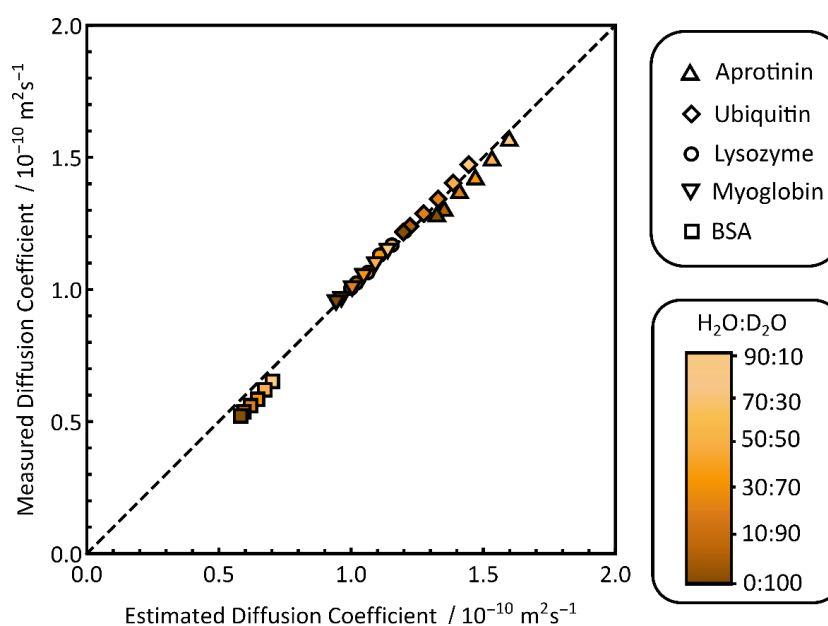
Figure 8.4.7 Measured diffusion coefficients plotted against calculated using the mixed viscosity modified SEGWE equation for various proteins at 298.15 K, with a range of solvent compositions 90:10 $H_2O:D_2O$, 70:30 $H_2O:D_2O$, 50:50 $H_2O:D_2O$, 30:70 $H_2O:D_2O$, 10:90 $H_2O:D_2O$, where 90:10 $H_2O:D_2O$ is the lightest shade and 10:90 $H_2O:D_2O$ is the darkest shade.

Two concentration-dependent factors will reduce the experimentally acquired diffusion coefficient. Firstly, proteins can aggregate in solution, forming larger species. Secondly, at high enough concentrations, the proteins present an inaccessible volume fraction of the sample and obstruct each other as they diffuse. The volume fraction of the solute can be related to the molecular weight, *MW*, a molar concentration C_M in a solvent with density *ρ,* the volume fraction can be estimated using Equation 8.4.5.[296] The volume fractions of lysozyme at various concentrations have been calculated and presented in

Table 8.4.1.

$$\phi = \frac{C_M M}{\rho + C_M M}$$

Equation 8.4.5

Table 8.4.1 The concentration and calculated volume fraction of the lysozyme.

Concentration (mM)	Φ
3.2	0.0439
1.6	0.0224
0.8	0.0114
0.4	0.0057
0.2	0.0029

The diffusion coefficient of molecules that aggregate can be calculated using the Einstein-Sutherland equation (Equation 8.4.6). The concentration dependent term does not change in $\left(\frac{\partial \ln \gamma}{\partial \ln c}\right)$, therefore, this term tends to zero. And thus, multiplied by essentially the Stokes-Einstein equation (kT/f). Since Φ for the different concentrations are very small for all likely concentration and certainly those used here, the effect on D will also be very small. Even for a 3.2 mM solution the (1− Φ) would be 0.9561, therefore, the estimated diffusion coefficient would be about *ca*. 5% lower. Therefore, for proteins at low concentrations the obstruction effect should have little affect the diffusion coefficient.

$$D = \frac{kT}{f}\left(1 + \frac{\partial \ln \gamma}{\partial \ln c}\right)(1 - \phi)$$

Equation 8.4.6

To experimentally confirm how the concentration of proteins affect the volume in space, the diffusion coefficients of lysozyme with concentrations from 0.2 mM to 3.2 mM were measured at 298.15 K, with solvent composition 90:10 H_2O:D_2O. All measurements with error were within the predicted diffusion coefficient of 1.205×10^{-10} m^2s^{-1}, as shown in Figure 8.4.8. Therefore, at low concentrations of proteins, the obstruction effect on the theoretically and experimentally determined diffusion coefficient is negligible. However, the possibility of obstruction should be considered if the protein solutions are concentrated.
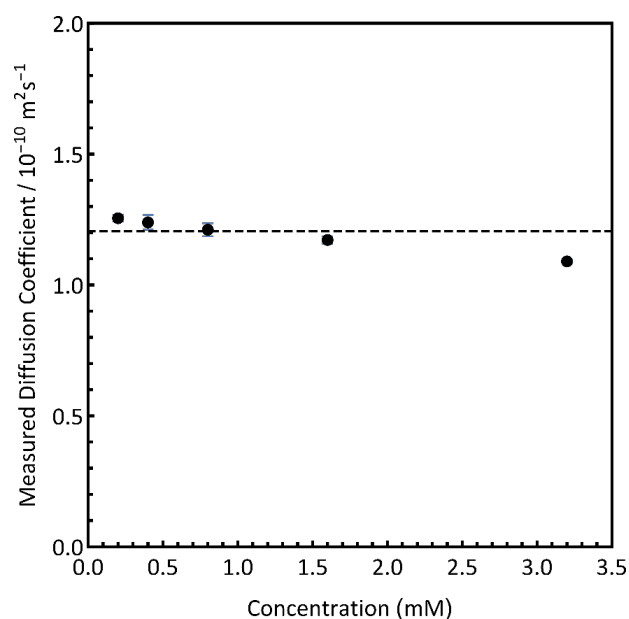
Figure 8.4.8 Concentration of lysozyme plotted against the measure diffusion coefficient. The diffusion measurements were at 298.15 K and the solvent composition is 90:10 $H_2O:D_2O$. The dashed line is the predicted diffusion coefficient in these conditions is 1.205×10^{-10} m^2s^{-1}.

A final assessment of the extended SEGWE method how well it can answer common relevant questions. The measurement of protein diffusion coefficients provides an important insight into their folding state in solution and function. Globular proteins, such as the set of five proteins used earlier in this work, have well-defined, compact structures which will be closer to the spherical approximation. On the other hand, intrinsically disordered proteins or IDPs lack order in their three-dimensional form. Their structure is more closely related to synthetic polymers than globular proteins. IDPs can be fully unstructured or only partially structured. Less tightly packed molecules will affect the shape and volume in space, reducing the experimental diffusion coefficient. The extended SEGWE model was applied to various proteins and IDPs with a range of molecular weights. All data presented in Figure 8.4.9 was provided by Dudás et al.[297]. The experimental diffusion coefficients of globular proteins (black) and IDP (blue) plotted against the calculated diffusion coefficients using the viscosity modified SEGWE model. The figure indicates that the extended SEGWE model, Equation 8.4.4, can distinguish between globular proteins close to the spherical approximation and IDP structurally closer to a synthetic polymer.
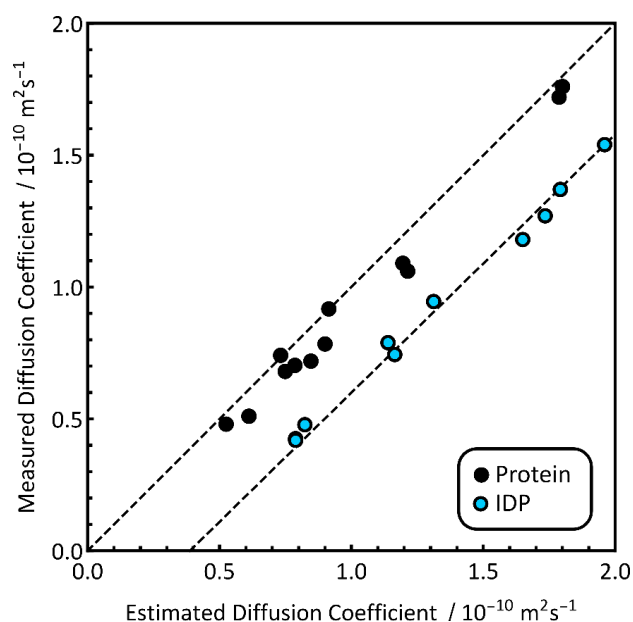
Figure 8.4.9 Measure diffusion coefficients of globular proteins (black) and intrinsically disordered proteins (blue) plotted against calculated using the mixed viscosity modified SEGWE equation for various IDP at 287 K in H_2O. Diffusion data from literature Dudás et al.[297]

8.5 Conclusion and Further Work

8.5.1 Conclusion

Diffusion coefficients have been used to provide information on size, shape and envoironment of molecules. One approach is the Stokes-Einstein model which works well for larger molecules. Combining the Stokes-Einstein equation with the well-established Gierer-Wirtz modification results in the SEGWE model which can accurately predict the diffusion coefficients of small molecules at a given temperature in a singular solvent. In this work, appropriate modifications to the viscosity term in the SEGWE equation enable a starting point for estimating diffusion coefficients of molecules in mixed protiated-deuteriated solvents. For this preliminary study of how mixed solvents effect the diffusion coefficient of moleucles, proteins were chosen as their size would minimise the effects of the Gierer-Wirtz term in the SEGWE equation. For an H_2O:D_2O solvent system, this extended SEGWE model effectively estimates diffusion coefficients for globular proteins. The equation is suitable for proteins at low concentrations where the obstruction effects of high macromolecule concentrations are minimal. At higher concentrations, these should be considered. The proposed model is accurate enough to solve chemical problems. When applied to IDPs of various molecular weights, it was observed that the prediction of diffusion coefficients was overestimated. Biomolecules such as proteins have various parameters contributing to the self-diffusion coefficient.

B.Tang, PhD Thesis, Aston University, 2024.

One such parameter is their shape and configuration, i.e. folded or non-folded. This can also vary depending on the environment and solvent conditions. The two states can be distinguished by using the SEGWE equation modified for mixed solvent systems. This allows users to understand if their protein has successfully folded, i.e. when estimation and measurement are similar, or if there is an unexpected physical or chemical change, such as aggregation or disordered protein, where the predicted diffusion coefficients are over-estimated. The solvent system (pyridine and $CDCl_3$) for the derivatisation methods in previous chapters not only are different in viscosity, but also in size and shape. Overall, this work acts as a foundation and starting point in order to understand the diffusion of molecules in mixed solvents.

8.5.2 Further Work

To expand the model further, the following future work has been proposed:

1. **Understanding the impact of different solute shapes**. The Perrin shape factors play an important role in solute-solvent friction. Systems studied should have solutes with similar or the same molecular weights but different shapes in an ideally mixed or pure solvent.

2. **Understanding how two differently-sized solvents contribute to the Gierer-Wirtz friction term**. To study this, mixed solvent systems consisting of two solvents with similar viscosity but different radii should be investigated. For example, toluene-d_8 and methanol-d_4 have similar viscosities where the viscosity ratio is closer to 1. The radii for toluene-d_8 and methanol-d_4 are 3.99×10^{-10} m^2s^{-1} and 2.84×10^{-10} m^2s^{-1} respectively.

3. **Understanding the impact of non-ideal mixing**. The simple solvent system here mixes nearly ideally. Other mixed solvent systems will not. To study this, mixed solvent systems consisting of solvents of broadly the same shape and size but very different viscosity and vice-versa will need to be studied. For example, it is known that water and DMSO have a non-linear mixing relationship.

CHAPTER 9 : CONCLUSION AND FURTHER WORKS

The overall aim of this thesis has been to develop multinuclear and multidimensional NMR tools to characterise pyrolysis oils and complex mixtures.

Biomass could be a potential source of sustainable, renewable fuel. However, with the increasing demand for agricultural land for food, there may be better alternatives to growing crops for fuel. The brewing industry generates waste in the form of Brewer's Spent Grains (BSG), which is utilised mostly for animal feed. This offers an opportunity to get a low-cost and readily available source of biomass. BSG can be thermally converted into pyrolysis oil, also known as bio-oil. Pyrolysis oils are often not suitable for direct use as fuel, mainly due to their acidic nature. The acidity of pyrolysis oils is mostly due to oxygen-containing compounds. As a result, improved knowledge and understanding of the chemical compositions of BSG pyrolysis oil is critical for future storage, ageing and upgrading. However, pyrolysis oils are complex mixtures and difficult to analyse using current techniques. NMR methods are chemically specific and can be quantitative. However, there are still challenges in simplifying the spectra acquired and improving the spectral resolution.

Prior to developing novel NMR techniques to characterise pyrolysis oils. the department purchased a new 500 MHz spectrometer, and its performance needed to be assessed. Temperature stability and gradient strengths are parameters that can affect the accuracy and precision of NMR measurements, particularly, for diffusion measurements. Chapter 3 describes how to calibrate temperature for both the Bruker iProbe and the diffusion probe. The temperature was measured using a *d*-methanol thermometer probe, revealing that the real sample temperature differed from the temperature stated on the spectrometer. The gradient strength calibration constant for the iProbe was also adjusted to ensure experimental diffusion coefficients were similar to that of literature values. A set of appropriate molecular liquids and a ^{13}C diffusion experiment based on a DEPT pulsed-field spin echo sequence was used to calibrate the gradient strengths of the diffusion probe to compensate for the larger gradient strengths.

Developing new analytical techniques will enable a better understanding of the chemical compositions of pyrolysis oil. Chapter 4 details how, for the first time, low-field NMR was used to quantify the amount of carbonyl groups in four pyrolysis oils produced from different feedstocks. The derivatisation of carbonyl groups using 4-

255

(trifluoromethyl)phenyl hydrazine was used to effectively tag carbonyl-containing compounds in pyrolysis oils, allowing them to be detected using ^{19}F NMR spectroscopy. Low-field NMR proves able to distinguish between different fluorine environments and therefore, able to distinguish between different carbonyl groups that have been tagged with fluorine-containing compounds. A comprehensive chemical shift map was produced using derivatised model compounds. Overall, low-field ^{19}F NMR estimates of the total carbonyl content but also provide accurate chemical information on the different types of carbonyl-containing compounds present. This is a clear advantage of the NMR approach. In addition, low-field spectrometers have some additional advantages. They are typically compact, requiring minimal laboratory space. They are cheaper, often require less technical maintenance and do not require cryogens, making NMR techniques more accessible to a wider range of users, particularly smaller research laboratories and institutions.

Developing renewable fuels have many challenges to overcome, one of the major issues is understanding the products produced from the pyrolysis process. The complex nature of these pyrolysis oils makes them very difficult to analyse. It is extremely important to understand what is present in these fuels to decide on the treatment process or upgrading techniques required. Current analytical techniques have various limitations therefore it is important to innovate new techniques to combat these issues. Overall, these novel NMR methods developed combination with existing methods will provide important information charectering pyrolysis oils.

Further works:

- Using Global Spectral Deconvolution for the estimation of integrals in the regions of interest such as aldehydes, ketones and quinones.
- Identify other derivatisation agents to further improve the resolution of ^{19}F NMR signals.
- Improve spectral resolution by developing pulse sequences such as ^{19}F DOSY.

Hydroxyl groups are an oxygen-containing groups that also contributes to the oil's acidity. ^{1}H NMR struggles to distinguish between various hydroxyl groups in the sample. The derivatisation of hydroxyl groups using 2-chloro-4,4,5,5-tetramethyl-1,3,2-

dioxaphospholane was used to effectively tag carbonyl-containing compounds in pyrolysis oils, allowing them to be detected using ^{31}P NMR spectroscopy. To reduce the crowding of the spectrum, the use of ^{31}P{^{1}H} NMR for qualitative and quantitative analysis is explored in Chapter 5. A bi-level WALTZ-16 composite decoupling pulse was chosen to minimise spectral artefacts that arise from compounds with larger coupling constants. An inverse gated ^{31}P sequence was used to acquire quantitative data. ^{31}P NMR was used to identify different alcohols present and quantify the amount of alcohol in four hand sanitisers. The alcohol content estimated by ^{31}P NMR were also compared to labels on the sample as well as more traditional methods such as oxidation followed by redox titration. Overall, ^{31}P NMR estimates of the total hydroxyl content but also provide accurate chemical information on the different types of hydroxyl-containing compounds present.

Even though ^{31}P NMR methods in Chapter 5 significantly simplifies the spectrum easing analysis, it can still be difficult to identify species based on chemical shifts and multiplicity analysis alone. This was seen in two of hand sanitiser samples from the previous chapter, where it was inconclusive whether the peak at 145.1 ppm belonged to 2-propanol or 2-butanol or other secondary alcohol. Another way to separate signals further is using pulsed field gradient techniques, such as diffusion NMR, which separates signals in the diffusion domain. In Chapter 6, novel ^{31}P DOSY pulse sequences were written and evaluated. Parameters such as convection, can directly and significantly affect the measured diffusion coefficients, were also explored. It was found that thick-walled NMR tubes were insufficient to compensate for the effects of convection in very convective liquids such as $CDCl_3$. Therefore, ^{31}P convection compensated sequences were written and successfully implemented. Quantitative chemical information such as molecular weight can be inferred using power law methods where internal calibrants are used to generate a calibration curve. The molecular weight of unknown alcohols can then be estimated, using the power law generated. This sequence was applied to four hand sanitisers studied in Chapter 5; the additional information acquired allowed for unknown species in the hand sanitiser samples to be identified.

Further works:

- Current diffusion experiments require 20 hours to acquire data however, the signal-to-noise ratio is still relatively low for some peaks, therefore address the limitation of signal-to-noise.

- Better choice of internal calibrants with a wider molecular weight range and check that they aren't involved in chemical exchange with other species present. The main issues with the current internal calibrants, first, TMDP concentration can vary from sample to sample depending on how much had been used up and second, second, the derivatised NHND degrades over time.

- Apply ^{31}P DOSY techniques to other model oils and real oils.

- An extensive library/ machine learning of diffusion data for the compounds in bio-oil can be produced for a rapid and precise way to characterise bio-oil samples.

- Once these protocols are developed, they can be implemented on NMR software or as standalone packages.

In Chapter 7, Brewers' Spent Grains were used as a feedstock to produce pyrolysis oil using both slow and fast pyrolysis. The BSG pyrolysis oils were characterised using wet chemistry and novel spectroscopy techniques. The pH of the pyrolysis oils was studied, it was found that BSG pyrolysis oils had pH ca. pH 5 to 6, which are less acidic compared to other pyrolysis oils produced from other biomasses in literature, typically pH 2 to 3. The water content of organic phases of the pyrolysis oils was low, where slow pyrolysis oil contained *ca*. 2.43 % water, and fast pyrolysis oil contained *ca*. 27.08 % water. BSG slow pyrolysis overall contained less oxygen compared to fast pyrolysis based on elemental analysis data. Both pyrolysis oils contained small amounts of oxygen-containing species characterised using GC/MS however the major limitation is that not all of the oil can be analysed. NMR revealed the amounts of different oxygen-containing species, the overall concentrations of hydroxyl and carbonyl containing species, alcohols, acids, ketones, and aldehydes were concordant with the lower oxygen content in slow pyrolysis oils. These properties all suggest the promising viability of Brewers' Spent Grains as a feedstock for fuel replacements, fuel additives or upgrading to added-value chemicals. Notably, the low acidity suggests the BSG pyrolysis oils can be used directly as fuel for boilers and the low oxygen content will reduce the needs for upgrading.

Further works:

Physiochemical analysis of feedstock.

- Lignocellulose content
- CHNS/O
- Moisture content

Comprehensive study of the BSG pyrolysis oils produced.

- Heating Values – the amount of heat released during the combustion of pyrolysis oils.
- TAN (Total acid number) – the quantity of KOH required to neutralise the acid component.
- Flash Point – the minimum temperature at which a liquid gives ff vapour at a sufficient concentration to for an ignitable mixture with air.

Diffusion NMR spectroscopy can be used to obtain quantitative information such as molecular weights of species. Chapter 6 explores one way to quantitatively interpret diffusion coefficient information using power-laws generated based on internal calibrants. An alternative method is the Stokes-Einstein Gierer-Writz (SEGWE) has been developed to simplify the complex relationship between diffusion coefficient and molecular mass, enabling the estimation of diffusion coefficients in a pure solvent of a molecule based on the molecular weight. In Chapter 9, the SEGWE equation was extended to handle mixed aqueous solvents by appropriate modification to the viscosity term, combining Andrade's equation and the Grunberg-Nissan mixing rule. It was shown to successfully estimate the diffusion coefficients of both globular proteins and intrinsically disordered proteins, in a wide range of mixed protiated–deuteriated aqueous solvents at a range of temperatures. This allows for confirmation or estimation of protein molecular mass and proves capable of distinguishing unstructured proteins from their globular counterparts. This acts as a starting point in developing a suitable, general, equation for handling diffusion coefficient in mixed solvents, such as those used in derivatisation reactions earlier in the thesis (pyridine and $CDCl_3$). The extension to mixed solvents will only further increase the scope and range of use of the method.

Further works:

General approach for Extend the SEGWE to handle mixed solvents:

- Understanding the impact of different solute shapes.
- Understanding how two differently sized solvents contribute to the Gierer-Wirtz friction term.
- Understanding the impact of non-ideal mixing.

Overall, these novel analytical methods developed combination with existing methods will provide important information on the composition of pyrolysis oils.

REFERENCES

1. V.f Manieniyan, M. Thambidurai and R. Selvakumar, *Proceedings of SHEE*, **2009**, *10*, pp.2234-3689.
2. V. Quaschning, **2014**, *Understanding Renewable Energy Systems*, Routledge.
3. Zohuri, B, **2017**, *Hybrid Energy Systems: Driving Reliable Renewable Sources of Energy Storage*. Springer.
4. T. B. Johansson, K. McCormick, L. Neij and W. C. Turkenburg, *In Renewable Energy, Routledge*, **2012**, pp.15-47.
5. Y. M. Bar-On, R. Phillips and R. Milo, *Proceedings of the National Academy of Sciences*, **2018**, *115*, pp.6506-6511.
6. B. Kumar and P. Verma, *Fuel*, **2021**, *288*, pp.119622.
7. V. I. Popa, **2018** *In Biomass as renewable raw material to obtain bioproducts of high-tech value*, Elsevier.
8. J. Barber, *Chemical Society Reviews*, **2009**, *38*, pp.185-196.
9. J. Popp, S. Kovács, J. Oláh, Z. Divéki and E. Balázs, *New Biotechnology*, **2021**, *60*, 76-84.
10. R. K. Srivastava, N. P. Shetti, K. R. Reddy, E. E. Kwon, M. N. Nadagouda and T. M. Aminabhavi, *Environmental Pollution*, **2021**, *276*, pp.116731.
11. E. Dahlquist, **2013**, *Technologies for Converting Biomass to Useful Energy: Combustion, Gasification, Pyrolysis, Torrefaction and Fermentation*, CRC Press.
12. T. Y. Fahmy, Y. Fahmy, F. Mobarak, M. El-Sakhawy and R. E. Abou-Zeid, *Environment, Development and Sustainability*, **2020**, *22*, pp.17-32.
13. M. Balat, M. Balat, E. Kırtay and H. Balat, *Energy Conversion and Management*, **2009**, *50*, pp.3158-3168.
14. M. Balat, M. Balat, E. Kırtay and H. Balat, *Energy Conversion and Management*, **2009**, *50*, pp.3147-3157.
15. P. Basu, J. Butler and M. A. Leon, *Renewable Energy*, **2011**, *36*, pp.282-288.
16. R. K. Srivastava, N. P. Shetti, K. R. Reddy and T. M. Aminabhavi, *Science of The Total Environment*, **2020**, *722*, pp.137927.
17. P. Basu, **2018**, *Biomass gasification, pyrolysis and torrefaction: practical design and theory*, Academic press.
18. D. Vamvuka, I*nternational Journal of Energy Research*, **2011**, *35*, pp.835-862.
19. S. D. Stefanidis, K. G. Kalogiannis, E. F. Iliopoulou, C. M. Michailof, P. A. Pilavachi and A. A. Lappas, *Journal of Analytical and Applied Pyrolysis*, **2014**, *105*, pp.143-150.
20. G. Meshitsuka and A. Isogai, **2017**, *In Chemical Modification of Lignocellulosic Materials*, Routledge.
21. A. Heredia, A. Jiménez and R. Guillén, *Zeitschrift für Lebensmittel-Untersuchung und Forschung*, **1995**, *200*, pp. 24-31.
22. S.S. Maleki, K. Mohammadi, A. Movahedi, F. Wu, and K.S. Ji, *Frontiers in Plant Science*, **2020**,*11*, pp.492374
23. V. I. Popa and J. Spiridon, **1998**, *Polysaccharides: Structural Diversity and Functional Versatility*. Marcel Dekker.
24. C. E. Wyman, S. R. Decker, M. E. Himmel, J. W. Brady, C. E. Skopec and L. Viikari, **2005**, *Polysaccharides: Structural Diversity and Functional Versatility*, Marcel Dekker.
25. R. Katahira, T. J. Elder and G. T. Beckham, **2018**, *Lignnin Valorization*, RSC.
26. J. Zakzeski, P. C. A. Bruijnincx, A. L. Jongerius and B. M. Weckhuysen, *Chemical Reviews*, **2010**, *110*, pp.3552-3599.
27. H. Wang, J. Male and Y. Wang, *ACS Catalysis*, **2013**, *3*, pp.1047-1070.
28. M. N. Belgacem and A. Gandini, **2011**, *Monomers, polymers and composites from renewable resources*, Elsevier.
29. W. Schutyser, T. Renders, G. Van den Bossche, S. Van den Bosch, S. F. Koelewijn, T. Ennaert and B. F. Sels, **2017**, *Nanotechnology in Catalysis: Applications in the Chemical Industry, Energy Development, and Environment Protection*, Wiley.
30. A. O. Balogun, F. Sotoudehniakarani and A. G. McDonald, J*ournal of Analytical and Applied Pyrolysis*, **2017**, *127*, pp8-16.
31. S. Wunderlich and W. Back, **2009**, *in Beer in health and disease prevention*, Elsevier.
32. D. E. Briggs, **2004**, *Brewing: science and practice*, Woodhead Publishing.
33. L. Nyhan, A. W. Sahin, H. H. Schmitz, J. B. Siegel and E. K. Arendt, *Journal of Agricultural and Food Chemistry*, **2023**, *71*, pp.10543-10564.

34. R. Willaert, **2007**, *Handbook of food products manufacturing*, Wiley.
35. M. Mosher, K. Trantham, M. Mosher and K. Trantham, **2021**, B*rewing Science: A Multidisciplinary Approach*, Springer.
36. R. Lordan, E. O'Keeffe, A. Tsoupras and I. Zabetakis, *Foods*, **2019**, *8*, pp.171.
37. S. I. Mussatto, *Journal of the Science of Food and Agriculture*, **2014**, *94*, pp.1264-1275.
38. M. Jackowski, Ł. Niedźwiecki, K. Jagiełło, O. Uchańska and A. Trusek, *Biomolecules*, **2020**, *10*, pp.1669.
39. D.-S. Tang, G.-M. Yin, Y.-Z. He, S.-Q. Hu, B. Li, L. Li, H.-L. Liang and D. Borthakur, *Biochemical Engineering Journal*, **2009**, *48*, pp.1-5.
40. N. G. Meneses, S. Martins, J. A. Teixeira and S. I. Mussatto, *Separation and Purification Technology*, **2013**, *108*, pp.152-158.
41. C. Xiros, E. Topakas, P. Katapodis and P. Christakopoulos, *Bioresource Technology*, **2008**, *99*, pp.5427-5435.
42. S. I. Mussatto and I. C. Roberto, *Journal of the Science of Food and Agriculture*, **2005**, *85*, pp.2453-2460.
43. O. Kanauchi, K. Mitsuyama and Y. Araki, *Journal of the American Society of Brewing Chemists*, **2001**, *59*, pp.59-62.
44. C. Xiros and P. Christakopoulos, *Waste and Biomass Valorization*, **2012**, *3*, pp.213-232.
45. S. Öztürk, Ö. Özboy, İ. Cavidoğlu and H. Köksel, *Journal of the Institute of Brewing*, **2002**, *108*, pp.23-27.
46. T. Stahn, R. Storandt, S. Grebenteuch, S. Rohn, D. May, C. Dolsdorf and D. Pleissner, *Sustainability*, **2023**, *15*, pp.13774.
47. N. Ishiwaki, H. Murayama, H. Awayama, O. Kanauchi and T. Sato, *Technical Quarterly-Master Brewers Association of the Americas*, **2000**, *37*, pp.261-265.
48. W. Russ, H. Mörtel and R. Meyer-Pittroff, *Construction and Building Materials*, **2005**, *19*, pp.117-126.
49. S. Liang and C. Wan, *Bioresource Technology*, **2015**, *182*, pp.179-183.
50. S. Wilkinson, K. A. Smart, S. James and D. J. Cook, *Bioenergy Research*, **2017**, *10*, pp.146-157.
51. J. A. Dávila, M. Rosenberg and C. A. Cardona, *AIMS Agriculture and Food*, **2016**, *1*, pp.52-66.
52. J. Buffington, **2014**, *Advances in Chemical Engineering and Science*, Scrip.
53. A. S. Mahmood, J. G. Brammer, A. Hornung, A. Steele and S. Poulston, *Journal of Analytical and Applied Pyrolysis*, **2013**, *103*, pp.328-342.
54. L. D. Borel, A. M. Reis Filho, T. P. Xavier, T. S. Lira and M. A. Barrozo, *Biomass and Bioenergy*, **2020**, *140*, pp.105698.
55. D. Yu, Y. Sun, W. Wang, S. F. O'Keefe, A. P. Neilson, H. Feng, Z. Wang and H. Huang, *International Journal of Food Science & Technology*, **2020**, *55*, pp.357-368.
56. K. M. Lynch, E. J. Steffen and E. K. Arendt, *Journal of the Institute of Brewing*, **2016**, *122*, pp.553-568.
57. E. El-Shafey, M. Gameiro, P. Correia and J. De Carvalho, *Separation Science and Technology*, **2004**, *39*, pp.3237-3261.
58. G. Terefe, *CABI Agriculture and Bioscience*, **2022**, *3*, pp.1-8.
59. S. Aliyu and M. Bala, *African Journal of Biotechnology*, **2011**, *10*, pp.324-331.
60. B. Biswas, N. Pandey, Y. Bisht, R. Singh, J. Kumar and T. Bhaskar, *Bioresource Technology*, **2017**, *237*, pp.57-63.
61. T. Kan, V. Strezov and T. J. Evans, *Renewable and Sustainable Energy Reviews*, **2016**, *57*, pp.1126-1140.
62. V. Dhyani and T. Bhaskar, **2019**, *In Biofuels: Alternative Feedstocks and Fonversion Processes For The Production of Liquid and Gaseous Biofuels*, Elsevier.
63. A. Demirbas and G. Arin, *Energy Sources*, **2002**, *24*, pp.471-482.
64. D. Neves, H. Thunman, A. Matos, L. Tarelho and A. Gómez-Barea, *Progress in Energy and Combustion Science*, **2011**, *37*, pp.611-630.
65. D. Chen, K. Cen, X. Zhuang, Z. Gan, J. Zhou, Y. Zhang and H. Zhang, *Combustion and Flame*, **2022**, *242*, pp.112142.
66. A. Singh, S. Nanda and F. Berruti, **2020**, *Biorefinery of Alternative Resources: Targeting Green Fuels and Platform Chemicals*, Springer.
67. F. H. Isikgor and C. R. Becer, *Polymer Chemistry*, **2015**, *6*, pp.4497-4559.
68. A. Shaw, X. Zhang, L. Kabalan and J. Li, *Fuel*, **2021**, *286*, p119444.

69. C. L. Waters, R. R. Janupala, R. G. Mallinson and L. L. Lobban, *Journal of Analytical and Applied Pyrolysis*, **2017**, *126*, pp.380-389.
70. G. Dorez, L. Ferry, R. Sonnier, A. Taguet and J.-M. Lopez-Cuesta, *Journal of Analytical and Applied Pyrolysis*, **2014**, *107*, pp.323-331.
71. M. Ramiah, *Journal of Applied Polymer Science*, **1970**, *14*, pp.1323-1337.
72. H. Yang, R. Yan, H. Chen, D. H. Lee and C. Zheng, *Fuel*, **2007**, *86*, pp.1781-1788.
73. E. Adler, *Industrial & Engineering Chemistry*, **1957**, *49*, pp.1377-1383.
74. R. Parthasarathi, R. A. Romero, A. Redondo and S. Gnanakaran, *The Journal of Physical Chemistry Letters*, **2011**, *2*, pp.2660-2666.
75. N. Giummarella, Y. Pu, A. J. Ragauskas and M. Lawoko, *Green Chemistry*, **2019**, *21*, pp.1573-1595.
76. J. Li, X. Bai, Y. Fang, Y. Chen, X. Wang, H. Chen and H. Yang, *Combustion and Flame*, **2020**, *215*, pp.1-9.
77. X. Bai and K. H. Kim, **2016**, *Production of Biofuels and Chemicals from Lignin*, Springer.
78. L. Fan, Y. Zhang, S. Liu, N. Zhou, P. Chen, Y. Cheng, M. Addy, Q. Lu, M. M. Omar and Y. Liu, *Bioresource Technology*, **2017**, *241*, pp.1118-1126.
79. S. S. Wong, R. Shu, J. Zhang, H. Liu and N. Yan, *Chemical Society Reviews*, **2020**, *49*, pp.5510-5560.
80. H. A.-H. Ibrahim, **2020**, *Recent Advances in Pyrolysis*, InTechOpen.
81. S. Al Arni, *Renewable Energy*, **2018**, *124*, pp.197-201.
82. R. Jenkins, A. Sutton and D. Robichaud, **2016**, *in Biofuels for Aviation*, Elsevier.
83. K. O. Albrecht, M. V. Olarte and H. Wang, **2019**, T*hermochemical Processing of Biomass: Conversion into Fuels*, *Chemicals and Power*, Wiley.
84. S. Giacobbe, A. Piscitelli, F. Raganati, V. Lettera, G. Sannia, A. Marzocchella and C. Pezzella, *Biotechnology for Biofuels*, **2019**, *12*, pp.1-8.
85. L. D. Borel, T. S. Lira, J. A. Ribeiro, C. H. Ataíde and M. A. Barrozo, *Industrial Crops and Products*, **2018**, *121*, pp.388-395.
86. S. Ferreira, E. Monteiro, P. Brito, C. Castro, L. Calado and C. Vilarinho, *Energies*, **2019**, *12*, pp.912.
87. M. del Mar Contreras, A. Lama-Muñoz, J. M. Romero-García, M. García-Vargas, I. Romero and E. Castro, 2021, in Waste Biorefinery, Elsevier.
88. G. d. C. Gonçalves, P. K. Nakamura, D. F. Furtado and M. T. Veit, J*ournal of Cleaner Production*, **2017**, *168*, pp.908-916.
89. A. Lorente, J. Remón, V. L. Budarin, P. Sánchez-Verdú, A. Moreno and J. H. Clark, *Energy Conversion and Management*, **2019**, *185*, pp.410-430.
90. Y. Yang, J. Brammer, M. Ouadi, J. Samanya, A. Hornung, H. Xu and Y. Li, *Fuel*, **2013**, *103*, pp.247-257.
91. Y. Xu, X. Hu, W. Li and Y. Shi, *Progress in Biomass and Bioenergy Production*, **2011**, pp.197-222.
92. M. J. Groom, E. M. Gray and P. A. Townsend, *Conservation Biology*, **2008**, *22*, pp.602-609.
93. F. Cheng, H. Luo, J. D. Jenkins and E. D. Larson, *Applied Energy*, **2023**, 331, pp.120388.
94. Q. Zhang, J. Chang, T. Wang and Y. Xu, *Energy Conversion and Management*, **2007**, *48*, pp.87-92.
95. X. Hu and M. Gholizadeh, *Renewable and Sustainable Energy Reviews*, **2020**, *134*, pp.110124.
96. Y. M. Isa and E. T. Ganda, *Renewable and Sustainable Energy Reviews*, **2018**, *81*, pp.69-75.
97. F. Stankovikj, A. G. McDonald, G. L. Helms and M. Garcia-Perez, *Energy & Fuels*, **2016**, *30*, pp.6505-6524.
98. M. D. G. de Luna, L. A. D. Cruz, W.-H. Chen, B.-J. Lin and T.-H. Hsieh, *Energy*, **2017**, *141*, pp.1416-1428.
99. M. Bertero, G. de la Puente and U. Sedran, *Fuel*, **2012**, *95*, pp.263-271.
100. D. Özçimen and F. Karaosmanoğlu, *Renewable Energy*, **2004**, *29*, pp.779-787.#
101. S. Beis, Ö. Onay and Ö. Koçkar, *Renewable Energy*, **2002**, *26*, pp.21-32.
102. J. A. Ramirez, R. J. Brown and T. J. Rainey, *Energies*, **2015**, *8*, pp.6765-6794.
103. A. Oasmaa and S. Czernik, *Energy & Fuels*, **1999**, *13*, 914-921.
104. J. Ancheyta and J. G. Speight, 2007, *Hydroprocessing of Heavy Oils and Residual*, CRC Press.

B.Tang, PhD Thesis, Aston University, 2024.

105.   A. H. Zacher, M. V. Olarte, D. M. Santosa, D. C. Elliott and S. B. Jones, *Green Chemistry*, **2014**, *16*, pp.491-515.
106.   H. J. Park, J.-K. Jeon, D. J. Suh, Y.-W. Suh, H. S. Heo and Y.-K. Park, *Catalysis Surveys from Asia*, **2011**, *15*, pp.161-180.
107.   Z. Tang, Q. Lu, Y. Zhang, X. Zhu and Q. Guo, *Industrial & Engineering Chemistry Research*, **2009**, *48*, pp.6923-6929.
108.   C. Xu and T. Etcheverry, *Fuel*, **2008**, *87*, pp.335-345.
109.   J.-P. Cao, X.-Y. Zhao, K. Morishita, L.-Y. Li, X.-B. Xiao, R. Obara, X.-Y. Wei and T. Takarada, *Bioresource Technology*, **2010**, *101*, pp.4242-4245.
110.   A. Ross, P. Biller, M. Kubacki, H. Li, A. Lea-Langton and J. Jones, *Fuel*, **2010**, *89*, pp.2234-2243.
111.   M. Ikura, M. Stanciulescu and E. Hogan, *Biomass and Bioenergy*, **2003**, *24*, pp.221-232.
112.   L. Ciddor, J. A. Bennett, J. A. Hunns, K. Wilson and A. F. Lee, *Journal of Chemical Technology & Biotechnology*, **2015**, *90*, pp.780-795
113.   P. K. Kanaujia, Y. Sharma, U. Agrawal and M. Garg, *TrAC Trends in Analytical Chemistry*, **2013**, *42*, pp.125-136.
114.   M. Staš, M. Auersvald, L. Kejla, D. Vrtiška, J. Kroufek and D. Kubička, *TrAC Trends in Analytical Chemistry*, **2020**, *126*, pp.115857.
115.   L. K. Park, J. Liu, S. Yiacoumi, A. P. Borole and C. Tsouris, *Fuel*, **2017**, *200*, pp.171-181.
116.   S. Black and J. R. Ferrell III, *Energy & Fuels*, **2016**, *30*, pp.1071-1077.
117.   A. H. Bennett and F. Donovan, *Analyst*, **1922**, *47*, pp.146-152.
118.   J. D. Adjaye, R. K. Sharma and N. N. Bakhshi, *Fuel Processing Technology*, **1992**, *31*, pp.241-256.
119.   A. Oasmaa, B. Van De Beld, P. Saari, D. C. Elliott and Y. Solantausta, *Energy & Fuels*, **2015**, *29*, pp.2471-2484.
120.   J. R. Ferrell III, M. V. Olarte, E. D. Christensen, A. B. Padmaperuma, R. M. Connatser, F. Stankovikj, D. Meier and V. Paasikallio, *Biofuels, Bioproducts and Biorefining*, **2016**, *10*, pp.496-507.
121.   E. Lazzari, T. Schena, M. C. A. Marcelo, C. T. Primaz, A. N. Silva, M. F. Ferrao, T. Bjerk and E. B. Caramao, *Industrial Crops and Products*, **2018**, *111*, pp.856-864.
122.   L. Zhou, Z.-M. Zong, S.-R. Tang, Y. Zong, R.-L. Xie, M.-J. Ding, W. Zhao, X.-F. Zhu, Z.-L. Xia and L. Wu, *Energy Sources, Part A: Recovery, Utilization, and Environmental Effects*, **2009**, *32*, pp.370-375.
123.   B. Scholze and D. Meier, J*ournal of Analytical and Applied Pyrolysis*, **2001**, *60*, pp.41-54.
124.   A. Fullana, J. A. Contreras, R. C. Striebich and S. S. Sidhu, *Journal of Analytical and Applied Pyrolysis*, **2005**, *74*, pp.315-326.
125.   T. Sfetsas, C. Michailof, A. Lappas, Q. Li and B. Kneale, *Journal of Chromatography A*, **2011**, *1218*, pp.3317-3325.
126.   O. Faix, D. Meier and I. Fortmann, *Holz als Roh-und Werkstoff*, **1990**, *48*, pp.351-354.
127.   M. Vlasiou and C. Drouza, *Analytical Methods*, **2015**, *7*, pp.3680-3684.
128.   K. David, M. Kosa, A. Williams, R. Mayor, M. Realff, J. Muzzy and A. Ragauskas, *Biofuels*, **2010**, *1*, pp.839-845.
129.   N. Hao, H. Ben, C. G. Yoo, S. Adhikari and A. J. Ragauskas, *Energy & fuels*, **2016**, *30*, pp.6863-6880.
130.   E. M. Purcell, H. C. Torrey and R. V. Pound, *Physical Review*, **1946**, *69*, pp.37.
131.   F. Bloch, *Physical Review*, **1946**, *70*, pp460.
132.   J. T. Arnold, S. Dharmatti and M. Packard, *The Journal of Chemical Physics*, **1951**, *19*, pp.507-507.
133.   T. D. Claridge, 2016, High-Resolution NMR Techniques in Organic Chemistry, Elsevier.
134.   W. Proctor and F. Yu, *Physical Review*, 1**950**, *77*, pp.717.
135.   W. Pauli, *Zeitschrift für Physik*, **1927**, *43*, pp.601-623.
136.   S. Goudsmit and G. Uhlenbeck, *Physica*, **1926**, *6*, pp.273-290.
137.   M. A. Bernstein, K. F. King and X. J. Zhou, 2004, Handbook of MRI pulse sequences, Elsevier.
138.   I. C. Felli and B. Brutscher, *ChemPhysChem*, **2009**, *10*, pp.1356-1368.
139.   H. Schwalbe, *Angewandte Chemie (International ed. in English)*, **2017**, *56*, pp.10252-10253.

140. E. Moser, E. Laistler, F. Schmitt and G. Kontaxis, *Frontiers in Physics*, **2017**, *5*, pp.33.
141. D. Park, Y. H. Choi and Y. Iwasa, *IEEE Transactions on Applied Superconductivity*, **2019**, *29*, pp.1-5.
142. O. Kirichek, P. Carr, C. Johnson and M. Atrey, *Review of Scientific Instruments*, **2005**, *76*, pp.055104.
143. M. Grootveld, B. Percival, M. Gibson, Y. Osman, M. Edgar, M. Molinari, M. L. Mather, F. Casanova and P. B. Wilson, *Analytica Chimica Acta*, **2019**, *1067*, pp.11-30.
144. H.-Y. Yu, S. Myoung and S. Ahn, *Magnetochemistry*, **2021**, *7*, pp.121.
145. L. Ingram, D. Mohan, M. Bricka, P. Steele, D. Strobel, D. Crocker, B. Mitchell, J. Mohammad, K. Cantrell and C. U. Pittman Jr, *Energy & Fuels*, **2008**, *22*, pp.614-625.
146. J. Joseph, C. Baker, S. Mukkamala, S. H. Beis, M. C. Wheeler, W. J. DeSisto, B. L. Jensen and B. G. Frederick, *Energy & Fuels*, **2010**, *24*, pp.5153-5162.
147. C. A. Mullen, G. D. Strahan and A. A. Boateng, *Energy & Fuels*, **2009**, *23*, pp.2707-2718.
148. N. Ozbay, A. E. Pütün and E. Pütün, *International Journal of Energy Research*, **2006**, *30*, pp.501-510.
149. J. Zhang, G. Wang and S. Xu, *Carbon Resources Conversion*, **2020**, *3*, pp.130-139.
150. Q. Wang, D. Cui, P. Wang, J. Bai, Z. Wang and B. Liu, *Fuel*, **2018**, *211*, pp.341-352.
151. F. Ateş, E. Pütün and A. E. Pütün, *Journal of Analytical and Applied Pyrolysis*, **2004**, *71*, pp.779-790.
152. N. S. Tessarolo, R. V. Silva, G. Vanini, A. Casilli, V. L. Ximenes, F. L. Mendes, A. de Rezende Pinho, W. Romão, E. V. de Castro and C. R. Kaiser, *Journal of Analytical and Applied Pyrolysis*, **2016**, *117*, pp.257-267.
153. K. Smets, P. Adriaensens, J. Vandewijngaarden, M. Stals, T. Cornelissen, S. Schreurs, R. Carleer and J. Yperman, *Journal of Analytical and Applied Pyrolysis*, **2011**, *90*, pp.100-105.
154. F. Dalitz, A. Steiwand, K. Raffelt, H. Nirschl and G. Guthausen, *Energy & Fuels*, **2012**, *26*, pp.5274-5280.
155. M. H. Levitt, R. Freeman and T. Frenkiel, *Journal of Magnetic Resonance (1969)*, **1982**, *47*, pp.328-330.
156. A. Shaka, J. Keeler and R. Freeman, *Journal of Magnetic Resonance (1969)*, **1983**, *53*, pp.313-340.
157. A. Shaka, P. B. Barker and R. Freeman, *Journal of Magnetic Resonance (1969)*, **1985**, *64*, pp.547-552.
158. P. Giraudeau and E. Baguet, *Journal of Magnetic Resonance*, **2006**, *180*, pp.110-117.
159. H. Ben and A. J. Ragauskas, *Bioresource Technology*, **2013**, *147*, pp.577-584.
160. L. Negahdar, A. Gonzalez-Quiroga, D. Otyuskaya, H. E. Toraman, L. Liu, J. T. Jastrzebski, K. M. Van Geem, G. B. Marin, J. W. Thybaut and B. M. Weckhuysen, *ACS Sustainable Chemistry & Engineering*, **2016**, *4*, pp.4974-4985.
161. M. Carrier, M. Windt, B. Ziegler, J. Appelt, B. Saake, D. Meier and A. Bridgwater, *ChemSusChem*, **2017**, *10*, pp.3212-3224.
162. M. R. Bendall and D. T. Pegg, J*ournal of Magnetic Resonance (1969)*, **1983**, *53*, pp.272-296.
163. D. Doddrell, D. Pegg and M. R. Bendall, *Journal of Magnetic Resonance (1969)*, **1982**, *48*, pp.323-327.
164. J. M. Dereppe and C. Moreaux, *Fuel*, **1985**, *64*, pp.1174-1176.
165. R. Wang, Y. Luo, H. Jia, J. R. Ferrell and H. Ben, *RSC Advances*, **2020**, *10*, pp.25918-25928.
166. G. D. Strahan, C. A. Mullen and A. A. Boateng, *Energy & Fuels*, **2011**, *25*, pp.5452-5461.
167. L. Zhang and G. Gellerstedt, *Magnetic Resonance in Chemistry*, **2007**, *45*, pp.37-45.
168. R. Samuel, Y. Pu, B. Raman and A. J. Ragauskas, Applied Biochemistry and Biotechnology, **2010**, *162*, pp.62-74.
169. A. Salanti, L. Zoia, M. Orlandi, F. Zanini and G. Elegir, Journal of Agricultural and Food Chemistry, **2010**, *58*, 10049-10055.
170. C. Qu, T. Kishimoto, M. Kishino, M. Hamada and N. Nakajima, *Journal of Agricultural and Food Chemistry*, **2011**, *59*, pp.5382-5389.
171. Y. Yu, Y. W. Chua and H. Wu, *Energy & Fuels*, **2016**, *30*, pp.4145-4149.
172. M. Fortin, M. Mohadjer Beromi, A. Lai, P. C. Tarves, C. A. Mullen, A. A. Boateng and N. M. West, *Energy & Fuels*, **2015**, *29*, pp.8017-8026.

173. H. Ben and A. J. Ragauskas, *Energy & Fuels*, **2011**, *25*, pp.5791-5801.
174. C.-L. Chen and D. Robert, *Methods in Enzymology*, **1988**, *161*, pp.137-174.
175. F. Stankovikj, A. G. McDonald, G. L. Helms, M. V. Olarte and M. Garcia-Perez, *Energy & Fuels*, **2017**, *31*, pp.1650-1664.
176. O. Faix, B. Andersons and G. Zakis, *Holzforschung*, **1998**, *52*, pp.268-274.
177. W.-J. Liu, X.-S. Zhang, Y.-C. Qv, H. Jiang and H.-Q. Yu, *Green Chemistry*, **2012**, *14*, pp.2226-2233.
178. E. Adler, G. Brunow and K. Lundquist, *Holzforschung*, **1987**, *41*, pp,199-207.
179. E. A. Capanema, M. Y. Balakshin and J. F. Kadla, *Journal of Agricultural and Food Chemistry*, **2004**, *52*, pp.1850-1860.
180. M. Balakshin and E. Capanema, *Journal of Wood Chemistry and Technology*, **2015**, *35*, pp.220-237.
181. D. R. Robert and G. Brunow, *Holzfordchung*, **1984**, *38*, pp.85-90.
182. P. Sleevi, T. Glass and H. Dorn, *Analytical Chemistry*, **1979**, *51*, pp.1931-1934.
183. M. Barrelle, *Holzforschung*, **1993**, *47*, pp.261-267.
184. C. Heitner, D. Dimmel and J. Schmidt, **2016**, *Lignin and Lignans: Advances in Chemistry*, CRC press.
185. S. L. Manatt, *Journal of the American Chemical Society*, **1966**, *88*, pp.1323-1324.
186. J. K. Kenny, J. W. Medlin and G. T. Beckham, A*CS Sustainable Chemistry & Engineering*, **2023**, *11*, pp.5644-5655.
187. W. D. Brittain and S. L. Cobb, *Organic & Biomolecular Chemistry*, **2019**, *17*, pp.2110-2115.
188. W. Glasser, S. Drew and P. Hall, *Annual Reports on Fermentation Processes*, **1980**, *4*, pp.67-103.
189. A. Lindner and G. Wegener, *Journal of Wood Chemistry and Technology*, **1988**, *8*, pp.323-340.
190. J.C. Fernandes, **1994**. *Modifications structurales apportées à la lignine lors de la cuisson kraft et des stades de blanchiment des pâtes papetières* (Doctoral dissertation, Grenoble INPG).
191. R. Sevillano, G. Mortha, M. Barrelle and D. Lachenal, *Holzforschung*, **2001**, *55*, pp.286-295.
192. F. Huang, S. Pan, Y. Pu, H. Ben and A. J. Ragauskas, *RSC Advances*, **2014**, *4,* pp.17743-17747.
193. S. Constant, C. S. Lancefield, B. M. Weckhuysen and P. C. A. Bruijnincx, *ACS Sustainable Chemistry & Engineering*, **2016**, *5,* pp.965-972.
194. L. Saikia, J. M. Baruah and A. J. Thakur, Organic and Medicinal Chemistry Letters, **2011**, *1*, pp.1-6.
195. L. D. Quin, **2000**, *A Guide to Organophosphorus Chemistry*, John Wiley & Sons.
196. A. Wroblewski, C. Lensink, R. Markuszewski and J. Verkade, *Energy & Fuels*, **1988**, *2*, pp.765-774.
197. M. Nagy, B. J. Kerr, C. J. Ziemer and A. J. Ragauskas, *Fuel*, **2009**, *88*, pp.1793-1797.
198. A. Zwierzak, *Canadian Journal of Chemistry*, **1967**, *45*, pp.2501-2512.
199. D. Argyropoulos, *Research on Chemical Intermediates*, **1995**, *21*, pp373.
200. Y. Archipov, D. Argyropoulos, H. Bolker and C. Heitner, *Journal of Wood Chemistry and Technology*, **1991**, *11*, pp.137-157.
201. D. S. Argyropoulos, H. I. Bolker, C. Heitner and Y. Archipov, Journal of Wood Chemistry and Technology, **1993**, *13*, pp.187-212.
202. D. S. Argyropoulos, H. I. Bolker, C. Heitner and Y. Archipov, *Holzforschung-International Journal of the Biology, Chemistry, Physics and Technology of Wood*, **1993**, *47*, pp.50-56.
203. D. S. Argyropoulos and C. Heitner, *Holzforschung-International Journal of the Biology, Chemistry, Physics and Technology of Wood*, **1994**, *48*, pp.112-116.
204. 2D. S. Argyropoulos, *Journal of Wood Chemistry and Technology*, **1994**, *14*, pp.45-63.
205. D. S. Argyropoulos, *Journal of Wood Chemistry and Technology*, **1994**, *14*, pp.65-82.
206. Y. Pu, S. Cao and A. J. Ragauskas, *Energy & Environmental Science*, **2011**, *4*, pp.3154-3166.
207. P. Korntner, I. Sumerskii, M. Bacher, T. Rosenau and A. Potthast, *Holzforschung*, **2015**, *69*, pp.807-814.
208. A. Granata and D. S. Argyropoulos, *Journal of Agricultural and Food Chemistry*, **1995**, *43*, pp.1538-1544.

209. X. Meng, C. Crestini, H. Ben, N. Hao, Y. Pu, A. J. Ragauskas and D. S. Argyropoulos, *Nature Protocols*, **2019**, *14*, pp.2627-2647.
210. Z. Wu, H. Ben, Y. Yang, Y. Luo, K. Nie, W. Jiang and G. Han, *RSC Advances*, **2019**, *9*, pp.27157-27166.
211. M. Zawadzki and A. Ragauskas, *Holzforschung*, **2001**, *55*, pp.283-285.
212. H. Ben and J. R. Ferrell III, *RSC Advances*, **2016**, *6*, pp.17567-17573.
213. M. Mazur and D. Argyropoulos, *Cellulose Chemistry and Technology*, **1995**, *29*, pp.589-601.
214. P. Sannigrahi, A. J. Ragauskas and S. J. Miller, *BioEnergy Research*, **2008**, *1*, pp.205-214.
215. S. Christophoridou and P. Dais, *Journal of Agricultural and Food Chemistry*, **2006**, *54*, pp.656-664.
216. J. F. Araneda, I. W. Burton, M. Paleologou, S. D. Riegel and M. C. Leclerc, *Canadian Journal of Chemistry*, **2022**, *100*, pp.799-808.
217. A. Einstein, *Annalen der Physik*, **1905**, *4*, pp.549-560.
218. E. O. Stejskal and J. E. Tanner, *The Journal of Chemical Physics*, **1965**, *42*, pp.288-292.
219. C. S. Johnson Jr, *Progress in Nuclear Magnetic Resonance Spectroscopy*, **1999**, *34*, pp.203-256.
220. C. A. Mullen, G. D. Strahan and A. A. Boateng, *ACS Sustainable Chemistry & Engineering*, **2019**, *7*, pp.19951-19960.
221. R. Evans, G. Dal Poggetto, M. Nilsson and G. A. Morris, *Analytical Chemistry*, **2018**, *90*, pp.3987-3994.
222. R. Evans, Z. Deng, A. K. Rogerson, A. S. McLachlan, J. J. Richards, M. Nilsson and G. A. Morris, *Angewante Chemie International Edition*, **2013**, *52*, pp.3199-3202.
223. Z. Lyu, F.-e. Gao, L. Wen, K. Shi, M. Ma, C. Li, Y. Wang and Y. Qiao, *Energy & Fuels*, **2018**, *32*, pp.3551-3558.
224. Z. Lyu, F. Yue, X. Yan, J. Shan, D. Xiang, C. M. Pedersen, C. Li, Y. Wang and Y. Qiao, *Fuel Processing Technology*, **2018**, *171*, pp.117-123.
225. M. Foroozandeh, G. A. Morris and M. Nilsson, *Chemistry–A European Journal*, **2018**, *24*, pp.13988-14000.
226. A. Le Gresley, G. Broadberry, C. Robertson, J.-M. R. Peron, J. Robinson and S. O'Leary, *Journal of Analytical and Applied Pyrolysis*, **2019**, *140*, pp.281-289.
227. Q. Zhao, H. Ma, C. M. Pedersen, M. Dou, Y. Qiao, X. Hou, Y. Qi and Y. Wang, *ACS Sustainable Chemistry & Engineering*, **2021**, *9*, pp.2456-2464.
228. M. Findeisen, T. Brand and S. Berger, *Magnetic Resonance in Chemistry*, **2007**, *45*, pp.175-178.
229. L. Longsworth, *The Journal of Physical Chemistry*, **1960**, *64*, pp.1914-1917.
230. M. Holz, S. R. Heil and A. Sacco, *Physical Chemistry Chemical Physics*, **2000**, *2*, pp.4740-4742.
231. M. D. Pelta, G. A. Morris, M. J. Stchedroff and S. J. Hammond, *Magnetic Resonance in Chemistry*, **2002**, *40*, pp.S147-S152.
232. C.-L. Chen, **1992** in *Methods in lignin chemistry*, Springer.
233. T. A. van Beek, *Phytochemical Analysis*, **2021**, *32*, pp.24-37.
234. A. Zivkovic, J. J. Bandolik, A. J. Skerhut, C. Coesfeld, M. Prascevic, L. Zivkovic and H. Stark, *Journal of Chemical Education*, **2017**, *94*, pp.121-125.
235. D. Galvan, A. A. C. Tanamati, F. Casanova, E. Danieli, E. Bona and M. H. M. Killner, *Food Chemistry*, **2021**, *365*, pp.130476.
236. R. C. Silva, G. F. Carneiro, L. L. Barbosa, V. Lacerda Jr, J. C. Freitas and E. V. de Castro, *Magnetic Resonance in Chemistry*, **2012**, *50*, pp.85-88.
237. J. Gracia-Vitoria, M. Rubens, E. Feghali, P. Adriaensens, K. Vanbroekhoven and R. Vendamme, *Industrial Crops and Products*, **2022**, *176*, pp. 14405.
238. S. Banks, M. Śnieg, D. Nowakowski, M. Stolarski and A. Bridgwater, *Waste and Biomass Valorization*, **2021**, *12*, pp.2375-2388.
239. Z. Yan, X. Gao, Q. Gao and J. Bao, *Applied and Environmental Microbiology*, **2019**, *85*, pp.e01443-01419.
240. K. Meyer, S. Kern, N. Zientek, G. Guthausen and M. Maiwald, *TrAC Trends in Analytical Chemistry*, **2016**, *83*, pp.39-52.
241. G. A. Barding, R. Salditos and C. K. Larive, *Analytical and Bioanalytical Chemistry*, **2012**, *404*, pp.1165-1179.

B.Tang, PhD Thesis, Aston University, 2024.

242.   W. Picheansathian, *International Journal of Nursing Practice*, **2004**, *10*, pp.3-9.

243.   D. R. Macinga, D. J. Shumaker, H.-P. Werner, S. L. Edmonds, R. A. Leslie, A. E. Parker and J. W. Arbogast, *BMC Infectious Diseases*, **2014**, *14*, pp.1-8.

244.   R. Freeman and E. Kupče, *NMR in Biomedicine: An International Journal Devoted to the Development and Application of Magnetic Resonance In Vivo*, **1997**, *10*, pp.372-380.

245.   M. Li, C. G. Yoo, Y. Pu and A. J. Ragauskas, *ACS Sustainable Chemistry & Engineering*, **2017**, *6*, pp.1265-1270.

246.   M. E. McNally, K. Usher, S. W. Hansen, J. S. Amoo and A. P. Bernstein, **2015,** pp.40-46

247.   P. Araujo, F. Couillard, E. Leirnes, K. Ask, A. Bøkevoll and L. Frøyland, *Journal of Chromatography A*, **2006**, *1121*, pp.99-105.

248.   M. Wang, C. Wang and X. Han, *Mass Spectrometry Reviews*, **2017**, *36*, pp.693-714.

249.   K. Altria and H. Fabre, *Chromatographia*, **1995**, *40*, pp.313-320.

250.   P. Haefelfinger, *Journal of Chromatography A*, **1981**, *218*, pp.73-81.

251.   P. Prasertpong, C. Jaroenkhasemmeesuk, N. Tippayawong and Y. Thanmongkhon, *Chiang Mai University Journal of Natural Sciences*, **2017**, *16*, pp.135-144.

252.   T. Rottreau, *Aston University*, **2018**.

253.   M. Nilsson, *Journal of Magnetic Resonance*, **2009**, *200*, pp.296-302.

254.   H. C. Chen and S. H. Chen, *The Journal of Physical Chemistry*, **1984**, *88*, pp.5118-5121.

255.   M. Tanaka, G. Girard, R. Davis, A. Peuto and N. Bignell, *Metrologia*, **2001**, *38*, pp.301.

256.   Lide, D.R. *ed.*, **2004**. *CRC handbook of chemistry and physics (Vol. 85)*. CRC press.

257.   R. A. Clará, A. C. Gómez Marigliano, D. Morales and H. N. Sólimo, *Journal of Chemical & Engineering Data*, **2010**, *55*, pp.5862-5867.

258.   I. Kul and T. Lieu, *Fluid Phase Equilibria*, **2010**, *290*, pp.95-102.

259.   I. Swan, M. Reid, P. Howe, M. A. Connell, M. Nilsson, M. Moore and G. Morris, *Journal of Magnetic Resonance*, **2015**, *252*, pp.120-129.

260.   P. Steele, M. E. Puettmann, V. K. Penmetsa and J. E. Cooper, *Forest Products Journal*, **2012**, *62*, pp.326-334.

261.   M. Garcia-Perez, A. Chaala, H. Pakdel, D. Kretschmer and C. Roy, *Biomass and Bioenergy*, **2007**, *31*, pp.222-242.

262.   D. Chen, Y. Li, K. Cen, M. Luo, H. Li and B. Lu, *Bioresource Technology*, **2016**, *218*, pp.780-788.

263.   R. Garg, N. Anand and D. Kumar, *Renewable Energy*, **2016**, *96*, pp.167-171.

264.   E. B. Hassan, H. Abou-Yousef, P. Steele and E. El-Giar, *Energy Sources, Part A: Recovery, Utilization, and Environmental Effects*, **2016**, *38*, pp.43-50.

265.   G. Kumar, A. K. Panda and R. Singh, *Journal of Fuel Chemistry and Technology*, **2010**, **38**, 162-167.

266.   O. Beaumont, *Wood and Fiber Science*, **1985**, pp.228-239.

267.   M. Gholizadeh, X. Hu and Q. Liu, *Renewable and Sustainable Energy Reviews*, **2019**, *114*, pp.109313.

268.   J. Challinor, *Journal of Analytical and Applied Pyrolysis*, **1996**, *37*, pp.1-13.

269.   H. Hu, W. Tan and B. Xi, *Environmental Science and Ecotechnology*, **2021**, *8*, pp.100131.

270.   S.-F. Koelewijn, S. Van den Bosch, T. Renders, W. Schutyser, B. Lagrain, M. Smet, J. Thomas, W. Dehaen, P. Van Puyvelde and H. Witters, *Green Chemistry*, **2017**, *19*, pp.2561-2570.

271.   M. Staš, D. Kubička, J. Chudoba and M. Pospíšil, *Energy & Fuels*, **2014**, *28*, pp.385-402.

272.   P. J. De Wild, W. J. Huijgen and R. J. Gosselink, *Biofuels, Bioproducts and Biorefining*, 2014, *8*, pp.645-657.

273.   M. B. Figueiredo, R. Venderbosch, H. Heeres and P. Deuss, *Journal of Analytical and Applied Pyrolysis*, **2020**, *149*, pp.104837.

274.   D. K. Wilkins, S. B. Grimshaw, V. Receveur, C. M. Dobson, J. A. Jones and L. J. Smith, *Biochemistry*, **1999**, *38*, pp.16424-16431.

275.   J. A. Jones, D. K. Wilkins, L. J. Smith and C. M. Dobson, *Journal of Biomolecular NMR*, **1997**, *10*, pp.199-203.

276.   R. D. Whitehead III, C. M. Teschke and A. T. Alexandrescu, *Protein Science*, **2022**, *31*, pp.e4321.

277.   F. Perrin, *Journal de Physique et le Radium*, **1936**, *7*, pp.1-11.

278. W. Sutherland, *The London, Edinburgh, and Dublin Philosophical Magazine and Journal of Science*, **1905**, *9*, pp.781-785.
279. A. Gierer and K. Wirtz, *Zeitschrift für Naturforschung A*, **1953**, *8*, pp.532-538.
280. R. Evans, *Progress in Nuclear Magnetic Resonance Spectroscopy*, **2020**, *117*, pp.33-69.
281. E. d. C. Andrade, *Nature*, **1930**, *125*, pp.309-310.
282. O. Reynolds, *Philosophical Transactions of the Royal Society of London*, **1886**, *177*, pp.157-234.
283. J. Kendall and K. P. Monroe, *Journal of the American Chemical Society*, **1917**, *39*, pp.1787-1802.
284. J. Kendall and K. P. Monroe, *Journal of the American Chemical Society*, **1917**, *39*, pp.1802-1806.
285. R. C. Reid, J. M. Prausnitz and B. E. Poling, **1987**, *The Properties of Gases and Liquids*, McGraw-Hill
286. S. Bretschneider, **1966**, *The Properties of Gases and Liquids. Engineering Methods of Calculation*, Khimiya, Moscow.
287. L. Grunberg and A. H. Nissan, *Nature*, **1949**, *164*, pp.799-800.
288. R. Powell, W. Roseveare and H. Eyring, *Industrial & Engineering Chemistry*, **1941**, *33*, pp.430-435.
289. S. Arrhenius, *Zeitschrift für Physikalische Chemie*, **1887**, *1*, pp.285-298.
290. D. S. Raiford, C. L. Fisk and E. D. Becker, *Analytical Chemistry*, **1979**, *51*, pp.2050-2051.
291. D. Wu, A. Chen and C. S. Johnson, *Journal of Magnetic Resonance, Series A*, **1995**, *115*, pp.260-264.
292. T.-L. Hwang and A. Shaka, *Journal of Magnetic Resonance, Series A*, **1995**, *112*, pp.275-279.
293. S. Balayssac, M.-A. Delsuc, V. Gilard, Y. Prigent and M. Malet-Martino, *Journal of Magnetic Resonance*, **2009**, *196*, pp.78-83.
294. L. Castañar, G. D. Poggetto, A. A. Colbourne, G. A. Morris and M. Nilsson, *Magnetic Resonance in Chemistry*, **2018**, *56*, pp.546-558.
295. M. Holz, X. a. Mao, D. Seiferling and A. Sacco, *The Journal of Chemical Physics*, **1996**, *104*, pp.669-679.
296. M. P. Renshaw and I. J. Day, *The Journal of Physical Chemistry B*, **2010**, *114*, pp.10032-10038.
297. E. F. Dudás and A. Bodor, *Analytical Chemistry*, **2019**, *91*, pp.4929-4933.

B.Tang, PhD Thesis, Aston University, 2024.

APPENDICES

CONTENTS

B.Tang, PhD Thesis, Aston University, 2024.

APPENDIX 1 Experimental Calibration

Table A1.1 Experimental parameters

Sample(s)	Δ (s)	δ (s)	% of max. gradient strength (1700 G cm^{-1})
cyclohexanol	0.1	0.001	5 - 20
DMSO	0.1	0.001	10 - 30
1-pentanol	0.1	0.001	10 - 50
squalane	0.1	0.001	10 - 90

Table A1.2 estimated gradient strength required to achieve a 10% and 90% attenuation for a ^{1}H DOSY

liquid	Signal Intensity	D m^{2}s^{-1}	Δ s	δ s	γ rads^{-1}T^{-1}	g G/cm
D2O	0.9	1.91E-09	0.1	0.001	267522187.4	8.779351823
	0.1	1.91E-09	0.1	0.001	267522187.4	41.04226818
cyclohexane	0.9	1.42E-09	0.1	0.001	267522187.4	10.18204389
	0.1	1.42E-09	0.1	0.001	267522187.4	47.59966161
DMSO	0.9	7.3E-10	0.1	0.001	267522187.4	14.20096009
	0.1	7.3E-10	0.1	0.001	267522187.4	66.38754479
1-pentanol	0.9	2.86E-10	0.1	0.001	267522187.4	22.68799513
	0.1	2.86E-10	0.1	0.001	267522187.4	106.063272
squalane	0.9	2.90E-11	0.1	0.001	267522187.4	71.24922388
	0.1	2.90E-11	0.1	0.001	267522187.4	333.0803701

Table A1.3 estimated gradient strength required to achieve a 10% and 90% attenuation for a ^{13}C DOSY

liquid	Signal Intensity	D m^{2}s^{-1}	Δ s	δ s	γ rads^{-1}T^{-1}	g G/cm
cyclohexanol	0.9	1.42E-09	0.1	0.001	67282800	40.48468
	0.1	1.42E-09	0.1	0.001	67282800	189.2603
DMSO	0.9	7.3E-10	0.1	0.001	67282800	56.46424
	0.1	7.3E-10	0.1	0.001	67282800	263.9626
1-pentanol	0.9	2.86E-10	0.1	0.001	67282800	90.20942
	0.1	2.86E-10	0.1	0.001	67282800	421.7167
squalane	0.9	2.90E-11	0.1	0.001	67282800	283.293
	0.1	2.90E-11	0.1	0.001	67282800	1324.356

APPENDIX 2 Low-field ^{19}F Analysis of Carbonyl Groups in Bio-oil

Table A2.1 Model carbonyl compounds

Compound	Supplier	Purity (%)
Acetone	Fisher Scientific	99
3-methyl-1,2-butanone	Sigma-Aldrich	99
2-butanone	Alfa Aesar	99
2-pentanone	Thermo Scientific	99
3-pentanone	Thermo Scientific	99
butyraldehyde	Alfa Aesar	98
valeraldehyde	Alfa Aesar	97+
hexanal	Fisher Scientific	96
octanal	Alfa Aesar	98
furfural	Sigma-Aldrich	99
benzaldehyde	Sigma-Aldrich	99
cinnamaldehyde	Fisher Scientific	99
anthraquinone	Acros Organics	98
1,4-benzoquinone	Thermo Scientific	98+
2-hydroxyl-1,4-napthoquinone	Alfa Aesar	98+
1,4-napthoquinone	Acros Organics	99
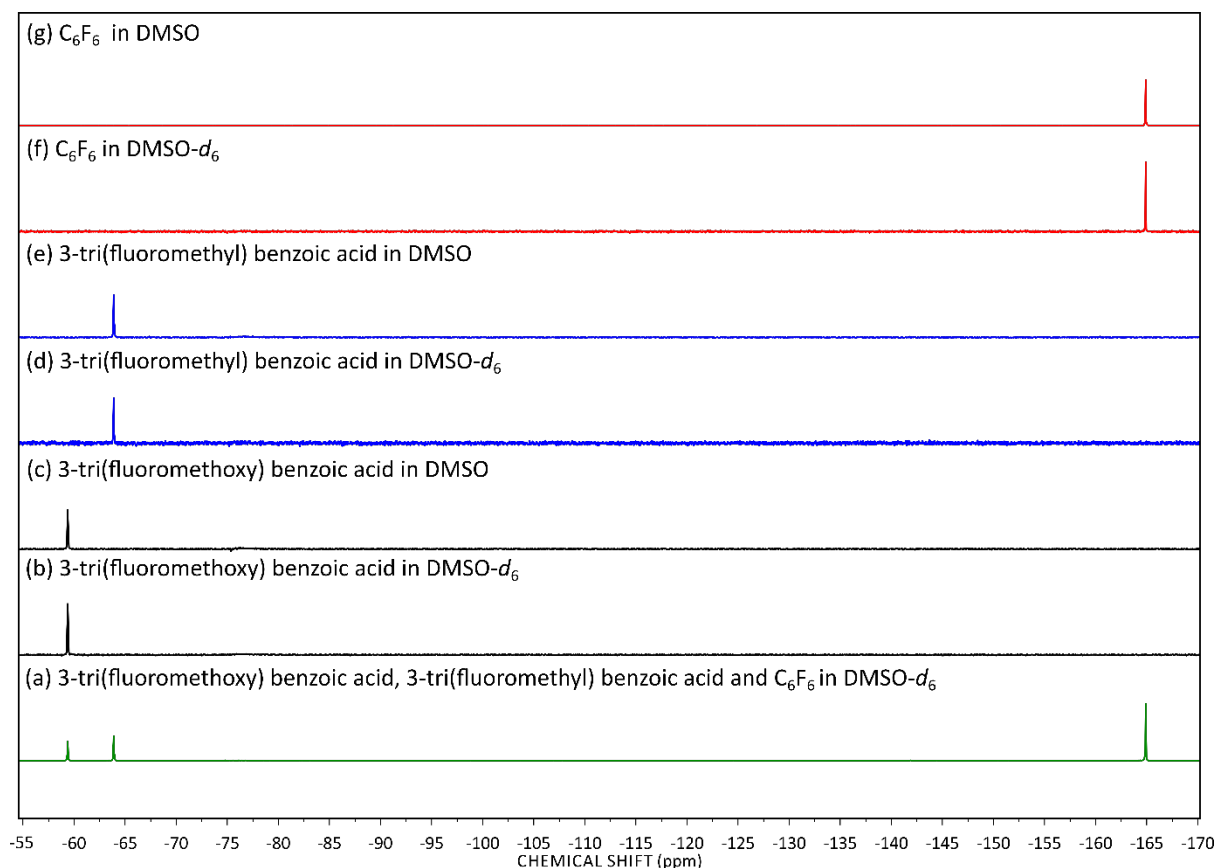
Figure A2.1 Stacked ^{19}F NMR spectrum of internal standards in protiated DMSO and deuteriated DMSO

Table A2.2 Summary of ^{19}F NMR chemical shifts of model compounds all references against C_6F_6 at −164.0 ppm

	Chemical	Chemical shift (ppm)
Ketones −61 to −61.7	acetone	− 61.63
	3-methyl-2-butanone	−61.68
	2-butanone	−61.63
	2-pentanone	−61.64
	3-pentaone	−61.61
Aldehydes −61.7 to −61.9	butyraldehyde	−61.72
	valeraldehyde	−61.67
	hexanal	−61.70
	octanal	−61.74
	benzaldehyde	−61.81
	furfural	−61.83
	cinnamaldehyde	−61.86
Quinones −61.9 to -64.0	2-hydroxy-1,4-naphthaquinone	−62.66 to −61.75
	1,4-naphthaqionone	−63.68 to −61.51
	anthraquinone	−63.47 to −61.52
	benzoquinone	−63.60 to 61.46

Figure A2.2 shows that 3-(trifluoromethyl)benzoic acid (−63.8 ppm) is a potential candidate for internal standard for quantification as the peak is far away from the acetone peak.
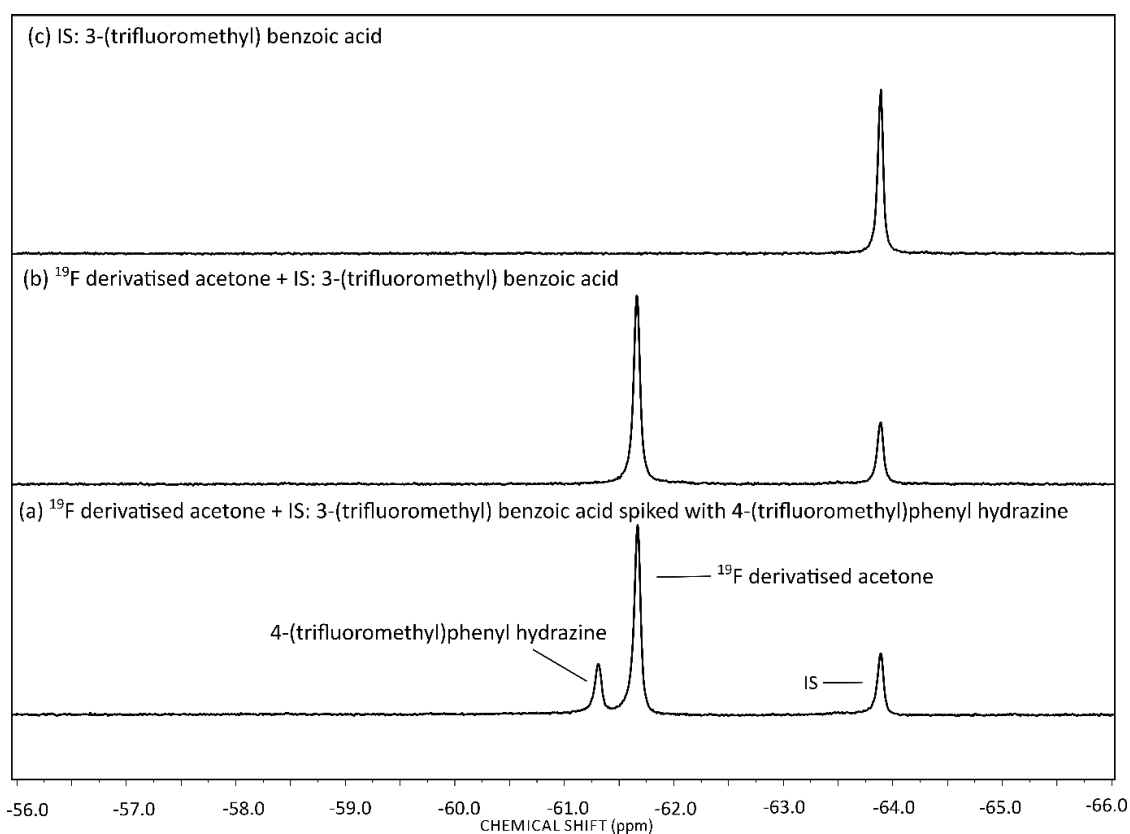
Figure A2.2 (a) ^{19}F NMR spectrum of derivatised acetone, internal standard (IS) 3-(trifluoromethyl) benzoic acid and 4-(trifluoromethyl)phenyl hydrazine. (b) ^{19}F NMR spectrum of derivatised acetone and internal standard (IS) 3-(trifluoromethyl) benzoic acid (c) internal standard (IS) 3-(trifluoromethyl)benzoic acid

277
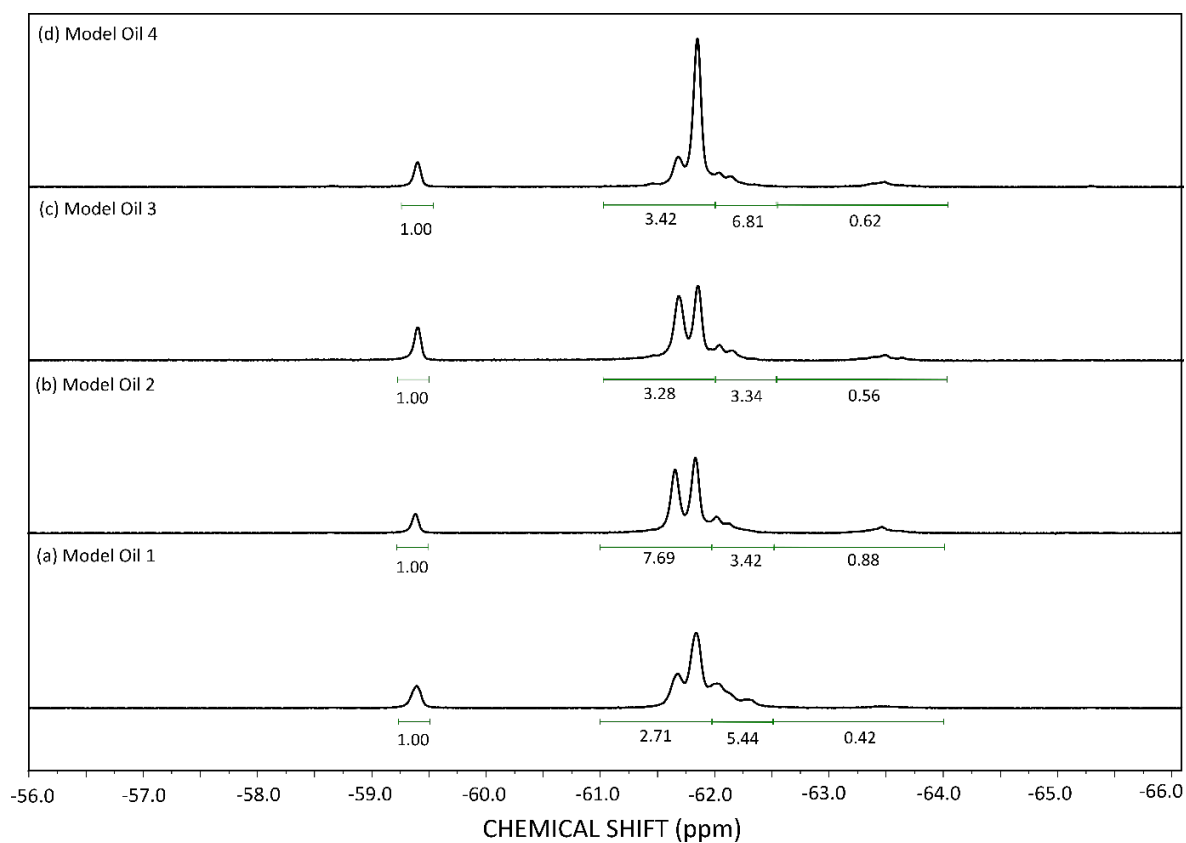
Figure A2.3 Stack plot of the ^{19}F NMR spectrum for the model oils

Table A.2a Summary integrals used for quantification using NMR spectroscopy

Sample	Internal Standard Mass (g)	Internal Standard MW (g mol^{-1})	Internal Standard Moles (×10^{-4})	Ketone Integral	Aldehyde Integral	Quinone Integral
Model Oil 1	0.0127	206.12	0.616	2.71	5.44	0.42
Model Oil 2	0.0118	206.12	0.572	7.69	3.42	0.88
Model Oil 3	0.0163	206.12	0.791	3.28	3.34	0.56
Model Oil 4	0.0134	206.12	0.650	3.42	6.81	0.62

Table A2.2b Summary of the theoretical moles of carbonyl containing compounds and the quantification using NMR spectroscopy

Sample	Theoretical Ketone Moles (×10⁻⁴)	Theoretical Aldehyde Moles (×10⁻⁴)	Theoretical Quinone Moles (×10⁻⁴)	Ketone Moles (×10⁻⁴)	Aldehyde Moles (×10⁻⁴)	Quinone Moles (×10⁻⁴)
Model Oil 1	2	2.8	0.3	1.68	3.35	0.26
Model Oil 2	4	3.8	0.3	4.40	1.95	0.50
Model Oil 3	2	2.8	0.3	2.59	2.64	0.44
Model Oil 4	2	4.6	0.3	2.22	4.43	0.40
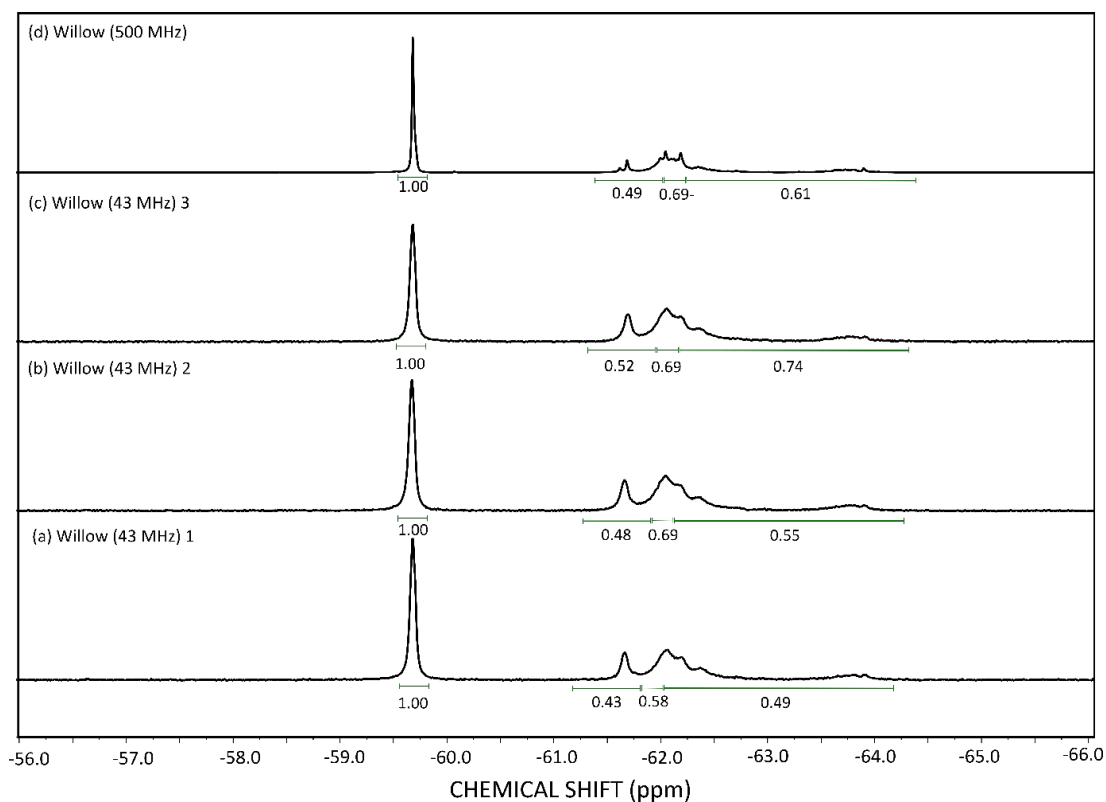
Figure A2.4 Stacked Plot of ¹⁹F NMR spectra of derivatised pyrolysis oil produced from willow at 43 MHz in triplicate (a-c) and ¹⁹F NMR spectrum of derivatised pyrolysis oil produced from willow at 500 MHz
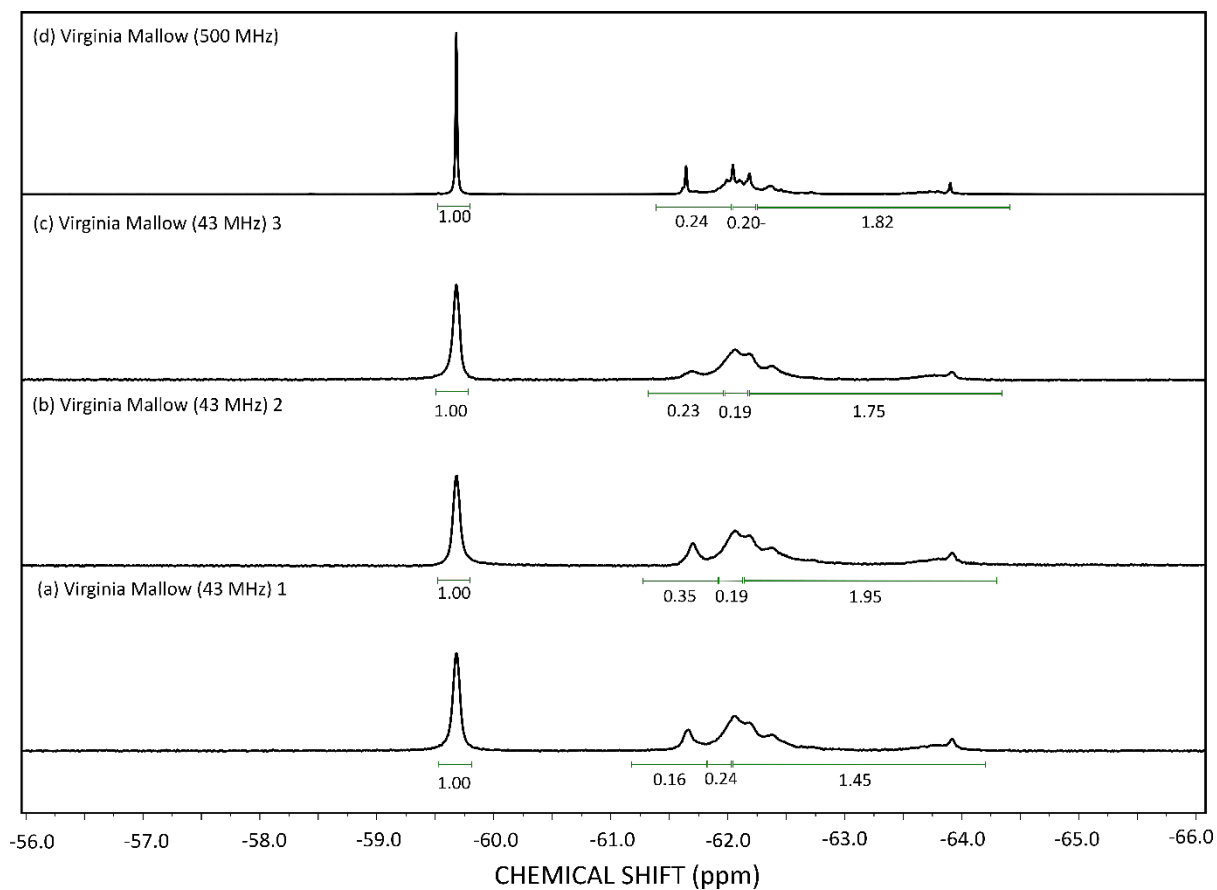
Figure A2.5 Stacked Plot of ^{19}F NMR spectra of derivatised pyrolysis oil produced from Virginia Mallow at 43 MHz in triplicate (a-c) and ^{19}F NMR spectrum of derivatised pyrolysis oil produced from Virginia Mallow at 500 MHz
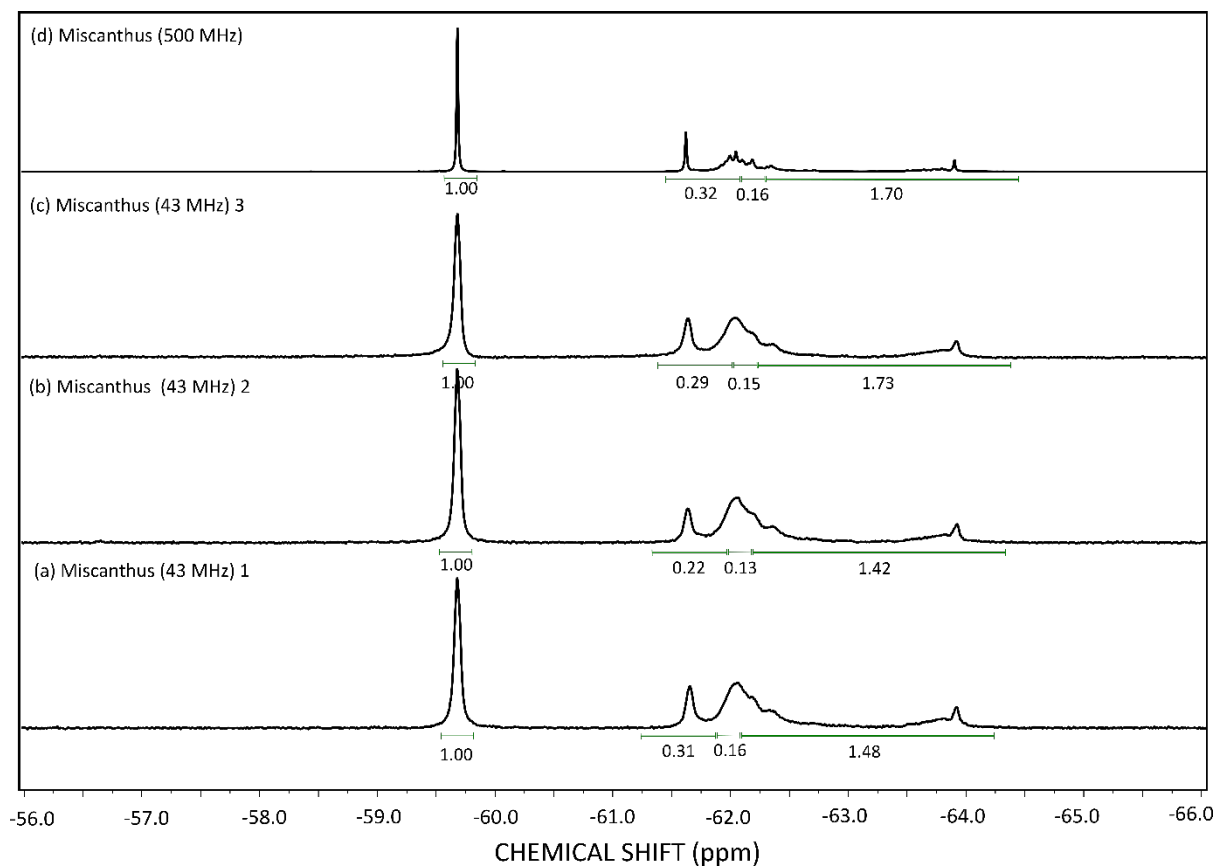
Figure A2.6 Stacked Plot of ^{19}F NMR spectrum of derivatised pyrolysis oil produced from Miscanthus at 43 MHz in triplicate (a-c) and ^{19}F NMR spectrum of derivatised pyrolysis oil produced from Miscanthus at 500 MHz

APPENDIX 3 ^{31}P NMR Analysis of Alcohol Groups in Bio-oils

A3.1 Chemicals and chemical shift map

Table A3.1 Model alcohol compounds

Compound	Supplier	Purity (%)
Methanol	Fisher Scientific	99.8
Ethanol	Fisher Scientific	99.8
1-propanol	Fisher Scientific	≥99
2-propanol	Fisher Scientific	99.5
1-butanol	Sigma-Aldrich	99.9
2-butanol	Acros Organics	99
t-butanol	Sigma-Aldrich	99.5
Glycerol	Fisher Scientific	99+
Cyclohexanol	Acros Organics	98
Phenol	Sigma-Aldrich	≥99

Table A3.2 Summary of ^{31}P NMR chemical shifts of derivatised model compounds all references against di-derivatised water at 132.2 ppm

	Chemical	Chemical Shift (ppm)
Tertiary Alcohols & Aromatics	Phenol	137.9
	t-butanol	142.0
Secondary Alcohols	Cyclohexanol	145.19
	2-propanol	145.2
	2-butanol	145.8
	Glycerol	146.4
Primary Alcohols	Ethanol	146.8
	1-propanol	147.1
	1-butanol	147.2
	Glycerol	147.3
	Methanol	148.0

Table A3.3 Summary of ^{31}P NMR chemical shifts of derivatised model compounds reproduced from M. Li, C. G. Yoo, Y. Pu and A. J. Ragauskas, ACS Sustainable Chemistry & Engineering, 2017, 6, 1265-1270.

Compound	COOH (ppm)	OH (ppm)
Acetic acid	134.6	-
Trans-aconitic acid	134.6 135.2 135.4	-
Citric acid	134.8 134.9	-
Formic acid	137.4	-
Fumaric acid	135.2	-
Glucuronic acid	134.5 (β) 135.3 (α)	-
Hexanoic acid	134.3	-
Isobutyric acid	134.8	-
L-lactic acid	134.9	-
Levulinic acid	134.6	-
Linoleic acid	134.3	-
Linolenic acid	134.3	-
Malonic acid	134.8	-
Oleic acid	134.4	-
Palmitic acid	134.7	-
Stearic acid	134.6	-
Succinic acid	134.6	-
cis-Vaccenic acid	134.7	-
Benzoic acid	136.0	-
trans-Cinnamic acid	135.0	-
Caffeic acids	135.1	138.6 (*p*) 139.6 (*m*)
Coniferyl alcohol	-	139.7 148.1
o-Coumaric acid	134.9	138.9
p-Coumaric acid	135.1	139.4
2',5'-Dihydroxyaceophenone	-	138.7 (*m*) 138.8 (*o*)
Ferulic acid	135.1	139.4
3-Methoxycatechol	-	142.7 (*m*) 138.6 (*o*)
4-Methly catechol	-	139.3 (*p*) 138.9 (*m*)
Sinapic acid	135.2	142.2
Syringic acid	135.1	141.9
Vanillic acid	136.0	139.8

B.Tang, PhD Thesis, Aston University, 2024.

A3.2 ^{31}P spectrum of initial calibration (qNMR)

This section shows a series of ^{31}P NMR spectra of derivatised cyclohexanol using TMDP at different concentrations. These spectra show the integration range used to calculate the ratio of I_{OH}/I_{NHND}
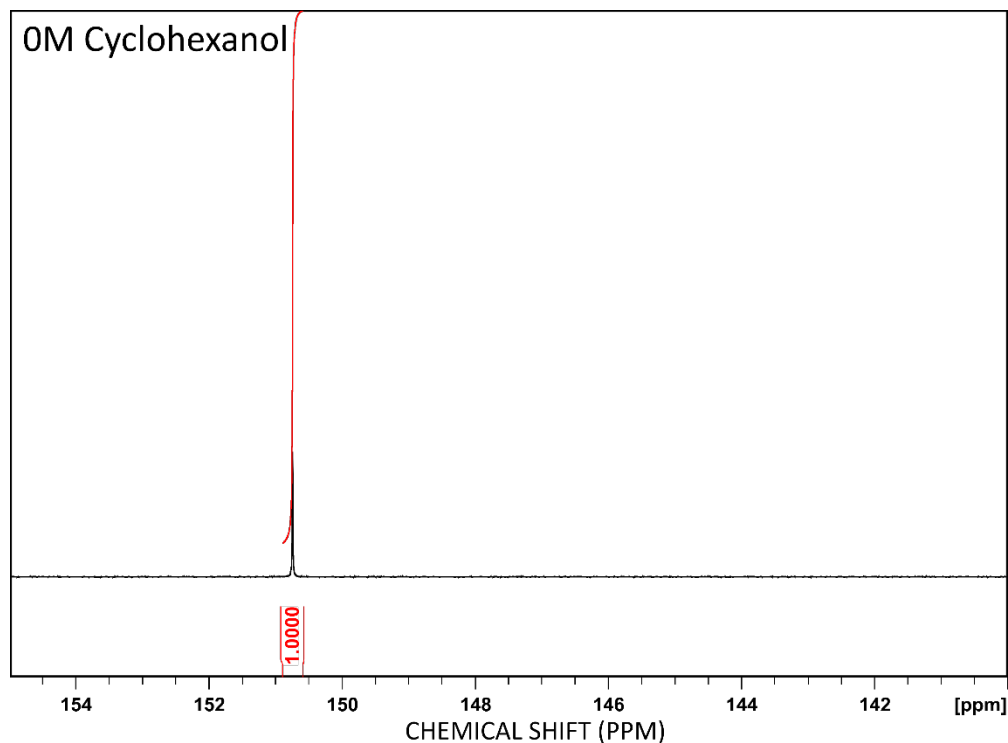
Figure A3.1 1D ^{31}P NMR spectrum of derivatised NHND (ca. 151 ppm)
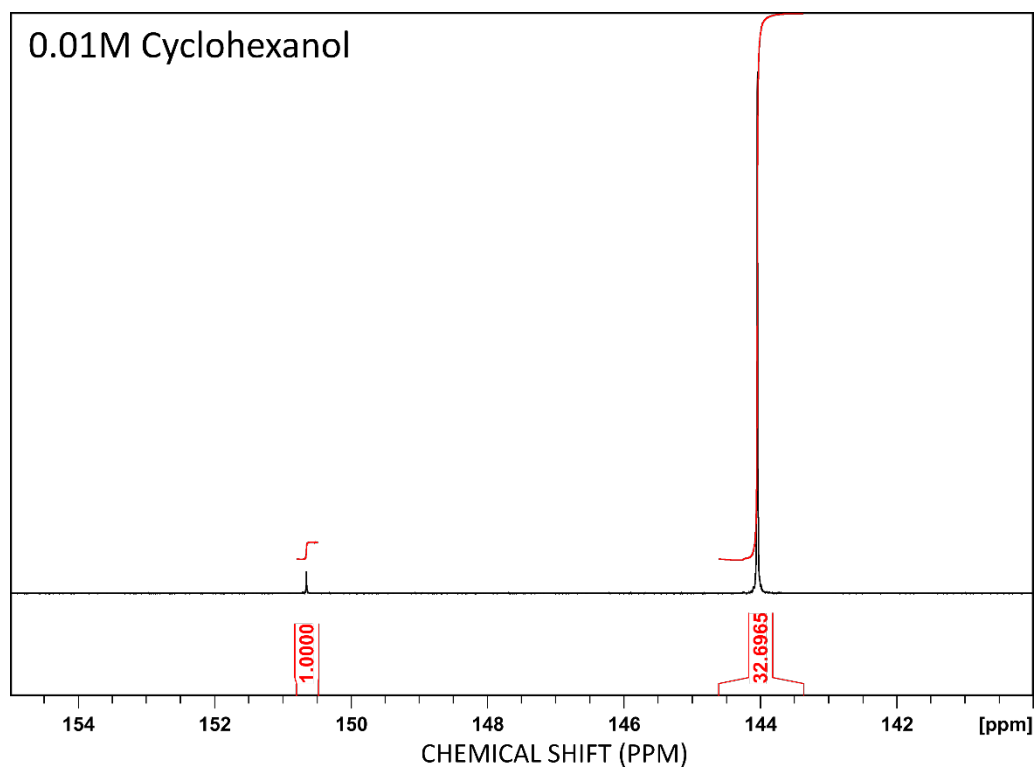
Figure A3.2 1D ^{31}P NMR spectrum of derivatised 0.1 M of cyclohexanol (ca. 145 ppm) and NHND (ca. 151 ppm)

B.Tang, PhD Thesis, Aston University, 2024.
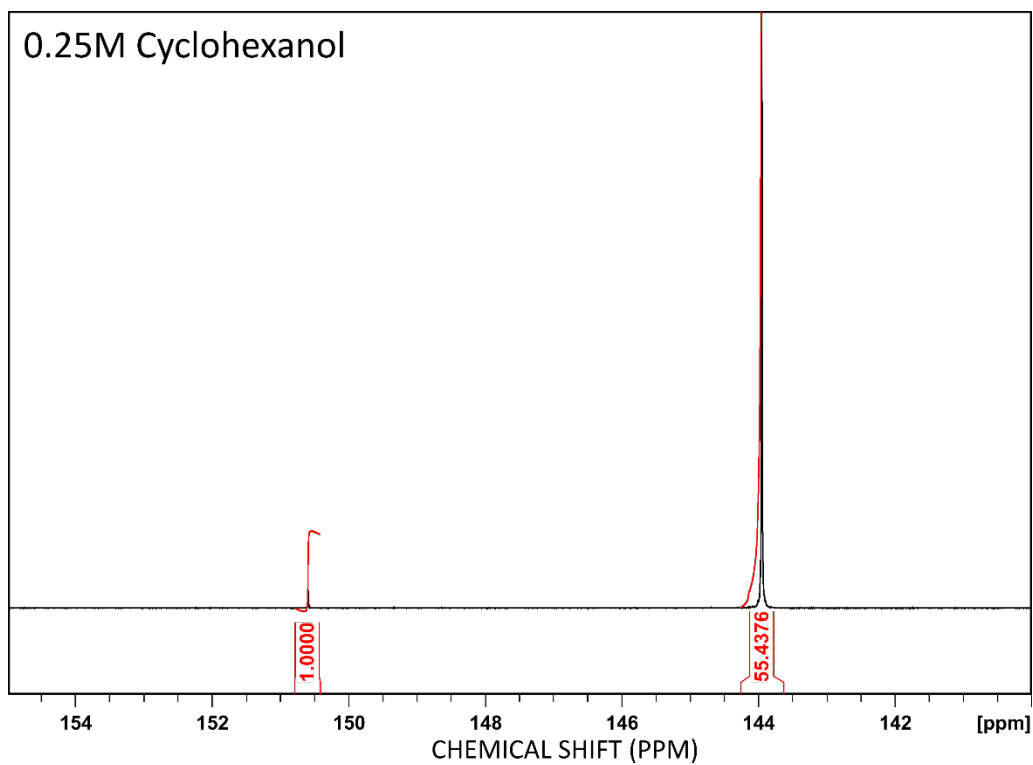
Figure A3.3 1D ^{31}P NMR spectrum of derivatised 0.25 M of cyclohexanol (ca. 145 ppm) and NHND (ca. 151 ppm)
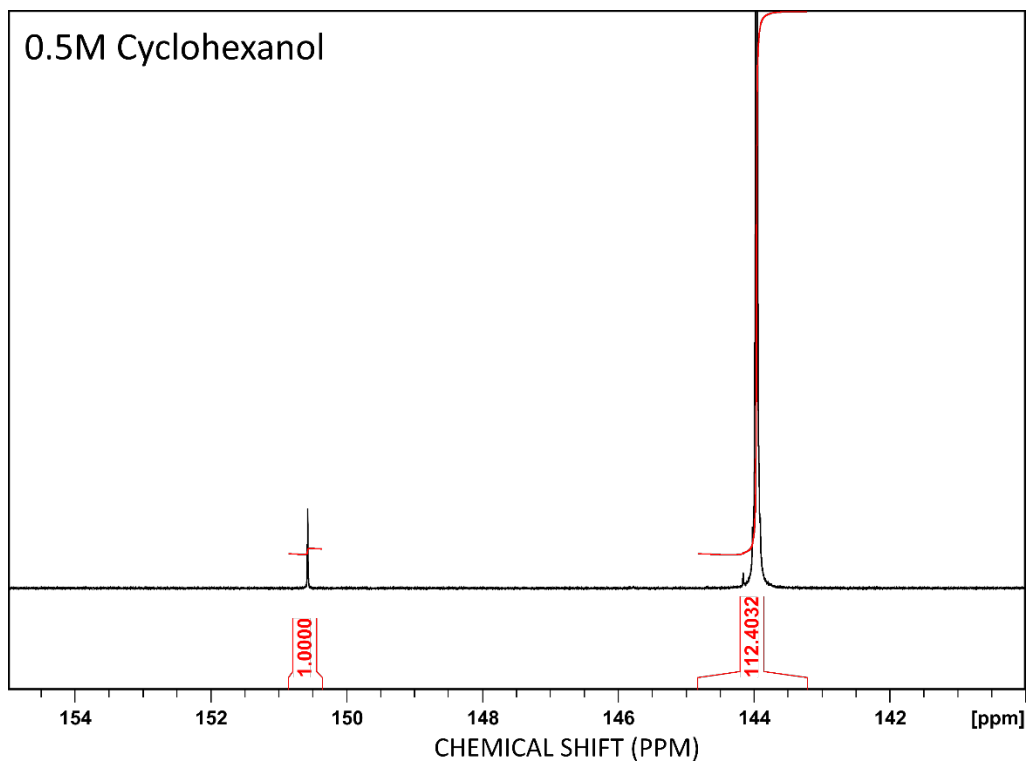
Figure A3.4 1D ^{31}P NMR spectrum of derivatised 0.5 M of cyclohexanol (ca. 145 ppm) and NHND (ca. 151 ppm)

286
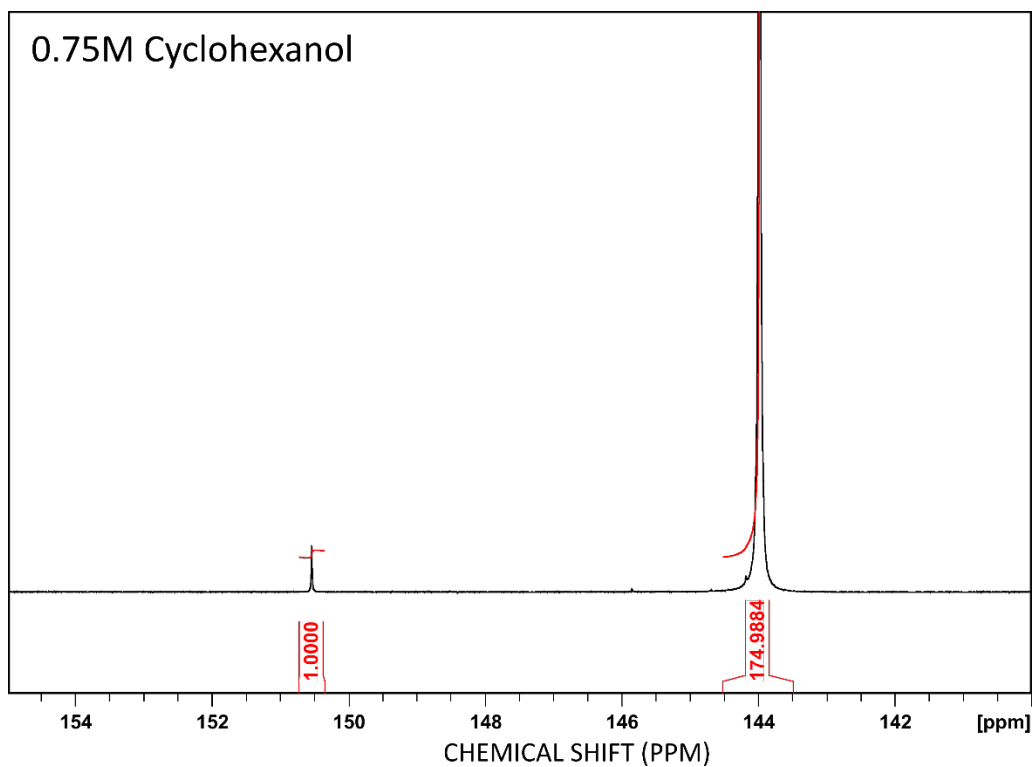
Figure A3.5 1D ^{31}P NMR spectrum of derivatised 0.75 M of cyclohexanol (ca. 145 ppm) and NHND (ca. 151 ppm)
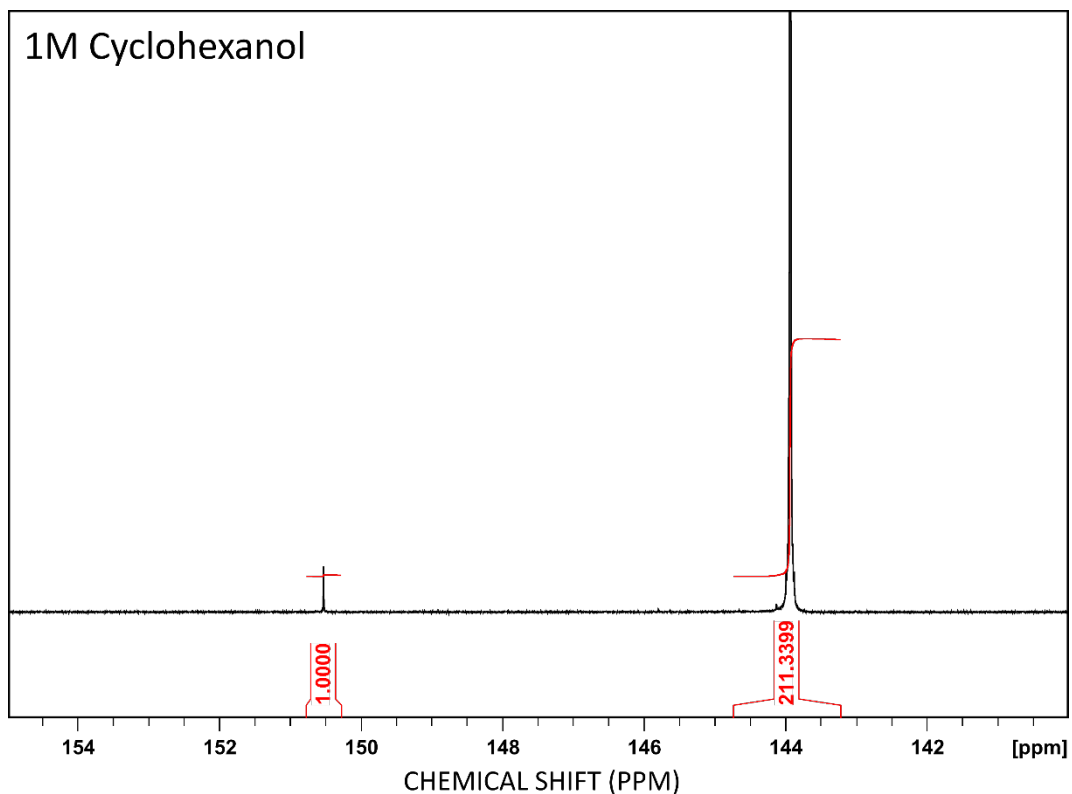
Figure A3.6 1D ^{31}P NMR spectrum of derivatised 1 M of cyclohexanol (ca. 145 ppm) and NHND (ca. 151 ppm)

B.Tang, PhD Thesis, Aston University, 2024.

A3.3 Hand Sanitisers

Table a3.1 Titration results for hand sanitisers

	Initial	Final	Titre
Blank 1	0.2	20.6	20.4
Blank 2	20.6	40.9	20.3
Blank 3	2.6	23	20.4
Garnier 1	0.8	13.2	12.4
Garnier 2	13.2	25.7	12.5
Garnier 3	25.7	38.2	12.5
Carex 1	0.7	14	13.3
Carex 2	14.1	27.4	13.3
Carex 3	27.4	40.9	13.5
Cuticura 1	1.3	13.1	11.8
Cuticura 2	13.3	25	11.7
Cuticura 3	25	36.8	11.8
Bondloc 1	0.2	11.8	11.6
Bondloc 2	13.4	25.1	11.7
Bondloc 3	25	36.6	11.6

Table A3.2 Estimation of alcohol content from titration results for hand sanitisers

Hand sanitiser	Hand sanitiser mass in 1 mL (g)	Titre (cm^3)	Moles of Ethanol (mol)	Mass of Ethanol (g)	Estimation of the amount ethanol using titration %(w/w)
Garnier 1	0.0040	20.4	5.70×10^{-5}	2.63×10^{-3}	65.6
Garnier 2	0.0041	20.3	5.63×10^{-5}	2.59×10^{-3}	63.8
Garnier 3	0.0041	20.4	5.63×10^{-5}	2.59×10^{-3}	63.8
Carex 1	0.0041	12.4	6.15×10^{-5}	2.83×10^{-3}	69.2
Carex 2	0.0041	12.5	6.23×10^{-5}	2.87×10^{-3}	70.0
Carex 3	0.0041	12.5	6.15×10^{-5}	2.83×10^{-3}	69.2
Cuticura 1	0.0041	13.3	5.03×10^{-5}	2.32×10^{-3}	56.9
Cuticura 2	0.0041	13.3	5.03×10^{-5}	2.32×10^{-3}	56.9
Cuticura 3	0.0041	13.5	4.88×10^{-5}	2.25×10^{-3}	55.2
Bondloc 1	0.0041	11.8	6.30×10^{-5}	2.90×10^{-3}	71.4
Bondloc 2	0.0041	11.7	6.23×10^{-5}	2.87×10^{-3}	70.6
Bondloc 3	0.0041	11.8	6.30×10^{-5}	2.90×10^{-3}	71.4

B.Tang, PhD Thesis, Aston University, 2024.

Table A3.3 Average alcohol content from itration results for hand sanitisers

Hand sanitiser	Average of the amount ethanol using titration %(w/w)	Error
Garnier	64.4	3.27
Carex	69.5	3.52
Cuticura	56.3	2.86
BondLoc	71.1	3.61
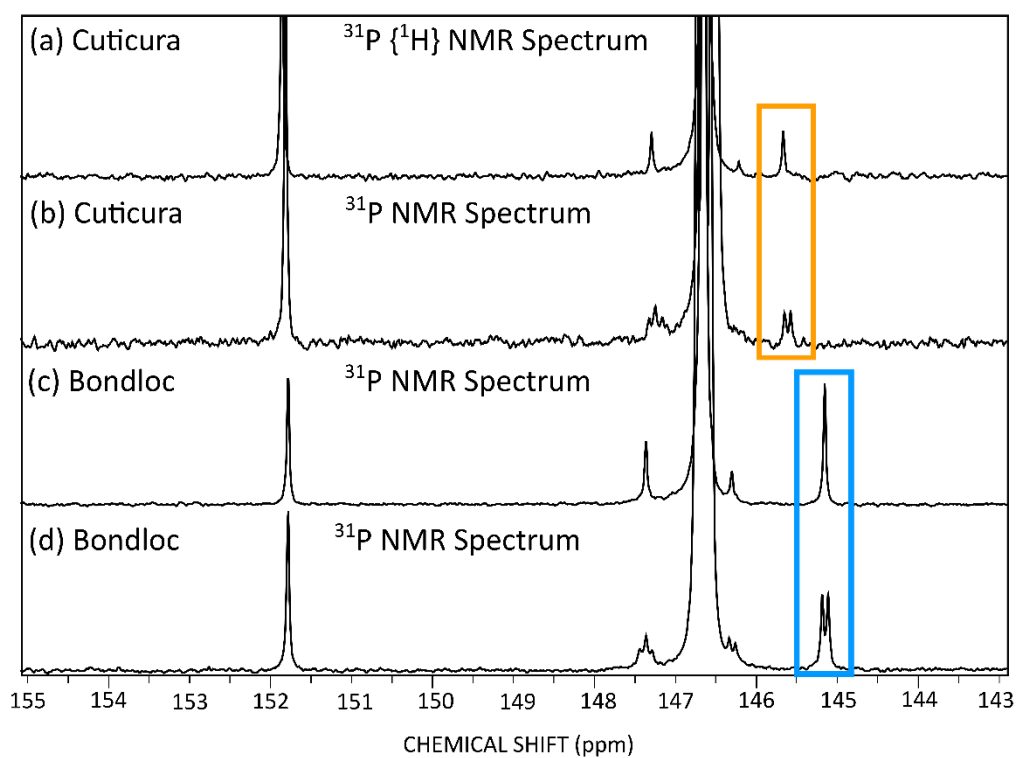
Figure A3.7 Stacked plot of (a) ^{31}P {1H} NMR spectrum of derivatised hand sanitiser (Cuticura) (b) ^{31}P NMR spectrum of derivatised hand sanitiser (Cuticura) (c) ^{31}P {1H} NMR spectrum of derivatised hand sanitiser (Bondloc) (d) ^{31}P NMR spectrum of derivatised hand sanitiser (Bondloc)
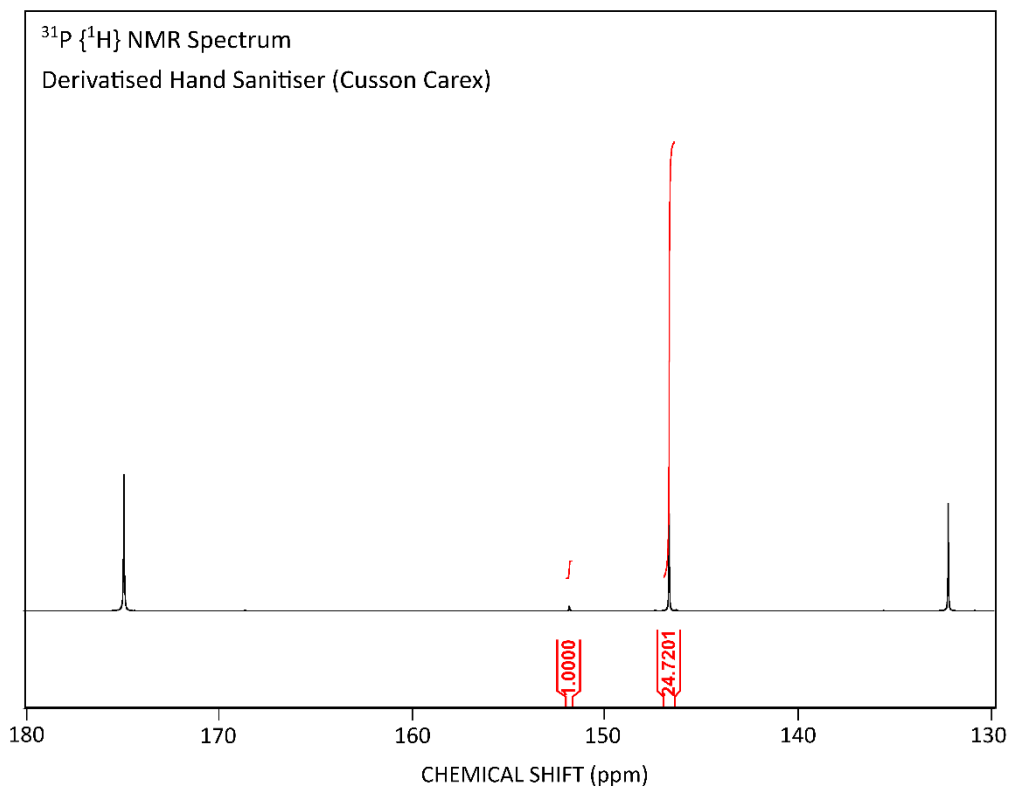
Figure A3.8 1D ^{31}P NMR spectrum of derivatised hand sanitiser (carex)
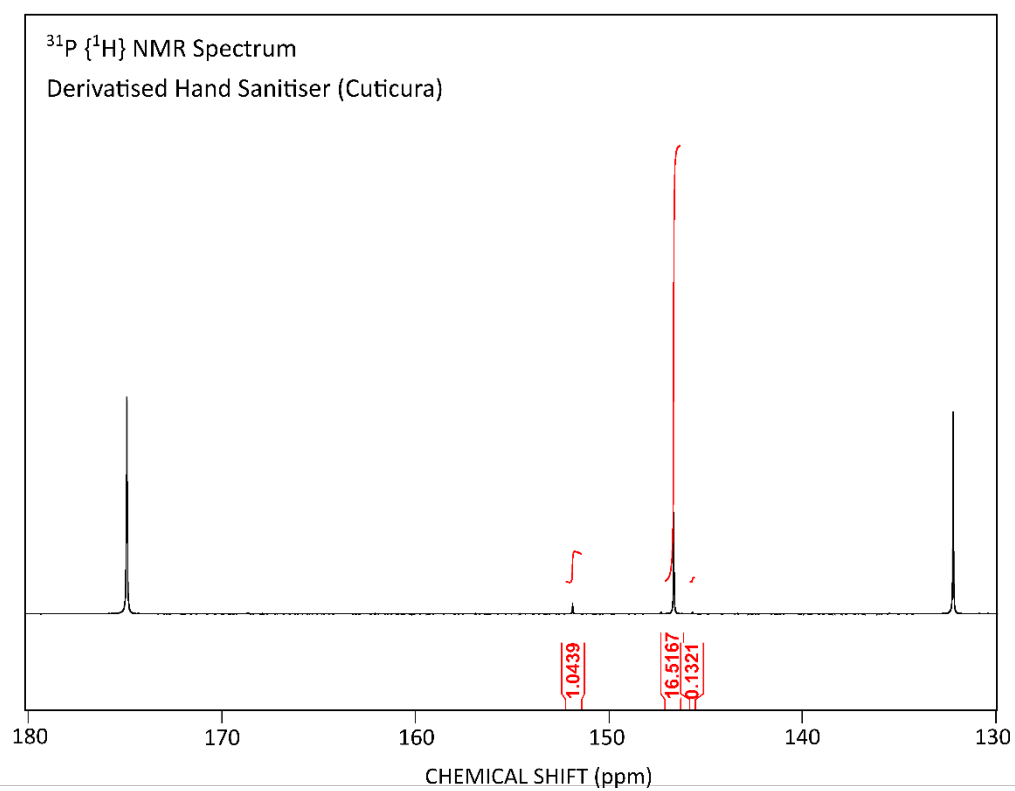
Figure A3.9 1D ^{31}P NMR spectrum of derivatised hand sanitiser (cuticura)

B.Tang, PhD Thesis, Aston University, 2024.

³¹P {¹H} NMR Spectrum
Derivatised Hand Sanitiser (BondLoc)
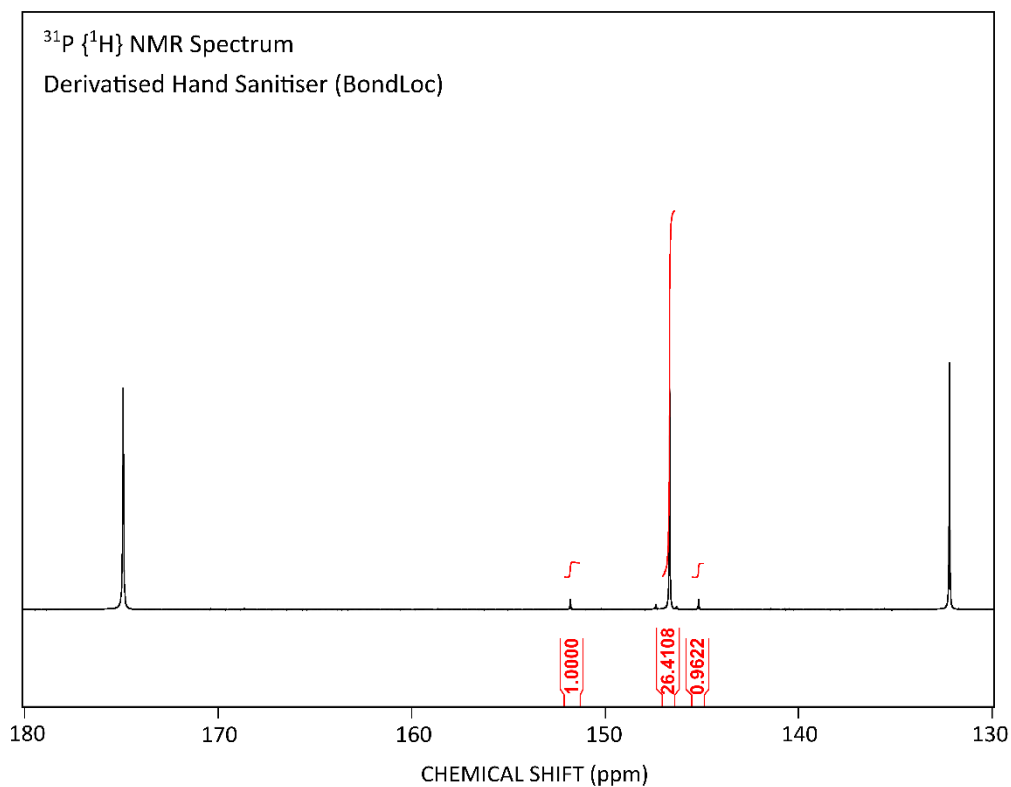
Figure A3.10 1D ³¹P NMR spectrum of derivatised hand sanitiser (bondloc)

Table A3.4 Estimation of alcohol content from ³¹P NMR results for hand sanitisers

Hand sanitiser	IS Mass (g)	Mass of whole solution (g)	Mass of IS in NMR (g)	R	Hand sanitiser Mass (g)	Ethanol (mmol/g)	Ethanol (mol/mol)
Garnier	0.1125	2.513	0.00940	37.8	0.0263	13.5156	0.62266
Carex	0.1236	2.513	0.01033	24.7	0.0166	15.3728	0.70823
Cuticura	0.1346	2.513	0.01125	16.5	0.0153	12.1334	0.55899
BondLoc	0.1383	2.513	0.01156	26.4	0.0200	15.2595	0.70301

Table A3.5 Estimation of alcohol content from ³¹P NMR results for hand sanitisers and errors

Hand sanitiser	Ethanol content on label %(w/w)	Estimation of the amount ethanol using qNMR %(w/w)
Garnier	62.4	62.3
Carex	70	70.8
Cuticura	57.5	55.8
BondLoc	70	70.3

B.Tang, PhD Thesis, Aston University, 2024.

A3.4 ^{31}P NMR of Spruce Pyrolysis Oil
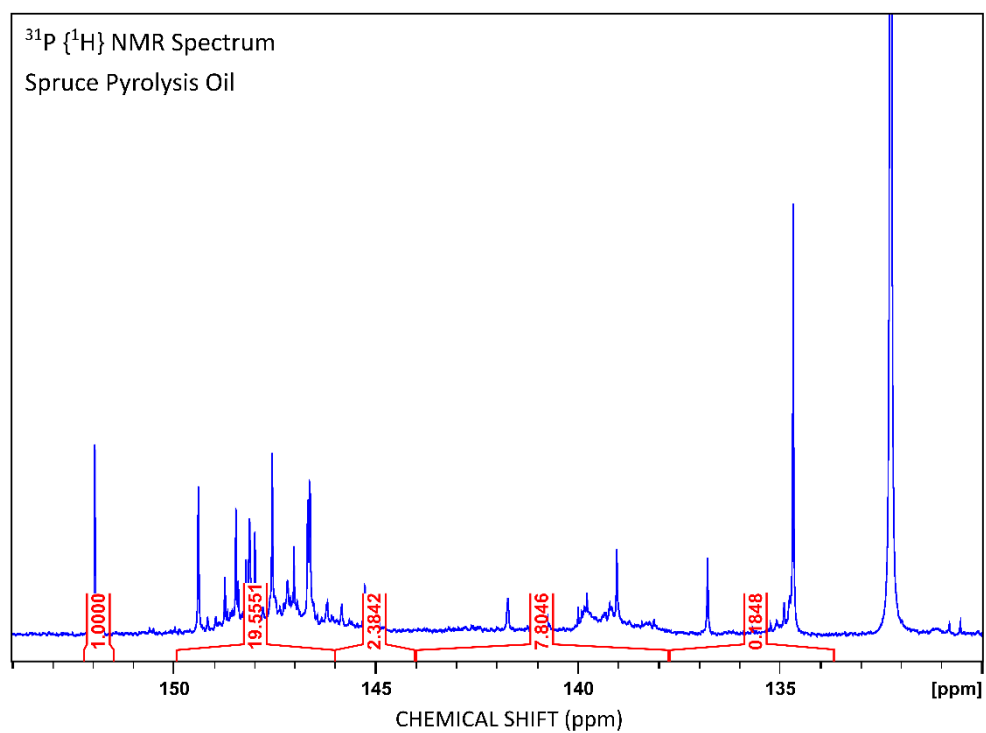
Figure A3.11 1D ^{31}P NMR spectrum of derivatised spruce pyrolysis oil.

APPENDIX 4 Development of ^{31}P DOSY

A4.1 Mathematica Scripts for Calculating Thermal Expansion Coefficient, β, from Density Data

Deuteriated Water

```
dir = "C:\\Users\\tangb2\\Desktop\\DOSY DATA.xlsx";
Data = Import[dir, "Data"];

xaxis = "T (K)"
yaxis = "V (cm³ mol⁻¹)"
Clear[T]
T = {Data[[5, 5, 9]]};
For[i = 6, i ≤ 14, i++, AppendTo[T, Data[[5, i, 9]]]];
T

ρwaterD = {Data[[5, 5, 10]]};
For[i = 6, i ≤ 14, i++, AppendTo[ρwaterD, Data[[5, i, 10]]]];
ρwaterD

ρwaterD⁻¹;

Mr = 20.0276;

V = Mr * (ρwaterD⁻¹);

plot = Partition[Riffle[T, V], 2];
DatPlot = ListPlot[plot, PlotStyle → Purple, LabelStyle → {10, Black, FontFamily → "Calibri"}, AxesLabel → {xaxis, yaxis}];

int = Interpolation[plot]
intplot = Plot[int[x], {x, 279, 340}, PlotStyle → {Red, Dashed}];
dint = int';
(*dint[205]*)
dintplot = Plot[dint[x], {x, 279, 340}, PlotStyle → {Blue, Dashed}];

img2 = Show[DatPlot, intplot]

BETAplot = Plot[dint[x] / int[x], {x, 279, 340}]
dint[298.15] / int[298.15]

Clear[a, b, c, d, x];
nlm1 = NonlinearModelFit[plot, a + b x + c x^2 + d x^3, {a, b, c, d}, x];
nlm1 = Normal[nlm1];
FitPlot = Plot[nlm1, {x, 279, 340}, PlotStyle → {Red, Dashed}];

img3 = Show[DatPlot, FitPlot]
BETA2 = Simplify[D[nlm1, x] / nlm1]
BETA2 /. x → 298.15
```


$\beta = 1.73 \times 10^{-4}$ K^{-1}

B.Tang, PhD Thesis, Aston University, 2024.

Protiated Water

```
dir = "C:\\Users\\tangb2\\Desktop\\DOSY DATA.xlsx";
Data = Import[dir, "Data"];

xaxis = "T (K)"
yaxis = "V (cm³ mol⁻¹)"
Clear[T]
T = {Data[[5, 4, 3]]};
For[i = 5, i ≤ 15, i++, AppendTo[T, Data[[5, i, 3]]]];
T


ρwater = {Data[[5, 4, 4]]};
For[i = 5, i ≤ 15, i++, AppendTo[ρwater, Data[[5, i, 4]]]];
ρwater

ρwater⁻¹;

Mr = 18.01528;

V = Mr * (ρwater⁻¹);

plot = Partition[Riffle[T, V], 2];
DatPlot = ListPlot[plot, PlotStyle → Purple, LabelStyle → {10, Black, FontFamily → "Calibri"}, AxesLabel → {xaxis, yaxis}];

int = Interpolation[plot];
intplot = Plot[int[x], {x, 279, 328}, PlotStyle → {Red, Dashed}];
dint = int';
(*dint[205]*)
dintplot = Plot[dint[x], {x, 279, 328}, PlotStyle → {Blue, Dashed}];

img2 = Show[DatPlot, intplot]

BETAplot = Plot[dint[x] / int[x], {x, 279, 328}]
dint[298.15] / int[298.15]

Clear[a, b, c, x];
nlm1 = NonlinearModelFit[plot, a + b x + c x^2, {a, b, c}, x];
nlm1 = Normal[nlm1];
FitPlot = Plot[nlm1, {x, 279, 328}, PlotStyle → {Red, Dashed}];


img3 = Show[DatPlot, FitPlot]
BETA2 = Simplify[D[nlm1, x] / nlm1]
BETA2 /. x → 298.15
```


$\beta = 2.43 \times 10^{-4} \text{ K}^{-1}$

B.Tang, PhD Thesis, Aston University, 2024.

Deuteriated Chloroform

```
dir = "C:\\Users\\tangb2\\Desktop\\DOSY DATA.xlsx";
Data = Import[dir, "Data"];

xaxis = "T (K)";
yaxis = "V (cm^3 mol^-1)";

T = {Data[[4, 3, 2]]};
For[i = 4, i ≤ 13, i++, AppendTo[T, Data[[4, i, 2]]]];
T;

ρchloroformD = {Data[[4, 3, 3]]};
For[i = 4, i ≤ 13, i++, AppendTo[ρchloroformD, Data[[4, i, 3]]]];
ρchloroformD;

ρchloroformD^-1;

Mr = 120.38;

V = Mr * (ρchloroformD^-1);

plot = Partition[Riffle[T, V], 2];
DatPlot = ListPlot[plot, PlotStyle → Purple, LabelStyle → {10, Black, FontFamily → "Calibri"}, AxesLabel → {xaxis, yaxis}];

int = Interpolation[plot];
intplot = Plot[int[x], {x, 279, 328}, PlotStyle → {Red, Dashed}];
dint = int';
(*dint[205]*)
dintplot = Plot[dint[x], {x, 279, 328}, PlotStyle → {Blue, Dashed}];

BETAplot = Plot[dint[x] / int[x], {x, 279, 328}];
img2 = Show[DatPlot, intplot]
img2b = Show[alphaplot];
dint[298.15] / int[298.15]

Clear[a, b, c, x];
nlm1 = NonlinearModelFit[plot, a + b x + c x^2, {a, b, c}, x];
nlm1 = Normal[nlm1];
FitPlot = Plot[nlm1, {x, 0, 600}, PlotStyle → {Red, Dashed}];


img3 = Show[DatPlot, FitPlot]
dint2 = D[nlm1, x];
BETA2 = Simplify[dint2 / nlm1];
BETA2 /. x → 298.15
```
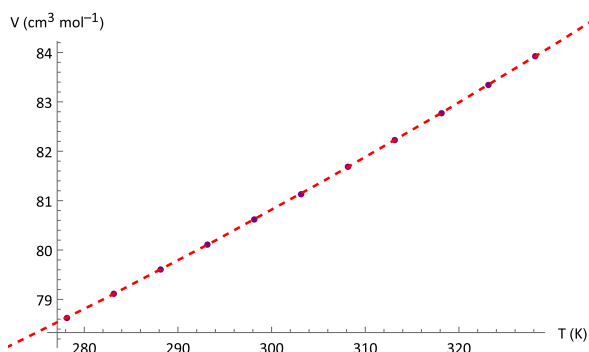

β = 1.29 × 10⁻³ K⁻¹

Protiated Chloroform

```
dir = "C:\\Users\\tangb2\\Desktop\\DOSY DATA.xlsx";
Data = Import[dir, "Data"];

xaxis = "T (K)";
yaxis = "V (cm³ mol⁻¹)";
Clear[T];
T = {Data[[4, 14, 13]]};
For[i = 15, i ≤ 22, i++, AppendTo[T, Data[[4, i, 13]]]];
T;

ρchloroform = {Data[[4, 14, 15]]};
For[i = 15, i ≤ 22, i++, AppendTo[ρchloroform, Data[[4, i, 15]]]];
ρchloroform;

ρchloroform⁻¹;

Mr = 119.38;

V = Mr * (ρchloroform⁻¹);

plot = Partition[Riffle[T, V], 2];
DatPlot = ListPlot[plot, PlotStyle → Purple, LabelStyle → {10, Black, FontFamily → "Calibri"}, AxesLabel → {xaxis, yaxis}];

int = Interpolation[plot];
intplot = Plot[int[x], {x, 279, 328}, PlotStyle → {Red, Dashed}];
dint = (int');
(*dint[205]*)
dintplot = Plot[dint[x], {x, 279, 328}, PlotStyle → {Blue, Dashed}];

img2 = Show[DatPlot, intplot]

BETAplot = Plot[dint[x] / int[x], {x, 279, 328}];
dint[298.15] / int[298.15]

Clear[a, b, c, x];
nlm1 = NonlinearModelFit[plot, a + b x + c x^2, {a, b, c}, x];
nlm1 = Normal[nlm1];
FitPlot = Plot[nlm1, {x, 279, 328}, PlotStyle → {Red, Dashed}];


img3 = Show[DatPlot, FitPlot]
BETA2 = Simplify[D[nlm1, x] / nlm1];
BETA2 /. x → 298.15
```
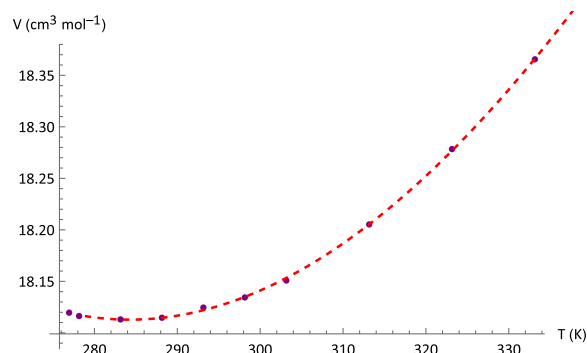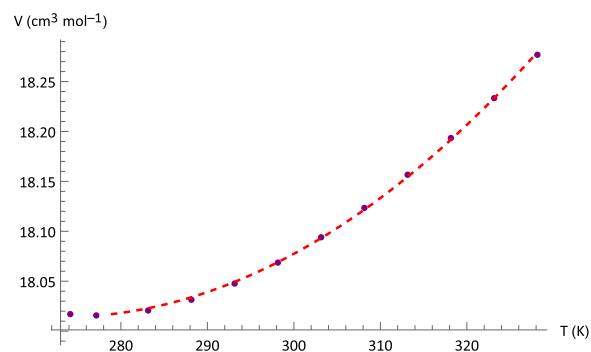

β = 1.24 × 10⁻³ K⁻¹

Deuteriated pyridine

```
dir = "C:\\Users\\tangb2\\Desktop\\DOSY DATA.xlsx";
Data = Import[dir, "Data"];

xaxis = "T (K)"
yaxis = "V (cm³ mol⁻¹)"

Clear[T]
T = {Data[[4, 3, 2]]};
For[i = 4, i ≤ 13, i++, AppendTo[T, Data[[4, i, 2]]]];
T

ρpyridineD = {Data[[4, 3, 8]]};
For[i = 4, i ≤ 13, i++, AppendTo[ρpyridineD, Data[[4, i, 8]]]]
ρpyridineD

ρpyridineD⁻¹;

Mr = 84.13071;

V = Mr * (ρpyridineD⁻¹);

plot = Partition[Riffle[T, V], 2];
DatPlot = ListPlot[plot, PlotStyle → Purple, LabelStyle → {10, Black, FontFamily → "Calibri"}, AxesLabel → {xaxis, yaxis}];

int = Interpolation[plot];
intplot = Plot[int[x], {x, 279, 328}, PlotStyle → {Red, Dashed}];
dint = int';
(*dint[205]*)
dintplot = Plot[dint[x], {x, 279, 328}, PlotStyle → {Blue, Dashed}];

img2 = Show[DatPlot, intplot]

BETAplot = Plot[dint[x] / int[x], {x, 279, 328}];
dint[298] / int[298]

Clear[a, b, c, x];
nlm1 = NonlinearModelFit[plot, a + b x + c x^2, {a, b, c}, x];
nlm1 = Normal[nlm1];
FitPlot = Plot[nlm1, {x, 279, 328}, PlotStyle → {Red, Dashed}];


img3 = Show[DatPlot, FitPlot]
BETA2 = Simplify[D[nlm1, x] / nlm1];
BETA2 /. x → 298
```
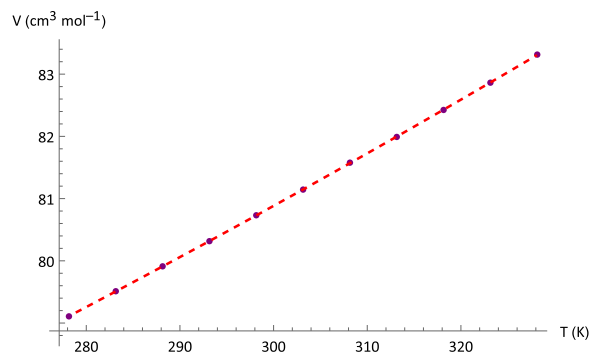

$\beta = 1.03 \times 10^{-3}$ K^{-1}

Protiated pyridine

A small number of values for β could be found, while no consistent density data was identified. This required a different approach to estimating β at 298 K.

```
T = {308.15, 318.15, 328.15};
BETA = {1.065, 1.073, 1.099};

Dat = Partition[Riffle[T, BETA], 2];
DatPlot = ListPlot[Dat];
nlm1 = NonlinearModelFit[Dat, a + b x + c x^2, {a, b, c}, x];
nlm1 = Normal[nlm1]
FitPlot = Plot[nlm1, {x, 200, 350}, PlotStyle → {Red, Dashed}];

img = Show[DatPlot, FitPlot]
nlm1 = Normal[nlm1] /. x → 298.15
```
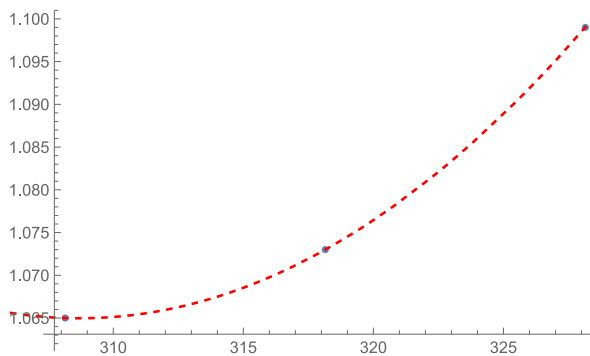

β = 1.08 × 10⁻³ K⁻¹

A4.2 Pulse Sequence (BRUKER): ^{31}P Oneshot Diffusion Sequence
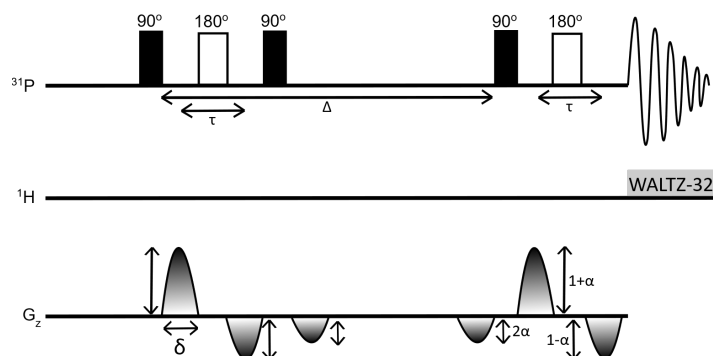
;avance-version (16/06/10)

;2D Doneshot DOSY pulse sequence

;$CLASS=HighRes

;$DIM=2D

;$TYPE=

;$SUBTYPE=

;$COMMENT=

;A one-shot sequence for high-resolution diffusion-ordered spectroscopy

;Michelle D. Pelta   Gareth A. Morris   Marc J. Stchedroff   Stephen J. Hammond

;Magnetic Resonance in Chemistry. Volume 40 Issue 13   Pages S147 - S152

;doi: 10.1002/mrc.1107

#include <Avance.incl>

#include <Grad.incl>

#include <Delay.incl>

define list<gradient> diff=<Difframp>

"p2=p1*2"

B.Tang, PhD Thesis, Aston University, 2024.

```
"d11=30m"

"cnst14=0.2"

"cnst15=1+cnst14"; cnst15

"cnst16=1-cnst14"

"cnst17=2*p1+d16+p30"

"cnst18=p30*2*p30*2*(d20+(p30/3)*(cnst14*cnst14-
2)+((2*p1+d16+p30)/2)*(cnst14*cnst14-1))"


"DELTA1=d20-4.0*p1-4.0*p30-5.0*d16-p19"


"acqt0=-p1*2/3.1416"

1 ze
  d11 pl12:f2
2 30m do:f2
  d1*0.5 ph10                          ;ph10+ph11= ph1
  d1*0.5 ph11                          ;ph10+ph11= ph1


  p19:gp7*-1.0                         ;Spoiler gradient balancing pulse
  d16


  p1 ph1                               ;1st 90


  p30:gp1*diff*cnst16                  ; 1 - alpha
  d16


  p2 ph2                               ;First 180


  p30:gp1*-1*diff*cnst15               ;1 + alpha
  d16
```

```
p1 ph3                          ; 2nd 90

p30:gp1*diff*2*cnst14           ;Lock refocusing pulse pulse
d16

p19:gp7                         ;Spoiler gradient balancing pulse
d16 ph12                        ;ph12+ph13=ph4


DELTA1

p30:gp1*diff*2*cnst14           ;Lock refocusing pulse pulse
d16 ph13                        ;ph12+ph13=ph4

p1 ph4        ; 1st 90

p30:gp1*diff*cnst16             ; 1 - alpha
d16*0.5 ph14                    ; ph14+ph15=ph5
d16*0.5 ph15                    ; ph14+ph15=ph5

p2 ph5

p30:gp1*-1*diff*cnst15          ; 1 + alpha
d16

4u BLKGRAD

go=2 ph31 cpd2:f2
30m do:f2 mc #0 to 2 F1QF(igrad diff)

exit

ph10={0}*4 {1}*4
```

```
ph11=0 2

ph12={0}*2 {2}*2
ph13={0}*8 {1}*8 {2}*8 {3}*8

ph14={0}*64 {1}*64
ph15={0}*16 {2}*16

ph1= ph10 + ph11

ph2={0}*128 {2}*128
ph3={0}*32 {2}*32
ph4= ph12 + ph13
ph5= ph14 + ph15

ph31=ph1 - ph2*2 + ph3 - ph4 + ph5*2

;pl1 : f1 channel - power level for pulse (default)
;p1  : f1 channel -  90 degree high power pulse
;p19: gradient pulse 2 (spoil gradient)
;p30: gradient pulse (little DELTA*0.5)
;d1  : relaxation delay; 1-5 * T1
;d16: delay for gradient recovery
;d20: diffusion time (big DELTA)

;NS: 1 * n
;DS: 1 * m
;td1: number of experiments
;FnMODE: QF

; cnst14 : alpha. Unbalancing factor. Use 0.2.

; use    gradient value  gpz1: 100  and  gpz7 : 100
```

B.Tang, PhD Thesis, Aston University, 2024.

```
;use AU-program dosy to calculate gradient ramp-file Diframp

;       use xf2 and DOSY processing

;       use "setdiffparm STEbp" instead of "setdiffparm"


;$Id: Doneshot        v 1.x 2010/06/16 xx:xx:xx ber Exp $
```

A4.3 Pulse Sequence (BRUKER): ^{31}P Convection Compensated Diffusion Sequence
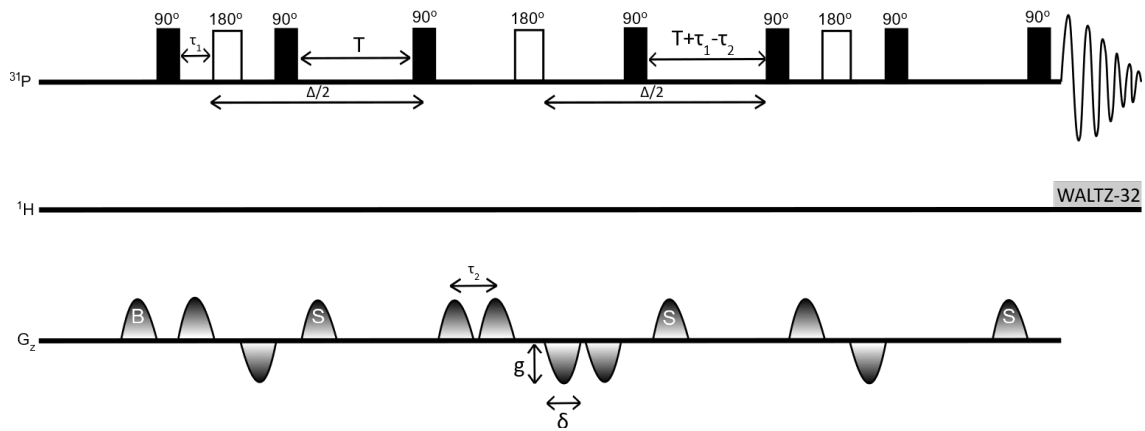
;dstebpgp3s

;avance-version (08/01/16)

;2D sequence for diffusion measurement using double stimulated

;   echo for convection compensation and LED

;using bipolar gradient pulses for diffusion

;using 3 spoil gradients, includes balancing gradient at the start

;

;A. Jerschow & N. Mueller, J. Magn. Reson. A 123, 222-225 (1996)

;A. Jerschow & N. Mueller, J. Magn. Reson. A 125, 372-375 (1997)

;

;$CLASS=HighRes

;$DIM=2D

;$TYPE=

;$SUBTYPE=

;$COMMENT=

#include <Avance.incl>

#include <Grad.incl>

#include <Delay.incl>

B.Tang, PhD Thesis, Aston University, 2024.

```
define list<gradient> diff=<Difframp>

"p2=p1*2"

"d11=30m"


"DELTA1=d20*0.5-p1*2-p2-p30*2-d16*3-p19"

"DELTA2=d21-p19-d16-4u"



"acqt0=-p1*2/3.1416"



1 ze
  d11 pl12:f2
2 30m do:f2
  d1
        p19:gp1
        d16
        50u
  p1 ph1
  p30:gp6*diff
  d16
  p2 ph2
  p30:gp6*-1*diff
  d16
  p1 ph3
  p19:gp7
  d16
  DELTA1
```

```
p1 ph4

p30:gp6*diff

d16

p30:gp6*diff

d16

p2 ph5

p30:gp6*-1*diff

d16

p30:gp6*-1*diff

d16

p1 ph6

p19:gp8

d16

DELTA1

p1 ph3

p30:gp6*diff

d16

p2 ph8

p30:gp6*-1*diff

d16

p1 ph3

p19:gp9

d16

DELTA2

4u BLKGRAD

p1 ph3

go=2 ph31 cpd2:f2

30m do:f2 mc #0 to 2 F1QF(igrad diff)
exit
```

```
ph1= 0 0 1 1 2 2 3 3
ph2= 1 2 2 3 3 0 0 1
ph3= 0
ph4= 2 2 3 3
ph5= 3 3 0 0 3 3 0 0  0 0 1 1 0 0 1 1
ph6= 2
ph8= 0 0 0 0 0 0 0 0  0 0 0 0 0 0 0 0
     2 2 2 2 2 2 2 2  2 2 2 2 2 2 2 2
ph31=0 2 0 2 2 0 2 0  2 0 2 0 0 2 0 2
```

;pl1 : f1 channel - power level for pulse (default)

;p1 : f1 channel - high power pulse

;p2 : f1 channel - 180 degree high power pulse

;p19: gradient pulse 2 (spoil gradient)

;p30: gradient pulse (little DELTA * 0.5)

;d1 : relaxation delay; 1-5 * T1

;d16: delay for gradient recovery

;d20: diffusion time (big DELTA)

;d21: eddy current delay (Te)   [5 ms]

;NS: 16 * n

;DS: 4 * m

;td1: number of experiments

;FnMODE: QF

;   use xf2 and DOSY processing

;use gradient ratio: gp 6 : gp 7   : gp 8   : gp 9

;   100 : -13.17 : -17.13 : -15.37

B.Tang, PhD Thesis, Aston University, 2024.

;for z-only gradients:

;gpz6: 100%

;gpz7: -13.17% (spoil)

;gpz8: -17.13% (spoil)

;gpz9: -15.37% (spoil)

;gpz1: +45.67% (balance, sum of spoil)

;use gradient files:

;gpnam1: SINE.100

;gpnam6: SINE.100

;gpnam7: SINE.100

;gpnam8: SINE.100

;gpnam9: SINE.100

;use AU-program dosy to calculate gradient ramp-file Diframp

;the gradients serve the following purpose:

;   p19   gradient balance

;   p30

;   p30   first STE dephase bipolar pulse pair

;   p19   spoiler

;   p30

;   p30   first STE rephase bipolar pulse pair

;   p30   and second STE dephase bipolar pulse pair

;   p30

;   p19   spoiler

;   p30

;   p30   second STE rephase bipolar pulse pair

;   p19   LED with spoiler

;$Id: dstebpgp3s,v 1.2.6.1 2008/01/16 15:46:23 ber Exp $

APPENDIX 5 Characterisation of Pyrolysis Oils Produced from Brewers' Spent Grains

Table A5.1 GC/MS analysis of slow pyrolysis oil produced from brewers' spent grain

Peak	Retention Time (s)	Compound
1	1.65	Methylamine, N,N-dimethyl-
2	1.82	1-Penten-3-yne
3	1.94	1-Hexene
4	1.98	Hexanal, 2-ethyl-
5	2.02	Furan, 2-methyl-
6	2.28	1,3-Cyclopentadiene, 1-methyl-
7	2.32	Cyclopentene, 1-methyl-
8	2.42	Benzene
9	2.48	1,3,5-Hexatriene, (Z)-
10	2.57	Cyclohexene
11	2.63	1-Heptene
12	2.82	Furan, 2,5-dimethyl-
13	3.04	Heptanedinitrile
14	3.68	Toluene
15	4.03	1-Octene
16	4.59	Pyridine, 2-methyl-
17	5.62	Ethylbenzene
18	5.81	o-Xylene
19	6.32	1-Nonene
21	6.43	Ethylbenzene
22	8.13	Benzene, propyl-
23	8.91	Benzene, 1-ethyl-3-methyl-
24	9.02	Phenol
25	9.20	1-Decene
26	9.42	Benzene, 1-ethenyl-2-methyl-
27	10.93	1H-Indene, 1-chloro-2,3-dihydro-
28	11.26	N-Benzyloxycarbonyl-D-aspartic acid
29	11.95	p-Cresol
30	12.31	1-Undecene
31	12.48	Bicyclo[2.2.1]hept-5-ene-2-carbonitrile
32	13.91	Benzyl nitrile
33	14.41	Benzene, pentyl-
34	14.76	Phenol, 4-ethyl-
35	15.30	Naphthalene
36	15.39	Cyclopropane, nonyl-
37	16.35	Benzofuran, 2,3-dihydro-
38	18.35	1-Tridecene
41	18.60	Naphthalene, 1-methyl-
42	21.16	1-Tetradecene
43	23.98	Pentadecane
44	33.35	Heptadecanenitrile
45	34.93	n-Hexadecanoic acid
46	36.83	Octadecanoic acid, 2-propenyl ester
47	38.29	9,12-Octadecadienoic acid (Z,Z)-
48	38.61	Octadecanoic acid
49	39.01	Hexadecanamide
50	39.18	Phenol, 4,4'-(1-methylethylidene)bis-

Table A5.2 GC/MS analysis of fast pyrolysis oils produced from brewers' spent grain

Peak	Retention Time (s)	Compound
1	1.655	Methylamine, N,N-dimethyl-
2	2.118	Acetic acid
3	2.415	Benzene
4	2.868	Propanoic acid
5	3.353	Pyridine
6	3.67	Toluene
7	4.219	2-Pentene, 3,4-dimethyl-, (E)-
8	4.605	Pyridine, 2-methyl-
9	5.46	2-Furanmethanol
10	5.616	Ethylbenzene
11	5.809	o-Xylene
12	6.369	Bicyclo[4.2.0]octa-1,3,5-triene
13	6.426	Ethylbenzene
14	9.023	Phenol
15	9.348	Benzene, 1-ethenyl-3-methyl-
16	9.417	Benzene, 1-ethenyl-2-methyl-
17	10.407	1,2-Cyclopentanedione, 3-methyl-
18	10.923	1H-Indene, 1-chloro-2,3-dihydro-
19	11.256	Phenol, 2-methyl-
20	11.903	p-Cresol
21	11.99	Phenol, 3-methyl-
22	12.777	Benzofuran, 7-methyl-
23	13.09	Maltol
24	13.894	Benzyl nitrile
25	14.387	1H-Indene, 3-methyl-
26	14.777	Phenol, 4-ethyl-
27	15.291	Naphthalene
28	16.131	1,4:3,6-Dianhydro-.alpha.-d-glucopyranose
29	16.375	Benzofuran, 2,3-dihydro-
30	19.084	Naphthalene, 2-methyl-
31	21.145	1-Tetradecene
32	21.216	Indole, 3-methyl-
34	23.989	Hexadecane
33	33.336	Hexadecanenitrile
34	34.929	n-Hexadecanoic acid
35	36.823	Octadecanoic acid, 2-propenyl ester
35	38.372	E-11-Hexadecenal
36	38.664	Octadecanoic acid
37	39.048	Hexadecanamide
38	39.216	Phenol, 4,4'-(1-methylethylidene)bis-
39	40.105	9-Octadecenoic acid, 1,2,3-propanetriyl ester, (E,E,E)-
40	42.163	Palmitoleamide
41	54.247	Cholest-5-en-3-ol (3.beta.)-, carbonochloridate

B.Tang, PhD Thesis, Aston University, 2024.

APPENDIX 6 Quantitative Interpretation of Protein Diffusion Coefficients in Mixed Protiated-Deuteriated Aqueous Solvent

A6.1 DOSY Spectra of 0.4 mM Lysozyme at a Range of Temperatures and in Different $H_2O:D_2O$ Compositions

Figure A6.1.1 DOSY spectrum of 0.4mM lysozyme in 0:100 $H_2O:D_2O$ solution at 278.15 K. Insert depicts protein methyl peaks (0 – 2 ppm), estimate of diffusion coefficient, D, and associated error estimate.

Figure A6.1.2 DOSY spectrum of 0.4mM lysozyme in 0:100 $H_2O:D_2O$ solution at 278.15 K. Insert depicts protein aromatic peaks (6 – 8 ppm), estimate of diffusion coefficient, D, and associated error estimate.

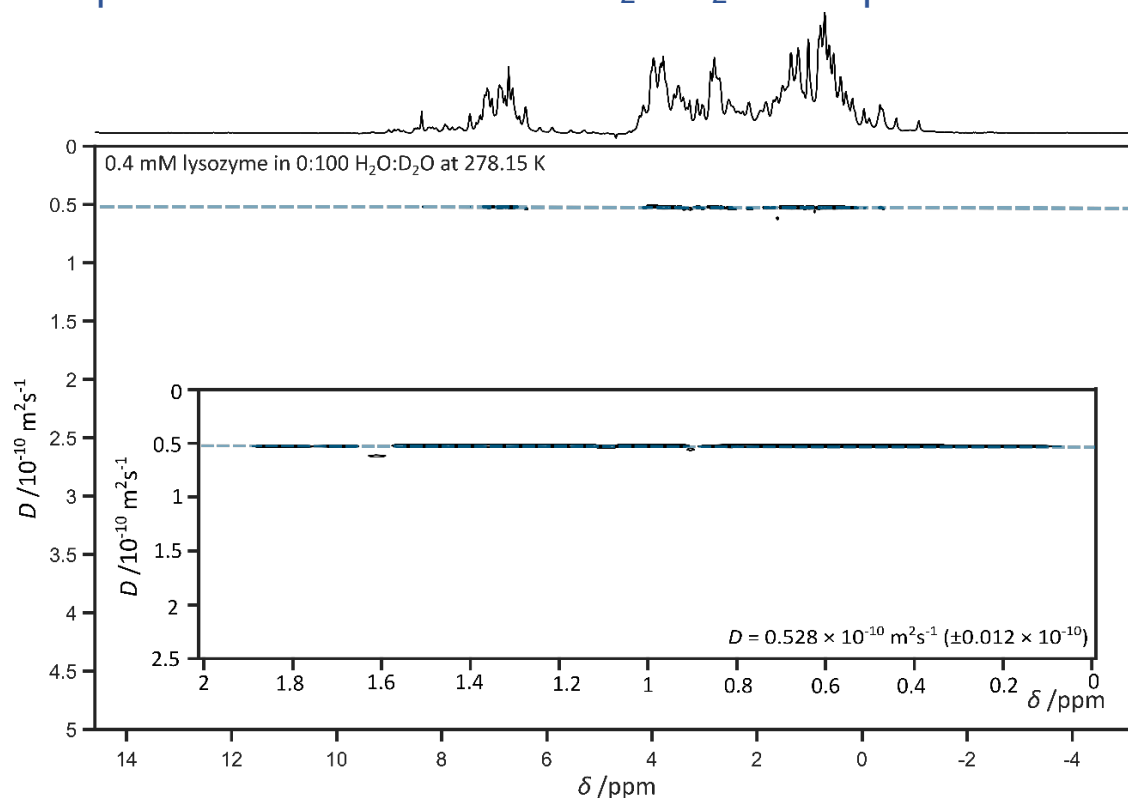B.Tang, PhD Thesis, Aston University, 2024.

Figure A6.1.3 DOSY spectrum of 0.4mM lysozyme in 10:90 H₂O:D₂O solution at 278.15 K. Insert depicts protein methyl peaks (0 – 2 ppm), estimate of diffusion coefficient, D, and associated error estimate.

Figure A6.1.4 DOSY spectrum of 0.4mM lysozyme in 10:90 H₂O:D₂O solution at 278.15 K. Insert depicts protein aromatic peaks (6 – 8 ppm), estimate of diffusion coefficient, D, and associated error estimate.

Figure A6.1.5 DOSY spectrum of 0.4mM lysozyme in 30:70 H₂O:D₂O solution at 278.15 K. Insert depicts protein methyl peaks (0 – 2 ppm), estimate of diffusion coefficient, D, and associated error estimate.
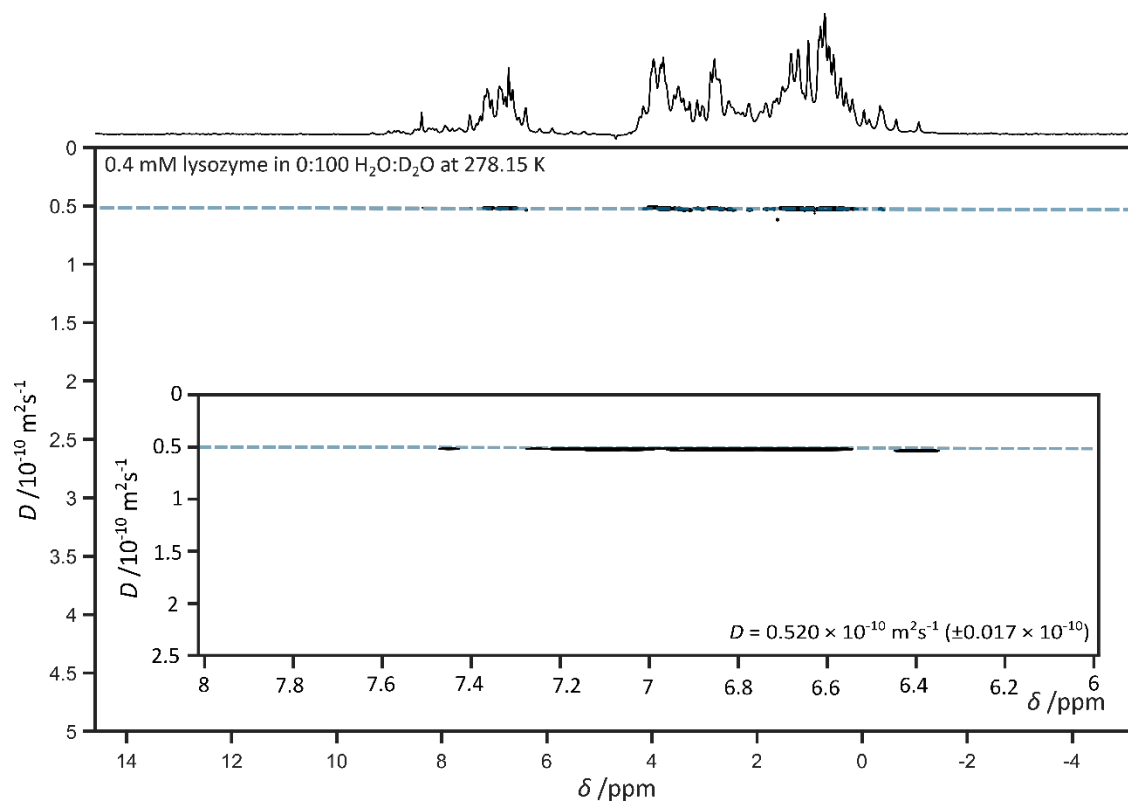

Figure A6.1.6 DOSY spectrum of 0.4mM lysozyme in 30:70 H₂O:D₂O solution at 278.15 K. Insert depicts protein aromatic peaks (6 – 8 ppm), estimate of diffusion coefficient, D, and associated error estimate.
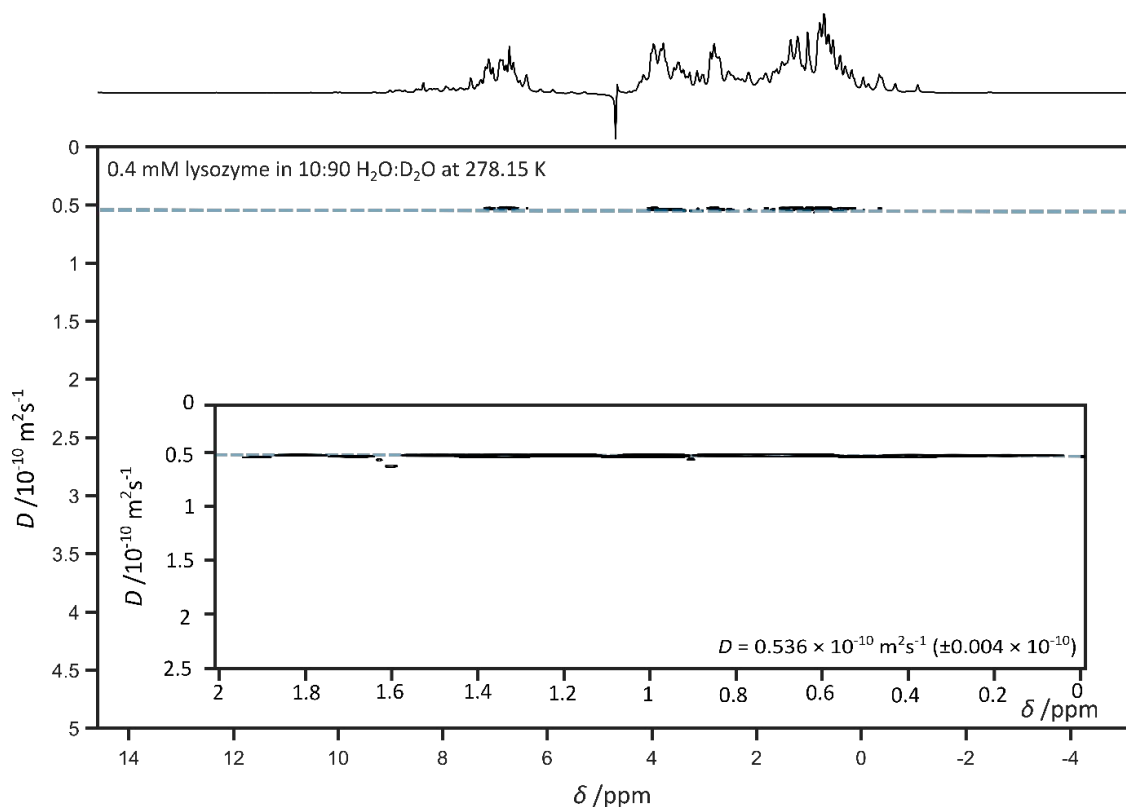
316

B.Tang, PhD Thesis, Aston University, 2024.

Figure A6.1.7 DOSY spectrum of 0.4mM lysozyme in 50:50 H₂O:D₂O solution at 278.15 K. Insert depicts protein methyl peaks (0 – 2 ppm), estimate of diffusion coefficient, D, and associated error estimate.
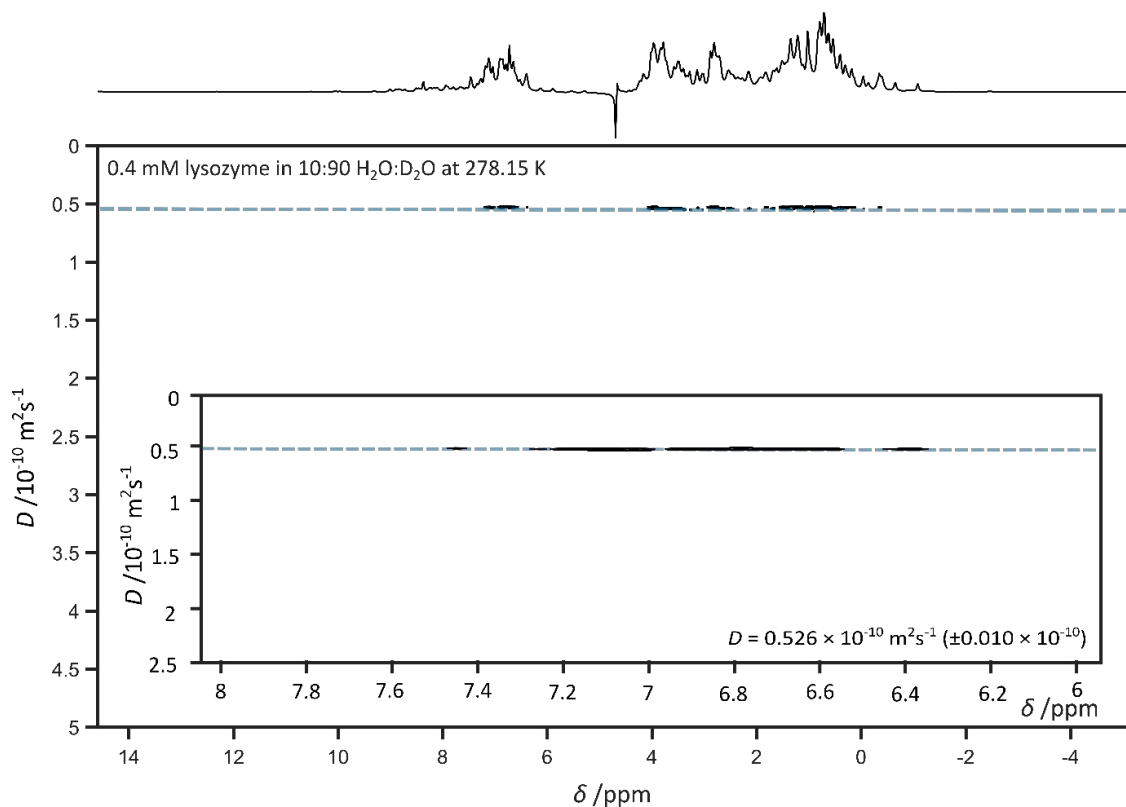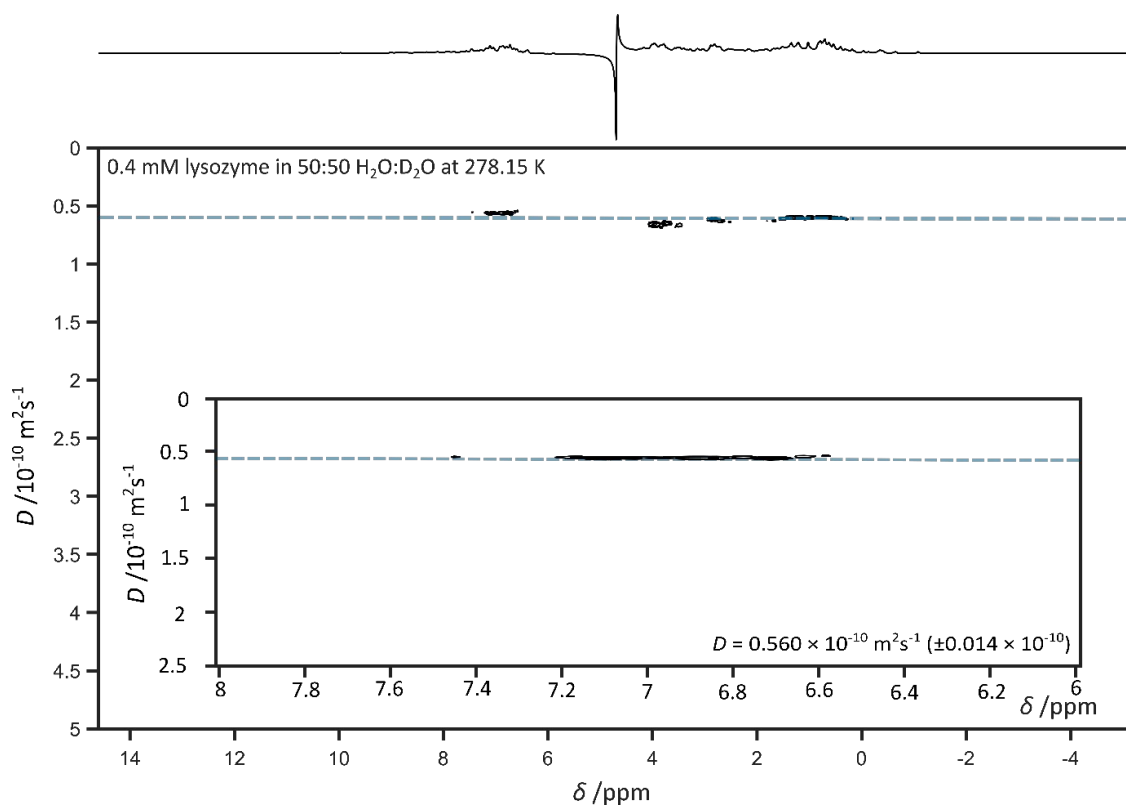

Figure A6.1.8 DOSY spectrum of 0.4mM lysozyme in 50:50 H₂O:D₂O solution at 278.15 K. Insert depicts protein aromatic peaks (6 – 8 ppm), estimate of diffusion coefficient, D, and associated error estimate.
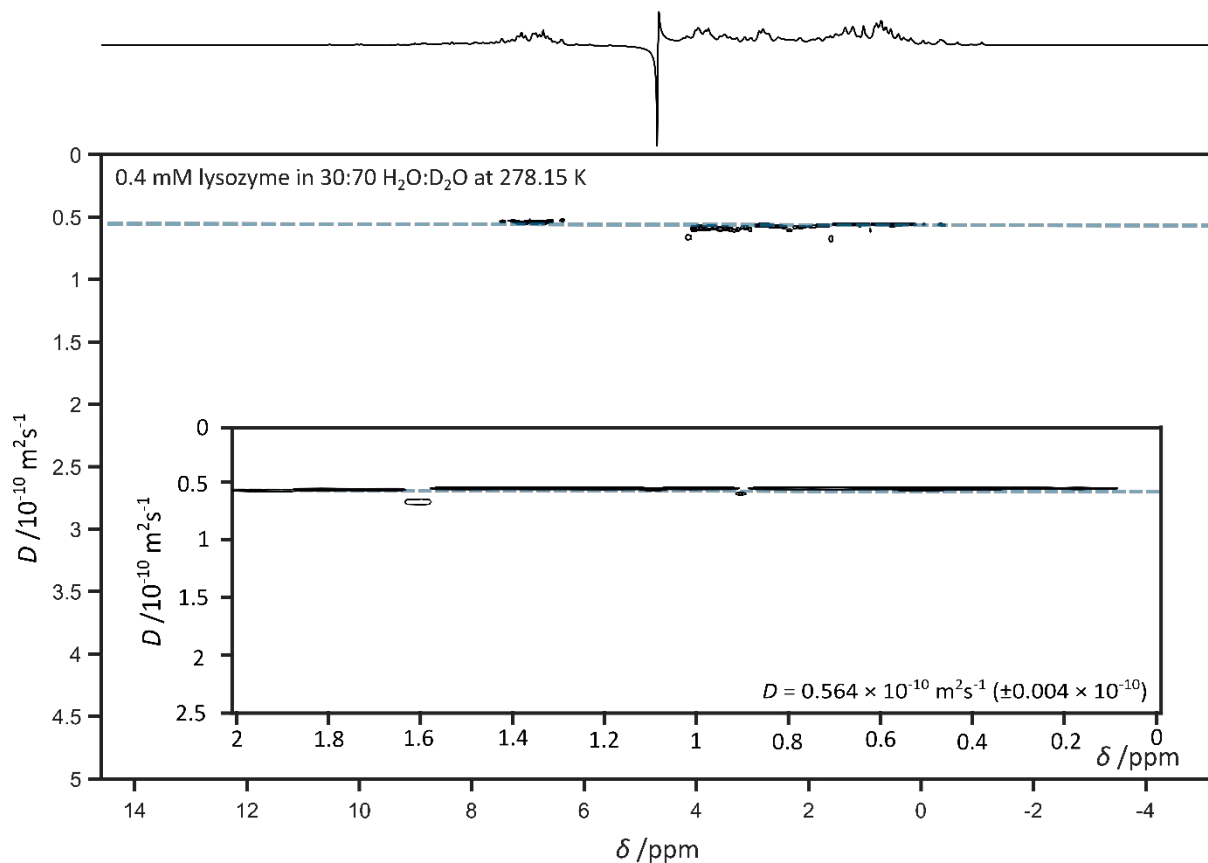
B.Tang, PhD Thesis, Aston University, 2024.
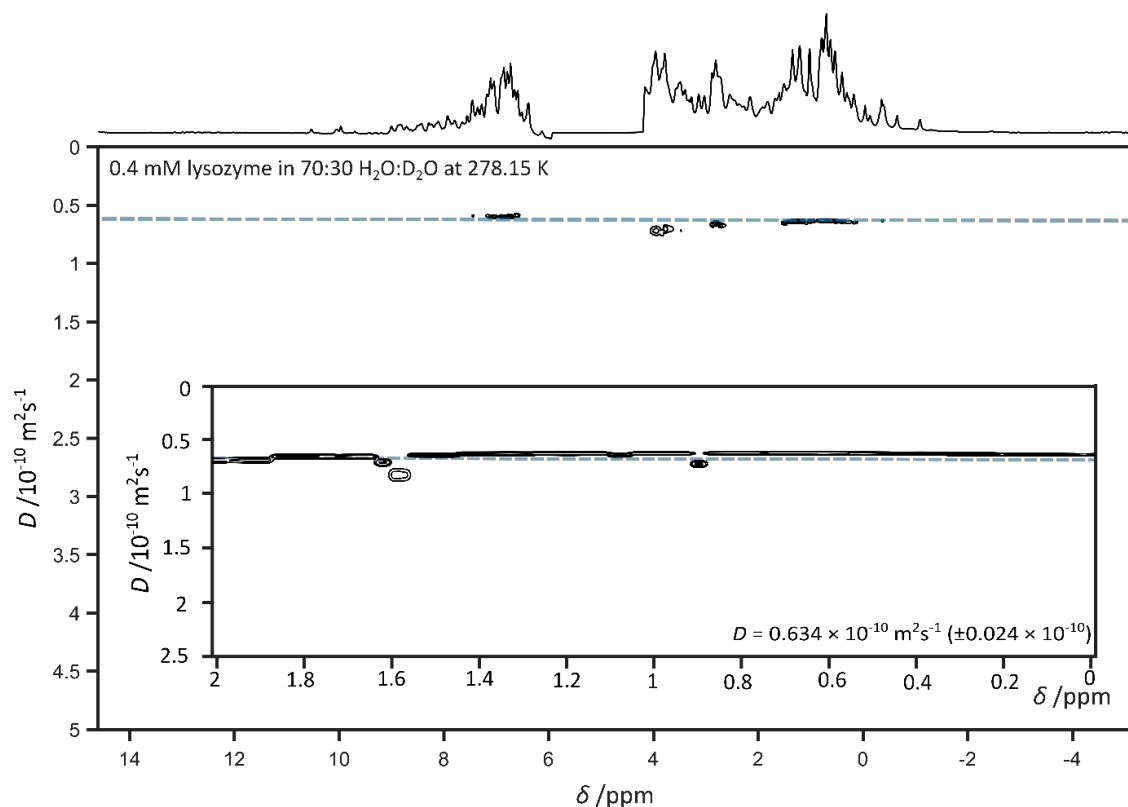
Figure A6.1.9 DOSY spectrum of 0.4mM lysozyme in 70:30 H₂O:D₂O solution at 278.15 K. Insert depicts protein methyl peaks (0 – 2 ppm), estimate of diffusion coefficient, D, and associated error estimate.

Figure A6.1.10 DOSY spectrum of 0.4mM lysozyme in 70:30 H₂O:D₂O solution at 278.15 K. Insert depicts protein aromatic peaks (6 – 8 ppm), estimate of diffusion coefficient, D, and associated error estimate.

318

B.Tang, PhD Thesis, Aston University, 2024.

Figure A6.1.11 DOSY spectrum of 0.4mM lysozyme in 90:10 H₂O:D₂O solution at 278.15 K. Insert depicts protein methyl peaks (0 – 2 ppm), estimate of diffusion coefficient, D, and associated error estimate.
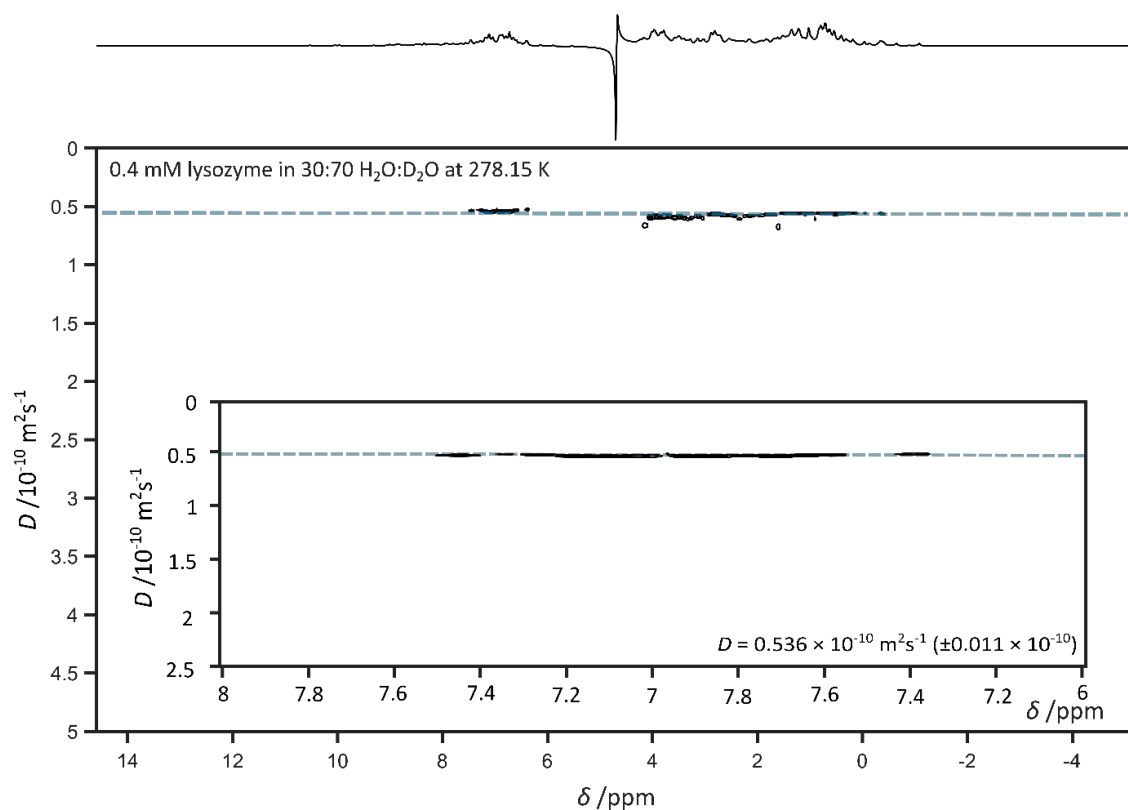

Figure A6.1.12 DOSY spectrum of 0.4mM lysozyme in 90:10 H₂O:D₂O solution at 278.15 K. Insert depicts protein aromatic peaks (6 – 8 ppm), estimate of diffusion coefficient, D, and associated error estimate.
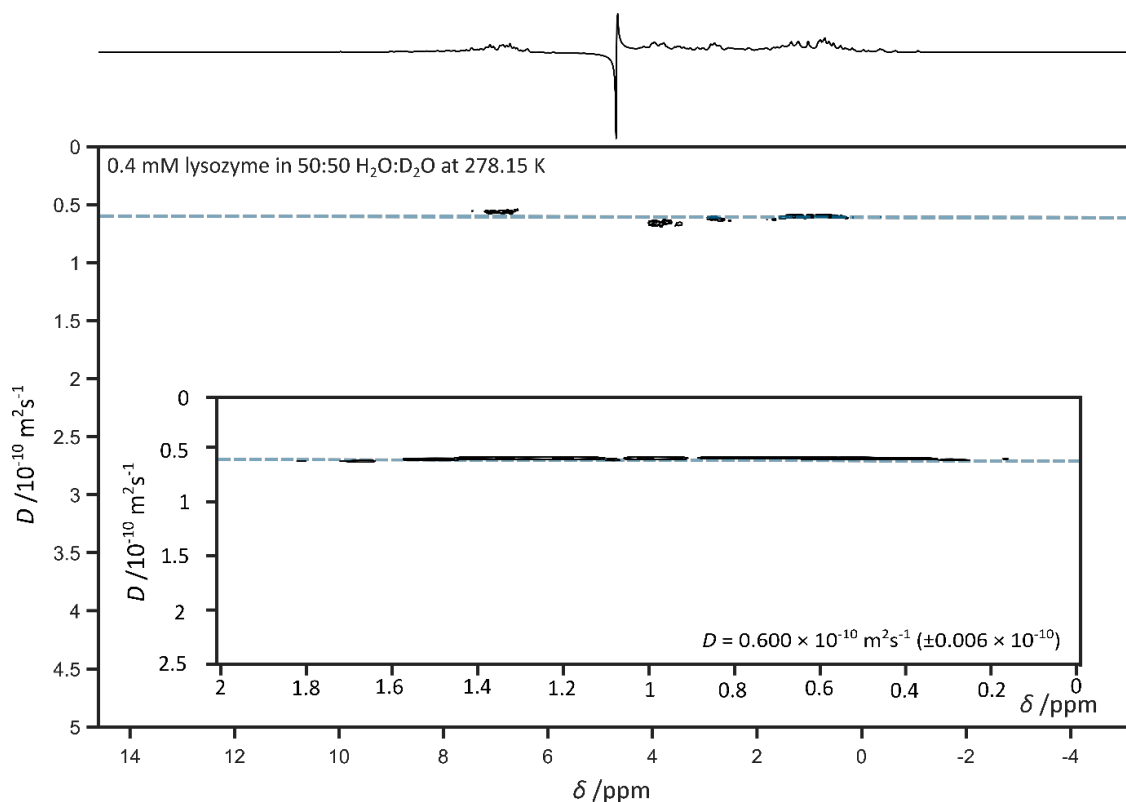
B.Tang, PhD Thesis, Aston University, 2024.

Figure A6.1.13 DOSY spectrum of 0.4mM lysozyme in 0:100 H₂O:D₂O solution at 283.15 K. Insert depicts protein methyl peaks (0 – 2 ppm), estimate of diffusion coefficient, D, and associated error estimate.

Inside the first figure insert: $D = 0.629 \times 10^{-10} \text{ m}^2\text{s}^{-1}\ (\pm 0.003 \times 10^{-10})$

Figure 1 label: 0.4 mM lysozyme in 0:100 H_2O:D_2O at 283.15 K

Figure A6.1.14 DOSY spectrum of 0.4mM lysozyme in 10:90 H₂O:D₂O solution at 283.15 K. Insert depicts protein methyl peaks (0 – 2 ppm), estimate of diffusion coefficient, D, and associated error estimate.

Inside the second figure insert: $D = 0.642 \times 10^{-10} \text{ m}^2\text{s}^{-1}\ (\pm 0.003 \times 10^{-10})$

Figure 2 label: 0.4 mM lysozyme in 10:90 H_2O:D_2O at 283.15 K

B.Tang, PhD Thesis, Aston University, 2024.

Figure A6.1.15 DOSY spectrum of 0.4mM lysozyme in 30:70 H₂O:D₂O solution at 283.15 K. Insert depicts protein methyl peaks (0 – 2 ppm), estimate of diffusion coefficient, D, and associated error estimate.
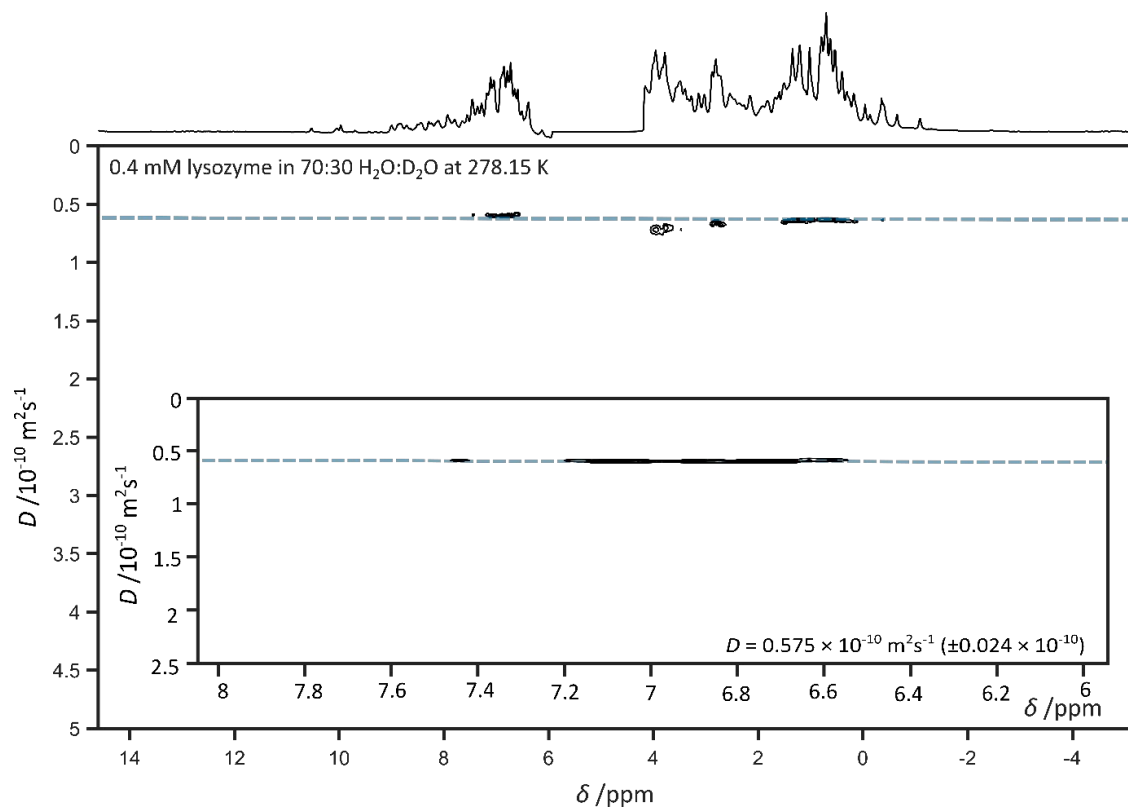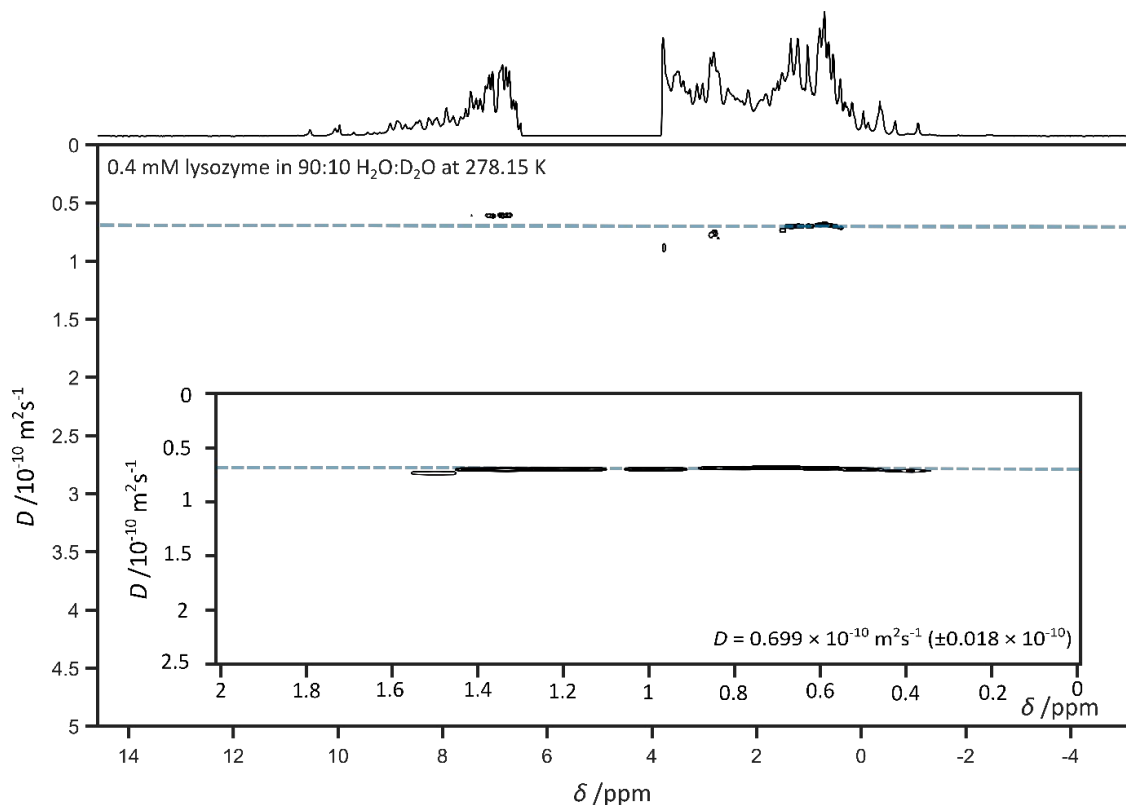

Figure A6.1.16 DOSY spectrum of 0.4mM lysozyme in 50:50 H₂O:D₂O solution at 283.15 K. Insert depicts protein methyl peaks (0 – 2 ppm), estimate of diffusion coefficient, D, and associated error estimate.

Figure A6.1.17 DOSY spectrum of 0.4mM lysozyme in 70:30 H₂O:D₂O solution at 283.15 K. Insert depicts protein methyl peaks (0 – 2 ppm), estimate of diffusion coefficient, D, and associated error estimate.
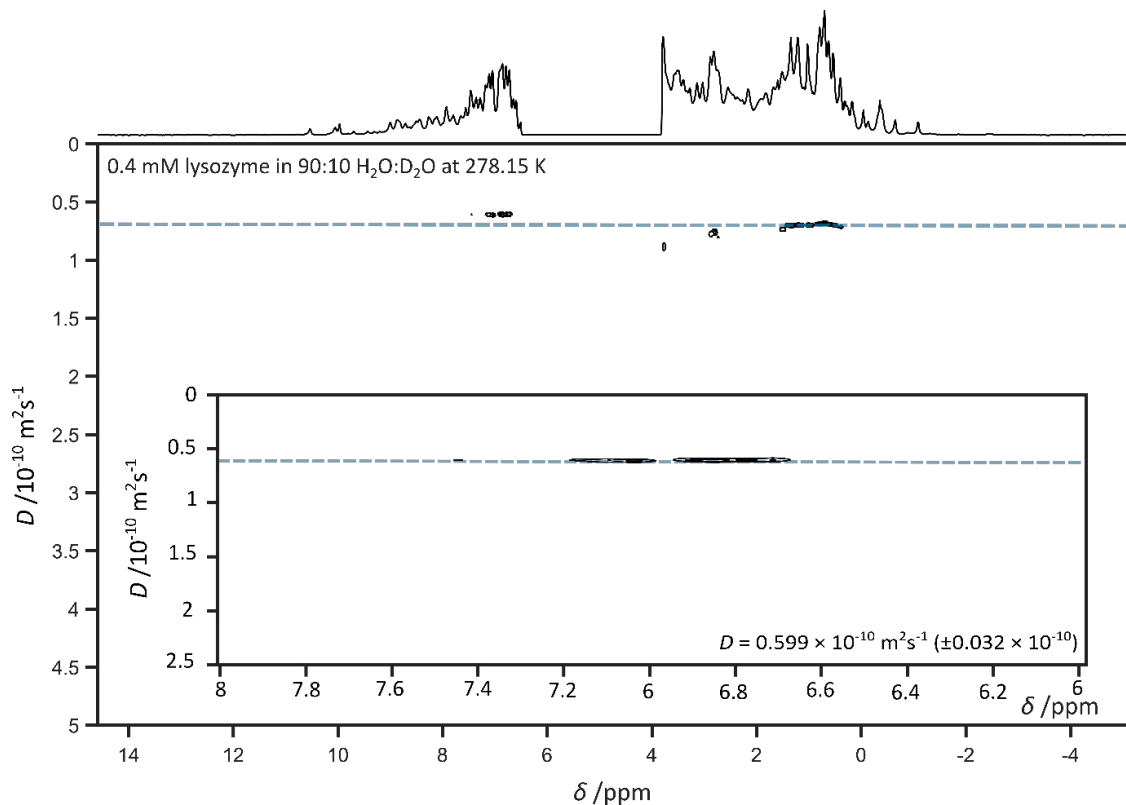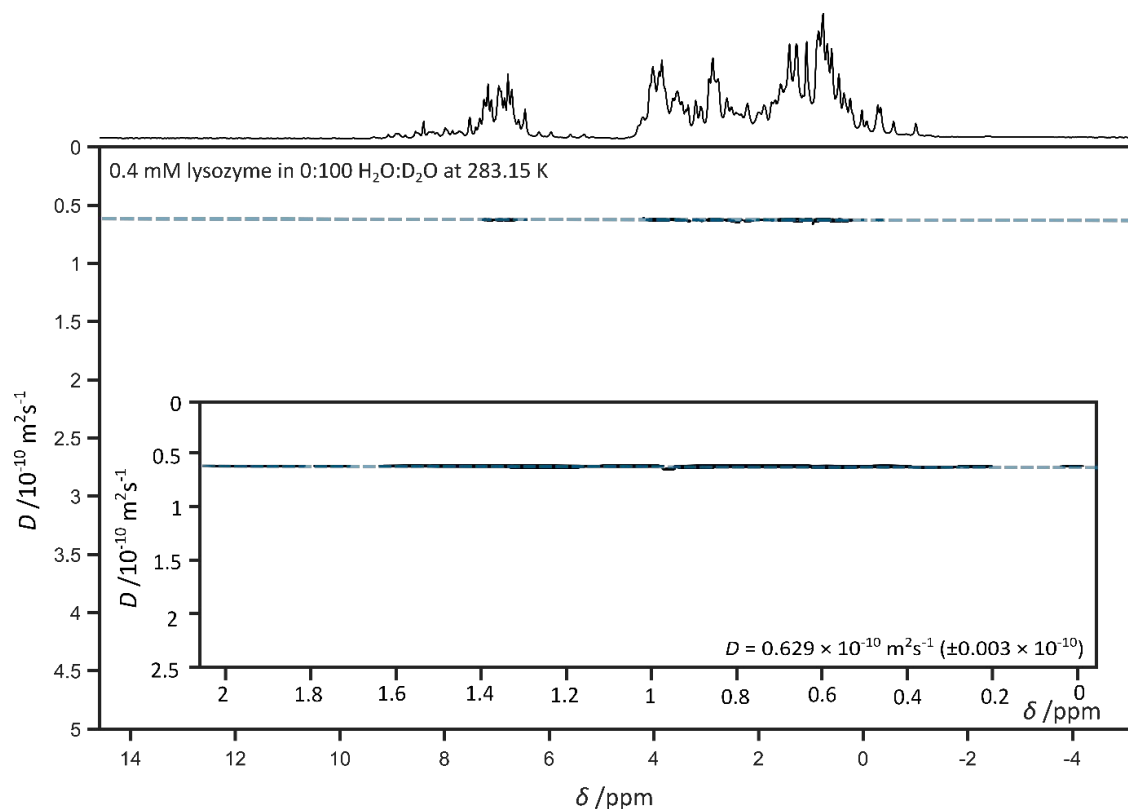

Figure A6.1.18 DOSY spectrum of 0.4mM lysozyme in 90:10 H₂O:D₂O solution at 283.15 K. Insert depicts protein methyl peaks (0 – 2 ppm), estimate of diffusion coefficient, D, and associated error estimate.

B.Tang, PhD Thesis, Aston University, 2024.

Figure A6.1.19 DOSY spectrum of 0.4mM lysozyme in 0:100 H_2O:D_2O solution at 288.15 K. Insert depicts protein methyl peaks (0 – 2 ppm), estimate of diffusion coefficient, D, and associated error estimate.

Insert text: $D = 0.748 \times 10^{-10}$ m^{2}s^{-1} ($\pm0.003 \times 10^{-10}$)

Label: 0.4 mM lysozyme in 0:100 H_2O:D_2O at 288.15 K

Figure A6.1.20 DOSY spectrum of 0.4mM lysozyme in 10:90 H_2O:D_2O solution at 288.15 K. Insert depicts protein methyl peaks (0 – 2 ppm), estimate of diffusion coefficient, D, and associated error estimate.

Insert text: $D = 0.763 \times 10^{-10}$ m^{2}s^{-1} ($\pm0.007 \times 10^{-10}$)

Label: 0.4 mM lysozyme in 10:90 H_2O:D_2O at 288.15 K
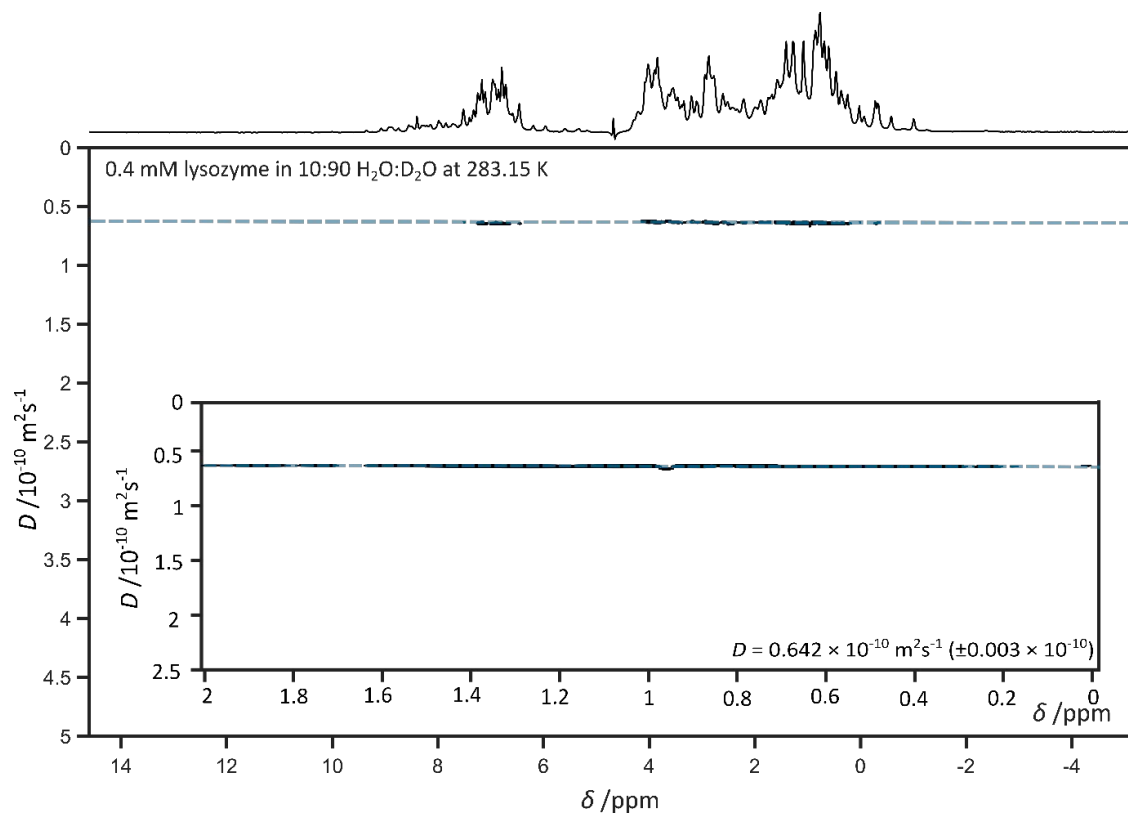
B.Tang, PhD Thesis, Aston University, 2024.

Figure A6.1.21. DOSY spectrum of 0.4mM lysozyme in 30:70 H₂O:D₂O solution at 288.15 K. Insert depicts protein methyl peaks (0 – 2 ppm), estimate of diffusion coefficient, D, and associated error estimate.
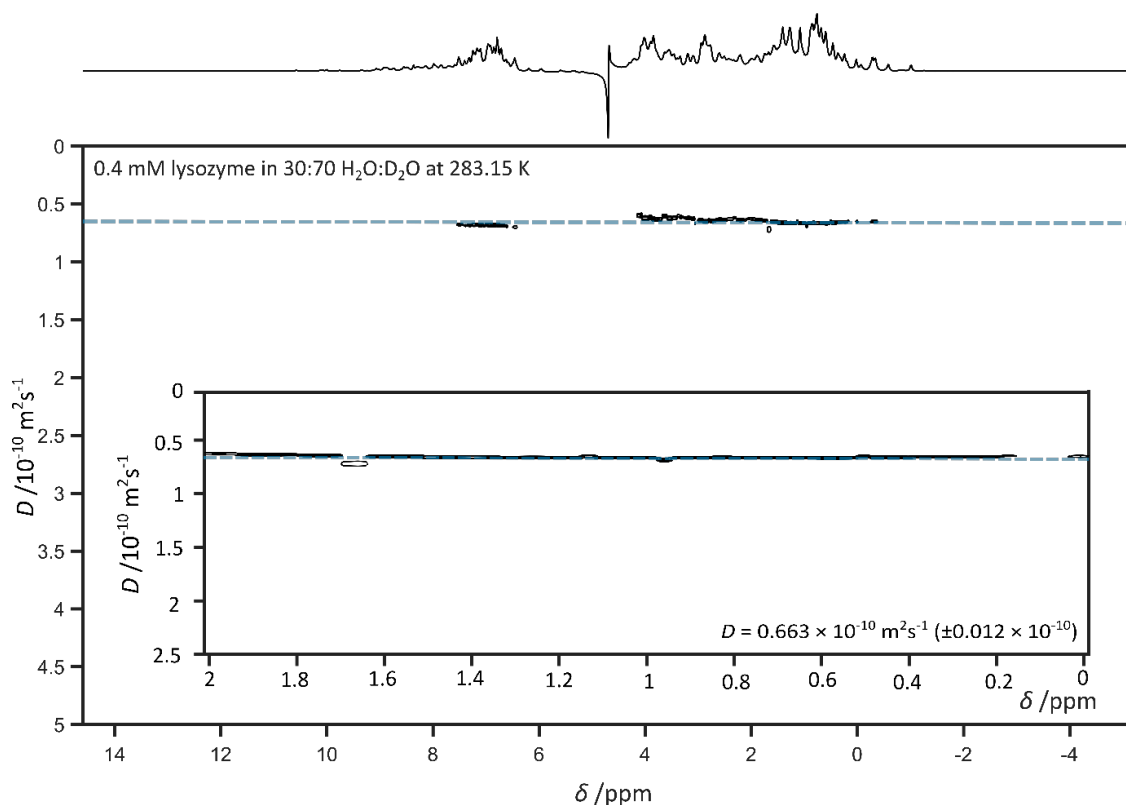

Figure A6.1.22 DOSY spectrum of 0.4mM lysozyme in 50:50 H₂O:D₂O solution at 288.15 K. Insert depicts protein methyl peaks (0 – 2 ppm), estimate of diffusion coefficient, D, and associated error estimate.
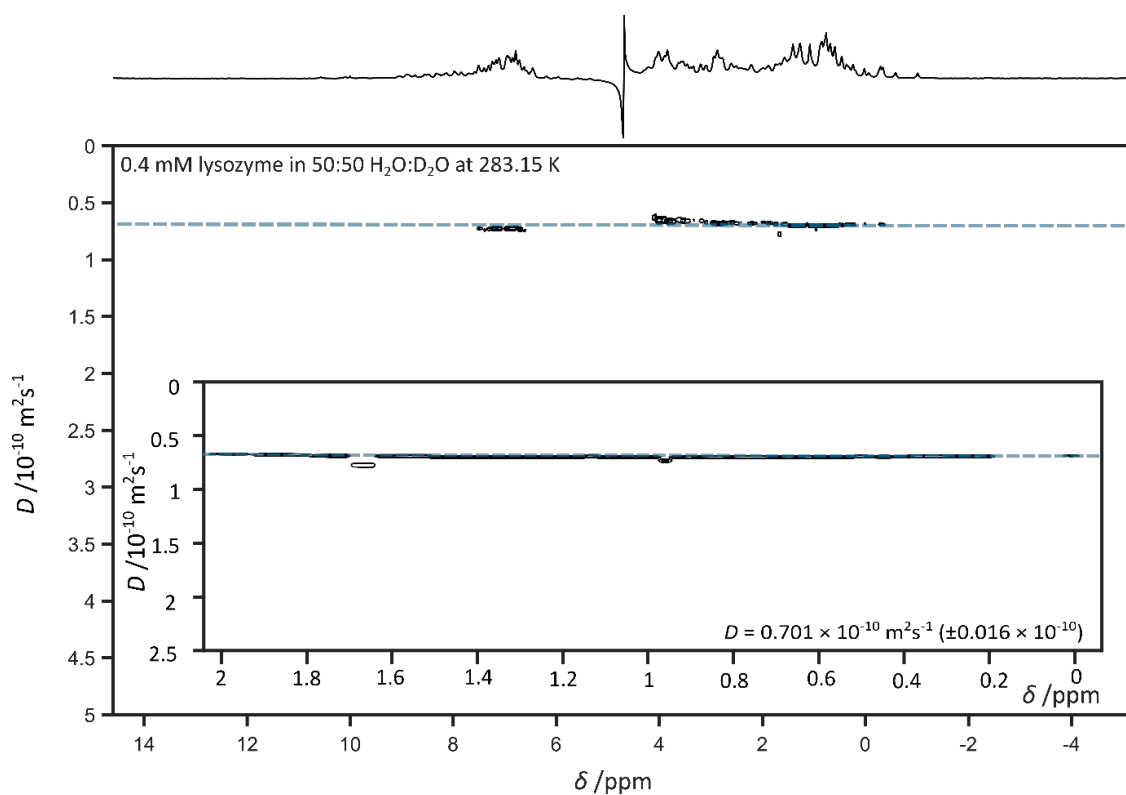
Figure A6.1.23 DOSY spectrum of 0.4mM lysozyme in 70:30 H₂O:D₂O solution at 288.15 K. Insert depicts protein methyl peaks (0 – 2 ppm), estimate of diffusion coefficient, D, and associated error estimate.
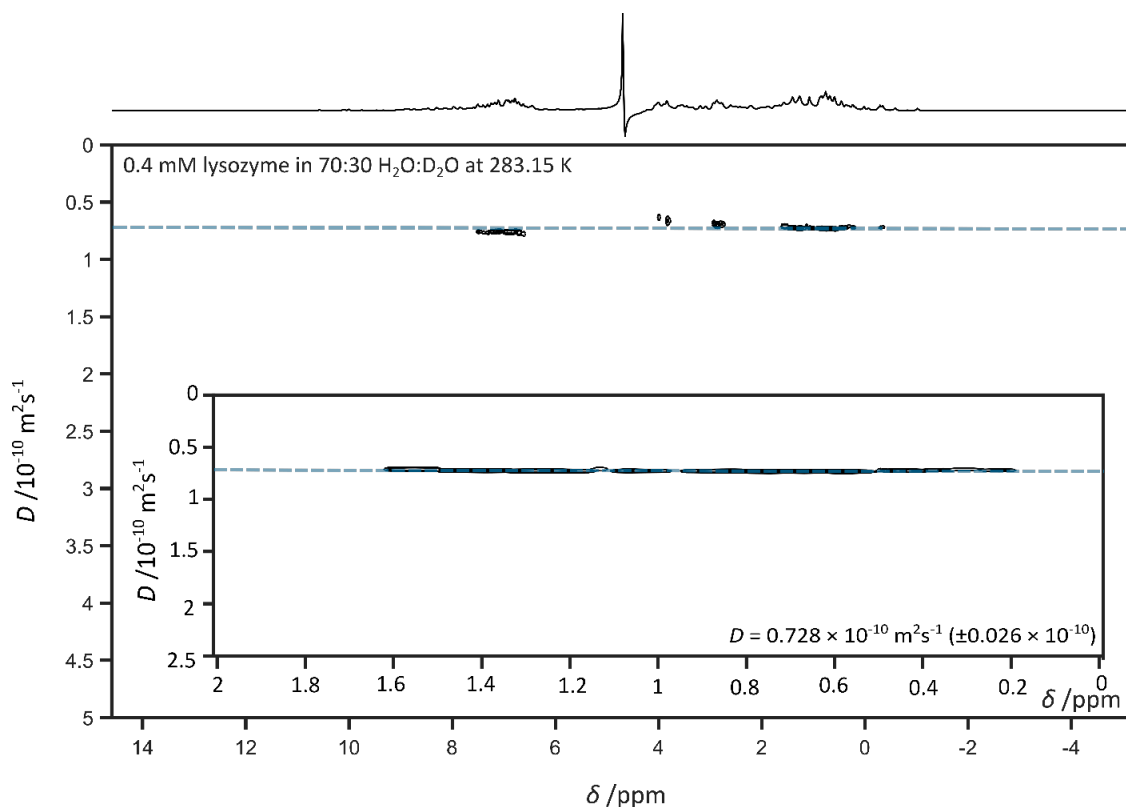
In the first spectrum: "0.4 mM lysozyme in 70:30 H_2O:D_2O at 288.15 K" and insert: $D = 0.878 \times 10^{-10}$ m²s⁻¹ (±0.014 × 10⁻¹⁰)

Figure A6.1.24 DOSY spectrum of 0.4mM lysozyme in 90:10 H₂O:D₂O solution at 288.15 K. Insert depicts protein methyl peaks (0 – 2 ppm), estimate of diffusion coefficient, D, and associated error estimate.
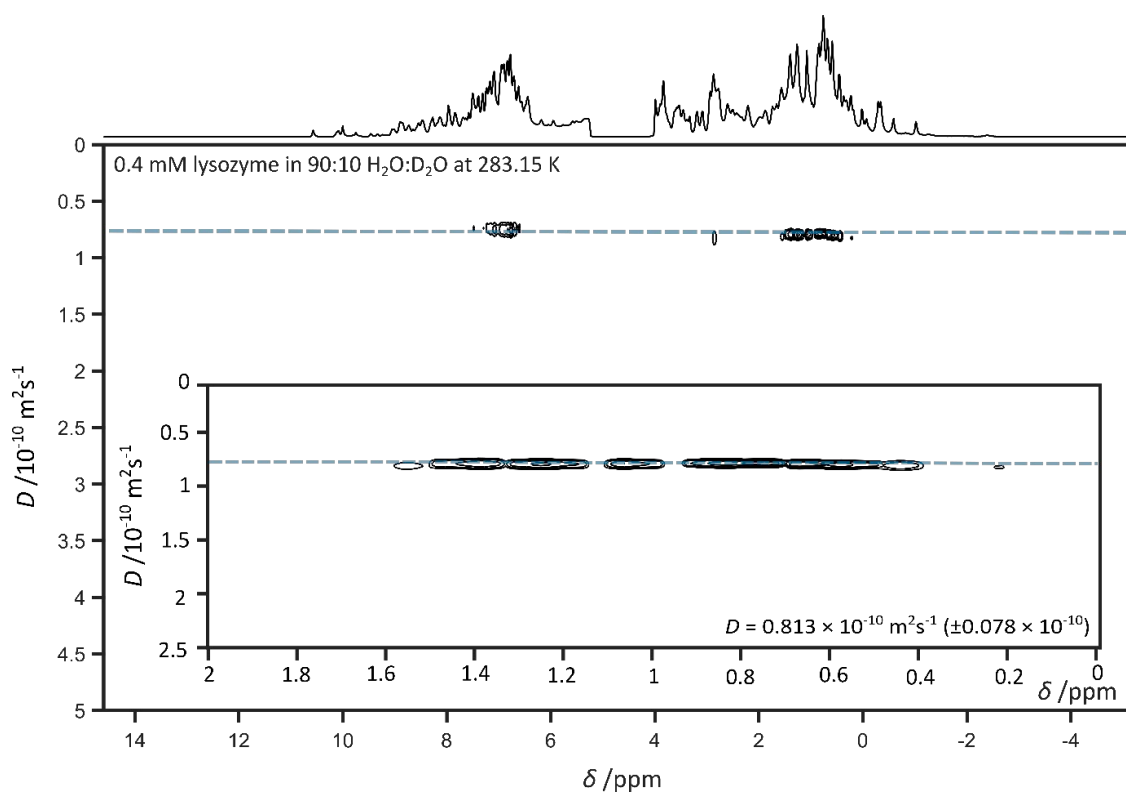
In the second spectrum: "0.4 mM lysozyme in 90:10 H_2O:D_2O at 288.15 K" and insert: $D = 0.910 \times 10^{-10}$ m²s⁻¹ (±0.020 × 10⁻¹⁰)

B.Tang, PhD Thesis, Aston University, 2024.

Figure A6.1.25 DOSY spectrum of 0.4mM lysozyme in 0:100 H₂O:D₂O solution at 298.15 K. Insert depicts protein methyl peaks (0 – 2 ppm), estimate of diffusion coefficient, D, and associated error estimate.
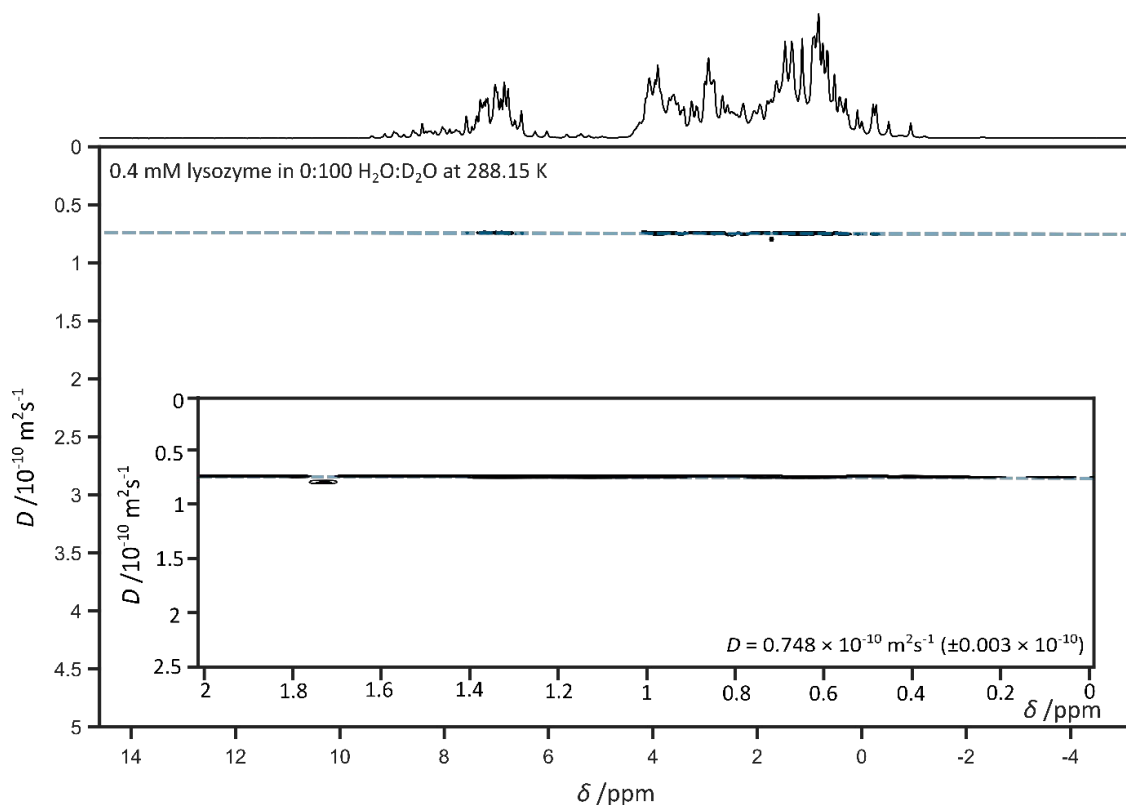

Figure A6.1.26 DOSY spectrum of 0.4mM lysozyme in 10:90 H₂O:D₂O solution at 298.15 K. Insert depicts protein methyl peaks (0 – 2 ppm), estimate of diffusion coefficient, D, and associated error estimate.
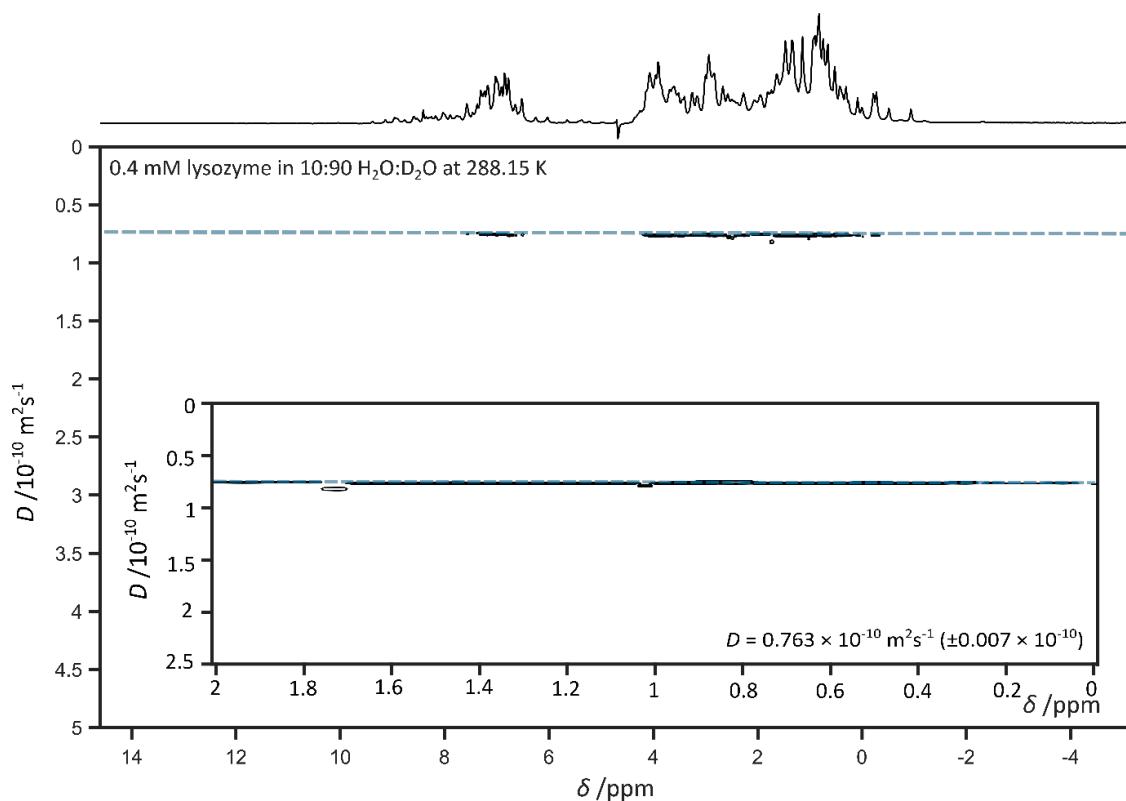
B.Tang, PhD Thesis, Aston University, 2024.

Figure A6.1.27 DOSY spectrum of 0.4mM lysozyme in 30:70 H_2O:D_2O solution at 298.15 K. Insert depicts protein methyl peaks (0 – 2 ppm), estimate of diffusion coefficient, D, and associated error estimate.
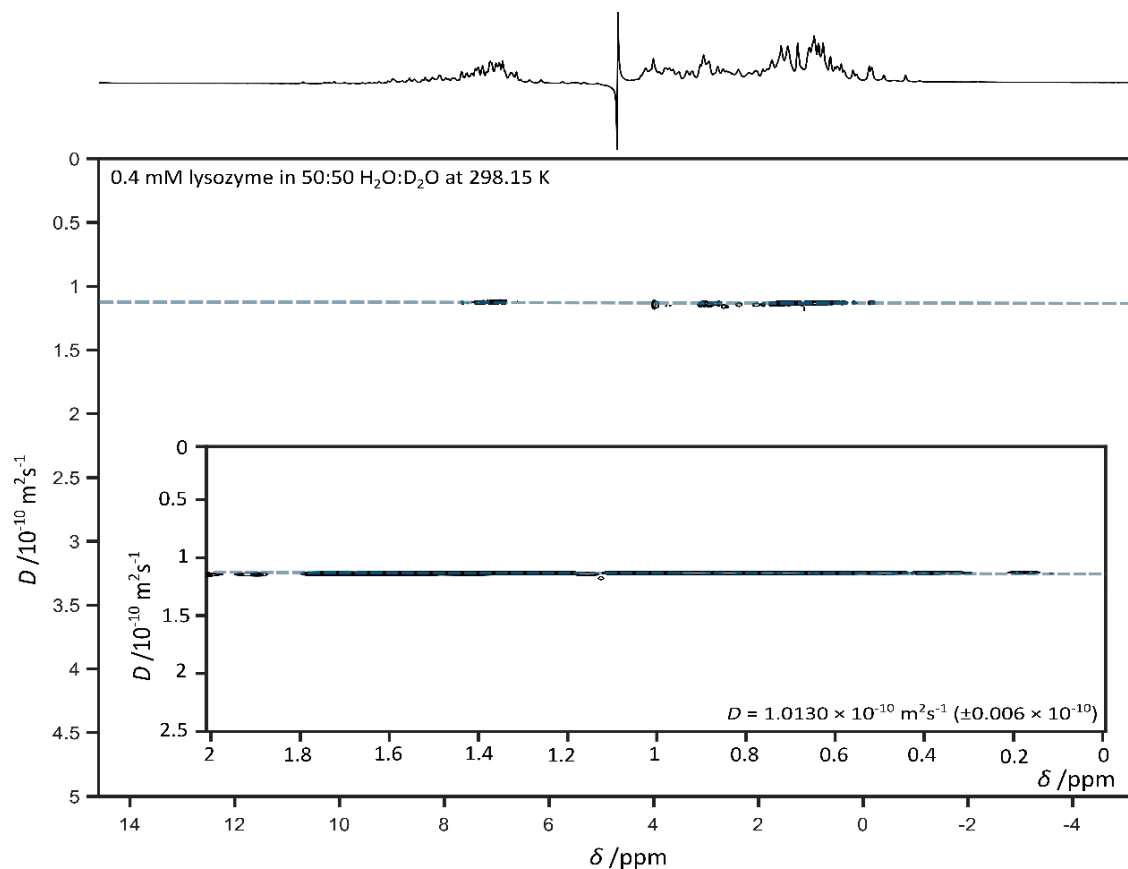
Figure A6.1.28 DOSY spectrum of 0.4mM lysozyme in 50:50 H_2O:D_2O solution at 298.15 K. Insert depicts protein methyl peaks (0 – 2 ppm), estimate of diffusion coefficient, D, and associated error estimate.
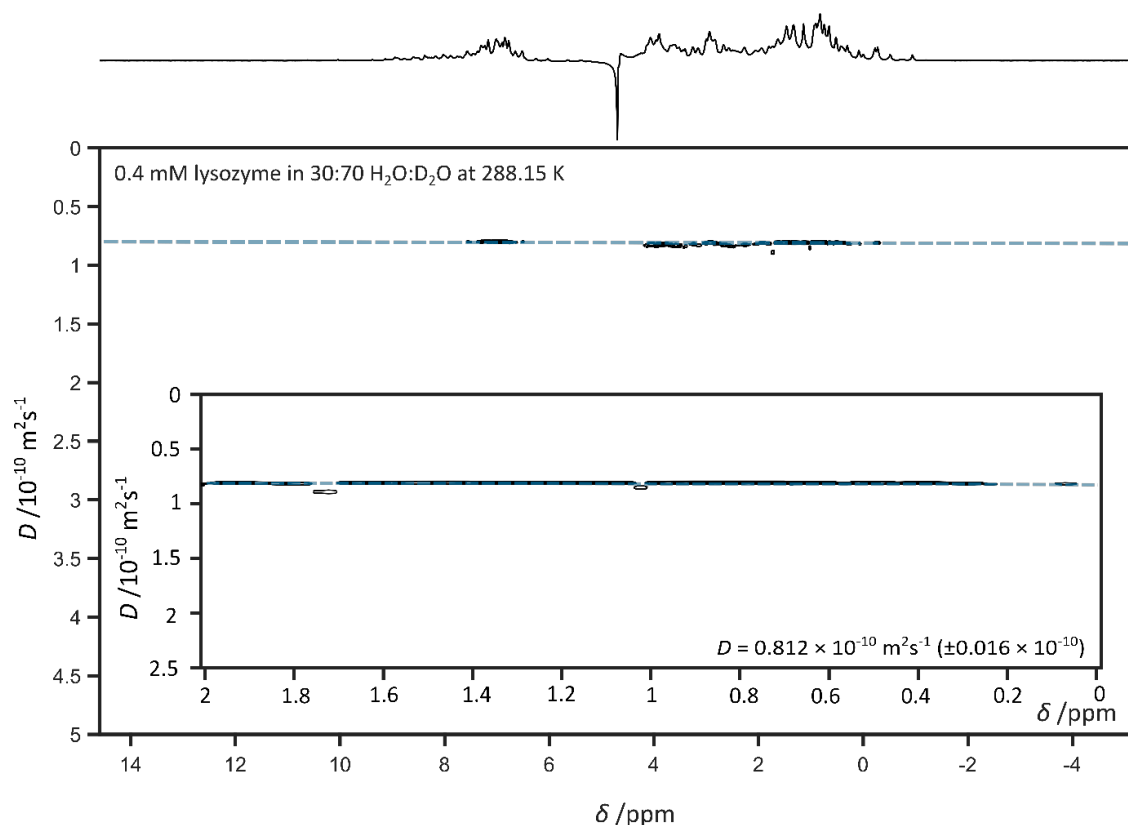
B.Tang, PhD Thesis, Aston University, 2024.
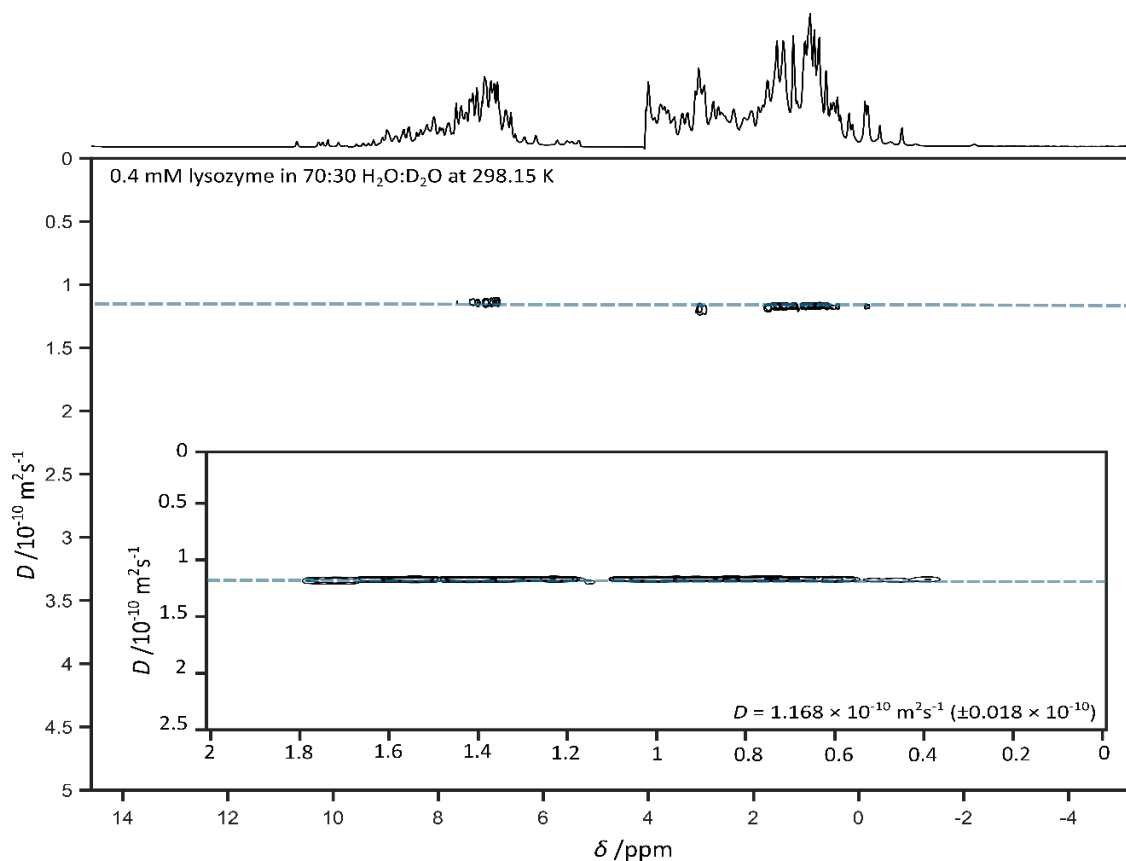
Figure A6.1.29 DOSY spectrum of 0.4mM lysozyme in 70:30 H_2O:D_2O solution at 298.15 K. Insert depicts protein methyl peaks (0 – 2 ppm), estimate of diffusion coefficient, D, and associated error estimate.
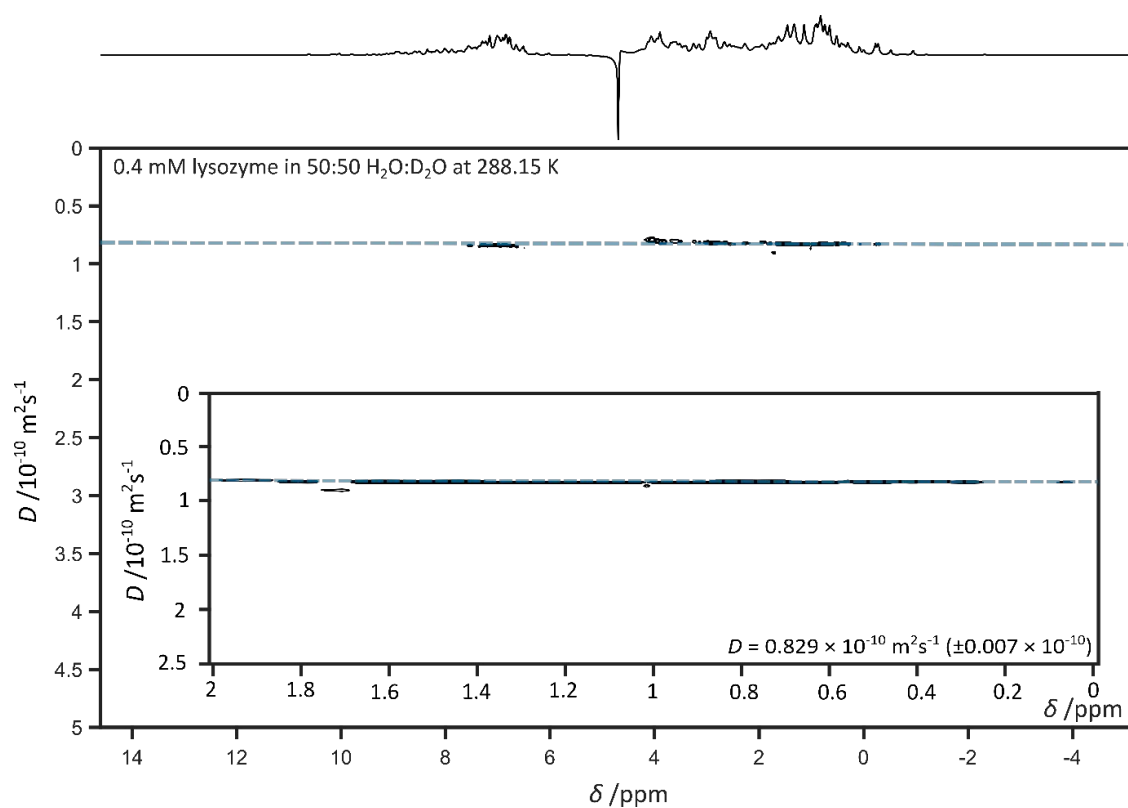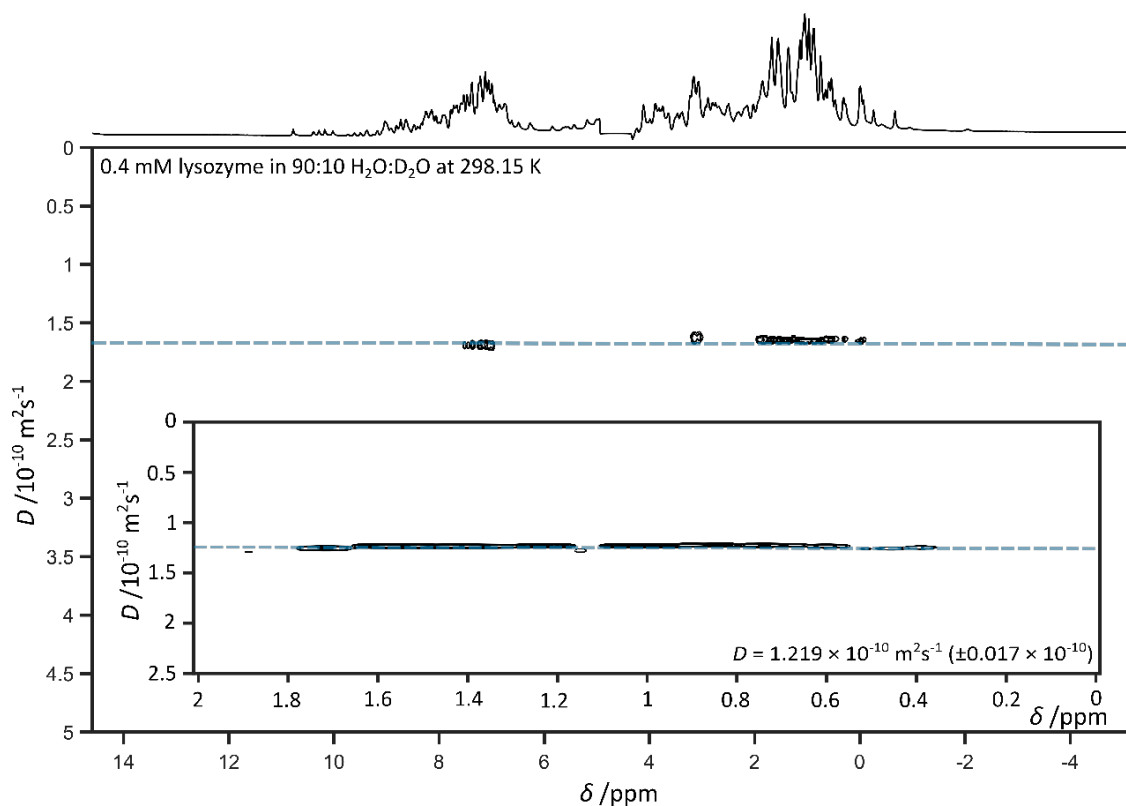

Figure A6.1.30 DOSY spectrum of 0.4mM lysozyme in 90:10 H_2O:D_2O solution at 298.15 K. Insert depicts protein methyl peaks (0 – 2 ppm), estimate of diffusion coefficient, D, and associated error estimate.

328

B.Tang, PhD Thesis, Aston University, 2024.
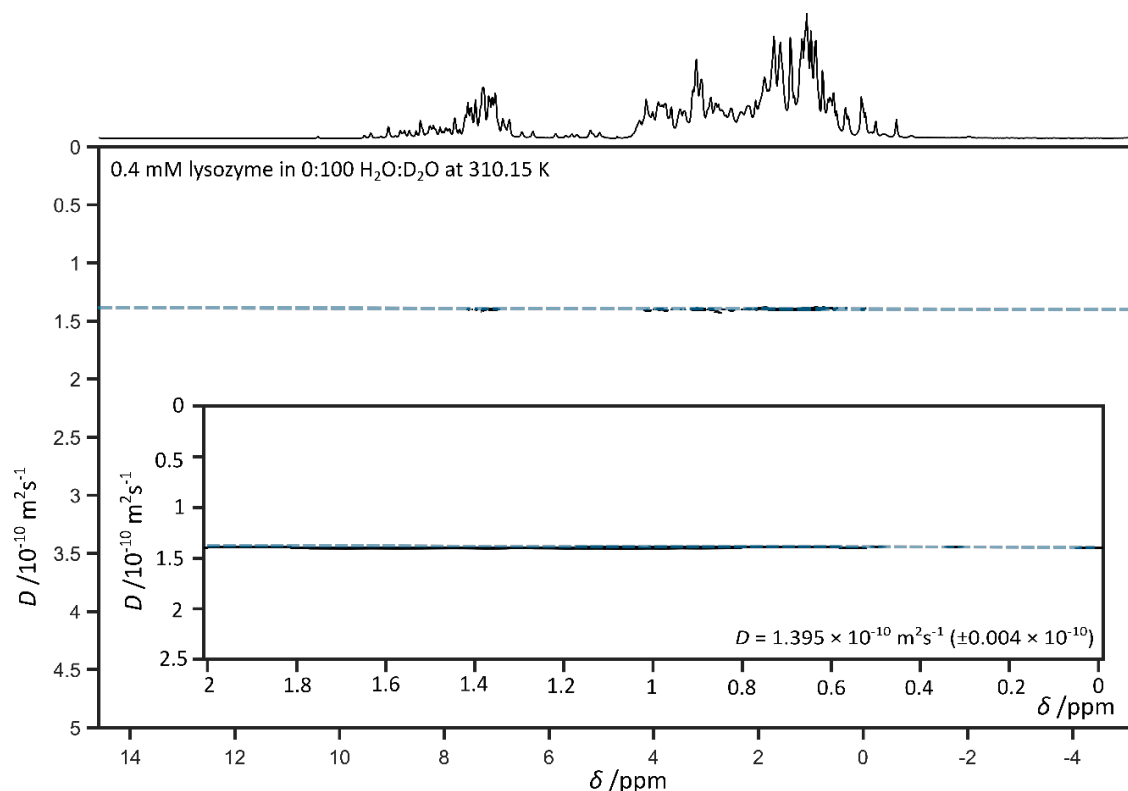
Figure A6.1.31 DOSY spectrum of 0.4mM lysozyme in 0:100 H₂O:D₂O solution at 310.15 K. Insert depicts protein methyl peaks (0 – 2 ppm), estimate of diffusion coefficient, D, and associated error estimate.
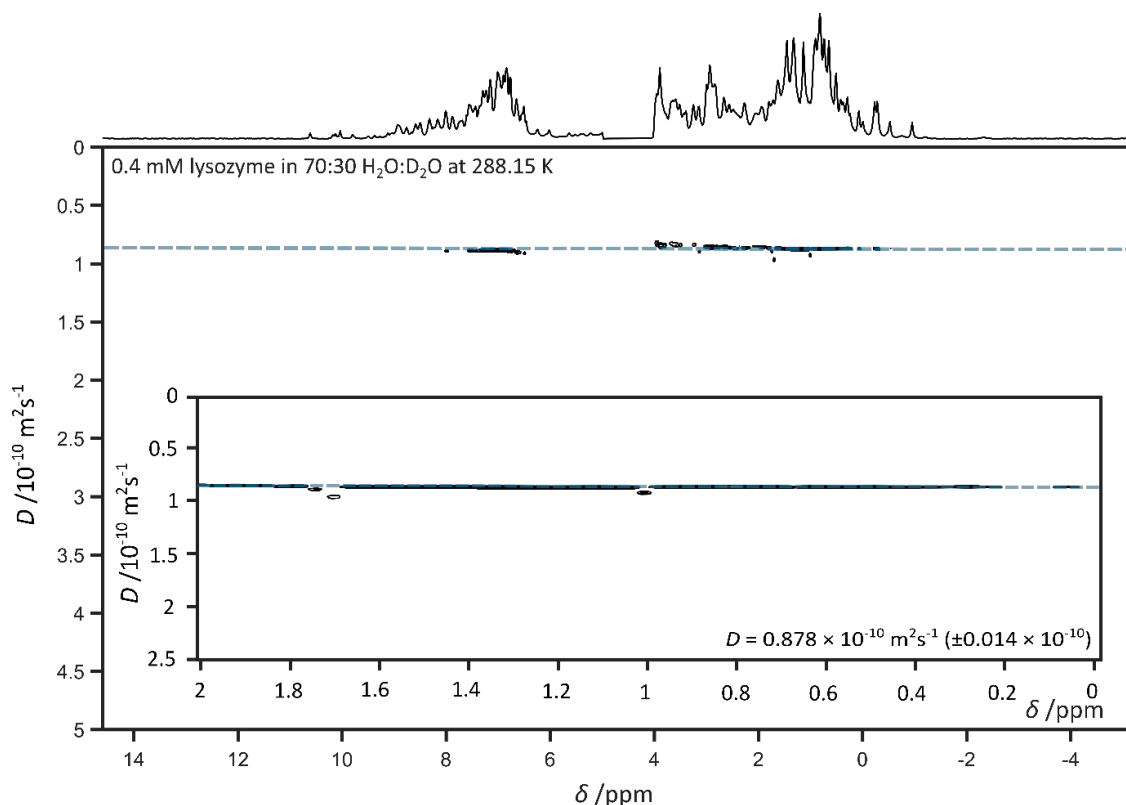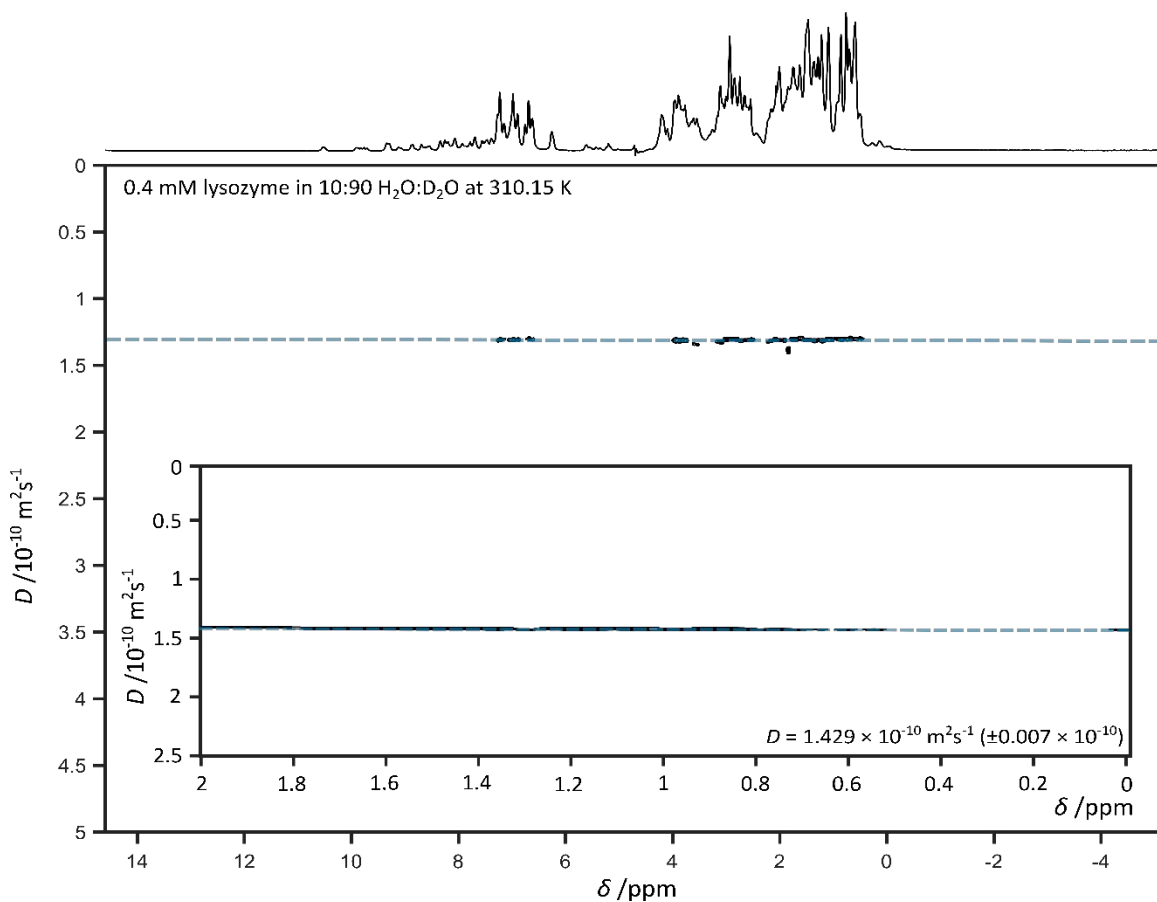

Figure A6.1.32 DOSY spectrum of 0.4mM lysozyme in 10:90 H₂O:D₂O solution at 310.15 K. Insert depicts protein methyl peaks (0 – 2 ppm), estimate of diffusion coefficient, D, and associated error estimate.
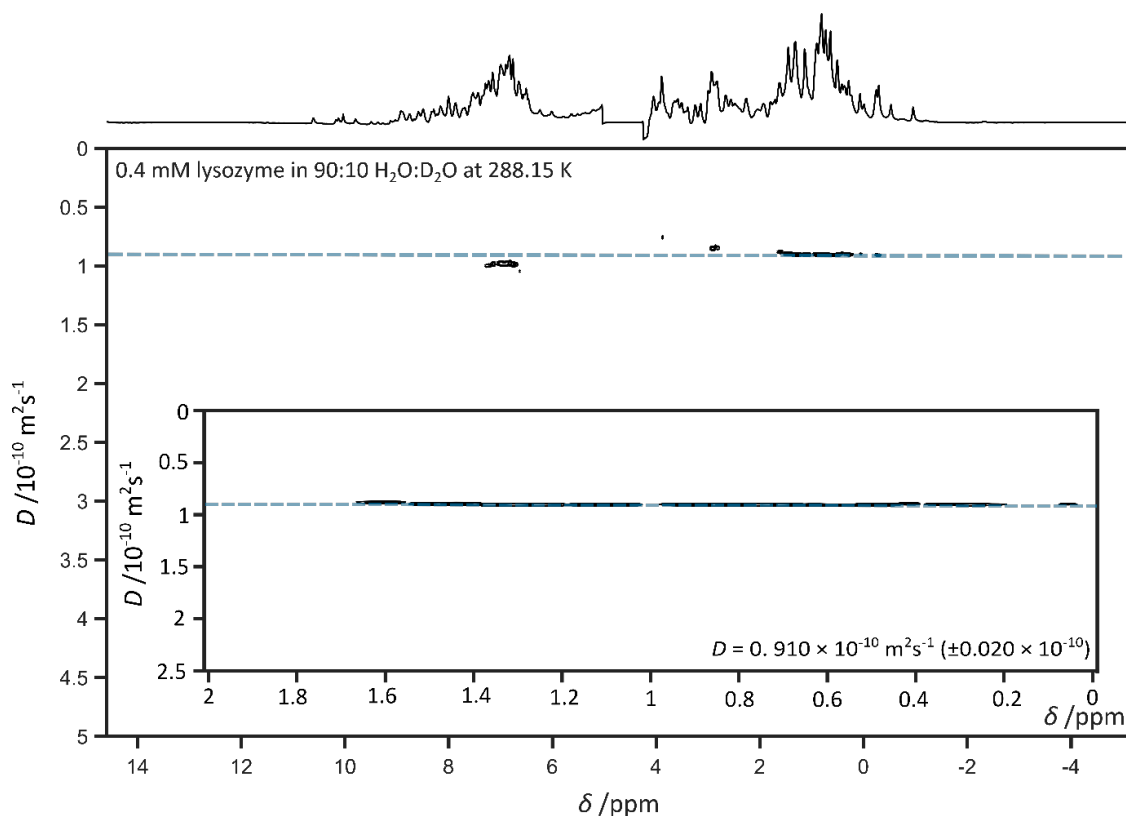
B.Tang, PhD Thesis, Aston University, 2024.
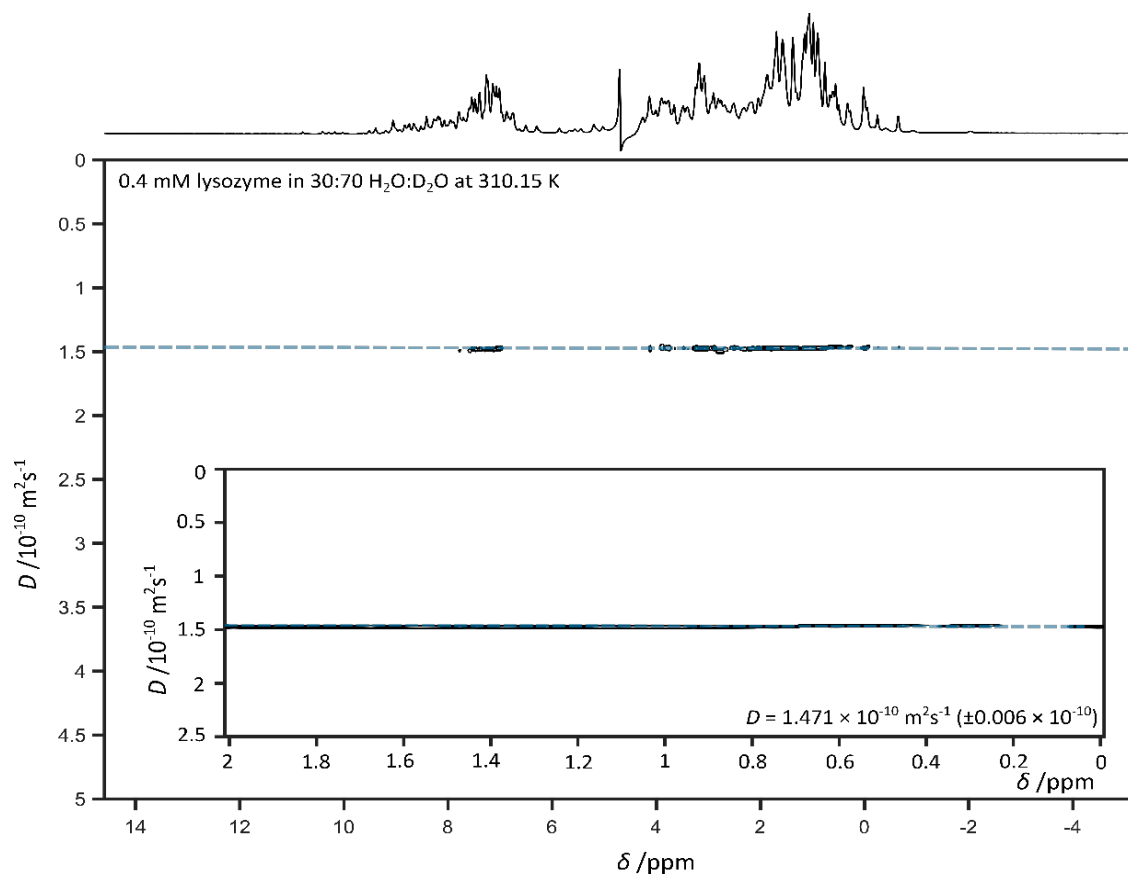
Figure A6.1.33 DOSY spectrum of 0.4mM lysozyme in 30:70 H₂O:D₂O solution at 310.15 K. Insert depicts protein methyl peaks (0 – 2 ppm), estimate of diffusion coefficient, D, and associated error estimate.
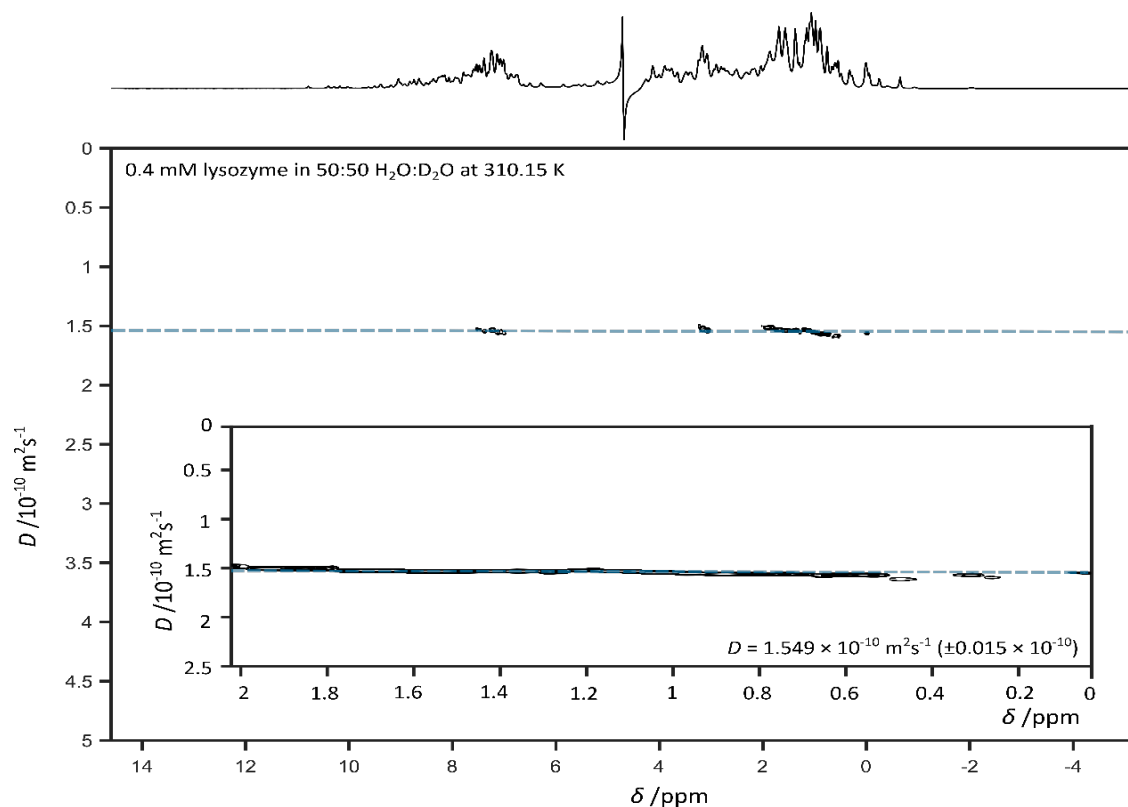
Figure 65.1.34 DOSY spectrum of 0.4mM lysozyme in 50:50 H₂O:D₂O solution at 310.15 K. Insert depicts protein methyl peaks (0 – 2 ppm), estimate of diffusion coefficient, D, and associated error estimate.
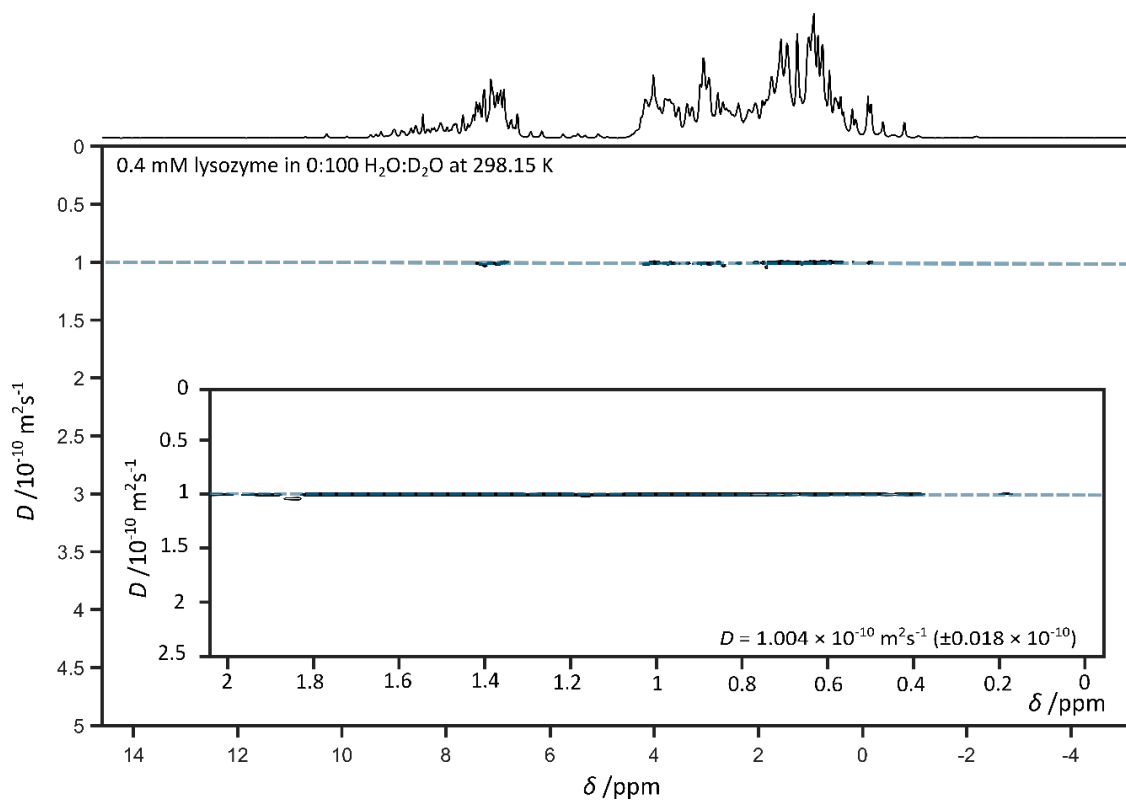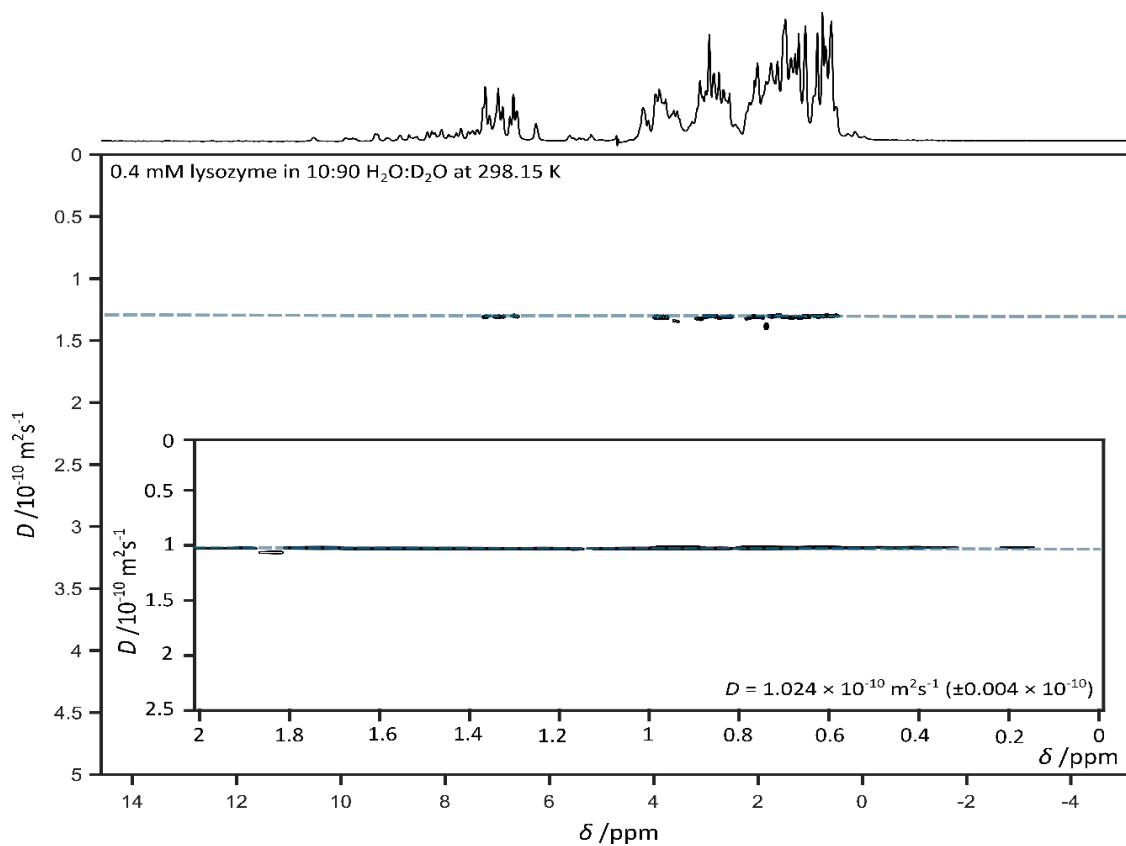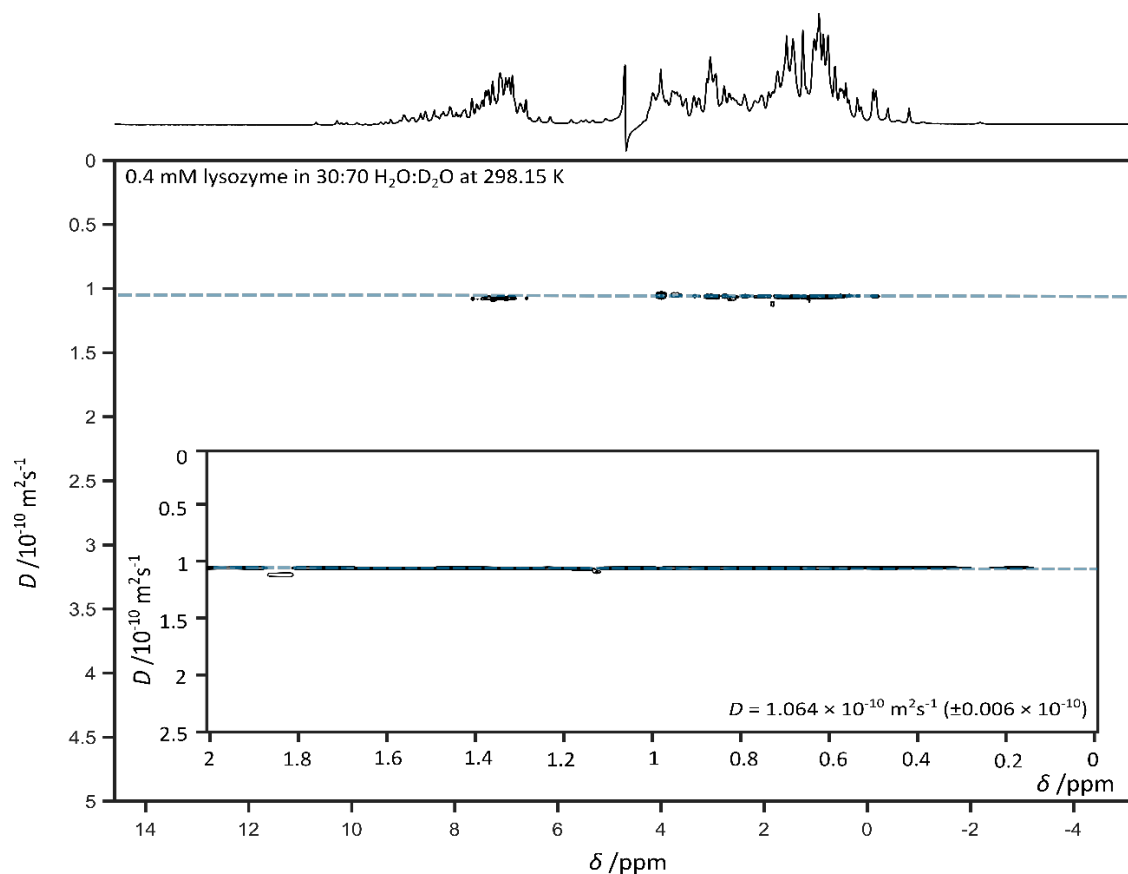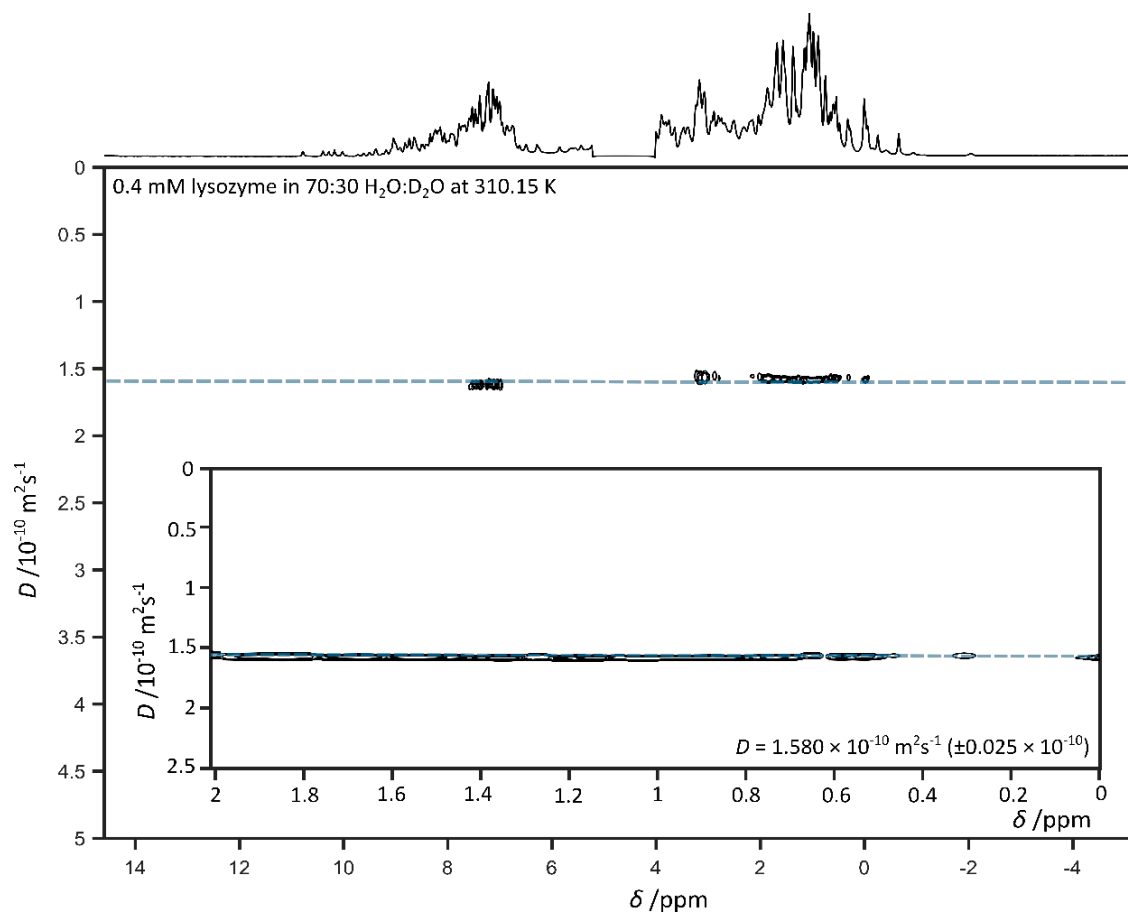
Figure A6.1.35 DOSY spectrum of 0.4mM lysozyme in 70:30 H_2O:D_2O solution at 310.15 K. Insert depicts protein methyl peaks (0 – 2 ppm), estimate of diffusion coefficient, D, and associated error estimate.
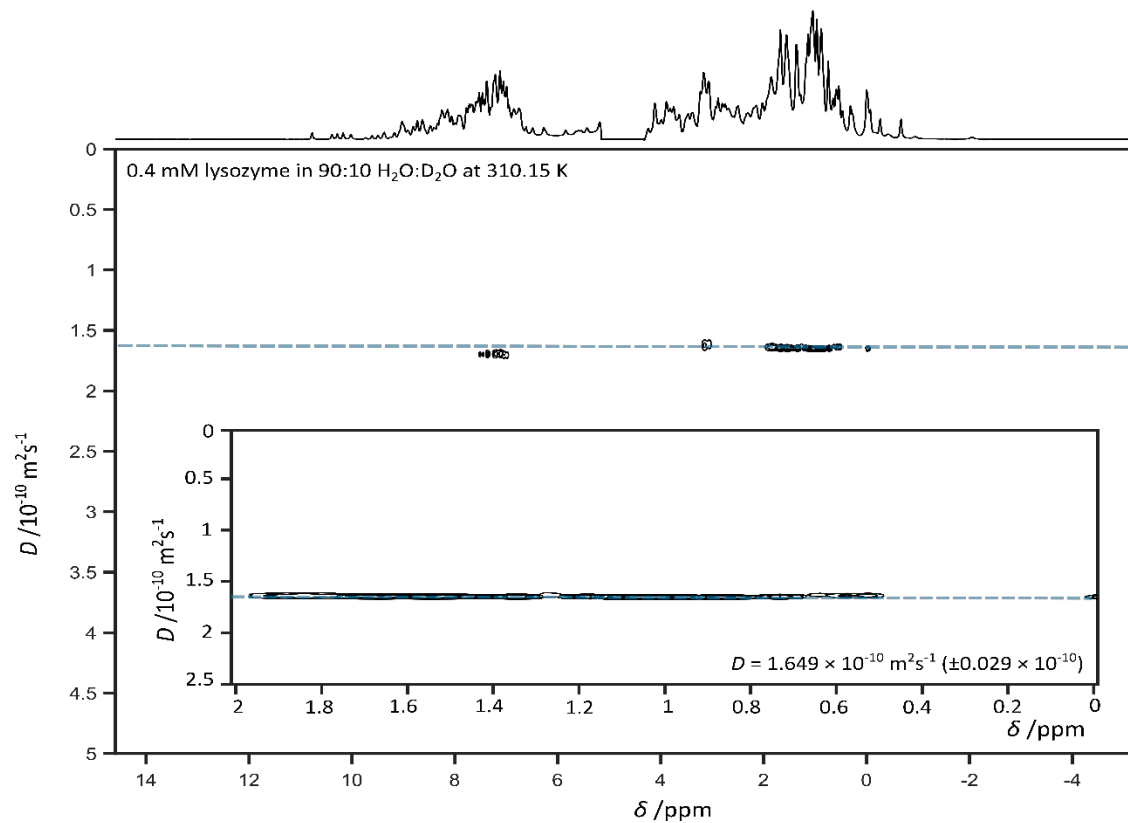
Figure A6.1.36 DOSY spectrum of 0.4mM lysozyme in 90:10 H_2O:D_2O solution at 310.15 K. Insert depicts protein methyl peaks (0 – 2 ppm), estimate of diffusion coefficient, D, and associated error estimate.

331

*Table 65.1.1 Summary of all experimentally-acquired diffusion coefficients of 0.4 mM lysozyme at a range of temperatures and for a range of solvent compositions*

$D \times 10^{-10}$ m^{2}s^{-1}	Temperature (K)				
%H$_2$O	278.15	283.15	288.15	298.15	310.15
90	0.699	0.813	0.910	1.219	1.649
70	0.634	0.728	0.878	1.168	1.580
50	0.600	0.701	0.829	1.130	1.549
30	0.564	0.663	0.812	1.064	1.471
10	0.536	0.642	0.763	1.024	1.429
0	0.528	0.629	0.748	1.004	1.395

Table A6.1.2 Summary of diffusion coefficients predicted using the Stokes-Einstein equation for 0.4 mM lysozyme at a range of temperatures and for a range of solvent compositions

$D \times 10^{-10}$ m^{2}s^{-1}	Temperature (K)				
%H$_2$O	278.15	283.15	288.15	298.15	310.15
90	0.633	0.737	0.854	1.130	1.547
70	0.600	0.701	0.814	1.084	1.493
50	0.569	0.666	0.776	1.039	1.440
30	0.539	0.634	0.741	0.997	1.390
10	0.511	0.603	0.706	0.956	1.341
0	0.498	0.588	0.690	0.936	1.318

Table A6.1.3 Summary of diffusion coefficients predicted using the extended SEGWE equation for 0.4 mM lysozyme at a range of temperatures and for a range of solvent compositions

$D \times 10^{-10}$ m^{2}s^{-1}	Temperature (K)				
%H$_2$O	278.15	283.15	288.15	298.15	310.15
90	0.674	0.784	0.909	1.203	1.647
70	0.639	0.746	0.867	1.154	1.590
50	0.606	0.710	0.828	1.108	1.535
30	0.575	0.676	0.790	1.063	1.482
10	0.546	0.643	0.754	1.020	1.431
0	0.531	0.626	0.734	0.996	1.403

A6.2 Calculation of Viscosity Using Anadrade's Equation for Common Solvents

Table A6.2.1 Molecular masses and Arrhenius viscosity parameters of common protiated solvent and their deuteriated counterparts. Parameters for chloroform-d are estimated from protiated solvent data.

Solvent	MW /g mol^{-1}	a /kg m^{-1} s^{-1}	b /K
water	18.02	8.12×10^{-7}	2093
water-d_2	20.03	4.52×10^{-7}	2330
methanol	32.04	9.57×10^{-6}	1203
methanol-d_4	36.07	8.62×10^{-6}	1268
chloroform	119.37	2.87×10^{-6}	878
chloroform-d	120.38	2.86×10^{-5}	878
dimethyl sulfoxide	78.13	8.35×10^{-6}	1631
dimethyl sulfoxide-d_6	84.17	6.32×10^{-5}	1742
toluene	92.14	1.55×10^{-5}	1068
toluene-d_8	100.19	1.50×10^{-5}	1099

Source: All viscosity data summarised was taken from the supporting information from *Evans, R., Dal Poggetto, G., Nilsson, M. and Morris, G.A., 2018. Improving the interpretation of small molecule diffusion coefficients. Analytical chemistry, 90(6), pp.3987-3994.* All viscosity data was taken from the Arrhenius plots presented in section SI.4.1 and SI.4.2.

Table A6.2.2 Estimated hydrodynamic radii of common protiated solvents and their deuteriated counterparts.

Solvent	Radii /m
water	2.25×10^{-10}
water-d_2	2.33×10^{-10}
methanol	2.73×10^{-10}
methanol-d_4	2.84×10^{-10}
chloroform	4.23×10^{-10}
chloroform-d	4.24×10^{-10}
dimethyl sulfoxide	3.67×10^{-10}
dimethyl sulfoxide-d_6	3.76×10^{-10}
toluene	3.88×10^{-10}
toluene-d_8	3.99×10^{-10}

All radii were calculated using the equation:

$$r = \sqrt[3]{\frac{3MW}{4\pi\rho_{eff}N_A}}$$

Using the data in Table SI.1.1, viscosities of protiated and deuteriated solvents were compared over the temperature range 273 K to 313 K in figures SI.1.1-5. Figure SI.1.6 summarises these data in a single figure showing the ratio of solvent viscosities as a function of temperature.

B.Tang, PhD Thesis, Aston University, 2024.

Figure A6.2.1 Solvent viscosity calculated at a range of temperature 273 - 313 K for H₂O (blue) and D₂O (black) using Andrade's equation.

Figure A6.2.2 Solvent viscosity calculated at a range of temperature from 273 - 313 K for CHCl₃ (blue) and CDCl₃ (black) using Andrade's equation.

B.Tang, PhD Thesis, Aston University, 2024.

Figure A6.2.3 Solvent viscosity calculated at a range of temperature from 273 - 313 K for DMSO (blue) and DMSO-d₆ (black) using Andrade's equation.
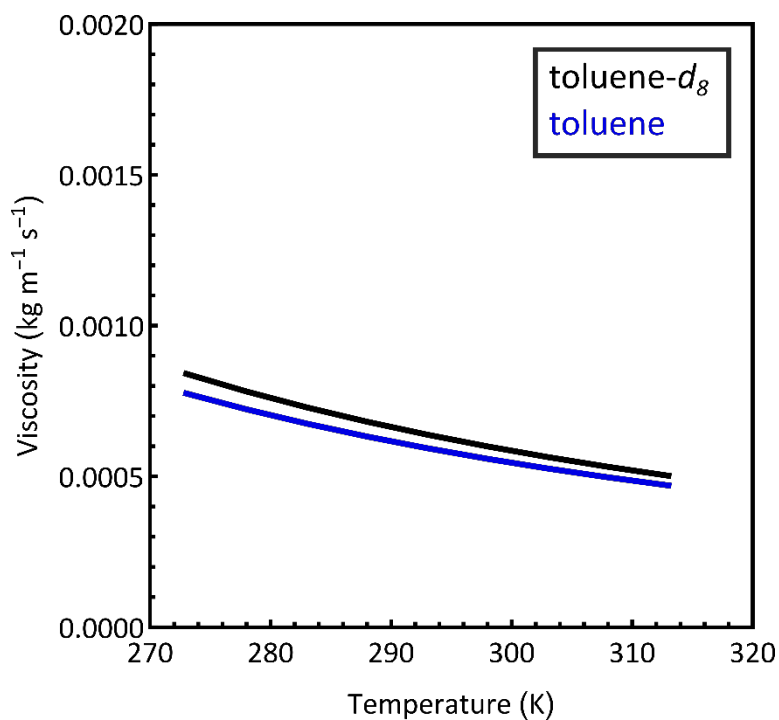
Figure A6.2.4 Solvent viscosity calculated at a range of temperature from 273 - 313 K for toluene (blue) and toluene-d₈ (black) using Andrade's equation.
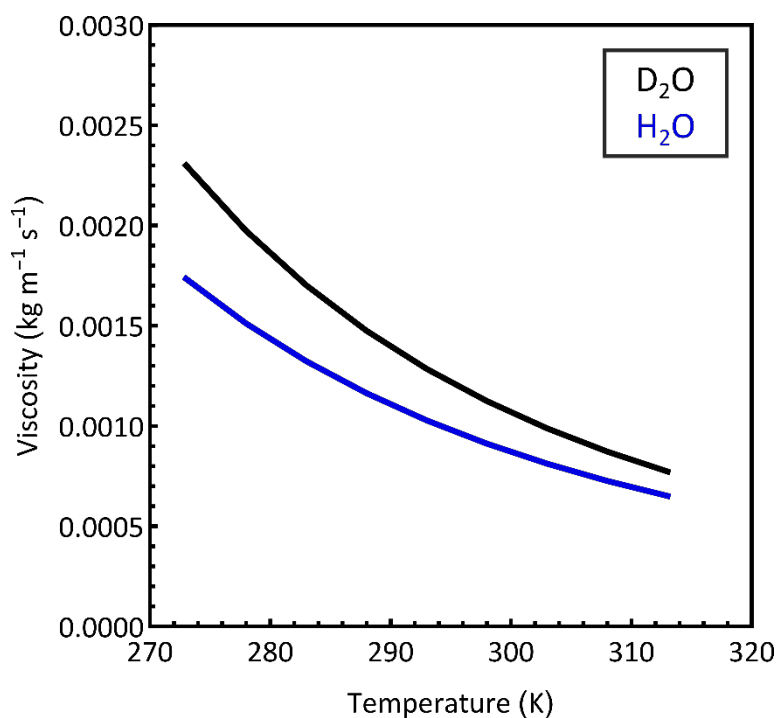
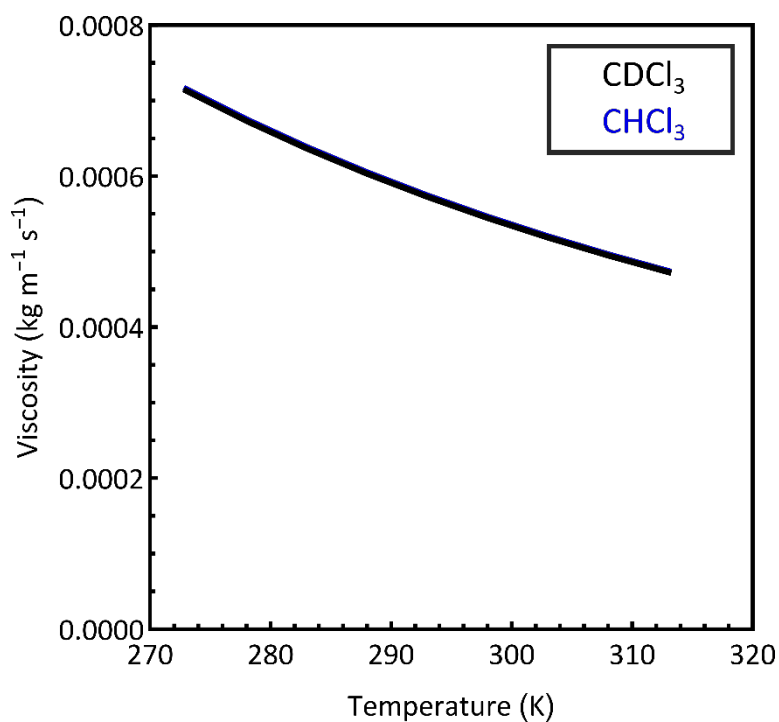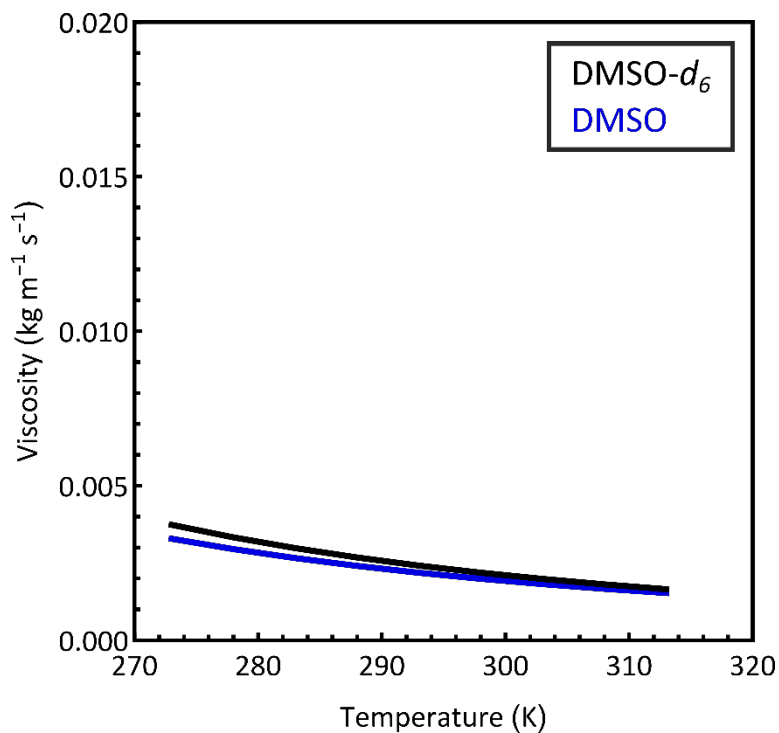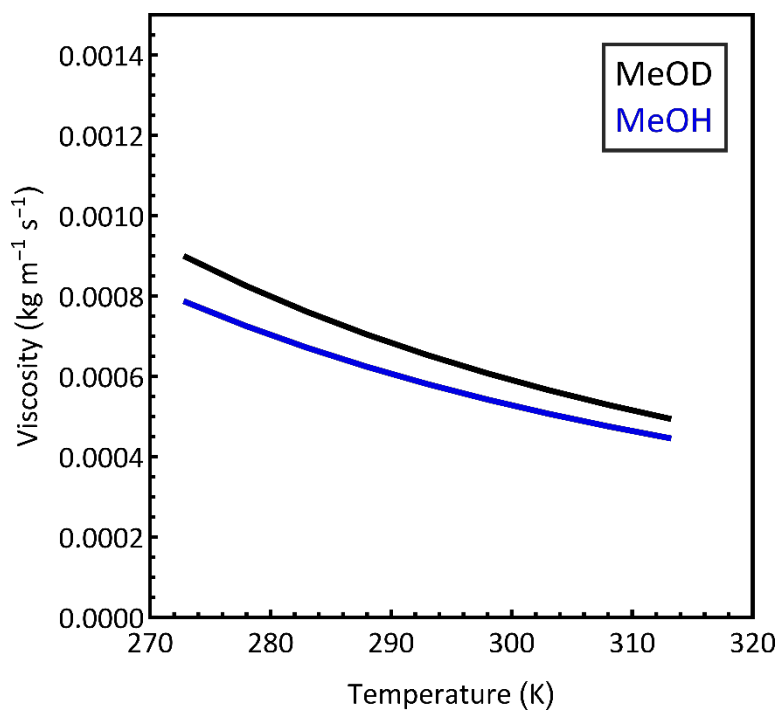*Figure A6.2.5 Solvent viscosity calculated at a range of temperature from 273 - 313 K for MeOH (blue) and MeOD (black) using Andrade's equation.*

B.Tang, PhD Thesis, Aston University, 2024.

A6.3 Mixing rules for viscosity (equations)

Three mixing rules for viscosity are summarised below. Here, each has been combined with Andrade's equation

$$\eta = a e^{\frac{b}{T}}$$

to create expressions for the viscosity of a mixed solvent on the basis of its composition and the relevant Arrhenius-like parameters used in Andrade's equation.

η = viscosity (kg m^{-1} s^{-1})

$\eta_{1,2}$ = combined viscosity of the component 1 (η_1) and component 2 (η_2) (kg m^{-1} s^{-1}).

T = Temperature (K)

a and b are Arrhenius-like parameters (kg m^{-1} s^{-1} and K, respectively)

ρ = density (kg m^{-3}), where ρ_1 and ρ_2 are densities of components 1 and 2, respectively.

x = mole fraction, where x_1 and x_2 are mole fractions of components 1 and 2, respectively.

1. **Kendall-Monroe (cubic) Equation**:

$$\eta_{1,2}^{1/3} = x_1 \eta_1^{1/3} + x_2 \eta_2^{1/3}$$

$$\eta_{1,2}^{1/3} = x_1 (a_1 e^{\frac{b_1}{T}})^{1/3} + x_2 (a_2 e^{\frac{b_2}{T}})^{1/3}$$

$$\eta_{1,2}^{1/3} = x_1 a_1^{1/3} e^{\frac{b_1}{3T}} + x_2 a_2^{1/3} e^{\frac{b_2}{3T}}$$

2. **Density Equation for salt solutions**:

$$\eta_{1,2} = \frac{x_1 \rho_1 + x_2 \rho_2}{x_1 \frac{\rho_1}{\eta_1} + x_2 \frac{\rho_2}{\eta_2}}$$

$$\eta_{1,2} = \frac{x_1 \rho_1 + x_2 \rho_2}{x_1 \frac{\rho_1}{(a_1 e^{\frac{b_1}{T}})} + x_2 \frac{\rho_2}{(a_2 e^{\frac{b_2}{T}})}}$$

$$\frac{1}{\eta_{1,2}} = \frac{\frac{x_1 \rho_1}{(a_1 e^{\frac{b_1}{T}})} + \frac{x_2 \rho_2}{(a_2 e^{\frac{b_2}{T}})}}{x_1 \rho_1 + x_2 \rho_2}$$

3. **Grunberg-Nissan model**:

$$\ln(\eta_{1,2}) = x_1 \ln(\eta_1) + x_2 \ln(\eta_2)$$

$$\ln(\eta_{1,2}) = x_1 \ln\left(a_1 e^{\frac{b_1}{T}}\right) + x_2 \ln\left(a_2 e^{\frac{b_2}{T}}\right)$$

$$\ln(\eta_{1,2}) = x_1 \ln(a_1) + \frac{x_1 b_1}{T} + x_2 \ln(a_2) + \frac{x_2 b_2}{T}$$

$$\eta_{1,2} = a_1^{x_1} a_2^{x_2} e^{(\frac{x_1 b_1 + x_2 b_2}{T})}$$

B.Tang, PhD Thesis, Aston University, 2024.

A6.4 DOSY Spectra of various Proteins at 298.15 K in Different H₂O:D₂O Compositions

Figure A6.4.1 DOSY spectrum of 0.4mM aprotinin in 0:100 H₂O:D₂O solution at 298.15 K. Insert depicts protein methyl peaks (0 – 2 ppm), estimate of diffusion coefficient, D, and associated error estimate.

Figure A6.4.2 DOSY spectrum of 0.4mM aprotinin in 10:90 H₂O:D₂O solution at 298.15 K. Insert depicts protein methyl peaks (0 – 2 ppm), estimate of diffusion coefficient, D, and associated error estimate.

Figure A6.4.3 DOSY spectrum of 0.4mM aprotinin in 30:70 H_2O:D_2O solution at 298.15 K. Insert depicts protein methyl peaks (0 – 2 ppm), estimate of diffusion coefficient, D, and associated error estimate.

Figure A6.4.4 DOSY spectrum of 0.4mM aprotinin in 50:50 H_2O:D_2O solution at 298.15 K. Insert depicts protein methyl peaks (0 – 2 ppm), estimate of diffusion coefficient, D, and associated error estimate.

B.Tang, PhD Thesis, Aston University, 2024.

Figure A6.4.5 DOSY spectrum of 0.4mM aprotinin in 70:30 $H_2O:D_2O$ solution at 298.15 K. Insert depicts protein methyl peaks (0 – 2 ppm), estimate of diffusion coefficient, D, and associated error estimate.
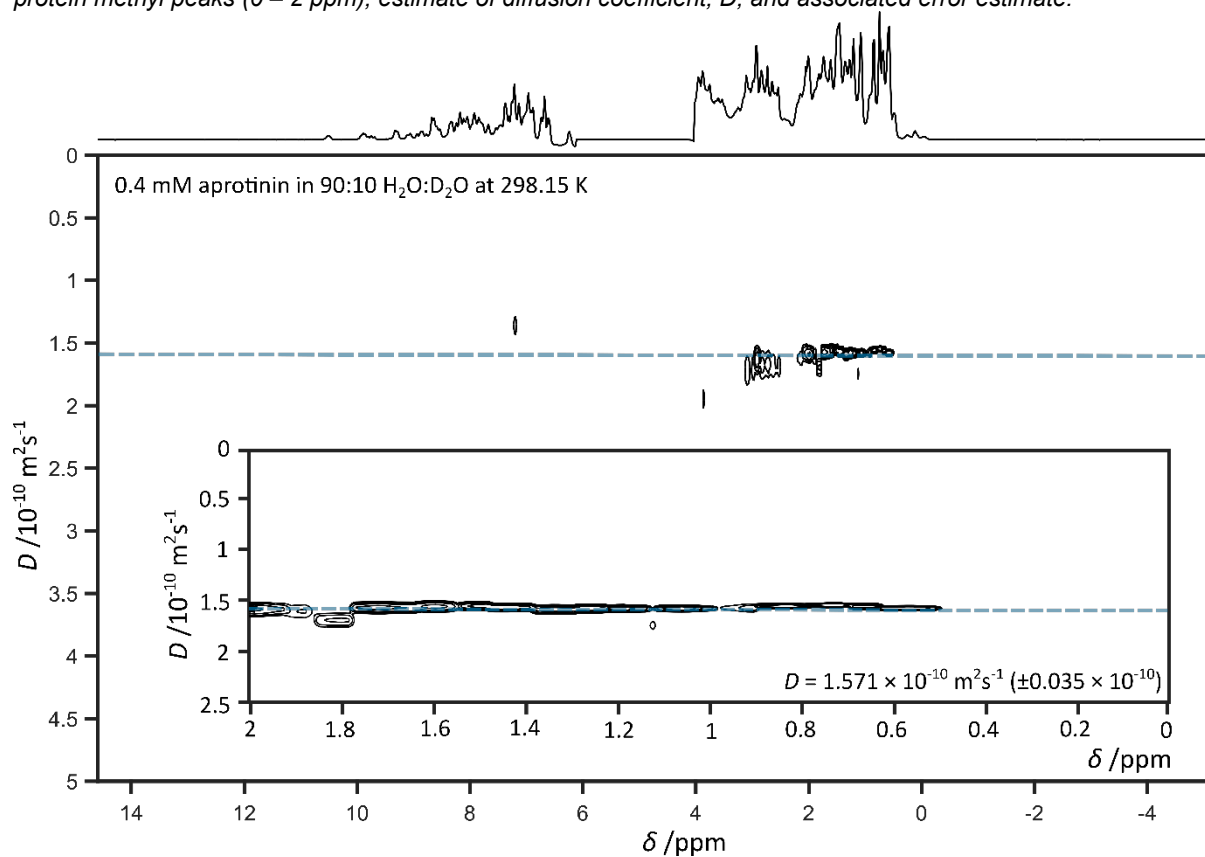
Figure A6.4.6 DOSY spectrum of 0.4mM aprotinin in 90:10 $H_2O:D_2O$ solution at 298.15 K. Insert depicts protein methyl peaks (0 – 2 ppm), estimate of diffusion coefficient, D, and associated error estimate.

B.Tang, PhD Thesis, Aston University, 2024.
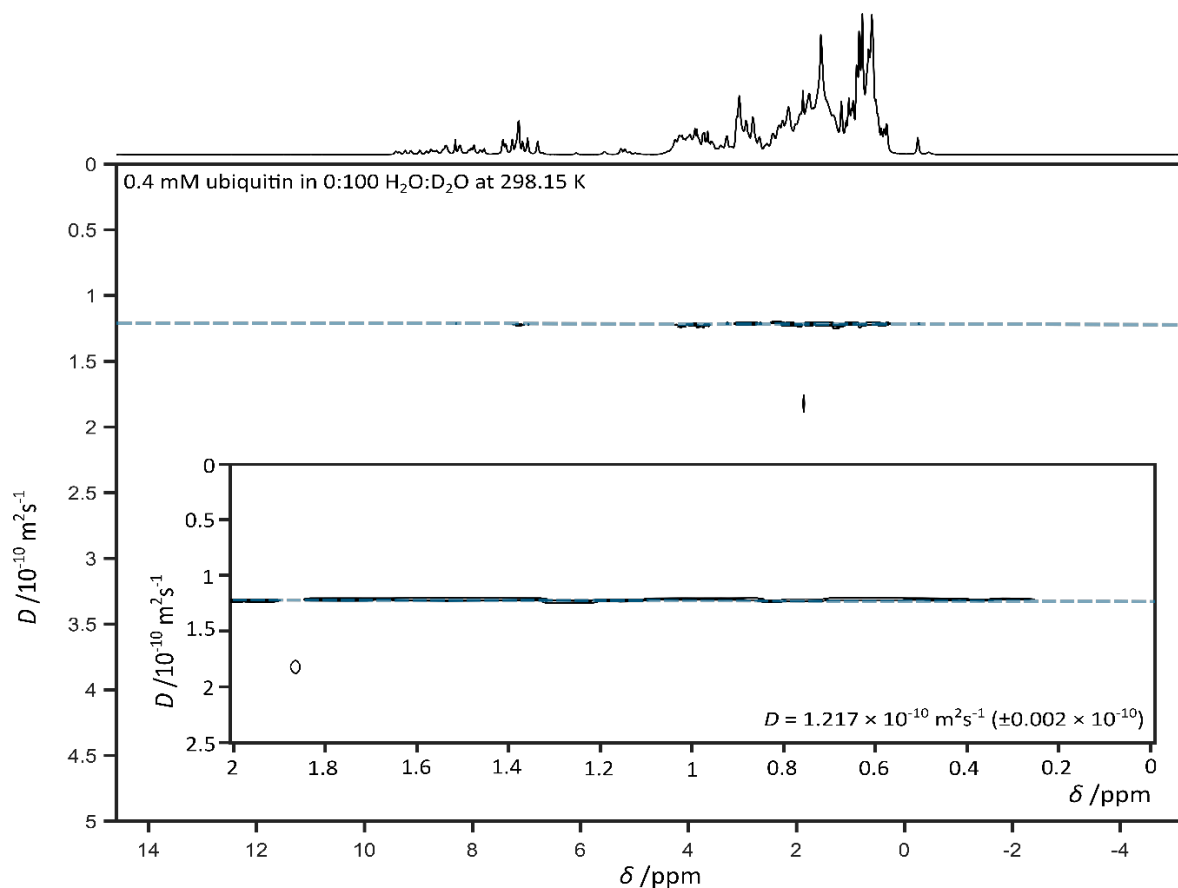
Figure A6.4.7 DOSY spectrum of 0.4mM ubiquitin in 0:100 $H_2O:D_2O$ solution at 298.15 K. Insert depicts protein methyl peaks (0 – 2 ppm), estimate of diffusion coefficient, D, and associated error estimate.

Figure A6.4.8 DOSY spectrum of 0.4mM ubiquitin in 10:90 $H_2O:D_2O$ solution at 298.15 K. Insert depicts protein methyl peaks (0 – 2 ppm), estimate of diffusion coefficient, D, and associated error estimate.

B.Tang, PhD Thesis, Aston University, 2024.
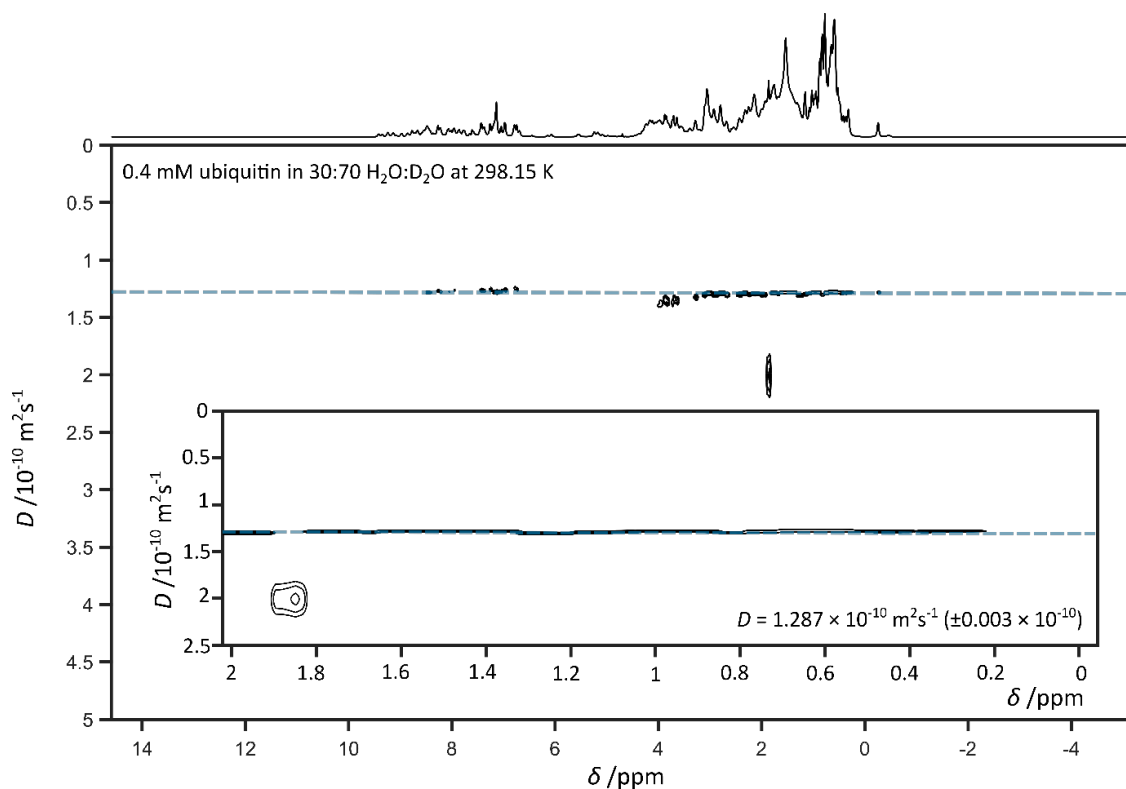
Figure A6.4.9 DOSY spectrum of 0.4mM ubiquitin in 30:70 $H_2O:D_2O$ solution at 298.15 K. Insert depicts protein methyl peaks (0 – 2 ppm), estimate of diffusion coefficient, D, and associated error estimate.
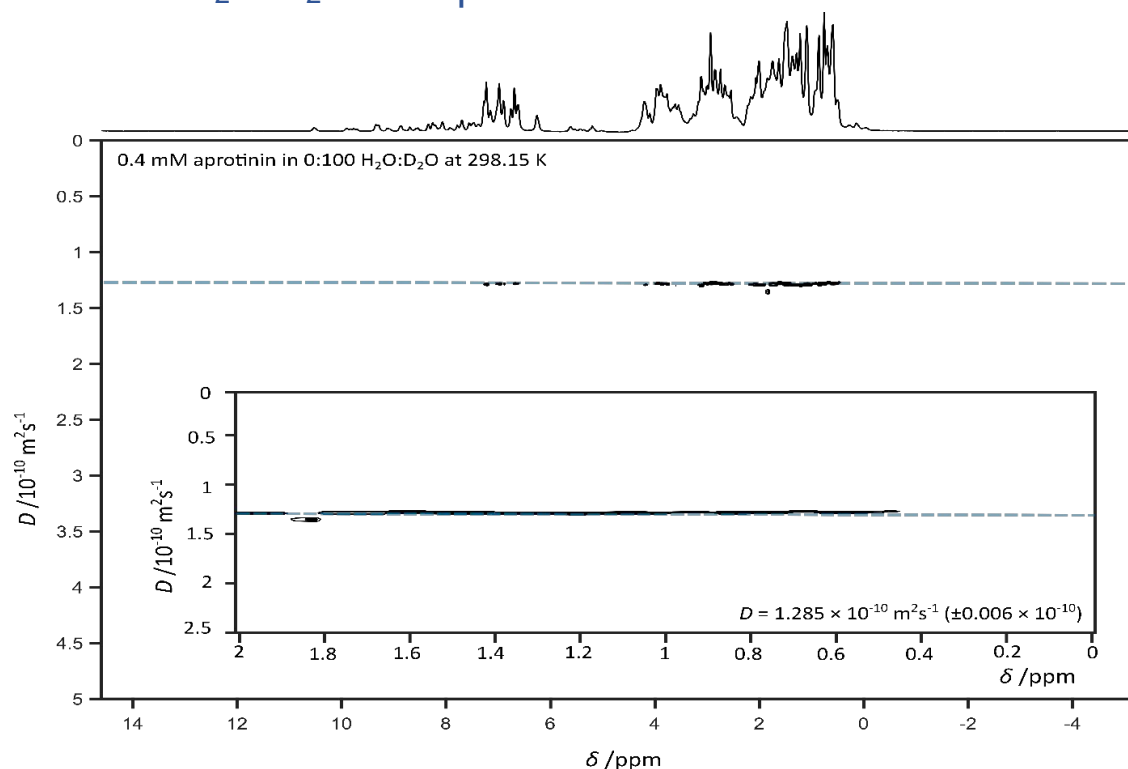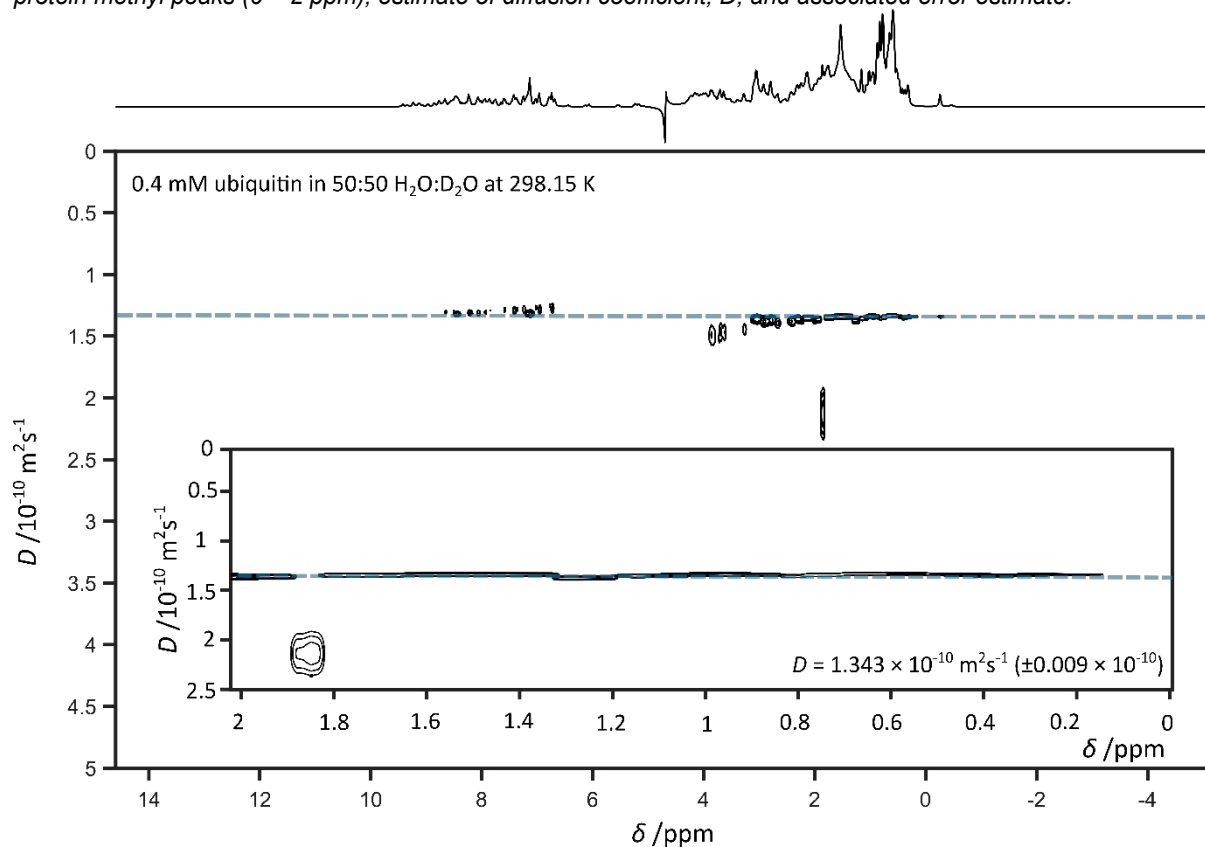

Figure A6.4.10 DOSY spectrum of 0.4mM ubiquitin in 50:50 $H_2O:D_2O$ solution at 298.15 K. Insert depicts protein methyl peaks (0 – 2 ppm), estimate of diffusion coefficient, D, and associated error estimate.

B.Tang, PhD Thesis, Aston University, 2024.
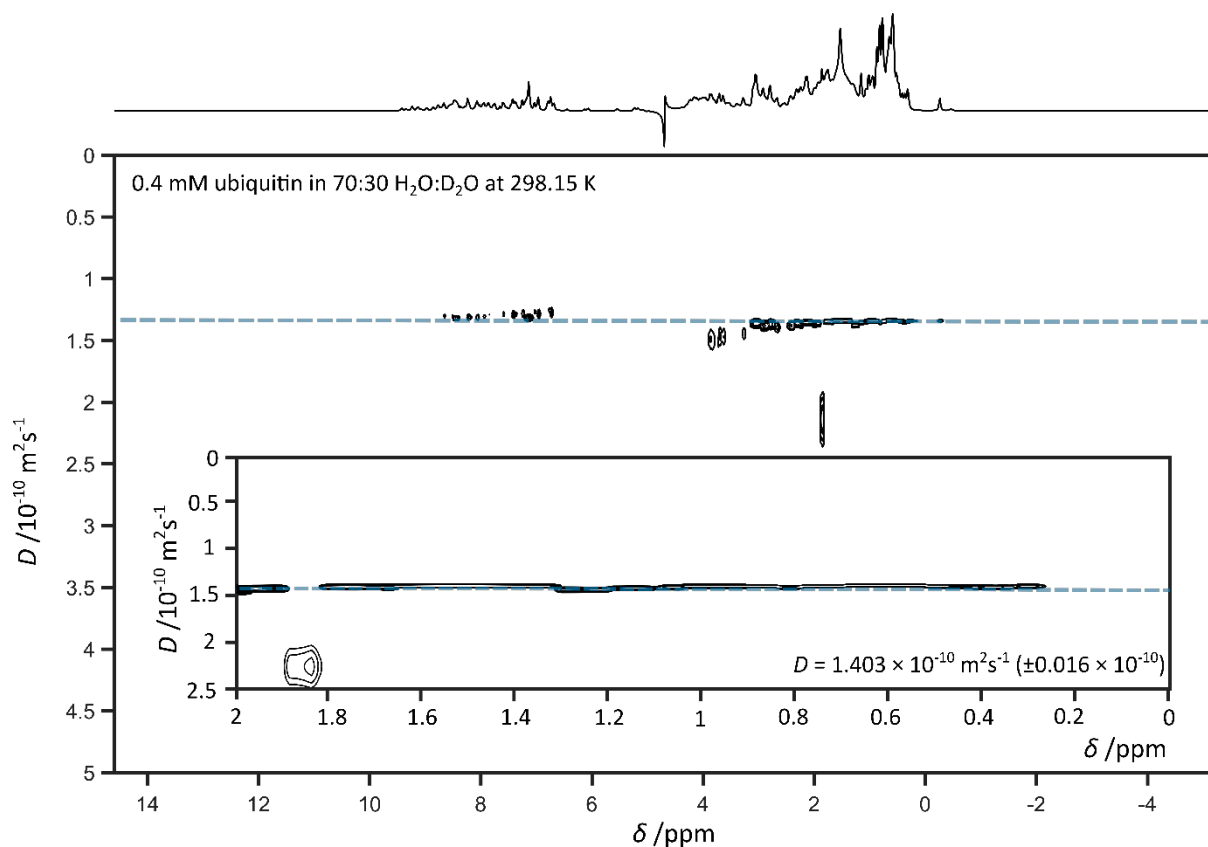
Figure A6.4.11 DOSY spectrum of 0.4mM ubiquitin in 70:30 $H_2O:D_2O$ solution at 298.15 K. Insert depicts protein methyl peaks (0 – 2 ppm), estimate of diffusion coefficient, D, and associated error estimate.

Figure A6.4.12 DOSY spectrum of 0.4mM ubiquitin in 90:10 $H_2O:D_2O$ solution at 298.15 K. Insert depicts protein methyl peaks (0 – 2 ppm), estimate of diffusion coefficient, D, and associated error estimate.
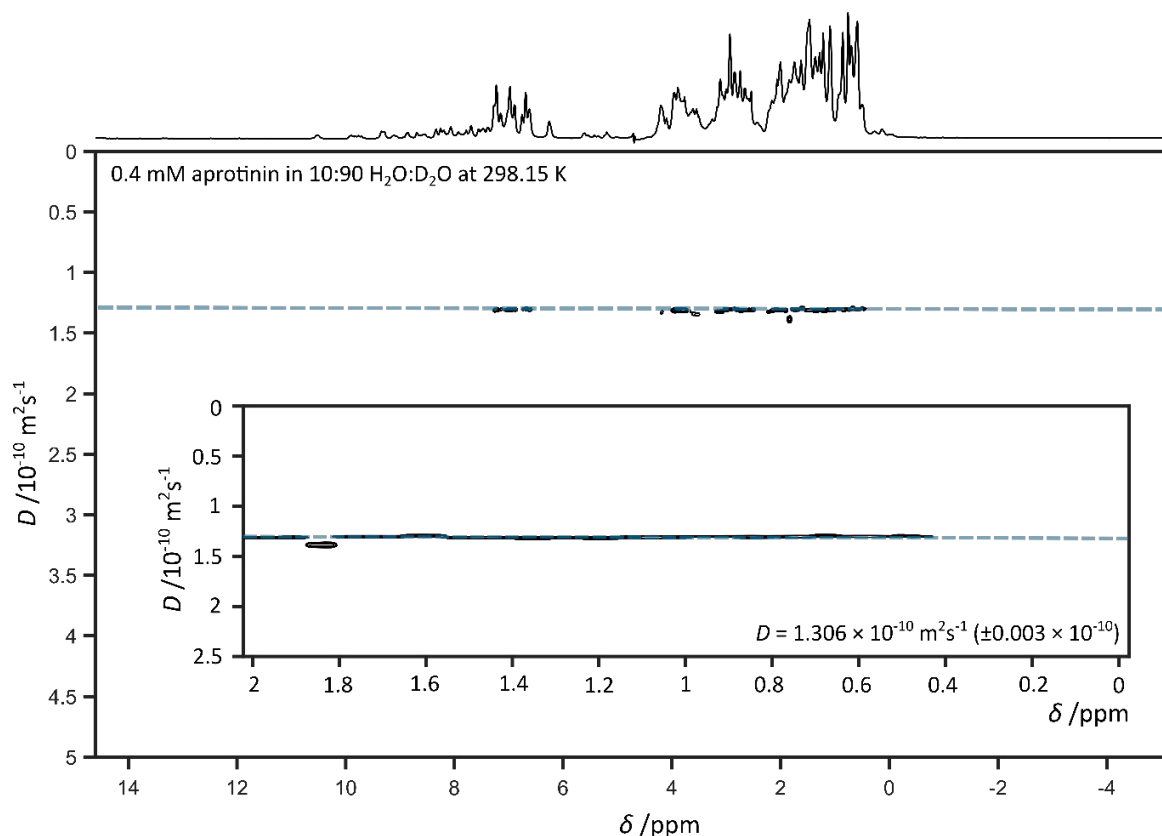
343
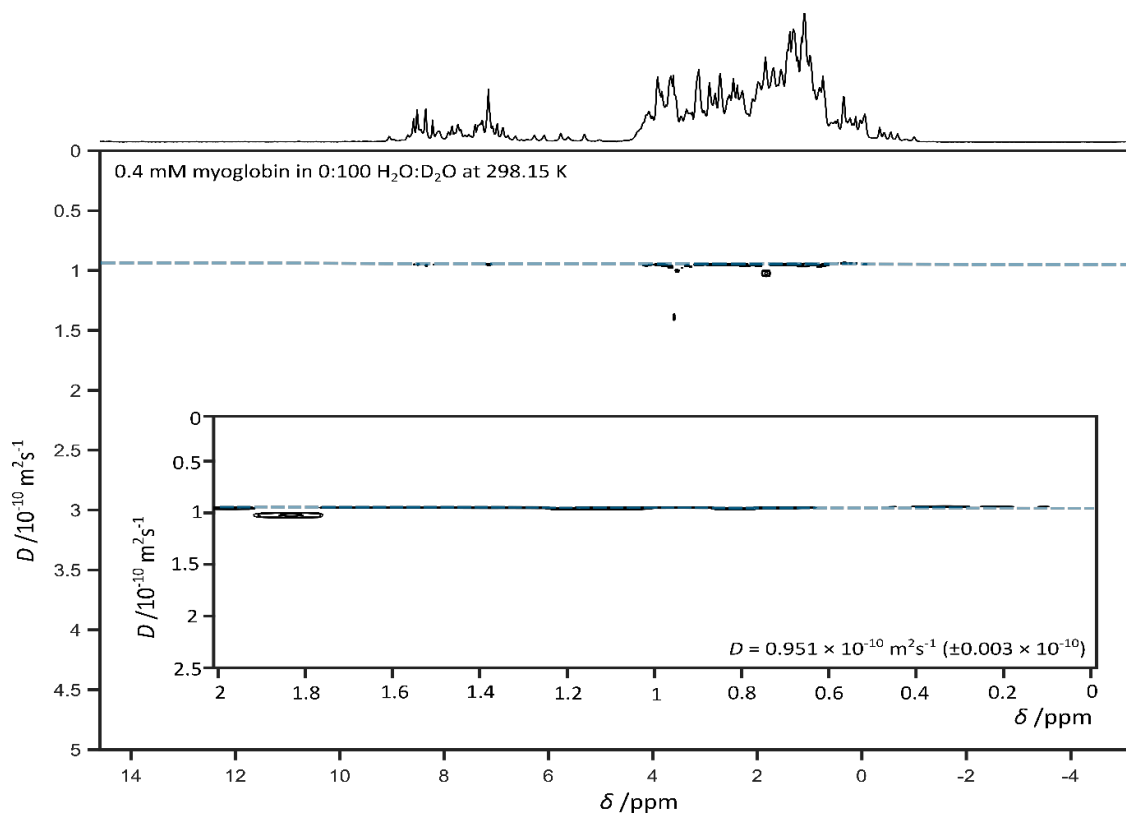
Figure A6.4.13 DOSY spectrum of 0.4mM myoglobin in 0:100 H_2O:D_2O solution at 298.15 K. Insert depicts protein methyl peaks (0 – 2 ppm), estimate of diffusion coefficient, D, and associated error estimate.
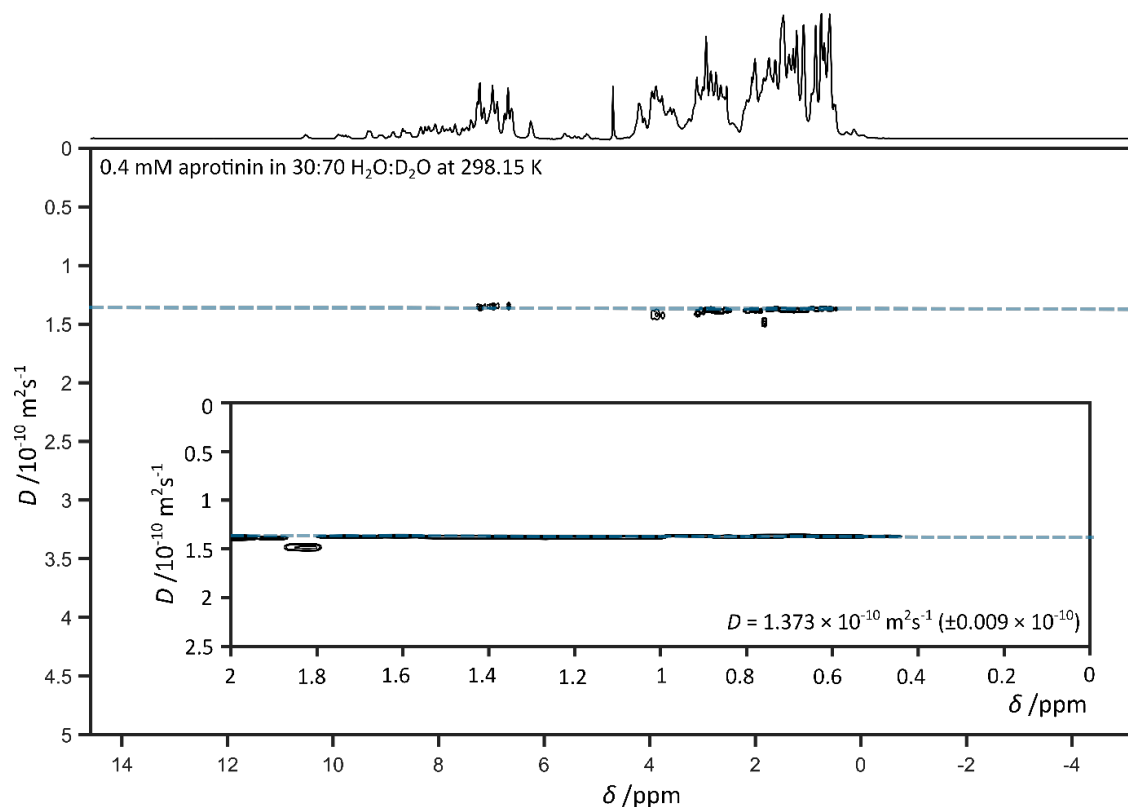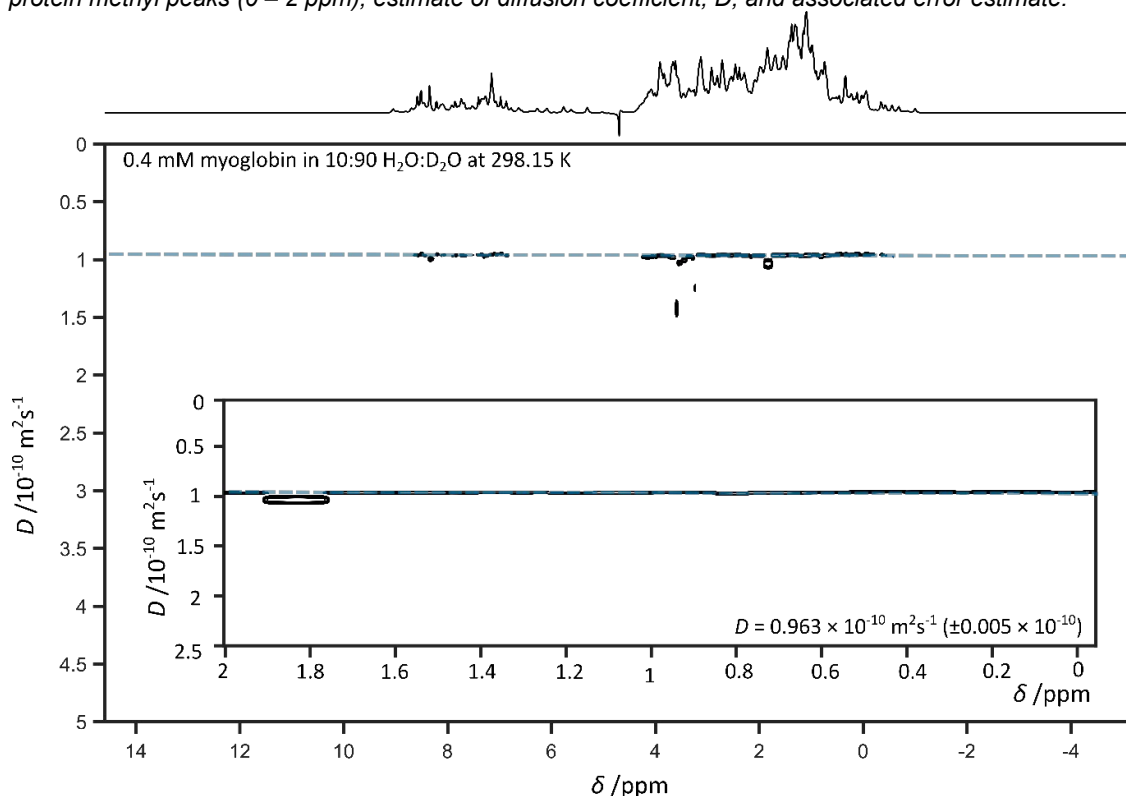

Figure A6.4.14 DOSY spectrum of 0.4mM myoglobin in 10:90 H_2O:D_2O solution at 298.15 K. Insert depicts protein methyl peaks (0 – 2 ppm), estimate of diffusion coefficient, D, and associated error estimate.

B.Tang, PhD Thesis, Aston University, 2024.
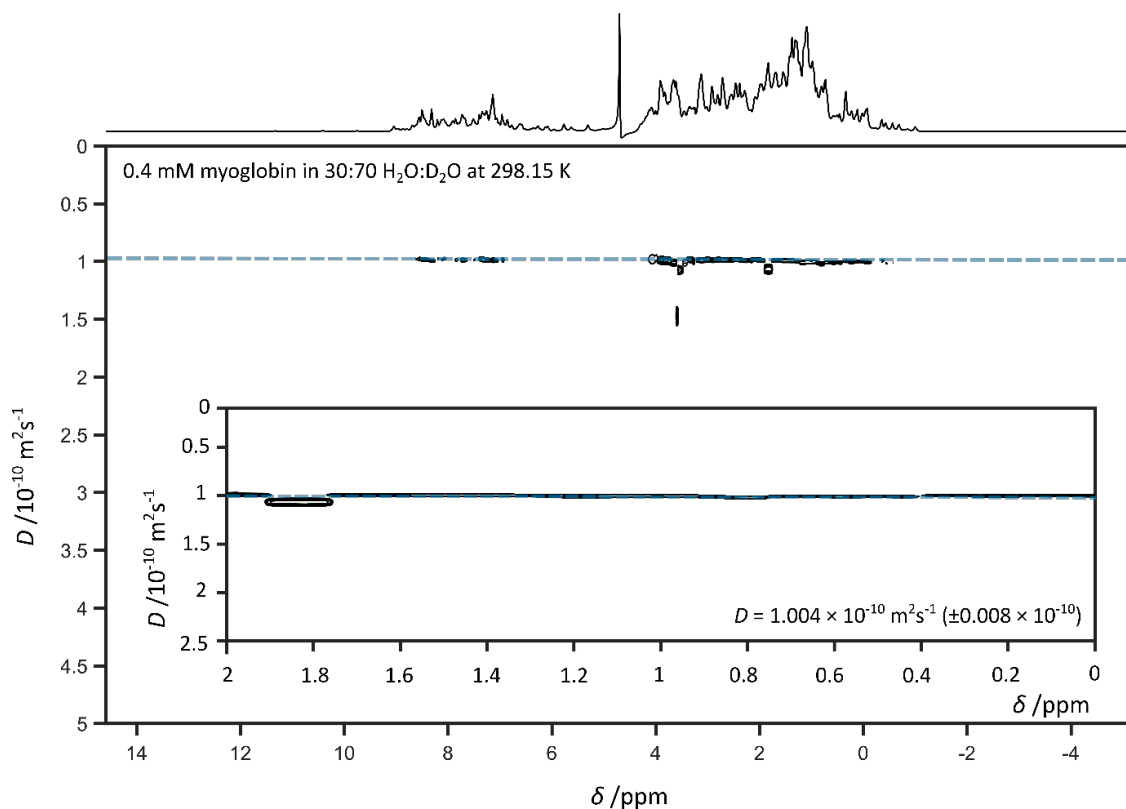
Figure A6.4.15 DOSY spectrum of 0.4mM myoglobin in 30:70 H2O:D2O solution at 298.15 K. Insert depicts protein methyl peaks (0 – 2 ppm), estimate of diffusion coefficient, D, and associated error estimate.
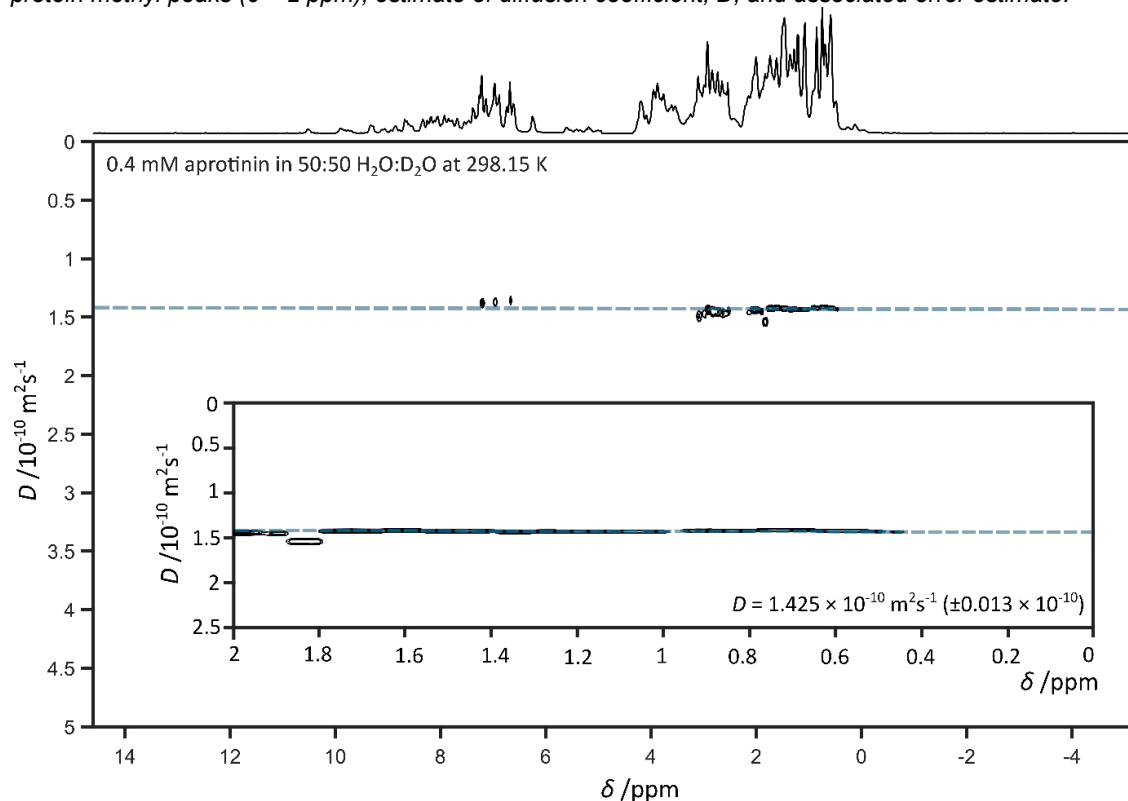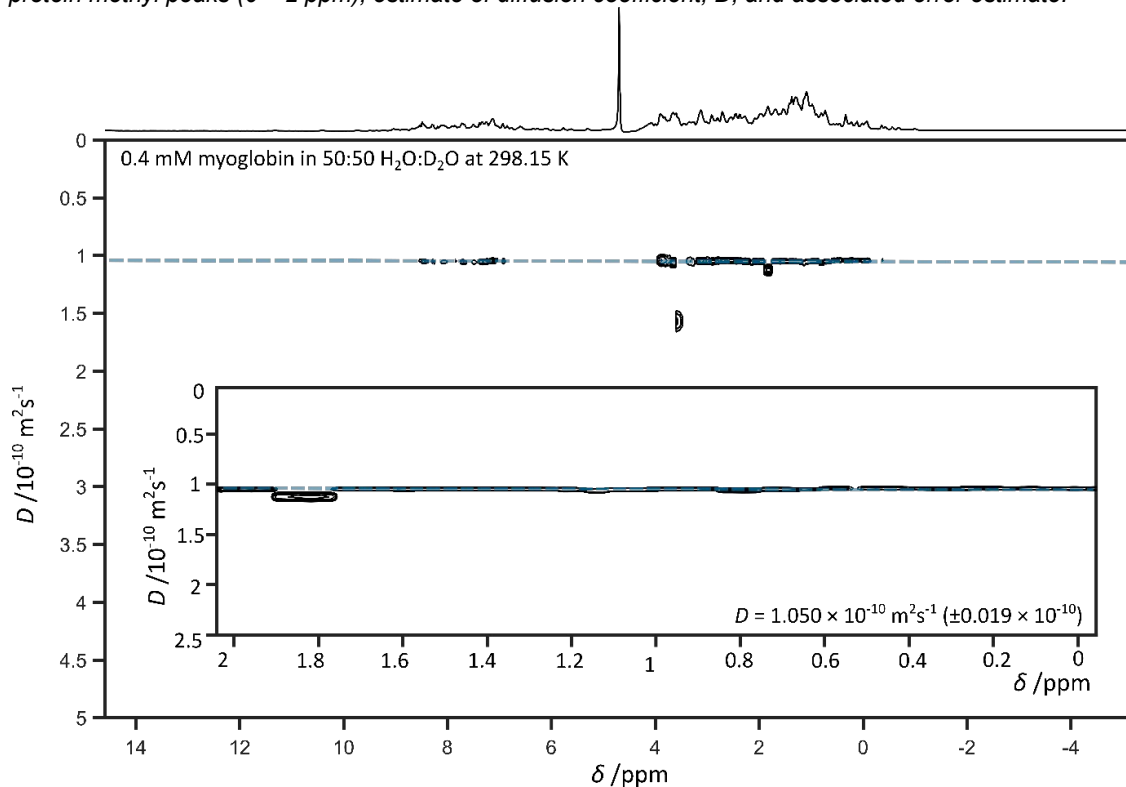

Figure A6.4.16 DOSY spectrum of 0.4mM myoglobin in 50:50 H2O:D2O solution at 298.15 K. Insert depicts protein methyl peaks (0 – 2 ppm), estimate of diffusion coefficient, D, and associated error estimate.
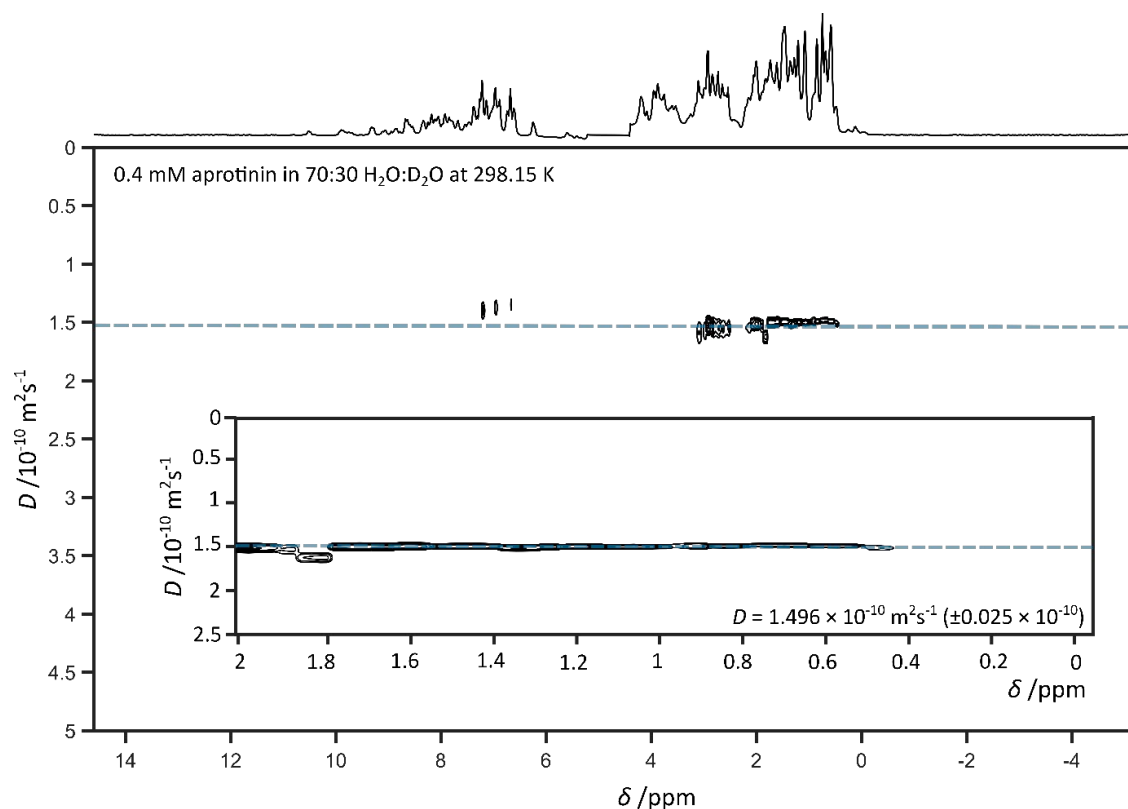
B.Tang, PhD Thesis, Aston University, 2024.

Figure A6.4.17 DOSY spectrum of 0.4mM myoglobin in 70:30 $H_2O:D_2O$ solution at 298.15 K. Insert depicts protein methyl peaks (0 – 2 ppm), estimate of diffusion coefficient, D, and associated error estimate.

In the insert: $D = 1.095 \times 10^{-10}$ m^{2}s^{-1} ($\pm 0.010 \times 10^{-10}$)

Label: 0.4 mM myoglobin in 70:30 $H_2O:D_2O$ at 298.15 K

Figure A6.4.18 DOSY spectrum of 0.4mM myoglobin in 90:10 $H_2O:D_2O$ solution at 298.15 K. Insert depicts protein methyl peaks (0 – 2 ppm), estimate of diffusion coefficient, D, and associated error estimate.

In the insert: $D = 1.145 \times 10^{-10}$ m^{2}s^{-1} ($\pm 0.019 \times 10^{-10}$)

Label: 0.4 mM myoglobin in 90:10 $H_2O:D_2O$ at 298.15 K

Figure A6.4.19 DOSY spectrum of 0.4mM BSA in 0:100 H_2O:D_2O solution at 298.15 K. Insert depicts protein methyl peaks (0 – 2 ppm), estimate of diffusion coefficient, D, and associated error estimate.
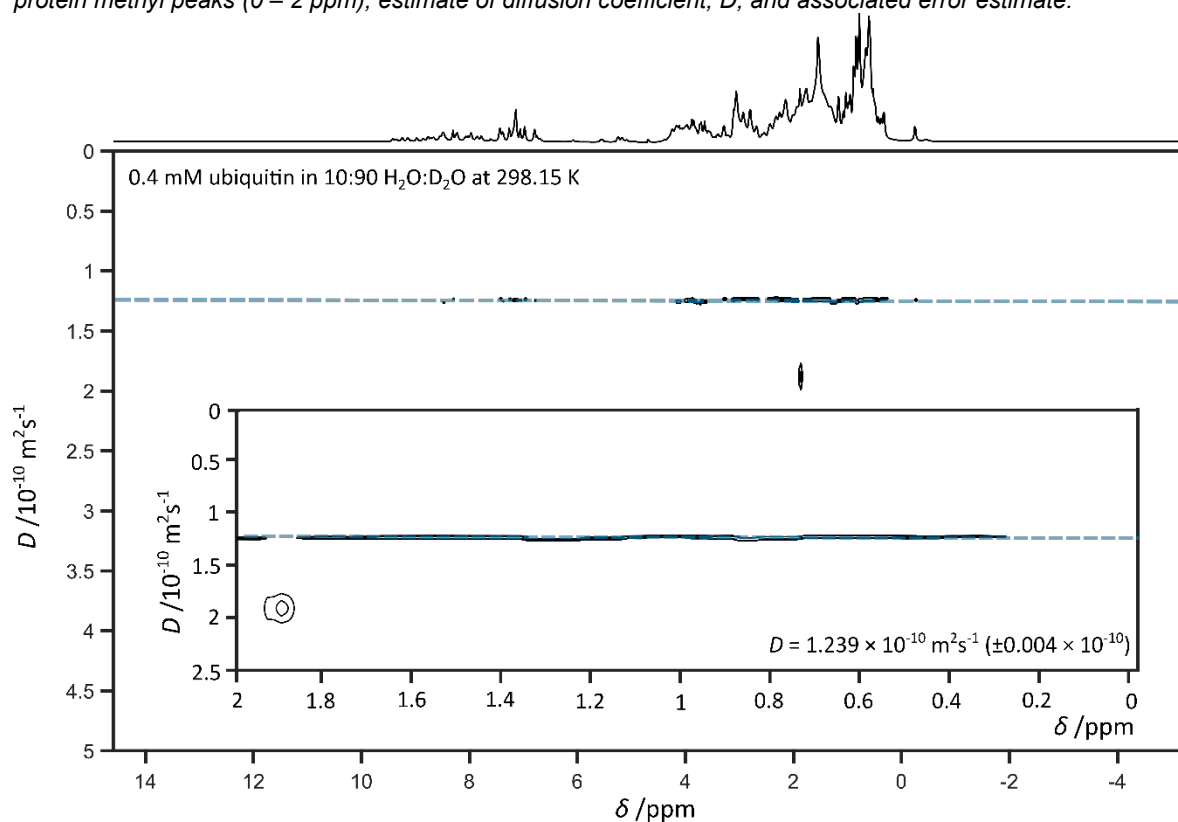

Figure A6.4.20 DOSY spectrum of 0.4mM BSA in 10:90 H_2O:D_2O solution at 298.15 K. Insert depicts protein methyl peaks (0 – 2 ppm), estimate of diffusion coefficient, D, and associated error estimate.

B.Tang, PhD Thesis, Aston University, 2024.
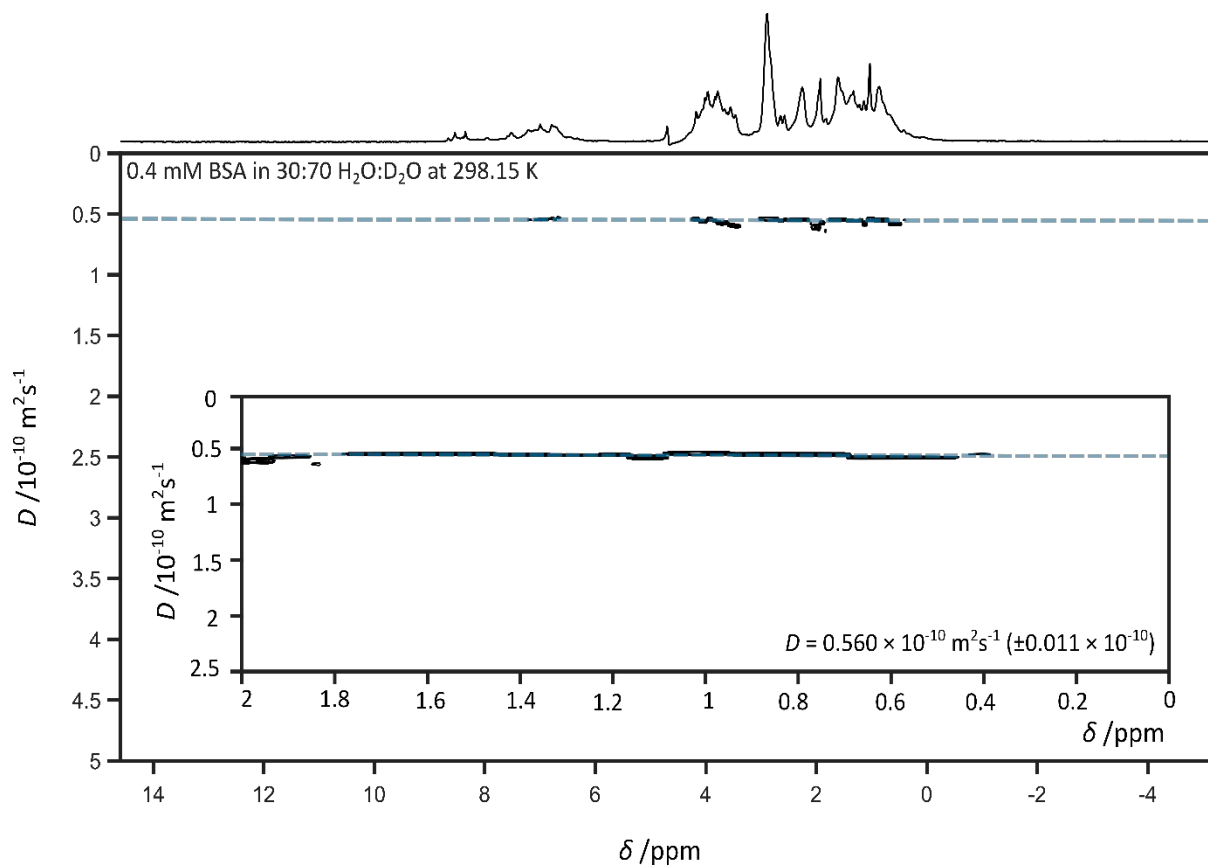
Figure A6.4.21 DOSY spectrum of 0.4mM BSA in 30:70 $H_2O:D_2O$ solution at 298.15 K. Insert depicts protein methyl peaks (0 – 2 ppm), estimate of diffusion coefficient, D, and associated error estimate.

The insert shows: $D = 0.560 \times 10^{-10} \text{ m}^2\text{s}^{-1}$ ($\pm 0.011 \times 10^{-10}$)

Main plot label: 0.4 mM BSA in 30:70 $H_2O:D_2O$ at 298.15 K

Figure A6.4.22 DOSY spectrum of 0.4mM BSA in 50:50 $H_2O:D_2O$ solution at 298.15 K. Insert depicts protein methyl peaks (0 – 2 ppm), estimate of diffusion coefficient, D, and associated error estimate.

The insert shows: $D = 0.584 \times 10^{-10} \text{ m}^2\text{s}^{-1}$ ($\pm 0.014 \times 10^{-10}$)

Main plot label: 0.4 mM BSA in 50:50 $H_2O:D_2O$ at 298.15 K

B.Tang, PhD Thesis, Aston University, 2024.

Figure A6.4.23 DOSY spectrum of 0.4mM BSA in 70:30 H_2O:D_2O solution at 298.15 K. Insert depicts protein methyl peaks (0 – 2 ppm), estimate of diffusion coefficient, D, and associated error estimate.
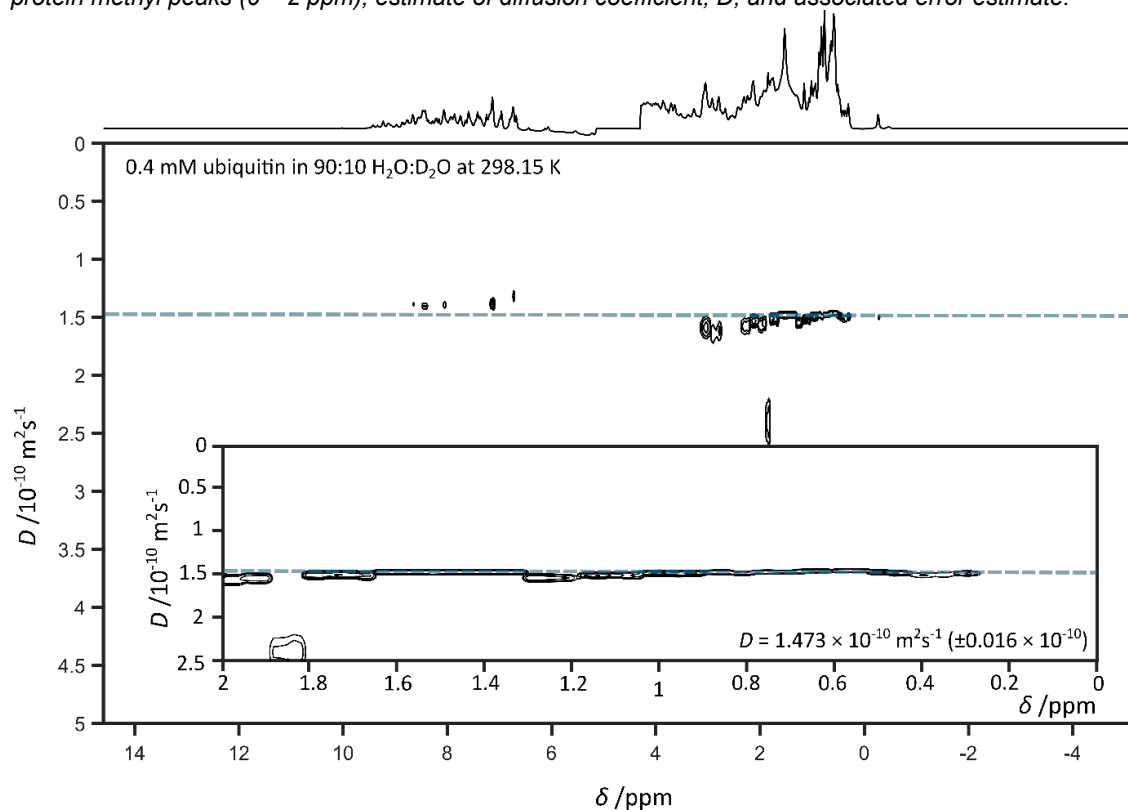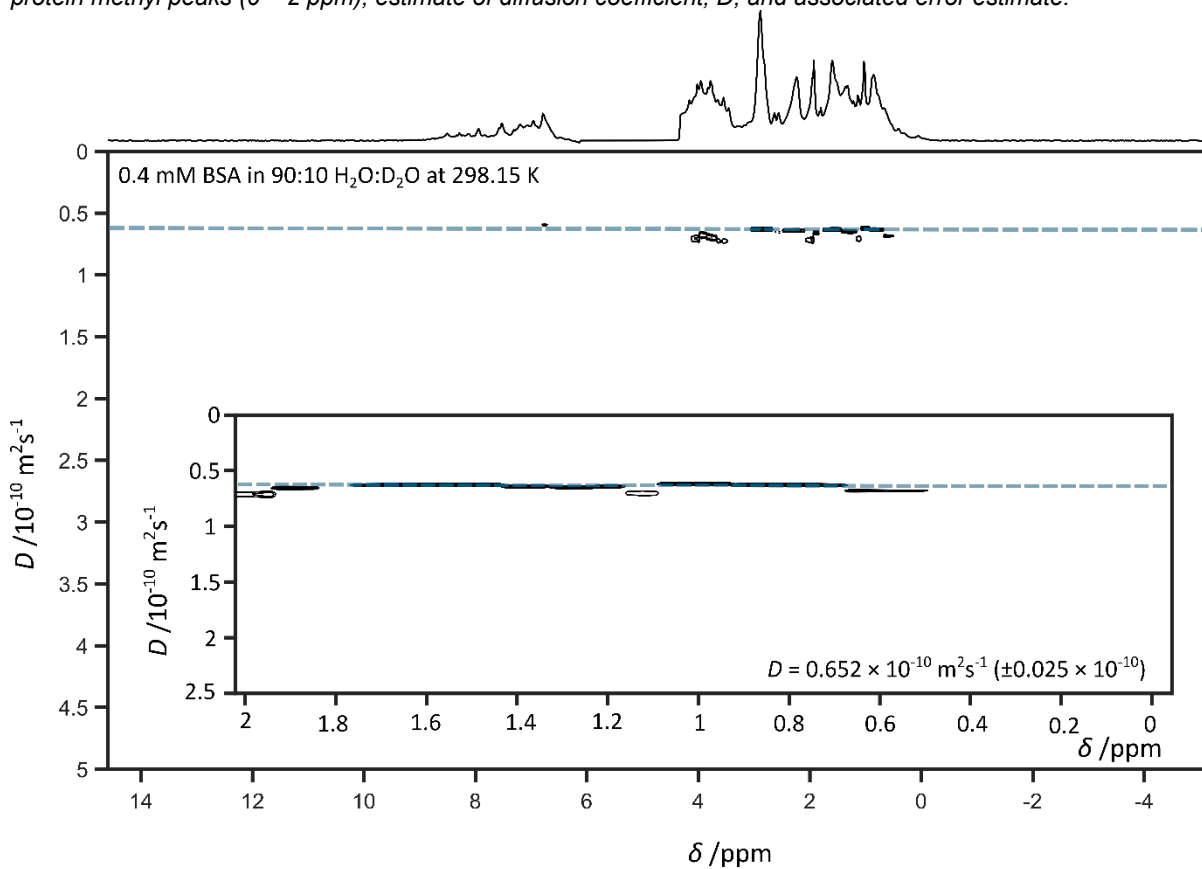

Figure A6.4.24 DOSY spectrum of 0.4mM BSA in 90:10 H_2O:D_2O solution at 298.15 K. Insert depicts protein methyl peaks (0 – 2 ppm), estimate of diffusion coefficient, D, and associated error estimate.

349

Table A6.4.4 Summary of all data for various proteins at 298.15 K, including MW, experimentally-acquired diffusion coefficients and diffusion coefficients predicted using the extended SEGWE equation.

Protein	*MW* /g mol^{-1}	%H$_2$O	*D* Measured × 10^{-10} m^{2}s^{-1}	*D* Estimated using extended SEGWE × 10^{-10} m^{2}s^{-1}
Aprotinin	6500	90	1.571	1.598
		70	1.496	1.533
		50	1.425	1.470
		30	1.373	1.410
		10	1.306	1.352
		0	1.285	1.324
Ubiquitin	8579	90	1.473	1.445
		70	1.403	1.386
		50	1.343	1.329
		30	1.287	1.275
		10	1.239	1.223
		0	0.217	1.197
Lysozyme	14307	90	1.220	1.203
		70	1.167	1.154
		50	1.130	1.108
		30	1.064	1.063
		10	1.024	1.020
		0	1.004	0.999
Myoglobin	16700	90	1.145	1.138
		70	1.095	1.092
		50	1.050	1.047
		30	1.004	1.004
		10	0.963	0.963
		0	0.951	0.934
BSA	66463	90	0.652	0.702
		70	0.620	0.673
		50	0.584	0.646
		30	0.560	0.620
		10	0.537	0.594
		0	0.521	0.582

Example calculation for volume fraction, for 1mM Lysozyme, 90:10 H₂O:D₂O

$$\Phi = \frac{C_M M}{\rho + C_M M}$$

ϕ = volume fraction of the solute
C_M = Molecular concentration (mol m^{-3})
M = molecular weight (kg mol^{-1})
ρ = density (kg m^{-3})

$$\phi = \frac{1\ mol\ m^{-3} \times 14307 \times 10^{-3} kg\ mol^{-1}}{997\ kg\ m^{-3} + (1\ mol\ m^{-3} \times 14307 \times 10^{-3} kg\ mol^{-1})} = 0.0141$$
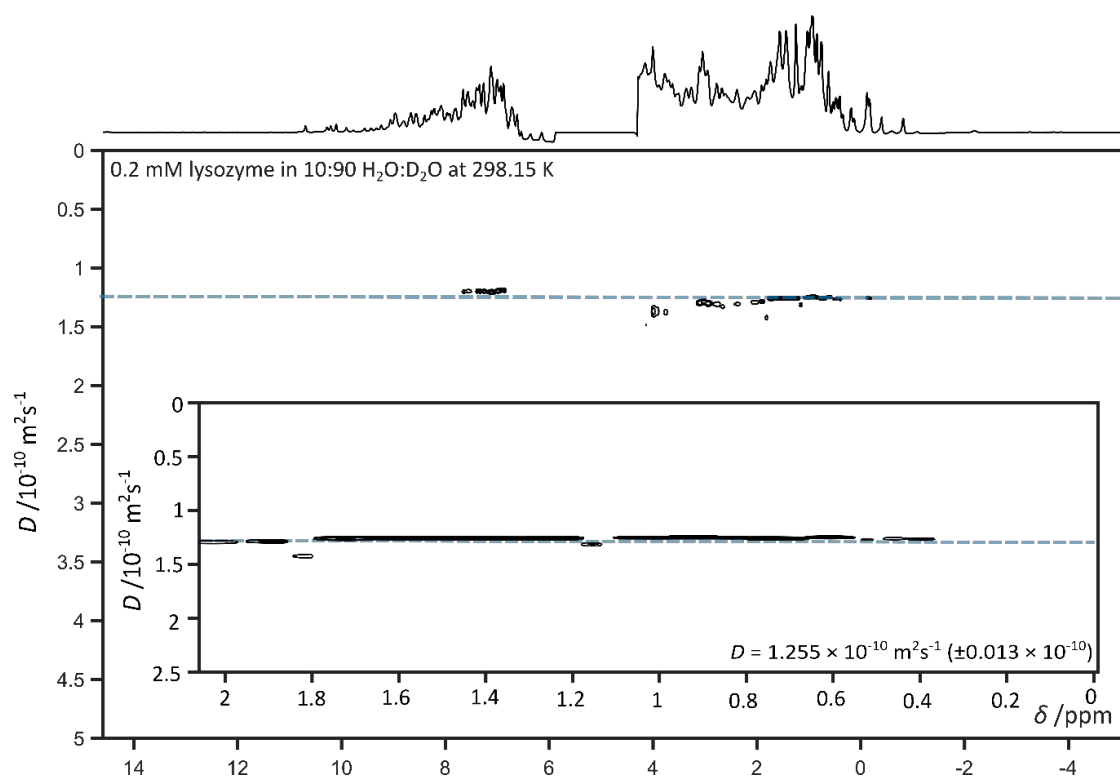
Figure A6.5.1 DOSY spectrum of 0.2mM lysozyme in 10:90 H₂O:D₂O solution at 298.15 K. Insert depicts protein methyl peaks (0 – 2 ppm), estimate of diffusion coefficient, D, and associated error estimate.
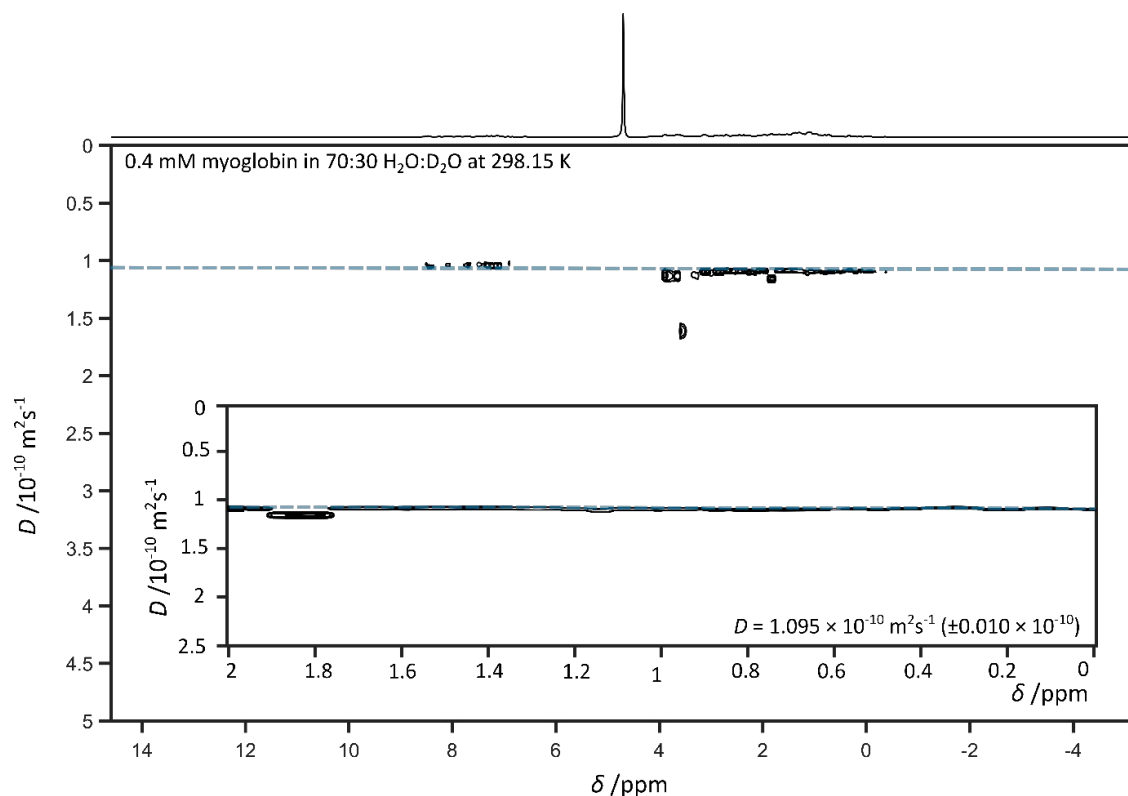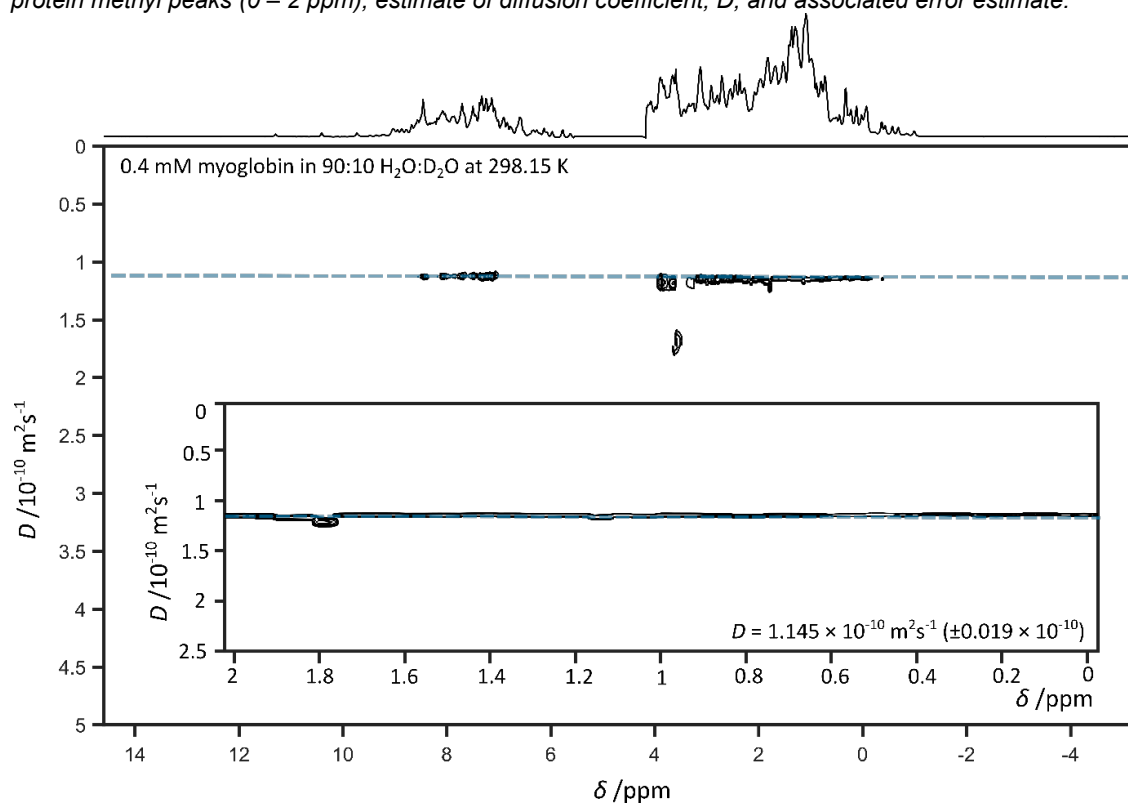
B.Tang, PhD Thesis, Aston University, 2024.
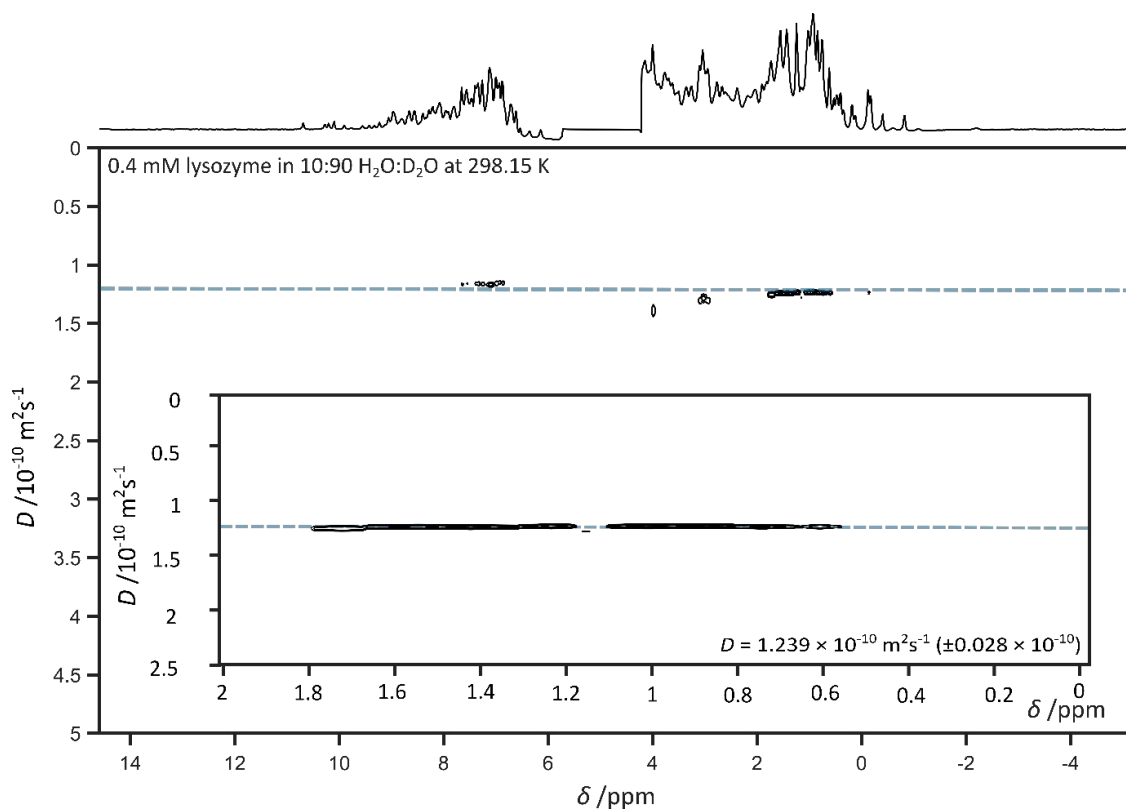
Figure A6.5.2 DOSY spectrum of 0.4mM lysozyme in 10:90 H₂O:D₂O solution at 298.15 K. Insert depicts protein methyl peaks (0 – 2 ppm), estimate of diffusion coefficient, D, and associated error estimate.
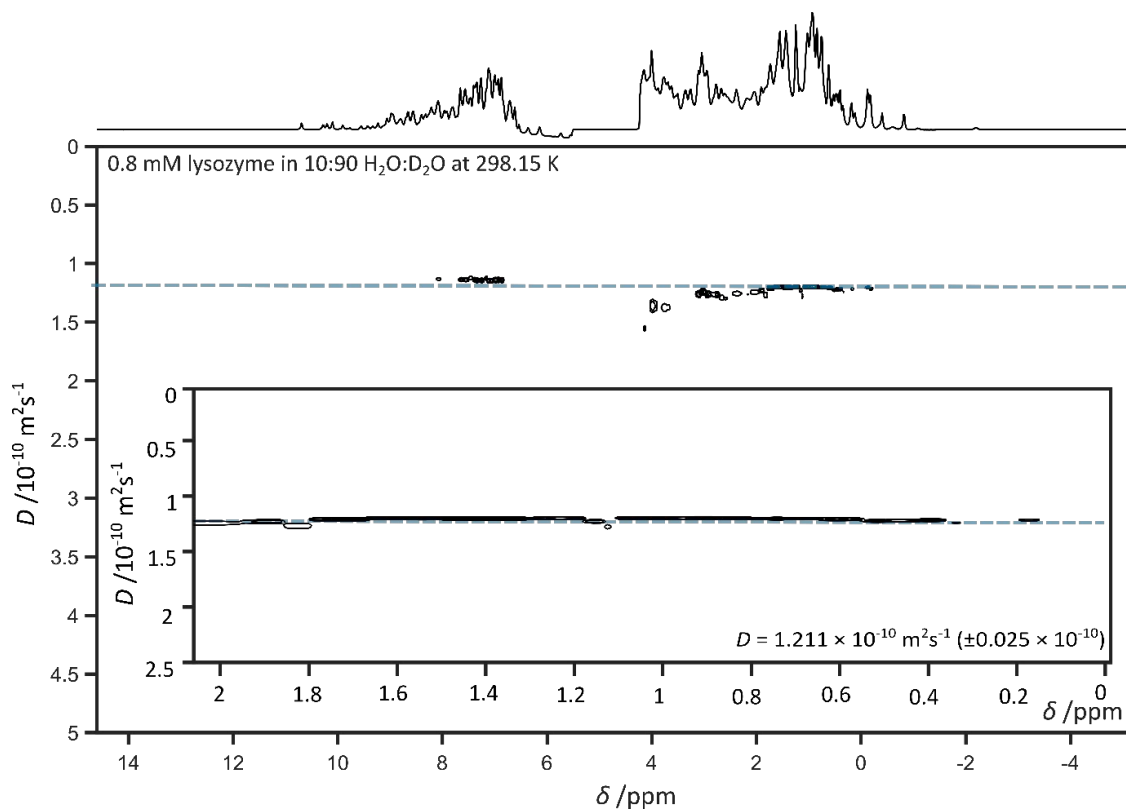
Figure A6.5.3 DOSY spectrum of 0.8mM lysozyme in 10:90 H₂O:D₂O solution at 298.15 K. Insert depicts protein methyl peaks (0 – 2 ppm), estimate of diffusion coefficient, D, and associated error estimate.
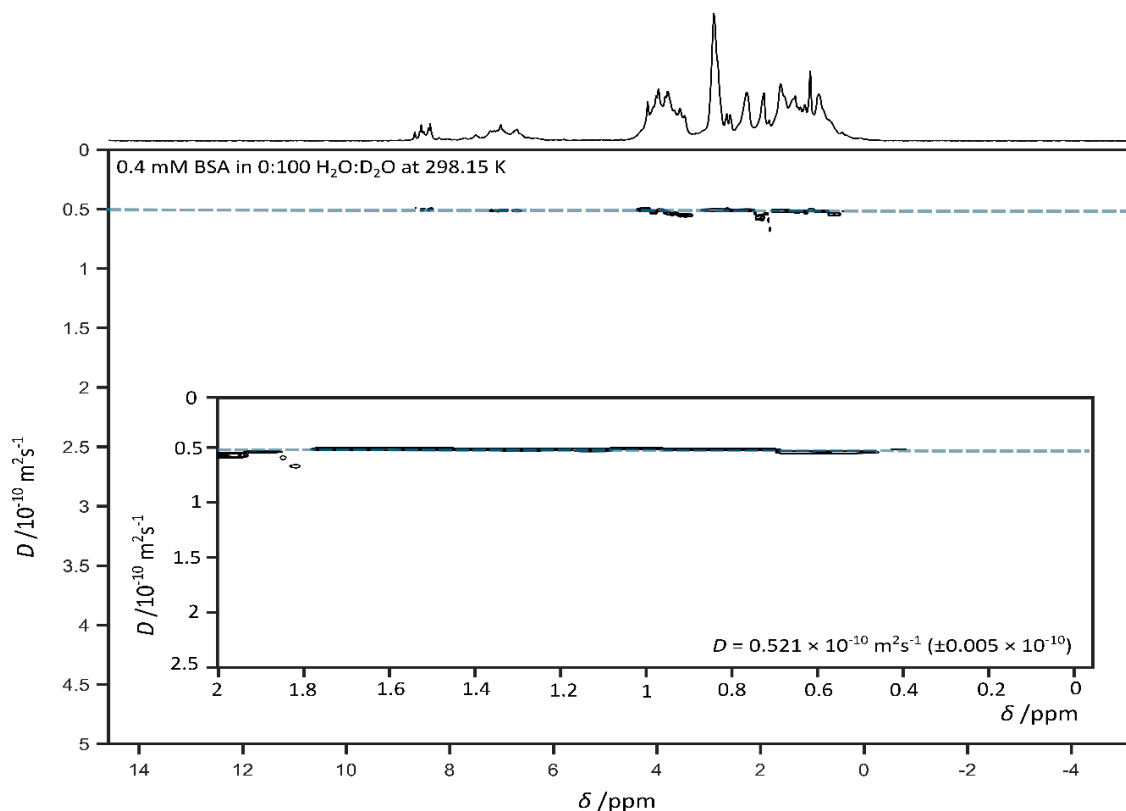
B.Tang, PhD Thesis, Aston University, 2024.
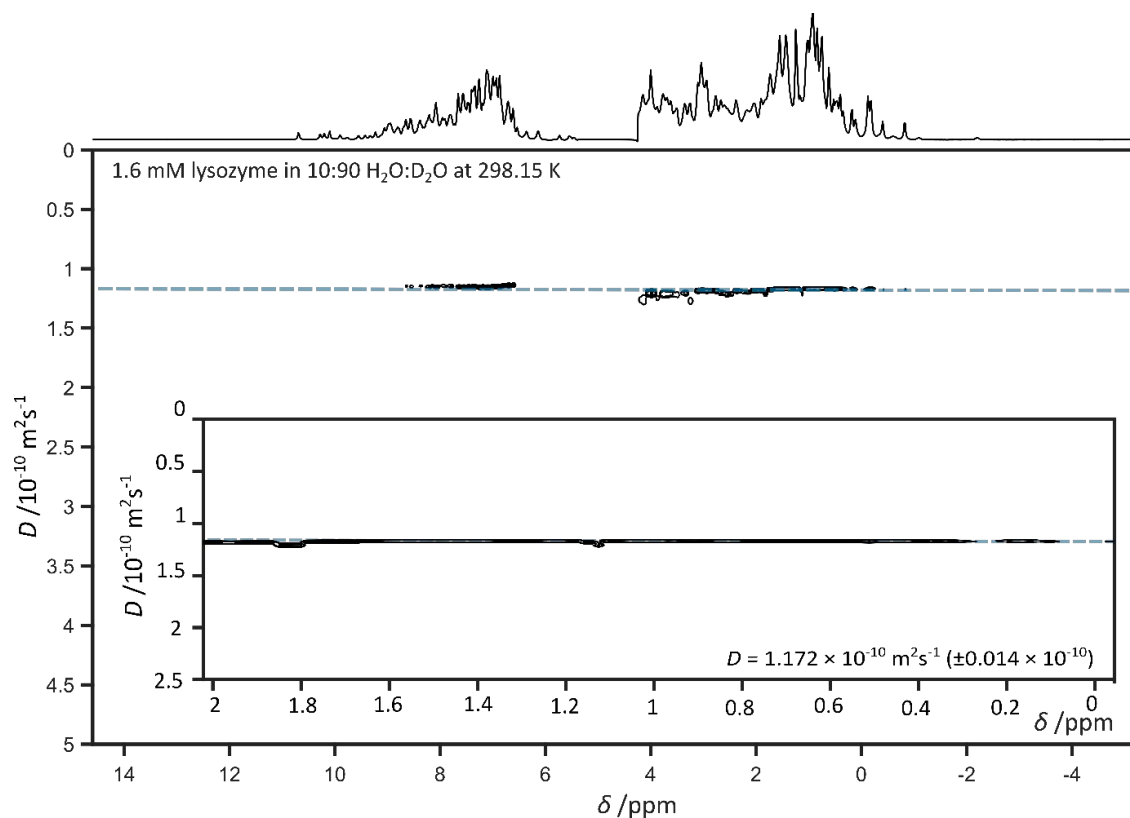
Figure A6.5.4 DOSY spectrum of 1.6mM lysozyme in 10:90 H_2O:D_2O solution at 298.15 K. Insert depicts protein methyl peaks (0 – 2 ppm), estimate of diffusion coefficient, D, and associated error estimate.
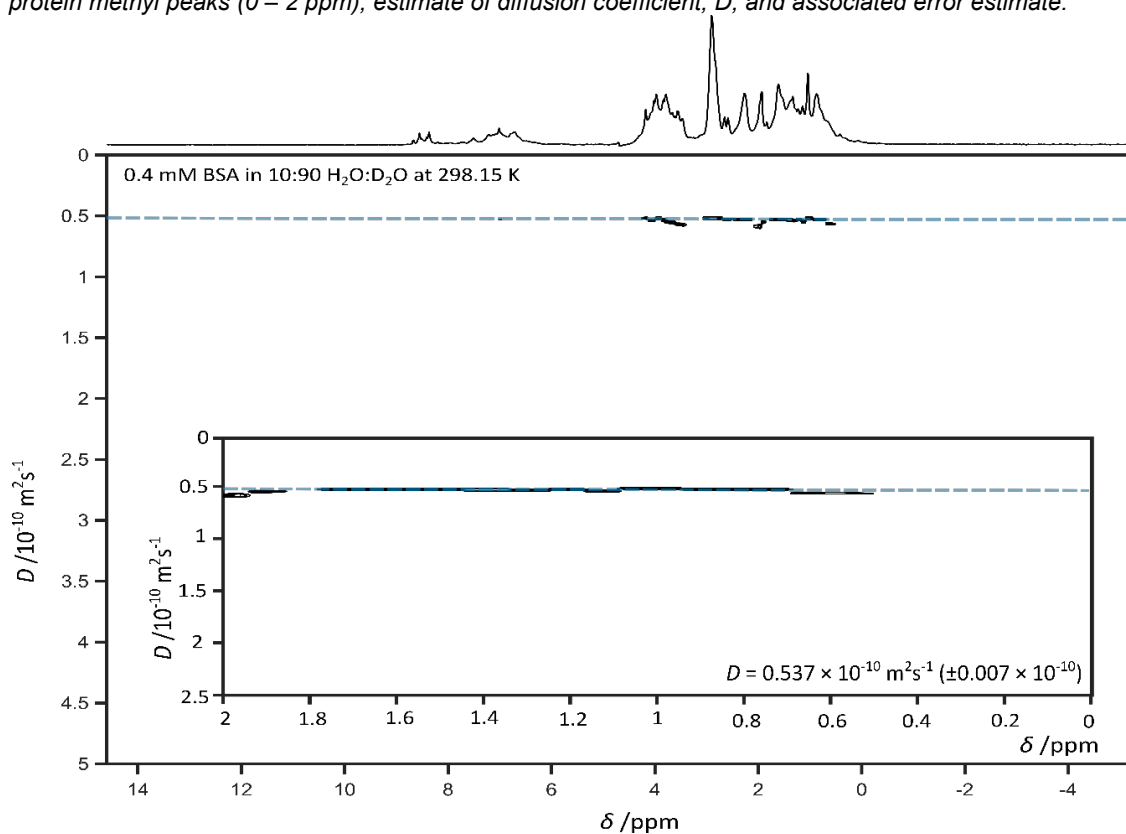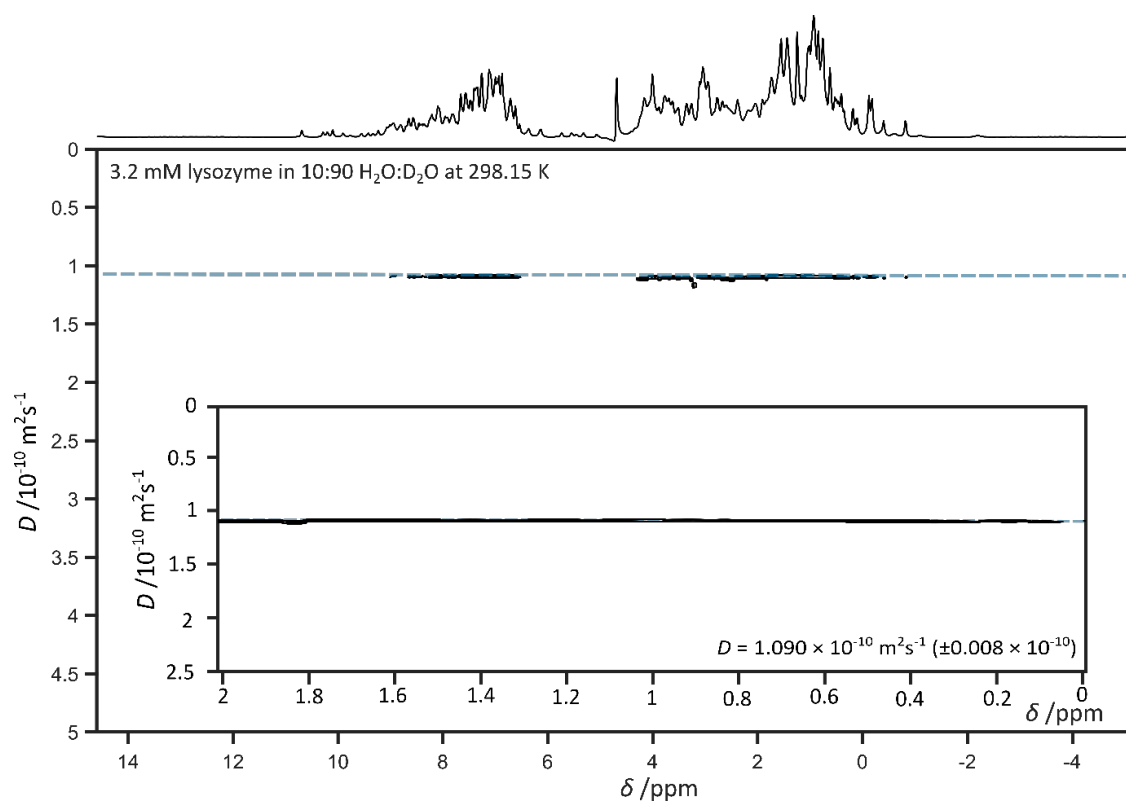

Figure A6.5.5 DOSY spectrum of 3.2mM lysozyme in 10:90 H_2O:D_2O solution at 298.15 K. Insert depicts protein methyl peaks (0 – 2 ppm), estimate of diffusion coefficient, D, and associated error estimate.
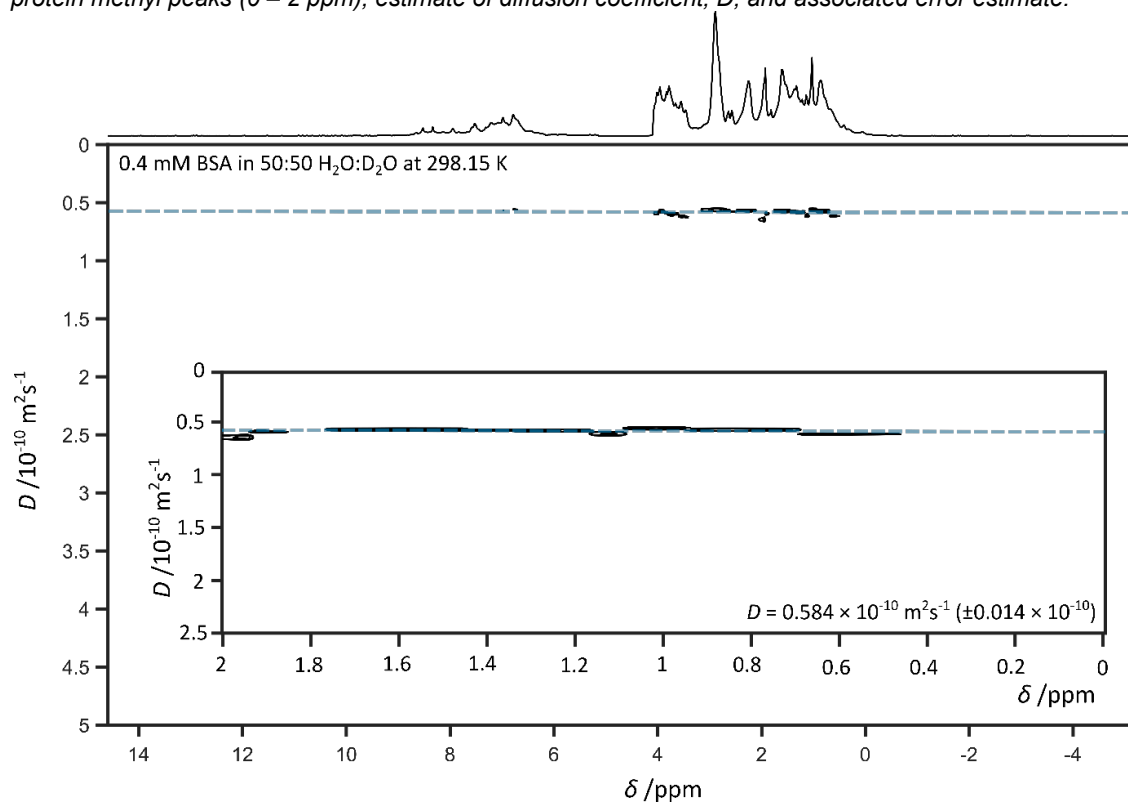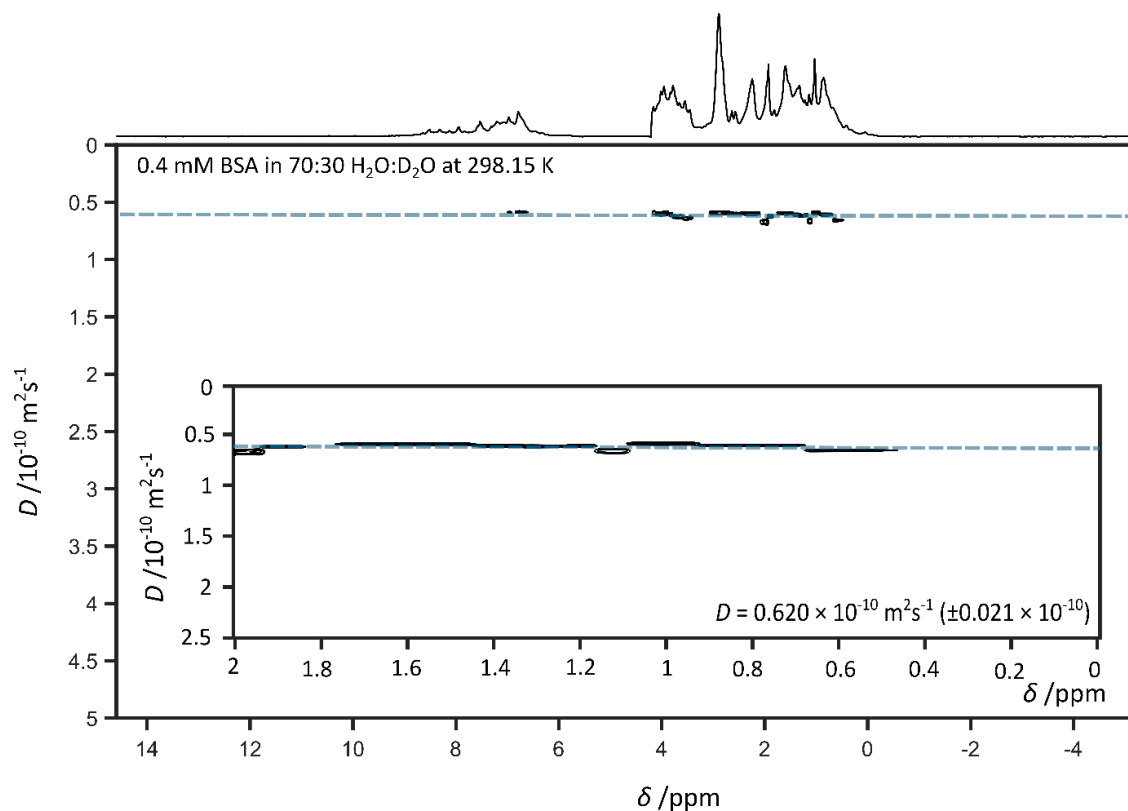
353

B.Tang, PhD Thesis, Aston University, 2024.

A6.6 Raw Data for Intrinsically Disordered Proteins and Proteins

Source: All data for protein and IDP measured diffusion coefficient was taken from the supporting information of *Dudás, E.F. and Bodor, A., 2019. Quantitative, diffusion NMR based analytical tool to distinguish folded, disordered, and denatured biomolecules. Analytical chemistry, 91(8), pp.4929-4933.*

Table A6.6.1 Physical properties, experimentally acquired diffusion coefficients and diffusion coefficients estimated using extended SEGWE equation for additional proteins listed in Dudás and Bodor.

Protein	MW /g mol^{-1}	Net charge	# of neg. charged res.	# of pos. charged res.	PI	D Measured × 10^{-10} m^{2}s^{-1}	D Estimated using extended SEGWE × 10^{-10} m^{2}s^{-1}
TC5b	2169	1	−1	2	3.8	1.760	1.800
TC5bS13E	2211	0	−2	2	6.8	1.720	1.787
PAF	6250	5	−8	13	8.93	1.060	1.213
BPTI	6517	6	−4	10	9.24	1.090	1.195
Ribonuclease	13690	6	−10	16	8.93	0.917	0.914
Lysozyme	14313	5	−8	13	8.98	0.784	0.900
CalmodulinCa2+	16997	−24	−38	14	4.09	0.719	0.847
S100A4d19a2+	20966	−6	−30	24	5.33	0.703	0.786
S100A4wt	24018	−2	−34	32	5.85	0.680	0.749
Chymotrypsinogen	25678	4	−14	18	8.52	0.741	0.732
Ovalbuim	42881	−12	-47	35	5.19	0.510	0.611
BSA	66463	−13	−99	86	5.82	0.480	0.525

B.Tang, PhD Thesis, Aston University, 2024.

Table A6.6.2 Physical properties, experimentally acquired diffusion coefficients and diffusion coefficients estimated using extended SEGWE equation for IDPs listed in Dudás and Bodor.

IDP	MW /g mol^{-1}	Net charge	# of neg. charged res.	# of pos. charged res.	PI	D Measured × 10^{-10} m^{2}s^{-1}	D Estimated using extended SEGWE × 10^{-10} m^{2}s^{-1}
NFAT	1738	−1	−3	2	5.45	1.540	1.960
MNK1	2195	7	0	7	12.6	1.370	1.792
MK2	2392	6	−2	8	10.66	1.270	1.735
RSK	2732	4	−1	5	11.72	1.180	1.649
Tb4	5053	−2	−11	9	5.02	0.945	1.312
p53 TAD	7000	−11	−12	1	3.43	0.744	1.164
M67	7440	−1	−15	14	5.45	0.789	1.139
SMAR3	18370	−19	−33	14	4.94	0.478	0.824
ERD14 wt	20786	−9	−46	37	7.70	0.425	0.788
fullscrERD14	20773	−7	−44	37	6.50	0.419	0.788

B.Tang, PhD Thesis, Aston University, 2024.

Figure A6.6.1 shows the positively charged proteins and IDPs in red and negatively charged proteins and IDPs in blue. The net charge of proteins and IDP are summarised in Tables SI.6.1 and SI.6.2 respectively. The net charge of these proteins and IDP raged from -24 to +7. Overall, the net charge of the protein or IDP does not appear to affect the diffusion coefficients of the proteins and IDP.
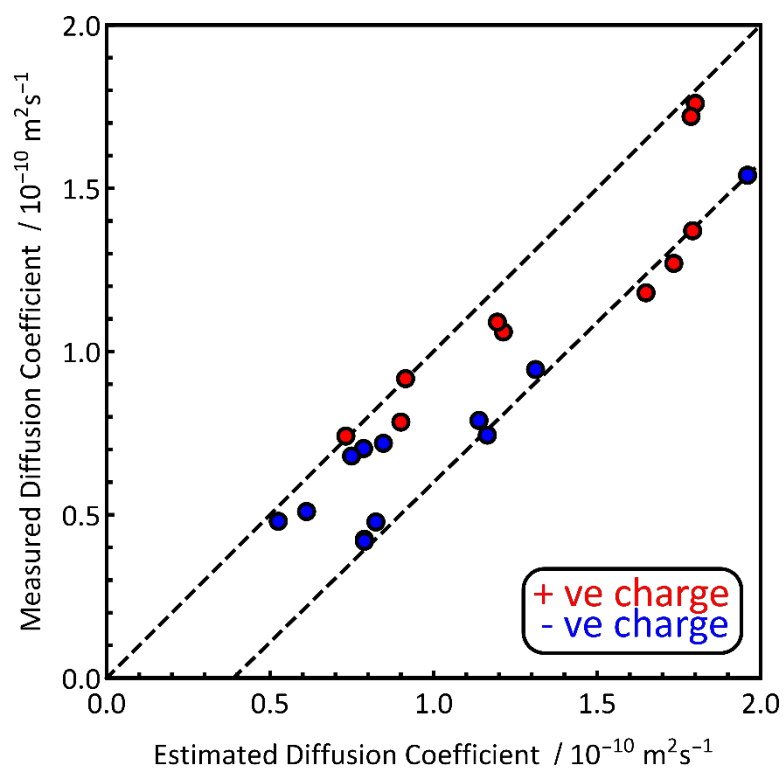
Figure A6.6.1 Experimentally-acquired diffusion coefficients of globular proteins and intrinsically disordered proteins plotted against diffusion coefficients predicted using the extended SEGWE equation at 287 K in H_2O. Positively charged proteins and IDP are shown in red and negatively charged proteins and IDP are shown in blue.

APPENDIX 7 Additional Publications

A7.1 Cover Art and Cover Profile
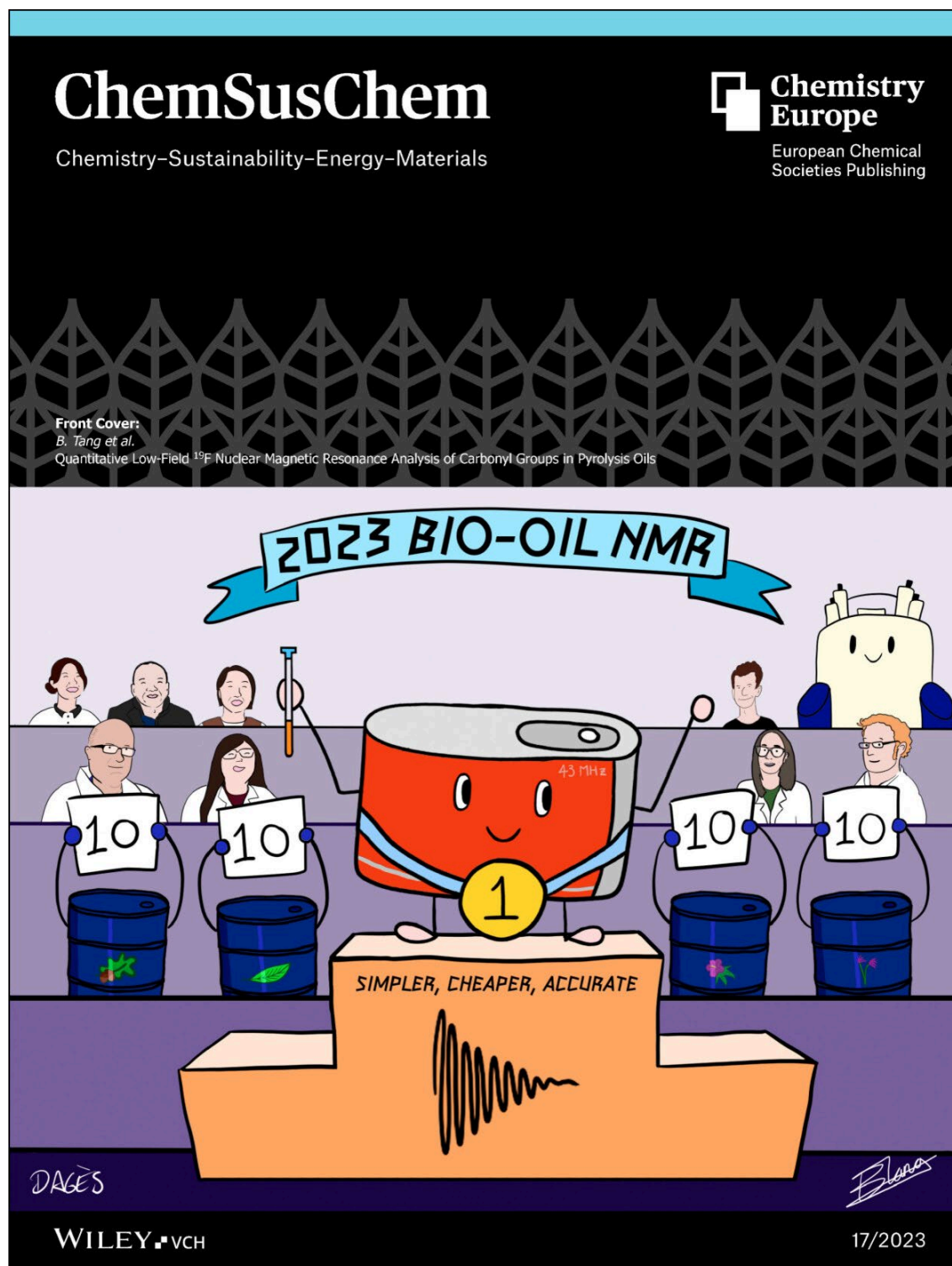
Quantitative Low-Field ^{19}F Nuclear Magnetic Resonance Analysis of Carbonyl Groups in Pyrolysis Oils

Bridget Tang Dr. Katie Chong Prof. Art Raguaskas Dr. Robert Evans

Aston University BIRMINGHAM UK

Invited for this month's cover is the collaboration between Dr Rob Evans at Aston University, Birmingham, UK and Prof. Art Ragauskas at University of Tennessee, Knoxville and Oak Ridge National Laboratory, Oak Ridge, USA. The image illustrates that low-field, or benchtop, NMR spectrometers can be as effective as their higher-field counterparts in the accurate, quantitative analysis of bio-oils.
The Research Article itself is available at 10.1002/cssc.202300625.

What was the inspiration for this cover design?

This work has been a team effort throughout and we wanted to convey that in the image. Katie and I have been working on using NMR to study bio-oils and fuels since I joined Aston in 2013. Bridget has been part of my group since she first joined as a summer research intern in 2017. Art has collaborated and supported us since a research seminar in autumn 2018. We had help in creating our cartoon from another Aston PhD student, Benjamin Dages, who can be found seated by the high field magnet. Finally, we decided to pay tribute to Bridget's family, who have supported her throughout.

Did serendipity play a part in this work?

Definitely! This particular project started from asking *"why don't we try it on the department's benchtop and see what it looks like … "*. From the very first results acquired, we realised we had found something worth pursuing. Sometimes it really is worth giving an experiment a go just to see what happens.

What are the main challenges in the broad area of your research?

In NMR research, there's always a balance between having too little information in a spectrum and too much. The biggest challenge is often resolving individual peaks in the spectra. In this work, it was not vital, hence the successful transfer to the benchtop. However, there are a few additional NMR 'tricks' to employ if single, well-resolved peaks could be obtained…

Acknowledgements
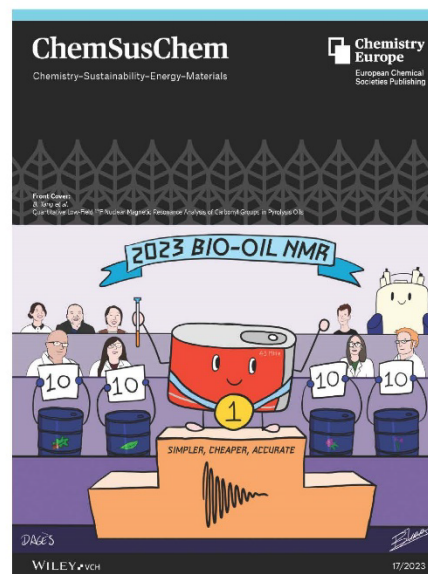
Improving the Analysis of Separated Bio-Fuels with Slice Selective Total Correlation NMR Spectroscopy

Jaskamal Singh Khangura[†], Bridget Tang[†], Katie Chong[‡] and Robert Evans[†]*, †

Aston Institute of Materials Research, School of Engineering and Applied Science, Aston University, Birmingham, B4 7ET, UK, United Kingdom.

‡ European Bioenergy Research Institute, Aston University, Aston Triangle, Birmingham B4 7ET, United Kingdom

ABSTRACT

Pyrolysis oil has been identified as a possible alternative fuel source, however widespread use is hindered by high acidity and water content. These negative characteristics can be mitigated by blending with, for example, mixtures of biodiesel, marine gas oil and butanol. These blended biofuel samples can be unstable and often separate into two distinct phases. Analysis of how the components of any blended biofuel samples partition between the two layers is an important step towards understanding the separation process and may provide insight into mitigating the problem. Slice-selective NMR, where the NMR spectrum of only a thin slice of the total sample is acquired, has been previously used to study, non-invasively, bio-oil samples. Here, the technique is extended and improved, with slice-selective two-dimensional TOCSY experiments used to resolve the distinct chemical spectra of the various components of the blended fuel mixtures.

INTRODUCTION

The use of biomass pyrolysis oils is one potential solution toward the development of sustainable and green energy platforms.[1,2] Pyrolysis is a thermochemical conversion process, involving irreversible heat-driven decomposition of materials, such as lignocellulosic biomass, in the absence of oxygen.[3] The pyrolysis products contain char, gas, and an oil, itself a complex mixture of alcohols, aldehydes, alkenes, carbohydrates, carboxylic acids, esters, furans, guaiacols, ketones, phenols, syringols, miscellaneous other oxygenates, nitrogen-containing compounds, and water.[3-5] This oil is a potential fuel, but typically cannot be used directly in unmodified engines as it contains too much water and the various other oxygen-containing species present render it too

361

acidic. There are several methods by which the utility of a pyrolysis product can be improved,[6-8] such as by blending with other products.[9-13] These multiple component blends are typically opaque and can readily separate into a multiple-phase solution.[12-14] Once separated, the blends are not suitable as fuel products and could cause significant damage to an engine if used. A key challenge to the successful blending of these fuel products is the analysis, understanding and mitigation of this phase separation.

The NMR analysis of pyrolysis oils is well-established and comprehensive reviews are available. [15-16] However, any analysis of these oils, blended or otherwise, is complicated by the large number of species present and the range of functional groups that may be present. Any analysis is rendered more difficult if the samples separate. Standard 1D NMR measurements of the separated sample will simply sum the signals of the two phases together. Additionally, the presence of a boundary between two phases will detrimentally affect the resolution and quality of the spectrum, due to the differences in magnetic susceptibility of the two phases. These issues can be avoided by using slice-selective, or spatially resolved, NMR.[17]

Excitation of a given slice of the sample is accomplished by applying a long, low-power, radiofrequency pulse in the presence of a pulsed magnetic field gradient. NMR spectrometers are now fitted with such pulsed magnetic field gradients as standard. On most standard NMR probes, these gradients are applied along the direction of the magnetic field or z-axis. When a linear field gradient, G_z , is applied to a sample, the magnetic field strength, $B(z)$, depends on the position along the axial direction of the NMR tube, z, such that $B(z) = B_0 + zG_z$. Therefore, all resonance frequencies experience an offset, Ω, that

362

depends on the vertical deviation (z) from the center of the gradient coil, see Equation (1), where γ is the gyromagnetic ratio of the spins being measured.

$$\Omega = \frac{\gamma G_z z}{2\pi}$$

<div align="right">Equation (1)</div>

A soft pulse, with a bandwidth ΔB, employed at this offset will selectively excite a horizontal slice of the sample, centred at z, with a thickness Δz obtained from Equation (2).

<div align="right">Equation (2)</div>

$$\Delta z = \frac{2\pi}{\gamma G_z} \Delta B$$

Only this thin horizontal slice of the sample will be excited by the soft radiofrequency pulse. Before acquisition of the NMR data, the field gradient is switched off and the spectrum of the slice is acquired as in a normal experiment. The use of slice-selective NMR in 1-dimensional chemical applications is a growing field and has been demonstrated in a number of studies, including idealised systems, such as benzene floating on water[18] or water and olive oil mixtures,[19] and the diffusion of small molecules in non-equilibrium systems, such as the mutual diffusion of small molecules,[20] CO_2 in ionic liquids,[21] and small molecules through gels.[22-24] Slice-selective NMR spectroscopy has more recently been utilized6 in increasingly complex analyses, such as separated biofuels,[25] crude oil emulsions,[26] and hydrophilic/hydrophobic metabolites.[27] Its use is not limited to observing ^1H, with application to the study of ^7Li ions in both polymer gels[28, 29] and in systems intended to resemble Li-ion batteries.[30]

Here, the performance of slice-selective NMR analysis of blended fuels is improved by combining slice-selective methods with two-dimensional NMR techniques. Total correlation spectroscopy (TOCSY) is used here, as the final

B.Tang, PhD Thesis, Aston University, 2024.

spectra produced can be phased to give pure absorption mode peaks. By extending the spectra into a second dimension, the resolution of individual peaks in the spectra are significantly improved and it is easier to identify specific species in the different layers of the sample. In addition, coupling information is now revealed, allowing for identification of more components in the mixtures, particularly the biooil present in the blend.

EXPERIMENTAL

METHODS AND MATERIALS

Six blended biofuel samples containing differing amounts of the bio-oil, marine gas oil, fatty acid methyl ester, and butanol were analysed.

Marine gas oil: Marine gas oil is made from the distillate fraction of petroleum oil. It is the fuel most used for inland marine transport. The oil used in this study was supplied by Statoil in Norway.

Fatty Acid Methyl Ester (biodiesel, FAME): A key component of the blended fuel is the methyl ester of a long chain fatty acid. The biodiesel used for this study was produced through the transesterification of pure rape seed oil, yielding methyl esters. It has previously been demonstrated that biodiesel and marine gas oil are miscible in all proportions.[31]

Bio-oil: All blends studied in this work contain fast pyrolysis oil produced at Aston University using a Norwegian Spruce feedstock in a 1 kg h^{-1} fast pyrolysis rig. The bio-oil used in this work is a mixture of phenolic compounds, carboxylic acids and water.

All blended biofuel samples contained both bio-oil and butanol and either one, or both, of the other components and are referred to as three- or four-component

364

mixtures. The blends were prepared by adding a weighed sample of bio-oil to butanol in a sample container, followed by biodiesel and/or marine gas oil. Finally, the solvent was added, the container sealed and lightly shaken. All blends were prepared at room temperature with a total weight of 20 grams. Table 1 summarizes the compositions of the six samples.

| Sample | Component composition / % | | | |
	Bio-oil	Butanol	FAME	Marine gas oil
A	10	80	10	0
B	20	40	40	0
C	15	45	0	40
D	30	20	50	0
E	20	50	7.5	22.5
F	30	40	15	15

Table 1. Summary of percentage by weight compositions of samples A, B, C, D, E and F.

NMR Experiments

All ^{1}H NMR measurements were performed on a 300 MHz Bruker Avance spectrometer at 298 K, using a 5 mm BBO probe equipped with a *z* gradient coil producing a maximum gradient strength of 0.55 T m^{-1}. For the slice-selective NMR experiments, a G4 cascade[32] was used for the selective pulse, with a 5000 Hz bandwidth and applied at offsets of + and − 5000 Hz, corresponding to the

upper and lower layers respectively. A gradient of 5 % of the maximum gradient strength was applied concurrently with the selective pulse. This corresponds to a slice 4.3 mm in width, exciting a slice centered 4.3 mm from the center of the G_z coils. No deuterated solvents were added to the samples. All NMR experiments were acquired without the use of the lock and shimming was achieved using the area of the acquired FID. The data presented here were all acquired with a slice-selective 2D TOCSY experiment with 256 increments, 8 scans and 16 dummy scans, for an experimental duration of 2 hours and 30 minutes. 1D ^{1}H experiments of all blended samples were also acquired, using 64 scans, for a duration of 16 seconds. All data were processed using TopSpin. The NMR analysis of the oils was performed blind. The identities and compositions of the oils were only revealed to the NMR spectroscopists after the analysis of the NMR spectra was completed.

RESULTS AND DISCUSSION

2D ^{1}H TOCSY of un-separated bio-oil blends

To first demonstrate the general utility of 2D TOCSY experiments in the analysis of biofuels, **Figures 1** and **2** depict spectra acquired from unseparated, three-component, samples. **Figure 1** has been enlarged to capture the smaller peaks present in the sample.

B.Tang, PhD Thesis, Aston University, 2024.
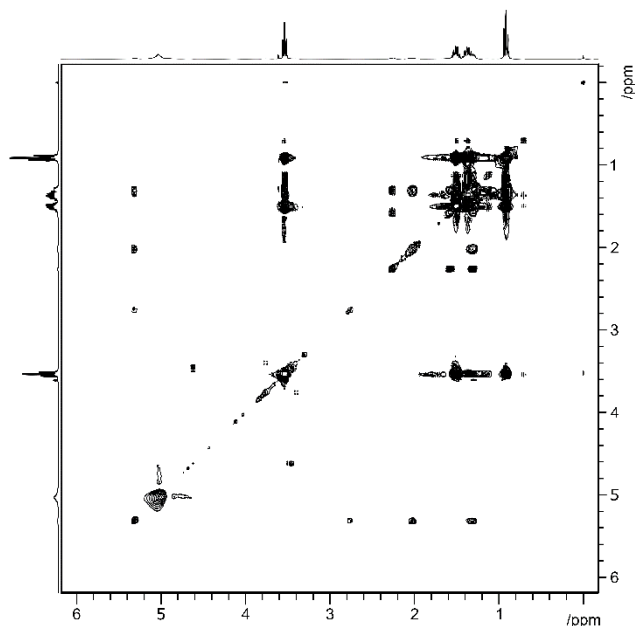
Figure 1: 2D ^{1}H TOCSY spectra of three-component unseparated sample A. The butanol peaks dominate the 1D 1H spectrum and, as expected, the TOCSY spectrum contains all expected cross peaks from butanol, the major component of sample A. However, the TOCSY spectrum reveals additional components of the mixture, both expected and unexpected. The fatty acid methyl ester can also be observed, as a row of resonances horizontally or vertically along 5.4 ppm. Additional peaks, belonging to neither butanol nor fatty acid methyl ester are observed as cross peaks between *ca*. 1.5 ppm and *ca*. 2 ppm.
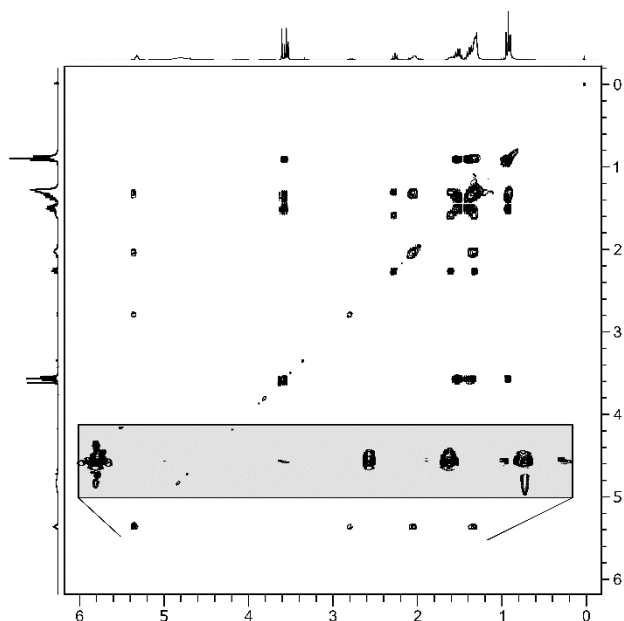
Figure 2: 2D ^{1}H TOCSY spectra of three-component unseparated sample B. Insert, in grey background, depicts enlarged row of peaks corresponding to FAME.

With the long alkyl chain on the fatty acid methyl ester, a suitably long spin-lock is needed to couple together the most distant protons on the chain. The signals highlighted in the insert confirm that the spin-lock period selected is appropriate for the sample. While the intensity of the methyl peak is low, particularly compared with the more plentiful methylene signals, it does appear along the same horizontal line as the other FAME signals. These two spectra show the advantages of the TOCSY pulse sequence. The complete NMR spectrum of individual components can be readily resolved.

Two-dimensional TOCSY spectra of a further two unseparated, four-component, samples, Samples E and F, are presented in the Supporting Information as **Figures S2** and **S3**. While these also contain bio-oil alongside butanol, marine gas oil and FAME, this pair of spectra share many of the features of Samples A and B.

B.Tang, PhD Thesis, Aston University, 2024.

Slice-Selective 2D ¹H TOCSY of Separated Samples

To demonstrate the effectiveness of slice-selective 2D TOCSY experiments in analysing bio-oil samples, two separated, three-component, samples were studied in this work. The NMR spectra of these separated samples were also acquired using both standard 1D ¹H and slice-selective ¹H NMR pulse sequences.

Figure 3 depicts the upper (left) and lower (right) layers of a separated three component blended biooil sample. The sample contains the bio-oil, butanol and marine gas oil. The proton spectra indicate the key differences between the samples, with the upper layer consisting mainly of the marine gas oil and an aqueous lower layer. The butanol is partitioned between the two layers, with *ca.* 93 % found in the lower, aqueous layer.

B.Tang, PhD Thesis, Aston University, 2024.
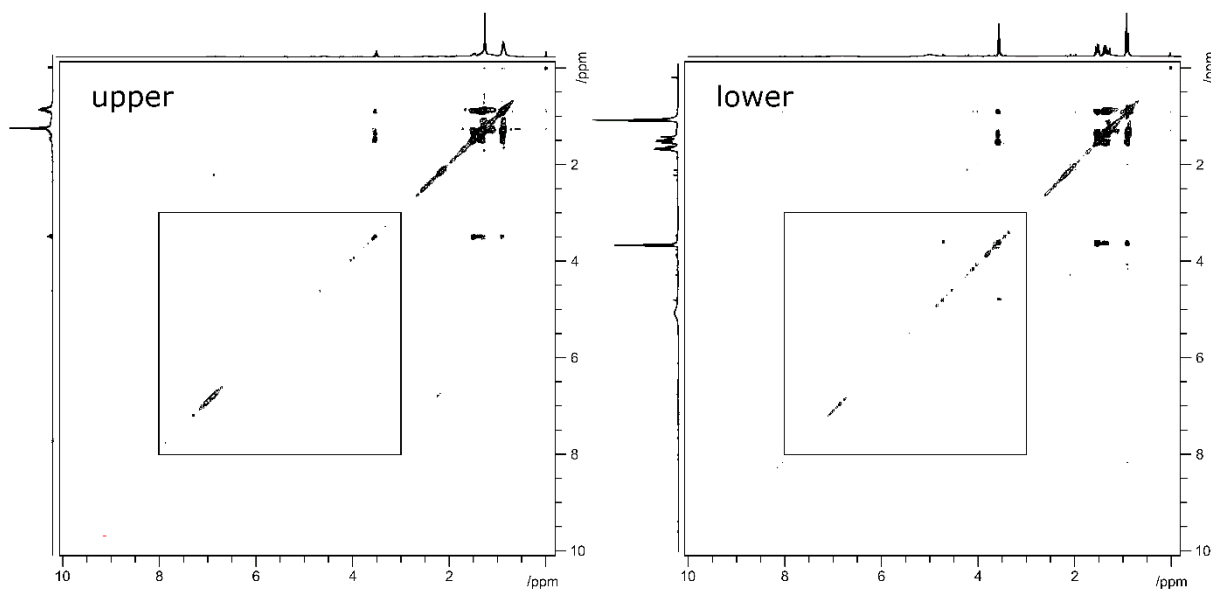
Figure 3: 2D ^{1}H TOCSY spectra of three-component separated sample C. Left-hand spectrum depicts the upper layer and right-hand spectrum depicts the lower later. Spectral regions indicated by boxes are reproduced, enlarged, in **Figure 4**.

The similarity in methyl and methylene chemical shifts render the full TOCSY spectra rather similar, particularly between 1 and 4 ppm. Less intense cross-peaks do appear in the spectra of both layers. In the upper layer, there is a cross peak indicating coupling between aromatic species and alkyl groups while in the lower, the cross peak indicating coupling between species at 3.5 and *ca*. 5 ppm suggests the presence of more polar species. In order to make a more detailed comparison between the two layers, the regions from 3 to 8 ppm, indicated by boxes in **Figure 3**, are magnified and overlaid. This comparison is depicted in **Figure 4**, with the upper layer in blue and the lower layer in red.

B.Tang, PhD Thesis, Aston University, 2024.
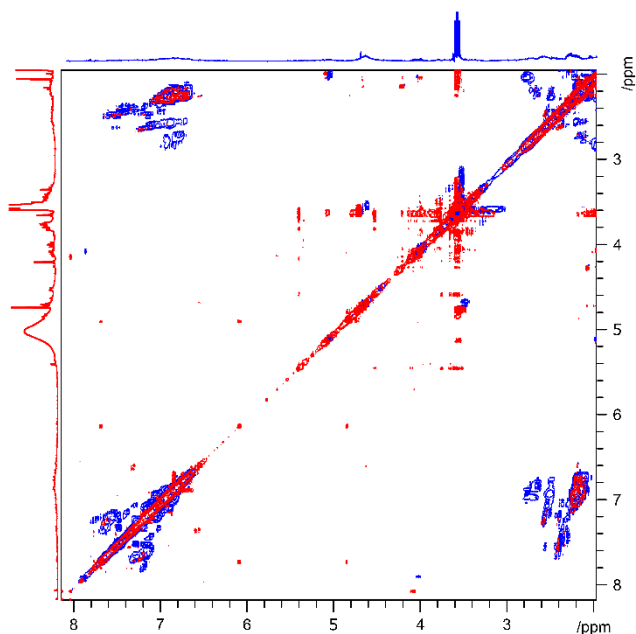
Figure 4: 2D ^{1}H TOCSY spectrum between 2 and 8 ppm (region indicated by box in **Figure 3**) of three-component separated sample C. Blue spectra indicates upper layer. Red spectra indicates lower layer. The individual slice-selective 2D TOCSY spectra of each layer are reproduced in Supporting Information as **Figures S4** and **S5**.

Figure 4 makes the differences between the two layers easily visible. The cross peaks between *ca*. 7 ppm and *ca*. 2 ppm in the upper layer spectrum indicates aromatic species with alkyl substituents. The broad nature of these peaks indicate a wide range of species, likely polymeric or fused ring systems. On the other hand, the cross peaks in the lower layer are both smaller in area and are clustered around 3.5 and 5.5 ppm, indicating a large number of smaller compounds with polar functional groups.

Figure 5 depicts overlaid 2D TOCSY spectra of both the upper layer, in blue, and the lower layer, in red, of a final separated, three component sample (**Sample D**). In this figure, a large range of chemical shifts with a broad dynamic range is depicted and the contour levels of the 2D plots have been adjusted to show as full a range of smaller, less intense, peaks as possible. These peaks are particularly evident in the lower layer, with a large number of small, sharp cross peaks between 3 and 5 ppm. Again, this indicates a larger number of small, polar, molecules present in the bio-oil.
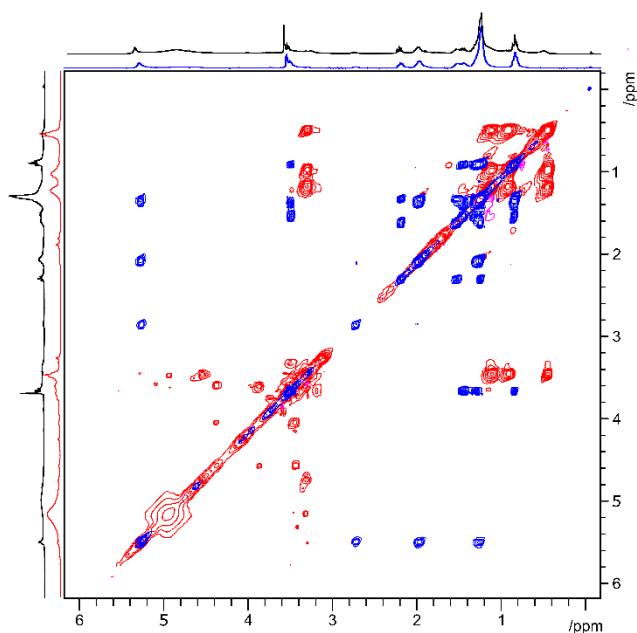
Figure 5: Slice-selective 2D ^{1}H TOCSY spectra of both upper and lower layers of three-component separated sample D. Blue spectrum indicates upper layer. Red spectrum indicates lower layer. Along the x- and y-axes, the blue and red 1D spectra depict the slice-selective spectra of the upper and lower layers, respectively, and the 1D spectrum of the whole sample has been overlaid on both axes, in black, for further comparison.

This sample contains no marine gas oil. Butanol is again partitioned between the upper and lower layers, more evenly than in the previous example with *ca*. 50 % in each layer. Practically all of the bio-oil components are found in the aqueous layer. This is confirmed by **Figure 6**, which depicts the 2D TOCSY of only the lower slice of the final separated sample for an expanded chemical shift range.
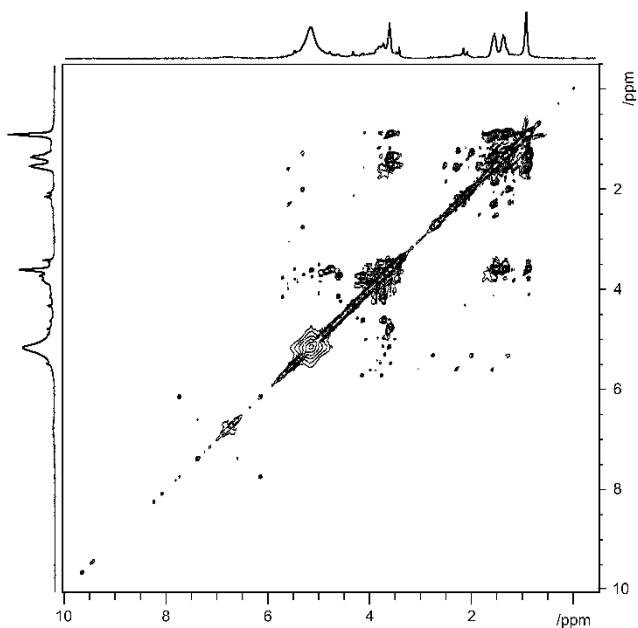
Figure 6: Slice-selective 2D ^{1}H TOCSY spectrum of lower layer of three-component separated **sample D**.

As with every 2D spectrum of the lower, aqueous, layer, there are many sharp peaks, with cross peaks between 3 and 5 ppm. In addition, what are likely to be small chain alcohols can be observed as horizontal lines along *ca*.5.5 ppm and also in the shadow of the intense butanol peaks at *ca*. 4 ppm. Each distinct cross peak in the two dimensional spectrum corresponds to a coupling between two distinct proton environments. Further analysis and identification of individual components in the bio-oil component of the mixture could be achieved through use of machine learning tools applied to this large set of NMR data.

CONCLUSIONS

In this paper, the extension, of slice-selective NMR using two-dimensional techniques has been successfully demonstrated. This extension should not end here. One of the main advantages of NMR spectrometry is the range of

373

experiments and nuclei that can be studied. For a start, NMR techniques are certainly not limited to studying protons. One-dimensional carbon experiments, such as the DEPT family, both improve spectral resolution and can provide additional information about the different species present in the samples.[33] Two-dimensional NMR techniques, of which TOCSY is only one example, have only been rarely used in the study of bio-fuels, bio-oils and related samples.[34] Recently, a slice-selective ^{1}H-^{13}C HSQC experiment has been successfully demonstrated for metabolomics in highly heterogeneous samples.[35]

NMR techniques can also be used to study physical parameters of systems. Diffusion NMR produces information on the sizes of species present[36] and the viscosity of the sample[37]. The relaxation times of water peaks have been shown to be related to the pH of some micellar systems[38] and could be used in such a manner in bio-oil-based fuel samples. Both diffusion and relaxation techniques can act as filters, to remove unwanted signals belonging to either small[39] or large[40] species. NMR spectrometers are now routinely equipped with the pulsed field gradients that enable slice-selective techniques. Thinner slices can be acquired, at the expense of reduced signal to noise, and slices can be easily moved by changing the offset of the selective pulse. The method is not limited to superconducting magnets; so long as the spectrometer has pulsed field gradients in an appropriate geometry, the method described here is transferable.

This paper demonstrates the improved analysis of blended bio-oil samples by the successful implementation of slice-selective two-dimensional TOCSY NMR. Blended bio-oil samples are often unstable, separating into two distinct, often opaque, phases. Improved analysis of how the components of any blended biofuel samples partition between the two layers is an important step towards

understanding the separation processes and may provide insight into mitigating the problem. With an increasing use of biofuel as a long term, sustainable resource and the wider use of NMR techniques in studying biofuel samples, slice-selective NMR techniques offer a powerful, additional analytical tool.

ASSOCIATED CONTENT

Supporting Information.

Supporting information includes photographs of all samples studied and additional spectra.

AUTHOR INFORMATION

Corresponding Author

Robert Evans, r.evans2@aston.ac.uk

Author Contributions

The manuscript was written through contributions of all authors. All authors have given approval to the final version of the manuscript.

REFERENCES

1.   Kamm, B.; Gruber, P.R.; Kamm, M., Eds. *Biorefineries—Industrial Processes and Products: Status Quo and Future Directions. Vol. 1*; Wiley-VCG, 2006.

2.   Kamm, B., Gruber, P.R., Kamm, M., Eds. *Biorefineries—Industrial Processes and Products: Status Quo and Future Directions. Vol. 2*; Wiley-VCG, 2006.

3.   Bridgwater, A.V. Review of fast pyrolysis of biomass and product upgrading. *Biomass Bioenerg.* **2012**, *38*, 68-94.

4.   Bridgwater, A.V. *Fast Pyrolysis of Biomass: A Handbook*. *Vol. 2*; CPL Press, 2002.

5.   Mohan, D; Pittman, Jr., C. U.; Steele P. H. Pyrolysis of Wood/Biomass for Bio-oil: A Critical Review. *Energy Fuels* **2006,** *20* (3), 848-889.

6.   Butler, E.; Devlin, G.; Meier, D.; McDonnell, K. A. A review of recent laboratory research and commercial developments in fast pyrolysis and upgrading. *Renew. Sustainable Energy Rev.* **2011**, *15* (8), 4171-4186.

7.   Mortensen, P.M.; Grunwaldt, J. D.; Jensen, P. A.; Knudsen, K. G.; Jensen, A. D. A review of catalytic upgrading of bio-oil to engine fuels. *Appl. Catal*. *A-Gen*. **2011**, *407* (1-2), 1-19.

8.   Zacher, A.H.; Olarte, M. V.; Santosa, D. M.; Elliott, D. C.; Jones, S. B. A review and perspective of recent bio-oil hydrotreating research. *Green Chem*. **2014**, *16* (2), 491-515.

9.   Garcia-Perez, M.; Shen, J.; Wang, X. S.; Li, C. Z. Production and fuel properties of fast pyrolysis oil/bio-diesel blends. *Fuel Process. Technol.* **2010**, *91* (3), 296-305.

10. Kim, T.Y., Lee, S.; Kang K.,Performance and emission characteristics of a high-compression-ratio diesel engine fueled with wood pyrolysis oil-butanol blended fuels. *Energy* **2015**, *93* (2), 2241-2250.

11. Zhang, M.; Wu, H. Phase Behavior and Fuel Properties of Bio-Oil/Glycerol/Methanol Blends. *Energy Fuels* **2014**, *28* (7), 4650-4656.

12. Krutof, A.; Hawboldt, K. Blends of pyrolysis oil, petroleum, and other bio-based fuels: A review. *Renew. Sustainable Energy Rev.* **2016**, *59*, 406-419.

13. Chong, K.J.; Bridgwater, A.V. Fast Pyrolysis Oil Fuel Blend for Marine Vessels. *Environ. Prog. Sustain. Energy*, 2016.

14. Alcala, A.; Bridgwater, A.V. Upgrading fast pyrolysis liquids: Blends of biodiesel and pyrolysis oil. *Fuel* **2013**, *109* (0), 417-426.

15. Mullen, C.A.; Strahan G.D.; Boateng A.A. Characterization of Various Fast-Pyrolysis Bio-Oils by NMR Spectroscopy. *Energy Fuels* **2009**, *23* (5), 2707-2718.

16. Hao, N.; Ben, H.; Yoo, C. G.; Adhikari, S.; Ragauskas, A. J. Review of NMR Characterization of Pyrolysis Oils. *Energy Fuels* **2016**, *30* (9), 6863-6880.

17. Dumez, J. N. Spatial encoding and spatial selection methods in high-resolution NMR spectroscopy. *Prog. Nucl. Magn. Reson. Spectrosc.* **2018**, *109*, 101-134.

18. Lambert, J.; Hergenroder, R.; Suter, D.; Deckert, V. Probing liquid-liquid interfaces with spatially resolved NMR spectroscopy. *Angew. Chem. Int. Ed.* **2009**, *48* (34), 6343-63435.

B.Tang, PhD Thesis, Aston University, 2024.

19. Mantel, C.; Bayle, P-A.; Hediger, S.; Berthon, C.; Bardet, M. Study of liquid–liquid interfaces by an easily implemented localized NMR sequence. *Magn*. *Reson*. *Chem*. **2010**, *48* (8), 600-606.

20. Pantoja, C. F.; J. A. Bolanos, J. A.; Bernal A.; Wist, J. Mutual Diffusion Driven NMR: a new approach for the analysis of mixtures by spatially resolved NMR spectroscopy. *Magn*. *Reson*. *Chem*. **2017**, *55*, 519-524.

21. Allen, J.; Damodaran, K. High-resolution slice selection NMR for the measurement of CO_2 diffusion under non-equilibrium conditions. *Magn*. *Reson*. *Chem*. **2015**, *53* (3), 200-202.

22. Garcia-Aparicio, C.; Quijada-Garrido, I.; Garrido, L. Diffusion of small molecules in a chitosan/water gel determined by proton localized NMR spectroscopy. *J. Colloid Interface Sci*. **2012**, *368* (1), 14-20.

23. Mitrev, Y.; Simova, S.; Jeannerat, D. NMR analysis of weak molecular interactions using slice-selective experiments via study of concentration gradients in agar gels. *Chem*. *Commun*. **2016**, *52*, 5418-5420.

24. Wisniewska, M. A.; Seland, J. G. Investigating structure-dependent diffusion in hydrogels using spatially resolved NMR spectroscopy. *J. Colloid Interface Sci*. **2019**, *533*, 671-677.

25. Evans, R; Sandhu, A.; Bridgwater, T.; Chong, K. Slice-Selective NMR: A Noninvasive Method for the Analysis of Separated Pyrolysis Fuel Samples. *Energy Fuels*, **2017**, *31*, 4135-4142.

26. Hjartnes, T. N.; Sorland, G. H., Simon, S.; Sjoblom, J. Demulsification of Crude Oil Emulsions Tracked by Pulsed Field Gradient (PFG) Nuclear Magnetic Resonance (NMR). Part I: Chemical Demulsification. *Ind*. *Eng*. *Chem*. *Res*. **2019**, *58*, 2310-2323.

B.Tang, PhD Thesis, Aston University, 2024.

27.   Seeger, K. Simple and Rapid (Extraction) Protocol for NMR Metabolomics—Direct Measurement of Hydrophilic and Hydrophobic Metabolites Using Slice Selection. *Anal. Chem.* **2021**, *93*, 1451-1457.

28.   Poppler, A. C.; Frischkorn, S.; Stalke, D.; John, M. Toluene and lithium amide diffusion into polystyrene: a slice-selective NMR-spectroscopic study. *ChemPhysChem* **2013**, *14* (13), 3103-3107.

29.   Niklas, T., Stalke D.; John, M. Single-shot titrations and reaction monitoring by slice-selective NMR spectroscopy. *Chem. Commun.* **2015**, *51* (7), 1275-1277.

30.   Krachkovskiy, S. A.; Pauric, A. D.; Halalay, I. C.; Goward, G. R. Slice-Selective NMR Diffusion Measurements: A Robust and Reliable Tool for In Situ Characterization of Ion-Transport Properties in Lithium-Ion Battery Electrolytes. *J. Phys. Chem. Lett.* **2013**, *4* (22), 3940-3944.

31.   Lin, C.-Y. Effects of Biodiesel Blend on Marine Fuel Characteristics for Marine Vessels. *Energies* **2013**, *6*(9), 4945-4955.

32.   Emsley, L.; Bodenhausen, G. Gaussian pulse cascades: New analytical functions for rectangular selective inversion and in-phase excitation in NMR. *Chem. Phys. Lett.* **1990**, *165* (6), 469-476.

33.   Doddrell, D. M.; Pegg, D.T.; Bendall, M. R. Distortionless enhancement of NMR signals by polarization transfer. *J. Magn. Reson.* **1982**, *48* (2), 323-327.

34.   Nielsen, J. B.; Jensen, A.; Schandel, C. B.; Felby, C.; Jensen, A. D. Solvent consumption in non-catalytic alcohol solvolysis of biorefinery lignin. *Sustain. Energy Fuels*, **2017**, *1*, 2006-2015.

35.   Lysak, D. H.; Bermel, W.; Moxley-Paquette, V.; Michal, C.; Ghosh-Biswas, R.; Soong, R.; Nashman, B.; Lacerda, A.; Simpson, A. J. Cutting without a Knife:

A Slice-Selective 2D 1H–13C HSQC NMR Sequence for the Analysis of Inhomogeneous Samples, *Anal. Chem.* **2023**, *95* (38), 14392–14401.

36.   Evans, R.; Deng, Z.; Rogerson, A. K.; McLachlan, A. S.; Richards, J. J.; Nilsson, M.; Morris, G. A. Quantitative interpretation of diffusion-ordered NMR spectra: can we rationalize small molecule diffusion coefficients? *Angew. Chem. Int. Ed.* **2013**, *52* (11), 3199-3202.

37.   Li, W.; Kagan, G.; Hopson, R.; Williard, P. G. Measurement of Solution Viscosity via Diffusion-Ordered NMR Spectroscopy (DOSY). *J. Chem. Edu.* **2011**, *88* (9), 1331-1335.

38.   Halliday, N.A.; Peet, A.C.; Britton, M.M.; Detection of pH in Microemulsions, without a Probe Molecule, Using Magnetic Resonance. *J. Phys. Chem. B*, **2010**, *114* (43), 13745-13751.

39.   Esturau, N.; Espinosa, J.F. Optimization of Diffusion-Filtered NMR Experiments for Selective Suppression of Residual Nondeuterated Solvent and Water Signals from ^{1}H NMR Spectra of Organic Compounds. *J. Org. Chem.* **2006**, *71* (11), 4103-4110.

40.   Aguilar, J. A.; Nilsson, M.; Bodenhausen, G.; Morris, G. A. Spin echo NMR spectra without J modulation. *Chem. Commun.* **2012**, *48* (6), 811-3.

B.Tang, PhD Thesis, Aston University, 2024.

GRAPHICAL ABSTRACT

B.Tang, PhD Thesis, Aston University, 2024.